Universität Hamburg
DER FORSCHUNG | DER LEHRE | DER BILDUNG

CLUSTER OF EXCELLENCE
QUANTUM UNIVERSE

Charting Cosmological History and New Particle Physics with Primordial Gravitational Waves

Dissertation
zur Erlangung des Doktorgrades
an der Fakultät für Mathematik, Informatik und Naturwissenschaften
Fachbereich Physik
der Universität Hamburg

vorgelegt von
Peera Simakachorn

Hamburg
2022

Gutachter/innen der Dissertation:	Prof. Dr. Géraldine Servant Dr. Thomas Konstandin
Zusammensetzung der Prüfungskommission:	Prof. Dr. Géraldine Servant Dr. Thomas Konstandin Prof. Dr. Günter H. W. Sigl Prof. Dr. Jochen Liske Dr. Bibhushan Shakya
Vorsitzende/r der Prüfungskommission:	Prof. Dr. Günter H. W. Sigl
Datum der Disputation:	28.10.2022
Vorsitzender Fach-Promotionsausschuss PHYSIK:	Prof. Dr. Wolfgang J. Parak
Leiter des Fachbereichs PHYSIK:	Prof. Dr. Günter H. W. Sigl
Dekan der Fakultät MIN:	Prof. Dr.-Ing. Norbert Ritter

Abstract

Our Universe – within its first second – evolved in a very high-energy stage, spanning at most 19 decades in energy scales from the time of primordial inflation to the epoch of Big Bang Nucleosynthesis (BBN) and typically involving new physics beyond the Standard Model (SM). Due to the weakness of gravitational interactions, gravitational waves (GW) from primordial sources convey information about the Universe that remains unaltered from their production time until today. They enable access to the early Universe and to particle physics at energy scales that are unreachable by other means of experiments. The particle physics of the SM and beyond can source GWs and determine the course of cosmic history; both imprint smoking-gun GW signatures.

The first part of this thesis starts by charting the landscape of primordial GW, assuming the standard ΛCDM Universe. Primary sources originate from the SMs of particle physics and cosmology (primordial inflation and thermal plasma) and beyond the SMs (preheating, first-order phase transitions, and cosmic strings). Almost half of the landscape is compatible within the sensitivities of the current and future-planned GW observatories. We discuss the dependence of GW signals on the parameters controlling the sources and derive, for each source, the relation between the GW frequency and the cosmic temperature when the GW is produced. Focusing on cosmic strings, we analyze their network evolution and calculate the GW spectrum in detail. The semi-analytic model allows the generalizations of string evolution in various non-trivial setups, e.g., metastable strings, global strings, and strings that evolve in arbitrary cosmology. We also show that cosmic strings can explain the exciting hint of stochastic GW background observed by the pulsar timing arrays.

Particle physics beyond the SM can change the course of the early evolution of the Universe with respect to the standard radiation-dominated Universe by temporarily inducing different cosmological eras. We list five possible schemes, ranging from matter, secondary inflation, and kination eras and occurring either right after the primordial inflation or inside the radiation era after reheating. The resulting non-standard expansion histories leave signatures in primordial stochastic GW backgrounds. The spectral suppressions are caused by matter and secondary inflationary eras, while the kination era enhances the GW signal. With the present and future generations of GW observatories, it is possible to map the Universe's expansion history and chart the new particle-physics parameter spaces.

In the second part, we consider the particle-physics realizations of the intermediate matter and kination eras. The former case can be induced by heavy and unstable particles, such as moduli, heavy scalars produced via gravitational and Higgs portals, and heavy dark photons. The next-generation GW experiments can remarkably extend the usual BBN constraint on the lifetime of new particles down to 10^{-16} sec by detecting the step-like feature in GW from cosmic strings. The intermediate kination era is realized by the rotating axion, which we analyze in great detail. We find for the first time a unique GW-peak signature of axion physics in the early Universe that applies in particular to the kinetic misalignment mechanism for axion dark matter. The peak position depends on the axion speed and decay constant. LISA, BBO, ET, and CE are sensitive to such kination era at MeV-EeV scales. Finally, we connect the kination peak to dark matter and baryogenesis from the rotating axions.

Zusammenfassung

Innerhalb der ersten Sekunde seiner Existenz befand sich unser Universum in einem hochenergetischen Zustand, dessen Energieskala von der Zeit primordialer Fluktuationen bis zur "Big-Bang" Nukleosynthese (BBN) bis zu 19 Dekaden überspannte und in dem typischerweise neue Physik, jenseits des Standardmodells (SM), involviert war. Aufgrund der Schwäche gravitativer Wechselwirkungen übermitteln Gravitationswellen (GW) primordialen Ursprungs Informationen über das Universum, die vom Zeitpunkt ihrer Produktion bis heute unverändert blieben. Sie ermöglichen Zugang zum frühen Universum und zu Teilchenphysik bei Energieskalen, welche mit anderen experimentellen Methoden unerreichbar sind. Die Teilchenphysik des Standardmodells, und jenseits davon, kann Gravitationswellen hervorbringen, die kosmologische Geschichte bestimmen, und damit "Smoking-Gun" Gravitationswellensignaturen erzeugen.

Der erste Teil dieser Arbeit beginnt damit, den Parameterraum primordialer GWs unter der Annahme des Standard-ΛCDM Universums zu kartieren. Primäre Quellen können aus dem Standardmodell der Teilchenphysik und Kosmologie stammen (primordiale Fluktuationen und thermisches Plasma), aber auch aus Physik jenseits des Standardmodells ("Preheating", Phasenübergänge erster Ordnung und kosmische "Strings"). Fast die Hälfte des Parameterraum ist mit den Empfindlichkeiten heutiger sowie geplanter GW-Observatorien kompatibel. Wir diskutieren die Abhängigkeit der GW-Signale von den Parametern, welche die Quellen kontrollieren, und leiten daraus für jede Quelle eine Relation zwischen GW-Frequenz und der kosmischen Temperatur, zur Zeit als die GW produziert wurde, ab. Wir konzentrieren uns auf kosmische Strings, analysieren die Evolution ihres Netzwerkes und berechnen das Gravitationswellenspektrum im Detail. Das semi-analytische Modell erlaubt die Generalisierung der String-Evolution in verschiedenen, nicht-trivialen Konfigurationen, z.B. für meta-stabile Strings, globale Strings, und Strings, die sich in beliebigen Kosmologien entwickeln. Wir zeigen außerdem, dass kosmische Strings den aufregenden Hinweis auf einen stochastischen GW-Hintergrund, der von den 'Pulsar Timing Arrays' beobachtet wurde, erklären können.

Teilchenphysik jenseits des Standardmodells kann die Entwicklung des jungen Universum dahingehend verändern, dass im typischerweise strahlungsdominierten Universum zeitweise andere kosmologische Epochen induziert werden. Wir listen fünf mögliche Schemen auf, welche von Materie-, über zweite Inflations-, zu "Kination"-Epochen reichen, und welche entweder direkt nach primordialer Inflation oder während der strahlungsdominierten Epoche nach dem Prozess der Wiederaufheizung ("Reheating") auftreten. Die resultierenden, nicht-standardmässigen Expansionsgeschichten hinterlassen Signaturen in stochastischen GW-Hintergründen. Eine Unterdrückung des Spektrums wird von Materie- und zweite Inflations-Epochen verursacht, wahrend eine "Kination"-Epoche das GW-Signal verstärkt. Mit den gegenwärtigen und zukünftigen Generationen von GW-Observatorien ist es möglich, die Expansionsgeschichte des Universums zu kartieren und die Parameterräume neuer Teilchenphysik zu erfassen.

Im zweiten Teil untersuchen wir die teilchenphysikalischen Realisierungen der zwischenzeitlichen Materie- und der "Kination"-Epochen. Der erste Fall kann durch die Produktion schwerer und instabiler Teilchen induziert werden, wie zum Beispiel Moduli, schwere skalare Teilchen, produziert durch gravitative Portale und Higgsportale, und schwere dunkle Photonen. Die GW-Experimente der nächsten Generation können die üblichen BBN-Limits an die Lebensdauer neuer Teilchen auf $10^{-16}\,\mathrm{sec}$ senken, indem ein stufenförmiges Merkmal in GWs von kosmischen Strings detektiert wird. Eine zwischenzeitliche "Kination"-Epoche wird durch ein rotierendes Axion realisiert, welches wir im Detail analysieren. Wir finden, zum ersten Mal, die einzigartige Signatur eines GW-Maximums durch Axionphysik im frühen Universum, die insbesondere auf den kinetischen "Misalignment"-Mechanismus für axionische dunkle Materie anwendbar ist. Die Position des Maximums hängt von der Geschwindigkeit des Axions und der Zerfallskonstante ab. LISA, BBO, ET und CE sind empfindlich für eine solche Kination-Epoche bei MeV-EeV Skalen. Abschließend schlagen wir eine Brücke vom GW-Maximum durch "Kination" zu dunkler Materie und Baryogenese durch rotierende Axionen.

Acknowledgements

First and foremost, I could not undertake this incredible journey without my supervisor, Prof. Dr. Géraldine Servant, who always encourages me to expand my knowledge and connection in particle-cosmology and beyond, e.g., the LISA cosmology working group. Moreover, she always motivates me to investigate many research topics, concluding four intensive studies. I am also very grateful that she accepted me as her advisee since my master's study and allowed me to pursue further in this exciting research direction.

I would like to express my gratitude to Dr. Thomas Konstandin, who accepted to be my co-supervisor and the reviewer of this manuscript. I am also extremely grateful to Dr. Bibhushan Shakya, my mentor and one of the committee members, for being patient with my slow progress on our project. Special thanks to Prof. Dr. Günter Sigl and Prof. Dr. Jochen Liske for accepting to be part of the examiners.

It had been a wonderful experience working with Yann Gouttenoire, who constantly stimulates valuable discussions/understandings and diligently solves many complex problems throughout our projects. It was him who introduced me, in my first class in Hamburg, to the particle-cosmology group at DESY. I appreciate every one of the office 1a-O1.135 for the past four years (alphabetically ordered): Baptiste Filoche, Felix Giese, Matthias "Koschi" Koschnitzke (who also helped translate the abstract), Henda Mansour, Henrique Rubira, and Stefan Sandner, for a stimulating, productive, and cheering atmosphere. Thanks to all people of the DESY *cosmorridor* (past and present) for always being opened to discussions (physics and many other things) which help in my professional and personal developments: Jorinde van de Vis, Yohei Ema, Ryusuke Jinno, Pablo Quilez, Hyungjin Kim, Philip Soerensen, Jacob Leedom, Cem Eröncel, Aleksandr Chatrchyan, and Alessandro Lenoci.

Many thanks to the excellence cluster *Quantum Universe* for funding my Ph.D. study and allowing me to attend workshops and conferences (virtual and in-person). I am grateful to Pedro Schwaller, Enrico Morgante, Wolfram Ratzinger, and Christiane Scherb (the second German translator) for a nice time in Mainz. Special thanks to the Cargése summer school 2022 for the hospitality while this manuscript was finalized. Moreover, this endeavor would not have been possible without helps from Delia and Popla.

Last but not least, I would like to extend my immense gratitude to my family (whom I have not seen for almost three years due to the pandemic) for the endless love, encouragement, and opportunity which allowed me to appreciate our puzzling but magnificent Universe a little further.

(To my grandfather, who now lives among the stars and within my memory.)

Eidesstattliche Versicherung / Declaration on oath

Hiermit versichere ich an Eides statt, die vorliegende Dissertationsschrift selbst verfasst und keine anderen als die angegebenen Hilfsmittel und Quellen benutzt zu haben.

Hamburg, den 21.11.2022

Peera Simakachorn

Unterschrift des Doktoranden

Contents

Publications

This thesis is based on the following publications:

[1] Y. Gouttenoire, G. Servant and P. Simakachorn, *Beyond the Standard Models with Cosmic Strings*, *JCAP* **07** (2020) 032, [1912.02569].

[2] Y. Gouttenoire, G. Servant and P. Simakachorn, *BSM with Cosmic Strings: Heavy, up to EeV mass, Unstable Particles*, *JCAP* **07** (2020) 016, [1912.03245].

[3] Y. Gouttenoire, G. Servant and P. Simakachorn, *Revealing the Primordial Irreducible Inflationary Gravitational-Wave Background with a Spinning Peccei-Quinn Axion*, [2108.10328].

[4] Y. Gouttenoire, G. Servant and P. Simakachorn, *Kination cosmology from scalar fields and gravitational-wave signatures*, [2111.01150].

Author's contributions

In all the works above, the author developed the analytical and numerical calculations of gravitational-wave (GW) spectra from primordial inflation and local/global cosmic strings in arbitrary cosmological history. The predictions for detectability at the current and future-planned GW observatories relied on the integrated power-law sensitivity curves; 9 of them (presented in this thesis: LISA, ET, CE, BBO, DECIGO, LIGO, GAIA, THEIA, AEDGE) are calculated from the detectors' noise sensitivities by the author.

In Ref. [1], the author was involved significantly in computing the cosmic-string network's evolution using the full semi-analytic method. He also participated substantially in the original texts and the theoretical discussions and produced all 34 figures.

The author provided, in Ref. [2], the numerical results of GW spectra from local cosmic strings that lead to the constraints on particle-physics parameter spaces made by Yann Gouttenoire. Moreover, the author also participated in active discussions and produced Fig. 1 and 3.

In Ref. [3, 4], the author engaged extensively in realizing the intermediate kination era from axion models. He also derived the analytical and numerical predictions of GW signatures and their detectability for all primordial sources, except the feature in the infrared GW tail from first-order phase transitions made by Yann Gouttenoire. The author contributed to most of the original texts in Ref.[4], except Sec. 10 and App. A, D, F, which were written by Yann Gouttenoire. In both Ref. [3, 4], 56 of 66 figures are produced by the author.

Other Publications

The author also contributed partially in section 9: *"Tests of non-standard pre-Big-Bang nucleosynthesis cosmology via the SGWB"* of the following publication:

[5] LISA Cosmology Working Group collaboration, P. Auclair et. al., *Cosmology with the Laser Interferometer Space Antenna*, [2204.05434].

This thesis also contains some parts of the ongoing works:

- *Probing particle couplings to cosmic strings via a signature in SGWB,*
  in collaboration with Bibhushan Shakya,
- *Limits on the duration of kination era from axion fluctuations,*
  in collaboration with Cem Eröncel, Ryosuke Sato, and Géraldine Servant,
- *Generalization kination and particle physics realizations,*
  in collaboration with Oleksii Matsedonskyi and Géraldine Servant.

Exclusive contents in this thesis

The following lists show the major content updates not presented in the above publications.

Chapter 2. — We provide the landscape of primordial GW backgrounds and the estimations for GW from all prime sources, including the new back-of-the-envelope calculation for cosmic-string GW. We also discuss the hint from the pulsar timing arrays and provide the corresponding analysis for local cosmic strings.

Chapter 3. — We derive the GW frequency of the formation cut-off Eq. (3.5) and the detectability of metastability strings in Fig. 3.7 and 3.8. We revise the global-string discussion, including axionic strings.

Chapter 4. — We list 5 non-standard cosmological schemes and the bounds on their durations in Sec. 4.1. The simple derivations for GW signatures and the spectral indices are provided in Sec. 4.2. We also revise the discussion regarding the constraint from scalar fluctuation in Sec. 4.4.4.

Chapter 6. — We revise the discussion on axion physics and the no-go argument for the intermediate kination era from a real scalar field. The GW probe of the axion parameter space $(m_a - f_a)$ for the model dependent is newly added in Fig. 6.5.

Appendices. — In App. A.1, we discuss different notions of SNR, main results shown in Fig. A.1. The field-theoretical cosmic-string section is added in App. B.1 with two new figures about string field profiles. We discuss the UV and IR tails of the SGWB from each population of cosmic-string loops and their impacts on the ability to trace the cosmological history in App. B.3.6. App. C derives the bound on an intermediate inflationary era.

Abbreviations

BAU	Baryon Asymmetry of the Universe
CC	Cosmological Constant
CMB	Cosmic Microwave Background
CS	Cosmic String
DM	Dark Matter
EOM	Equation of Motion
EOS	Equation of State
FOPT	First Order Phase Transition
GW	Gravitational Wave
pNGB	Pseudo-Nambu-Goldstone Boson
SNR	Signal-to-Noise Ratio
SGWB	Stochastic Gravitational-Wave Background
SM	Standard Model
SNR	Signal-to-Noise Ratio

Notations and Conventions

This work uses *natural* units: $\hbar = c = k_b = 1$ where $\hbar$ is the reduced Planck constant, c the speed of light, and k_b the Boltzmann constant. Therefore, every physical quantity is in the unit of energy:

$$[\texttt{energy}] = [\texttt{mass}] = [\texttt{length}]^{-1} = [\texttt{time}]^{-1} = [\texttt{temperature}].$$

Typically, energy is measured in the unit of electronvolt (eV). We use the following conversion rules between the SI units and the *natural* units:

$$\text{GeV} \simeq 1.78 \cdot 10^{-27}\ \text{kg} \simeq 5.06 \cdot 10^{15}\ \text{m}^{-1} \simeq 1.52 \cdot 10^{24}\ \text{s}^{-1} \simeq 1.16 \cdot 10^{13}\ \text{K}.$$

The Planck mass and the reduced Planck mass are:

$$m_{\text{Pl}} \equiv \frac{1}{\sqrt{G}} \simeq 1.221 \cdot 10^{19}\ \text{GeV}, \quad M_{\text{Pl}} \equiv \frac{1}{\sqrt{8\pi G}} \simeq 2.435 \cdot 10^{18}\ \text{GeV},$$

respectively.

"The effort to understand the Universe is one of the very few things that lifts human life a little above the level of farce, and gives it some of the grace of tragedy."

— Steven Weinberg, *The First Three Minutes*

Chapter 1

Introduction

A decade ago, the Higgs-boson discovery at the Large Hadron Collider [6, 7] concluded the search for Standard Model (SM) particles and confirmed our understanding of their behavior at the TeV scale. Nonetheless, the entire picture is incomplete; some theoretical puzzles – such as the hierarchy problem, the neutrino masses, the flavor puzzle, and the strong-CP problem – cannot be addressed by the SM and require new particle physics beyond the Standard Model (BSM). Most of the solutions introduce a new mass scale that would lie beyond the current collider capability (if they are not already relying on the electroweak scale).

Embedded into our Universe's history, the SM cannot account for many observational facts. The flat and homogeneous Universe suggests an inflationary period emerging from the BSM sector and happening long before the presence of hot and dense plasma of the SM particles. Later, the Universe follows the Standard Model of cosmology or the Λ-Cold-Dark-Matter (ΛCDM) model, cf. Sec. 1.1, which needs at least the presence of Dark Matter (DM), cosmological constant (CC), and the matter-antimatter asymmetry. In the era of precision cosmology, many experiments utilize electromagnetic (EM) probes, e.g., the cosmic microwave background (CMB), large-scale structures, and other astrophysical observations. They strongly constrain our Universe to be dominated by the SM thermal plasma at the Big-Bang Nucleosynthesis (BBN) scale around the energy of MeV. Except for the limit on the inflationary scale at 10^{16} GeV, no EM probe of cosmology reaches beyond this threshold.

The first direct detection at LIGO [8, 9] marked the dawn of the gravitational wave (GW) physics era. Many future experiments with higher sensitivity will be soon running and observing GW in various frequency bands. Due to the weakness of gravity, GW allows us to directly explore the first second of our Universe that spans at most 19 decades in energy scales and possibly the new physics addressing the problems of the SM. The BSM physics could either prominently source GW or non-trivially alter the course of cosmic history, imprinting smoking-gun GW signatures. By searching for these features, the current and future planned observatories can exclude or discover various new particle physics; this is the main idea of this thesis.

The following section briefly reviews the Standard Models of cosmology and particle physics. The outline of this thesis is presented in Sec. 1.2.

1.1 Standard Models of Cosmology and Particle Physics

The cosmological principle – i.e., the homogeneity and isotropy of the Universe – is consistent with observations [10–12] and is described by the Friedmann-(Lemaître-)Robertson-Walker (FRW) metric [13–16],

$$ds^2 = -dt^2 + \sum_{i=1}^{3} a^2(t) dx^i dx_i, \tag{1.1}$$

where t is the cosmic time, x_i is the spatial coordinate, and $a(t)$ is the scale factor describing the Universe's expansion. We neglect the small curvature term [17] throughout this thesis. The evolution of the Universe described by $a(t)$ depends on its energy contents and follows from the Einstein equation [18], $G_{\mu\nu} = 8\pi G T_{\mu\nu} - \Lambda g_{\mu\nu}$, where $G_{\mu\nu}$ is the Einstein tensor related to the curvature of spactime, G is the Newton's constant, $T_{\mu\nu}$ is the energy-momentum tensor of the Universe's components, and Λ is the cosmological constant.

At large scales, the energy content is assumed to be a perfect fluid whose $T_{\mu\nu}$ is described by its pressure and energy density, or the equation of state (EOS): $\omega \equiv p/\rho$. The pressureless matter ($p = 0$) has $\omega = 0$; the radiation ($p = \rho/3$) has $\omega = 1/3$; the cosmological constant (CC) ($\rho \gg p$) has $\omega = -1$. Let us emphasize the particular case of the so-called *kination* where $\omega = 1$ is the maximum value allowed by cauasality, i.e., the speed of perturbation ($c_s^2 \equiv \partial p/\partial\rho \leq 1$) is smaller than the light's speed; see Chap. 4. Solving the Einstein equation with the perfect-fluid contents, one yields the Friedmann equations,

$$H^2 \equiv \left(\frac{\dot{a}}{a}\right)^2 = \frac{\sum_i \rho_i}{3M_{\rm Pl}^2}, \quad \frac{\ddot{a}}{a} = -\frac{\sum_i(\rho_i + p_i/3)}{6M_{\rm Pl}^2}, \tag{1.2}$$

where H is the Hubble rate describing the expansion, we sum all energy densities and pressures contributions. Combining the two equations or considering the energy conservation, the continuity equation for such a fluid reads

$$\dot{\rho} + 3H(1+\omega)\rho = 0 \quad \Rightarrow \quad \rho \propto a^{-3(1+\omega)}, \tag{1.3}$$

which describes how the energy density of the Universe gets diluted along the cosmological history. Moreover, if such a fluid dominates over the total energy density of the Universe, the first Friedmann equation yields the solution to the scale factor, $a \propto t^{2/3(1+\omega)}$. The matter energy density ($\omega_m = 0$) scales as $\rho_m \propto a^{-3}$, and the matter-dominated era has $a \propto t^{2/3}$. The radiation ($\omega_r = 1/3$) has $\rho_r \propto a^{-4}$, and $a \propto t^{1/2}$ during the radiation-dominated era. For the extreme limit of $\omega = -1$, the energy density does not dilute, and the CC-dominated Universe leads to an exponential expansion: $a \propto e^{Ht}$. The special case of kination ($\omega_{\rm kin} = 0$) has the energy density red-shifts the fastest $\rho_{\rm kin} \propto a^{-6}$ and the Universe expands at the slowest rate $a \propto t^{1/3}$.

In the standard cosmological history (ΛCDM + inflation), the Universe starts with an exponential expansion, the so-called *inflation*. Though inflation is not required by the Standard Model (SM) of particle physics, it solves the horizon and flatness problems of the ΛCDM cosmology [19]. The observations constrain the inflationary scale to be at most $E_{\rm inf}^{\rm max} \simeq 1.4 \cdot 10^{16}$ GeV [20, 21]. After the inflation, the Universe converts its energy budget into the hot thermal plasma of particles in the SM. (Note that the reheating period could lead to the non-standard cosmological history, namely the matter or kination eras, cf. Chap. 4.) The Universe is then in the radiation-dominated era. Due to interactions, the thermal equilibrium is reached and has the energy and entropy densities,

$$\rho_r = \frac{\pi^2}{30} g_*(T) T^4, \quad s = \frac{2\pi^2}{45} g_{*s}(T) T^3, \tag{1.4}$$

where $g_*(T), g_{*,s}(T)$ is the effective number of relativistic particle species contributing to the energy and entropy densities of the thermal plasma. For bosons, $g_* = \sum_i g_i$, while $g_* = \frac{7}{8}\sum_i g_i$ for fermions. When all of the SM particles are in equilibrium, we obtain $g_* = g_{*s} = 106.75$.

After the electroweak (EW) phase transition, many SM particles receive a mass from the non-zero vacuum expectation value of the Higgs field. They become non-relativistic and annihilate once the Universe cools sufficiently. Note that the temperature of the Universe (or thermal bath) drops with the expansion rate: $T \propto a^{-1} g_{*s}^{-1/3}$, determined by the entropy conservation $a^3 s =$ constant. The effective number of relativistic particles decreases over time, as shown in Fig. 1.1. We take the evolutions of g_* and $g_{*,s}$ from the fitted formulae in Ref. [22]. The sharp drop at QCD scale ($T_{\rm QCD} \sim 150$ MeV) is due to the condensation of quarks into baryons. The last fall is due to

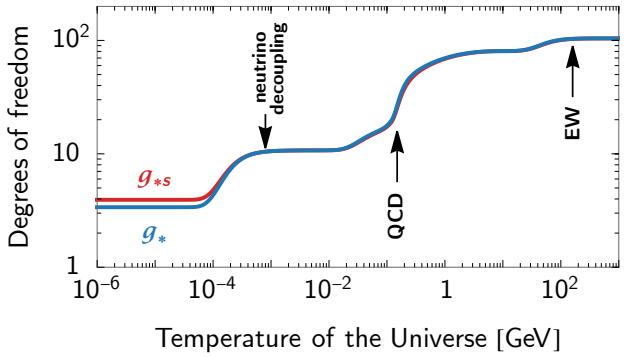

Figure 1.1: Evolution of the effective numbers of relativistic SM-particle species, contributing to the energy and entropy densities. Obtained from the fitted formulae in Ref. [22].

the neutrino decoupling and the electron-positron annihilation. The final values – $g_*(T_0) = 3.36$, $g_{*,s}(T_0) = 3.94$ – are of the photons and neutrinoes; their difference is due to the electron-positron annihilation happening after the neutrino decoupling and leading the heating of photons.

At around temperature $T_{\rm eq} \simeq 0.75$ eV, the radiation bath becomes subdominant to the matter-type energy density: baryon and cold dark matter. The Universe enters the matter domination regime. The primordial perturbations imprinted since the time of inflation can grow and lead to structure formations. The matter era ends with the CC (Λ) domination only when $T \simeq 0.33$ meV. The Universe today expands exponentially with rate of $H_0 = 67.4\,{\rm km\,s^{-1}\,Mpc^{-1}}$ [23].

Let us comment on two of the milestones of cosmological evolution. First, the *cosmic microwave background* (CMB) radiation is generated when photons decouple from the rest of the particles and carry the direction information about the Universe around $T \sim 0.1$ eV. By fitting to observations, the energy contents of the Universe in the standard ΛCDM cosmology is

$$\rho_{{\rm ST},0}(a) = \rho_{r,0}\, G[T(a), T_0] \left(\frac{a_0}{a}\right)^4 + \rho_{m,0} \left(\frac{a_0}{a}\right)^3 + \rho_{\Lambda,0}, \tag{1.5}$$

where r, m, and Λ denote radiation, matter, and the CC, respectively. The energy density is written in terms of the relic density Ω_i as $\rho_{i,0} = \Omega_{i,0}\,(3M_{\rm Pl}^2 H_0^2)$, where the term in bracket defines the critical energy density today. Each of the components is measured to be $\Omega_{r,0} \simeq 5.4 \times 10^{-5}$, $\Omega_{m,0} \simeq 0.31$, $\Omega_\Lambda \simeq 0.69$ [23]. The presence of the function

$$G(T, T_0) \equiv \left[\frac{g_*(T)}{g_*(T_0)}\right] \left[\frac{g_{*s}(T_0)}{g_{*s}(T)}\right]^{4/3}, \tag{1.6}$$

comes from the conservation of the comoving entropy.

Another milestone – the *Big-Bang Nucleosynthesis* (BBN) – sits earlier back in time at temperature $T_{\rm BBN} \sim$ MeV or around the time ~ 1 sec, when nuclei of the light elements (H, D, He, Li) form for the first time. The theoretical predictions based on the standard cosmological history are consistent with the observations of the abundances of light elements [24], suggesting that the Universe must be in the radiation-dominated era at least at BBN.

1.2 Outline of this thesis

At most, 19 decades in energy scale lie above BBN up to the inflation scale. The standard cosmological paradigm suggests the radiation-domination era along the way; however, other scenarios are not unlikely. For example, some energy densities beyond the Standard Model (BSM) might dominate the total energy density of the Universe, leading to a non-standard cosmological history that ends well before BBN. This thesis focuses on charting this pre-BBN cosmology – *the primordial dark age*[1] or the first second of our Universe – through gravitational waves (GW) from

[1] This is not the late-time *cosmic dark age* that happened between the recombination and the reionization and can be probed by EM waves such as Lyman-α forest, cf. review [25].

primordial sources. Due to the weakness of the gravitational interaction, GW conveys information about the Universe from its production time to our GW observatories today, allowing access to the early Universe and particle physics at energy scales unreachable by other means of experiments.

In the first part of this thesis, Chap. 2 starts discussing GW from primordial sources in the form of stochastic GW background (SGWB). We chart the landscape of primordial SGWB, populated by prominent sources from and beyond the SM. Almost half of it is compatible with the sensitivities of the current and future-planned GW experiments. We comment on the exciting SGWB hint from pulsar timing arrays. Chap. 3 focuses on the cosmic-string network where we calculate the corresponding GW in detail, assuming the standard cosmology and employing the semi-analytic model. We also study the metastability effect and the global strings. Chap. 4 turns to the effect of BSM physics that changes the course of cosmological history. We list possible schemes – ranging from matter, secondary inflation, and kination eras – and study their imprints/features in the primordial SGWBs. With the present and future generations of GW observatories, it is possible to map almost the full Universe's expansion history.

In the second part, we consider the particle-physics realizations of some attractive schemes in Chap. 4. The intermediate matter era – induced by heavy and unstable particles – is investigated in Chap. 5. Chaps. 6 and 7 scrutiznize the intermediate kination era from the *rotating axion*, which leads to the exciting GW signatures. We devote the discussion in Chap. 6 to the model-independent phenomenology of rotating axion (e.g., dark matter and baryogenesis) and its detectability of the kination-induced GW signature. In Chap. 7, we list all the required ingredients in the rotating-axion model for the successful intermediate kination era and construct the cosmological history in terms of model parameters step-by-step. We conclude in Chap. 8 and defer all additional details to appendices.

PART I

Beyond the Standard Models with Primordial Gravitational Waves

Chapter 2

Primordial Gravitational Waves

The first direct detection of gravitational waves (GW) – predicted by Einstein as a consequence of *general relativity* [26, 27] – by LIGO collaboration in 2015 [8, 9] has initiated a new era of exploration of our Universe into uncharted territory. Subsequently, many observations have been made from astrophysical sources with great precision, along with their electromagnetic (EM) counterparts, e.g., binaries systems of black holes and neutron stars, cf. the living review [28]. On the other hand, GW can also be originated during the primordial Universe, across ~ 26 decades in energy scales from the end of primordial inflation to the first light of our Universe, e.g., [29–32].

The EM observations observe up to the scale of recombination, $T_{\rm rec} \sim 0.1$ eV, or at best the Big Bang Nucleosynthesis (BBN) scale, $T_{\rm BBN} \sim$ MeV, while the particle colliders probe up to the TeV scales [12, 33]. The so-called *primordial* GW are produced by very high-energy physics that any other experiment cannot test. Because the gravitational interaction is extremely weak; GW decouples from other particles in the thermal plasma as soon as they are produced:

$$\frac{\Gamma_{\rm grav}}{H} \sim \frac{n\sigma v}{T^2/M_{\rm Pl}} \simeq \frac{G^2T^5}{T^2/M_{\rm Pl}} \simeq \left(\frac{T}{M_{\rm Pl}}\right)^3 \ll 1 \text{ for the sub-Planckian Universe,} \tag{2.1}$$

where $n \sim T^3$ is the number density of particles in thermal equilibrium, $\sigma \sim G^2T^2$ is the cross-section of the gravitational interaction[1], and $v \simeq 1$. Any primordial GW travels freely, up to the cosmic expansion, and carries direct information about its generation mechanism from the production time to our GW observatories today.

In this chapter, Sec 2.1 first reviews the primordial GW in the form of a stochastic GW background (SGWB) observed today. In Sec. 2.2, two parts of information can be learned from the SGWB spectrum – the sources' strength and length/time scale – allowing us to chart the landscape of the primordial GWs, as shown in Fig. 2.1. We discuss the prime sources from the SM (of particle physics and cosmology) in Sec. 2.3 and the beyond SM in Sec. 2.4. Sec. 2.5 review the prospects of detection, expanding over 21 decades in frequency Finally, Sec. 2.6 comments on the exciting hint of SGWB, observed by pulsar timing arrays and probably explained by cosmic strings.

2.1 Stochastic Gravitational-Wave Background

Consider the cosmological perturbation theory on the isotropic-homogeneous expanding Universe, described by the Friedmann-Robertson-Walker (FRW) metric,

$$ds^2 = -dt^2 + a^2(t)(\delta_{ij} + h_{ij})dx^i dx^j, \tag{2.2}$$

where the presence of scalar and vector modes are neglected, and a slight spatial tensor perturbation $|h_{ij}| \ll 1$ represents gravitational waves (GW), satisfying the *transverse-traceless* (TT)

[1] In standard textbook [34], the neutrino decoupling is estimated by replacing $G \to G_F$ (Fermi's constant) for the weak interaction: $\Gamma/H \sim (T/\text{MeV})^3$.

conditions $h^i{}_i = \partial^i h_{ij} = 0$ and leaving h_{ij} with two propagating degrees-of-freedom, i.e., the GW polarizations. The equation-of-motion (EOM) of the GW follows from the linearized Einstein equation,

$$\ddot{h}_{ij}(\mathbf{x},t) + 3H\dot{h}_{ij}(\mathbf{x},t) - \frac{\nabla^2}{a^2}h_{ij}(\mathbf{x},t) = 16\pi G\Pi_{ij}^{\rm TT}(\mathbf{x},t), \tag{2.3}$$

where $\dot{(\cdot)} \equiv d(\cdot)/dt$, $\nabla^2 \equiv \partial_i\partial_i$. GW is sourced by $\Pi_{ij}^{\rm TT}(\mathbf{x},t)$ the transverse-traceless part of the anisotropic stress tensor, defined by $a^2\Pi_{ij} = T_{ij} - pa^2(\delta_{ij}+h_{ij})$ where T_{ij} is the spatial component of the source's energy-momentum tensor, and p is the homogeneous background pressure.

Let us write the above equation in terms of Fourier components for convenience. The tensor perturbation in the TT gauge becomes

$$h_{ij}(\mathbf{x},t) = \sum_{\lambda=+,\times}\int \frac{d^3k}{(2\pi)^3}e^{i\mathbf{k}\cdot\mathbf{x}}h^\lambda(\mathbf{k},t)\epsilon_{ij}^\lambda(\hat{\mathbf{k}}), \tag{2.4}$$

where λ represents the two polarizations, and the polariztion tensor $\epsilon_{ij}^\lambda(\hat{\mathbf{k}})$ is symmetric ($\epsilon_{ij}^\lambda = \epsilon_{ji}^\lambda$) and TT ($k^i\epsilon_{ij}^\lambda = 0 = \epsilon_{ii}^\lambda$) conditions. Moreover, the polarization tensor also has the orthonormal and completeness relations

$$\sum_{i,j}\epsilon_{ij}^\lambda(\hat{\mathbf{k}})\epsilon_{ij}^{\lambda'}(\hat{\mathbf{k}}) = 2\delta_{\lambda\lambda'}, \quad \sum_{\lambda=+,\times}\epsilon_{ij}^\lambda(\hat{\mathbf{k}})\epsilon_{lm}^\lambda(\hat{\mathbf{k}}) = P_{il}P_{jm} + P_{im}P_{jl} - P_{ij}P_{lm}, \tag{2.5}$$

where $P_{ij}(\hat{\mathbf{k}}) \equiv \delta_{ij} - \hat{k}_i\hat{k}_j$ is the projector on the direction orthogonal to $\mathbf{k}$ ($P_{ij}k_i = 0,\ P_{ij}P_{jl} = P_{il}$). Similarly, the source term can be written as

$$\Pi_{ij}^{\rm TT}(\mathbf{x},t) = \mathcal{O}_{ijlm}(\hat{\mathbf{k}})\int \frac{d^3k}{(2\pi)^3}e^{i\mathbf{k}\cdot\mathbf{x}}\Pi_{lm}(\mathbf{k},t), \tag{2.6}$$

with $\mathcal{O}_{ijlm}(\hat{\mathbf{k}}) \equiv P_{il}(\hat{\mathbf{k}})P_{jm}(\hat{\mathbf{k}}) - \frac{1}{2}P_{ij}(\hat{\mathbf{k}})P_{lm}(\hat{\mathbf{k}})$ is the TT projection and $\mathcal{O}_{ijlm}(\hat{\mathbf{k}})\Pi_{lm}(\mathbf{k},t) = \Pi_{ij}^{\rm TT}(\mathbf{k},t)$, leading to conditions $k_i\Pi_{ij}^{\rm TT} = 0 = \Pi_{ii}^{\rm TT}$. The Fourier decomposition of the GW EOM reads

$$\ddot{h}_{ij}(\mathbf{k},t) + 3H\dot{h}_{ij}(\mathbf{k},t) + \frac{k^2}{a^2}h_{ij}(\mathbf{k},t) = 16\pi G\Pi_{ij}^{\rm TT}(\mathbf{k},t), \tag{2.7}$$

A freely propagating GW ($\Pi_{ij}^{\rm TT} = 0$) evolves differently in two limits, depending on its co-moving wavenumber k,

$$h_\lambda(\mathbf{k},\tau) = \begin{cases} \frac{A_\lambda(\mathbf{k})}{a(\tau)}e^{ik\tau} + \frac{B_\lambda(\mathbf{k})}{a(\tau)}e^{-ik\tau}, & \text{for } k \gg aH \text{ (sub-horizon)}, \\ A_\lambda(\mathbf{k}) + B_\lambda(\mathbf{k})\int^\tau \frac{d\tau'}{a^2(\tau')}, & \text{for } k \ll aH \text{ (super-horizon)}, \end{cases} \tag{2.8}$$

where $d\tau \equiv dt/a$ is the conformal time, A_λ and B_λ are arbitrary constants set when the source term $\Pi_{ij}^{\rm TT}$ becomes inactive. The sub-horizon GW exhibits an oscillatory behavior with its size being red-shifted by the cosmic expansion. The super-horizon mode stays frozen due to the first term, and it later re-enters the horizon and starts oscillating. By observing GW today, we obtain two parts of information: the *dynamics* related to the production mechanism $\Pi_{ij}^{\rm TT}$ and the *kinematics* related to the expansion history of the Universe.

GW from the early Universe and relic density. — A GW production process during the early Universe operates only within a causal patch (i.e. $\lambda_{\rm GW} \leq H_{\rm prod}^{-1}$), much smaller than the horizon size today,

$$\frac{\lambda_{\rm GW,0}}{H_0^{-1}} \leq \frac{H_{\rm prod}^{-1}}{H_0^{-1}}\left[\frac{a_0}{a_p}\right] \simeq \Omega_{r,0}^{-1/2}\left[\frac{T_0}{T_p}\right] \simeq 2\cdot 10^{-13}\left[\frac{100\ \text{GeV}}{T_p}\right], \tag{2.9}$$

where we use $a \sim T^{-1}$. Therefore, the primordial GW sources from many uncorrelated patches would randomize the amplitude of $h_{ij}(\mathbf{x}, t)$ observed today and contribute to the so-called *stochastic GW background* (SGWB). Since there is only one Universe, an observable is not well characterized by an ensemble average in the context of statistics; instead, we trade it with the spatial/temporal average via the *ergodic* theorem [31]. For an isotropic, homogeneous, unpolarized, stationary, and gaussian background, the correlation function reads,

$$\left\langle h_\lambda(\mathbf{k},\tau)\, h_{\lambda'}(\mathbf{k}',\tau')\right\rangle = \frac{8\pi^5}{k^3} h_c^2(k,\tau)\delta^{(3)}(\mathbf{k}-\mathbf{k}')\delta(\tau-\tau')\delta_{\lambda\lambda'}, \tag{2.10}$$

$$\text{and} \quad \left\langle h_{ij}(\mathbf{x},\tau)\, h_{ij}(\mathbf{x},\tau)\right\rangle = 2\int d(\log k)\, h_c^2(k,\tau) \tag{2.11}$$

where h_c is the dimensionless characteristic strain of GW, and all statistical information is captured due to gaussianity. The delta functions and the Dirac delta in Eq. (2.10) suggest other four properties: 1) $\delta^{(3)}(\mathbf{k}-\mathbf{k}')$ for isotropy and homogeneity, 2) $\delta(\tau-\tau')$ for stationary, and 3) $\delta_{\lambda\lambda'}$ for unpolarization. Note that these properties are typical for primordial GW; however, there could be deviations for a particular source that would serve as smoking-gun signatures from other stochastic sources, e.g., [35–38].

The energy density of GW is the 00^{th} component of the energy-momentum tensor,

$$\rho_{\rm GW} = \frac{\left\langle \dot{h}_{ij}(\mathbf{x},t)\dot{h}_{ij}(\mathbf{x},t)\right\rangle}{32\pi G} = \frac{\left\langle h'_{ij}(\mathbf{x},\tau)h'_{ij}(\mathbf{x},\tau)\right\rangle}{32\pi G a^2}. \tag{2.12}$$

For the sub-horizon GW ($k \gg aH$), we deduce from Eq. (2.8) that ${h_c'}^2(k,\tau) \simeq k^2 h_c^2$, leading to

$$\rho_{\rm GW} = \int d(\log k)\frac{k^2 h_c^2(k,\tau)}{16\pi G a^2(\tau)} \equiv \int d(\log k)\frac{d\rho_{\rm GW}}{d\log k}, \tag{2.13}$$

where the last step defines the energy density spectrum of GW. Due to $h_c^2 \propto a^{-2}$ for sub-horizon mode, we emphasize the most critical aspect of GW, i.e., *the GW energy density of some mode k red-shifts as radiation a^{-4}*. The relic density of SGWB observed by GW experiments with some frequency today – corresponding to some comoving wavenumber ($k/a_0 = 2\pi f$) – reads

$$\Omega_{\rm GW,0}(f) = \frac{k^2 h_c^2(k,\tau_0)}{16\pi G a_0^2} = \frac{\rho_{\rm GW}^{\rm prod}(f)}{\rho_{\rm tot,0}}\left(\frac{a_{\rm prod}}{a_0}\right)^4, \tag{2.14}$$

where we used again that $\rho_{\rm GW} \propto a^{-4}$. Despite its simplicity, this equation leads to many interesting consequences. For instance, we can redshift the SGWB from the production time to estimate the SGWB today from each primordial source. Moreover, this simple equation allows us to derive signatures from non-standard cosmological effects in Chap. 4.

In this thesis, all predicted stochastic GW frequency spectra will be expressed in terms of $\Omega_{\rm GW}h^2$, which differs from the usual characterization of the GW signal in terms of the strain h_c. For comparison, we show in Fig. A.2, how the typical stochastic spectra computed in this thesis would look like In h_c units.

2.2 Landscape of Primordial SGWBs

Many early-Universe processes generate SGWB of various signal shapes and frequency ranges. In this section, we scrutinize the plane (frequency $f_{\rm GW}$, amplitude $\Omega_{\rm GW}$) where the energy-density spectra of primordial SGWBs would reside today, regardless of the nature of their sources. The critical aspect is that the GW propagates freely and carries direct information about its origin, from the production time to the GW observatories today. Ultimately, the amplitude and frequency relate to the production mechanism's strength and time scale, respectively. The generic theoretical

constraints on the primordial sources are discussed in Secs. 2.2.1 and 2.2.2, limiting the SGWB landscape down to Fig. 2.1. The prime sources of primordial SGWB[2] discussed in Secs. 2.3 and 2.4 populate the region widely, while the experimental prospects probe almost half of it.

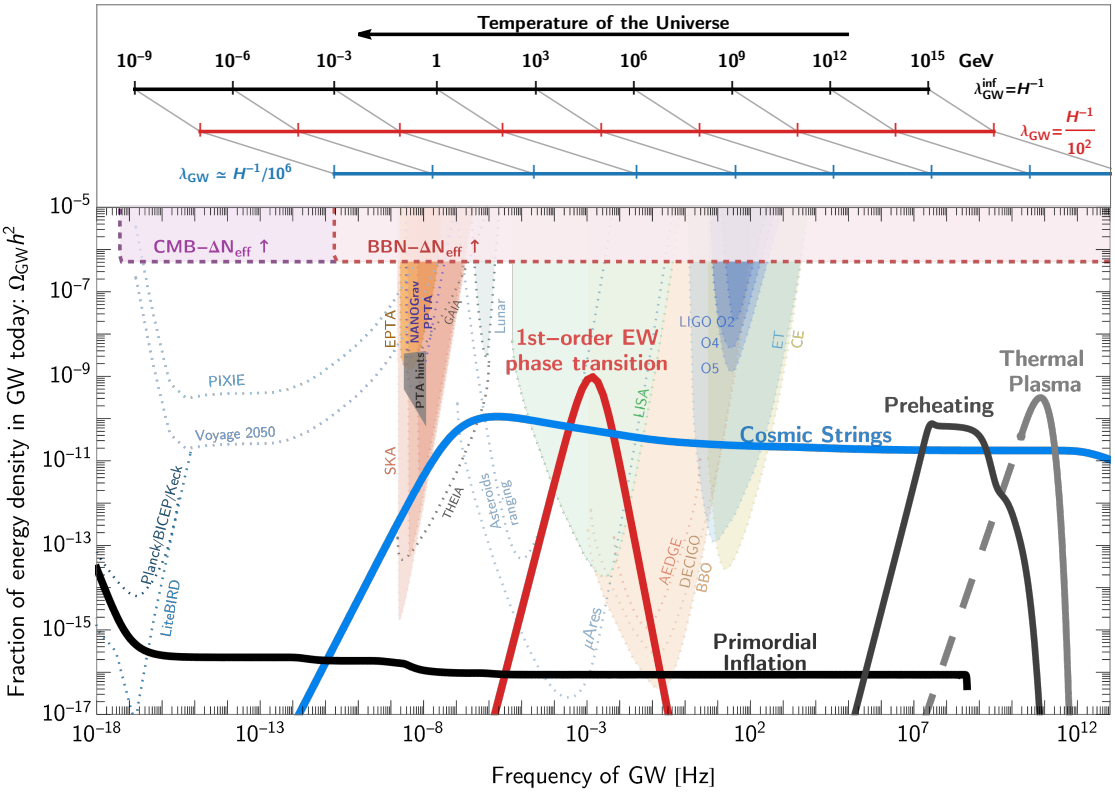

Figure 2.1: The landscape of primordial SGWBs and the sensitivities of the future-planned GW observatories, cf. Sec. 2.5. Assuming the standard ΛCDM cosmology, we show the SGWB spectra from the Standard Models (primordial inflation and thermal plasma) in Sec. 2.3 and beyond SM (preheating, first-order phase transition, cosmic strings) in Sec. 2.4. See footnote for the chosen parameters. The GW frequency today corresponds to its production time, shown in the above-colored lines for different sizes $\lambda_{\rm GW}$ of sources (colors match that of spectra). The maximum amplitude is bounded by the $\Delta N_{\rm eff}$ constraints at BBN/CMB scales, cf. Sec. 2.2.2.

From signals to their origins. — Due to the cosmic expansion, GW energy density today is redshifted from the production time as radiation,

$$\Omega_{\rm GW,0} = \left(\frac{\rho_{\rm GW,prod}}{\rho_{\rm tot,0}}\right)\left(\frac{a_{\rm prod}}{a_0}\right)^4 \simeq \Omega_{r,0}\left(\frac{\rho_{\rm GW}}{\rho_{\rm tot}}\right)_{\rm prod}, \tag{2.15}$$

where the last step assumes the standard ΛCDM cosmology, and $\Omega_{r,0} = 5.38 \cdot 10^{-5}$ [39] is the abundance of radiation today. The last bracket suggests that the observed signal depends on the strength of the GW generation process. The strongest source $\rho_{\rm GW} \to \rho_{\rm tot}$ leads to the extreme bound $\Omega_{\rm GW,0} \lesssim 10^{-5}$ on primordial SGWB assuming the standard cosmology. Nonetheless, the CMB/BBN observations put a more stringent constraint $\Omega_{\rm GW,0} \lesssim 10^{-7}$; see Sec. 2.2.2.

The GW frequency today relates to the source's characteristic length scale $\lambda_{\rm GW}$, through the red-shift factor,

$$f_{\rm GW} = \lambda_{\rm GW}^{-1}\left(\frac{a_{\rm prod}}{a_0}\right) \simeq 10^{-6}\ {\rm Hz}\left(\frac{H_{\rm prod}^{-1}}{\lambda_{\rm GW}}\right)\left(\frac{T_{\rm prod}}{100\ {\rm GeV}}\right), \tag{2.16}$$

[2]In Fig. 2.1: primordial inflation ($E_{\rm inf} = 10^{16}$ GeV), thermal plasma ($T_{\rm reh} = 10^{16}$ GeV), preheating ($T_{\rm reh} = 10^{16}$ GeV, $\{g_i\} = \{10^{-2}, 10^{-3}\}$), phase transition ($T_* = 150$ GeV, $\beta/H_* = 100$, $\alpha = 2$), and local cosmic strings ($G\mu = 10^{-12}$).

where we use $T \propto a^{-1}$. We can also write this relation in terms of the production time,

$$t_{\rm prod} \simeq \text{ sec } \left(\frac{H_{\rm prod}^{-1}}{\lambda_{\rm GW}}\right)^2 \left(\frac{10^{-11}\text{ Hz}}{f_{\rm GW}}\right)^2, \tag{2.17}$$

where we use $t_{\rm prod} \simeq (\text{MeV}/T_{\rm prod})^2 \times$ sec. For higher frequencies, the SGWB is a probe of the hotter and earlier stages of the Universe, well beyond the reach of traditional particle physics experiments.

The frequency-temperature relations for several sources' sizes are shown on the top panel of Fig. 2.1. Due to causality, the horizon size at production $H_{\rm prod}^{-1}$ is the largest possible length scale of the source: $\lambda_{\rm GW} \to H_{\rm prod}^{-1}$. Furthermore, we can understand that the long-lasting GW sources (e.g., primordial inflation and cosmic strings) generate SGWBs that span a broad range of frequencies; many contributions at different frequencies add up. The signals from the short-lasting sources are localized at particular frequencies associated with their production times (e.g., first-order phase transition) or length scales (e.g., preheating and thermal GW).

2.2.1 Naive frequency limits on the landscape

The naive theoretical constraints on the highest and lowest frequencies of the SGWB can be derived from Eq. (2.16). The lowest frequency of GW is that of those GW produced today; their source has the largest possible size, i.e., the Hubble horizon today,

$$f_{\rm GW,lowest} = H_0 \simeq 10^{-18}\text{ Hz}. \tag{2.18}$$

Despite this late-time GW production, we still call this a primordial GW from many primordial sources that could still exist today. The highest frequency of primordial GW arises from the highest energy scale[3] $H_{\rm prod} \simeq M_{\rm Pl}$, and the GW source of the smallest size, the Planck length $\lambda_{\rm GW}^{-1} \sim M_{\rm Pl}$. The highest possible frequency of primordial GW is

$$f_{\rm GW,highest} \simeq 10^{13}\text{ Hz}. \tag{2.19}$$

Such highest frequencies could still be reached in principle by experiments like axion helioscopes, probing GW at 10^{14} Hz; see Ref. [40] for a review. Smaller-size sources could populate the ultra-high frequency region at late times, e.g., primordial black-hole inspirals [41].

At the high-frequency end, the smallest source of the Planck length $\lambda_{\rm GW}^{-1} \sim M_{\rm Pl}$ produced GW at the end of inflation $H_{\rm inf}^{\rm max} \simeq 6 \cdot 10^{13}$ GeV [20, 21] at the frequency

$$f_{\rm GW,highest} \simeq 10^{13}\text{ Hz}. \tag{2.20}$$

Such ultra-high frequencies could still be reached in principle by experiments like axion helioscopes, probing GW at 10^{14} Hz; see Ref. [40] for a review. The Planck-size sources at late times might populate the signals beyond the above naive limit, e.g., primordial black-hole inspirals [41], which is beyond the scope of this thesis.

2.2.2 Largest Possible Amplitude: $\Delta N_{\rm eff}$ bound

The amount of GW – even as a sub-component of the total energy density – can impact the Universe's expansion rate. More precisely, any relativistic energy density beyond the ΛCDM components can act as an effective number of neutrino relics,

$$N_{\rm eff} = \frac{8}{7}\left(\frac{\rho_{\rm tot} - \rho_\gamma}{\rho_\gamma}\right)\left(\frac{11}{4}\right)^{4/3}, \tag{2.21}$$

[3] The bound becomes smaller for $H_{\rm prod} \lesssim H_{\rm planck} \simeq 6 \cdot 10^{13}$ GeV.

which is strongly constrained by CMB measurements [17] to $N_{\rm eff} = 2.99^{+0.34}_{-0.33}$ and by BBN predictions [42, 43] to $N_{\rm eff} = 2.90^{+0.22}_{-0.22}$ whereas the SM predicts $N_{\rm eff} \simeq 3.045$ [44–46]. Using $\Omega_\gamma \simeq 5.38 \times 10^{-5}$ [39], we obtain the following bound on the primordial GW spectrum, produced before CMB/BBN,

$$\int_{f_{\rm BBN,CMB}}^{f_{\rm max}} \frac{df}{f} \Omega_{\rm GW}(f) \leq 5.6 \times 10^{-6} \Delta N_\nu, \tag{2.22}$$

where $f_{\rm BBN,CMB}$ are the frequencies corresponding to the BBN/CMB scales, $f_{\rm max}$ is the highest frequency of the GW spectrum (which might not be the same as the Planck-scale limit frequency in Eq. (2.20)), and we set $\Delta N_\nu \leq 0.2$. Note that CMB stage-4 experiments is expected to improve the bound or discovery region to $N_{\rm eff} < 0.03$ [47].

In Fig. 2.1, we show the $\Delta N_{\rm eff}$ bound on a primordial SGWB – spanning only an order of magnitude in $\log(f)$ and located at frequencies higher than BBN/CMB scales – such that the bound reads $\Omega_{\rm GW} \leq 5.6 \times 10^{-6} \Delta N_\nu$. Nonetheless, there are *two* important points when applying this bound to a more realistic SGWB. *First*, the GW spectral shape matters. Let us consider two of the most generic shapes: a flat spectra $\Omega_{\rm GW} = \Omega_{\rm GW,*}$ for $f_{\rm min} < f < f_{\rm max}$, and a peak $\Omega_{\rm GW}(f) = \Omega_{\rm GW,*}(f/f_{\rm peak})^\beta$ assuming[4] the spectrum cut-off exponentially beyond $f_{\rm peak}$. Eq. (2.22) reads

$$\Omega_{\rm GW,*} \leq 5.6 \times 10^{-6} \Delta N_\nu \cdot \begin{cases} \log^{-1}\left[\frac{f_{\rm max}}{\max(f_{\rm ref}, f_{\rm min})}\right] & \text{for flat spectrum,} \\ \beta \left[1 - \left(\frac{f_{\rm ref}}{f_{\rm peak}}\right)^\beta\right]^{-1} & \text{for peak,} \end{cases} \tag{2.23}$$

where $f_{\rm ref}$ is the GW frequency corresponding to CMB/BBN scales, and the constraint for the peaked spectrum is dominated by $f_{\rm peak}$. Because of these multiplicative factors, the $\Delta N_{\rm eff}$ bound on the realistic SGWB can be slightly stronger or weaker than the naive bound shown in Fig. 2.1.

Second, the integral cut-off matters. For example, the BBN frequency of inflationary SGWB is sensitive to the horizon size of temperature $T_{\rm BBN} \sim$ MeV, much larger than those of local cosmic strings, which is boosted by a factor 10^6 for string tension $G\mu = 10^{-12}$, as we shall see later. Precisely, the BBN-scale frequencies for SGWB from primordial inflation and local cosmic strings of tension $G\mu$ read

$$f^{\rm inf}_{\rm BBN} \simeq 1.8 \times 10^{-11}\ {\rm Hz}, \quad f^{\rm cs}_{\rm BBN} \simeq 8.9 \times 10^{-5}\ {\rm Hz} \left(\frac{10^{-11}}{G\mu}\right)^{1/2}. \tag{2.24}$$

We emphasize that the $\Delta N_{\rm eff}$ bound applies to GW, already existing by the time of $N_{\rm eff}$ measurements. For example, the astrophysical GW with a strong signal is not bounded because GW is produced late. On the challenging ultra-high-frequency range [40], the current probes far weaker than the BBN bound could potentially constrain the primordial black-hole binaries, cf. Ref. [41] and references therein.

After charting the landscape of primordial SGWB, the following section reviews prime sources[5] from SM (of particle physics and cosmology) and beyond SM physics, illustrated in Fig. 2.1. We assume that the Universe is in the radiation-dominated era right after the primordial inflation, the *standard* cosmological history. The presence of non-standard eras imprints interesting signatures on SGWB, discussed in Chap. 4.

2.3 From Standard Models of Particle Physics and Cosmology

In the standard (ΛCDM) cosmological model, there is an early period of primordial inflation followed by a radiation-dominated Universe due to the thermal plasma of SM particles (the matter

[4] One would expect also that $\beta \leq 3$ due to causality. However, some sources of SGWB lead to a sharp peak, e.g., the scalar-induced SGWB; see Ref. [48]

[5] See, for examples, Refs. [49, 50] for excellent derivations of SGWB from arbitrary sources.

domination and cosmological constant eras arise at very late times). These two necessary ingredients in the SM of particle physics and cosmology generate a SGWB, shown in Fig. 2.1. We shall see that these two signals are probes of the Universe at the highest scales: the inflationary scale and the reheating scale.

2.3.1 Primordial Inflation

The quantum fluctuations of some comoving scale k during inflation classicalize upon horizon exit ($k > aH$) and stay frozen afterward. After the end of the inflation phase, the increasing comoving horizon catches up with these modes; they re-enter ($k < aH$). Tensor perturbations are particularly interesting as they correspond to SGWB [51–54], whose observation would be a signature of inflationary models [20, 21, 55]. The irreducible SGWB today from inflationary tensor perturbations[6] of comoving wave number $k = a_k H_k$, denoted by its fraction of the total energy density, reads [31]

$$\Omega_{\rm GW}^{\rm inf}(k) = \frac{k^2 a_k^2}{24 H_0^2} \Omega_T^{\rm inf}, \tag{2.25}$$

which re-entered the cosmic horizon when the scale factor of the universe was a_k and the Hubble rate was H_k. H_0 is the Hubble rate today. The first factor reflects the evolution of the perturbation after the horizon re-entry and is known as *transfer function*. It could be altered by further damping effects, e.g., the change in the number of relativistic degrees-of-freedom [22] and the free-streaming particles [64].

The metric tensor perturbation $\Omega_T^{\rm inf}$ set during the inflationary stage are well-known to lead to a nearly scale-invariant power spectrum at the horizon re-entry,

$$\Omega_T^{\rm inf} \simeq \frac{2}{\pi^2} \left(\frac{H_{\rm inf}}{M_{\rm pl}}\right)^2 \left(\frac{k}{k_p}\right)^{n_t}, \tag{2.26}$$

where $H_{\rm inf}$ the Hubble rate during inflation, and k_p is the pivot scale used for CMB observation $k_p/a_0 \simeq 0.002\ {\rm Mpc}^{-1}$ [20] (equivalent to the GW frequency $f_p = 3.1 \times 10^{-18}$ Hz). In slow-roll inflation, the spectral index n_t is expected to be only slightly red-tilted $n_t \simeq -2\epsilon \simeq -r/8 \gtrsim -0.0045$, since the non-observation of primordial B-modes by BICEP/Keck Collaboration constrains the tensor-to-scalar ratio to be $r \lesssim 0.036$ [21]. The presence of this red-tilt suppresses the GW energy density by $\mathcal{O}(10\%)$ correction in the ranges of Pulsar-Timing-Arrays (PTA) and Earth-based interferometers. The rest of this thesis neglects this suppression and assumes $n_t = 0$ for simplicity. Combining Eqs. (2.25) and (2.26), tensor modes entering during the radiation era have the standard flat spectrum,

$$\Omega_{\rm GW}^{\rm inf} \simeq 2.9 \cdot 10^{-17} G(T_k) \left(\frac{E_{\rm inf}}{10^{16}\ {\rm GeV}}\right)^4, \tag{2.27}$$

where $E_{\rm inf}$ is the inflationary energy scale, $G(T_k) = (g_*(T_k)/106.75)(g_{*,s}(T_k)/106.75)^{-4/3}$ and T_k is the temperature when a given mode enters the Hubble horizon. Fig. 2.1 shows the maximal possible signature allowed by the largest inflationary scale constrained by CMB data [20, 21]. This GW background is beyond the sensitivity of future GW observatories: LISA [65] and Einstein Telescope [66, 67]; only Big Bang Observer [68] could be sensitive.

Frequency-temperature relation. — The inflationary GW of mode $k = aH$ at re-entry has the horizon-size wavelength H^{-1} corresponding to the frequency today,

$$f_{\rm GW}^{\rm inf} = f_{\rm GW}^{H} = \frac{H}{2\pi}\frac{a}{a_0} \simeq 2.7 \cdot 10^{-6}\ {\rm Hz} \left[\frac{g_*(T)}{106.75}\right]^{1/2} \left[\frac{g_{*,s}(T)}{106.75}\right]^{-1/3} \left[\frac{T}{10^2\ {\rm GeV}}\right]. \tag{2.28}$$

[6] The scalar (density) perturbation can also source SGWB at second-order of the perturbation theory; its SGWB is subdominant to the leading scale-invariant tensor fluctuation, unless the density perturbation is enhanced [56–63]. See Ref. [48] for a review.

Since many modes re-enter during cosmological history, the primordial inflation acts as a long-lasting source of GW. The high-frequency cut-off of the spectrum corresponds to the inflationary scale [69] $k_{\rm inf} = a_{\rm inf} H_{\rm inf}$ where $a_{\rm inf}$ is the scale factor at the end of inflation, and reads $f_{\rm inf}^{\rm max} \simeq 4 \cdot 10^8 {\rm Hz}\ (E_{\rm inf}/10^{16}\ {\rm GeV})$, as shown in Fig. 2.1.

Furthermore, the shape of SGWB is sensitive to cosmological history. For example, when the total energy of the Universe is $\rho \propto a^{-3(1+\omega)}$ with ω being the EOS of the universe, we have $f \propto a_k^{-(1+3\omega)/2}$; Eq. (2.25) gives

$$\Omega_{\rm GW} \propto f^\beta, \ \text{ with } \ \beta \equiv -2\left(\frac{1-3\omega}{1+3\omega}\right), \tag{2.29}$$

where the non-trivial scaling comes from a_k^2 in Eq. (2.25), i.e., the transfer function of GW after re-entry [70]. Modes entering the horizon during radiation ($\omega = 1/3$), matter ($\omega = 0$) and kination ($\omega = 1$) eras contribute to spectral indices $\beta = 0, -2$, and 1, respectively[7]. The signatures of non-standard cosmological evolution – beyond the radiation-dominated Universe – will be the main topic of Chap. 4.

2.3.2 Thermal Plasma

In the standard model of cosmology, primordial inflation is followed by a radiation era involving the radiation bath of the SM particles, which interact and reach a thermal equilibrium of some temperature T. These interactions are responsible for accelerations among particles that source GW [72–76]. The SGWB spectra today from the thermal SM are shown in Fig. 2.2, calculated from the full and complex formula in Ref. [73], for a given reheating temperature $T_{\rm reh}$.

$$h^2\Omega^{\rm th}_{\rm GW,full}(f) \simeq 10^{-8}\left[\frac{T_{\rm reh}}{10^{16}\ {\rm GeV}}\right]\left[\frac{f}{50\ {\rm GHz}}\right]^3 \times, \tag{2.30}$$
$$\times \begin{cases} 1, & \text{for } 2\pi f \lesssim \alpha_1^2 T_0, \\ \frac{f}{1600 T_0} n_B\left[f\left(\frac{a(T_0)}{a(T_{\rm reh})}\right)\right] \sum_{i=1}^3 d_i \bar{m}_{Di}^2 \left(\ln\frac{5}{\bar{m}_{Di}} + \ldots\right), & \text{for } 2\pi f > T_0, \end{cases}$$

where $n_B(p)$ is the Bose-Einstein distribution, $d_1 = 1$, $d_2 = 3$, $d_3 = 8$, $\alpha \equiv g^2/4\pi$, and the normalized Debye masses are defined by $\bar{m}_1 = g_1\sqrt{11/6}$, $\bar{m}_2 = g_2\sqrt{11/6}$, $\bar{m}_3 = g_3\sqrt{2}$. The index i runs for the SM gauge group ${\rm U}(1)$, ${\rm SU}(2)$ and ${\rm SU}(3)$.

To understand the physics, let us consider two regimes of GW: the small wavelength ($p \gg T$ where p is the physical momentum of GW) and the large wavelength ($p < T$) regimes, discussed below. We will show that the order-of-magnitude estimation of the peak amplitude and spectrum agrees well with the numerical results shown in Fig. 2.2.

Small-wavelength regime. — Particles in the thermal plasma of number density $n \sim T^3$ interact and produce GW with a Planck-suppressed rate $\Gamma_{\rm int} \sim \alpha n e^{-p/T}/M_{\rm Pl}^2$, where $\alpha \equiv g^2/4\pi$ and g is the coupling constant between particles. The thermal plasma produces only a small amount of GW with $p \gg T$ because the particles' distribution functions suppress its interaction rate $e^{-p/T}$. Per one Hubble time, the number of GW emissions with rate $\Gamma_{\rm int}$ determines the fraction of energy density in GW $\rho^{\rm th}_{\rm GW}$ extracted from the thermal plasma of $\rho_{\rm rad}$

$$\frac{\rho^{\rm th}_{\rm GW}}{\rho_{\rm rad}}(T) \sim \frac{\Gamma_{\rm int}}{H} \sim \left[\frac{\alpha}{M_{\rm Pl}^2}\right] T^3 e^{-p/T} \times \frac{M_{\rm Pl}}{T^2} = \frac{\alpha T}{M_{\rm Pl}} e^{-p/T}. \tag{2.31}$$

Translating this into the SGWB observed today, we deduce the GW spectrum from the thermal plasma of temperature T

$$\Omega^{\rm th}_{\rm GW}(f) \sim \Omega_{r,0}\frac{\alpha T}{M_{\rm Pl}} e^{-p/T} \simeq 4 \cdot 10^{-9}\left[\frac{\alpha}{10^{-2}}\right]\left[\frac{T}{10^{16}\ {\rm GeV}}\right] e^{-p(f)/T}, \tag{2.32}$$

[7] For a more realistic power spectrum, i.e., by solving the full GW EOM, the non-standard cosmology alters the behavior of the GW transfer function.The effect on the amplitude is of order $\mathcal{O}(1)$ [71], while the transition between eras could feature a spectral oscillation from the change of Bessel function's orders.

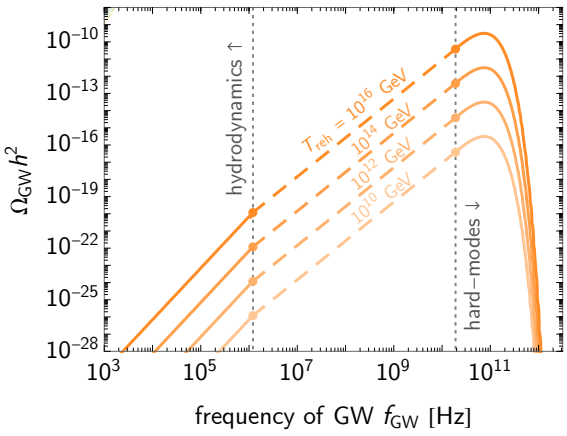

Figure 2.2: **SGWB from the SM thermal plasma** assuming the reheating at $T_{\rm reh}$. It does not follow the usual temperature-frequency relation since GW is produced with a wavelength of order T^{-1} rather than H^{-1}. The hydrodynamical fluctuations contribute to the low-frequency GW, while the high-frequency regime is dominated by microscopic particle scatterings. At very large frequencies, the spectrum is exponentially cut off as the distribution of thermalized particles is suppressed by $e^{-p/T}$.

where $p(f)$ is the momentum associated to frequency f today. The GW spectrum indeed cut-offs exponentially for $p \gg T$, as shown in Fig. 2.2. However, it becomes significant when $p \to T$. Our simple estimation matches the result from the more precise method, i.e., from *hard thermal loops* calculations [73, 74]. We also see that the maximum contribution comes from the hottest plasma; the maximum is at the reheating $T_{\rm reh}$.

At first sight, it seems complicated to determine the frequency range of the GW spectrum observed today; the result is a sum of GW produced at different temperatures, which peak around the frequency $f_* \simeq \lambda_{\rm GW}^{-1} \simeq p/2\pi \sim T/2\pi$ at production. By red-shifting it until today, Eq. (2.16), all contributions point to the peak frequency

$$f_{\rm GW}^{\rm th}(T) \simeq f_* \frac{a_*}{a_0} \simeq T_0/2\pi \simeq 5 \cdot 10^{10}\ {\rm Hz}. \tag{2.33}$$

Although the thermal plasma is a long-lasting source, its SGWB is localized at a particular frequency, which is beyond the reach of planned interferometers as it resides in the region of ultra-high frequencies targeted by other types of experiments [40].

Large-wavelength regime. — The plasma of particles also fluctuates collectively on a large wavelength $p \ll T$ – so-called *hydrodynamics* fluctuation [77] – and sources GW production via the transverse-traceless part of the stress tensor of the plasma, $\langle TT \rangle_{\rm TT} \simeq \eta T$, which is proportional to the *shear viscosity* $\eta \sim T^3/g^4$ [78, 79], growing as the coupling constant g gets weaker. This can be understood as the energies of particles after scatterings fluctuate slightly from the averaged value of the plasma and settle to thermal equilibrium within the time scale determined by the size of their couplings. The weaker the coupling, the longer the lifetime of the fluctuation. In the weak-coupling limit, it is found that the energy density spectrum of GW per unit time is [73]

$$\frac{d\rho_{\rm GW}}{dt d\ \ln p}(p \ll \alpha^2 T) \sim \frac{p^3 \eta T}{M_{\rm Pl}^2}, \tag{2.34}$$

such that the slope of the GW spectrum is $\Omega_{\rm GW} \propto f^3$, as shown in Fig. 2.2. Ref. [73] also shows that this behavior continues up to some corrections being cut off at $p \sim T$ as the thermal plasma is better described by particle scattering for $\alpha^2 T < p < T$.

2.4 Beyond the Standard Models

The SM of particle physics and cosmology predicts SGWBs – either too small or too high in frequency – which are difficult be observe. On the other hand, physics beyond the Standard Models can lead to various sources with huge GW signals, allowing future-planned GW observatories to probe the underlying BSM parameters. This section discusses three prime BSM sources: the preheating, the first-order phase transitions, and cosmic strings.

2.4.1 Preheating

The first BSM source of SGWB relates to how the inflationary phase – which dilutes all particles away – gives rise to the hot Big-Bang cosmology; the (p)reheating stage supposes to convert the energy budget of the Universe (via coupling with inflaton) into the SM particle species and the thermal plasma [80–83]. See Refs. [84–86] for reviews. The converting channels can be either perturbative [80, 81, 87, 88] or non-perturbative [82, 89–101]. In the latter case, particles are produced violently and out of equilibrium, leading to a large amount of GW [102–121]. The resulting SGWB depend entirely on the structure of preheating process: the number of daughter particles, their masses, and their couplings to the inflaton. Moreover, interactions among themselves complicate the analysis and results, e.g., [120]. In this section, we follow Ref. [119] for estimating the SGWB from preheating into the non-interacting daughter boson fields.

As an example, consider the inflationary α-attractor model where the inflaton ϕ coupled to a set of daughter scalar fields $\{\chi_i\}$

$$V(\phi,\{\chi_i\}) = \frac{1}{2}\Lambda^4 \tanh^2\left[\frac{\phi}{M}\right] + \frac{1}{2}g_i^2\chi_i^2\phi^2 = \frac{1}{2}g_i^2\chi_i^2\phi^2 + \begin{cases} \frac{\omega_*^2 M^2}{2} & \text{for } \phi \gg M \\ \frac{1}{2}\omega_*^2\phi^2 & \text{for } \phi \ll M \end{cases}, \quad (2.35)$$

where the inflaton in the large-field regime slow-rolls towards the origin and eventually oscillates in the quadratic potential with frequency $\omega_* = \Lambda^2/M$. This induces the parametric growth of $\{\chi_i\}$ fluctuation/particles in the broad resonance regime, defined by the *resonance* parameter: $q \equiv g^2\phi_*^2/\omega_*^2$ with ϕ_* being the inflaton field value when inflation ends. The daughter-field fluctuations get pumped with inflaton energy for modes with comoving momentum $\omega_* \lesssim k_{\rm lin} \lesssim \omega_* q^{0.25}$ during the linear regime and up to $k_p \simeq \omega_* q^{\sim 0.5}$, taking into account mode interactions [118]. Beyond this point, no mode is populated, and the energy spectrum is expected to fall off. In the following, we suppose that the energy spectrum has a smoothened plateau from the linear-regime scale ω_* up to k_p due to the self-interaction distributing energy among all modes. Note that a precise result of the full spectrum requires a dedicated simulation at large scales.

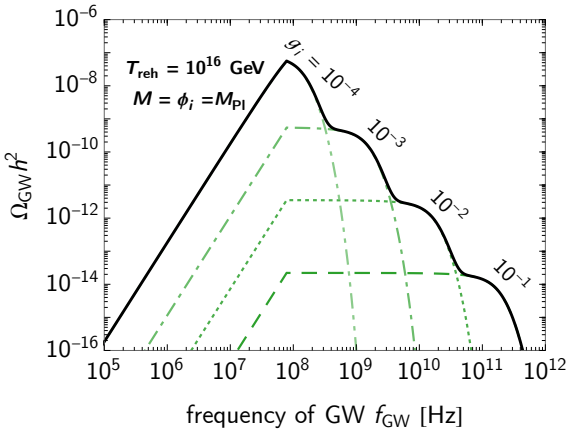

Figure 2.3: **SGWB from the preheating** assuming the instantaneous reheating at $E_{\rm inf} \simeq T_{\rm reh}$ and the inflaton coupled to four non-interacting bosonic particles with coupling $g_i = 10^{-4}$, 10^{-3}, 10^{-2}, 10^{-1}. The total spectrum exhibits a *stairway* shape due to each daughter particle's contribution, neglecting the interaction among them. The spectra are estimated from the result in Ref. [119].

These sudden and violent particle productions produce time-dependent inhomogeneities that lead to an anisotropic stress tensor, roughly due to the gradient energies. The authors of Ref. [119] measure the peak momentum and amplitude of the GW spectrum, using the recent $\mathcal{C}$osmo$\mathcal{L}$attice simulations [122, 123]. Suppose the Universe reheats quickly after the end of inflation at temperature $T_{\rm reh} \simeq \sqrt{\omega_* M} \simeq 10^{16}$ GeV, i.e., the resonance parameter is controlled by the coupling $q \simeq g^2(M_{\rm Pl}/T_{\rm reh})^4$, choosing $M = \phi_* = M_{\rm Pl}$. We obtain the peak GW amplitude today by red-shifting their result with $\Omega_{r,0}$,

$$\Omega_{\rm GW}^{\rm preh} \simeq \Omega_{r,0} \times 10^{-5}\left(\frac{q}{10^4}\right)^{-1.1\pm1.2} \simeq 10^{-11}\left(\frac{10^{-2}}{g}\right)\left(\frac{T_{\rm reh}}{10^{16}\ {\rm GeV}}\right)^4. \quad (2.36)$$

The overall amplitude is suppressed for stronger coupling because a larger g means a broader resonance band, and the available energy is distributed over a wider range of modes. The range of GW frequency today – corresponding modes within $\omega_* \lesssim k \lesssim k_p$ – to be,

$$8 \cdot 10^7 \text{ Hz} \left(\frac{T_{\rm reh}}{10^{16} \text{ GeV}}\right) \lesssim f_{\rm GW}^{\rm preh} \lesssim 10^{10} \text{ Hz} \left(\frac{g}{10^{-2}}\right) \left(\frac{10^{16} \text{ GeV}}{T_{\rm reh}}\right). \tag{2.37}$$

The high-frequency cut-off $f_{\rm GW}^{\rm preh}(k_p)$ depends on the coupling g which would be observed directly at future GW observatories; nonetheless, the future-planed experiments would be sensitive to $T_{\rm reh} \lesssim 10^9$GeV and require a miniscule $g \lesssim 10^{-14}$ for a detectable amplitude. In the presence of many daughter fields, the SGWB of each species adds up and contributes to the *stairway* signature [119], as shown in Fig. 2.3 neglecting the interactions among daughters. The IR tail below $f_{\rm GW}^{\rm preh}(\omega_*)$ falls off with f^3 as expected from causality.

Finally, many other early-Universe systems abruptly produce particles, leading to a strong SGWB. For example, gauge-field production [36, 124–128], and scalar-field fragmentation [129–132].

2.4.2 First-Order Phase Transition

The (p)reheating stage produces the radiation bath of particles, later cooled down by the cosmic expansion. Several phase transitions can take place; for example, the electroweak (EW) and QCD phase transitions in the SM occur relatively smoothly [133–135], so-called *crossover* or the second-order transition. Conversely, the system could be trapped in the metastable vacuum due to the barrier separating it from the true vacuum state; this is the first-order phase transition (FOPT), which is generic in many extensions of SM addressing many open problems, e.g., [19, 136–147]. For example, the vacuum structure could depend on the potential of some extra scalar field.

In some regions of space, the quantum transition or thermal fluctuation causes the system to transit; bubbles of the true vacuum nucleate and expand out in the surrounding of the false vacuum state [148, 149]. Bubble walls also drag the thermal plasma along their motions [150, 151]. Their collisions eventually complete the phase transition. Together with fluid motions, they source GW that would be observed in the future-planned observatories [152–154], as shown in Fig. 2.4. The detectability of SGWB – calculating from PLS curves of SNR = 10 – is also shown on the right panel[8].

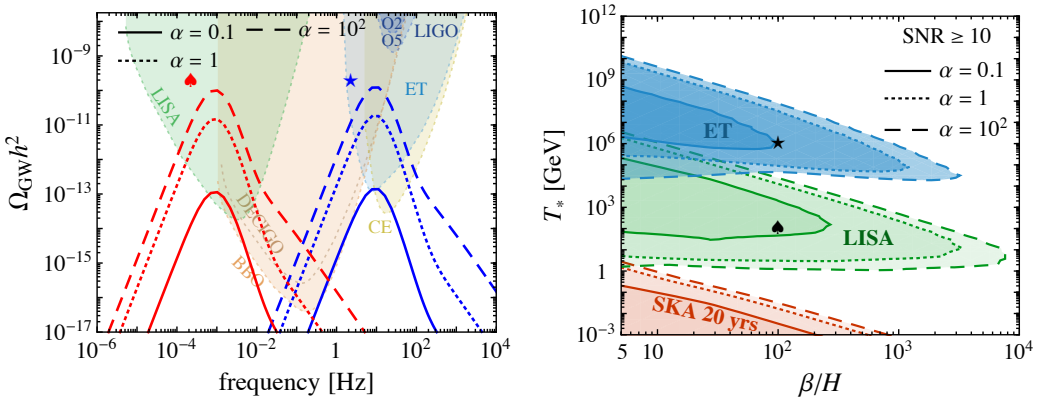

Figure 2.4: **SGWB from first-order phase transition (FOPT)** assuming the GW contribution from fluid motions and varying the transition strength α. The benchmark points correspond to β/H and temperature T_* at GW production shown on the right panel. The right plot shows the detectability of SGWB in several future-planned experiments. LISA probes TeV-scale physics, while ET explores PeV-EeV scales.

[8] A convenient way to obtain detectability is using `PTPlot` tools [153].

The peak GW amplitude observed today can be written, in a unified way, as [152–154]

$$\Omega^{pt}_{\rm GW,0}(f) \simeq \left(\frac{a_*}{a_0}\right)^4 \left(\frac{\rho_{\rm tot,*}}{\rho_{\rm tot,0}}\right) \left(\frac{H_*}{\beta}\right)^m \left(\frac{\kappa\alpha}{1+\alpha}\right)^2 \mathcal{F}(f,\beta), \tag{2.38}$$
$$\simeq \Omega_{r,0} \left(\frac{H_*}{\beta}\right)^m \left(\frac{\kappa\alpha}{1+\alpha}\right)^2 \mathcal{F}(f,\beta),$$

where $*$ denotes the time when GW is produced, $\rho_{{\rm tot},i}$ is the total energy density of the Universe at time i, β^{-1} is the duration of the transition, α is the ratio of the vacuum energy difference over the radiation energy density, κ is the efficiency for converting energy into GW, and we expect $m = 1$ for GW from long-lived fluid motion and $m = 2$ for GW from short-lived fluid motion or bubble wall collisions. Here the factors involving the wall velocity $v_{\rm w}$ are neglected. The spectral shape $\mathcal{F}(k,\beta)$ has the broken power-law scaling where

$$\text{Bubble walls [152, 155–160]: } \mathcal{F}_B(f) \simeq \frac{3.8(f/f_{\rm peak})^{2.8}}{1+2.8(f/f_{\rm peak})^{3.8}}, \tag{2.39}$$

$$\text{Sound waves [150, 153, 161–168]: } \mathcal{F}_{\rm sw}(f) \simeq \frac{(f/f_{\rm peak})^3}{\left[1+\frac{3}{4}(f/f_{\rm peak})^2\right]^{7/2}}, \tag{2.40}$$

$$\text{Turbulence [153, 169–179]: } \mathcal{F}_{\rm turb}(f) \simeq \frac{(f/f_{\rm peak})^3}{[1+(f/f_{\rm peak})]^{11/3}\left(1+\frac{2\pi f}{H_*}\frac{a_0}{a_*}\right)}. \tag{2.41}$$

The IR and UV slopes read $(2.8,-1)$, $(3,-4)$, and $\left(3,-\frac{5}{3}\right)$ for the bubble collision, the sound wave, and the turbulence, respectively.

Since the GW production is relatively short compared to Hubble time, the spectral shape $\mathcal{F}(f,\beta)$ peaks around the bubble size at collision, which is estimated to be a fraction of the horizon size, $\lambda_{\rm GW} \sim \beta^{-1}$. The peak frequency of SGWB from FOPT is

$$f^{\rm pt}_{\rm GW}(H_*) \simeq H_* \frac{a_*}{a_0}\left(\frac{\beta}{H_*}\right) \sim 10^{-5}\ {\rm Hz} \left(\frac{\beta}{H_*}\right)\left(\frac{g_*(T_*)}{106.75}\right)^{1/6}\left(\frac{T_*}{10^2\ {\rm GeV}}\right), \tag{2.42}$$

where we replace frequency of the horizon-size GW in Eq. 2.28. For a benchmark of $\beta/H_* = 10^2$, the frequency-temperature relation is shown for $\lambda_{\rm GW} = H^{-1}/10^2$.

2.4.3 Cosmic Strings

The exhaustive review of cosmic strings (CS) and the derivation of their precise SGWB will be discussed in Chap. 3 and App. B. In this section, we propose a back-of-envelope method for obtaining GW spectra for both local and global cosmic strings[9]. This calculation could be generalized for estimating any relic from the string network, e.g., light or heavy particles and Baryogenesis.

A cosmic string is a line-like topological defect arising after some cosmological phase transition [181–183] and involving a certain type of spontaneous symmetry breaking (SSB), cf. Chap. 3. The broken symmetry can be either local or global; the cosmic string is called local or global. After SSB at some energy scale η, the network of strings forms with tension

$$\mu \sim \eta^2 \times \begin{cases} 1, & \text{for local,} \\ \ln(m_\phi/H), & \text{for global,} \end{cases} \tag{2.43}$$

where the global string has the extended core energy. and separates from its neighbor by a correlation length L. Initially, the network of infinite strings (with length determined by the horizon size $L_{\rm form} \sim H^{-1}_{\rm form}$) has the energy density, $\rho^{\rm form}_\infty \sim EL^{-3}_{\rm form} \simeq \mu L^{-2}_{\rm form} \sim G\mu\rho^{\rm form}_{\rm tot}$ where $\rho^{\rm form}_{\rm tot}$ is the

[9] Similar derivation has been considered in [180].

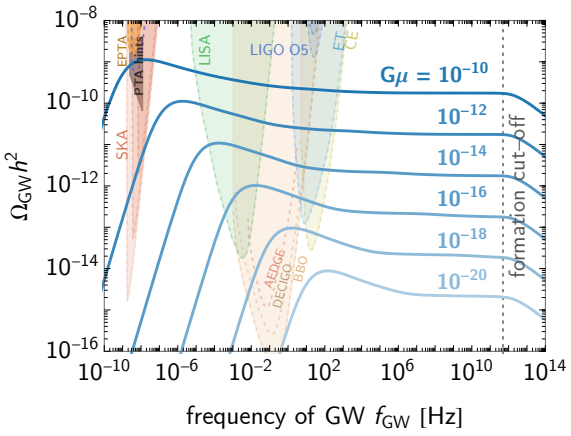

Figure 2.5: **SGWB from local cosmic strings (CS)** for the string tension $G\mu$ (specified on each colored line). The formation cut-off is independent of $G\mu$ due to the delayed GW emission by a factor $(G\mu)^{-1/2}$, cf. Sec. 3.2.5. Interestingly, CS might explain the SGWB hint in the PTA band, discussed in Sec. 2.6.

total energy density of the Universe at the time of the string-network formation. If strings do not interact, their length scale grows $L \propto a$ as the Universe expands. This is the misconception about the unacceptable cosmic-string domination $\rho_\infty \propto L^{-2} \propto a^{-2}$. Nonetheless, the cosmic strings continuously lose energy by decaying or forming loops that later radiate away, including GW.

The dynamics of the string network reach the attractor behavior called *scaling* regime where $\rho_\infty^{\rm scaling} = \xi(t)\mu(t)/t^2$ for $\xi(t) \sim \mathcal{O}(0.1)$ is the correlation length per Hubble horizon, justified by simulations [184–193] ; see Chap. 3 for more details. The string network never dominates the Universe because it tracks the total energy density, $\rho_\infty^{\rm scaling} \simeq \mu(t)/t^2 \simeq G\mu\rho_{\rm tot}$, regardless of the background. The energy lost per unit volume $\tilde{\Gamma}$ is found from $\dot{\rho}_\infty + 2H\rho_\infty = \tilde{\Gamma}$. Requiring that $\tilde{\Gamma}$ guides the network into scaling $\rho_\infty \to \rho_\infty^{\rm scaling}$, we deduce

$$\tilde{\Gamma} = -\rho_\infty^{\rm scaling}\left[(n-2)H - \dot{\xi}\xi^{-1} - \dot{\mu}\mu^{-1}\right] \tag{2.44}$$

where we assume $H \sim a^{-n/2}$ which gives $H = 2/nt$.

Local strings. — The string tension μ and the correlation length ξ are constant: $\tilde{\Gamma}(t) = -(n-2)H\rho_\infty^{\rm scaling}(t)$. Within one Hubble time, the network emits energy[10] in the form of loops

$$\rho_{\rm emit}(t) = -\tilde{\Gamma}/H = (n-2)\rho_\infty^{\rm scaling}(t) = 4(n-2)\xi\mu H^2. \tag{2.45}$$

which behaves as a gas of particles ($\rho_{\rm emit} \simeq \rho_{\rm loop} \sim a^{-3}$) and later decays into GW ($\rho_{\rm GW} \sim a^{-4}$) at the time $t_M \simeq t/G\mu$; see App. B.4. The energy density of GW today from loops produced at $a(t)$ and decayed at a_M is

$$\rho_{\rm GW,0}^{\rm total}(a) = \left[\frac{a}{a_M}\right]^3\left[\frac{a_M}{a_0}\right]^4\rho_{\rm loop}(t) = 4(n-2)\xi\mu\Omega_{r,0}H_0^2\left[\frac{1}{2G\mu}\right]^{\frac{1}{2}}\left[\frac{t_\Delta}{t}\right]^{\frac{3(n-4)}{2n}}, \tag{2.46}$$

where we consider that loops are produced when the total energy density is $\rho \sim a^{-n}$ and ends at a_Δ, and loops decay during the subsequent radiation era. Therefore we obtain the famous scale-invariant GW spectrum for cosmic-string in the radiation era ($n = 4$)

$$\Omega_{\rm GW,0} = \rho_{\rm GW,0}/\rho_{c,0} \simeq 1.1\cdot 10^{-10}\left(\frac{\xi}{0.1}\right)\left(\frac{G\mu}{10^{-10}}\right)^{1/2} \tag{2.47}$$

where we use $\Omega_{r,0} \simeq 5.38\cdot 10^{-5}$ [23]. This simple estimation agrees well with the precise calculation, illustrated in Fig. 2.5, from the precise method in Chap. 3.

[10] This estimation assumes that all energy loss goes into the relic, which might not be the case for strings losing their energy in several channels. Moreover, simulations have found that around 90% of loops are produced with small lengths and high velocities [194]. The energy in small loops red-shifts away, such that only 10% of the total energy loss from the network contribute to the relic abundance.

Global strings. — The string tension μ and the correlation length ξ experience the log dependence due to the existence of Goldstone, cf. App. B.1. It is still under debate whether ξ receives the log-dependence due to a mild violation of scaling behavior found in simulations [195–198]. However, the VOS equations – derived from the NG approximation – suggest a mild violation, less than a factor log [1, 199]. Thus we parametrize both quantities by [200]

$$\xi(t) = \xi_0 \log^p\left(\frac{m_\phi}{H}\right), \quad \mu(t) = \mu_0 \log\left(\frac{m_\phi}{H}\right), \tag{2.48}$$

where ξ_0, μ_0 are evaluated at the time of string formation, Γ is a constant of $\mathcal{O}(1)$, and $p = 0, 1$ for the scaling network and the log-violation of the scaling, respectively.

Unlike local strings, the global-strings loops also release energy in the form of massless goldstone particles, whose branching fraction is much larger than the GW emission. We denote the efficiency of GW production as

$$\epsilon \equiv \frac{P_{\rm GW}}{P_{\rm total}} \simeq \frac{P_{\rm GW}}{P_{\rm gold}} \simeq \frac{\Gamma G\mu}{\Gamma_{\rm gold}/\log(m_\phi/H)}, \tag{2.49}$$

where $P_{\rm total} = P_{\rm gold} + P_{\rm GW} \simeq P_{\rm gold}$, $P_{\rm GW} = \Gamma G\mu^2$, and $P_{\rm gold} = \Gamma_{\rm gold}\eta^2$. See Sec. 3.6 for more details. The second difference is that the GW emission happens shortly after the loop formation[11], i.e. $t_M \sim t$. Therefore, the energy density of the GW today from loops produced at $a(t)$ reads

$$\rho_{\rm GW,0}(a) = \left(\frac{a_M}{a_0}\right)^4 \left(\frac{a}{a_M}\right)^3 \rho_{\rm loop}(t)\,\epsilon(t) \simeq 8\xi G\mu^2 \Omega_{r,0} H_0^2 \left(\frac{\Gamma}{\Gamma_{\rm gold}}\right) \log(m_\phi/H), \tag{2.50}$$

where we consider the radiation-dominated Universe. The GW abundance today reads

$$\Omega_{\rm GW,0} \simeq 7.9\cdot 10^{-18}\left(\frac{\xi_0}{0.1}\right)\left[\frac{\eta}{10^{15}\ {\rm GeV}}\right]^4 \log^{p+3}\left[2\cdot 10^{27}\left(\frac{\eta}{10^{15}\ {\rm GeV}}\right)\left(\frac{\rm mHz}{f}\right)^2\right], \tag{2.51}$$

where we assume $\Gamma \simeq 50$ and $\Gamma_{\rm gold} \simeq 65$, $p = 0, 1$ is for the scaling network and the log-violation in ξ, respectively. Here we obtain the consistent parameter dependence (e.g., μ, log) as the VOS model in Sec. 3.6.

Frequency-temperature relation. — The GW frequency today relates to the loop's size at emission redshifted until today. Consider loops formed at some length scale H_*^{-1}. The delayed emission of the local strings allows the string loop to attain its size until later times[12]. The GW frequency today from local strings thus is higher compared to the global-string case, which follows the formula of the horizon-size GW sources ($f_{\rm GW}^H \simeq H_* a_*/a_0$) in Eq. (2.28):

$$f_{\rm GW}^{\rm cs}(H_*) \simeq H_*\frac{a_*}{a_0} \times \begin{cases} 1 & \text{for global,} \\ \frac{a_M}{a_*} = (G\mu)^{-1/2} & \text{for local,} \end{cases} \tag{2.52}$$

where we use that the delayed emission happens at $a_M/a_* = (t_M/t_*)^{1/2} = 1/\sqrt{G\mu}$. For example, the local-string SGWB with $G\mu = 10^{-12}$ has the frequency-temperature relation with $\lambda_{\rm GW} = 10^{-6}H^{-1}$ in Fig. 2.1. Interestingly, the local-string GW frequency associated to the network-formation scale ($H_* \propto \mu$, $a_*/a_0 \propto \mu^{-1/2}$) is $f_{\rm form} \simeq 10^{11}$ Hz$[g_*(\eta)/106.75]^{1/6}$, insensitive to $G\mu$ as illustrated in Fig. 2.5.

[11] To justify, we consider the length evolution: $l(t) = \alpha t_i - (P_{\rm GW} + P_{\rm gold})(t - t_i)$. The dominant emission occurs when $l(t_M) = \alpha t_I/2$. Hence, we have $t_M/t = (\alpha/2 + P_{\rm GW} + P_{\rm gold})/(P_{\rm GW} + P_{\rm gold}) \simeq 1$ when $P_{\rm gold} \gg \alpha \gg P_{\rm GW}$.

[12] Tension makes loops decoupled from Hubble flow.

2.5 Prospect of Detections

Fig. 2.1 shows the landscape of primordial SGWBs along with the prospects of GW experiments, which can be classified in Tab. 2.1 by their techniques of measurements. The sensitivity curves for LISA, ET, CE, BBO, DECIGO, LIGO, GAIA, THEIA, and AEDGE are the power-law integrated sensitivity curves with $\mathrm{SNR} = 10$, discussed in App.A. The pulsar timing-array curves are taken from [201]; other experiments are taken from references shown in Tab. 2.1. Fig. 2.1 also shows the hint of SGWB observed by pulsar timing arrays, cf. Sec. 2.6.

The synergy among all experiments enables us to probe almost half of the landscape populated by the primordial SGWB. Nonetheless, the high-frequency side ($f_{\rm GW} > \mathrm{kHz}$) has no current proposal of experiments that can beat the $\Delta N_{\rm eff}$ bound [40]. Interestingly, some of these techniques are borrowed from the ongoing axion-search experiments. It would be an exciting direction for future research since this high-frequency GW probes the Universe at very early times and at extraordinarily high energies.

Observatories/Experiments	Techniques
Planck/BICEP/KECK [20, 30, 32], LiteBIRD [202]	CMB B-mode polarization
FIRAS/PIXIE/Voyage 2050 [203]	CMB spectral (μ, y) distortion
EPTA [204], NANOGrav [205], PPTA [206], SKA [207], **Fermi-LAT [208]**	Pulsar timing arrays
GAIA [209], THEIA [210]	Astrometry
Asteroids [211], lunar ranging [212]	Radio and laser ranging
Particle-accelerator's storage rings [213, 214]	Storage-ring GW observatories
LISA [5, 65], DECIGO/BBO [68] Taiji [215, 216], TainQin [217–219], μAres [220]	Space-based laser interferometry
AEDGE [221], MARGIS/AION [222–225]	Atomic interferometry
LIGO/VIRGO/KAGRA [28, 226, 227], ET [66, 67], CE [228]	Terrestrial laser interferometry

Table 2.1: List of GW experiments/observatories. Some are not shown in Fig. 2.1, and some references are reviews on the topics. Bold-faced are currently operating or completed their missions.

2.5.1 Perspectives on Astrophysical Foregrounds

On top of the primordial sources, SGWB can also be produced by the astrophysical sources at late times. It is crucial for studying the primordial SGWB to be able to rely on the assumption that the astrophysical foreground can be subtracted.

LIGO/VIRGO have observed three binary black hole (BH-BH) merging events [229–231] during the first 4-month observing run O1 in 2015, and seven additional BH-BH [232–235] as well as one binary neutron star (NS-NS) [236] merging events during the second 9-month observing run O2 in 2017. In the first part of the 6-month observing run O3a in 2019, the number of events is raised to 55 events [237, 238]. After a 5-month run O3b (joined by KAGRA) in 2019-2020, the recently released catalog lists up to 90 events [239]. Hence, one might worry about the difficulty of distinguishing the primordial SGWB from the one generated by the astrophysical foreground.

In the BBO and ET/CE windows, the NS and BH foreground might be substracted with respective reached sensibilities $\Omega_{\rm GW} \simeq 10^{-15}$ [240] and $\Omega_{\rm GW} \simeq 10^{-13}$ [241]. In the LISA window,

the binary white dwarf (WD-WD) foreground dominates over the NS-NS, and BH-BH foregrounds [242–244]. The WD-WD galactic foreground, one order of magnitude higher than the WD-WD extragalactic [245], might be substracted with reached sensibility $\Omega_{\rm GW} \simeq 10^{-13}$ at LISA [246, 247]. Hence, in the optimistic case where the foreground can be *subtracted* and the latter sensibility is reached, one might be able to distinguish the primordial signal from the one generated by the astrophysical foreground, e.g., [241, 248–252].

The GW spectrum generated by the astrophysical foreground increases with frequency as $f^{2/3}$ [253], which might be distinguished from the primordial sources using the *spectral separation* methods [247, 254–258]. Furthermore, the assumption of an isotropic, homogeneous, unpolarized, stationary, and gaussian SGWB might be violated by different sources and can be used to distinguish them [37, 38, 259, 260].

2.6 A Hint of SGWB from Pulsars

The SGWB-hunting effort over 23 decades in frequencies may be about to pay off. Recently, PTA collaborations (NANOGrav, EPTA, PPTA) have reported noises in the time-of-arrival signal [204–206], which are spatially-uncorrelated and common to all pulsars and could result from SGWB. Also, the IPTA collaboration has recently found similar results [261] by reanalyzing a joint data set of the previous data releases, containing pulsars with $0.5 - 30$ years baselines.

In the left panel of Fig. 2.6, the residual in the time-delay signal of the common-spectrum process (or CP delay) spans over the frequency range and can be interpreted as the SGWB with strain amplitude h_c and relic abundance $\Omega_{\rm GW}$

$$\text{Res} = \sqrt{\frac{\mathcal{O}(\Gamma_{\rm HD})h_c^2}{12\pi^2 f_{\rm yr}^2}\left(\frac{f_{\rm yr}}{f}\right)^3} \simeq (0.45\,\mu\text{s})h^{-1}\left[\frac{\Omega_{\rm GW}h^2}{10^{-9}}\right]^{\frac{1}{2}}\left[\frac{\mathcal{O}(\Gamma_{\rm HD})}{0.1}\right]^{\frac{1}{2}}\left[\frac{2.5\,\text{nHz}}{f}\right]^{\frac{5}{2}}, \quad (2.53)$$

where $f_{\rm yr} = 1/\text{yr} \simeq 31.7\,\text{nHz}$, $\mathcal{O}(\Gamma_{\rm HD}) \sim 0.1$ is a factor depending on the overlap reduction function, assumed to follow the *Hellings-Downs* relation, and in the last step we use $\Omega_{\rm GW} = 2\pi^2 h_c^2 f^2/(3H_0^2)$. The right panel of Fig. 2.6 shows the 1σ, 2σ, 3σ fitted spectral shapes of h_c, assuming $h_c = A_{\rm CP}(f/f_{\rm yr})^{(3/2-\gamma_{\rm CP})}$. Notice that the NANOGrav region differs from ITPA, EPTA, and PPTA. Because the shown NANOGrav result is fitted for the first 5 frequency bins ($2.5\,\text{nHz} < f < 12\,\text{nHz}$), which corresponds to $\gtrsim 99.98\%$ of the signal-to-noise ratio [205], while the other results fitted over total of 30 bins ($\text{nHz} < f < f_{\rm yr}$) where the other noises (e.g., white noises) could contaminate the actual signal cf. for $f > 10\,\text{nHz}$ in Fig. 2.6. We translate these regions into a plane of SGWB amplitude $\Omega_{\rm GW}$ and its spectral index β via $\Omega_{\rm GW}(f_*) = \Omega_{\rm GW}(f_{\rm yr})(f_*/f_{\rm yr})^\beta$ for $\beta = 5 - \gamma_{\rm CP}$ in Fig. 2.7. One caveat of identifying this observation as SGWB is the inconclusive result [204–206, 261] of the quadrupole (Hellings-Downs) correlation [262], the characteristic angular correlations among pairs of pulsars which is unique to an isotropic SGWB. Newer PTA observatories will join further measurements by EPTA, PPTA, and NANOGrav: InPTA, CPTA, and MeerKAT, to resolve this issue. The increasing precision and statistic might allow one to pinpoint whether this signal is of astrophysical or primordial origin.

There are several explanations for SGWB that fit this result: astrophysical and primordial sources. One prime astrophysical candidate is the background from super-massive black hole binaries (SMBH), whose SGWB contribution has a spectral index of $\beta = 2/3$ [263][13]. A large variety of BSM physics are also well motivated for primordial SGWBs ranging from: topological defects [264–266], quantum fluctuations during inflation (e.g. leading to primordial black holes) [267–269], first-order phase transitions around temperature $T_p \sim \mathcal{O}(\text{MeV})$ [270–273], and modified cosmological history [274]. As an example, Fig. 2.7 shows the shape of a SGWB coming from a CS network with tension $G\mu$ cf. Chap. 3 for more detail. We see that CS with $G\mu \simeq 10^{(-9,-10)}$

[13] However, the amplitude has some uncertainties from the merger rates in particular.

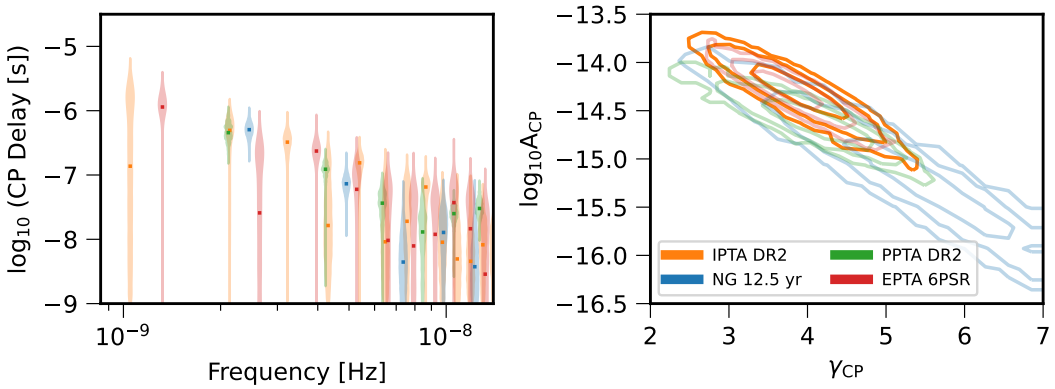

Figure 2.6: left: The time-delay caused by a common-spectrum process (CP) has been observed by the PTA collaborations: NANOGrav [205], PPTA [206], and EPTA [204]. The IPTA's second data released (DR2) provides a fit of the joint data set of the previous NANOGrav, EPTA, and PPTA releases. *right:* By fitting with the broken power-law SGWB strain, the amplitude, and spectral index are shown for 1σ, 2σ, and 3σ confidence levels from inner to outer, respectively. Figure copied from [261].

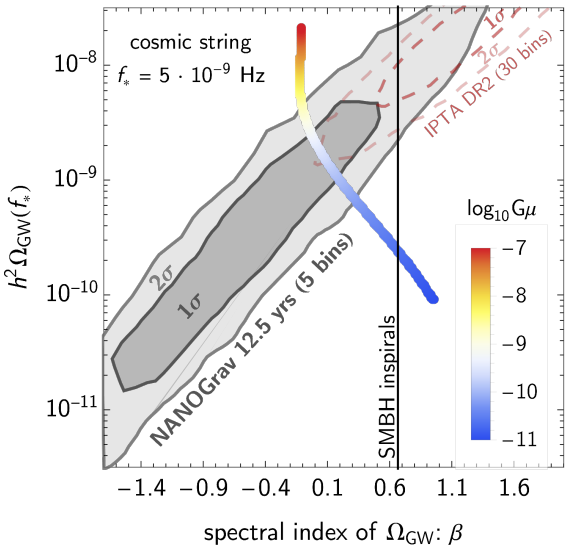

Figure 2.7: Result of fitted SGWB assuming power-law shape at the frequency f_*. The NANOGrav 12.5 yrs result uses the first 5 bins data and differs from the combined result of IPTA DR2 that uses 30 bins which other noises could highly contaminate. The colored line shows the spectral shape of SGWB from CS where $G\mu \simeq 10^{(-9,-10)}$ are preferred.

could well explain the PTA data, suggesting the existence of a phase transition around temperature $T \simeq M_{\rm Pl}\sqrt{G\mu} \simeq 10^{13}$ GeV.

2.7 Chapter Summary

Any primordial GW source operates within a limited length scale – the horizon size – which is tremendously smaller than the horizon today; many GWs from numerous causal uncorrelated patches contribute to the signal observed today in the form of stochastic GW background (SGWB). The extreme weakness of the gravitational interaction allows GW to propagate freely, up to the cosmic expansion, and to carry direct information about the source's strength and length/time scale. The observed spectrum of SGWB is characterized by the relic density $\Omega_{\rm GW}$ and the frequency $f_{\rm GW}$, which are simply redshifted from the production time, i.e., $\rho_{\rm GW} \propto a^{-4}$ and $f_{\rm GW} \propto a^{-1}$.

By applying simple theoretical arguments in Sec. 2.2, we chart the landscape of primordial GW in Fig. 2.1, spanning over 31 decades in frequency (10^{-18} Hz $\lesssim f_{\rm GW} \lesssim 10^{13}$ Hz), while the BBN/CMB-$\Delta N_{\rm eff}$ bounds strongly constrain the GW amplitude ($\Omega_{\rm GW} \lesssim 10^{-7}$). Furthermore, a crucial aspect of primordial GW is that its frequency range is typically associated with the horizon

size and the Universe's temperature at the production time, cf. Eq. (2.16). This means that primordial SGWB is a probe of cosmological history; the earlier the production time, the higher the GW frequency.

As shown in Fig. 2.1, the early Universe has several prime sources of GW, classified as those from the SM (primordial inflation and thermal plasma) in Sec. 2.3 and beyond the SM (preheating, FOPT, and cosmic strings) in Sec. 2.4. Moreover, we can also categorize them according to the time interval of GW production. For the short-lasting sources, SGWBs from FOPT and preheating localize at some particular frequency. In contrast, SGWB from long-lasting sources (primordial inflation and cosmic strings) span a broad frequency range. The thermal plasma is also a long-lasting source, but its SGWB sits only at frequency $f_{\rm GW} \sim T_0$ (due to $\lambda_{\rm GW}^{-1} \sim T_{\rm prod}$). The SM sources barely lead to observable SGWB in future-planned experiments as their spectra have either too small amplitudes or too high frequencies. Nonetheless, BSM sources can typically reside within the visible windows, and the experimental efforts in GW physics will significantly contribute to new physics searches.

In Sec. 2.5, we list the current and planned GW experiments involving many techniques from CMB, pulsar, astrometry, asteroid rangings, lunar rangings, laser interferometers, atomic interferometers, and storage rings of some particle accelerators. They span about 22 decades in frequency, more than half of the primordial GW landscape. However, the ultra-high frequency range remains untouched; the challenges and prospects of experiments in this region are reviewed in [40], including the application of the exciting axion searches. We comment briefly on the possibility of astrophysical foreground cleaning using several methods and properties of SGWB.

Lastly, Sec.2.6 reviews the recent hint of SGWB observed by pulsar timing arrays, compatible with $\Omega_{GW} \simeq 10^{-9 \div -10}$ and a spectral index of $(-1.5, 0.5)$. One possible explanation would be cosmic strings with tension $G\mu \sim 10^{-9 \div -10}$. Nevertheless, the smoking-gun signature of SGWB – the quadrupolar (*Hellings-Downs*) relation – remains inconclusive. The next NANOGrav data release in 2023 should deliver a decisive result.

In the next chapter, we focus on the cosmic strings whose SGWB spans a wide frequency range with a large amplitude; this allows us to probe new particle physics. Besides, SGWBs shown in Fig. 2.1 assume the standard cosmological history, i.e., the radiation-dominated era up to very high-energy scales. In Chap. 4, we shall see that the non-standard cosmological history leads to many exciting signatures. In some cases, the inflationary SGWB can also be enhanced in the observable windows.

Chapter 3

Cosmic Strings & Gravitational Waves

Based on
[1] Y. Gouttenoire, G. Servant and P. Simakachorn, ***Beyond the Standard Models with Cosmic Strings****,* JCAP **07** *(2020) 032, [1912.02569].*

Cosmic strings (CS) act as a long-lasting source of gravitational waves (GW) from the time of their production – presumably very early on – until today [275–293]. The resulting frequency spectrum, therefore, encodes information from the almost entire cosmic history of our Universe and could possibly reveal precious details about the high-energy particle physics responsible for cosmological histories [1–4, 199, 274, 294–297], discussed as the main topic of Chap. 4.

In this chapter, we first recap the key features of CS networks, their cosmological evolution, decay channels, and the pulsar timing array constraints on the string tension. Sec. 3.2 reviews the computation of the SGWB from Nambu-Goto CS. We first discuss the underlying assumptions on the small-scale structure and the loop distribution and then derive the master formula of the GW frequency spectrum. A critical discussion concerns the non-trivial frequency-temperature relation and how it depends on the cosmological scenario. Sec. 3.3 is devoted to deriving the loop production efficiency beyond the scaling regime, taking into account transient effects from the change in the equation of state of the Universe. We apply this to predict the SGWB in the standard cosmological model in Sec. 3.4. Sec. 3.5 illustrates the possibilities for the GW spectrum to exhibit different types of peak structures due to the presence of both a high and a low-frequency cutoff, e.g., the metastable string network. The interesting case of global strings is discussed in Sec.3.6.6 which includes: the evolution of the network, SGWB calculation, differences from the local case, and some comments on axion strings.

Additional details are moved to appendices, such as a simple UV completion of cosmic strings in App. B.1, non-GW constraints on the string tension $G\mu$ in App. B.2, a back-of-the-envelope estimation of SGWB in App. 2.4.3, a precise step-by-step derivation of the GW spectrum as well as the values of its slopes in App. B.3, the formulae of the various turning-point frequencies in App. B.4, the derivation of the equations which govern the evolution of the long-string network in the Velocity-dependent One-Scale (VOS) model in App. B.5, a discussion of the extensions to the original VOS model in App. B.6, and the impact of the cosmology on the size of loops at formation in App. B.7.

3.1 Recap on Cosmic Strings

Cosmic strings are extended objects of cosmological sizes[1] that have been the subject of numerous studies since the pioneering paper [181], see [183, 301, 302] for reviews. They can originate as fundamental or composite objects in string theory [303–310] or as topological defects from spontaneous symmetry breaking (SSB) in field theories. In superstring theory, strings are the fundamental new degrees of freedom, which are usually unstable and decay before they can stretch to

[1] Although the cosmological size is required for cosmic string, the string-liked solution arises and are observed in laboratory scales as a consequence of field theory in condensed matter physics, e.g., superfluid helium [298–300].

cosmological scales. However, the so-called F-, D-, and (p,q)-strings can grow large and could influence significantly cosmological phenomena [306, 310–312].

3.1.1 Field-theoretic strings

In field theories, the existence of a sting-liked solution is rather generic but not automatic. It is a classical field configuration that arises whenever there is a symmetry-breaking $G \to H$ with a non-trivial homotopy group[2] $\pi_1(G/H) \neq \mathbf{Id}$ where **Id** denotes the identity map, i.e. there exists an equivalent class of maps from a circle to a non-deformable line in the vacuum manifold G/H. For example, any theory with a broken-$U(1)$ symmetry has a string solution since $\pi_1(U(1)) = \mathbb{Z}$.

More complex vacuum manifolds with string solutions can appear in various grand unified theories [313–315], e.g., $SO(10) \to SO(5) \times \mathbb{Z}_2$. However, we emphasize that there is no string solution in the Standard Model (SM) because the symmetry breaking pattern of the SM is trivial,

$$SU(2)_L \times U(1)_Y \to U(1)_{\rm EM}, \tag{3.1}$$

whose corresponding homotopy group[3] is

$$\pi_1(SU(2) \times U(1)/U(1)) \cong \pi_0(U(1)) \cong \mathbf{Id}. \tag{3.2}$$

Thus no string solution is allowed in the SM, and the existence of cosmic strings requires physics beyond the Standard Model (BSM)[4].

The Abelian-Higgs model. The classic example of field theories with a string-liked solution is the Abelian-Higgs (AH) model, a field theory with a complex scalar field ϕ charged under a $U(1)$ gauge interaction. Note that the symmetry can also be global. The resulting string solutions corresponding to local and global symmetries are called local and global strings. CS corresponds to lines where the scalar field sits on the top of its *Mexican hat potential* $V(\phi)$ and approaches its vacuum expectation value (VEV) at a considerable distance, the *Nielsen-Olesen* vortex [319, 320]. When following a closed path around the string, the phase of the complex scalar field returns to its original value after winding around the Mexican hat an integer n number of times. The energy per unit of length, also known as the *string tension* reads [301]

$$\mu \approx 2\pi\eta^2\, n^2 \times \begin{cases} 1 & \text{for local strings,} \\ \ln\left(\frac{m_\phi}{H}\right) & \text{for global strings,} \end{cases} \tag{3.3}$$

with η the scalar field VEV. The Hubble horizon H^{-1} and the string core width m_ϕ^{-1} play the role of IR and UV cut-offs. The logarithmic divergence of the tension of global strings is due to a long-range interaction mediated by the massless Goldstone mode (the complex phase of ϕ). We refer the reader to App. B.1 for more details on Abelian-Higgs cosmic strings and the string-tension calculations.

3.1.2 Cosmic-string network formation and evolution

Kibble mechanism. The formation of cosmic strings occurs during a cosmological phase transition associated with spontaneous symmetry breaking, occurring at a temperature approximately

[2] Other topological defects also defined in the same way, e.g. $\pi_n(G/H) \neq \mathbf{Id}$ for $n = 1, 2, 3$ associate to domain walls, monopoles, and textures, respectively.

[3] The calculation of a homotopy group is done via the so-called *fundamental theorem*: $\pi_n(G/H) \cong \pi_{n-1}(H)$.

[4] Actually, a non-topological string solution exists for the electroweak theory [316]. This is the weak-gauge coupling limit of the so-called *semi-local* strings [317] whose unbroken symmetry is mixed between local and global groups. The string configuration exists due to the gradient energy from global symmetry. However, the realistic SM parameters are in the regime where the string solution is unstable [318].

given by the VEV acquired by the scalar field

$$T_p \simeq 10^{11}\ \text{GeV} \left(\frac{G\mu}{10^{-15}}\right)^{1/2}. \tag{3.4}$$

As shown in Fig. 2.5, the string formation scale can lead to an interesting GW signature: the high-frequency cut-off. As we will discuss later, the GW frequency in Eq. (3.33) – corresponding to the formation temperature – is

$$f_{\text{form}} \simeq 206\ \text{GHz} \left(\frac{0.1 \times 50}{\alpha\Gamma}\right)^{1/2} \left[\frac{g_*(T_{\text{form}})}{g_*(T_0)}\right]^{1/4}, \tag{3.5}$$

which is interestingly independent of $G\mu$.

At the time of the phase transition associated with an energy scale η, CS are randomly distributed and form a network characterized by its correlation length L, which can be defined as

$$L \equiv \sqrt{\mu/\rho_\infty}, \tag{3.6}$$

where μ is the string tension – the energy per unit length – of the order η^2, see Eq. (3.3), and ρ_∞ is the energy density of long strings. More precisely, long strings form infinite random walks [321] which can be visualized as collections of segments of length L.

Loop chopping. Each time two segments of a long string cross, they inter-commute, with a probability P, and form a loop. Loop formation is the primary energy-loss mechanism of the long string network. In numerical simulations [322] and analytical modeling [323], the probability of inter-commutation has been found to be $P = 1$ but in some models it can be lower. This is the case of models with extra-dimensions [304, 324], strings with junctions [325] or peeling [326], or the case of highly relativistic strings [327].

Scaling regime. The strings may interact strongly with the thermal plasma just after the network is formed, so their motion is damped. When the damping stops, cosmic strings oscillate and enter the phase of *scaling* evolution. During this phase, the network experiences two competing dynamics:

1. Hubble stretching: the correlation length scale stretches due to the cosmic expansion, $L \sim a$.

2. Fragmentation of long strings into loops: a loop is formed after each segment crossing. Right after their formation, loops evolve independently of the network and start to decay through gravitational radiation and particle production.

It has been known since a long time [184–188], that out of the two competing dynamics, Hubble expansion and loop fragmentation, there is an attractor solution, called the *scaling regime*, where the correlation length scales as the cosmic time,

$$L \sim t. \tag{3.7}$$

Note, however, that in the case of a global-string network, it has been claimed that the scaling property in Eq. (3.7), is logarithmically violated due to the dependence of the string tension on the Hubble horizon [195, 328–332]. More recently, an opposite conclusion has been drawn in [333].

Number of strings. During the scaling regime, the number of strings per Hubble patch is conserved

$$\frac{\rho_\infty H^{-3}}{\mu L} = \text{constant}. \tag{3.8}$$

Moreover, the energy density of the long-string network, which scales as $\rho_\infty \sim \mu/t^2$, has the same equation-of-state as the main background cosmological fluid $\rho_{\rm bkg} \sim a^{-n}$,

$$\frac{\rho_\infty}{\rho_{\rm bkg}} \sim \frac{a^n}{t^2} \sim \text{constant}, \tag{3.9}$$

where we used $a = t^{2/n}$. Hence, the long-string energy density redshifts as matter during matter domination and as radiation during radiation domination. The scaling regime allows cosmic strings not to dominate the energy density of the Universe, unlike other topological defects. A string network's scaling property was checked fifteen years ago in numerical Nambu-Goto simulations [189–192] and more recently with larger simulations [193]. During the scaling regime, the loop production function is scale-free, with a power-law shape, meaning that loops are produced at any size between the Hubble horizon t and the scale $\sim \Gamma G\mu\, t$, below which the gravitational backreaction has smoothened the strings and there is no further segment crossing.

A scale-invariant SGWB. An essential outcome is the scale-invariance of the Stochastic GW Background generated by loops during the scaling regime [275–291]. Expanding from the back-of-the-envelope estimation given in Sec. 2.4.3, we construct the GW spectrum in Sec. 3.2.3 and give further details in App. B.3. Remarkably, the spectrum generated by loops produced during radiation domination is flat, $\propto f^0$, whereas an early matter domination or an early kination-domination era turns the spectral index from f^0 to respectively $f^{-1/3}$ or f^1. As recently pointed out by [334], in presence of an early matter, the slope f^{-1} predicted by [294, 295], is changed to $f^{-1/3}$ due to the high-k modes. We give more details on the impact of high-k modes on the GW spectrum in the presence of a decreasing slope due to an early matter era, a second period of inflation, particle production, thermal friction or network formation in App. B.3.7. Hence, the detection of the SGWB from CS by LIGO [226], DECIGO, BBO [68], LISA [65], Einstein Telescope [66, 67] or Cosmic Explorer [228] would offer an unique observation window on the equation of state of the Universe at the time when the CS loops responsible for the detected GW are formed. In Secs. 4.3, 4.5 and 4.6, we study the possibility for probing particular non-standard cosmological scenario: long matter/kination era, intermediate matter and intermediate inflation, respectively.

3.1.3 Decay channels of Cosmic Strings

Cosmic strings can decay in several ways, as we discuss below.

GW radiation from long strings. Because of their topological nature, straight infinitely-long strings are stable against decay. However, small-scale structures of long wiggly strings can generate gravitational radiation. Intuitively, a highly wiggly string can act as a gas of tiny loops. The GW emission from long strings can be neglected compared to the GW emission from loops, as loops live much longer than a Hubble time [281, 301]. Indeed, the GW signal emitted by loops is enhanced by many loops (continuously produced). Exceptions are strings with small inter-commutation probability and global strings where loops are short-lived due to efficient Goldstone production. In such cases, the GW emission from long strings can give a major contribution to the SGWB [335–339]. Nambu-Goto numerical simulations have shown that the loop energy density is at least 100 times larger than the long-string energy density [194]. Recently, NG simulations also finds that the SGWB from the local CS network attains a spectral shape similar to the GW from loops, but with unobservable amplitude $\Omega_{\rm GW}^{\rm long} \simeq 10^{-2}(G\mu)^2$ [339]. In what follows, we only consider the emission from loops.

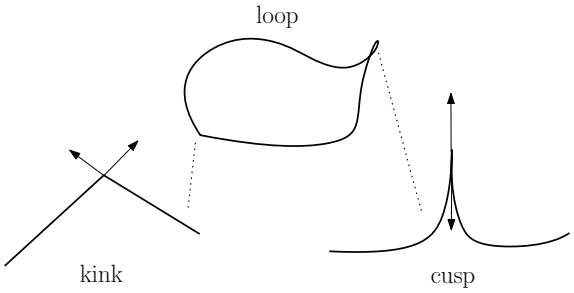

Figure 3.1: Cartoon showing the geometry of a kink and a cusp which are singular structures formed on loops. The arrows denote the tangent vectors of the string segments.

GW radiation from loops (local strings): In contrast to long strings, loops do not contain any topological charge and are free to decay into GW. The GW radiation power is found to be [301, 340]

$$P_{\rm GW} = \Gamma G\mu^2, \tag{3.10}$$

where the total GW emission efficiency Γ is determined from Nambu-Goto simulations, $\Gamma \simeq 50$ [341]. Note that the gravitational power radiated by a loop is independent of its length. This can be understood from the quadrupole formula $P = G/5(Q''')^2$ [277, 342] where the triple time derivative of the quadrupole, $Q''' \propto [\texttt{mass}][\texttt{length}]^2[\texttt{time}]^{-3} \propto \mu$, is indeed independent of the length. The resulting GW are emitted at frequencies [183, 343]

$$\tilde{f} = \frac{2k}{l}, \qquad k \in \mathbb{Z}^+, \tag{3.11}$$

corresponding to the proper modes k of the loop. The symbol $\tilde{\cdot}$ is used to distinguished the frequency emitted at $\tilde{t}$ from the frequency today

$$f = a(\tilde{t})/a(t_0)\ \tilde{f}. \tag{3.12}$$

The frequency dependence of the power spectrum $P_{\rm GW}(k)$ relies on the nature of the loop small-scale structures [344, 345], e.g., kinks or cusps, cf. Fig. 3.1.

More precisely, the spectrum of the gravitational power emitted from one loop reads

$$P_{\rm GW}^{(k)} = \Gamma^{(k)} G\mu^2, \qquad \text{with} \quad \Gamma^{(k)} \equiv \frac{\Gamma\, k^{-n}}{\sum_{p=1}^{\infty} p^{-n}}\,, \quad n = \begin{cases} 4/3 & \text{cusps} \\ 5/3 & \text{kinks} \\ 2 & \text{kink-kink collisions} \end{cases} \tag{3.13}$$

where the spectral index $n = 4/3$ when the small-scale structure is dominated by cusps [277, 285, 346], $n = 5/3$ for kink domination [285], or $n = 2$ for kink-kink collision domination [344, 345]. A discussion on how to read information about the small-scale structure of CS from the GW spectrum, is given in App. B.3.7. In particular, we show that the high-frequency slope of the GW spectrum in the presence of an early matter era, a second period inflation, particle production or network formation, which is expected to be f^{-1} from the fundamental, $k = 1$, GW spectrum alone, is actually given by f^{1-n}. Immediately after a loop gets created, at time t_i with a length $\alpha\, t_i$, its length $l(\tilde{t})$ shrinks through emission of GW with a rate $\Gamma G\mu$

$$l(\tilde{t}) = \alpha t_i - \Gamma G\mu(\tilde{t} - t_i). \tag{3.14}$$

Consequently, the string lifetime due to decay into GW is given by

$$\tau_{\rm GW} = \frac{\alpha\, t_i}{\Gamma G\mu}. \tag{3.15}$$

The superposition of the GW emitted from all the loops formed since the creation of the long-string network generates a SGWB. Also, cusp formations can emit high-frequency, short-lasting GW bursts [284, 285, 344, 345, 347]. If the rate of such events is lower than their frequency, they might be subtracted from the SGWB.

Goldstone boson radiation (global strings): For global strings, the massless Goldstone particle production is the main decay channel. The radiation power has been estimated [301]

$$P_{\rm Gold} = \Gamma_{\rm Gold}\, \eta^2, \tag{3.16}$$

where η is the scalar field VEV and $\Gamma_{\rm Gold} \approx 65$ [199, 348]. We see that the GW emission power in Eq. (3.10) is suppressed by a factor $G\mu$ with respect to the Goldstone emission power in Eq. (3.16). Therefore, for global strings, the loops decay into Goldstone bosons after a few oscillations before having the time to emit much GW [301, 349]. However, as shown in Sec. 3.6, the SGWB from global string is detectable for large values of the string scale, $\eta \gtrsim 10^{14}$ GeV. Other recent studies of GW spectrum from global strings in standard and non-standard cosmology include [199, 350–352]. A well-motivated example of a global string is the axion string coming from the breaking of a $U(1)$ Peccei-Quinn symmetry [195, 197, 331, 348, 353–357]. Ref. [351] shows the detectability of the GW from the axionic network of QCD axion Dark Matter (DM) after introducing an early-matter era that dilutes the axion DM abundance and increases the corresponding Peccei-Quinn scale η.

Massive particle radiation: When the string curvature size is larger than the string thickness, one expects the quantum field nature of the CS, e.g., massive particle radiation (a constituent of string), to give negligible effects. One may instead consider the CS as an infinitely thin 1-dimensional classical object with tension μ: the Nambu-Goto (NG) string. This statement, however, fails once the string interaction is enhanced. For example, an additional scalar – coupled to the string's scalar – can boost the perturbative decay rate for the cubic [358] and quartic [359] couplings. The coupling to fermions and gauge fields have also been studied, e.g., in the context of [180, 360]. These massive radiation from CS could interestingly source the non-thermal DM or Baryon Asymmetry of the Universe [180, 195–197, 358–365]. Since this enhanced perturbative particle emission becomes one of the main energy-loss mechanisms, it leads to the cut-off in the GW spectrum, similar to the non-perturbative emission discussed in the next paragraph. We leave the analysis of prospects for probing additional CS couplings and their phenomenology via GW signatures for future work[5].

Moreover, due to small-scale structures on the strings, regions with curvature comparable to the string core size can develop, and the Nambu-Goto approximation breaks down. In that case, massive radiation can be emitted non-perturbatively during processes known as cusp annihilation [366, 367] or kink-kink collisions [368]. We discuss non-perturbative massive-particle emission in more details in Sec. 3.2.1.

3.1.4 Constraints on the string tension from GW emission

The observational signatures of Nambu-Goto cosmic strings are mainly gravitational. The GW emission can be probed by current and future pulsar timing arrays and GW interferometers, while CMB, 21 cm, and lensing observables can investigate the static gravitational field around the string; see app. B.2 for more details on non-GW probes. The strongest constraints come from pulsar timing array EPTA, $G\mu \lesssim 8 \times 10^{-10}$ [369], and NANOGrav, $G\mu \lesssim 5.3 \times 10^{-11}$ [370]. Comparison with the theoretical predictions from the SGWB from cosmic strings leads to $G\mu \lesssim 2 \times 10^{-11}$ [295, 341] or $G\mu \lesssim 10^{-10}$ [345], even though it can be relaxed to $G\mu \lesssim 5 \times 10^{-7}$ [287], after taking into account uncertainties on the loop size at formation and on the number of emitting modes. Note that it can also be strengthened by decreasing the inter-commutation probability [289, 371, 372].

By using the EPTA sensitivity curve derived in [201], we obtain the upper bound on $G\mu$, one order of magnitude higher, 2×10^{-10}, instead of 2×10^{-11}, cf. Fig. 3.4. This bound becomes $\sim 5 \times 10^{-11}$ by using the NANOGrav sensitivity curve derived in [201]. Another significant source of uncertainty is the nature of the GW spectrum generated by a loop, which depends on the assumption of the small-scale loop structure (e.g., the number of cusps, kinks, and kink-kink

[5] Many thanks go to Bibhushan Shakya regarding this future work.

collisions per oscillations) [289, 345]. For instance, the EPTA bound can be strengthened to $G\mu \lesssim 6.7 \times 10^{-14}$ if the loops contain many kinks [345]. CS can also emit highly-energetic and short-lasting GW bursts due to cusp formation [284, 285, 344, 345, 347]. From the non-observation of such events with LIGO/VIRGO/KAGRA [373–375], one can constrain $G\mu \lesssim 10^{-10}$ with the loop distribution function from [376]. However, the constraints are completely relaxed with the loop distribution function from [194].

Interestingly, the recent PTA observations of the red-noise process – that is common to all observed pulsars – suggest the presence of SGWB within the (1–10 nHz) frequency band and with $\Omega_{\rm GW} \sim 10^{-9 \div -11}$ [204–206, 261]. The SGWB from the simple NG CS with $G\mu \sim 10^{-10 \div -11}$ explains the signal well while still satisfying other bounds. Nonetheless, the smoking-gun signature for identifying the SGWB is still inconclusive, namely the *spatial quadrupole (Hellings-Downs)* correlation [262]. The next observation runs with more pulsars should clarify the nature of these red-noise processes. We refer the reader to Sec. 2.6 for more details on these interesting observations.

3.2 Gravitational Waves from Local Cosmic Strings

In this section, we do not consider the case of global strings where the presence of a massless Goldstone in the spectrum implies that particle production is the main energy loss so that GW emission is suppressed [301, 348]. However, in detail, we discuss the GW spectrum from global strings in Sec. 3.6, which can be detectable for string scales $\eta \gtrsim 10^{14}$ GeV. Other studies of the sensitivity of next-generation observatories to GW from global strings are [199, 350–352, 357].

There has been a long debate in the community whether local cosmic strings mainly lose their energy via GW emission or by particle production. We summarise the arguments and clarify the underlying assumptions below.

3.2.1 Beyond the Nambu-Goto approximation

Quantum field string simulations. Field-theoretic string (Abelian-Higgs) lattice simulations run by Hindmarsh et al. [377–379] have shown that decay into massive radiation is the primary energy loss and is sufficient to lead to scaling. Then, loops decay within one Hubble time into scalar and gauge boson radiation before having the time to emit GW. It is suggested that the presence of small-scale structures, kinks, and cusps at the string core size are responsible for the energy loss in particle production. In these regions of large string curvature, the Nambu-Goto approximation, which considers CS as infinitely thin 1-dimensional classical objects, is no longer valid.

However, Abelian-Higgs simulations run by [380–382] have claimed the opposite result, that energy loss into massive radiation is exponentially suppressed when the loop size is large compared to the thickness of the string.

Small-scale structure. At formation time, loops are not smooth but made of straight segments linked by kinks [383]. Kinks are also created in pairs after each string intercommutation, see [384] or Fig. 2.1 in [385]. The presence of straight segments linked by kinks prevents the formation of cusps. However, backreaction from GW emission smoothens the shapes, hence allowing for the formation of cusps [383] (see Fig. 3.1). Because of the large hierarchy between the gravitational backreaction scale and the cosmological scale H, the effects of the gravitational backreaction on the loop shape are not easily tractable numerically. The effects of backreaction from particle emission are shown in [384]. Nevertheless, it has been proposed since long [386] that the small-scale structures are smoothened below the gravitational backreaction scale $\sim \Gamma G\mu t$,. Particularly, based on analytical modeling on simple loop models, it has been shown in [387, 388] that due to gravitational backreaction, kinks get rounded off, become closer to cusps, and then cusps get weakened. In earlier works, the same authors [389, 390] claimed that whether the smoothening has the time

to occur within the loop lifetime strongly depends on the initial loop shape. In particular, for a four-straight-segment loop, the farther from the square shape, the faster the smoothening, whereas for more general loop shapes, the smoothening may not always occur.

To summarize the last two paragraphs, the efficiency of the energy loss into massive radiation depends on the nature of the small-scale structure, which can be understood as a correction to the Nambu-Goto approximation. The precise nature of the small-scale structure, its connection with the gravitational backreaction scale, and the conflict between Nambu-Goto and Abelian Higgs simulations remain to be explained. Moreover, the value of the gravitational backreaction scale itself, see Sec. 3.2.2 is a matter of debate. For our study, we follow the proposal of [391] for investigating how the GW spectrum is impacted for two benchmark scenarios: when cusps dominate the small-scale structures or when kinks dominate them. We will give more details in the next paragraph. In App. B.3.7, we show that if the high-frequency slope of the fundamental, $k = 1$, GW spectrum is f^{-1}, as expected in presence of an early matter era or in presence of an Heaviside cut-off in the loop formation time, then the existence of the high-k modes, turns it to $f^{-1} \to f^{1-n}$, where n, defined in Eq. (3.13), depends on the small-scale structure. We can therefore read information about the small-scale structure of CS from the high-frequency GW spectrum.

Massive radiation emission. In the vicinity of a cusp, the topological charge vanishes where the string cores overlap. Hence, the corresponding portions of the string can non-perturbatively decay into massive radiation. The length of the overlapping segment has been estimated to be $\sqrt{rl}$ [366, 367, 392] where $r \simeq \mu^{-1/2}$ is the string core size and l is the loop length. Hence, the energy radiated per cusp formation is $\mu\sqrt{rl}$, from which we deduce the power emitted from a loop

$$P_{\rm cusp}^{\rm part} \simeq N_{\rm c} \frac{\mu^{3/4}}{l^{1/2}}, \tag{3.17}$$

where $N_{\rm c}$ is the average number of cusps per oscillation, estimated to be $N_{\rm c} \sim 2$ [383]. Note that the consideration of pseudo-cusps, pieces of string moving at highly relativistic velocities, might also play a role [393, 394].

Even without the presence of cusps, Abelian-Higgs simulations [368] have shown that kink-kink collisions produce particles with a power per loop

$$P_{\rm kink}^{\rm part} \simeq N_{\rm kk} \frac{\epsilon}{l}, \tag{3.18}$$

where $N_{\rm kk}$ is the average number of kink-kink collisions per oscillation. Values possibly as large as $N_{\rm kk} \sim O(10^3)$ have been considered in [345] or even as large as 10^6 for the special case of strings with junctions [395], due to kink proliferations [396]. In contrast to the cusp case, the energy radiated per kink-kink collision, ϵ, is independent of the loop size l, and we expect $\epsilon \sim \mu^{1/2}$.

Upon comparing the power of GW emission in Eq. (3.10) with either Eq. (3.17) or (3.18), one expects gravitational production to be more efficient than particle production when loops are larger than [391]

$$l \gtrsim l_c \equiv \beta_c \frac{\mu^{-1/2}}{(\Gamma G \mu)^2}, \tag{3.19}$$

for small-scale structures dominated by cusps, and

$$l \gtrsim l_k \equiv \beta_k \frac{\mu^{-1/2}}{\Gamma G \mu}, \tag{3.20}$$

for kink-kink collision domination. $\beta_{\rm c}$ and $\beta_{\rm k}$ are numbers which depend on the precise refinement. We assume $\beta_{\rm c}$, $\beta_{\rm k} \sim O(1)$. Therefore, loops with length smaller than the critical value in Eq. (3.19) or (3.20) are expected to decay into massive radiation before they have time to emit GW, which means that they should be subtracted when computing the SGWB. Eqs. (3.19) and (3.20) are crucial to determine the cutoff frequency, as we discuss in Sec. 3.2.5.

The cosmological and astrophysical consequences of the production of massive radiation and the corresponding constraints on CS from different experiments are presented in Sec. B.2.4.

3.2.2 Assumptions on the loop distribution

The SGWB resulting from the emission by CS loops strongly relies on the distribution of loops. In the present section, we introduce the loop-formation efficiency and discuss the assumptions on the loop-production rate, inspired by Nambu-Goto simulations. The loop-formation efficiency is computed later, in Sec. 3.3.

Loop-formation efficiency. The equation of motion of a long Nambu-Goto string in a expanding Universe implies the following evolution equation for the long string energy density, cf. Sec. B.5

$$\frac{d\rho_\infty}{dt} = -2H(1+\bar{v}^2)\rho_\infty - \left.\frac{d\rho_\infty}{dt}\right|_{\rm loop}, \tag{3.21}$$

where $\bar{v}$ is the long string mean velocity. The energy loss into loop formation can be expressed as [301]

$$\left.\frac{d\rho_\infty}{dt}\right|_{\rm loop} \equiv \mu \int_0^\infty l f(l,t) dl \equiv \frac{\mu}{t^3}\tilde{C}_{\rm eff}, \tag{3.22}$$

with $f(l,t)$ the number of loops created per unit of volume, per unit of time t and per unit of length l and where we introduced the loop-formation efficiency $\tilde{C}_{\rm eff}$. The loop-formation efficiency $\tilde{C}_{\rm eff}$ is related to the notation introduced in [294, 295] by

$$\tilde{C}_{\rm eff} \equiv \sqrt{2}\, C_{\rm eff}. \tag{3.23}$$

In Sec. 3.3, we compute the loop-formation efficiency $C_{\rm eff}$ as a function of the long string network parameters $\bar{v}$ and L, which themselves are solutions of the Velocity-dependent One-Scale (VOS) equations.

Only loops produced at the horizon size contribute to the SGWB. As pointed-out a long time ago by [186, 386] and more recently in large Nambu-Goto simulations [194], the most numerous loops are the ones of the size of the gravitational backreaction scale

$$\Gamma G\mu \times t, \tag{3.24}$$

which acts as a cut-off below which, small-scale structures are smoothened and such that smaller loops cannot be produced below that scale. However, it has been claimed that only large loops are relevant for GW [194, 284, 397]. In particular, Nambu-Goto numerical simulations realized by Blanco-Pillado et al. [194] have shown that a fraction $\mathcal{F}_\alpha \simeq 10\%$ of the loops are produced with a length equal to a fraction $\alpha \simeq 10\%$ of the horizon size, and with a Lorentz boost factor $\gamma \simeq \sqrt{2}$. The remaining 90% of the energy lost by long strings goes into highly boosted smaller loops whose contributions to the GW spectrum are sub-dominant. Under those assumptions, the number of loops, contributing to the SGWB, produced per unit of time can be computed from the total energy flow into loops in Eq. (3.22)

$$\frac{dn}{dt_i} = \frac{\mathcal{F}_\alpha}{\gamma\mu\alpha t_i}\left.\frac{d\rho_\infty}{dt}\right|_{\rm loop}, \tag{3.25}$$

with $\mathcal{F}_\alpha = 0.1$, $\gamma = \sqrt{2}$ and $\alpha = 0.1$. In App. B.7.2, we discuss the possibility to define the loop-size as a fixed fraction of the correlation length L instead of a fixed fraction of the horizon size t. Especially, we show that the impact on the GW spectrum is negligible. The latter can be recast as a function of the loop-formation efficiency $\tilde{C}_{\rm eff}$ defined in Eq. (3.22)

$$\frac{dn}{dt_i} = \mathcal{F}_\alpha \frac{\tilde{C}_{\rm eff}(t_i)}{\gamma\,\alpha\, t_i^4}. \tag{3.26}$$

This is equivalent to choosing the following *monochromatic horizon-sized loop-formation* function

$$f(l,\, t_i) = \frac{\tilde{C}_{\rm eff}}{\alpha\, t_i^4}\delta(l - \alpha t_i), \tag{3.27}$$

where δ is the delta function. The assumptions leading to Eq. (3.26) are the ones we followed for our study and which are also followed by [294, 295]. Our results strongly depend on these assumptions and would be dramatically impacted if, instead, we consider the model discussed in the next paragraph.

A second population of smaller loops. The previous assumption – that the only loops relevant for the GW signal are the loops produced at horizon size – which is inspired by the Nambu-Goto numerical simulations of Blanco-Pillado et al. [194, 398], conflicts with the results from Ringeval et al. [345, 376, 399]. In the latter works, the loop production function is derived analytically starting from the correlator of tangent vectors on long strings, within the Polchinski-Rocha model [400–403]. In the Polchinski-Rocha model, which has been tested in Abelian-Higgs simulations [378], the gravitational back-reaction scale, i.e., the lower cut-off of the loop production function, is computed to be

$$\Upsilon (G\mu)^{1+2\chi} \times t, \tag{3.28}$$

with $\Upsilon \simeq 10$ and $\chi \sim 0.25$. Consequently, the gravitational back-reaction scale in the Polchinski-Rocha model is significantly smaller than the usual gravitational back-reaction scale, commonly assumed to match the gravitational radiation scale, $\Gamma G\mu\, t$. Therefore, the model of Ringeval et al. predicts the existence of a second population of smaller loops which enhances the GW spectrum at high frequencies by many orders of magnitude [345]. However, as raised by [404], the model of Ringeval et al. predicts the amount of long-string energy converted into loops to be ~ 200 times larger than the one computed in the numerical simulations of Blanco-Pillado et al. [194]. These discrepancies between Polchinski-Rocha analytical modeling and Nambu-Goto numerical simulations remain to be understood.

3.2.3 The gravitational-wave spectrum

For our study, we compute the GW spectrum observed today generated from CS as follows (see app. B.3 for a derivation)

$$\Omega_{\rm GW}(f) \equiv \frac{f}{\rho_c}\left|\frac{d\rho_{\rm GW}}{df}\right| = \sum_k \Omega^{(k)}_{\rm GW}(f), \tag{3.29}$$

where

$$\Omega^{(k)}_{\rm GW}(f) = \frac{1}{\rho_c}\cdot\frac{2k}{f}\cdot\frac{\mathcal{F}_\alpha\,\Gamma^{(k)}G\mu^2}{\alpha(\alpha+\Gamma G\mu)}\int_{t_{\rm osc}}^{t_0} d\tilde{t}\,\frac{C_{\rm eff}(t_i)}{t_i^4}\left[\frac{a(\tilde{t})}{a(t_0)}\right]^5\left[\frac{a(t_i)}{a(\tilde{t})}\right]^3\Theta(t_i-t_{\rm osc})\Theta(t_i-\frac{l_*}{\alpha}), \tag{3.30}$$

with

Θ $\equiv$ Heaviside function,

μ, G, ρ_c $\equiv$ string tension, Newton constant, critical density,

a $\equiv$ scale factor of the Universe
(we solve the full Friedmann equation for a given energy density content),

k $\equiv$ proper mode number of the loop (effect of high-k modes are discussed in App. B.3.7.
For technical reasons, in most of our plots, we restrict to 2×10^4 modes),

Γ $\equiv$ gravitational loop-emission efficiency, ($\Gamma\simeq50$ [398])

$\Gamma^{(k)}$ $\equiv$ Fourier modes of Γ, dependent on the loop small-scale structures,
($\Gamma^{(k)}\propto k^{-4/3}$ for cusps, e.g., [285]),

$\mathcal{F}_\alpha$ $\equiv$ fraction of loops formed with size α ($\mathcal{F}_\alpha\simeq0.1$), cf. Sec. 3.2.2,

$C_{\rm eff}$ $\equiv$ loop-production efficiency, defined in Eq. (3.39),
($C_{\rm eff}$ is a function of the long-string mean velocity $\bar{v}$ and correlation length ξ,
both computed upon integrating the VOS equations, cf. Sec. 3.3)

α $\equiv$ loop length at formation in unit of the cosmic time, ($\alpha\simeq0.1$)
(we consider a monochromatic, horizon-sized loop-formation function, cf. Sec. 3.2.2),

$\tilde{t}$ $\equiv$ the time of GW emission,

f $\equiv$ observed frequency today
(related to frequency at emission $\tilde{f}$ through $f\,a(t_0)=\tilde{f}\,a(\tilde{t})$,
related to loop length l through $\tilde{f}=2k/l$,
related to the time of loop production t_i through $l=\alpha t_i-\Gamma G\mu(\tilde{t}-t_i)$),

t_i $\equiv$ the time of loop production,
(related to observed frequency and emission time $\tilde{t}$ through
$t_i(f,\tilde{t})=\frac{1}{\alpha+\Gamma G\mu}\left[\frac{2k}{f}\frac{a(\tilde{t})}{a(t_0)}+\Gamma G\mu\,\tilde{t}\right]$),

t_0 $\equiv$ the time today,

$t_{\rm osc}$ $\equiv$ the time at which the long strings start oscillating, $t_{\rm osc}=\mathrm{Max}[t_{\rm fric},\,t_F]$,
t_F is the time of CS network formation, defined as $\sqrt{\rho_{\rm tot}(t_F)}\equiv\mu$ where $\rho_{\rm tot}$ is
the Universe total energy density. In presence of friction, at high temperature,
the string motion is damped until the time $t_{\rm fric}$, computed in app. B.5.4,

l_* $\equiv$ $l_{\rm c}$ for cusps and $l_{\rm k}$ for kinks in Eq. (3.19) and Eq. (3.20)
(critical length below which the emission of massive radiation
is more efficient than the gravitational emission, cf. Sec. 3.2.1).

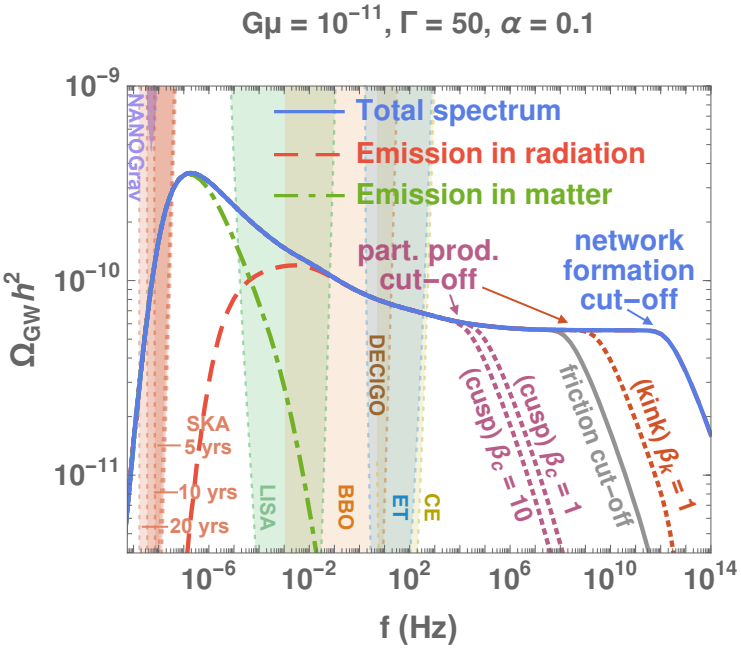

Figure 3.2: GW spectrum from the scaling cosmic-string network evolving in a standard cosmology. Contributions from GW emitted during radiation and matter eras are shown with red and green dashed lines respectively. The high-frequency cut-offs correspond to either the time of formation of the network, cf. Eq. (3.4), the time when friction-dominated dynamics become irrelevant, cf. App. B.5.4, or the time when gravitational emission dominates over massive particle production, for either kink or cusp-dominated small-scale structures, cf. Sec. 3.2.1. The cut-offs are described by Heaviside functions in the master formula in Eq. (3.29). In App. B.3.7, we show that the slopes beyond the high-frequency cut-offs are given by $f^{-1/3}$. Colored regions indicate the integrated power-law sensitivity of future experiments, as described in Sec. 2.5.

A first look at the GW spectrum. Fig. 3.2 shows the GW spectrum computed with Eq. (3.29). The multiple frequency cut-offs follow from the Heaviside functions in Eq. (3.29), subtracting loops formed before network formation, cf. Eq. (3.4), or when thermal friction freezes the network, cf. App. B.5.4, or subtract loops decaying via massive particle emission from cusps and kinks instead of GW, cf. Sec. 3.2.1. We indicate separately the contributions from the emission occurring before and after the matter-radiation equality. One can see that loops emitting during the radiation era contribute to a flat spectrum, whereas loops emitting during the matter era lead to a slope decreasing as $f^{-1/3}$. Similarly, the high-frequency cut-offs due to particle production, thermal friction, and network formation, but also due to the second period of inflation (discussed in Sec. 4.6), give a slope $f^{-1/3}$. In App. B.3.7, we show that the presence of high-frequency modes are responsible for changing the slope f^{-1}, expected from the $(k = 1)$-spectrum, to $f^{-1/3}$.

3.2.4 Impact of the cosmology on the GW spectrum

The frequency dependence of the GW spectrum receives two contributions: a red tilt from the redshift of the GW energy density and a blue tilt from the loop-production rate $\propto t_i^{-4}$. On the one hand, the higher the frequency, the earlier the GW emission, so the larger the redshift of the GW energy density and the more suppressed the spectrum. On the other hand, high frequencies correspond to loops formed earlier, those being more numerous; this increases the GW amplitude. Interestingly, during radiation domination, the two contributions cancel such that the spectrum is flat.

Concretely, the GW spectrum from the master formula, Eq. (3.30), depends on GW frequency

as

$$\Omega_{\rm GW}^{\rm local} \propto f^{-1}\,\tilde{t}\,t_i^{-4}\,a^2(\tilde{t})\,a^3(t_i) \propto f^{\beta}, \text{ with } \beta = 2\left[\frac{3m+n-nm}{n(2-m)}\right], \tag{3.31}$$

where we assume that the formation and the emission happen when the universe is dominated by the energy densities $\rho \propto a^{-n}$ and a^{-m}, respectively. The emission time and the loop formation time are related to frequency via Eq. (3.32): $t_i, \tilde{t}_M \propto f^{m/(2-m)}$. The flatness of the GW spectrum during radiation is intimately related to the independence of the GW emission power on the loop length. As the main topic of Chap. 4, a change in the equation of state of the Universe impacts the GW spectrum because it modifies the two following redshift factors: the redshift of the number of emitting loops and the redshift of the emitted GW.

For instance, when GW emission occurs during radiation $(m = 4)$ but loop formation occurs during matter $(n = 3)$, the loop density redshifts faster. Then, the larger the frequency, the earlier the loop formation, and the more suppressed the GW spectrum (as f^{-1} for $k = 1$ and as $f^{-1/3}$ when including high-k modes cf. App. B.3.7). Conversely, if loop formation occurs during kination, the loop density redshift slower, and the GW gets enhanced at a large frequency (as f^1).

Lastly, we would like to mention that Eq. (3.31) is valid for $\beta \geq -1$. Since the SGWB from the string network is contributed by various loop populations. Discussed in App. B.3.6, the spectrum from a single population has the UV tail with slope -1. So if the peak contributions (at $\tilde{t} = \tilde{t}_M$) lead to $\beta < -1$, the resulting final spectrum is dominated by the UV tail of the loop population produced at the latest time and thus has the slope of -1 for each $k^{\rm th}$ mode (and $-1/3$ when summing higher harmonics).

3.2.5 The frequency–temperature relation

In App. B.4, it is argued that most of loops – created at time t_i – decay at much later time: $\tilde{t}_M \simeq (\alpha/2\Gamma G\mu)t_i$. Their coresponding GW has the frequency today f related to the loop length $\alpha t_i/2$,

$$\left(\frac{2}{f}\right)\left[\frac{a(\tilde{t}_M)}{a(t_0)}\right] = \frac{\alpha t_i}{2} \quad \Rightarrow \quad f = \frac{4}{\alpha t_i}\left[\frac{a(\tilde{t}_M)}{a(t_0)}\right], \tag{3.32}$$

where the fundamental mode is considered here. The delay in GW emission leads to the non-trivial relation between the GW frequency today and the temperature of the Universe when the loops, mostly responsible for f, are formed

$$f \simeq (6.7\times10^{-2}\ \text{Hz})\left(\frac{T}{\text{GeV}}\right)\left(\frac{0.1\times50\times10^{-11}}{\alpha\,\Gamma G\mu}\right)^{1/2}\left(\frac{g_*(T)}{g_*(T_0)}\right)^{1/4}. \tag{3.33}$$

We emphasize that Eq. (3.33) is very different from the relation obtained in the case of GW generated by a first-order cosmological phase transition. In the latter case, the emitted frequency corresponds to the Hubble scale at T_p [31]

$$f_{\rm FOPT} \simeq (19\times10^{-3}\ \text{mHz})\left(\frac{T_p}{100\ \text{GeV}}\right)\left(\frac{g_*(T_p)}{100}\right)^{1/4}. \tag{3.34}$$

In the case of cosmic strings, instead of being set by the Hubble scale at the loop-formation time t_i, the emitted frequency is further suppressed by a factor $(\Gamma G\mu)^{-1/2}$, which we now explain. From the scaling law $\propto t_i^{-4}$ of the loop-production function in Eq.(3.26), one can understand that the most numerous population of emitting loops at a given time $\tilde{t}$ is the population of loops created at the earliest epoch. They are the oldest loops[6]. Hence, a loop created at time t_i contributes to the SGWB much later, at a time given by the loop half-lifetime $\tilde{t}_{\rm M} = \alpha\, t_i/2\Gamma G\mu$, cf. Eq. (3.15). Therefore, the

[6]Note that they are also the smallest loops, with a length given by the gravitational radiation scale $\Gamma G\mu\, t$.

emitted frequency is dispensed from the redshift factor $a(\tilde{t}_{\rm M})/a(t_i) = (\tilde{t}_{\rm M}/t_i)^{1/2} \sim (\Gamma G\mu)^{-1/2}$, and so, is higher. See App. B.4 and its Fig. B.5 for more details.

Another striking consequence is that the formation cut-off in Eq. (3.5) (depicted in Fig. 2.5) is $G\mu$-independent. Indeed, string networks with smaller $G\mu$ are formed at later times, but the associated loops decay much slower. By varying $G\mu$, the GW frequency today remains constant by the compensation of a smaller redshift.

The detection of a non-standard cosmology: During a cosmology change, e.g., from a matter to a radiation-dominated era, the long-string network evolves from one scaling regime to the other. The network's response to the change in cosmology is quantified by the VOS equations, which are presented in Sec. 3.3. As a result of the transient evolution towards the new scaling regime, the turning-point frequency Eq. (B.51) associated with the change of cosmology is lower in VOS than in the scaling network. The detection of a turning point in a GW spectrum from CS by a future interferometer would be a smoking-gun signal for non-standard cosmology, as we shall discuss in Chap. 4. Notably, in Fig. 4.5, we show that LISA can probe a non-standard era ending around the QCD scale, ET/CE can probe a non-standard period ending around the TeV scale, whereas DECIGO/BBO can probe the intermediate range. We show examples of a long-lasting era in Sec. 4.3. We focus on the case of a short matter era in Sec. 4.5 and a short inflation era in Sec. 4.6, respectively. In the latter case, the turning-point frequency is further decreased due to the string stretching, which we explain in the next paragraph.

The detection of a non-standard cosmology (intermediate-inflation case): If the Universe undergoes a period of inflation lasting N_e e-folds, the correlation length of the network is stretched outside the horizon. After inflation, the network achieves a long transient regime lasting $\sim N_e$ other e-folds until the correlation length re-enters the horizon. Hence, the turning-point frequency in the GW spectrum, cf. Eq. (4.39), receives a $\exp(N_e)$ suppression compared to Eq. (3.33) due to the duration of the transient. We give more details in Sec. 4.6.

Cut-off frequency from particle production: As discussed in the Sec. 3.2.1, particle production is the main decay channel of loops shorter than

$$l_* = \beta_m \frac{\mu^{-1/2}}{(\Gamma G\mu)^m}, \tag{3.35}$$

where $m = 1$ or 2 for loops kink-dominated or cusp-dominated, respectively, and $\beta_m \sim \mathcal{O}(1)$. The corresponding characteristic temperature above which loops, decaying preferentially into particles, are produced, is

$$T_* \simeq \beta_m^{-1/2}\,\Gamma^{m/2}\,\sqrt{\alpha}\,(G\mu)^{(2m+1)/4}\,M_{\rm pl} \simeq \begin{cases} (0.2\text{ EeV})\,\sqrt{\dfrac{\alpha}{0.1}}\,\sqrt{\dfrac{1}{\beta_c}}\left(\dfrac{G\mu}{10^{-15}}\right)^{3/4} & \text{for kinks,} \\ (1\text{ GeV})\,\sqrt{\dfrac{\alpha}{0.1}}\,\sqrt{\dfrac{1}{\beta_k}}\left(\dfrac{G\mu}{10^{-15}}\right)^{5/4} & \text{for cusps.} \end{cases} \tag{3.36}$$

We have used $l_* = \alpha\, t_i$, $H = 1/(2t_i)$ and $\rho_{\rm rad} = 3M_{\rm pl}^2 H^2$. Upon using the frequency-temperature correspondence in Eq. (3.33), we get the cut-off frequencies due to particle production

$$f_* \simeq \begin{cases} (1\text{ GHz})\,\sqrt{\dfrac{1}{\beta_c}}\left(\dfrac{G\mu}{10^{-15}}\right)^{1/4} & \text{for kinks,} \\ (31\text{ Hz})\,\sqrt{\dfrac{1}{\beta_k}}\left(\dfrac{G\mu}{10^{-15}}\right)^{3/4} & \text{for cusps.} \end{cases} \tag{3.37}$$

and which we show in most of our plots with dotted red and purple lines. Particularly, in Fig. 3.5, we see that particle production in the cusp-dominated case would start suppressing the GW signal in the ET/CE windows for string tension lower than $G\mu \lesssim 10^{-15}$. However, in the kink-dominated case, the spectrum is only impacted at frequencies much higher than the interferometer windows. In App. B.3.7, we show that the slope of the GW spectrum beyond the high-frequency cut-off f_* is given by $f^{-1/3}$.

3.3 The Velocity-dependent One-Scale (VOS) Model

The master formula (3.29) crucially depends on the loop-production efficiency encoded in $C_{\rm eff}$. In this section, we discuss its derivation within the framework of the Velocity-dependent One-Scale (VOS) model [405–408].

3.3.1 The loop-production efficiency

In a correlation volume L^3, a segment of length L must travel a distance L before encountering another segment. L is the correlation length of the long-string network. The collision rate, per unit of volume, is $\frac{\bar{v}}{L} \cdot \frac{1}{L^3} \sim \frac{\bar{v}}{L^4}$ where $\bar{v}$ is the long-string mean velocity. At each collision forming a loop, the network looses a loop energy $\mu L = \rho_\infty L^3$. Hence, the loop-production energy rate can be written as [184]

$$\left.\frac{d\rho_\infty}{dt}\right|_{\rm loop} = \tilde{c}\,\bar{v}\frac{\rho_\infty}{L}, \tag{3.38}$$

where one can compute $\tilde{c} = 0.23 \pm 0.04$ from Nambu-Goto simulations in expanding Universe [407]. $\tilde{c}$ is the only free parameter of the VOS model. Hence, the loop-formation efficiency, defined in Eq. (3.22), can be expressed as a function of the long-string parameters, $\bar{v}$ and $\xi \equiv L/t$,

$$\tilde{C}_{\rm eff} \equiv \sqrt{2}\,C_{\rm eff}(t) = \frac{\tilde{c}\,\bar{v}(t)}{\xi^3(t)}. \tag{3.39}$$

In app. B.6, we discuss how our results are changed when considering a recent extension of the VOS model with more free parameters, fitted on Abelian-Higgs field theory numerical simulations [409], and taking into account the emission of massive radiation. Basically, the loop-formation efficiency $C_{\rm eff}$ is only decreased by a factor ~ 2. In the following, we derive $\bar{v}$ and ξ as solutions of the VOS equations.

3.3.2 The VOS equations

The VOS equations describe the evolution of a network of long strings in term of the mean velocity $\bar{v}$ and the correlation length $\xi = L/t$ [405–408]. The latter is defined through the long string energy density $\rho_\infty \equiv \mu/L^2$. Starting from the equations of motion of the Nambu-Goto string in a FRW Universe, we can derive the so-called VOS equations (see app. B.5 for a derivation)

$$\frac{dL}{dt} = HL\,(1+\bar{v}^2) + \frac{1}{2}\tilde{c}\,\bar{v}, \tag{3.40}$$

$$\frac{d\bar{v}}{dt} = (1-\bar{v}^2)\left[\frac{k(\bar{v})}{L} - 2H\bar{v}\right], \tag{3.41}$$

$$\text{where} \qquad k(\bar{v}) = \frac{2\sqrt{2}}{\pi}(1-\bar{v}^2)(1+2\sqrt{2}\bar{v}^3)\frac{1-8\bar{v}^6}{1+8\bar{v}^6}, \tag{3.42}$$

is the so-called momentum parameter and is a measure of the deviation from the straight string, for which $k(\bar{v}) = 1$ [408]. The first VOS equation describes the evolution of the long string correlation length under the effect of Hubble expansion and loop chopping. The second VOS equation is

nothing more than a relativistic generalization of Newton's law, where the string is accelerated by its curvature $1/L$ but is damped by the Hubble expansion after a typical length H^{-1}.

Numerical simulations [189–193] have shown that a network of long strings is first subject to a transient regime before reaching a scaling regime, in which the long string mean velocity $\bar{v}$ is constant. The correlation length grows linearly with the Hubble horizon $L = \xi\, t$. The values of the quantities $\bar{v}$ and ξ depend on the cosmological background, namely the equation of state of the Universe. Hence, when passing from a cosmological era #1 to era #2, the network accomplishes a transient evolution from the scaling regime #1 to the scaling regime #2. We use the VOS equations to compute the time evolution of $\bar{v}$ and ξ during cosmology change and then compute their impact on the CS SGWB.

3.3.3 Scaling regime solution and beyond

Scaling solution vs. VOS solution: Fig. 3.3 shows the evolutions of ξ, $\bar{v}$, and $C_{\rm eff}$, from solving the VOS equations in Eq. (3.40) with three equations of state: matter, radiation and kination. Regardless of the initial-condition choice, the network approaches a scaling solution where all parameters become constant. The energy scale of the Universe has to decrease by some 4 orders of magnitude before reaching the scaling regime after the network formation. For a cosmological background evolving as $a \propto t^{2/n}$ with $n \geq 2$, the scaling regime solution is

$$\xi = \frac{n}{2}\sqrt{\frac{k(\bar{v})[k(\bar{v})+\tilde{c}]}{2(n-2)}} = \text{constant}, \quad \bar{v} = \sqrt{\frac{n}{2}\frac{k(\bar{v})}{[k(\bar{v})+\tilde{c}]}\left(1-\frac{2}{n}\right)} = \text{constant}. \tag{3.43}$$

In order to fix the notation used in our plots, we define

- **(Instantaneous) scaling network**: The loop-formation efficiency $C_{\rm eff}$, defined in Eq. (3.39), is taken at its steady state value, given by Eq. (3.43). In particular for matter, radiation and kination domination, one has

$$C_{\rm eff} \simeq 0.39,\ 5.4,\ 29.6 \qquad \text{for} \quad n = 3,\ 4,\ 6. \tag{3.44}$$

  During a change of era #1→#2, $C_{\rm eff}$ is assumed to change instantaneously from the scaling regime of era #1 to the scaling regime of era #2. This is the assumption adopted in [294, 295].

- **VOS network**: The loop-formation efficiency $C_{\rm eff}$, defined in Eq. (3.39), is computed upon integrating the VOS equations in Eq. (3.40). During a change of cosmology, the long-string network experiences a transient regime.

In Fig. 3.4 and Fig. 3.5, we compare the GW spectra and the $C_{\rm eff}$ evolution, obtained with a scaling and VOS network. They are quite similar. The main difference arises from relativistic degrees of freedom change near the QCD confining temperature and from the matter-radiation transition. In contrast, predictions differ significantly when considering non-standard cosmology in Chap. 4. In Fig. 4.4, in dashed vs. solid, we compare the loop-production efficiency factor $C_{\rm eff}$ and the corresponding GW spectra for a scaling network and a VOS network. The VOS frequency of the turning point due to the change of cosmology is shifted to a lower frequency by a factor ~ 22.5 with respect to the corresponding scaling frequency[7]. The shift results from the extra time needed by the network's transient evolution to the new scaling regime. In the rest of this work, we go beyond the instantaneous scaling approximation used in [294, 295].

[7]The turning-point frequency can even be smaller by $\mathcal{O}(400)$ if, in a far-future, the precision of the order of 1% can be reached in the measurement of the SGWB, cf. Eq. (B.51).

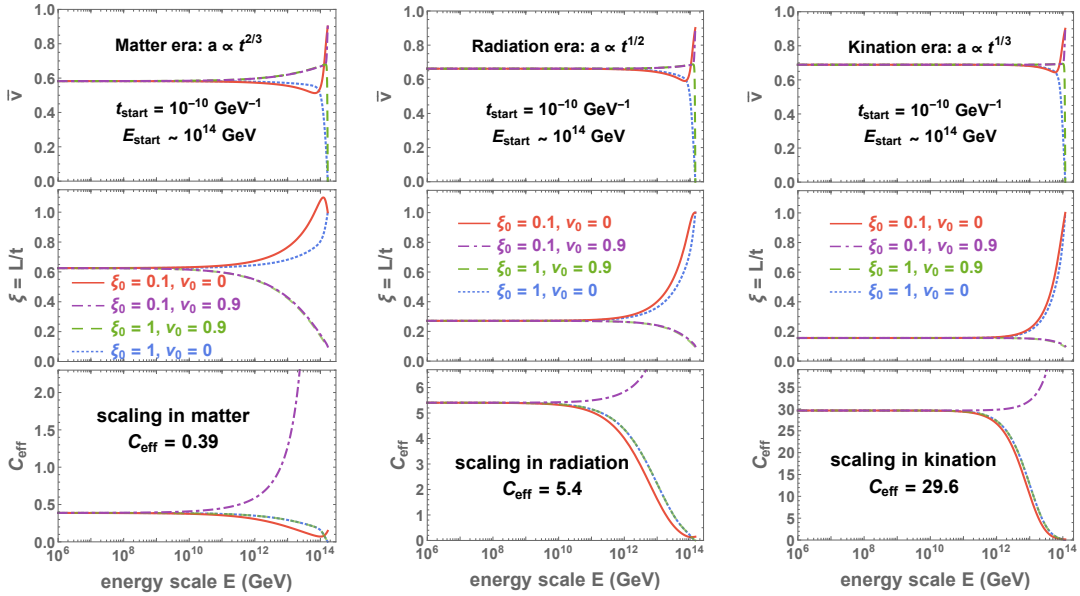

Figure 3.3: Cosmic-string network evolving in the one-component Universe with energy density $\rho \sim a^{-n}$ where $n = 3$, 4 and 6 correspond to matter, radiation and kination, respectively. The long-string-network mean velocity $\bar{v}$, the correlation length ξ and the corresponding loop-production efficiency $C_{\rm eff}$ reach the scale-invariant solutions after the Hubble expansion rate has dropped by 2 orders of magnitude, independently of the initial conditions.

3.4 Standard Cosmology

The SGWB from CS, cf. master formula in Eq. (3.29), depends on the cosmology through the scale factor a. We compute the later upon integrating the Friedmann equation, Eq. (1.2), for a given energy density ρ as in the standard ΛCDM scenario,

$$\rho_{\rm ST,0}(a) = \rho_{r,0}\,\Delta_R(T(a),T_0)\left(\frac{a}{a_0}\right)^4 + \rho_{m,0}\left(\frac{a}{a_0}\right)^3 + \rho_{k,0}\left(\frac{a}{a_0}\right)^2 + \rho_{\Lambda,0}, \tag{3.45}$$

where r, m, k and Λ denote radiation, matter, curvature, and the cosmological constant, respectively. We take $\rho_i = \Omega_i h^2\, 3M_{\rm pl}^2 H_0^2$, where $H_0 = 100$ km/s/Mpc, $\Omega_r h^2 \simeq 4.2\times10^{-5}$, $\Omega_m h^2 \simeq 0.14$, $\Omega_k \simeq 0$, $\Omega_\Lambda h^2 \simeq 0.31$ [39]. The presence of the function

$$\Delta_R = \left(\frac{g_*(T)}{g_*(T_0)}\right)\left(\frac{g_{*s}(T_0)}{g_{*s}(T)}\right)^{4/3}, \tag{3.46}$$

comes from imposing the conservation of the comoving entropy $g_{*s}\,T^3\,a^3$, where the evolutions of g_* and $g_{*,s}$ are taken from appendix C of [22]. In the next chapter, we discuss the possibility of adding an extra source of energy density, long matter/kination in Sec. 4.3, intermediate matter in Sec. 4.5, intermediate inflation in Sec. 4.6, and intermediate kination in Sec. 4.7.

Fig. 3.4 shows the dependence of the spectrum on the string tension. The amplitude decreases with $G\mu$ due to the lower energy stored in the strings. Moreover, at lower $G\mu$, the loops decay slower, and the GW is emitted later, implying a lower redshift factor and a global spectrum shift to higher frequencies. The figure also shows how the change in SM relativistic degrees of freedom introduces a slight red tilt which suppresses the spectrum by a factor $\Delta_R^{-1} \sim 2.5$ at high frequencies. We find that the amplitude of the GW spectrum at large frequency, assuming a standard cosmology,

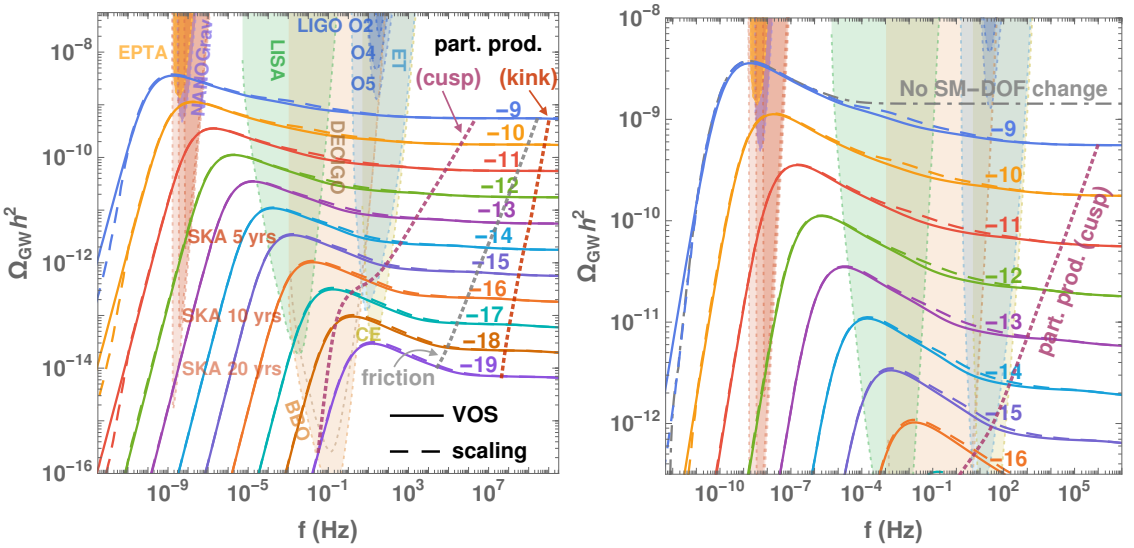

Figure 3.4: left: GW spectra from cosmic strings assuming either the scaling or VOS network, cf. Sec. 3.3.3, evolving in the standard cosmological background. Each line corresponds to string tension $G\mu = 10^x$, where x is specified by a number on each line. Dotted lines show the spectral cut-offs expected due to particle production, cf. Sec. 3.2.5 and thermal friction, cf. Sec. B.5.4, which depend on the nature of the loop small-scale structures: cusp or kink-dominated. *right:* The zoom-in plot of the left panel shows the effects from the change of SM degrees of freedom on the scaling and VOS networks.

is given by

$$\Omega_{\rm GW}h^2 \simeq 15\pi\,\Delta_R\,\Omega_r h^2\,C_{\rm eff}^{\rm rad}\,\mathcal{F}_\alpha\left(\frac{\alpha G\mu}{\Gamma}\right)^{1/2} \simeq 6\cdot 10^{-11}\left[\frac{G\mu}{10^{-11}}\right]^{1/2}\left[\frac{\alpha\times 50}{0.1\times\Gamma}\right]^{1/2}, \quad (3.47)$$

where $\Omega_r h^2 \simeq 4.2\times 10^{-5}$ is the present radiation energy density of the Universe [39]. We provide a back-of-the-envelope estimation in App. 2.4.3 and an intuitive derivation based on the quadrupole formula in App. B.3.5.

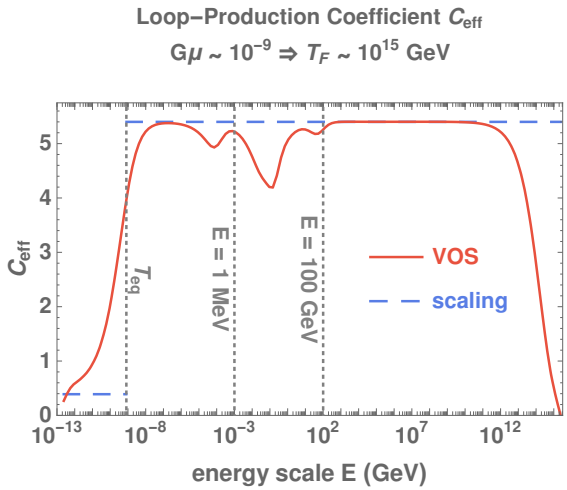

Figure 3.5: Comparison of the loop-production efficiency under the scaling assumption, where the attractor solution of the VOS equations is assumed to be reached instantaneously, and under the VOS assumptions, where one integrates the VOS equations. A standard cosmology is assumed.

Deviation from the scaling regime.

Fig. 3.5 shows how the loop-formation efficiency $C_{\rm eff}$ varies during the change of SM relativistic degrees of freedom and the matter-radiation equality upon solving the VOS equations, cf. Sec. 3.3. We see the associated corrections to the spectrum in Fig. 3.4, which were already pointed out in

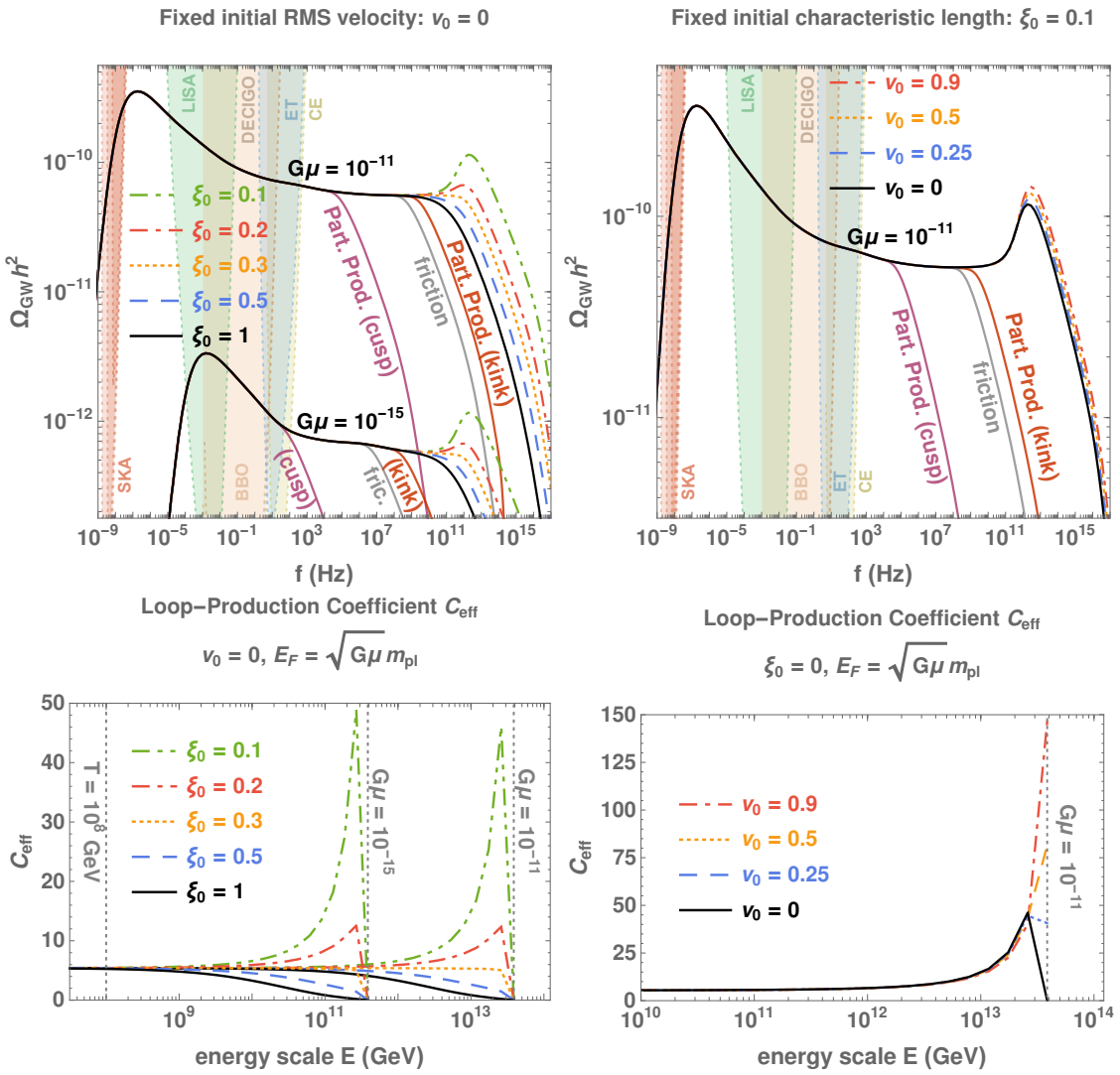

Figure 3.6: top: GW spectra assuming a standard cosmology. The network is formed at the temperature specified by the string tension: $T_F \sim m_{pl}\sqrt{G\mu}$. Initial conditions with a fixed initial mean velocity $\bar{v}_0$ (left) and a fixed initial correlation length scale ξ_0 (right) are applied. The cut-offs due to particle production, cf. Sec. 3.2.5, and thermal friction, cf. App. B.5.4, are shown with purple, red and gray lines. *bottom:* The bumps at high frequencies come from the over-production of loops right after the network formation when $\xi/\bar{v}$ are taken smaller/larger than their scaling values.

[296, 410]. The spectrum is enhanced at low frequencies because more loops are produced than when assuming that the matter era ($t > t_{\rm eq}$) is reached instantaneously, cf. Fig. 3.5.

Beyond the Nambu-Goto approximation.

Fig. 3.4 shows the possibility of a cut-off at high frequencies due to particle production for two different assumptions regarding the loop small-scale structures: cusps or kinks domination, cf. Sec. 3.2.1. Above these frequencies, loops decay into massive radiation before they have time to emit GW. For kinky loops, the cut-off is outside any future-planned observational bands, while for cuspy loops, the cut-off might be in the observed windows for $G\mu \lesssim 10^{-15}$.

Initial network configuration

Fig. 3.6 shows how the spectrum depends on the choice of initial conditions $\bar{v}_0$, ξ_0. Only the region near the high-frequency cut-off is impacted, corresponding to loops created just after the network

formation. Such initial values lead to an overproduction of loops during the initial transient regime and an enhancement of the spectrum. The impact of ξ_0 is stronger than the one of $\bar{v}_0$ because the loop-production efficiency scales as $C_{\rm eff} \propto \bar{v}/\xi^3$. The smaller/larger $\xi_0/\bar{v}_0$, the higher the bump.

Note that the frequency of the bump is independent of $G\mu$. This can be understood upon plugging the temperature when the network is formed, $T_F \sim m_{\rm pl}\sqrt{G\mu}$ into the $(f-T)$-correspondence formula in Eq. (3.33). Also, note that at such a high temperature, the friction of the strings with the plasma might play a major role [411].

The high-frequency bump could be a probe of the nature of the PT in the early Universe, e.g., the initial correlation length, or a probe of the plasma-string interaction cf. App. B.5.4. For example, the initial correlation length would be at smaller sizes for FOPT because the field fluctuates at the size of nucleated bubbles. In the second-order case, the scalar field tends to take VEV everywhere when the transition happens, such that the correlation length could be much larger, cf. [412] and references therein. This could be, in principle, motivation for high-frequency GW experiments. However, the loops contributing to such high-frequency GW might rather decay into particles, cf. solid purple and red line in Fig. 3.6.

In the next chapter, we will study the impact of different non-standard cosmologies on the SGWB from cosmic strings. Each cosmological history not only yields a distinct value for the scale factor of the Universe today, a_0, thus a different amount of redshifting of gravitational waves in Eq. (3.30), but also a distinct loop-production rate $\propto C_{\rm eff}/t_i^4$ due to a different formation time t_i and a different loop-production efficiency $C_{\rm eff}$. In Sec. 4.3, we assume that the radiation era was preceded by a long period of matter domination or kination after inflation. In Sec. 4.5 and Sec. 4.6, we assume instead some short eras of either matter domination or inflation, inside the radiation era.

3.5 Metastable Strings and Peaked GW Spectrum

In this section, we point out the possibility for the GW spectrum to exhibit a peak structure whenever high and low-frequency cut-offs are close to each other. As discussed in the previous sections and the next chapter, a high-frequency cut-off can arise:

- either in standard cosmology, mainly from particle production beyond the Nambu-Goto approximation, cf. blue dotted line in Fig. 3.10, whose corresponding cut-off frequency is computed in Eq. (3.37), but also possibly from friction or network formation, cf. Fig. 3.2,

- or in non-standard cosmology, in the presence of an intermediate matter era, cf. Sec. 4.5, or inflation era, cf. Sec. 4.6. The associated cut-off frequencies are computed in Eq. (4.21) and Eq. (4.38), respectively.

Beyond the high-frequency cut-off, the GW spectrum is suppressed with a slope $f^{-1/3}$. In App. B.3.7, we show that the $f^{-1/3}$ behavior, instead of f^{-1} as expected from the $(k=1)$-spectrum, is due to the presence of the high-k modes [334].

Conversely, there are also phenomena which suppress the GW spectrum at *low frequency*.

- Simply because such low frequencies have not been emitted yet, cf. blue line in Fig. 3.10 below 0.1 Hz, or Fig. 3.2 below $f \lesssim 10^{-7}$ Hz. The corresponding low-frequency cut-off is computed in Sec. 3.5.1.

- Or the string network is metastable, as discussed in Sec. 3.5.2

In Sec. 3.5.3, we show a variety of peak spectra and compare them to peak spectra generated by bubble collision in first-order phase transitions.

3.5.1 Low-energy cut-off of stable strings

The lowest frequency observed today is set by the inverse size of the main population of loops decaying today. This leads to the distinguished maximum of the standard GW spectrum around 0.1 Hz of the blue line in Fig. 3.10 or around 10^{-7} Hz in Fig. 3.2. As discussed in App. B.4, loops contributing to the frequency f dominantly decay at $\tilde{t}_M$ defined by

$$\frac{2k}{f} \cdot \frac{a(\tilde{t}_{\rm M})}{a(t_0)} = \Gamma G\mu \times \tilde{t}_{\rm M}. \tag{3.48}$$

Upon setting $\tilde{t}_M = t_0$, we deduce the frequency of the low-energy cut-off of any stable string network

$$f_{\rm low}^{\rm stable} = \frac{2}{\Gamma G\mu t_0} \simeq (1.48 \cdot 10^{-7}\ {\rm Hz}) \left(\frac{50 \cdot 10^{-11}}{\Gamma G\mu}\right), \tag{3.49}$$

where we have numerically adjusted the coefficient to fit with the GW spectrum. This formula agrees with EPTA/NANOGrav constraints which bound $G\mu \lesssim 10^{-10}$ for $f \sim 10^{-9} - 10^{-8}$ Hz.

3.5.2 Low-energy cut-off of metastable strings

So far, we have only been considering a stable CS network. However, there are mechanisms which can make the network decay, such as breaking into monopole (M) antimonopole ($\overline{M}$) pairs [413–416], Hubble-induced mass of flat direction in supersymmetric theories [417, 418], symmetry restoration in runaway quintessential scenarios [350], or the formation of domain walls in the case of axionic string network [351, 419–421]. The decay of the string network can imprint a low-energy cut-off in the GW spectrum at a frequency much higher than the low-energy cut-off of stable string networks, cf. Sec. 3.5.1.

In this work, we focus for illustration on the case of string breaking via nucleation of monopole-antimonopole pairs. Such a metastable string network can arise from a two-stage pattern of symmetry breaking [416]

$$G \to H \times U(1) \to H, \tag{3.50}$$

in which the first step generates monopoles, while the second one produces CS[8]. If the overall vacuum manifold G/H is simply connected, the CS (S) are topologically unstable [413, 423]. They can break under Schwinger production of monopole-antimonopole pairs ($M\bar{M}$), hence producing 'dumbbells' $MS\bar{M}$, namely segments of the string with monopoles attached at the two ends.[9] If the monopoles have unconfined flux which propagates outside the strings, their acceleration under the effect of the string tension up to ultra-relativistic velocities can lead to the emission of ultra-high-energetic gauge radiation, possibly leading to observable ultra-high-energy cosmic rays [431, 432] or CMB distortion [425]. If the monopoles do not carry unconfined flux, the only source of energy loss is through GW emission, whose emitted power is of the same order of magnitude as the one from CS loops [415] but with a spectrum extending to higher frequencies [414, 416]. More precisely, the GW power radiated by a straight dumbbell is [415]

$$P_{\rm GW}^{\rm M\bar{S}M} \simeq \tilde{\Gamma}\, G\mu^2, \qquad \text{with} \quad \tilde{\Gamma} \equiv 8 \ln(\gamma_0), \tag{3.51}$$

where γ_0 is the maximal Lorentz factor reached by the monopoles. We follow [416] and we set $\tilde{\Gamma} \sim 50$. We note the interesting possibility for dumbbells to explain Dark Matter if their lifetime is larger than the age of the Universe [433, 434].

[8] The two-stage symmetry breaking can have a large variety of breaking patterns. Many systems of hybrid defects: e.g., monopole-string and string-wall networks, could form and lead to various GW signatures [422].

[9] More complex hybrid topological objects, called $\mathcal{Z}_N$-string, can be generated from the breaking pattern $G \to H \times U(1) \to H \times \mathcal{Z}_N$ [424]. They are monopoles connected to N strings and are called 'cosmic necklaces' for $N = 2$ or 'string web' for $N \geq 3$ [425]. Their evolution is expected to be close to the scaling regime [424, 426–429] if the energy loss due to the presence of monopoles is not too large [430].

The monopole-anti-monopole pair nucleation rate per unit length is [416]

$$\Gamma_d = \frac{\mu}{2\pi} \exp(-\pi\kappa), \tag{3.52}$$

where $\kappa \equiv m^2/\mu \gtrsim 1$ is the ratio of the monopole mass m to the CS tension μ. As explained in Sec. 3.2.2, the main sources of SGWB generated by a stable network are the loops formed with a length $l = \alpha\, t_i$ where t_i is the loop formation time and $\alpha \simeq 0.1$. The breaking rate growing linearly with the string length, the later the loops are formed, the more likely they break under $M\bar{M}$ nucleation. More precisely, the loops break when the age of the Universe is equal to their lifetime upon breaking

$$t_i \sim (\Gamma_d \times \alpha\, t_i)^{-1}\,. \tag{3.53}$$

After $M\bar{M}$ nucleation, the loops become dumbbells $MS\bar{M}$ which shrinks under GW emission with power given by Eq. (3.51), until they totally disappear (or at least have their length divided by two) after a time

$$\tilde{t} \simeq \frac{\alpha\, t_i}{2\tilde{\Gamma} G\mu}. \tag{3.54}$$

Upon plugging the large-loop-breaking time in Eq. (3.53), in the dumbbell-lifetime under GW emission in Eq. (3.54), we obtain the age of the Universe after which no loops remain[10] and after which GW emission stops

$$\tilde{t}_{\rm stop} \sim (\Gamma_d \times \tilde{\Gamma} G\mu)^{-1/2}, \tag{3.55}$$

which agrees with the estimation in [416]. The frequency $f_{\rm break}$ emitted by this population of broken large-loops just before they disappear, at $\tilde{t}_{\rm stop}$, corresponds to the lowest frequency of the GW spectrum, and it obeys, cf. Eq. (3.54) and Eq. (3.33),

$$\frac{2k}{f_{\rm break}} \cdot \frac{a(\tilde{t}_{\rm stop})}{a(t_0)} = \Gamma G\mu \times \tilde{t}_{\rm stop}. \tag{3.56}$$

For string breaking during a radiation-dominated era, $\frac{a(\tilde{t}_{\rm stop})}{a(t_0)} = \left(\frac{\tilde{t}_{\rm stop}}{t_{\rm eq}}\right)^{1/2} \left(\frac{\tilde{t}_{\rm eq}}{t_0}\right)^{2/3}$, and we get

$$f_{\rm break} \simeq 2 \left(2\pi z_{\rm eq} G \tilde{\Gamma}^3\right)^{-1/4} (G\mu \cdot t_0)^{-1/2} \exp(-\pi\kappa/4). \tag{3.57}$$

Taking into account the summation of higher frequency modes and the more accurate cosmological history, we give the numerically-fitted version of the cut-off frequency due to string breaking through monopole-anti-monopole nucleation

$$f_{\rm break} \simeq (1.82 \times 10^{19}\ {\rm Hz}) \left(\frac{50}{\tilde{\Gamma}}\right)^{3/4} \left(\frac{10^{-11}}{G\mu}\right)^{1/2} \exp(-\pi\kappa/4). \tag{3.58}$$

where we have used $z_{\rm eq} = 3360$. The smaller the separation between the monopole mass and the string tension $\kappa = m^2/\mu > 1$, the faster the string breaking, and the higher the cut-off frequency $f_{\rm break}$.

GW signature of metastable strings The GW spectrum and their detectability from metastable strings can be visualized in Fig. 3.7, with different monopole-mass to string-tension ratios $\kappa \equiv m^2/\mu$, leading to different low-frequency cut-offs in Eq. (3.58). Three possible signatures – the cut-off, the slope, and the usual flat parts – are observable depending on the cut-off's position. Fig. 3.8 provides the current constraints and the projected detectability of the future-planned experiments. By decreasing $\kappa \lesssim 65$, we can evade the current GW constraints from EPTA/NANOGrav on the string tension, but also from the CMB, such that the current constraint comes from LIGO O2, $G\mu \lesssim 10^{-6}$. The latter can also be relaxed if $\kappa \lesssim 40$. Hence, Schwinger production of monopole-anti-monopole pairs constitutes an interesting proposal to revive GUT strings following the symmetry-breaking pattern $SO(10) \to G_{\rm SM} \times U(1)_{\rm B-L} \to G_{\rm SM}$ [435].

[10] Note that we have only considered broken loops and we have neglected the additional GW emission coming from the broken long strings of the network.

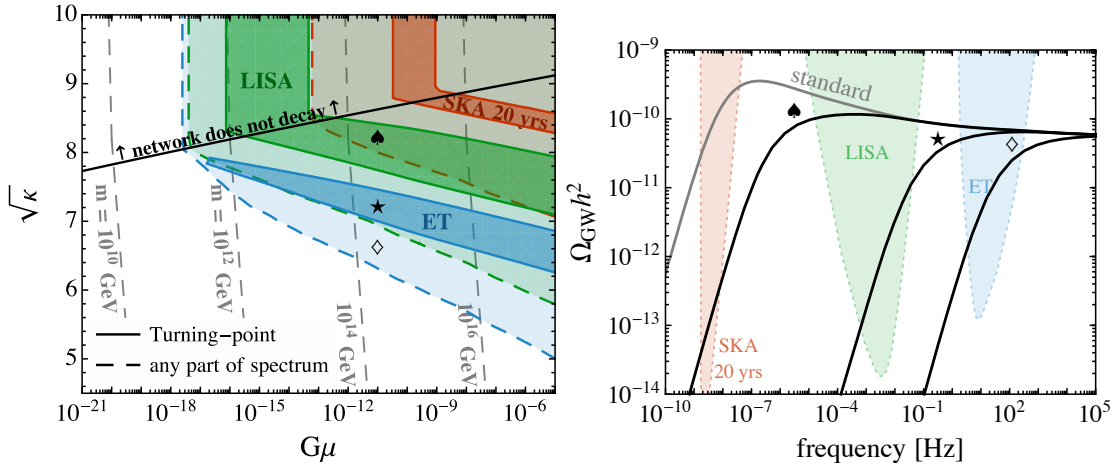

Figure 3.7: left: Parameter space reachable by future experiments. The cut-off could reside within the sensitivity range (solid contour); otherwise, the slope and flat parts are observable for regions below and above the solid contour, respectively. *right:* Three possible signatures of metastable strings at future-planned GW observatories. The GW spectra correspond to the three benchmark scenarios indicated in the left plot.

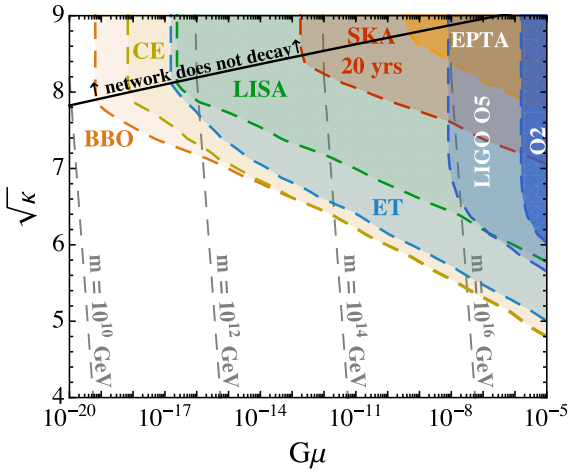

Figure 3.8: Constraints from LIGO O2 and EPTA and projected sensitivities at future planned observatories on the metastable string-network scenario. For larger κ, the suppressed monopole-antimonopole nucleation rate pushes the metastable strings signature to lower frequencies, cf. Eq. (3.58). Above the black line, κ is large enough such that the metastable strings are present today. The cut-off becomes κ-independent, dictated by Eq. (3.49).

3.5.3 Peaked spectrum

Fig. 3.9 represents the GW spectrum from stable strings in the presence of an early long-lasting matter era, leading to a high-frequency cut-off $f_{\rm High} = f_\Delta$ in Eq. (4.21) of the next chapter. Eventually, a peaked spectrum can be generated when $f_{\rm Low} \geq f_{\rm High}$. We can analytically locate the peaked spectrum to be at amplitude and frequency

$$\Omega_{\rm peak} = \Omega_{\rm GW,flat}(f_{\rm peak}) \left(\frac{f_{\rm High}}{f_{\rm Low}}\right)^{4/33}, \quad f_{\rm peak} = \left(f_{\rm High}^{1/3} f_{\rm Low}^{3/2}\right)^{6/11}, \tag{3.59}$$

with high- and low-frequency shapes to be

$$\Omega_{\rm GW}(f, G\mu, \kappa, T_\Delta) = \begin{cases} \Omega_{\rm peak} \left(\frac{f}{f_{\rm peak}}\right)^{2/3} & \text{for } f \leq f_{\rm peak}, \\ \Omega_{\rm peak} \left(\frac{f}{f_{\rm peak}}\right)^{-1/3} & \text{for } f > f_{\rm peak}. \end{cases} \tag{3.60}$$

The higher the ratio $f_{\rm Low}/f_{\rm High}$, the more suppressed the peak amplitude relative to the spectrum without a peak. In the right plot in Fig. 3.9, we lower the temperature T_Δ at which the matter era ends to bring the peak spectrum within the GW interferometers windows and show in red the

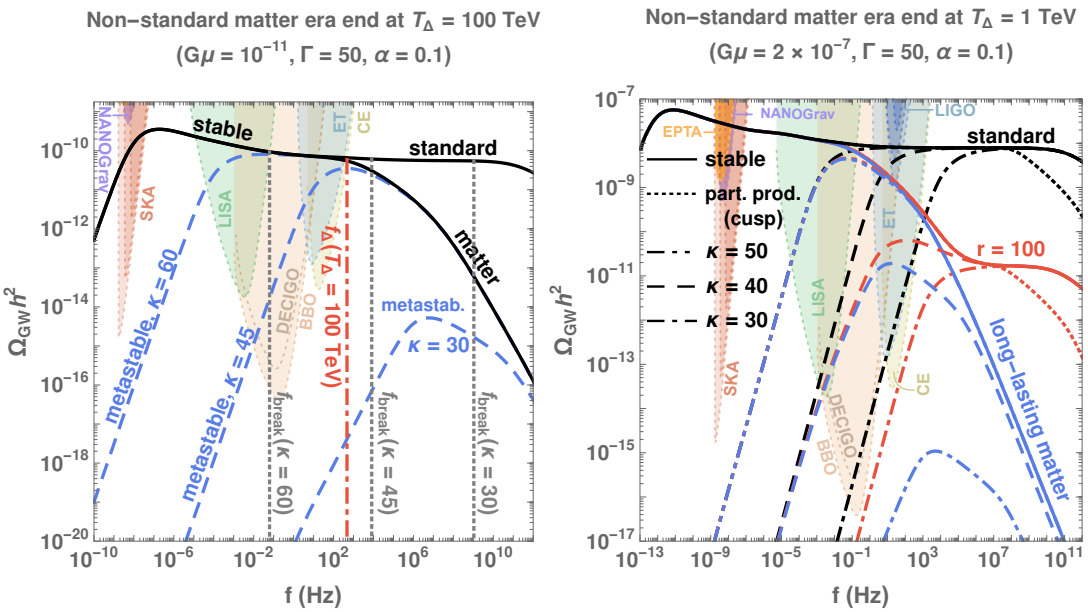

Figure 3.9: GW spectra from metastable string networks for different ratios of monopole mass to CS tension $\kappa \equiv m^2/\mu$, leading to different low-frequency cut-offs $f_{\rm break}$ (vertical gray dotted). By decreasing κ, the different GW constraints can be relaxed. *left:* Upon introducing a matter era with high-frequency cut-off f_Δ (vertical red dot-dashed), we can get a peak shape when $f_{\rm break} \gtrsim f_\Delta$. *right:* A rich variety of spectral shapes can be obtained by combining cut-off from metastability to long-lasting matter era (blue), short-lasting matter era (red) with duration $r = T_{\rm start}/T_\Delta = 100$, or particle production (dotted).

case of a short-matter era $T_{\rm start}/T_\Delta = 100$. A wide variety of spectral shapes can be obtained by combining different cut-off effects.

Fig. 3.10 shows three types of peaks, whose precise parameter choices are detailed in Table 3.1.

I. In black dashed lines, we show GW spectra from metastable string networks, cf. Sec. 3.5.2, in the presence of an early long-lasting matter-dominated era, cf. Sec. 4.5, for two different metastable-to-matter cut-off-frequency ratios. The same high-frequency cut-off can also be produced from an intermediate inflation era, cf. Sec. 4.6. The slopes are $f^{3/2}$ and low frequencies and $f^{-1/3}$ are high frequencies, cf. App. B.3.7.

II. In blue lines, we show a GW spectrum from a stable network, which low-frequency cut-off is discussed in Sec. 3.5.1. We assume the presence of cusps responsible for particle production, leading to the high-frequency cut-off in the dotted line, cf. discussion in Sec. 3.2.5. The slopes are $f^{3/2}$ at low frequencies, and $f^{-1/3}$ are high frequencies, cf. App. B.3.7.

III. In the red line, we show a GW spectrum from a first-order phase transition assuming non-runaway bubble-walls generated by sound waves [152]. It should be distinguishable from the peak spectrum from CS since the peak is thinner and the slopes are steeper: f^3 at low frequencies and f^{-4} at high frequencies ($f^{-5/3}$ for turbulence). Also, the slopes of a GW spectrum from first-order phase transitions assuming run-away bubble-walls, generated by scalar gradient, are also steeper than the CS case [152]: f^3 at low frequencies (or f^1 [160]) and f^{-1} at high frequencies (or $f^{-1.5}$ [436]).

3.6 Gravitational Waves from Global Cosmic Strings

The local CS as sources of SGWB is so far concerned. Yet, the symmetry that gets broken and generates strings can be global. A similar approach can study the global cosmic strings and calculate

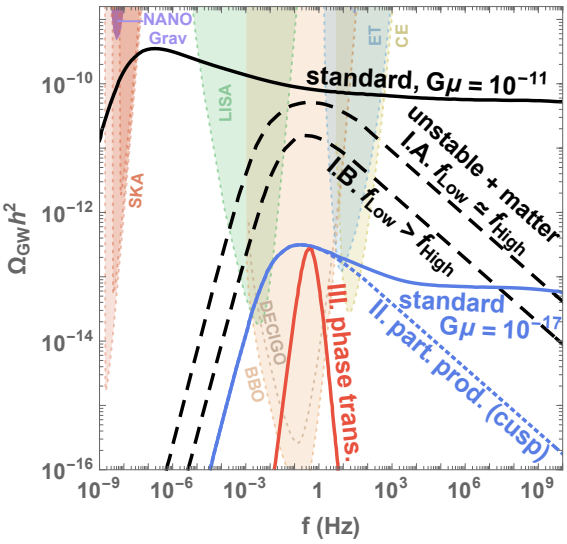

Figure 3.10: Peaked spectra with same peak frequencies, corresponding to the benchmark scenarios I, II and III, described in the text and in Table 3.1. Here we extrapolate the $f^{-1/3}$ behavior to arbitrary large frequencies, which is equivalent to sum over an infinite number of proper modes k, see App. B.3.7.

scenario	lower cut-off	higher cut-off
I.A. metastable strings with long-lasting matter era: $G\mu = 10^{-11}$, $T_\Delta = 200$ GeV, $\kappa = 55$	$f_{\rm break} \simeq 3.2$ Hz	$f_\Delta \simeq 1$ Hz
I.B. metastable strings with long-lasting matter era: $G\mu = 10^{-11}$, $T_\Delta = 10$ GeV, $\kappa = 52.5$	$f_{\rm break} \simeq 23$ Hz	$f_\Delta \simeq 0.04$ Hz
II. stable strings with standard cosmology and particle production (cusps): $G\mu = 10^{-17}$, $\beta_c = 1$	$f_{\rm low}^{\rm stable} \simeq 0.15$ Hz	$f_{\rm cusp} \simeq 2.9$ Hz
III. first-order phase transition generated from acoustic waves in standard cosmology [152]: $T_p = 5$ TeV, $\alpha = 0.1$, $\beta = 10^3$, $v_w \simeq 1$	$f_{\rm peak} \simeq 0.41$ Hz	

Table 3.1: Benchmark scenarios I, II and III, described in the text. The corresponding GW spectra are shown in Fig. 3.10.

the corresponding GW signals. The main distinction between global-string loops is that they are short-lived, whereas loops from local strings are long-lived. This results in different GW spectra in frequency and amplitude, as discussed in detail below.

3.6.1 The presence of a massless mode

For global string, the absence of gauge field implies the existence of a massless Goldstone mode, with logarithmically-divergent gradient energy, discussed in App. B.1. Hence the tension $\mu_{\rm g}$, cf. Eq. (3.3), reads

$$\mu_{\rm g} \equiv \mu_{\rm l} \ln\left(\frac{H^{-1}}{\delta}\right) \simeq \mu_{\rm l} \ln(\eta\, t)\,, \quad \text{with} \quad \mu_{\rm l} \equiv 2\pi\eta^2, \tag{3.61}$$

where η is the scalar field VEV, $\mu_{\rm l}$ is the tension of the would-be local string (when the gauge coupling is switched on) and $\delta \sim \eta^{-1}$ is the string thickness. Goldstones are efficiently produced by loop dynamics with the power

$$P_{\rm Gold} = \Gamma_{\rm Gold}\, \eta^2, \tag{3.62}$$

where $\Gamma_{\rm Gold} \approx 65$ [348], causing loops to decay with a rate

$$\frac{dl_{\rm g}}{dt} = \frac{dE}{dt}\frac{dl}{dE} \equiv \kappa \equiv \frac{\Gamma_{\rm Gold}}{2\pi\,\ln(\eta\, t)}, \tag{3.63}$$

Therefore, the string length evolving upon both GW and Goldstone bosons emission reads

$$l_{\rm g}(t) = \alpha t_i - \Gamma G\mu_{\rm g}(t - t_i) - \kappa(t - t_i), \tag{3.64}$$

which is dominated by the Goldstone emission because the rate is unsuppressed by $G\mu$ like GW emission.

3.6.2 Evolution of the global network

The Velocity-One-Scale equations for local strings – presented in Sec. 3.3 – can be modified by including the additional-loss due to Goldstone production [437]

$$\frac{dL}{dt} = HL\,(1+\bar{v}^2) + F(\bar{v})|_{\rm global}\,, \tag{3.65}$$

$$\frac{d\bar{v}}{dt} = (1-\bar{v}^2)\left[\frac{k(\bar{v})}{L} - \frac{\bar{v}}{l_d}\right], \tag{3.66}$$

where the energy-loss coefficient $F(\bar{v})$ is defined by

$$F(\bar{v})|_{\rm local} = \frac{\tilde{c}\bar{v} + d[k_0 - k(\bar{v})]^r}{2} \quad \Rightarrow \quad F(\bar{v})|_{\rm global} = F(\bar{v})|_{\rm local} + \frac{sv^6}{2\ln(\eta t)}, \tag{3.67}$$

where the constant s controlling the efficiency of the Goldstone production, is inferred from lattice simulations to be $s \simeq 70$ [332]. However, the momentum operator $k(v)$ in Eq. (3.66), is unchanged with respect to the local case

$$k(\bar{v}) = k_0\frac{1-(q\bar{v}^2)^\beta}{1+(q\bar{v}^2)^\beta}. \tag{3.68}$$

with the simulation-calibrated parameters: $k_0 = 1.37$, $q = 2.3$, $\beta = 1.5$, $\tilde{c} = 0.34$, $d = 0.22$, $r = 1.8$ [409]. Here through Eqs. (3.67) and (3.68), we follow [438] and consider the extended VOS model based on Abelian-Higgs simulations, proposed in [409] and already discussed in App. B.6.3. Namely, we have simply added the backreaction of Goldstone production on long strings in Eq. (3.67). We have checked that we can neglect the thermal friction due to the contact interaction of the particles in the plasma with the string, cf. Eq. (B.65) for which the interaction cross-section is given by the Everett formula in [301].

In order to later compute the GW spectrum, we define the loop-formation efficiency, analog of the local case in Eq. (3.39)

$$C_{\rm eff}^{\rm g} = \tilde{c}\bar{v}/\xi^3, \tag{3.69}$$

with $\bar{v}$ and $\xi \equiv L/t$ obeying the VOS equations in Eq. (3.65) and Eq. (3.66). Due to the logarithmic dependence of the string tension on the cosmic time, the scaling regime is slightly violated. Consequently, the loop-formation efficiency plotted in Fig. 3.11, never reaches a constant value. Hence, in this study we model the network based on VOS evolution, rather than using the scaling solutions. Only for enormous value of $\ln(\eta\, t)$ corresponding to cosmic times much larger than the age of the Universe today, we find that the solutions to the modified VOS equations in Eqs. (3.65) and (3.66) reach a scaling regime $C_{\rm eff} \to 0.46,\ 2.24,\ 6.70$ for matter-, radiation-, and kination-dominated Universe, respectively. By comparing to the values found in [199], our results agree only for the radiation case.

As shown in Fig. 3.11, the coefficient $C_{\rm eff}$ receives a correction from the logarithmically-time-dependent string tension, that enters in the energy loss via Goldstone, Eq. (3.67). However, a mild violation less than a factor log factor is found [1, 199], in contrast to the order-log correction found in simulations [195–197].

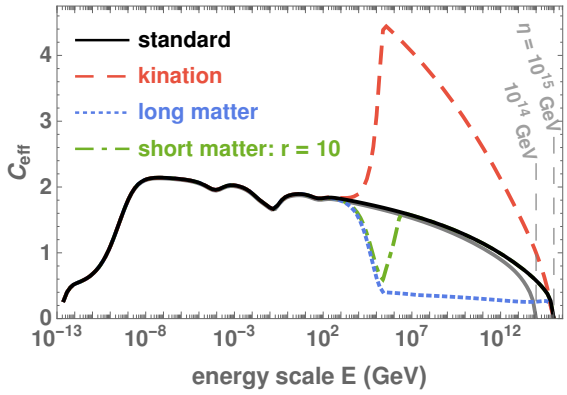

Figure 3.11: The evolution of the loop-production efficiency $C_{\rm eff}$, for each cosmological background never reaches a plateau, in contrast to local strings in which case the scaling regime is an attractor solution, cf. Fig. 3.5 and right panel of Fig. 4.4. Indeed, for global strings the scaling behavior is logarithmically violated due to the energy loss through Goldstone production in the VOS equations, cf. Sec. 3.6.2.

3.6.3 GW spectrum

While the back-of-the-envelope estimation can be found in App. 2.4.3, the precise GW spectrum generated by global-string loops is given by a master formula, similar to the local case in Eq. (3.29),

$$\Omega^{\rm g}_{\rm GW}(f) \equiv \frac{f}{\rho_c}\left|\frac{d\rho^{\rm g}_{\rm GW}}{df}\right| = \sum_k \Omega^{(k),\,{\rm g}}_{\rm GW}(f), \tag{3.70}$$

where

$$\Omega^{(k),\,{\rm g}}_{\rm GW}(f) = \frac{1}{\rho_c}\cdot\frac{2k}{f}\cdot\frac{\mathcal{F}_\alpha\,\Gamma^{(k)}G\mu_{\rm g}^2}{\alpha(\alpha+\Gamma G\mu_{\rm g}+\kappa)}\int_{t_F}^{t_0} d\tilde{t}\,\frac{C^{\rm g}_{\rm eff}(t^{\rm g}_i)}{(t^{\rm g}_i)^4}\left[\frac{a(\tilde{t})}{a(t_0)}\right]^5\left[\frac{a(t^{\rm g}_i)}{a(\tilde{t})}\right]^3\Theta(t^{\rm g}_i - t_F).s \tag{3.71}$$

We have checked that we can safely neglect massive radiation. The loop formation time $t^{\rm g}_i$ is related to the emission time $\tilde{t}$ after using $l_{\rm g}(\tilde{t}) = 0$ in Eq. (3.64)

$$t^{\rm g}_i = \frac{\Gamma G\mu_{\rm g}+\kappa}{\alpha+\Gamma G\mu_{\rm g}+\kappa}\tilde{t}. \tag{3.72}$$

The GW spectrum from global strings is shown in Fig. 3.12 and compare to the spectrum computed in [199]. Concerning [199], we find a lower value for $C_{\rm eff}$ during the late matter-dominated Universe (0.46 instead of 1.32), which implies a smaller spectral bump, while the radiation contributions are considered the same. Moreover, the shapes of the spectra are different. An explanation could be the summation over the high-frequency modes (up to $k = 2\times10^4$ in our case), which smoothens the spectrum. The spectrum from [199] resembles the first mode of our spectrum.

The contribution from the radiation-dominated era deviates from the scale-invariance due to log-correction,

$$\Omega^{\rm global}_{\rm std,1st}h^2 \simeq 2.5\,\Omega_r h^2\,C^{\rm rad}_{\rm eff}\left(\frac{\Gamma}{\Gamma_{\rm Gold}}\right)\log^3(\eta\tilde{t}_M)\left(\frac{\eta}{M_{\rm Pl}}\right)^4, \tag{3.73}$$

$$\Omega^{\rm global}_{\rm std,sum}h^2 \simeq 1.2\cdot10^{-17}\,\log^3\left[(5.6\cdot10^{30})\left(\frac{\eta}{10^{15}\ {\rm GeV}}\right)\left(\frac{1\ {\rm mHz}}{f}\right)^2\right]\left[\frac{\eta}{10^{15}\ {\rm GeV}}\right]^4, \tag{3.74}$$

where the last line uses $\tilde{t}_M \sim t_i \sim f^2$ from Eq. (3.32), and also multiplies the factor 3.6 coming from the inclusion of higher-modes (cusp) [294]. Compared to the local-string case, we summarize their differences in Sec. 3.6.5. As shown in Fig. 3.12, in consequence of the strong dependence of the GW amplitude on the string scale η, only global networks above $\eta \gtrsim 5\times10^{14}$ GeV can be detected by LISA or CE, whereas EPTA or BBO/DECIGO can probe $\eta \gtrsim 10^{14}$ GeV. Also, note the logarithmic spectral tilt due to the extra $\log^3$-dependence from Eq. (3.71): two of the log-factors come from the string tension μ and another one from the particle production rate κ in Eq. (3.63).

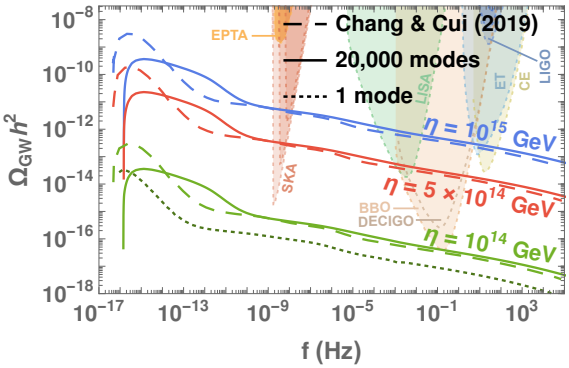

Figure 3.12: GW spectrum from global cosmic strings assuming VOS network formed at energy scale η, evolved in the standard cosmology. The shape of the GW spectrum computed in [199] resembles the first mode $k = 1$ of our spectrum.

There is also another mild log-dependence from the loop formation efficiency $C_{\rm eff}$ cf. Fig 3.11, which could lead to the $\log^4$-dependence as observed in the recent field-theoretic simulations [357].

The constraints on the inflation scale, $H_{\rm inf} \lesssim 6 \times 10^{13}$ GeV, from the non-detection of the fundamental B-mode polarization patterns in the CMB [20, 55], implies the upper bound on the reheating temperature $T_{\rm reh} \lesssim 5 \times 10^{16}$ GeV, assuming instantaneous reheating. Hence, assuming that the network is generated from a thermal phase transition, we impose $\eta \lesssim 5 \times 10^{16}$. A stronger restriction arises because of the direct CMB constraint on strings tensions

$$G\mu_{\rm g}\big|_{\rm CMB} = 2\pi \left(\frac{\eta}{m_{\rm pl}}\right)^2 \log(\eta\, t_{\rm CMB}) \lesssim 10^{-7} \quad \rightarrow \quad \eta \lesssim 1.4 \times 10^{15}, \tag{3.75}$$

where we use $t_{\rm CMB} \simeq 374$ kyr. Hence, we restrict to $\eta \lesssim 10^{15}$ GeV as in [199].

3.6.4 Impact of the cosmology on the GW spectrum

As same as the local case, the GW spectrum is sensitive to the expansion history of the Universe. Global-string loops – produced and emitted GW during $\rho \sim a^{-n}$ – has the spectral index from Eq. 3.71,

$$\begin{aligned}\Omega_{\rm GW}^{\rm global} &\propto f^{2\left(\frac{n-4}{n-2}\right)} \log^3\left[\eta t_\Delta \left(\frac{\tilde{t}_M}{t_\Delta}\right)\right], \\ &\propto f^{2\left(\frac{n-4}{n-2}\right)} \log^3\left[(5.6\times 10^{30})\left(\frac{\eta}{10^{15}\ {\rm GeV}}\right)\left(\frac{1\ {\rm mHz}}{f_\Delta}\right)^2\left(\frac{f_\Delta}{f}\right)^{n/(n-2)}\right],\end{aligned} \tag{3.76}$$

where f_Δ is the turning-point frequency when there is a non-standard cosmological era, and we took $(n = m)$-limit of the local case in Eq. (3.31) for global-string loops decay right after their formation: $t_i \sim \tilde{t}_M \propto f^{n/(2-n)}$. Up to the log factor, the spectral indices for global-string loops resemble the local case. As shown in Fig. 3.12, the log-factor mainly sources the violation of scale-invariance during the radiation era.

Eq. (3.76) is valid as long as the slope is not smaller than -1 because the slope of -1 is the minimum allowed by the UV tail of a single loop population; see App. B.3.6. Although Eq. (3.76) gives a slope of -2 for the matter-dominated era, Fig. 3.12 shows that, in fact, it leads to f^{-1} behavior in low-frequency range of $k = 1$ spectrum. Moreover, the summation over modes provides $f^{-1/3}$. The drop to f^1 behavior about $f \simeq 10^{-12}$ Hz can be related to the truncation of our summation at $k = 2 \times 10^5$. If we extrapolate the $f^{-1/3}$-behavior further, it becomes sub-dominant to the contribution from the radiation era around $f \simeq 10^{-8}$ Hz. I.e., the highest summation mode would be 10^8, which is technically a time-consuming calculation. Moreover, particle physics should limit the highest possible mode (e.g., $k_{\rm max} \sim \eta L$) and imprint a spectrum signature. We leave this compelling aspect for future study.

3.6.5 Global versus local strings

Parametrically, the GW spectra from local and global CS scale as, cf. Eq. (3.47) and (3.74)

$$\Omega_{\rm GW}^{\rm local} \simeq \Omega_r \frac{\eta}{M_{\rm pl}}, \qquad \text{and} \qquad \Omega_{\rm GW}^{\rm global} \simeq \Omega_r \left(\frac{\eta}{M_{\rm pl}}\right)^4 \log^3(\eta t_i). \tag{3.77}$$

In order to understand the scaling difference, let us consider the contribution to the GW spectrum coming from loops produced at time t_i. For local strings, the corresponding GW are dominantly emitted at time $\tilde{t}_M^{\rm local} \simeq \alpha t_i/(2\Gamma G\mu_{\rm local})$, see Eq. (3.15), which means that GW emission occurs $(M_{\rm pl}/\eta)^2$ Hubble times after loop production. Instead, global loops decay at $\tilde{t}_M^{\rm global} \simeq t_i$, so within one Hubble time after production, even though their tension is logarithmically enhanced. Therefore, with respect to local strings, the GW spectrum from global strings in standard radiation cosmology is:

- suppressed by the shorter Hubble time $\tilde{t}_M$ at the time of GW emission: factor $\tilde{t}_{\rm M}^{\rm global}/\tilde{t}_{\rm M}^{\rm local} \propto G\mu_{\rm local} \propto (\eta/M_{\rm pl})^2$,
- suppressed by the larger GW redshift due to earlier emission: factor $\left[a\left(\tilde{t}_{\rm M}^{\rm global}\right)/a\left(\tilde{t}_{\rm M}^{\rm local}\right)\right]^4 \propto (\eta/M_{\rm pl})^4$,
- enhanced by the lower loop redshift factor since GW emission occurs right after loop production: factor $\left[a\left(\tilde{t}_{\rm M}^{\rm local}\right)/a\left(\tilde{t}_{\rm M}^{\rm global}\right)\right]^3 \propto (\eta/M_{\rm pl})^{-3}$,
- increased by the log-enhanced GW power emission rate: factor $\log^2(\eta t_i)$,
- increased by the log-enhanced loop lifetime: factor $\log(\eta t_i)$.

Additionally, the global-loop GW emission does not delay as the local case. The associated frequency today is directly sensitive to the loop size at production αt_i. Compared to the frequency-temperature of local strings Eq. (3.33), the global-string GW frequency from Eq. (3.32) reads

$$\frac{f_{\rm global}}{f_{\rm local}} \simeq \frac{a\left(\tilde{t}_{\rm M}^{\rm global}\right)}{a\left(\tilde{t}_{\rm M}^{\rm local}\right)} \simeq \left(\frac{\Gamma G\mu}{\alpha}\right)^{1/2}, \tag{3.78}$$

which leads to

$$f_{\rm global} \simeq (4.7\times10^{-6}\ {\rm Hz})\left(\frac{T}{\rm GeV}\right)\left(\frac{0.1}{\alpha}\right)\left(\frac{g_*(T_i)}{g_*(T_0)}\right)^{1/4}. \tag{3.79}$$

The frequency-temperature relation of global strings is independent of the string tension, in contrast to local strings. It is therefore numerically similar to that of SGWB from a horizon-size source, e.g., inflationary GW. SGWB from global strings has an interesting detectability for probing the change in cosmological history, as shown in the next chapter in Fig. 4.8 of the next chapter.

3.6.6 A popular example: Axion Strings

A fascinating theory with global CS is the *axion-string* scenario. Discussed in more details in Chap. 6, the minimal extension of SM with a $U(1)$-symmetry (so-called *Peccei-Quinn* symmetry) can solve the strong CP problem by its psuedo-Nambu-Goldstone boson (pNGB) or the *QCD axion* [439–445]. The term *axion* or *axion-liked-particle* (ALP) has been also adopted widely for any pNGB arising from the spontaneous symmetry breaking (SSB) of any global $U(1)$ symmetry. At late times, the mass of the pNGB becomes more relevant to its dynamics and leads to the homogeneous-mode oscillation of the axion. Remarkably, this allows axion to explain the DM

abundance through several production mechanisms, mainly the misalignment [446–448], and kinetic misalignment [449, 450] mechanisms.

Moreover, another production channel relies on the axion field's inhomogeneity: axions from the decay of topological defect from the $U(1)$ SSB. The post-inflationary SSB leads to the axion-string formation[11] [181, 182, 195, 332, 333, 353–355, 451–453] that attains its scaling regime and produces an axion relic abundance and a SGWB [195–198, 200, 331, 356, 357, 421, 452, 454–456]. It is found from axion-string simulations that the ALPs from strings overproduces Dark Matter unless [357]

$$f_a^{\rm string} \lesssim 6 \cdot 10^{13}\ {\rm GeV} \left(\frac{10^{-18}\ {\rm GeV}}{m_a}\right)^{1/4}, \tag{3.80}$$

where f_a is the $U(1)$-symmetry breaking scale, and m_a is its mass. For the QCD axion, its $f_a - -m_a$ relation restricts the constraint further to be $f_a \lesssim 10^{10}$ GeV. QCD axion cannot lead to any observable SGWB due to its required small string tension, $\mu \sim f_a^2$, as shown in Fig. 3.12. Nonetheless, the future-planned observatories could potentially probe the signal from ultralight ALP DM. The presence of axion mass at late times could also give rise to the formation of domain walls attaching to strings. The collapse of the string-wall system contributes to a relic abundance that is of the same order as the one from strings and potentially leads to observable GW signals [421, 456].

3.7 Chapter Summary

In standard cosmology, the GW spectrum generated by a network of Nambu-Goto cosmic strings (mainly due to emission by loops) is nearly scale-invariant. Its potential observation by the future-planned GW observatories would be a unique probe of new effects beyond the standard models of particle physics and cosmology. Deriving firm conclusions is still premature as theoretical predictions of the GW spectrum from CS are subject to several large uncertainties, cf. [296] and references therein. Still, we found that the extraordinary potential offered by future GW observatories to probe high energy physics has not yet been explored, and in the later chapters of this thesis, we are starting to scrutinize how much can be learned, even if only in the far future, after those planned GW observatories have reached their expected long-term sensitivity and the astrophysical foreground will have been fully understood.

This chapter presents predictions for the resulting GW spectra under several assumptions which we have comprehensively reviewed. We integrate the recent developments and go beyond in several directions:

- We consider the transient period between scaling regimes by computing the time evolution of the string network parameters (long string mean velocity and correlation length) and thus the loop-production efficiency during the evolution of the Universe, see Fig. 3.5 for the standard cosmological history and the right panel of Fig. 4.4 for the non-standard case. Including these transient effects results in a turning-point frequency smaller by $\mathcal{O}(20)$ compared to the prediction from the scaling regime[12]. As a result, the energy scale of the Universe associated with the frequency of SGWB from CS is correspondingly larger than the one predicted from scaling networks.

- We include high-frequency cutoff effects from particle production, which can limit observations for small value of the string tension $G\mu \lesssim 10^{-15}$ and high-frequency cutoff from thermal friction, see Fig. 3.2 and top left panel of Fig. 3.4, as well as a low-frequency cutoff from unstable CS networks, see Fig. 3.9.

[11] The string density is greatly diluted in the pre-inflationary scenario, $f_a \gg H_{\rm inf}$.

[12] The turning-point frequency can even be smaller by $\mathcal{O}(400)$ if, in a far-future, the precision of the order of 1% can be reached in the measurement of the SGWB, cf. Eq. (B.51).

- We provide the relation between the observed frequency of a given spectral feature and the energy scale of the Universe when CS loops are formed, Eq. (3.33). Importantly, we can expect GW signatures which associate to different physical effects, see Figs. 2.5 and 3.4: i) the CS network formation; ii) the time when particle emissions dominate; iii) the moment when thermal friction becomes negligible.

- We discuss how to read information about the small-scale structure of CS from the high-frequency tail of the GW spectrum; see App. B.3.7.

- Assuming the standard cosmology, the SGWB from local CS can manifest a peaked shape due to the metastability of the string network, as shown in Sec. 3.5.

- We derive the SGWB from global CS using a simple semi-analytic method and discuss the comparison between local and global string networks, see Sec. 3.6.

A particular feature of SGWB from local CS is the relation between the observed frequency and the GW production mechanism. In contrast with short-lasting cosmological sources of SGWB, such as phase transitions, where the frequency is simply related to the Hubble radius at the time of GW emission, for local cosmic strings, the time of the dominant GW emission is much later than the time of loop production, by a factor $\sim 1/(G\mu)$, such that the observed frequency is higher due to a smaller redshift. We stressed that a given interferometer might be sensitive to very different energy scales, depending on the value of the string tension (the nature and duration of the non-standard era also matter and will be discussed in the next chapter). This goes against usual paradigms. For instance, it is customary to talk about LISA as a window on the EW scale [140, 153]. This does not apply to GW from cosmic strings, as LISA could be a window on a BSM physics at the QCD scale. Interestingly, the Einstein Telescope and Cosmic Explorer offer a window of observation on the EW and TeV scales and up to 10^{14} GeV for the intermediate inflationary eras (see the next chapter). We apply these findings to probe the non-standard cosmological eras in Chap. 4 and their well-motivated particle physics scenarios in Chaps. 5, 6, and 7.

One final important aspect of cosmic strings is the massive particle radiation, which could allow additional production mechanisms for DM and Baryon asymmetry [180, 195–197, 358–365]. On the one hand, particle production can be probed through cosmic rays and bring complementary non-gravitational information to the SGWB. On the other hand, the particle emission competes with the GW generation and would leave some imprints on the SGWB from CS, e.g., [391, 457] for the standard local cosmic strings. In some ongoing work of the author together with Bibhushan Shakya, we show that future GW observatories could probe the couplings between CS and other particles via the measurement of spectral cutoffs inherited from particle production.

Chapter 4

Cosmic Archeology of Non-Standard Cosmological Histories

Based on
[1] Y. Gouttenoire, G. Servant and P. Simakachorn, ***Beyond the Standard Models with Cosmic Strings****,* JCAP **07** *(2020) 032, [*1912.02569*] &*
[4] Y. Gouttenoire, G. Servant and P. Simakachorn, ***Kination cosmology from scalar fields and gravitational-wave signatures****, [*2111.01150*].*

As predicted by the theory of Big-Bang Nucleosynthesis (BBN), the measurement of the abundances of the light elements constrains the Universe to be dominated by radiation when the temperature was 1 MeV. The smoothness and flatness of the universe, and the temperature anisotropies in the Cosmic Microwave Background (CMB), support the idea that much earlier than BBN, the universe was inflating exponentially, dominated by the energy density of a slowly-rolling scalar field. The non-detection of the fundamental B-mode polarization patterns in the CMB suggests that the maximal Hubble rate during inflation $H_{\rm inf}$ was 5×10^{13} GeV, which corresponds to a maximal energy scale of 10^{16} GeV [20, 21, 55].

The equation of state (EOS) of the Universe between the end of inflation and the onset of BBN, encoded by the parameter $\omega = p/\rho$, where p and ρ are the local pressure and energy densities, is currently unconstrained [458]. The standard paradigm assumes that the energy density of the post-inflationary Universe is radiation-dominated, $\omega = 1/3$, by the thermal equilibrium of the SM particles; nonetheless, alternative cosmological histories are not unlikely. For example, the *reheating* phase connecting the end of primordial inflation and the radiation-dominated Universe could evolve with different EOS depending on the reheating mechanisms. Alternatively, some energetic sources – related to BSM of particle physics – could dominate the SM radiation bath, leading to the non-standard cosmological history.

The cosmological histories beyond the standard radiation-dominated Universe also modify predictions of cosmological abundances. The cosmic expansion dilutes any energy density produced during the early Universe, and its abundance today is sensitive to the evolution of our Universe. E.g., the relic abundances of DM and matter-antimatter asymmetry get diluted or boosted. Furthermore, the evolutions of the primordial perturbations/fluctuations depend on the expansion rate, leading to the altered small-scale structure formations, e.g., DM microhalos, axion mini clusters, and primordial black holes. By confronting these predictions with observations, the pre-BBN cosmological histories could be constrained. We refer to the comprehensive review on these broad topics [458], including an extensive list of references.

This thesis focuses on the effects of non-standard cosmological histories on the SGWB from primordial sources. As discussed in Chap. 2, GW is freely propagating after its production and is directly sensitive to the expansion rate of the Universe. It red-shifts as radiation $\rho_{\rm GW} \propto a^{-4}$, and its frequency also relates to the energy scale of the Universe at its production. Therefore, the SGWB frequency spectrum encodes the whole history of our Universe; any deviation from the prediction of the standard radiation-dominated Universe hints at the non-standard phase of expansion. This

is the so-called *cosmic archeology* with primordial GW.

Previous works of cosmic-archeology using long-lasting GW are [1–4, 22, 70, 71, 199, 274, 294, 295, 334, 459–464]; see [5, 458] for reviews. As discussed exhaustively in this chapter, the effect of the non-standard cosmological era imprints a smoking-gun signature – the spectral index – that differs completely from the prediction assuming the standard radiation-dominated Universe. For a short-lasting source, GW is produced at a specific time, and the spectrum localizes at a specific frequency. The effect of the non-standard cosmological histories shifts the spectrum as a whole [5, 458, 465], except the causality tail (IR tail)[462, 466].

In this chapter, Sec. 4.1 starts classifying the non-standard cosmological schemes: mainly those happening right after inflation and the intermediate ones occurring inside the radiation era. We investigate the effect of the non-standard expansion history on the SGWB from long-lasting sources in Sec. 4.2. A simple argument allows us to derive the shape of smoking-gun signatures and spectral indices, depending on whether the Universe is in the matter-, kination-, or secondary inflationary eras. In the following five sections, we discuss in detail each cosmological scheme, show precisely the modified SGWB, and provide the prospects of detecting these features with future-planned experiments. We also provide some introductory discussion about the interesting case of the kination era in Sec. 4.4. The signature imprinted on SGWB from short-lasting sources is derived in Sec. 4.8, where we choose the GW from FOPT as an example. The chapter is summarized in Sec. 4.9. While we motivate the non-standard eras right after inflation by connecting them to the inflation dynamics, we refer the reader to Chaps. 5, 6, and 7 for the particle-physics implementation of the intermediate non-standard eras. The GW observatories can uniquely probe the heavy-unstable particles and the axion.

4.1 Schemes of Non-Standard Cosmological Histories

Non-standard cosmological eras, where the EOS of the Universe is not radiation-like, can arise in many schemes. In this section, we classify them by the times when these eras happen, illustrated by the cartoon in Fig. 4.1.

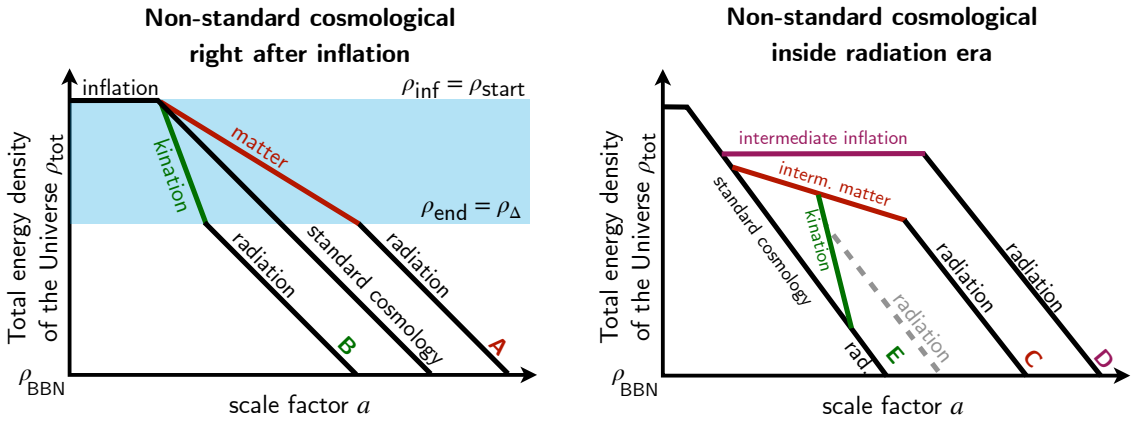

Figure 4.1: Evolutions of the total energy density of the Universe in two main classes of non-standard cosmological histories. **left:** Periods of matter (scheme A) and kination (scheme B) domination right after inflation, e.g., due to the inflaton dynamics after inflation. **right:** Non-standard eras happen during the radiation era much after the reheating of the Universe: the intermediate matter (scheme C), the intermediate inflation era (scheme D), and the intermediate (matter-)kination era (scheme E). The gray dashed line indicates the intermediate kination with an entropy injection. The well-motivated yet non-trivial realizations of these C, D, and E scenarios are unrelated to the inflaton dynamics.

Non-standard era right after inflation. — After the end of the inflationary stage, the Universe evolves with EOS beyond radiation-like ($\omega \neq 1/3$). For example, the inflaton after inflation could oscillate inside the power-law potential near the potential minimum. The scalar Virial theorem, cf.

Eq. (G.141), states that the averaged energy density of the scalar field – in the power-law potential and in the expanding Universe – redshifts as a function of scale factor a as

$$\langle \rho_\Phi \rangle \propto a^{-6p/(2+p)} \text{ for } V(\Phi) \propto \Phi^p, \tag{4.1}$$

is equivalent to the EOS: $\omega = (p-2)/(p+2)$. For $p = 2$, the Universe after inflation is matter-like (scheme A), the fast-rolling field (equivalent to $p \to \infty$) gives the *stiffest* EOS, or the so-called *kination* era (scheme B). See Sec. 4.4 for more histories and detail on kination. While the potential with $p > 2$ indeed provides the EOS that is stiffer than matter, e.g., $p = 4$ for radiation and $p > 10$ for $\rho \propto a^{-5}$, we only focus on the kination era where the effect on SGWB is maximized, as we shall see later. We parametrize the total energy density of the Universe, which is the input for evolving the Universe using the Friedmann equations, as

$$\rho_{\rm tot}(a) = \begin{cases} \rho_{\rm start} \left(\frac{a_{\rm start}}{a}\right)^n + \rho_{\rm late}(a) & \text{for } \rho_{\rm start} > \rho > \rho_{\rm end}, \\ \rho_{\rm end}\, G(T_{\rm end}, T) \left(\frac{a_{\rm end}}{a}\right)^4 + \rho_{\rm late}(a) & \text{for } \rho < \rho_{\rm end}, \end{cases} \tag{4.2}$$

where $\rho_{\rm start}, \rho_{\rm end} \equiv$ the starting and ending energy density of the non-standard cosmology, (i.e., $\rho_{\rm start} = \rho_{\rm inflation}$),

$\rho_{\rm late} \equiv$ the standard-cosmology energy density dominating at late times, (e.g. the standard matter density, and cosmological constant),

and the function

$$G(T,\, T_0) = \left[\frac{g_*(T)}{g_*(T_0)}\right] \left[\frac{g_{*s}(T_0)}{g_{*s}(T)}\right]^{4/3}, \tag{4.3}$$

the change in the number of relativistic degrees of freedom, assuming the conservation of the comoving entropy $g_{*s}\, T^3\, a^3$. We take the functions g_* and g_{*s} from App. C of [22].

Intermediate non-standard era inside radiation era. — After the Universe is reheated and dominated by the radiation bath, another source of energy density – sub-dominant early on – might dominate the radiation bath. This class of non-standard eras requires this energy density to redshift slower than radiation. For example, the intermediate matter era ended by reheating into the thermal bath (scheme C), the intermediate inflation (scheme D), and the intermediate kination after the matter era with or without partially reheating (scheme E). The last scheme is an example of generating the stiff intermediate era, which was not studied in detail until recently [3, 4, 274]. Furthermore, Chaps. 5, 6, and 7 show that these intermediate non-standard eras mostly connect to BSM of particle physics, unrelated to the inflaton. The energy density profile is illustrated in Fig. 4.12 and can be written as

$$\rho_{\rm tot}(a) = \begin{cases} \rho^{\rm st}_{\rm rad}(a) + \rho_{\rm late}(a) & \text{for } \rho > \rho_{\rm start}, \\ \rho_{\rm start} \left(\frac{a_{\rm start}}{a}\right)^n + \rho_{\rm late}(a) & \text{for } \rho_{\rm start} > \rho > \rho_{\rm end}, \\ \rho_{\rm end} G(T_{\rm end}, T) \left(\frac{a_{\rm end}}{a}\right)^4 + \rho_{\rm late}(a) & \text{for } \rho < \rho_{\rm end}. \end{cases} \tag{4.4}$$

where $\rho_{\rm start}, \rho_{\rm end} \equiv$ the starting and ending energy density of the non-standard cosmology,

$\rho_{\rm late} \equiv$ the standard-cosmology energy density dominating at late times, (e.g. the standard matter density, and cosmological constant)

$G(T, T_0)$ is given in Eq.(4.2).

Bounds from the radiation-dominated era at BBN. — The successful predictions for the primordial abundances of light elements are highly sensitive to the expansion history of the Universe. Together with the observations[1], they suggested that the Universe must be in the radiation

[1] Combined also with CMB observations which constrain the effect of neutrinos in CMB.

era at the time of BBN [467–470], meaning that the non-standard eras discussed above should end at temperature $T_\Delta \gtrsim T_{\rm BBN} \simeq 1$ MeV before BBN. We define the time when the non-standard era ends to be t_Δ. The constraint on the end of a non-standard era can be translated into the general bound on the duration of each era, characterized by the number of e-folds

$$N \equiv \log(a_{\rm start}/a_\Delta). \tag{4.5}$$

The following bounds suppose that the non-standard era happens at the highest energy scale, the inflationary scale $E_{\rm inf} \simeq 1.4 \cdot 10^{16}$ GeV [21], even for the intermediate-era cases. For secondary inflation, we require that the observed CMB comes from the first (primordial) stage of inflation, derived in App. C.

$$\begin{aligned}
&\text{Scheme A:} \quad N_{\rm MD} \lesssim 58 + \frac{4}{3}\log\left(\frac{E_{\rm inf}}{1.4\times 10^{16}\ \text{GeV}}\right),\\
&\text{Scheme B:} \quad N_{\rm KD} \lesssim 29 + \frac{2}{3}\log\left(\frac{E_{\rm inf}}{1.4\times 10^{16}\ \text{GeV}}\right),\\
&\text{Scheme C:} \quad N_{\rm MD} \lesssim 58 + \frac{4}{3}\log\left(\frac{E_{\rm reh}}{1.4\times 10^{16}\ \text{GeV}}\right),\\
&\text{Scheme D:} \quad N_{\rm inf}^{\rm 2nd} \lesssim 27.7 + \frac{1}{4}\log\left(\frac{E_{\rm Inf}^{\rm 2nd}}{\text{TeV}}\right),\\
&\text{Scheme E:} \quad N_{\rm KD} \lesssim 14.6 + \frac{1}{3}\log\left(\frac{E_{\rm reh}}{1.4\times 10^{16}\ \text{GeV}}\right).
\end{aligned} \tag{4.6}$$

where $E_{\rm reh}$ is the energy scale when the Universe becomes radiation-dominated right after inflation, and $E_{\rm Inf}^{\rm 2nd}$ is the energy scale of the intermediate inflationary era.

The rest of this chapter focuses on how each scheme of non-standard eras leads to a very distinct signature in SGWB and how the next-generation GW experiments can be tools for learning cosmological history.

4.2 Signatures in SGWB

An exciting prospect for deciphering the pre-BBN universe history and high-energy physics – inaccessible by particle physics experiments – comes from the possible detection of SGWB, originating from the primordial sources discussed in Chap. 2. We now discuss the effect of each non-standard history scheme on the SGWB and later derive the signature (e.g., the spectral indices) using a simple argument. While we focus only on the non-standard era, let us comment on other effects from pre-BBN-scale physics that can also leave some signatures in the SGWB.

Number of relativistic species. — The change in the number of relativistic species can modify the expansion rate of the radiation-dominated Universe; we see this concretely in the factor $G(T, T_0)$. Physically, the thermal bath red-shifts slower due to the entropy dumped by the particle species decoupling from the thermal bath. Similar to the fast expansion during the matter and the intermediate inflation eras, this leaves the signature in SGWB [22, 294, 295, 352, 464]. An effect of the order of $\mathcal{O}(10\%)$ in the SGWB spectrum requires an $\mathcal{O}(100)$ change in the number of relativistic species.

Free-streaming particles. — Another effect that imprints suppression signatures on the SGWB is the damping caused by the free-streaming particles. First pointed out by Weinberg [64], the tensor perturbation transfers the energy of the free-streaming particles, changing their distribution. The well-known effect is the damping due to free-streaming neutrinos, which suppresses the SGWB amplitude by $\sim 35\%$, while the decoupling of photons also decreases the spectrum further by $\sim 10\%$ [22]. Moreover, the free-streaming particles do not only damp the sub-horizon SGWB but also induce a signature in the causality tail (IR tail) [462, 466].

4.2.1 A simple argument

The exact spectrum of the SGWB is obtained from solving the EOM of the metric tensor perturbation in Chap. 2. Nonetheless, the effect of the non-standard history on the SGWB can be captured by a simple observation: the sub-horizon GW evolves in the same way as radiation, $\rho_{\rm GW} \propto a^{-4}$. The SGWB spectrum observed today and produced at H_* (corresponding to some frequency f_*) is,

$$\Omega_{\rm GW}(f_*) \;=\; \left(\frac{\rho_{{\rm GW},*}}{\rho_{{\rm tot},*}}\right)\left(\frac{H_*}{H_0}\right)^2\left(\frac{a_*}{a_0}\right)^4, \tag{4.7}$$

assuming the absence of entropy injection into the thermal bath. For most of the primordial sources discussed in Chap. 2, the GW energy density inherits a fraction of the total energy density of the Universe at the time of production; see the next subsection for examples of inflation and cosmic strings. Consider a production of SGWB at some time a_*/a_0. The SGWB amplitude is larger than the standard prediction if the total energy density during the non-standard era is larger at that time, i.e.,

$$\frac{\Omega_{\rm GW}^{\rm NS}}{\Omega_{\rm GW}^{\rm ST}} \;=\; \frac{\rho_{\rm tot}^{\rm NS}}{\rho_{\rm tot}^{\rm ST}} \;\geq\; 1. \tag{4.8}$$

leading to the shift in the amplitude of SGWB, localizing at some frequency f_*. Interestingly, the long-lasting GW sources – such as inflation and cosmic strings – produce GW along cosmological history and contribute to signals over a wide range of frequencies. Each part of their spectra, therefore, reflects the expansion history of our Universe. For GW from the short-lasting source, the GW spectrum will shift entirely since the main contribution of the spectrum is produced at a specific time. Nonetheless, the super-horizon modes of GW re-enter over a long cosmological history and can also be regarded as long-lasting GW sources. We study the effect of the non-standard era on the short-lasting GW source, particularly the FOPT, in Sec. 4.8.

Non-standard era right after inflation. — Fig. 4.2-left illustrates the evolution of the total energy density of the Universe in the presence of the matter and kination eras right after inflation (schemes A and B). Notice that the scale factor has already been normalized from Fig. 4.1, with the factor today a_0, so that the last bracket of Eq. (4.7) remains constant in all scenarios. The dashed lines show the amount of GW produced along the cosmological history, assuming $\rho_{\rm GW} \propto \rho_{\rm tot}$ at production. The GW produced during the matter (kination) era has a smaller(larger) energy density in GW compared to the standard radiation-domination scenario. We then translate the time scale of the Universe to the frequency of GW; the earlier the production, the higher the frequency of GW. Fig. 4.2-right shows the effect of the non-standard eras right after inflation. The kination era enhances the GW spectrum up to the scale at which GW is firstly produced, while the matter era suppresses it. We can obtain the precise spectral indices – depending on the sources – using this simple argument; see the following subsection.

Intermediate non-standard era inside radiation era. — Fig. 4.3 displays the effect of the non-standard intermediate eras on SGWB from long-lasting sources (schemes C and E). Note that the intermediate inflation (scheme D) will induce an effect close to the intermediate matter era. Similar to schemes A and B, the non-standard expansion histories suppress/enhance depending on whether the total energy density of the Universe at GW production is smaller/larger than that of the radiation era. The distinct signature of the intermediate era is that the GW signature is only present for some time scales or, equivalently, for some range of frequency. Interestingly, the intermediate matter era leads to the step-like suppression, while the intermediate matter-kination era generates the peak-like spectrum. The parts beyond the step and peak correspond to the radiation domination before the non-standard intermediate era, reflecting the spectral index of the radiation era.

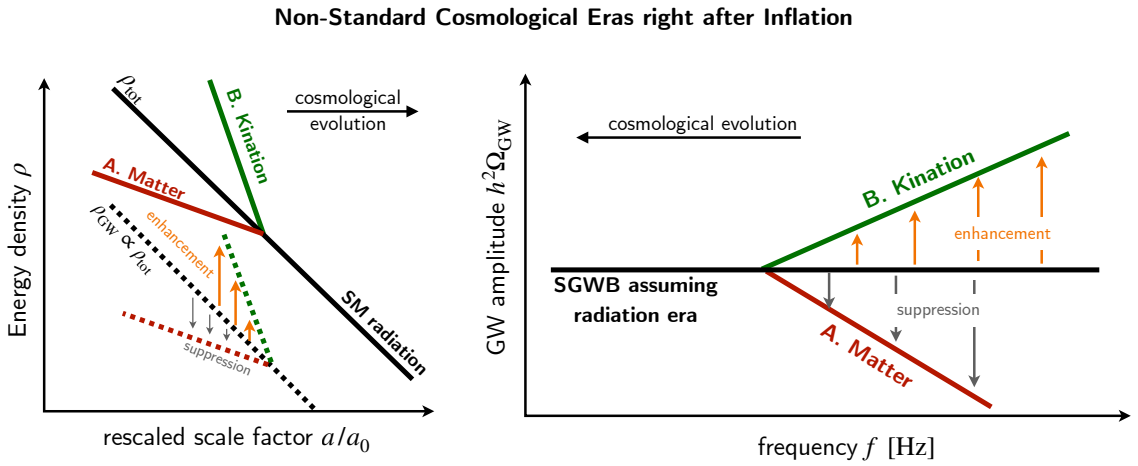

Figure 4.2: The effect of **the non-standard eras right after inflation**, Eq. (4.2), on SGWB. **left:** The energy density in SGWB is suppressed by the matter era (scheme A) and enhanced by the kination era (scheme B), compared to the standard radiation domination. **right:** The SGWB – from the long-lasting GW sources during the radiation domination – leads to a scale-invariant spectrum because the SGWB also redshifts as radiation. The effect of non-standard eras after inflation imprints a suppression and enhancement at high-frequency ranges, associated with the energy scales towards the inflationary scale.

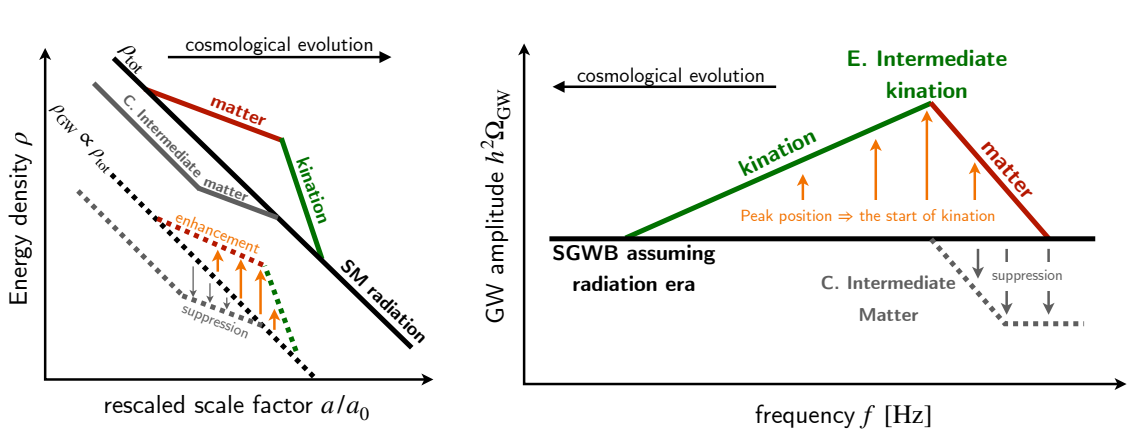

Figure 4.3: The effect of **the intermediate non-standard eras inside the radiation era**, Eq. (4.4), on SGWB. **left:** The energy density in SGWB is suppressed due to the intermediate matter era (scheme C) and enhanced into a peak by an intermediate (matter-)kination era (scheme E). A similar suppression is also expected for the intermediate inflationary era (scheme D). **right:** The intermediate matter and kination eras imprint a step-like suppression and a peaked enhancement on SGWB from long-lasting sources, respectively. The position of the signature – amplitude and frequency – carries the information about the energy scale of the non-standard eras.

4.2.2 Spectral indices from long-lasting sources

The previous section has shown the effects of the non-standard cosmological histories on SGWB: the suppression and enhancement whose amounts are specified by the spectral indices. This subsection quantifies the exact spectral indices which can, fortunately, be done using the simple argument in Eq. (4.7).

Inflation

The inflationary GW energy density is sourced by the scale-invariant tensor perturbation from the primordial inflation; Fourier modes remain frozen until they re- enter the Hubble horizon in

Eq. (2.26). Modes continuously re-enter the horizon, perturb the total energy density within the horizon, and act as a long-lasting source of GW: $\rho_{\rm GW} \propto \rho_{\rm tot}$ at production.

Consider a scenario where the non-standard era ($\rho_{\rm tot} \propto a^{-n}$) ending at scale factor a_Δ and the energy density is ρ_Δ. Eq. (4.7) is rewritten as

$$\Omega_{\rm GW}^{\rm inf}(f_*) = \Omega_{\rm st}^\Delta \left(\frac{\rho_{{\rm GW},*}}{\rho_{{\rm GW},\Delta}}\right)\left(\frac{a_*}{a_\Delta}\right)^4 = \Omega_{\rm st}^\Delta \left(\frac{\rho_{{\rm tot},*}}{\rho_{{\rm tot},\Delta}}\right)\left(\frac{a_*}{a_\Delta}\right)^4 = \Omega_{\rm st}^\Delta \left(\frac{a_*}{a_\Delta}\right)^{4-n}, \tag{4.9}$$

where the second step use $\rho_{\rm GW} \propto \rho_{\rm tot}$, and $\Omega_{\rm st}^\Delta$ is the GW spectrum where it recovers the standard prediction, cf. Fig. 4.2 for example. Now let us rewrite this in terms of frequency. The frequency of inflationary GW corresponds to the horizon size at production, redshifting until today

$$f_* \sim H_* a_*/a_0 = f_\Delta \left(\frac{H_*}{H_\Delta}\right)\left(\frac{a_*}{a_\Delta}\right) = f_\Delta \left(\frac{a_*}{a_\Delta}\right)^{\frac{2-n}{2}}, \tag{4.10}$$

where f_Δ is the GW frequency today corresponding to the end of the non-standard era, given by

$$f_\Delta = \frac{H_\Delta a_\Delta}{2\pi a_0} \simeq 2.7\cdot 10^{-6}\ {\rm Hz}\ \left[\frac{g_*(T_\Delta)}{106.75}\right]^{\frac{1}{2}}\left[\frac{g_{*,s}(T_\Delta)}{106.75}\right]^{-\frac{1}{3}}\left[\frac{T_\Delta}{10^2\ {\rm GeV}}\right]. \tag{4.11}$$

Trading a_*/a_Δ for f_*/f_Δ, we obtain the spectral index of the GW spectrum from inflation,

$$\Omega_{\rm GW}^{\rm inf}(f_*) = \Omega_{\rm st}^\Delta \left(\frac{f_*}{f_\Delta}\right)^\beta \quad \text{with} \quad \beta \equiv 2\left(\frac{n-4}{n-2}\right). \tag{4.12}$$

Indeed, the GW spectrum is scale-invariant for the radiation domination era. For the kination era ($n = 6$), the spectral index is $\beta = 1$, while the matter era ($n = 3$) suppressed the spectrum $\beta = -2$. For a more realistic power spectrum, i.e., by solving the full GW EOM, the non-standard cosmology alters the behavior of the GW transfer function. The effect on the amplitude is of order $\mathcal{O}(1)$ [70, 71, 459], while the transition between eras could feature a spectral oscillation from the change of Bessel function's orders.

Cosmic strings

Consider a cosmic-string network that forms at the end of inflation with tension given by $G\mu \sim (E_{\rm form}/m_{\rm pl})^2$, regardless of the presence of thermal bath at $E_{\rm form}$ (the string formation happens through non-thermal phase transition [313, 471–477]). The SGWB from strings originates mainly from loops – produced in the *scaling* regime along the cosmological history – with $\rho_{\rm loop} \propto \rho_{\rm tot}$, cf. Chap. 3. The energy density of GW then inherits that of loops, produced at some time a_*,

$$\frac{\rho_{\rm GW}}{\rho_{\rm loop}} \simeq \begin{cases} (a_*/a_{\rm emit})^3 & \text{for local strings,} \\ 1 & \text{for global strings,} \end{cases} \tag{4.13}$$

where the local strings have a delayed GW emission, cf. Eq. (3.15), while the global strings decay quickly after loop formation. For global strings, the GW frequency reflects the horizon size (or loop size) at production; the spectral index is obtained to be similar to the inflationary SGWB, up to some log-factor due to the divergent string tension.

For local cosmic strings. — Because of the delayed decay of string loops, loops red-shifts as a pressure-less matter (a^{-3}) before emitting GW. Consider the GW from loops formed at time a_*, during the non-standard era ($\rho_{\rm tot} \propto a^{-n}$) ending at scale factor a_Δ and the energy density ρ_Δ; the GW emission happens at $\tilde{a}_*$, during the era with $\rho_{\rm tot} \propto a^{-m}$. Eq. (4.7) becomes

$$\Omega_{\rm GW}^{\rm cs}(f_*) = \Omega_{\rm st}^\Delta \left(\frac{\rho_{{\rm GW},*}}{\rho_{{\rm GW},\Delta}}\right)\left(\frac{\tilde{a}_*}{\tilde{a}_\Delta}\right)^4 = \Omega_{\rm st}^\Delta \left(\frac{H_*}{H_\Delta}\right)^2\left(\frac{a_*\tilde{a}_\Delta}{\tilde{a}_* a_\Delta}\right)^3\left(\frac{a_*}{a_\Delta}\right)^4, \tag{4.14}$$

where $\Omega_{\rm st}^{\Delta}$ is the GW spectrum where it recovers the standard prediction. The delayed GW emission is considered, and the energy density of loops at production is $\rho_{\rm loop} \propto \rho_{\rm tot}$. Using that $(\tilde{a}_*/\tilde{a}_\Delta) = (t_*/t_\Delta)^{2/m} = (a_*/a_\Delta)^{n/m}$, we obtain

$$\Omega_{\rm GW}^{\rm cs}(f_*) = \Omega_{\rm st}^{\Delta}\left(\frac{a_*}{a_\Delta}\right)^{\frac{3m-nm+n}{m}}, \tag{4.15}$$

Moreover, the loop keeps its initial size H_*^{-1} until GW emission starts because the tension decouples it from the Hubble flow. The frequency of GW today from loops created at H_* is non-trivial,

$$f_* \sim H_*\tilde{a}_*/a_0 = f_\Delta\left(\frac{H_*}{H_\Delta}\right)\left(\frac{\tilde{a}_*}{\tilde{a}_\Delta}\right) = f_\Delta\left(\frac{a_*}{a_\Delta}\right)^{\frac{n(2-m)}{2m}}, \tag{4.16}$$

where the GW frequency is only red-shifted after the emission, and the turning-point frequency f_Δ is defined in Eq. (3.33). Trading a_*/a_Δ for f_*/f_Δ, we obtain the spectral index of the GW spectrum from local cosmic strings,

$$\Omega_{\rm GW}^{\rm cs}(f_*) = \Omega_{\rm st}^{\Delta}\left(\frac{f_*}{f_\Delta}\right)^{\beta} \quad \text{with} \quad \beta \equiv 2\left[\frac{3m-nm+n}{n(2-m)}\right]. \tag{4.17}$$

This is the same result obtained in Chap. 3.

We now see the SGWB signature due to the non-standard cosmological history. For the intermediate inflationary era and matter eras, right after inflation and the intermediate one, we only focus on the SGWB from CS. Because these eras induce suppression that would be hardly probed for the scale-invariant SGWB from inflation[2]. On the other hand, the kination era enhances the SGWB and leaves an observable signature even for the most conservative SGWB from inflation. We shall discuss the detectability due to the kination era on all prime GW sources. Nonetheless, we extensively derive the detectability for the intermediate kination case (scheme E) because the kination era after inflation is subject to various theoretical constraints.

4.2.3 Detectability of spectral features

We aim to use the would-be detection of a SGWB spectrum to constrain early non-standard cosmological histories motivated by particle physics. Assuming the a detector (i) with sensitivity $\Omega_{\rm sens}^{(i)}(f)$, the detection of SGWB is claimed if

$$\Omega_{\rm sens}^{(i)}(f) \gtrsim \Omega_{\rm GW}(f), \tag{4.18}$$

i.e., a GW spectrum is observable when its amplitude is large than the detector's sensitivity. We adopt the power-law integrated sensitivity (PLS) curves of the different experiments, cf. App. A.2, which follow a graphical detection criterion [478]. The precise data analysis on whether the signal is detectable or whether one can reconstruct the frequency profile of SGWB requires more dedicated techniques and algorithms, see for example [256, 479, 480].

We propose two prescriptions, based on the GW signature – deviating from the standard cosmology prediction – due to the non-standard era, happening at temperature T_Δ:

- **Rx 1** *(turning-point prescription)*: The frequency f_Δ of the turning-point is where the non-standard spectrum starts deviating from the standard prediction by some percentage of the amplitude inside the experiment's windows. For example, we derive the turning point f_Δ with a numerically fitted coefficient for 1% and 10% deviations.

[2] Some inflationary theories generate a blue-tilted power spectrum that allows the observable spectral suppression due to the matter era [460].

- **Rx 2** *(spectral-index prescription)*: The absolute value of the observed spectral index β, defined as $\Omega_{\rm GW}(f) \propto f^{\beta}$, is not zero (signature of the standard cosmology), and we choose the benchmark to be the spectral index larger than ± 0.15. Note that the effect of the non-standard era leads to a spectral index larger than a benchmark value. We checked that the choice of the precise benchmark value, e.g., 0.15, has minimal impact on the results.

In principle, both prescriptions would give the same results because the turning point is where the spectral index changes suddenly. Unless further specified, most of the analyses in the thesis adopt Rx 1 due to its technological convenience.

Now we shall start inspecting each scheme of the non-standard cosmological histories and discussing their theoretical limitations and detectability at the future-planned observatories. The particle-physics implementations for the intermediate matter era (scheme C) and kination era (scheme E) are postponed to Chaps. 5, 6, and 7.

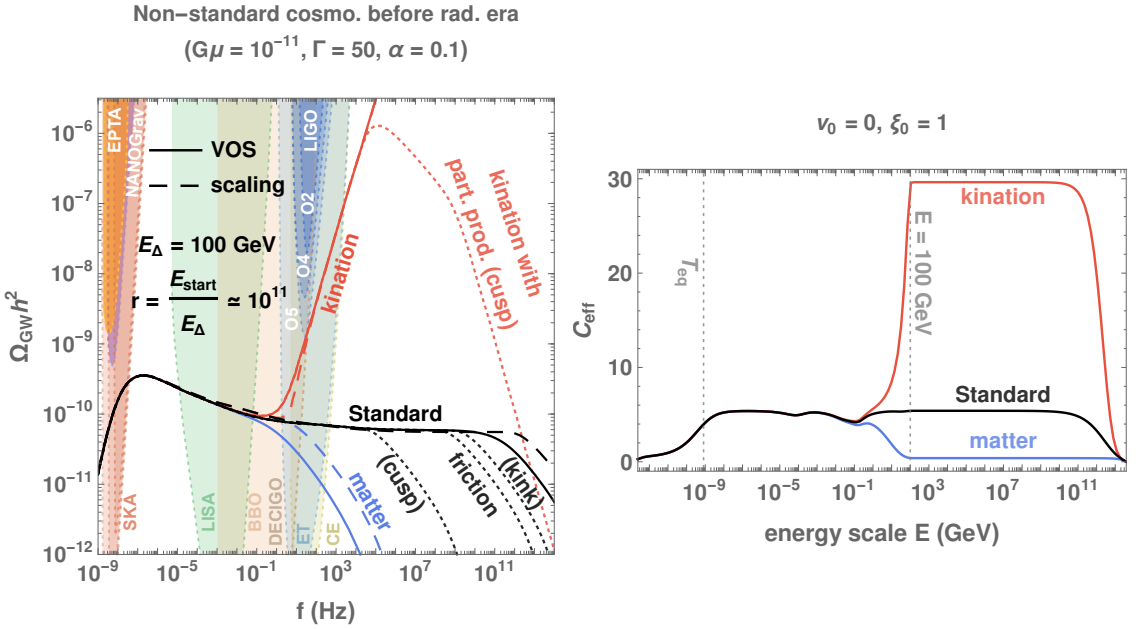

Figure 4.4: **Left:** GW spectra from cosmic strings assuming either the scaling (dashed) or the VOS network (solid), cf. Sec. 3.3.3, evolved in the presence of a non-standard era, either matter (blue) or kination-dominated (red), before the standard radiation era. The transient VOS evolution of the long-string network during the change of cosmology shifts the turning-point towards lower frequencies by $\mathcal{O}(25)$. The cut-offs due to particle production, cf. Sec. 3.2.5, or thermal friction, cf. App. B.5.4, are shown with dotted lines. **Right:** The evolution of the loop-production efficiency for each cosmological background shows that the scaling solution is reached after a transient evolution corresponding to the Hubble rate dropping by an order of magnitude. The slower the expansion rate $a \propto t^{2/n}$, the slower the dilution of the long-string energy density $\rho_\infty \propto a^{-2}$ and the higher the needed loop-production efficiency $C_{\rm eff}$ in order to reach the scaling regime $\rho_\infty \propto t^{-2}$.

4.3 Scheme A: Matter-Domination right after Inflation

We consider the first scenario in the non-standard cosmological histories: the matter era after inflation. In this case, the inflaton behaves as pressure-less matter during its oscillation around the potential bottom – approximately quadratic. This coherent-oscillation stage might be crucial for the reheating of the Universe [82, 83]. Remaining agnostic about the coupling between inflaton and other particles, we treat the energy scale of inflation $E_{\rm inf}$ and the end of matter era E_Δ as free parameters. We only consider the SGWB from local and global cosmic strings because the matter has the suppressed GW signature, which renders SGWB from inflation highly unobservable. Note

also that we will present the case of the kination right after inflation (scheme B) along with the discussion of scheme A below. Except for the difference in the slopes, the feature called *the turning point* is universal for both cases.

4.3.1 Impact on the spectrum: a turning-point

The GW spectra from local cosmic strings are shown in Fig. 4.4 for long-lasting matter and kination eras, starting before the string formation at $E_{\rm start} = m_{pl}\sqrt{G\mu}$ and ending at $E_{\rm end} = E_\Delta = 100$ GeV with duration

$$r \equiv \left(\frac{\rho_{\rm start}}{\rho_{\rm end}}\right)^{1/4} \equiv \left(\frac{E_{\rm start}}{E_\Delta}\right) \simeq 10^{11}. \tag{4.19}$$

For matter domination, we have the suppressed spectrum, while the kination leads to enhancement, as discussed previously by the simple argument. Note that the duration of the kination era might be subjected to the $\Delta N_{\rm eff}$ and fluctuation constraints in the next section, i.e., $N_{\rm KD} < 11$. However, these bounds strongly depend on the inflationary scale and the size of curvature perturbation which could be relaxed.

The turning-point frequency: — A key observable is a frequency above which the GW spectrum differs from the one obtained in standard cosmology. This is the so-called *turning-point* frequency f_Δ. It corresponds to the redshifted frequency emitted by the loops created during the change of cosmology at the temperature T_Δ. In the instantaneous scaling approximation, cf. dashed line in Fig. 4.4, the turning-point frequency f_Δ is given by the $(T,\ f)$-correspondence relation

$$f_\Delta^{\rm scaling} = (4.5\times10^{-2}\ {\rm Hz})\left(\frac{T_\Delta}{\rm GeV}\right)\left(\frac{0.1\times50\times10^{-11}}{\alpha\,\Gamma G\mu}\right)^{1/2}\left(\frac{g_*(T_\Delta)}{g_*(T_0)}\right)^{1/4}. \tag{4.20}$$

However, the deviation from the scaling regime during the change of cosmology, cf. Sec. 3.3.3, implies a shift to lower frequencies of the $(T,\ f)$-correspondence, by a factor ~ 22.5, cf. solid vs dashed lines in Fig. 4.4. The correct $(T,\ f)$-correspondence when applied to a change of cosmology is

$$f_\Delta^{\rm VOS} = (2\times10^{-3}\ {\rm Hz})\left(\frac{T_\Delta}{\rm GeV}\right)\left(\frac{0.1\times50\times10^{-11}}{\alpha\,\Gamma G\mu}\right)^{1/2}\left(\frac{g_*(T_\Delta)}{g_*(T_0)}\right)^{1/4}. \tag{4.21}$$

We fit the numerical factor in Eq. (4.21) (but also in Eq. (4.39)) by imposing[3] the non-standard-cosmology spectrum $\Omega_{\rm NS}$ to deviate from the standard-cosmology one $\Omega_{\rm ST}$ by 10% at the turning-point frequency (**Rx 1**),

$$\left|\frac{\Omega_{\rm NS}(f_\Delta)-\Omega_{\rm ST}(f_\Delta)}{\Omega_{\rm ST}(f_\Delta)}\right| \simeq 10\%. \tag{4.22}$$

We are conservative here. Choosing 1% instead of 10% would lead to a frequency shift of the order of $\mathcal{O}(400)$, cf. Eq. (B.51). Note that our Eq. (4.21) is numerically very similar to the one in [294–296] although an instantaneous change of the loop-production efficiency $C_{\rm eff}$ at T_Δ is assumed in [294–296]. This can be explained if in Ref. [294–296], the criterion in Eq. (4.22) is smaller than the percent level.

4.3.2 Detectability

Turning points due to the matter or kination after inflation, cf. Eq. (4.21), are plotted in the left panel of Fig. 4.5, for different values of $G\mu$ and temperatures T_Δ at the end of the non-standard era. We show the shift to lower frequencies by a factor $\sim$ 22.5 due to the deviation from the

[3]The coefficient in Eq. (4.21) has been fitted upon considering the matter case $\Omega_{\rm NS} = \Omega_{\rm matter}$. Note that the turning-point in the kination case is slightly higher frequency by a factor of order 1, cf. Fig. 4.4.

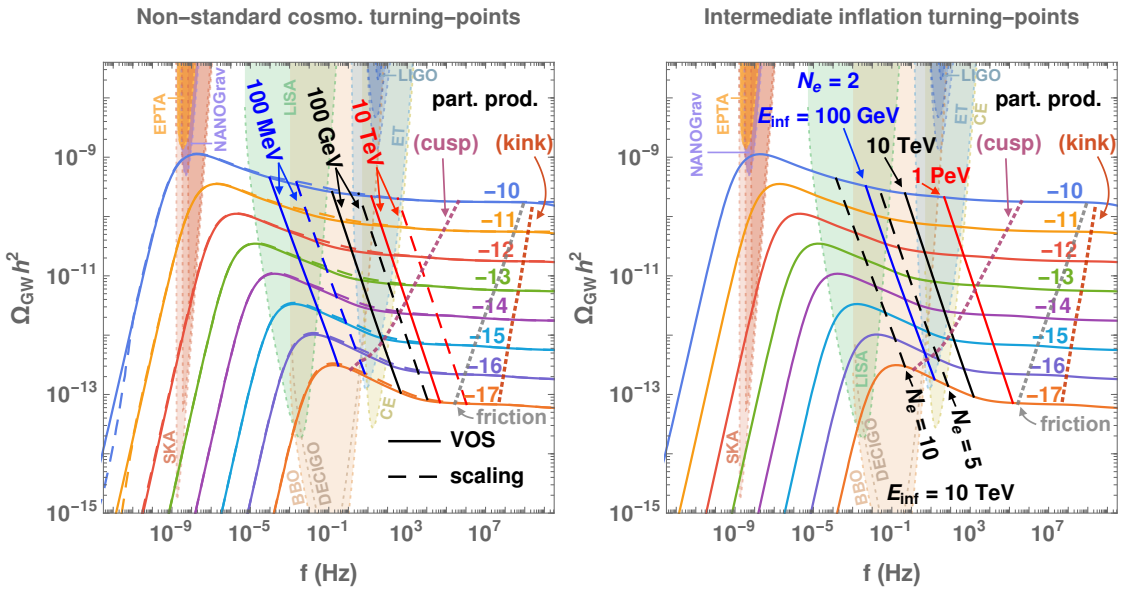

Figure 4.5: **left:** Straight solid and dashed lines are a collection of VOS and scaling turning points, given by Eq. (4.21) and Eq. (3.33) respectively, for general non-standard cosmologies ending at temperature T_Δ. The displayed spectra assume a standard cosmology. Each spectrum corresponds to string tension $G\mu = 10^x$, where a number on each line specifies x. **right:** We show the turning-points, given by Eq. (4.39), for intermediate inflation lasting for N_e e-folds and taking place at the energy scale $E_{\rm inf}$. The dotted lines in the two panels show the cut-off frequencies due to particle productions, cf. Sec. 3.2.5, and thermal friction, cf. Sec. B.5.4, for each value of $G\mu$.

scaling regime during the change of cosmology. With the solid purple and red lines, we show the expected cut-off frequencies above which the GW spectrum is expected to be suppressed due to the domination of massive particle production over gravitational emission in the benchmark cases where the small-scale loop structures are dominated either by cusps or kinks. Hereby, we show the possibility of losing information about the cosmological evolution when the turning points are at higher frequencies than the particle-production cut-off.

In Fig. 4.6, we show the detectability of a turning point at frequency f_Δ, corresponding to a change of cosmology taking place at the temperature T_Δ, in the plane $G\mu - T_\Delta$, $f_\Delta - T_\Delta$, and $G\mu - f_\Delta$. We compare the turning-point formula, defined in Eq. (4.21) in the VOS regime with the one defined in eq (3.33) in the scaling regime. We see that LISA, BBO/DECIGO and ET/CE can probe non-standard eras ending below $T_\Delta \simeq 10$ GeV, 1 TeV and 100 TeV, respectively. Particle production limits the observation for $G\mu \lesssim 10^{-15}$. Some of these plots were already presented in [294, 295] (for long matter and kination era), assuming that the scaling regime holds during the change of cosmology. Our plots turn out to be similar due to their different choice of precision in the determination of the turning point frequency, see criterion in Eq. (4.22).

Furthermore, the right panel of Fig. 4.5 also shows the turning points for the intermediate inflationary case (scheme D), cf. Eq. (4.39), for different inflation scales $E_{\rm inf}$ and e-fold numbers $N_{\rm e}$. Due to the stretching of the correlation length outside the horizon and the necessity to wait for it re-enters to reach the scaling regime, the longer the inflation, the lower the turning-point frequency. See Sec. 4.6 for further detail.

4.3.3 Global string as a probe of non-standard cosmology

The impact of non-standard cosmology on the GW spectra of global strings is shown in Fig. 4.7. The frequency of the turning point corresponding to a change of cosmology at a temperature T_Δ

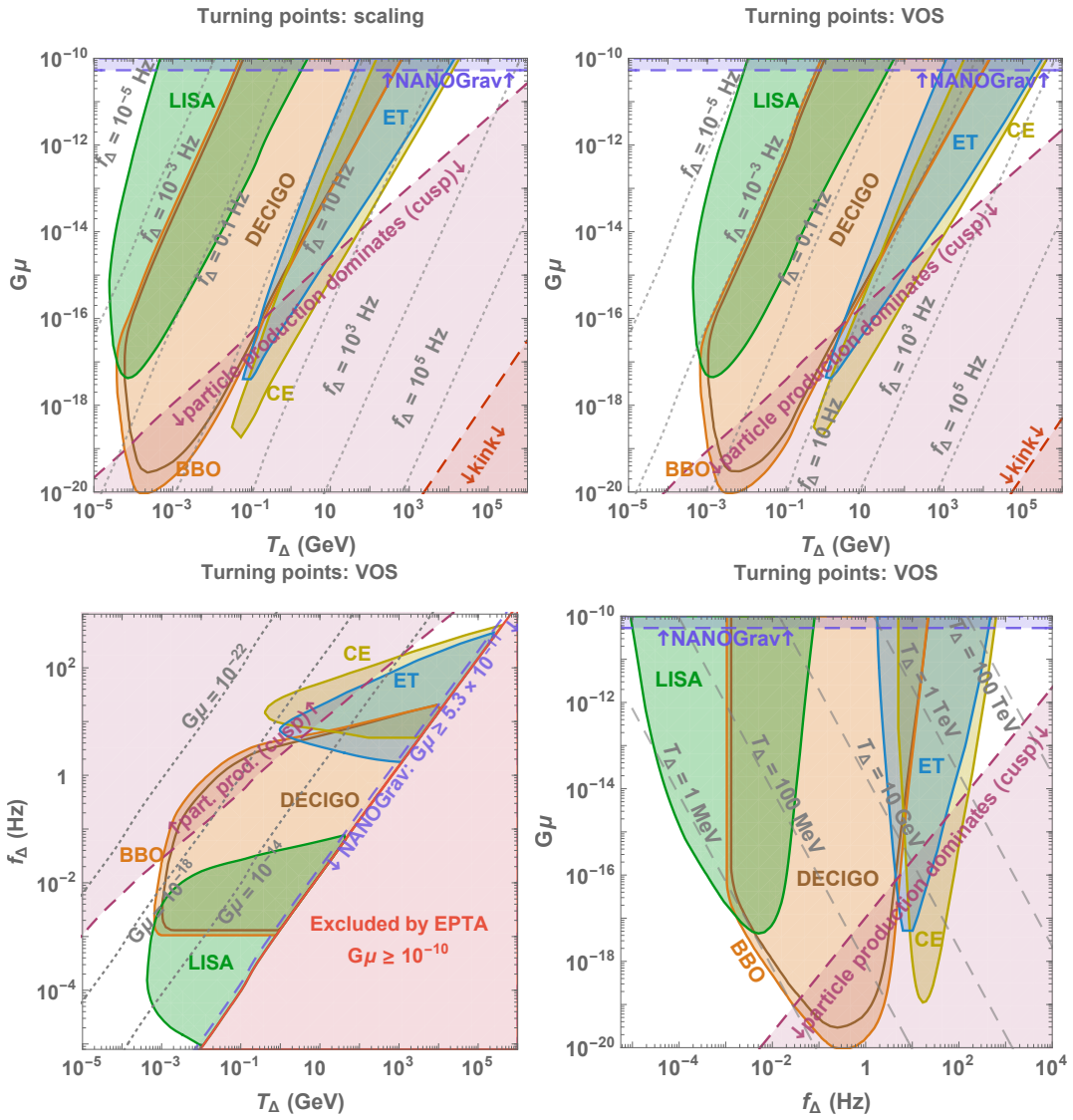

Figure 4.6: **top:** Comparison between the detectability of the turning-points in $G\mu - T_\Delta$ planes assuming a scaling network (left) with the one assuming the full VOS evolution (right), cf. Sec. 3.3.3, evolved in non-inflationary-non-standard-eras. Gray dotted lines are turning points for given frequencies, cf. Eq. (3.33) for scaling network and Eq. (4.21) for VOS network. **bottom:** Detectability of turning points in the planes $f_\Delta - T_\Delta$ and $G\mu - f_\Delta$ assuming a VOS network. Limitations from particle production (see Sec. 3.2.5) and bounds from EPTA are also included.

is given by Eq. (3.79). We report here a numerically-fitted version

$$f_\Delta^{\rm glob} \simeq \text{Hz} \left(\frac{T}{\text{GeV}}\right) \left(\frac{0.1}{\alpha}\right) \left(\frac{g_*(T)}{g_*(T_0)}\right)^{1/4} \times \begin{cases} 8.9 \times 10^{-7} & \text{for } 10\% \\ 7.0 \times 10^{-8} & \text{for } 1\% \end{cases}, \tag{4.23}$$

where the detection criterion is defined as in Eq. (4.22). In contrast to local strings, the global string decays quickly into particles and does not experience the delayed GW emission. In this case, the turning point is independent of the string tension and is sensitive to the Universe at higher energy scales. We now consider the reach of global strings for probing a non-standard cosmology. Fig. 4.8 shows the detectability of the turning-points by future GW experiments. Due to the string-scale independence, the global-string detectability collapses onto a line.

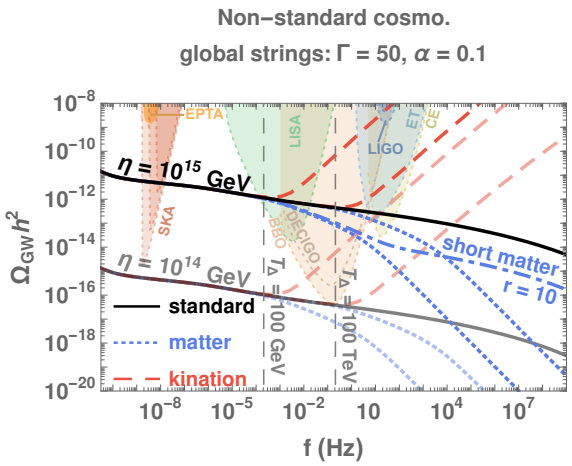

Figure 4.7: GW spectrum from the global cosmic strings assuming VOS network, evolving in the presence of a non-standard era, either long-lasting matter (dotted), intermediate matter (dot-dashed), or kination (dashed), ending at the temperature $T_\Delta = 100$ GeV or 100 TeV. The turning-point frequency is independent of the string tension.

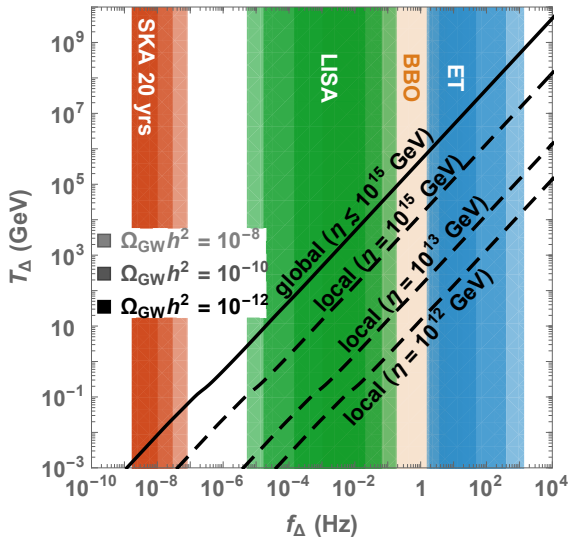

Figure 4.8: Detectability of the turning-points in the $T_\Delta - f_\Delta$ plane. The solid line represents turning points for global strings formed at any energy scale η, while dashed lines are turning points from local strings, similar to lines in the bottom-left panel of Fig. 4.6. Shaded areas correspond to the frequencies probed by each observatory assuming SGWB of amplitudes $\Omega_{\rm GW}h^2 = 10^{-8}$, 10^{-10} and 10^{-12}. The plot is inspired by [199].

4.4 Scheme B: Kination-Domination right after Inflation

The kination era has recently been at the center of attention because any relic density of the Universe gets amplified. The above simple argument has shown that the SGWB receives a significant enhancement that would allow the current and next-generation GW observatories to probe the particle physics related to the kination era. In this section, we first introduce the reader to the kination era; however, only the kination right after inflation (scheme B) is focused on. Due to some theoretical limitations, we shall see that there cannot be any spectral enhancement observable in the planned experiments. The intermediate (matter-)kination (scheme E) will be discussed in detail in Sec. 4.7 along with its compelling GW signatures, which could be a unique probe of *axion* physics as we shall see later in Chaps. 6 and 7.

4.4.1 A Brief Introduction to Kination

The term *kination* was introduced for the first-time[4] in [482] for describing a homogenous scalar field whose kinetic energy dominates the total energy of the Universe. The corresponding EOS is $\omega = \frac{p}{\rho} = \frac{KE-PE}{KE+PE} \simeq 1$, where p is the pressure, ρ denotes the energy density, and KE and PE denote kinetic and potential energy density, respectively. For example, the inflaton potential becomes steep; the inflaton fast-rolling ends the inflationary stage and induces a kination EOS.[483],

[4] Actually, the presence of kination dates back to the exotic cosmological model by Zel'dovich [481] if we consider the generalized definition of the kination: a cosmological epoch with EOS $\omega = 1$.

illustrated as scheme B in Fig. 4.1 and type (i) scenario in Fig. 4.9.

Kination has the maximal EOS allowed by causality, i.e., the speed of perturbations or the *sound* speed ($c_s^2 = \partial p/\partial\rho = 1$) becomes the light's speed. Due to the cosmic expansion, its energy density red-shits the fastest $\rho \propto a^{-6}$, where a is the scale factor of the Universe, while the Universe expands at the slowest rate, $a \propto t^{1/3}$. Any kination era at early times ends by becoming subdominant to the radiation bath without the need for decay[5]. Such a slow expansion rate has various phenomenological consequences, for example: reheating after inflation [485–491], electroweak baryogenesis [482, 492], the enhancement of DM relics [484, 493–503], matter perturbations and small-scale structure formation [504, 505], GW signals from inflation [70, 71, 459, 461, 506–511], GW from both local and global cosmic strings [1, 3, 4, 199, 274, 294, 295, 350, 352], and GW from phase transitions [4, 5, 458, 462, 512]. Before moving on to the kination and GW signature, we comment on other ideas about a non-scalar-field kination era.

Kination beyond the fast-rolling scalar. — The small-scale anisotropic stress in the coarse-grained homogenous expanding background has the energy density $\propto a^{-6}$ [513, 514]. Pointed out in [515, 516], the remnant fluid after a strong first-order phase transition also produces the kination-liked anisotropy. I.e., the intermediate kination era after the second-stage inflation – from a supercooling phase transition – as shown in type (iii) scenario in Fig. 4.9. The EOS evolution after bubble collisions would require a dedicated study, and we shall not consider kination after secondary inflation in this work.

The kination in the rest of this thesis focuses on two schemes in Fig. 4.1:

- **Scheme B**: Inflation → Kination → Radiation (type i in Fig. 4.9)
- **Scheme E**: Inflation → Radiation → Matter → Kination → Radiation without and without entropy injection (type ii.1 & ii.2 in Fig. 4.9)

For scheme E, we shall see the necessity of the prior matter era in Sec. 4.7.

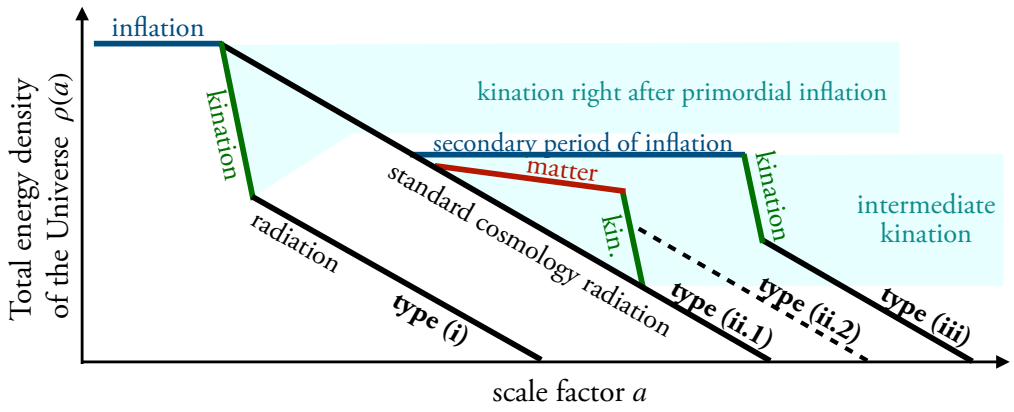

Figure 4.9: Possible cosmological histories involving a period of kination.

4.4.2 Some UV completions

In the literature, two classes of models predict a stiff EOS, $\omega > 1/3$, following primordial inflation.

Steep oscillatory potential. — Models where the inflaton ends up oscillating in a steep potential, $V(\phi) \propto \phi^p$ with $p > 4$ [482, 483, 517] has stiff EOS but hardly lasts longer than a few e-folds [518–521].

Steep non-oscillatory potential. — Quintessential inflation models [522, 523] where the inflaton potential has a sudden drop responsible for the fast-rolling scalar field after the end of inflation.

[5] Though the kination-decaying scenario can be considered [484].

On both sides of the drop, the inflaton potential features two asymptotically flat regions – the inflationary plateau and the quintessence tail – in which the scalar field slow-rolls and generates both primordial inflation and the late dark energy with a unified description. The first problem of this model is the super-Planckian field excursion. Indeed, during a period of kinetic energy domination, a canonically-normalized scalar field ϕ varies over $\mathcal{O}(M_{\rm Pl})$ during each e-fold of kination

$$\ddot{\phi} + 3H\dot{\phi} = 0 \quad \text{with } H = \sqrt{\frac{\dot{\phi}^2/2}{3M_{\rm pl}^2}} \;\Rightarrow\; \Delta\phi \simeq \sqrt{6} M_{\rm pl} N_{\rm KD}, \;\text{ with }\; N_{\rm KD} \equiv \Delta \log a, \quad (4.24)$$

which is a no-go if one takes seriously the swampland distance conjecture [524–526]. One way to circumvent this is by considering non-canonical kinetic terms, as in α-attractor models. See App. D. The second problem relates to the reheating of the Universe because the kination does not feature the coherent oscillations that can lead to the usual reheating or preheating mechanism. Extra ingredients are required: either additional non-minimal couplings or extra fields. We do not discuss this further as a myriad of models have been discussed in the literature and defer to App. D, reporting status with references on model-buildings related to the scenario of kination following inflation. In the following subsection, we present the GW signature from inflation and cosmic strings and discuss theoretical constraints on the kination after inflation, e.g., the recently realized limitation from scalar fluctuations [527].

4.4.3 GW signatures and $N_{\rm eff}$ constraints

In Sec. 4.2, we derived the spectral indices for inflationary and cosmic-string SGWB. We saw that the kination greatly enhanced their detectability, especially boosting the inflationary one into the observable range. However, a large GW relic – produced before BBN and CMB – contributes to the energy density of the extra relativistic species and is strongly constrained by the $\Delta N_{\rm eff}$ from BBN and CMB observations, cf. Eq. (2.22).

SGWB from inflation. — As illustrated in the left panel of Fig. 4.10, the kination after inflation boosts the SGWB at high-frequency ranges. At the same time, the flat behavior appears at low frequencies, corresponding to the radiation domination at late times. The position of the turning point in Eq. (4.54) is controlled by the inflationary scale $H_{\rm inf} \simeq E_{\rm inf}^2/M_{\rm pl}$ and the reheating temperature $T_{\rm RH}$, defined when the kination era ends. Nonetheless, this large enhancement leads to no observability due to the $\Delta N_{\rm eff}$ bounds in Eq. (2.22), as shown on the right panel of Fig. 4.10. The $\Delta N_{\rm eff}$ bound is roughly interpreted that the largest GW amplitude, which also has the highest frequency corresponded to the end of inflation,

$$f_{\rm max} \;\simeq\; 9.6 \cdot 10^{11}\ {\rm Hz} \left[\frac{g_*(T_{\rm RH})}{106.75}\right]^{\frac{1}{6}} \left[\frac{g_{*,s}(T_{\rm RH})}{106.75}\right]^{-\frac{1}{3}} \left[\frac{H_{\rm inf}}{10^{13}\ {\rm GeV}}\right]^{\frac{2}{3}} \left[\frac{1\ {\rm TeV}}{T_{\rm RH}}\right]^{\frac{1}{3}}. \quad (4.25)$$

In App. F.2, we show that $\Delta N_{\rm eff}$ bound on inflationary GW leads to the following upper bound on the duration of kination, which applies for both schemes B and E in Fig. 4.1,

$$N_{{\rm KD},\Delta N_{\rm eff}} \;\lesssim\; 11.9 + \log\left(\frac{5 \cdot 10^{13}\ {\rm GeV}}{H_{\rm inf}}\right). \quad (4.26)$$

The $\Delta N_{\rm eff}$ bound excludes the region where the too-long kination leads to a too-large GW signal. All future planned experiments cannot beat this bound, so we expect no discovery of the enhanced signal from a kination era right after inflation. Nonetheless, this region will be potentially probed by the high-frequency (HF) experiments discussed in [40]. In Fig. 4.10, we show how HF experiments – operating at 10 MHz and 10 GHz with sensitivity $h^2\Omega_{\rm sens}^{\rm min} = 10^{-10}$ – will be able to probe the parameter space beyond the BBN bound. We also find that HF experiments operating at 1 kHz, 1 MHz, and 1 GHz need at least $h^2\Omega_{\rm sens}^{\rm min} \lesssim 10^{-14}, 10^{-11},$ and 10^{-8}, respectively – for making a

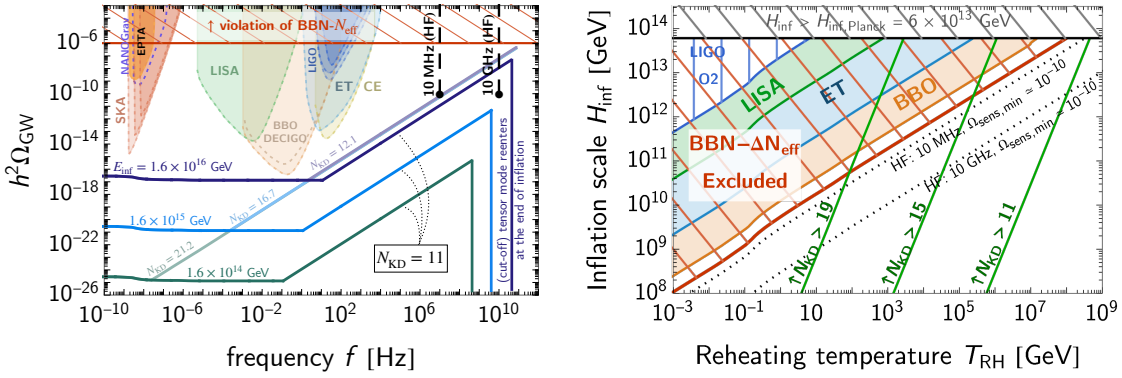

Figure 4.10: Ability of future GW experiments to probe a kination era right after inflation (scheme B) via the spectral enhancement on the inflationary SGWB, assuming an inflation scale $H_{\rm inf} = E_{\rm inf}^2/\sqrt{3}M_{\rm Pl}$. The $\Delta N_{\rm eff}$ bound – shown in red, cf. Eq. (4.26) – prevents all discoveries of the planned experiments, even for the highest allowed inflationary scale $H_{\rm inf,Planck} \simeq 6{\cdot}10^{13}$ GeV. Above the black dotted lines of the right panel, the high-frequency (HF) experiments – operating at a given frequency and the sensitivity $\Omega_{\rm sens,min}$ on the left panel – could probe the kination's enhancement. Alternatively, the pale spectra on the left panel – with a specific value of the number of kination-efolds $N_{\rm KD}$– satisfy the BBN bound for a given $H_{\rm inf}$. However, these spectra are unphysical due to the scalar fluctuation bound, $N_{\rm KD} \lesssim 11$ for $\rho/\delta\rho\,(H_{\rm inf}) \lesssim 10^{9\div10}$ cf. Eq. (4.29) and Ref. [132], as shown as the green lines on the left panel. By imposing $N_{\rm KD} \lesssim 11$ (relaxed in some inflation model), the spectra in the right panel can never violate the $\Delta N_{\rm eff}$ bound.

discovery. For experiments operating at $\gtrsim$ THz range, the cut-off frequency in Eq. (4.25) is smaller such that they cannot probe the GW signal.

Let us briefly comment on the arbitrary stiff era and the corresponding constraint from $\Delta N_{\rm eff}$. A similar analysis was performed for an arbitrary stiff era in [71], considering LIGO and LISA prospects. The conclusion was that only $\omega \simeq 1/2$ could still lead to signals at LISA while not being excluded by BBN, but they would correspond to a very low-energy stiff era below a GeV. In App. E, we provide analogues of Fig. 4.10 for a stiff era with $\omega = 1/2$ and $\omega = 2/3$. For $\omega = 1/2$, there is no $\Delta N_{\rm eff}$ bound; LISA, ET, and BBO can probe the enhanced GW signal from inflation. The high-frequency experiments would not bring additional insight due to the gentle slope of the signal. For $\omega = 2/3$, the $\Delta N_{\rm eff}$ bound prevents LISA's detectability, while there is a potential for ET and BBO.

SGWB from cosmic strings. — Similar to the inflationary SGWB, the kination era greatly enhances GW from cosmic strings, where the turning-point frequency for local strings is determined by Eq. (4.21). The example spectra are shown in Fig. 4.11 for different kination durations. Interestingly, a short kination period can generate a bump in the spectrum. In the left panel of Fig. 4.11, the network has no time to reach the scaling regime. Particularly, on the right panel of Fig. 4.11, we show how the efficiency of the loop production grows with the duration of the kination era, without reaching its scaling value $C_{\rm eff} = 29.6$, cf. Eq. (3.44). The bump increases for a longer kination epoch since the network gets closer to its scaling solution. However, this high-frequency bump may not be observable due to the high-frequency cutoff from particle production, cf. solid purple and red lines in the left panel of Fig. 4.11. In any case, the turning point of the spectrum might reside within the observable window without violating the $\Delta N_{\rm eff}$ bound due to the particle production cut-off. The prospect of detecting the turning point is the same as the matter era after inflation, as shown in Fig. 4.6. The turning-point signature in the global-string SGWB is presented in Fig. 4.8. The formation of the cosmic-string network during the kination era and before the reheating might be non-trivial and probably relies on the non-thermal phase transition [313, 471–477]. We leave the investigation of the cosmic-string formation during the kination era for future works.

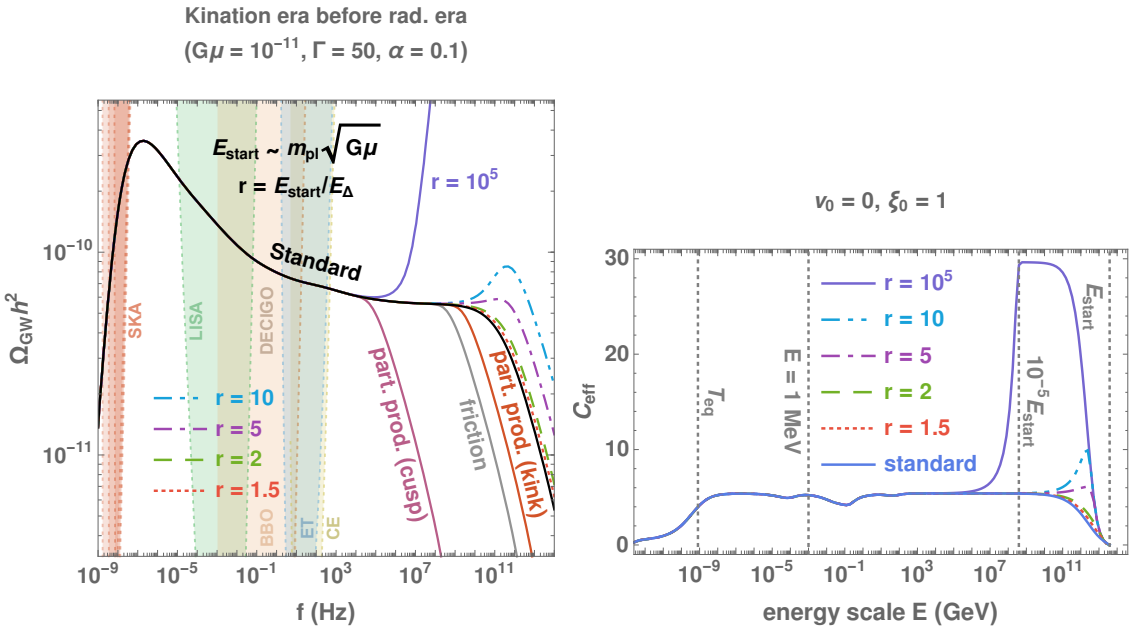

Figure 4.11: **left:** GW spectrum from the local cosmic-string network evolved in the presence of a short kination era after inflation. The peak at high frequencies generated by loops created just after the network formation (see Fig. 3.6) is enhanced by the effect of the kination era. The cut-offs due to particle production, cf. Sec. 3.2.5, and thermal friction, cf. App. B.5.4, are shown with purple, red, and gray lines. **right:** The corresponding evolution of the loop-production efficiency shows that the scaling regime is never reached for short kination eras.

4.4.4 Constraints from Scalar Fluctuations

So far, the strongest bound on the kination duration comes from the requirement of radiation era at the time of BBN. However, the scalar fluctuations in the early Universe could lead to a stronger bound as the fluctuation's growth depends on the Universe's expansion history. For example, an extended matter era can lead to the non-linear behavior of fluctuations [528–530] or enhanced formation of primordial black holes [531]. Similarly, the fluctuations of the massless field, which behave as radiation, grow during the kination era and could eventually dominate over the zero-mode, which scales as a^{-6}. One probable source of the fluctuations is the adiabatic curvature perturbation Φ that induces the fluctuation in the density of the homogeneous free-axion field. One can show that the EOM of the fluctuation from the freely-moving scalar satisfies (see Ref. [132] for a precise derivation)

$$\phi_k'' + 2\mathcal{H}\phi_k' + k^2\phi_k = -4\Phi_k'\phi_{\rm zero}', \tag{4.27}$$

where k is the comoving momentum ($k = ak_{\rm phys}$), $\cdot' \equiv d/d\tau = a(t)\cdot d/dt$ for t, τ are physical and conformal times, respectively. The non-vanishing scalar's speed sources the $k^{\rm th}$-mode axion fluctuation with help from the adiabatic fluctuation of the same mode Φ^k. Approximating the $k^{\rm th}$-mode fluctuation as a harmonic oscillator of mass k, its energy density is $\delta\rho_k \sim k_{\rm phys}^2\phi_k^2 = (k/a)^2\phi_k^2$. By averaging the EOM over many oscillations, the approximated energy density reads

$$\delta\rho(k) \sim \Phi^2\dot{\phi}_{\rm zero}^2 = \Phi^2\rho_{\rm zero}\big|_{k=aH}\,, \tag{4.28}$$

where we use $\Phi_k' \sim k\Phi$ in the second step, and the energy density of the freely-moving field is $\rho_{\rm zero} = \dot{\phi}_{\rm zero}^2$. The ratio between energy densities in fluctuation and zero-mode tracks the power spectrum of the curvature perturbation

$$\frac{\delta\rho}{\rho_{\rm zero}}(k) = \Phi^2(k) \simeq 10^{-9\div-10}, \tag{4.29}$$

where we assume the scale-invariant curvature perturbation at the level of CMB observation [20].

Assuming that the fluctuation with energy density $\delta\rho$ is generated at the end of inflation, it dominates the zero-mode of energy density ρ after the kination era expands by $N_{\rm KD} \simeq \log(\rho_{\rm inf}/\delta\rho_{\rm inf})/2$. For instance, the scalar might fluctuate as the same order as the curvature fluctuation – $\rho/\delta\rho \sim 10^{9\div10}$ which leads to $N_{\rm KD}^{\rm max} \sim 11$ [132]. For a suppressed fluctuation, the bound on kination duration can be relaxed for some particular inflation models. Fig. 4.10 shows that the theoretical kination-constraint from fluctuation is stronger than the usually-considered $\Delta N_{\rm eff}$ bound. These exciting implications of the fluctuation from the kination-like field will be discussed in [527].

4.5 Scheme C: Intermediate Matter Era

A matter-like energy density that is sub-dominant early on can dominate the SM radiation bath due to its slower red-shifting and lead to the matter domination era. Nonetheless, it must decay and injects energy/entropy into the thermal bath because the radiation-dominated Universe at BBN is required. One of the motivating scenarios for the intermediate matter era is the heavy particles or some oscillating moduli field that later decay into the radiation bath; see Chap. 5 for various UV completions and references therein. The faster expansion rate during the intermediate matter era, cf. Fig. 4.12, imprints the step-like suppression, as discussed in Sec. 4.2. Due to spectral suppression, this section only focuses on the large and highly observable SGWB from cosmic strings.

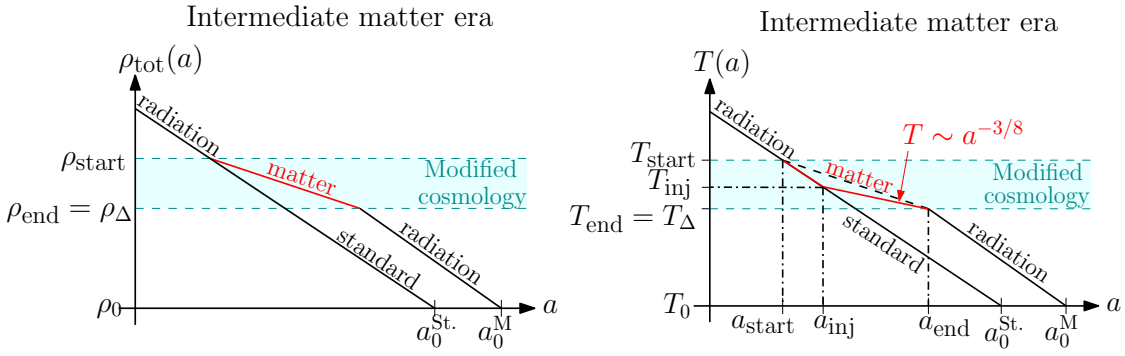

Figure 4.12: Evolution of the total energy density **(left)** and the temperature **(right)**, assuming an intermediate matter era. $T_{\rm inj}$ and $a_{\rm inj}$ are the temperature and scale factor when the entropy injection from a constant decay becomes effective, cf. Fig. 2 in [532]. Abbreviations: St for standard, and M for matter.

4.5.1 GW signature: a step-like suppression

The GW spectra from local cosmic strings on the left panel of Fig. 4.13 show that an intermediate matter era red-tilts the spectrum. The turning-point frequency in Eq. (4.21) determines the point of red-tilt, similar to the matter era right after inflation (scheme A). However, the spectrum in the intermediate matter scenario recovers a flat scaling at higher frequencies, corresponding to loops produced during the radiation era preceding the matter era. This flat part has its amplitude suppressed – compared to the later radiation era – because the intermediate matter ends with the entropy injection and dilutes any earlier-existing GW. The step size between two flat parts is suppressed by the duration r of the matter era

$$r = \frac{T_{\rm start}}{T_\Delta}, \tag{4.30}$$

where $T_\Delta = T_{\rm end}$ is the temperature of the Universe when the matter era ends. If the future-planned experiment observes the turning point and the step size, we can precisely imply the energy scale and the duration of the intermediate matter era.

Note also that the intermediate matter era changes the dynamics of the string network, i.e., the loop formation becomes less efficient and further suppresses the GW amplitude, as seen in the difference between VOS and scaling spectra. In the right panel of Fig. 4.13, we show that a short intermediate matter era, $r = 2$ or $r = 10$, cannot bring the string network into the scaling regime of the matter era ($C_{\rm eff} = 0.39$), cf. Eq. (3.44).

Fig. 4.14 shows the sensitivity of future GW experiments for probing the the intermedaite matter era – starting at the temperature $r\,T_\Delta$ and ending at the temperature T_Δ. Matter eras as short as $r = 2$ and ending at temperature as large as 100 TeV could be probed by GW interferometers. We assume that an early-matter era is detectable if the spectral index is smaller than -0.15, cf. *spectral-index prescription (Rx 2)* in Sec. 4.2.3.

We refer the reader to Chap. 5 for model-independent constraints on the abundance and lifetime of heavy and unstable particles, giving rise to such a non-standard intermediate matter era. We shall see that the next-generation GW observatories can largely extend the constraint on lifetime ($\tau_{\rm GW-CS} \gtrsim 10^{-16}$ s) beyond the usually-considered BBN bound ($\tau_{\rm BBN} \gtrsim 0.1$ s).

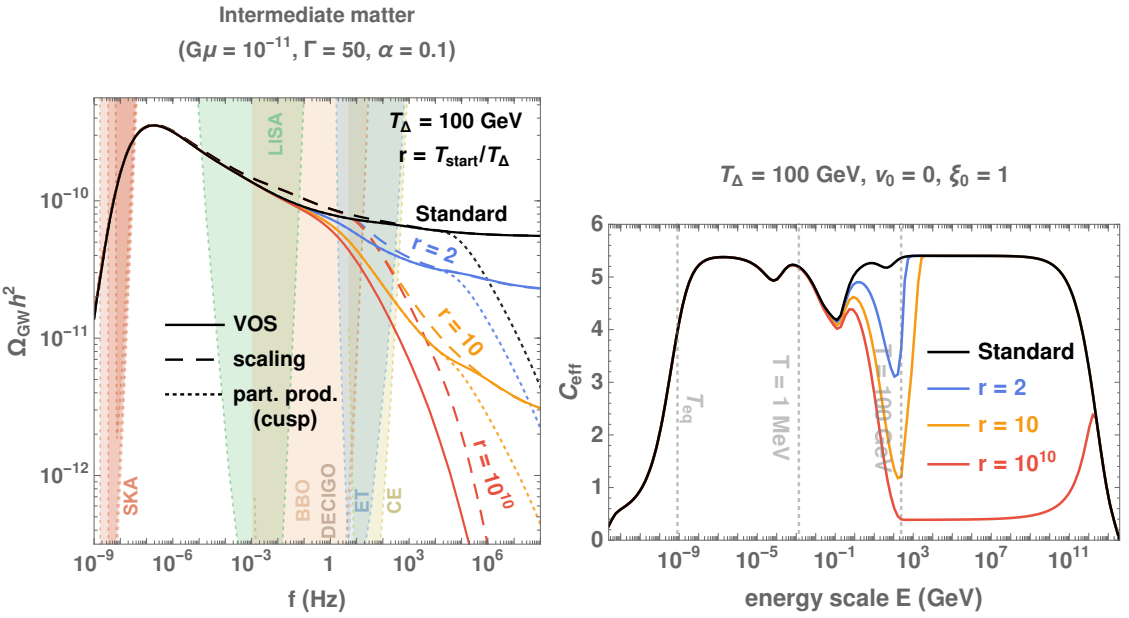

Figure 4.13: GW spectrum from an intermediate matter era starting at the temperature $T_{\rm start}$ and ending at $T_\Delta = 100$ GeV. **left:** The dashed lines assume that the scaling regime in the matter era switches instantaneously to the scaling regime in the radiation era, i.e., $C_{\rm eff}$ is a step function.. In contrast, the plain lines incorporate the transient behavior solution of the VOS equations, shown on the right panel. The cut-offs due to particle production, cf. Sec. 3.2.5, are shown with dotted lines. **right:** Time evolution of the loop-production efficiency $C_{\rm eff}$ after solving the VOS equations, cf. Sec. 3.3.3.

4.6 Scheme D: Intermediate Inflationary Era

Consider a short inflationary period – happening much later than another inflation at a higher scale that solves the flatness and horizon problems. The e-foldings of the cosmic expansion parametrize its duration,

$$N_e \equiv \log\left(\frac{a_{\rm start}}{a_{\rm end}}\right), \tag{4.31}$$

smaller than $N_e \lesssim 20 \ll 60$, in order not to alter the predictions from the first inflation era regarding the CMB power spectrum, cf. App. C for the precise condition. We define the energy

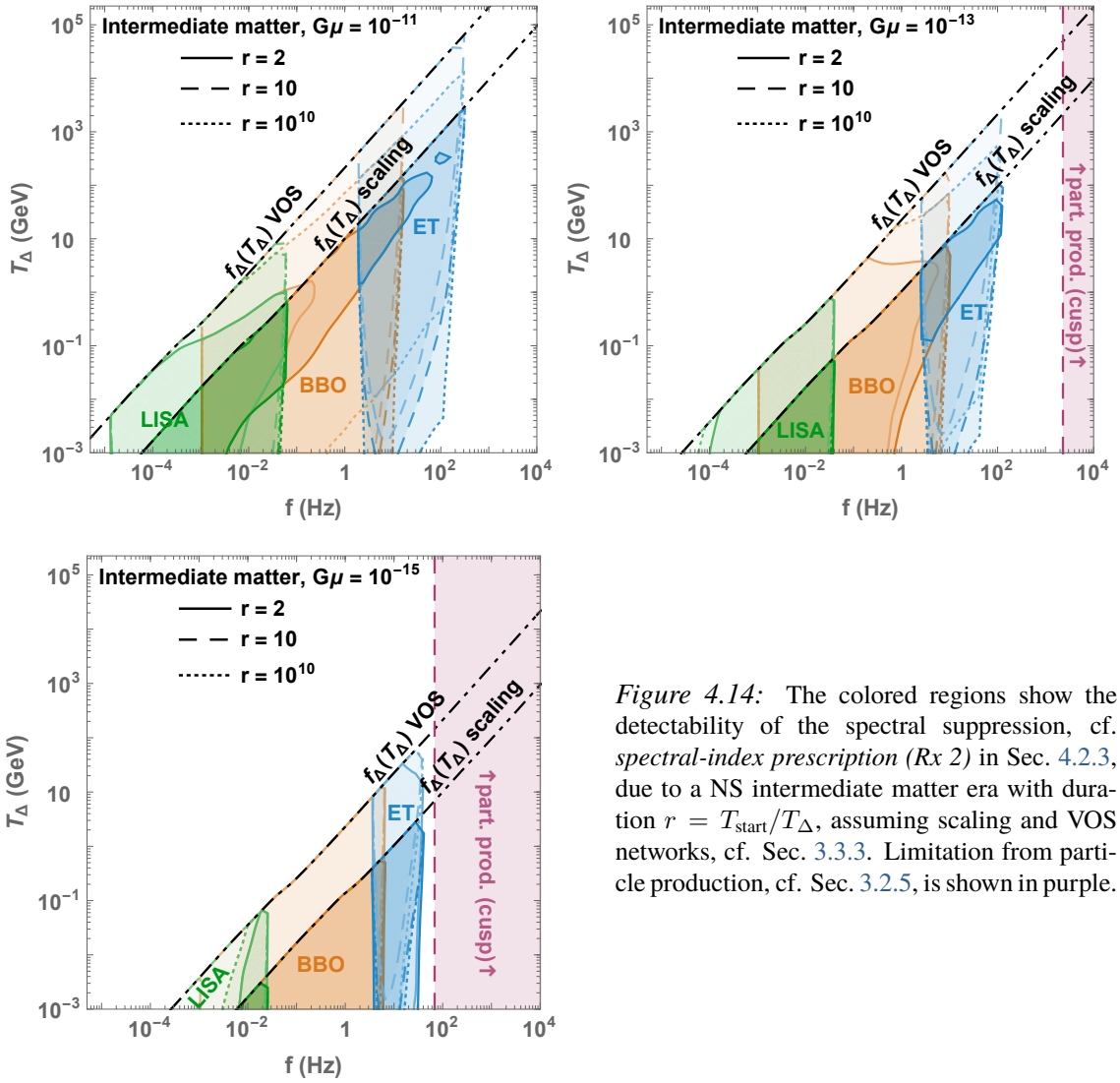

Figure 4.14: The colored regions show the detectability of the spectral suppression, cf. *spectral-index prescription (Rx 2)* in Sec. 4.2.3, due to a NS intermediate matter era with duration $r = T_{\rm start}/T_\Delta$, assuming scaling and VOS networks, cf. Sec. 3.3.3. Limitation from particle production, cf. Sec. 3.2.5, is shown in purple.

density profile as, cf. Fig. 4.15

$$\rho_{\rm tot}(a) = \begin{cases} \rho^{\rm st}_{\rm rad}(a) + \rho_{\rm late}(a) & \text{for } \rho > \rho_{\rm inf}, \\ \rho_{\rm inf} = E^4_{\rm inf} & \text{for } \rho = \rho_{\rm inf}, \\ \rho_{\rm inf}\Delta_R(T_{\rm end}, T)\left(\frac{a_{\rm end}}{a}\right)^4 + \rho_{\rm late}(a) & \text{for } \rho < \rho_{\rm inf}, \end{cases} \tag{4.32}$$

where $\rho_{\rm inf}$ is the total energy density of the Universe during inflation and $E_{\rm inf} \equiv \rho_{\rm inf}^{1/4}$ is the corresponding energy scale. The function Δ_R is defined in (4.3).

Indeed, the second-stage or the multiple-stage inflation can arise due to the non-trivial scalar dynamics in many inflationary theories [83, 533–544], leading to many phenomenological consequences. For example, many phases of expanding and shrinking Hubble horizon – dubbed the *rollercoaster* cosmology [545] – would alleviate some constraints on the $\mathcal{O}(60)$-efold single inflation scenario. The curvature perturbation from this scenario also possesses many scales corresponding to each inflationary stage that might appear in the small-scale CMB observations. Besides, many reheating between each inflation produces relic particles that hardly dilute due to short inflationary stages and affect particle-production mechanisms during the early times. We leave this exciting aspect of probing the multi-stage inflation with primordial SGWB for future work.

On the high-energy particle physics side, disconnected from the inflaton dynamics, such a short

inflationary period can be generated by a highly supercooled first-order phase transition. It was stressed that nearly-conformal scalar potentials naturally lead to such short, with $N_e \sim 1-15$ [546–548]. Those are well-motivated in new strongly interacting composite sectors arising at the TeV scale, as invoked to address the Higgs hierarchy problem, and were first studied in a holographic approach [141, 549] (see also the review [153]). As the results on the scaling of the bounce action for tunneling and on the dynamics of the phase transitions do essentially not depend on the absolute energy scale, but only on the shallow shape of the scalar potential describing the phase transition, those studies can thus be extended to a large class of confining phase transitions arising at any scale. In this section, we shall consider the energy scale and duration as free parameters[6].

This section focuses again on the SGWB from cosmic strings, whose amplitude lies in the sensitivity windows, even when the intermediate inflation imprint a significant spectral suppression. Unlike the intermediate matter era, the secondary inflation not only dilutes the earlier-existing SGWB but also seriously affects the dynamics of the string network and GW production, as we shall see below and in Fig. 4.16.

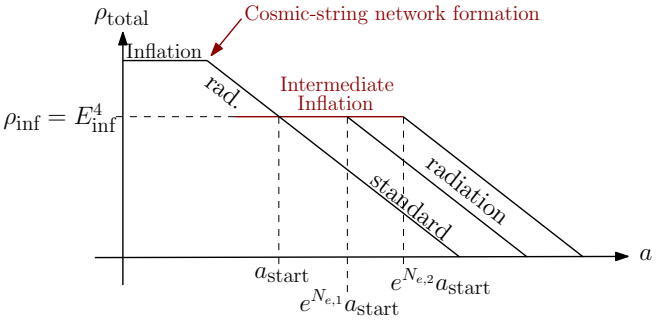

Figure 4.15: Evolution of the total energy density assuming the presence of an intermediate inflationary era characterised by the energy density $\rho_{\rm inf}$, for two different durations (number of efolds), $N_{e,1}$ and $N_{e,2}$.

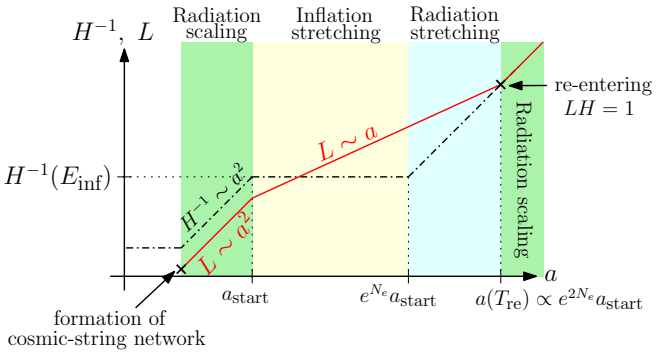

Figure 4.16: After its formation, before inflation, the network enters the scaling regime with $L \sim a^2$ due to loop formation. During the N_e e-folds of inflation, the network correlation length gets stretched out of the horizon by the rapid expansion, and loop formation stops, thus $L \sim a$. After inflation, during radiation, the correlation length starts to re-enter the horizon and scales again as $L \sim a^2$.

4.6.1 The intermediate inflation & the cosmic-string network

Let us review the chronology of the network in the presence of an intermediate-inflation period (see Fig. 4.16) to derive the frequency-temperature relation in Eq. (4.39). Assuming the network during the early radiation era has already been produced and reached the scaling regime before the secondary inflation starts, the correlation length scale is of order $(0.1)t$ or equivalently

$$L_{\rm start} H_{\rm start} \sim \mathcal{O}(0.1), \tag{4.33}$$

where L is the correlation length of strings, and H is the Hubble rate. When inflation begins, it stretches cosmic strings beyond the horizon within a few e-foldings,

$$L \propto a \quad \text{leading to} \quad LH \gg 1. \tag{4.34}$$

[6] An example of probing a model with the intermediate inflation using SGWB from cosmic strings has been shown in Ref. [50].

Indeed, during inflation, the loop-production efficiency $C_{\rm eff} \propto \xi^{-3}$ is severely suppressed, cf. Fig. 4.17, by stretching the correlation length ξ beyond the Hubble horizon, and loop production freezes [297]. Later, the late-time energy density takes over inflation, but the network is still in the *stretching* regime $L \propto a$, i.e.,

$$LH \propto t^{(2-n)/n} \quad \text{during the era with } \rho \propto a^n. \tag{4.35}$$

For $n > 2$, the Hubble horizon will eventually catch up with the string length, allowing them to re-enter and initiate the loop production. We consider the case where the Universe is radiation-dominated after the inflation period and define the temperature $T_{\rm re}$ of the Universe when the long-string correlation length L re-enters the horizon

$$L_{\rm re} H_{\rm re} = 1, \tag{4.36}$$

where $L_{\rm re}$ and $H_{\rm re}$ are the correlation length and Hubble rate at the re-entering time. We can use Eq. (4.35) to evolve the correlation length, starting from the start of inflation up to the re-entering time

$$1 = L_{\rm re} H_{\rm re} = \left(\frac{t_{\rm re}}{t_{\rm end}}\right)^{-1/2} L_{\rm end} H_{\rm end} \simeq \left(\frac{T_{\rm re}}{T_{\rm end}}\right) e^{N_e} (0.1), \tag{4.37}$$

where we assume the radiation era $t \propto T^{-2}$ after the end of inflation, use $L_{\rm start} H_{\rm start} \sim \mathcal{O}(0.1)$, and introduce the number N_e of inflation e-folds. Finally, we obtain the re-entering temperature in terms of the number of e-folds N_e and the inflationary energy scale $E_{\rm inf}$ as

$$T_{\rm re} \simeq \frac{E_{\rm inf}}{(0.1)\, g_*^{1/4}(T_{\rm re})\, \exp(N_e)}. \tag{4.38}$$

Crucially, the network must wait for another N_e foldings for the correlation length to re-enter the horizon before it can reach the scaling regime and produce GW again. The simple argument in Sec. 4.2, which considers only the effect of non-trivial expansion rate, does not apply to this current scenario; the turning-point relation of the cosmic-string SGWB in Eq. (4.21) is now sensitive to the energy scale when the strings re-enter the horizon, instead of the secondary inflation's scale.

After plugging Eq. (4.38) into the VOS turning-point formula Eq. (4.21), with $T_\Delta = T_{\rm re}$, and adjusting the numerical factor with the GW spectrum computed numerically, we obtain the relation between the turning-point frequency and the inflation parameters N_e and $E_{\rm inf}$,

$$f_\Delta^{\rm 2nd-inf} = (1.5 \times 10^{-4}\ {\rm Hz}) \left(\frac{T_{\rm re}}{\rm GeV}\right) \left(\frac{0.1 \times 50 \times 10^{-11}}{\alpha\, \Gamma G \mu}\right)^{1/2} \left(\frac{g_*(T_{\rm re})}{g_*(T_0)}\right)^{1/4}. \tag{4.39}$$

Note that the numerical factor in Eq. (4.39) comes from the demanded precision of 10% deviation, cf. Eq. (4.22). It can be lower by a factor $\sim$ 300 if the 1% precision is applied, as shown in Eq. (B.52).

4.6.2 GW signature: a step-like suppression

Fig. 4.17 shows how the fast expansion during inflation suppresses the GW spectrum for frequencies above a turning-point frequency f_Δ which depends on the number of e-folds. The SGWB spectrum exhibits a step-like feature for a short inflation duration, similar to the intermediate matter era. However, the inflation duration also changes the turning-point frequency, unlike in the matter case; the larger the number of e-folds, the lower f_Δ. Fig. 4.18 shows how a sufficiently long period of intermediate inflation can lead to SGWB with peak shapes in the future GW interferometer bands. We emphasize that the signatures in the GW spectrum from CS in the presence of a non-standard matter-dominated era, short inflation, and particle production look similar. Therefore, the question

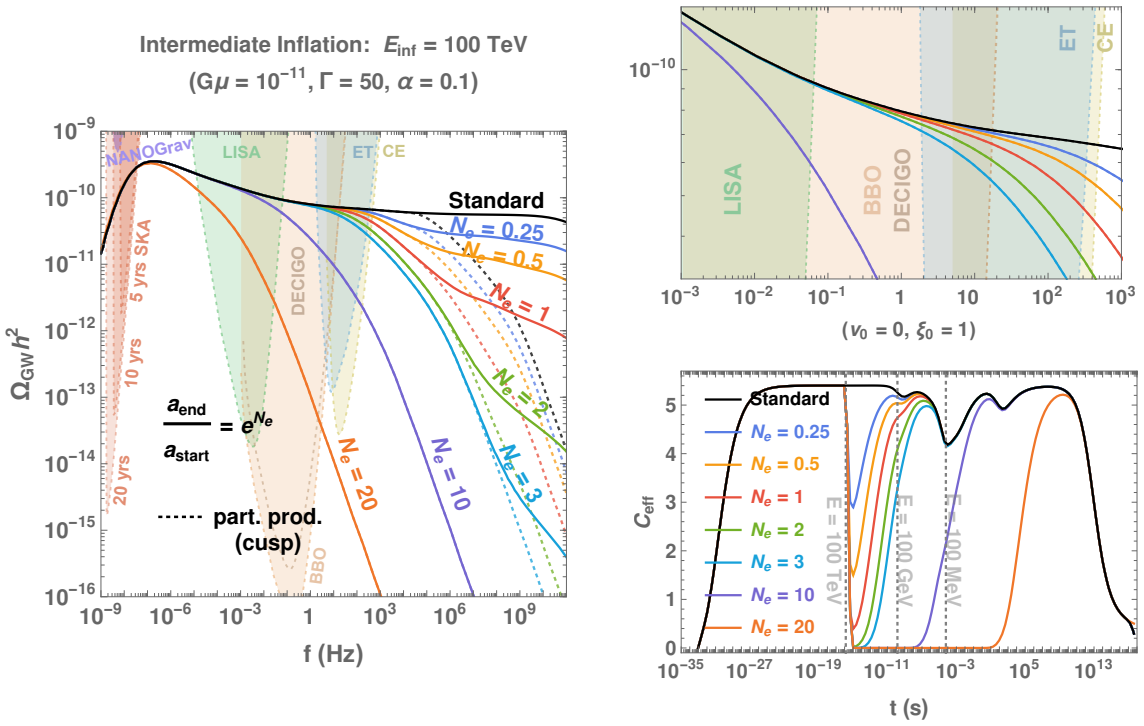

Figure 4.17: **Top:** GW spectra from cosmic strings assuming either the scaling or the VOS network evolved in a non-standard intermediate inflation era. Inflation directly affects the VOS parameters by stretching the strings beyond the horizon. The transition between the $f^{-1/3}$ scaling after the turning point, to the f^{-1} scaling at even larger frequencies, is an artefact due to total number of modes k being fixed to 2×10^4, see Fig. 4.18 for an extrapolation of the $f^{-1/3}$ behavior to arbitrary large frequencies and App. B.3.7 for more details. **Bottom:** The loop-production is suppressed and only becomes significant again when the correlation length re-enters the horizon. Limitations due to particle production, cf. Sec. 3.2.5, are shown with dotted lines.

of how disentangling each effect from one another deserves further studies. In Sec. 4.6.3, we provide the dictionary between the intermediate matter and inflationary eras.

Interestingly, in contrast with the SGWB which is dramatically impacted by an intermediate period of inflation, the short-lasting GW burst signals [284, 285, 344, 345, 347] remain preserved if the correlation length re-enters the horizon at a redshift higher than $\sim 5 \times 10^4$ [550]. Indeed, the bursts generated by the small-scale structures have higher frequencies and are emitted later than the SGWB, cf. Fig. 2 in [345].

4.6.3 Cosmic-string GW degeneracy: intermediate matter & inflationary eras

The intermediate matter and inflationary eras lead to similar spectral-suppression signatures in SGWB from cosmic strings. Suppose an SGWB is detected with a step-like suppression at high frequencies. It is interesting to ask where the degeneracy between their parameter lies for describing the spectral signatures – the turning point and the step height.

Turning-point. — By equating the turning-point formulae for intermediate matter in Eq. (4.21) and inflationary eras in Eq. (4.39), we obtain the relation between the energy scales of the two scenarios and the duration of inflation,

$$\textbf{condition \#1:}\quad E_{\rm inf} \simeq \exp(N_e)\, T_\Delta\, g_*^{1/4}(T_\Delta) \times \begin{cases} 1.33 & \text{for 10 \% precision} \\ 0.8 & \text{for 1 \% precision} \end{cases}, \tag{4.40}$$

where the precision means the deviation from the spectrum assuming the standard cosmology.

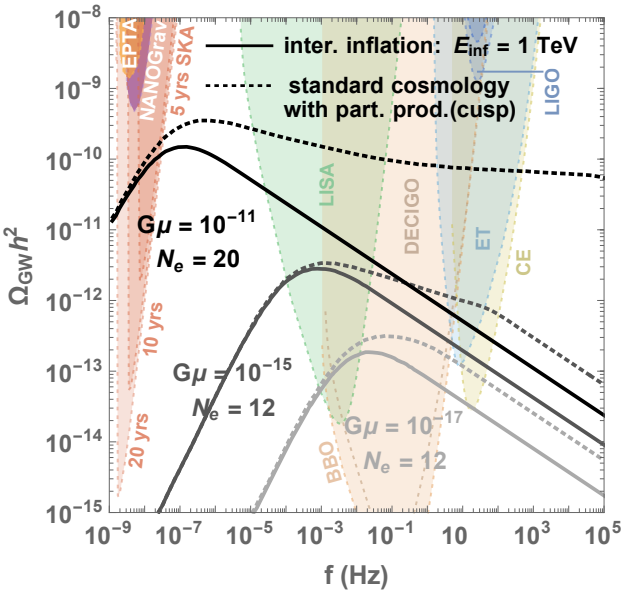

Figure 4.18: With an intermediate inflationary era lasting for $\mathcal{O}(10)$ efolds, the SGWB from CS completely loses its scale-invariant shape and has a peak structure. A TeV scale inflation era can lead to broad peaks either in the LISA or BBO band or even close to the SKA band, depending on the string tensions $G\mu$, and the number of efolds N_e. For $G\mu \lesssim 10^{-17}$, the spectrum manifests a peak structure even in standard cosmology because of the emission of massive particles at large frequencies, cf. Sec. 3.2.1. We introduce other realizations presenting a peak structure in Sec. 3.5. Here we extrapolate the $f^{-1/3}$ behavior to arbitrary large frequencies, equivalent to sum over an infinite number of proper modes k, see App. B.3.7.

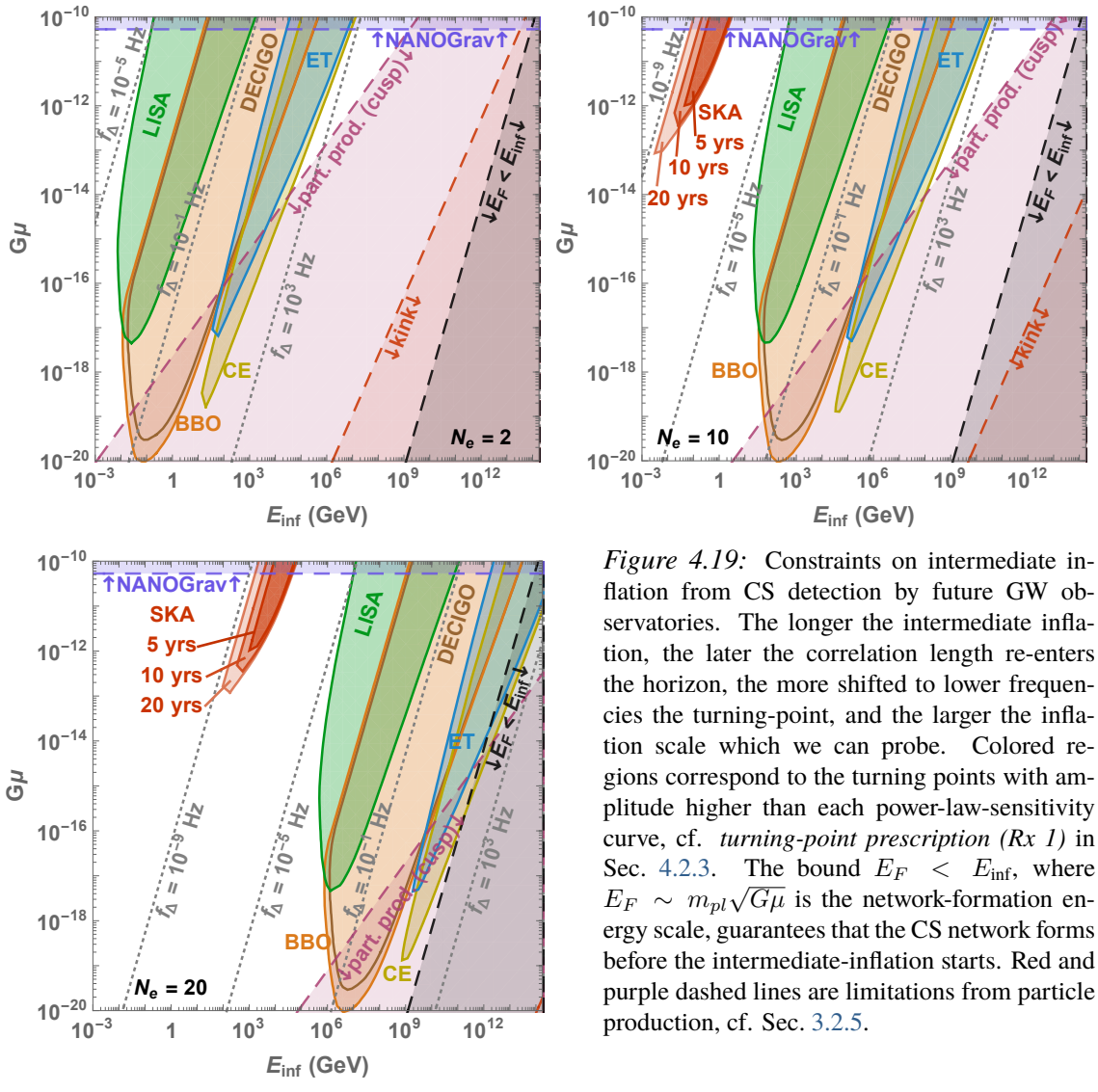

Figure 4.19: Constraints on intermediate inflation from CS detection by future GW observatories. The longer the intermediate inflation, the later the correlation length re-enters the horizon, the more shifted to lower frequencies the turning-point, and the larger the inflation scale which we can probe. Colored regions correspond to the turning points with amplitude higher than each power-law-sensitivity curve, cf. *turning-point prescription (Rx 1)* in Sec. 4.2.3. The bound $E_F < E_{\rm inf}$, where $E_F \sim m_{pl}\sqrt{G\mu}$ is the network-formation energy scale, guarantees that the CS network forms before the intermediate-inflation starts. Red and purple dashed lines are limitations from particle production, cf. Sec. 3.2.5.

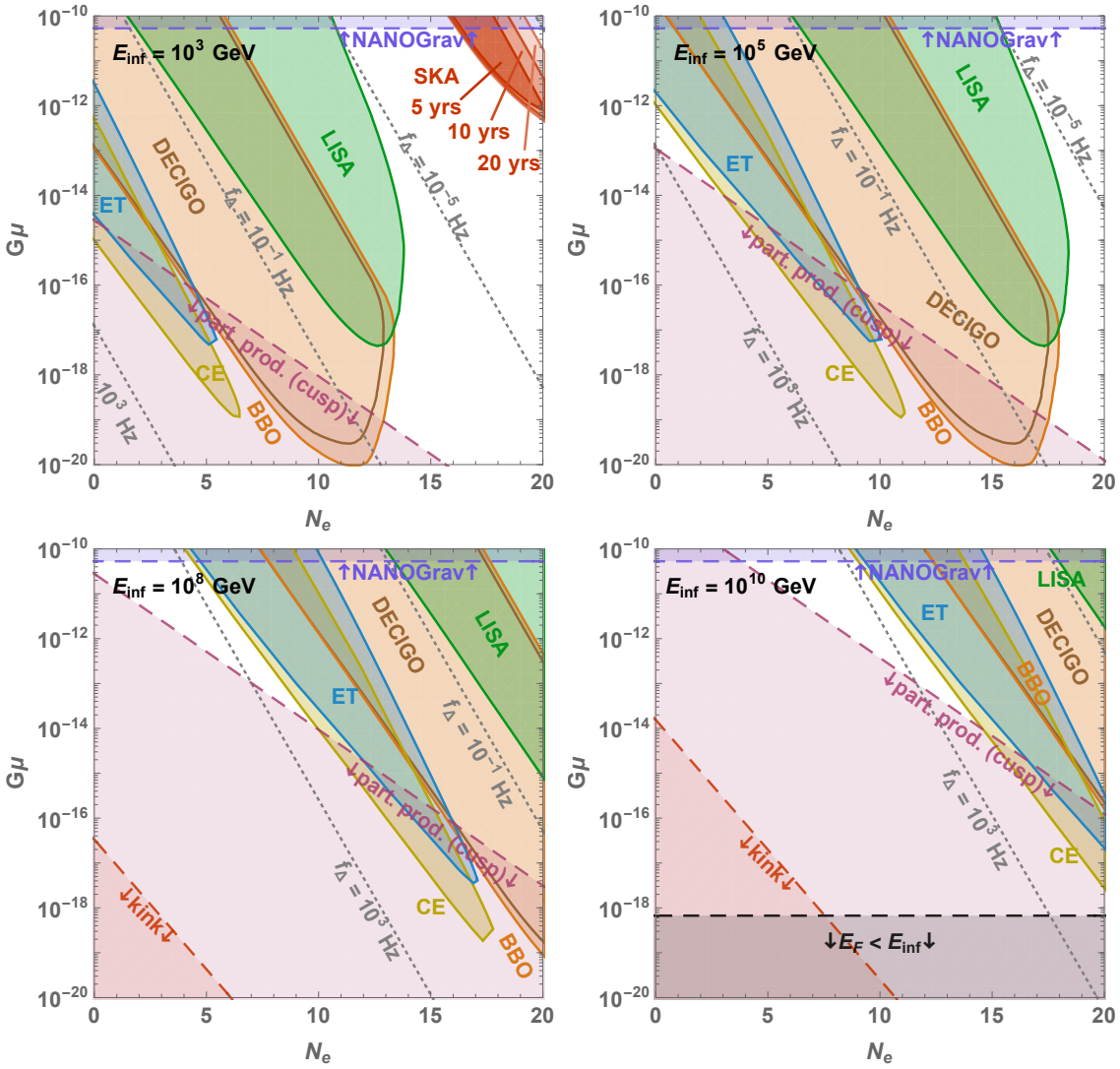

Figure 4.20: Prospective constraints on an intermediate inflationary stage if a GW interferometer detects a SGWB from CS with tension $G\mu$. The freezing of the long-string network due to stretching the correlation length outside the horizon allows for probing large inflationary scale $E_{\rm inf}$ for a large number of efolds N_e. Colored regions correspond to the turning points with amplitude higher than each power-law-sensitivity curve, cf. *turning-point prescription (Rx 1)* in Sec. 4.2.3. Red and purple dashed lines are limitations from particle production, cf. Sec. 3.2.5.

Step-height. — The intermediate matter and inflation imprint a step-like feature, whose suppressed flat plateau corresponds to the radiation era before each non-standard era. We can quantify its amount by comparing its amplitude to the spectrum assuming the radiation domination,

$$\frac{\Omega_{\rm GW,ST}}{\Omega_{\rm GW,NS}}(f \gg f_\Delta) = \frac{\Omega^p_{\rm GW,ST}}{\Omega^p_{\rm GW,NS}} \left(\frac{a_p}{a_0}\right)^4\Big|_{\rm ST} \left(\frac{a_0}{a_p}\right)^4\Big|_{\rm NS} = \left(\frac{a_{\rm start}}{a_{\rm end}}\right)^4\Big|_{\rm ST} \left(\frac{a_{\rm end}}{a_{\rm start}}\right)^4\Big|_{\rm NS}, \quad (4.41)$$

where the superscript "p" denotes when GW of frequency f is produced, and the condition $f \gg f_\Delta$ ensures that we consider the suppressed flat plateau. In the last step, the total mismatch between the standard and non-standard scenarios is from the start $a_{\rm start}$ to the end $a_{\rm end}$ of the non-standard

era. Since we know how the Universe evolves during the non-standard era, we deduce

$$\left(\frac{a_{\rm end}}{a_{\rm start}}\right)\Big|_{\rm NS} = \begin{cases} \left(\frac{\rho_{\rm start}}{\rho_{\rm end}}\right)^{1/3} \simeq \left(\frac{T_{\rm end}}{T_{\rm start}}\right)^{4/3} \simeq r^{4/3} & \text{for int. matter era,} \\ \exp(N_e) & \text{for int. inflationary era,} \end{cases} \tag{4.42}$$

$$\text{and} \quad \left(\frac{a_{\rm end}}{a_{\rm start}}\right)\Big|_{\rm ST} = \begin{cases} \left(\frac{\rho_{\rm start}}{\rho_{\rm end}}\right)^{1/4} \simeq \left(\frac{T_{\rm end}}{T_{\rm start}}\right) \simeq r & \text{for int. matter era,} \\ 1 & \text{for int. inflationary era,} \end{cases} \tag{4.43}$$

where we use that the total energy density before and after the inflationary era is constant. Thus the suppression of the GW spectrum due to intermediate matter and inflationary eras is given by

$$\frac{\Omega_{\rm GW,ST}}{\Omega_{\rm GW,NS}}(f \gg f_\Delta) = \begin{cases} r^{4/3} & \text{for int. matter era,} \\ \exp(4N_e) & \text{for int. inflationary era.} \end{cases} \tag{4.44}$$

The two non-standard scenarios provide a degenerate step height if

$$\textbf{condition \#2:} \;\; r \simeq \exp(3N_e). \tag{4.45}$$

4.6.4 Detectability and constraints

In Figs. 4.19 and 4.20, we show the constraints on the intermediate inflation scenario in the planes $E_{\rm inf} - N_e$, $G\mu - E_{\rm inf}$, and $G\mu - N_e$, respectively. We follow the *turning-point prescription (Rx 1)*, defined in Sec. 4.2.3, which constrains a non-standard cosmology by using the detectability of the turning-point frequency in Eq. (4.39). The longer the intermediate inflation; the later the correlation length re-enters the horizon; the latter the long-string network goes back to the scaling regime; the lower the frequency of the turning point; and the larger the inflationary scale, which can be probed. The detection of a GW spectrum generated by CS by future GW observatories would allow to probe an inflationary energy scale $E_{\rm inf}$ between 10^{-2} GeV and 10^{13} GeV assuming a number of e-folds $N_e \lesssim 20$.

4.7 Scheme E: Intermediate kination

This section focuses on the intermediate kination from a scalar field, unrelated to the inflation dynamics. One of the simplest yet non-trivial scenarios is when a scalar field leads to the matter domination era (e.g., oscillation in quadratic potential) and later the kination domination. The particle-physics realizations of the matter-kination era naturally arise in *axion* physics[7], as we shall see in Chaps. 6 and 7. The preceding matter era brings the energy density of the Universe above the radiation energy density, enabling a period of kination that redshifts faster than radiation. The longer the matter era dominates, the longer kination lasts.

Already discussed in Sec. 4.2, the intermediate matter-kination era imprints an interesting peak signature in SGWB of the long-lasting sources. We shall consider SGWB from the primordial inflation, local, and global cosmic strings. The intermediate kination era enhances the GW only some frequency range, allowing it to satisfy the $\Delta N_{\rm eff}$ which kills the whole discovery band for the kination right after inflation in scheme B. Let us now consider which information can be extracted from such a peaked SGWB and discuss the detectability within windows of GW observatories.

[7]The pre-kination period beyond the matter era could also be realized in a more complex model, e.g., involving the non-canonical scalar field. This is the main goal of the work in progress [551].

A matter-kination era. — The cosmological history is described by the total energy density of the Universe

$$\rho(a) = \rho_{r,0}\, G[T(a), T_0] \left(\frac{a}{a_0}\right)^4 + \rho_{m,0} \left(\frac{a}{a_0}\right)^3 + \rho_{\Lambda,0} + \rho_\phi(a), \tag{4.46}$$

where the function $G(T, T_0)$ is defined in Eq. (4.3). The first three terms of Eq. (4.46) follow from the ΛCDM assumption, while ρ_ϕ is the scalar field energy density that generates the non-standard matter and kination eras.

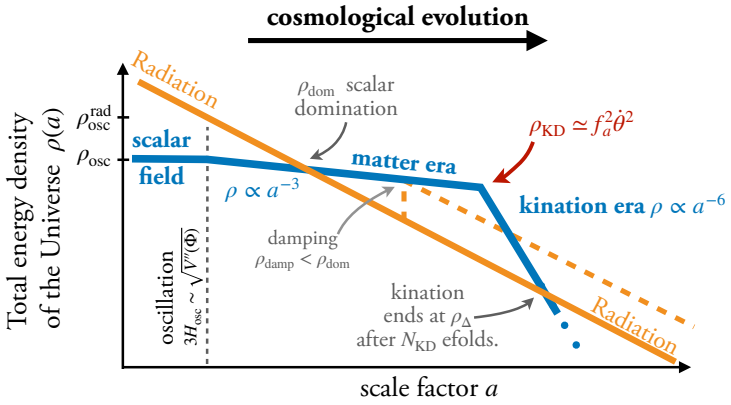

Figure 4.21: Scalar field dynamics that generate a matter-kination era inside the radiation epoch. The solid orange line shows where the entropy injection is absent or happens before the scalar domination. For the orange dashed line, the entropy injection occurs after scalar domination and suppresses the kination duration. f_a denotes the radius of the circular orbit of the field spinning with velocity $\dot{\theta}$, discussed in Chap. 6 and 7.

The cosmological evolution is sketched in Fig. 4.21; it starts with the SM radiation domination, while the scalar field ϕ is frozen and contributes to a subdominant cosmological constant. After the expansion rate becomes small, it can start to oscillate and behaves as pressure-less matter, leading to the matter era. Later, its kinetic energy dominates and generates the kination EOS. In the most model-independent way, the total energy density of the Universe is described by the following quantities that can be related to the model-dependent quantities in Chaps. 6 and 7:

- $\rho_{\rm osc}^{\rm rad}$ – Energy density of the background radiation at the oscillation onset $a_{\rm osc}$,
- $\rho_{\rm osc}$ – Energy density of the scalar field at oscillation,
- $\rho_{\rm KD}$ – Energy density of the scalar field when the kination era starts,

For convenience, we define the energy scale at each event by $\rho_i \equiv E_i^4$.

The non-standard matter era starts at the so-called time of scalar domination, $a = a_{\rm dom}$ when the scalar field energy density is

$$\rho_{\rm dom} = \rho_{\rm osc} \left(\frac{a_{\rm osc}}{a_{\rm dom}}\right)^3 = \rho_{\rm osc} \left(\frac{\rho_{\rm osc}}{\rho_{\rm osc}^{\rm rad}}\right)^3. \tag{4.47}$$

It lasts until kination starts at $a = a_{\rm KD}$ after some e-folds,

$$\exp(N_{\rm MD}) \equiv \frac{a_{\rm KD}}{a_{\rm dom}} = \left(\frac{\rho_{\rm dom}}{\rho_{\rm KD}}\right)^{1/3}, \tag{4.48}$$

and kination ends when the radiation bath dominates again at $a = a_\Delta$

$$\rho_\Delta = \frac{\rho_{\rm KD}^2}{\min(\rho_{\rm dom}, \rho_{\rm damp})}, \tag{4.49}$$

with the duration of kination, given by the e-folding number,

$$e^{N_{\rm KD}} \equiv \frac{a_\Delta}{a_{\rm KD}} = \left[\frac{\min(\rho_{\rm dom}, \rho_{\rm damp})}{\rho_{\rm KD}}\right]^{1/6}, \tag{4.50}$$

where $\rho_{\rm damp}$ is the energy density of radiation after the entropy injection. The transfer of energy is inevitable in the particle physics implementations, considered Chap. 7, and shortens the duration of kination, see orange dashed line in Fig. 6.2.

Absence of entropy injection. — The longest kination era is obtained when the Universe evolves adiabatically during the whole matter-kination era; no entropy injects during the matter-kination era and, therefore, $\rho_{\rm damp} > \rho_{\rm dom}$. In that case, $\rho_\Delta = \rho_{\rm dom}\,(a_{\rm dom}/a_\Delta)^4$ together with Eq. (4.47) and (4.49) imply

$$N_{\rm KD} = N_{\rm MD}/2. \tag{4.51}$$

Except when explicitly specified, we assume Eq. (4.51) to hold in our plots. Finally, the matter-kination scenario can be described, in the most model-independent way, simply by the newly defined parameters: the energy scale of the kination era $E_{\rm KD} = \rho_{\rm KD}^{1/4}$ and the duration of kination era $N_{\rm KD}$. The total energy density of the Universe reads,

$$\rho_{\rm tot}(a) \simeq E_{\rm KD}^4 \times \begin{cases} \exp(12N_{\rm KD})\left(\frac{a}{a_M}\right)^4, & \text{for } a < a_{\rm M} < a, \\ \left(\frac{a}{a_{\rm KD}}\right)^3, & \text{for } a_{\rm M} < a < a_{\rm KD}, \\ \left(\frac{a_{\rm KD}}{a}\right)^6, & \text{for } a_{\rm KD} < a < a_\Delta, \\ \exp(-6N_{\rm KD})\left(\frac{a_\Delta}{a}\right)^4, & \text{for } a > a_\Delta, \end{cases} \tag{4.52}$$

where the Universe evolves chronologically in radiation, matter, kination, and radiation eras, from top to bottom rows.

4.7.1 GW signature: a peak (triangular spectrum)

The signature of the matter-kination era contains a red tilt from the matter era and a blue tilt from the kination era. The shape of this spectrum is unique and very different from any other predictions of stochastic GW signals of cosmological origins. For instance, the peak that results from a FOPT is very narrow as the source is active at a specific temperature [153], while here, the matter-kination era is responsible for the peak lasts for several efolds. Another primary source is cosmic strings, whose spectrum has a different shape and gets a peak-like structure from the intermediate kination, depending on the precise cosmological history. If such cosmic strings are present, a multiple-peak structure may arise. Finally, another source of enhanced SGWB may come from the couplings of the inflaton. A well-known example is axion inflation which may lead to an enhanced signal due to parametric resonance effects induced by the inflaton coupling to gauge fields [125]. The spectral shape of this signal is also very different from what we predict from a short kination era.

Now we shall discuss the peak signature in SGWB – from inflation, local cosmic strings, and global cosmic strings – and their detectability. Since these sources could arise independently, their co-existence would lead to an exciting multiple-peak GW signal.

Inflationary SGWB

The spectral index of SGWB from inflation in Eq. (4.12) changes its sign: the high-frequency slope -2 is associated with the matter era, while the low-frequency slope +1 is related to the kination era.

The GW spectrum in the presence of the matter-kination era reads

$$\Omega_{\rm GW,0}h^2(f) = \Omega^{\rm st}_{\rm GW}(f_\Delta)h^2 \times \begin{cases} 1 & ; f < f_\Delta \quad \text{(late-time radiation)}, \\ (f/f_\Delta) & ; f_\Delta < f < f_{\rm KD} \quad \text{(kination)}, \\ (f_{\rm KD}/f_\Delta)\,(f_{\rm KD}/f)^2 & ; f_{\rm KD} < f < f_{\rm dom} \quad \text{(matter)}, \\ (f_{\rm KD}/f_\Delta)\,(f_{\rm KD}/f_{\rm dom})^2 & ; f_{\rm dom} < f \quad \text{(early-time radiation)}, \end{cases} \tag{4.53}$$

where the GW abundance assuming the standard radiation-dominated cosmology $\Omega^{\rm st}_{\rm GW}$ is given by Eq. (2.27), and f_Δ, $f_{\rm KD}$ (peak frequency), $f_{\rm dom}$ are the characteristic frequencies corresponding to the modes re-entering the horizon right after the end of the kination era, at the beginning of the kination era, and at the end of the matter era, respectively. They are defined as:

$$f_\Delta = \frac{H_\Delta a_\Delta}{2\pi a_0} \simeq 2.7\cdot 10^{-6}\ {\rm Hz}\ \left[\frac{g_*(T_\Delta)}{106.75}\right]^{\frac{1}{2}} \left[\frac{g_{*,s}(T_\Delta)}{106.75}\right]^{-\frac{1}{3}} \left[\frac{T_\Delta}{10^2\ {\rm GeV}}\right], \tag{4.54}$$

$$f_{\rm KD} = \frac{H_{\rm KD}a_{\rm KD}}{2\pi a_0} = f_\Delta e^{2N_{\rm KD}} \simeq 1.1\cdot 10^{-3}{\rm Hz}\ G^{\frac{1}{4}}(T_\Delta) \left[\frac{\rho_{\rm KD}^{1/4}}{10\ {\rm TeV}}\right] \left[\frac{e^{N_{\rm KD}/2}}{10}\right], \tag{4.55}$$

where the e-folding of the kination era is $e^{N_{\rm KD}} \equiv (\rho_{\rm KD}/\rho_\Delta)^{1/6}$. This peak frequency $f_{\rm KD}$ thus contains information about the energy scale and the duration of the kination era. The peak amplitude at $f_{\rm KD}$ is

$$\begin{aligned} \Omega_{\rm GW,KD}h^2 &= h^2\Omega^{\rm st}_{\rm GW}(f_\Delta)\left(\frac{f_{\rm KD}}{f_\Delta}\right) = \Omega^{\rm st}_{\rm GW}h^2(f_\Delta)e^{2N_{\rm KD}} \\ &\simeq 2.8\cdot 10^{-13}\left[\frac{g_*(T_\Delta)}{106.75}\right]\left[\frac{g_{*,s}(T_\Delta)}{106.75}\right]^{-\frac{4}{3}}\left[\frac{E_{\rm inf}}{10^{16}\ {\rm GeV}}\right]^4\left[\frac{e^{2N_{\rm KD}}}{e^{10}}\right], \end{aligned} \tag{4.56}$$

and is enhanced by the duration of the kination era. Finally, the frequency corresponding to the start of the matter era is

$$f_{\rm dom} = \frac{H_{\rm dom}a_{\rm dom}}{2\pi a_0} = f_{\rm KD}\left(\frac{\rho_{\rm dom}}{\rho_{\rm KD}}\right)^{1/6}. \tag{4.57}$$

The amplitude difference between flat parts from radiation eras before and after the matter-kination era is

$$\frac{\Omega_{\rm GW}(f > f_{\rm dom})}{\Omega_{\rm GW}(f < f_\Delta)} = \left(\frac{f_{\rm KD}}{f_\Delta}\right)\left(\frac{f_{\rm KD}}{f_{\rm dom}}\right)^2 = \left(\frac{1}{\rho_\Delta}\cdot\frac{\rho_{\rm KD}^2}{\rho_{\rm dom}}\right)^{1/3} \leq 1. \tag{4.58}$$

The above equality is satisfied when no entropy dilution occurs during the whole completion of the matter domination era and $\rho_\Delta = \rho^2_{\rm KD}/\rho_{\rm dom}$, cf. Eq. (4.49). Otherwise, the amount of dilution is imprinted in the difference between the amplitudes of the two flat parts of the spectrum.

Detectability. — The resulting typical spectra are plotted in the right panel of Fig. 4.22 for three benchmark points reported in the left panel and corresponding to different choices of kination energy scales and kination durations. A large parameter space allows the peak from the matter-kination era to be probed by LISA [65], BBO [68], ET [66, 67], CE [228], and SKA [207], where we have used the integrated power-law sensitivity curves[8] of [1]. Note that a kination era lasting more than ~ 12 e-folds is not viable as a too large energy density in GW violates the $\Delta N_{\rm eff}$ bound, see Eq. (2.22). Fig. 4.23 shows that the longer duration of the kination era enhances the detectability of the peak signature.

[8] We denote a signal to be detectable when its amplitude surpasses the power-law sensitivity curve for a given signal-to-noise ratio (SNR). We note that the SNR formula given in [1] is an approximated one which works within the limit of large detector noise. The generic formula can be found in [466, 552, 553]. We have checked that the two formulae agree for the power-law sensitivity curves with SNR $\lesssim 10$ used in this paper.

The peak signature we are exploring should be distinguished from GW peaked signals produced by cosmological first-order phase transitions, e.g., [140, 153], or by the network of cosmic strings [1, 351]. Another scenario with large primordial GW from inflation is axion inflation [125, 126]. This signal's spectral shape differs from what we predict from an intermediate matter-kination era.

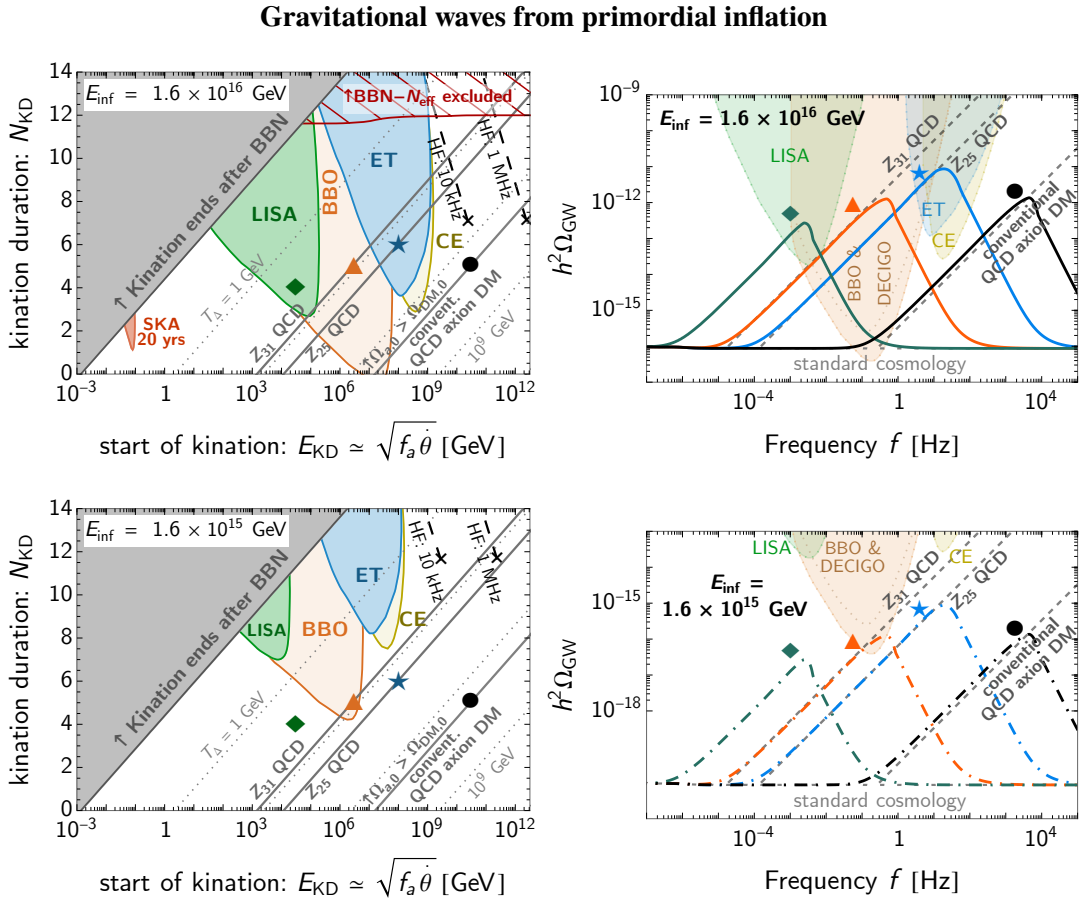

Figure 4.22: **Left**: Detectability of the irreducible GW background from inflation with energy scale $E_{\rm inf}$, enhanced by a period of matter-kination lasting for $(2N_{\rm KD} + N_{\rm KD})$ efolds with no entropy injection, cf. Eq. (4.51). The kination era starts at energy scale $E_{\rm KD}$ and ends when the temperature of the Universe is T_Δ (gray dotted lines). The observable windows of the peak signal are shown in the colored regions. BBN constrains the late kination eras (gray) and the duration of kination (red-hatched) (see Sec. 4.4.4). The QCD axion that allows a kination era could be DM along the solid-gray lines for the conventional and $\mathbb{Z}_\mathcal{N}$ QCD-axion models, assuming kinetic misalignment (see Sec. 6.4). The smaller the inflation scale, the weaker the GW amplitude. The black dashed lines show the prospects for the detectability by hypothetical high-frequency experiments operating at 10 kHz and 1 MHz with sensitivity $h^2\Omega_{\rm sens} = 10^{-10}$. **Right:** GW spectra corresponding to the benchmark points shown in the left panel. Dashed lines show the peak position for the matter-kination era from the QCD axion DM.

Local strings SGWB

The intermediate matter-kination era affects the SGWB from local cosmic strings by changing its slope, cf. Eq. (4.17), from +1 (for loops produced during kination) to -1/3 (for loops produced during matter). The estimation for the peak frequency becomes non-trivial, unlike the inflationary SGWB case, due to the delayed decay of the string loops, cf. Chap. 3. Besides, another signature also arises- the secondary peak- from loops produced deep inside the earlier radiation era and decay only during the matter kination era.

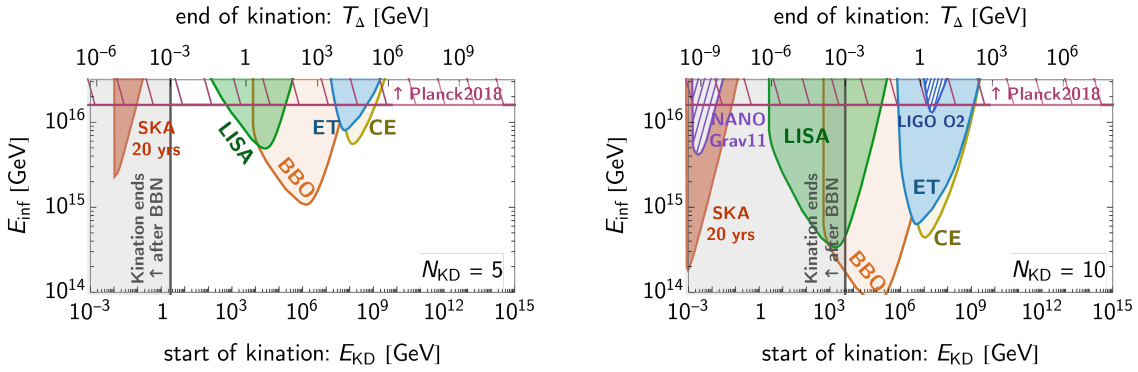

Figure 4.23: Observability regions when varying the inflation scale for two kination durations, $N_{\rm KD} = 5$ (**left**) and $N_{\rm KD} = 10$ (**right**). Planck2018 data [20, 55] implies the upper bound $E_{\rm inf} \lesssim 1.6 \times 10^{16}$ GeV (purple-hatched).

Peak frequency. — Local-string loops produced at the start of kination $t_{\rm KD}$ could decay long after the end of a short kination era at t_Δ. The condition for the GW emission at $\tilde{t}_M^{\rm KD}$ to take place during the late-radiation era is

$$1 < \frac{\tilde{t}_M^{\rm KD}}{t_\Delta} \simeq \left(\frac{\alpha}{2\Gamma G\mu}\right)\left(\frac{a_{\rm KD}}{a_\Delta}\right)^3 \quad \Rightarrow \quad N_{\rm KD} < \frac{1}{3}\log\left(\frac{\alpha}{2\Gamma G\mu}\right), \tag{4.59}$$

where we used Eq. (3.15) to relate GW emission times $\tilde{t}_M^x$ and loop production times t_x. For $\tilde{t}_M^{\rm KD} > t_\Delta$, the peak frequency $f_{\rm KD}$ follows from Eq. (3.32)

$$f_{\rm KD} \;=\; f_\Delta\left[\frac{a(\tilde{t}_M^{\rm KD})}{a(\tilde{t}_M^{\Delta})}\right]\left(\frac{t_\Delta}{t_{\rm KD}}\right) \;=\; f_\Delta\left(\frac{t_\Delta}{t_{\rm KD}}\right)^{1/2} \;=\; f_\Delta\left(\frac{\rho_{\rm KD}}{\rho_\Delta}\right)^{1/4}, \tag{4.60}$$

where we used Eq. (3.15) once again. For $\tilde{t}_M^{\rm KD} < t_\Delta$, the peak frequency $f_{\rm KD}$ is

$$f_{\rm KD} = f_\Delta\left[\frac{a(\tilde{t}_M^{\rm KD})}{a(t_\Delta)}\right]\left[\frac{a(t_\Delta)}{a(\tilde{t}_M^{\Delta})}\right]\left(\frac{t_\Delta}{t_{\rm KD}}\right) = f_\Delta\left(\frac{2\Gamma G\mu}{\alpha}\right)^{1/6}\left(\frac{\rho_{\rm KD}}{\rho_\Delta}\right)^{1/3}. \tag{4.61}$$

From the expression for f_Δ in Eq. (4.21), we deduce the frequency of the peak signature of the presence of a matter-kination era in the GW spectrum from local strings

$$f_{\rm KD} \simeq \begin{cases} 1.8\cdot 10^3\ {\rm Hz}\left[\frac{0.1\times 50\times 10^{-11}}{\alpha\Gamma G\mu}\right]^{\frac{1}{2}}\left[\frac{E_{\rm KD}}{10^5\ {\rm GeV}}\right] & \text{for } N_{\rm KD} < \frac{1}{3}\log\left(\frac{\alpha}{2\Gamma G\mu}\right), \\ 6.1\cdot 10^2\ {\rm Hz}\left[\frac{0.1}{\alpha}\right]^{\frac{2}{3}}\left[\frac{50\times 10^{-11}}{\Gamma G\mu}\right]^{\frac{1}{3}}\left[\frac{E_{\rm KD}}{10^5\ {\rm GeV}}\right]\left[\frac{\exp(N_{\rm KD}/2)}{10}\right] & \text{for } N_{\rm KD} > \frac{1}{3}\log\left(\frac{\alpha}{2\Gamma G\mu}\right). \end{cases} \tag{4.62}$$

Peak amplitude. — The amplitude at the peak is obtained from Eq. (4.17)

$$\Omega_{\rm GW,KD} \;\simeq\; \frac{1}{2.5}\Omega_{\rm GW,st}(10 f_\Delta)\left(\frac{f_{\rm KD}}{10 f_\Delta}\right), \tag{4.63}$$

where the factor 2.5 accounts for the change of relativistic degrees of freedom[9], and we multiply the factor 10 to f_Δ, which is fitted well with the peak from numerical simulations, in order to account for VOS evolution and mode summation. An analytical estimate of the GW amplitude $\Omega_{\rm GW,st}(f)$ emitted by local strings in standard cosmology is given by Eq. (3.47).

[9]Precisely, Eq. (3.31) has a factor of $\left(\frac{g_*(T)}{g_*(T_0)}\right)\left(\frac{g_{*s}(T_0)}{g_{*s}(T)}\right)^{4/3}$, which goes to 2.5^{-1} in high-temperature limit.

Detectability. — The peak signature of a matter-kination era in the GW spectrum from local cosmic strings is potentially observable by future observatories, as shown in Fig. 4.24. As the GW spectrum from local CS assuming standard cosmology is already at the observable level, even a few e-folds of the kination era can induce the smoking-gun peak signature. On the top panel, we show the string tension of $G\mu \sim 10^{-11}$ [264, 265], which could explain hints from NANOGrav 12.5 years [205], PPTA 15 years [206] and EPTA 24 years [204]. The planned observatories cannot probe a large parameter space (white), but ultra-high frequency experiments could do so. We expect the ability to probe such a high-energy kination era to get reduced by other cut-offs, i.e., friction and particle production in Chap. 3. We leave the dedicated study for further work. In Fig. 4.25, a few e-folds of kination render GW signal from strings of tension $G\mu \simeq 10^{-19}$ observable, but at the price of having kination ending after BBN.

Second kination peak at high-frequency. — The delayed decay of local string loops introduces another spectral enhancement at a high frequency; see the top left panel in Fig. 4.24. In contrast to the main peak from loops produced at the start of kination, the smaller second peak corresponds to loops created deep inside the earlier radiation era. Eq. (4.17) tells us that the spectral index changes sign between loops from radiation which decay in matter era, $\beta = -1/2$, and those decay during kination era, $\beta = 1/4$. So the second peak corresponds to loops produced during the radiation era and decay right at the start of the kination era, i.e.

$$\tilde{t}_M^{\rm KDII} \;=\; t_{\rm KD} \;\;\Rightarrow\;\; t_{\rm KDII} \;=\; \frac{2\Gamma G\mu}{\alpha} t_{\rm KD}, \tag{4.64}$$

where we applied Eq. (3.15) to relate GW emission times $\tilde{t}_M^x$ and loop production times t_x. The visibility of the second peak depends on the separation with respect to the first biggest kination peak, which we can derive from Eq. (3.32)

$$\frac{f_{\rm KDII}}{f_{\rm KD}} \;=\; \left[\frac{a(\tilde{t}_M^{\rm KDII})}{a(\tilde{t}_M^{\rm KD})}\right]\left(\frac{t_{\rm KD}}{t_{\rm KDII}}\right) \;=\; \left[\frac{a(t_{\rm KD})}{a(\tilde{t}_M^{\rm KD})}\right]\left(\frac{\alpha}{2\Gamma G\mu}\right), \tag{4.65}$$

where the first bracket depends on the two limits of $N_{\rm KD}$, as in Eq. (4.62). Here we report the separation between two kination peaks

$$\frac{f_{\rm KDII}}{f_{\rm KD}} \;=\; \begin{cases} 10^4 \left(\frac{\alpha \times 50 \times 10^{-11}}{0.1 \times \Gamma G\mu}\right)^{1/2} \exp(N_{\rm KD}/2) & \text{for } N_{\rm KD} < \frac{1}{3}\log\left(\frac{\alpha}{2\Gamma G\mu}\right), \\ 2.15 \times 10^5 \left(\frac{\alpha \times 50 \times 10^{-11}}{0.1 \times \Gamma G\mu}\right)^{2/3} & \text{for } N_{\rm KD} > \frac{1}{3}\log\left(\frac{\alpha}{2\Gamma G\mu}\right). \end{cases} \tag{4.66}$$

Eq. (4.66) underestimates the two-peak separation in Fig. 4.24 by approximately one order of magnitude because the EOS change only impacts the network evolution, which results in correcting the loop formation and, thus, the position of the most prominent peak. It takes a few e-folds for the network to adapt to the change of cosmology, which moves the first biggest peak to a lower frequency than naively expected, same as the factor $\mathcal{O}(0.1)$ in Eq. (4.21). On the other hand, the position of the smallest peak depends only on the loop's emission time and is not affected by the time the network adapts to a change in the cosmological era. Before moving to the global strings, let us emphasize that the second peak will not be seen in the global string spectrum. This peak is linked to delayed GW emission of local strings, while global loops decay almost instantaneously after formation.

Global strings

The short-lived global strings emit GW right after loop production, much earlier than for local strings. As a consequence, GW redshift for a longer time, at fixed loop-formation time t_i, and the frequency observed today is lowered by a factor equal $\eta/M_{\rm pl}$, see Eq. (3.78). Hence, for fixed

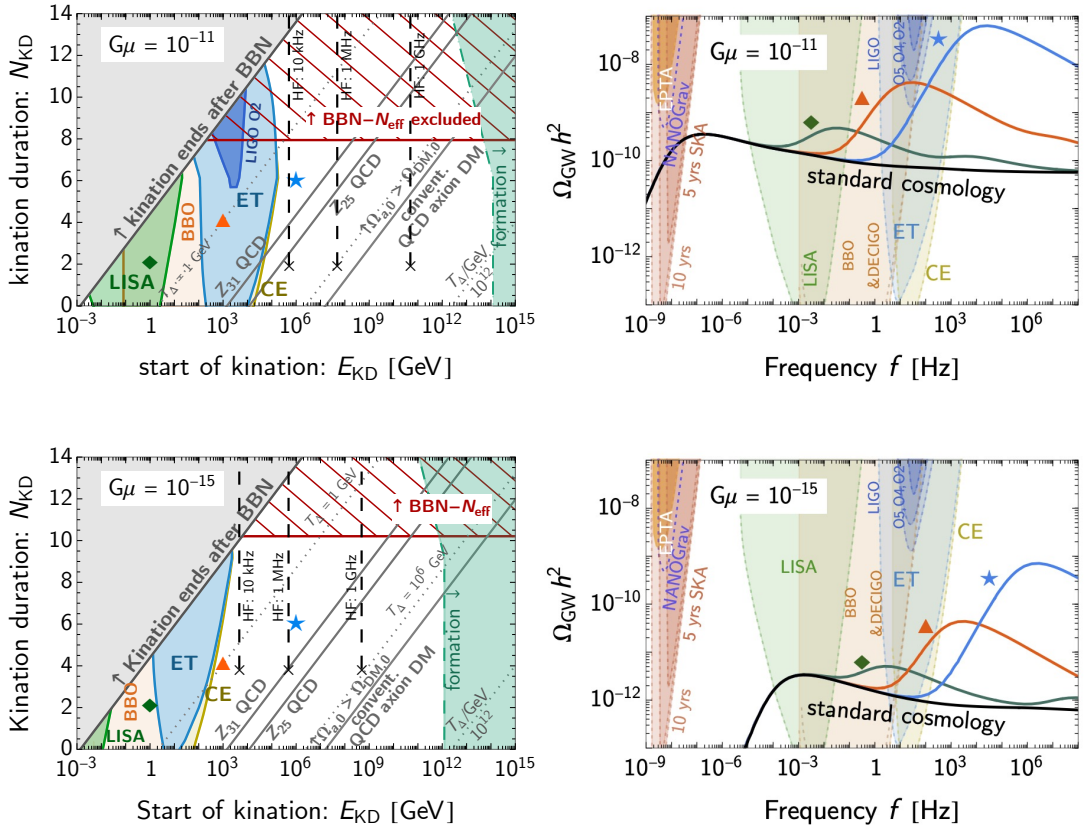

Figure 4.24: The GW background from local strings with tension $G\mu$ is enhanced by a period of matter-kination lasting for $(2N_{\rm KD} + N_{\rm KD})$ efolds, cf. Eq. (4.51). The kination era starts at energy scale $E_{\rm KD}$ and ends when the temperature of the Universe is T_Δ (dashed lines). **Left panel:** In the coloured regions, the peak is observable. BBN constrains late kination eras (gray) and long kination eras (red-hatched) (see Sec. 4.4.4). The black dashed lines show the detectability prospects of hypothetical HF experiments operating at 10 kHz, 1 MHz, and 1 GHz frequencies with sensitivity $h^2\Omega_{\rm sens} = 10^{-10}$. The QCD axion that allows a kination era could be DM along the solid-gray lines for the conventional and $\mathbb{Z}_\mathcal{N}$ QCD-axion models, assuming kinetic misalignment (see Sec. 6.4). **Right panel:** The GW spectra correspond to benchmark points in the left panel. Note the second peak at high-frequency for the green line, which comes from loops produced during the radiation era and decaying at the start of kination, cf. Eq. (4.66).

string scale η, the peak signature from the matter-kination era from global strings sits at a lower frequency than in the local-string case.

Due to PTA constraints $G\mu \lesssim 10^{-11}$ [369, 554], we only consider local strings with scale $\eta \lesssim 3\times10^{12}$ GeV. In contrast, the scale of global strings is only bounded by the largest inflationary scale $\eta \lesssim 10^{16}$ GeV. Hence, in our plots, the peak frequencies from global and local strings can only be compared if we consider that the string scales η, which we consider for both are different.

Peak frequency. — The peak GW frequency $f_{\rm KD}$ from loops that formed at the start of the kination era $t_{\rm KD}$ is written, via Eq. (3.32), in terms of the frequency f_Δ corresponding to the end of kination at time t_Δ,

$$f_{\rm KD} \;=\; f_\Delta \left[\frac{a(\tilde{t}_M^{\rm KD})}{a(\tilde{t}_M^{\Delta})}\right]\left(\frac{t_\Delta}{t_{\rm KD}}\right), \tag{4.67}$$

where $\tilde{t}_M^x$ and t_x are the emission and loop-production times, respectively. Applying $a \propto t^{1/3} \propto \rho^{1/6}$ during kination and $a \propto t^{1/2} \propto \rho^{1/4}$ during radiation era, the peaked frequency for global

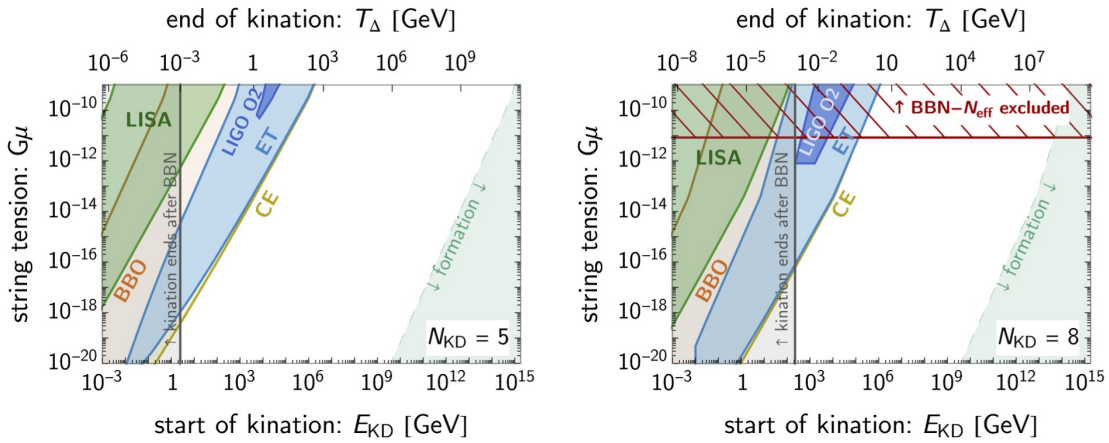

Figure 4.25: Detectability of the GW peak for varying string tension $G\mu$. The longer the matter-kination era, the higher the peak signature, allowing strings with smaller tension $G\mu$ to be probed.

strings is

$$f_{\rm KD} = f_\Delta \left[\frac{a(\tilde{t}_M^{\rm KD})}{a(t_\Delta)}\right]\left[\frac{a(t_\Delta)}{a(\tilde{t}_M^{\Delta})}\right]\left(\frac{t_\Delta}{t_{\rm KD}}\right) = f_\Delta \left(\frac{\rho_{\rm KD}}{\rho_\Delta}\right)^{1/3}, \tag{4.68}$$

where we apply $\tilde{t}_M^x \simeq t_x$ for global strings, see Eq. (3.72). Acquiring f_Δ from Eq. (3.79), we obtain the peak frequency from the presence of a matter-kination era in the global-string GW spectrum

$$f_{\rm KD} \simeq (0.9\ {\rm Hz})\left(\frac{0.1}{\alpha}\right)\left(\frac{E_{\rm KD}}{10^5\ {\rm GeV}}\right)\left[\frac{\exp(N_{\rm KD}/2)}{10}\right], \tag{4.69}$$

where the numerically-fitted f_Δ is used to account for the transition between two scaling regimes of the string network.

Peak amplitude. — From the relation in Eq. (3.76), the GW amplitude at the peak is

$$\Omega_{\rm GW,KD} \simeq \Omega_{\rm GW,st}(10 f_\Delta)\left(\frac{f_{\rm KD}}{10 f_\Delta}\right) L, \tag{4.70}$$

where the factor $10 f_\Delta$ fits well with the peak from numerical simulations, accounting for VOS evolution and mode summation and where $L = \mathcal{O}(1)$ is a ratio of log factors.[10] An analytical estimate of the GW amplitude $\Omega_{\rm GW,st}(f)$ emitted by global strings in standard cosmology is given by Eq. (3.74). In terms of the kination parameters, we have

$$\Omega_{\rm GW}^{\rm KD} \simeq 1.2\cdot 10^{-18}\left[\frac{\eta}{10^{15}\ {\rm GeV}}\right]^4 e^{2N_{\rm KD}} \log^3\left[2.2\cdot 10^{18}\left[\frac{\eta}{10^{15}\ {\rm GeV}}\right]\left[\frac{\alpha}{0.1}\right]^2\left[\frac{10^9\ {\rm GeV}}{E_{\rm KD}}\right]^2\right] \tag{4.71}$$

Detectability. — Fig. 4.26 shows the detectability of GW produced by global strings and enhanced by the intermediate matter-kination era. The spectra shown on the right panel correspond to the benchmark points in the contour plot on the left panel. The GW amplitude scales as η^4 up to the log suppression; therefore, the string tension η must be significant for detectability. The spectral index corresponding to loops formed during the matter era goes like $f^{-1/3}$ due to the summation of higher harmonics, instead of f^{-1} in the spectrum of the only fundamental Fourier

[10] $L \equiv \left\{\frac{\log^3\left[(5.6\times10^{30})\left(\frac{\eta}{10^{15}\ {\rm GeV}}\right)\left(\frac{1\ {\rm mHz}}{10 f_\Delta}\right)^2\left(\frac{10 f_\Delta}{f_{\rm KD}}\right)^{3/2}\right]}{\log^3\left[(5.6\times10^{30})\left(\frac{\eta}{10^{15}\ {\rm GeV}}\right)\left(\frac{1\ {\rm mHz}}{10 f_\Delta}\right)^2\right]}\right\}$.

mode [1, 334, 352]. The drop at some high frequency is an artifact because we only sum up to 5×10^5 modes.

GW from strings could experience a high-frequency cut-off due to the friction effect. This could shift the spectral peak if the friction cut-off has a frequency lower than the matter-kination era's peak. We leave the dedicated study for future work. On the other hand, the spectrum could exhibit the low-frequency cut-off (black dotted lines in Fig. 4.26) if the CS network manifests the metastability similar to [1, 435, 555] in the context of local strings. The contour plot in Fig. 4.26-left shows the compromise between the enhancement of the GW signal and the BBN bound when the kination duration is increased.

A common origin for matter-kination era and GW source: axion strings. — An intriguing possibility is if the physics responsible for kination induced by a spinning axion and the physics responsible for the cosmic strings have a common origin. A $U(1)$-breaking phase transition generates cosmic strings at early times, and the dynamics of the axion at later times generate a kination era. In this paper, we consider models (Sec. 7.1) where the radial mode of the complex scalar field obtains a large VEV at early times during inflation, so all topological defects are diluted away. However, in alternative constructions [551], the $U(1)$ could be broken after inflation. This can lead to the formation of a cosmic string network. A few efolds of kination for large f_a values would then be compatible with global strings with considerable tension and a detectable GW signal. For this class of models, the axion could generate the multiple-peak GW signals from both inflation and cosmic strings. We discuss the detectability of the axion-string GW enhanced by kination from spinning axion in Fig. 6.6 in Sec. 6.4.3.

4.7.2 Multiple-peak signature: inflation + local cosmic strings

Three types of peaks. The physics explaining the presence of the cosmic strings is generally unrelated to the inflationary sector. In the presence of multiple SGWB, the intermediate matter-kination era can lead to a multiple-peak GW signal which the synergy of future detectors could probe.

1. Peak signature of matter-kination era in inflationary GW, cf. Eq. (4.55).
2. Peak signature of matter-kination era in SGWB from local CS, cf. Eq. (4.62).
3. Peak in SGWB from local CS due to the transition between radiation and later matter era around the temperature 0.75 eV, and whose frequency reads [1]

$$f_{\rm low}^{\rm cs} \simeq 1.48 \cdot 10^{-7}\ \text{Hz} \left(\frac{50 \times 10^{-11}}{\Gamma G\mu}\right). \tag{4.72}$$

The inflationary peak (1) can be easily distinguished from the CS peaks (2 and 3), which are broader because the CS network takes time to react to the change of cosmology [1]. In this section, we point out the possibility of a two-peak spectrum (two matter-kination peaks) and a three-peak spectrum (two matter-kination peaks + one radiation-matter peak at lower frequency, Eq. (4.72)).

Peaks separation. We could observe either two (left panel) or three peaks (right panel) depending on the separation between each peak, which are estimated from Eqs. (4.55), (4.62), and (4.72)

$$\frac{f_{\rm peak}^{\rm cs}}{f_{\rm low}^{\rm cs}} \simeq 1.2 \cdot 10^{9} \left[\frac{E_{\rm KD}}{10\ \text{TeV}}\right] \left[\frac{\Gamma G\mu}{50 \times 10^{-11}}\right]^{\frac{1}{2}} \left[\frac{0.1}{\alpha}\right]^{\frac{1}{2}}, \tag{4.73}$$

$$\frac{f_{\rm peak}^{\rm cs}}{f_{\rm peak}^{\rm inf}} \simeq 1.6 \cdot 10^{5} \left[\frac{10}{e^{N_{\rm KD}/2}}\right] \left[\frac{0.1 \times 50 \times 10^{-11}}{\alpha\Gamma G\mu}\right]^{\frac{1}{2}}, \tag{4.74}$$

$$\frac{f_{\rm peak}^{\rm inf}}{f_{\rm low}^{\rm cs}} \simeq 7 \cdot 10^{3} \left[\frac{E_{\rm KD}}{10\ \text{TeV}}\right] \left[\frac{e^{N_{\rm KD}/2}}{10}\right] \left[\frac{\Gamma G\mu}{50 \times 10^{-11}}\right], \tag{4.75}$$

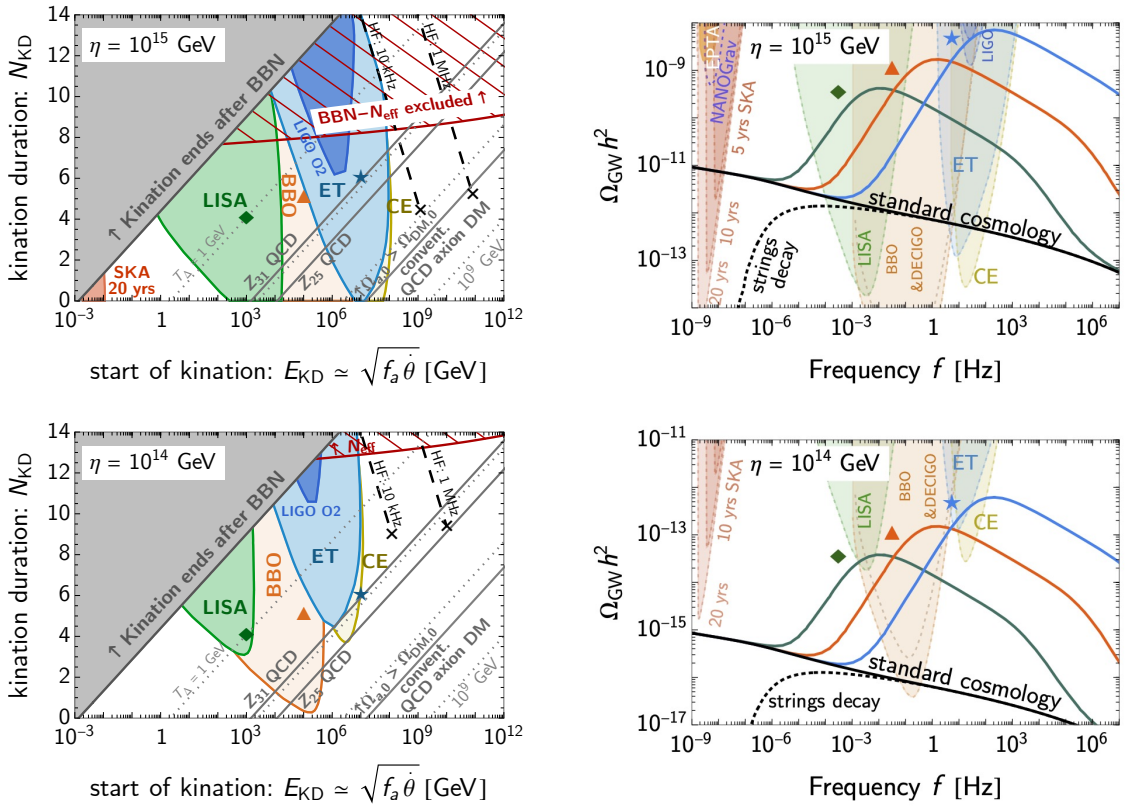

Figure 4.26: The GW spectrum from global strings with tension η is enhanced by a period of matter-kination lasting for $(2N_{\rm KD} + N_{\rm KD})$ efolds, cf. Eq. (4.51). The kination era starts at energy scale $E_{\rm KD}$ and ends when the temperature of the Universe is T_Δ (dashed lines). **Left panel:** In the coloured regions, the peak is observable. BBN constrains late kination eras (gray) and long kination eras (red-hatched). The peak is described by Eq. (4.69) and (4.71). The black dashed lines show the detectability prospects of hypothetical HF experiments operating at 10 kHz, 1 MHz, and 1 GHz frequencies with sensitivity $h^2\Omega_{\rm sens} = 10^{-10}$. The QCD axion that allows a kination era could be DM along the solid-gray lines for the conventional and $\mathbb{Z}_\mathcal{N}$ QCD-axion models, assuming kinetic misalignment (see Sec. 6.4). **Right panel:** The GW spectra correspond to benchmark points in the left panel. The effect of metastable strings cut the spectrum at a low frequency, as shown by the black dashed line for a network decay at $T \sim 100$ MeV.

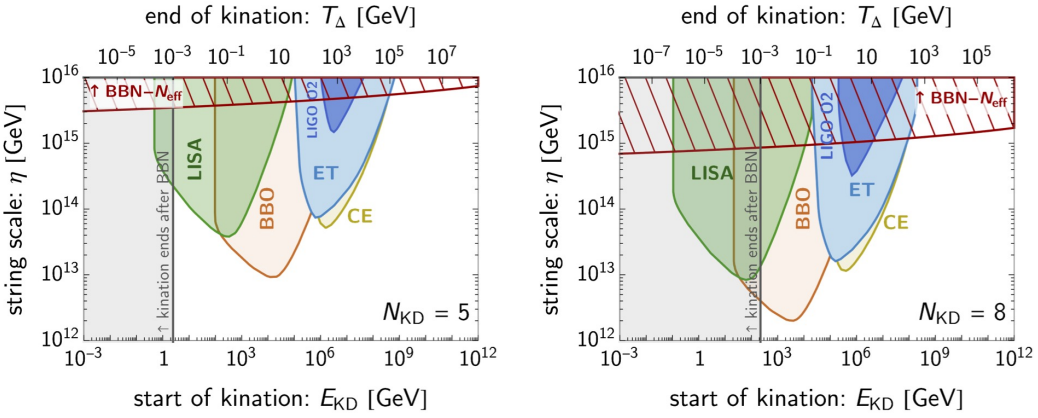

Figure 4.27: The longer kination era enhances the peak, allowing strings with smaller string scale η to be probed.

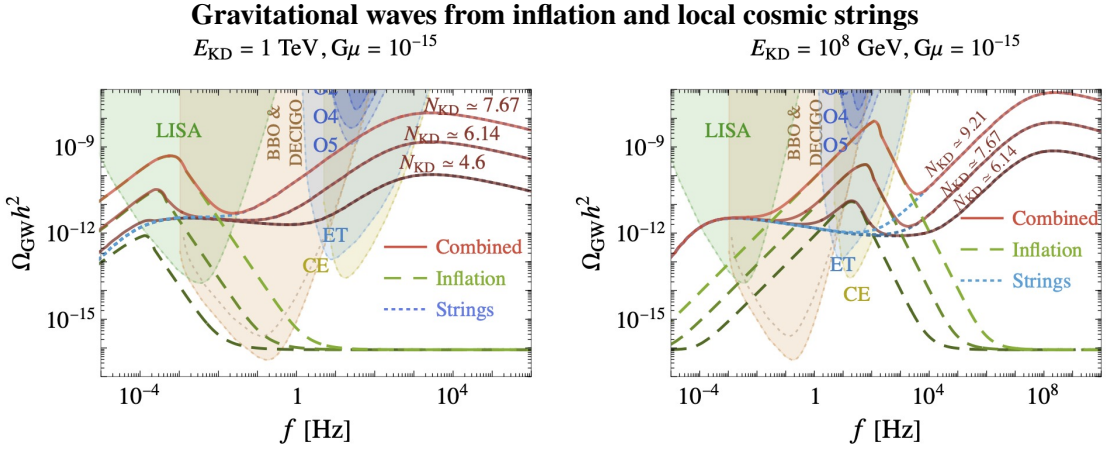

Figure 4.28: Two-peak (**left**) and three-peak (**right**) GW spectra from inflation and local CS network. We assume the maximum inflationary scale allowed by CMB data $E_{\rm inf} = 1.6 \times 10^{16}$ GeV [20, 55].

where we have assumed for simplicity that loops from kination era decay in the radiation era, $N_{\rm KD} < \log(\alpha/2\Gamma G\mu)/3$. For multiple observable peaks, the separations should be slight but not overlapping.

Detectability of two peaks. — The combined GW spectra are shown in Fig. 4.28. LISA and ET/CE can observe the two-peak spectrum in synergy.

Detectability of three peaks. — The lowest-frequency peak in the CS spectrum receives no boost from kination but requires a large $G\mu$ for its observability in the PTA range. However, the flat part of CS in Eq. (3.47) could dominate over the boosted inflationary peak, Eq. (4.56). The ratio between them is

$$\frac{\Omega^{\rm inf}_{\rm peak}}{\Omega^{\rm cs}_{\rm flat}} \approx 0.8 \times 10^{-3} \left(\frac{E_{\rm inf}}{10^{16}\ {\rm GeV}}\right)^4 \left(\frac{0.1 \times 10^{-11}}{\alpha G\mu}\right)^{1/2} \left(\frac{\Gamma}{50}\right)^{1/2} \left[\frac{\exp(N_{\rm KD}/2)}{10}\right]^4 . \quad (4.76)$$

For $N_{\rm KD} = 5$ and $E_{\rm inf} = 1.6 \times 10^{16}$ GeV, the string network with tension $G\mu \lesssim 10^{-15}$ allows the inflationary peak to emerge. However, as shown in Fig. 4.28-right, the simultaneous observation of the three peaks could be possible with the help of HF experiments [40].

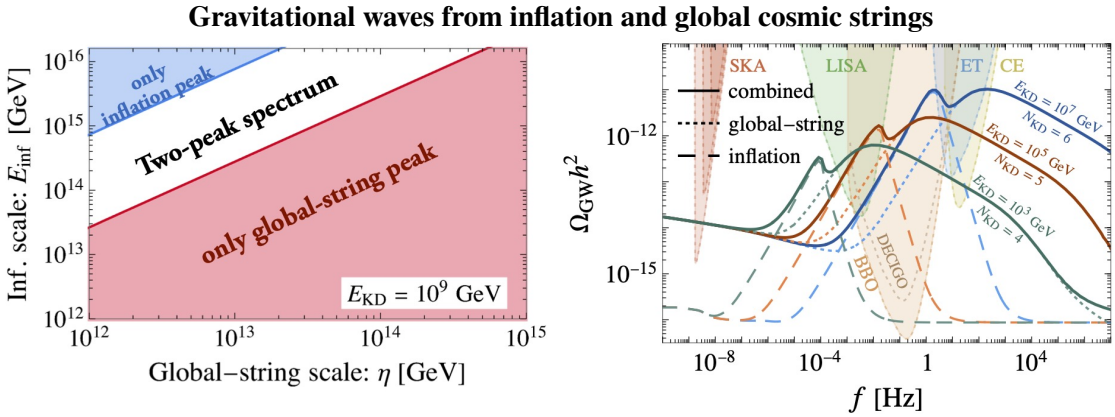

Figure 4.29: **Left**: In the presence of GW from both inflation and global strings, as well as a matter-kination era, the signal can have either one or two peaks. **Right**: Two-peak GW spectra from inflation at the maximum inflation scale allowed by CMB data $E_{\rm inf} = 1.6 \times 10^{16}$ GeV [20, 55] and from global strings with energy scale $\eta = 2 \times 10^{14}$ GeV.

Multiple-peak signature: inflation + global cosmic strings

Peaks separation. — The separation between the matter-kination peak in SGWB from global string and primordial inflation can be read out from Eqs. (4.55) and (4.62)

$$\frac{f_{\rm KD}^{\rm inf}}{f_{\rm KD}^{\rm glob}} \simeq (1.2 \times 10^{-2}) G^{1/4}(T_\Delta) \left(\frac{\alpha}{0.1}\right). \tag{4.77}$$

Interestingly, the peak separation is independent of the matter-kination parameters. The reason is that global-string loops decay right after their production. So the GW frequency reflects the horizon size directly at that time, similar to the inflationary GW.

Detectability of two peaks. — The visibility of each peak depends on their respective height, determined by the string scale η and the inflationary scale $E_{\rm inf}$. The matter-kination peak in the global-string spectrum, Eq. (4.71), is visible if its amplitude exceeds the inflation shoulder, Eq. (4.56),

$$\begin{aligned} 1 < \left.\frac{\Omega_{\rm GW}^{\rm glob}}{\Omega_{\rm GW}^{\rm inf}}\right|_{f_{\rm KD}^{\rm glob}} &= \frac{\Omega_{\rm GW,KD}^{\rm glob}}{\Omega_{\rm GW,KD}^{\rm inf}\left(\frac{f_{\rm KD}^{\rm inf}}{f_{\rm KD}^{\rm glob}}\right)^2} \\ &= 6.4 \cdot 10^2 \left[\frac{\eta}{10^{15}\ {\rm GeV}}\right]^4 G^{-\frac{3}{2}}(T_\Delta) \left[\frac{0.1}{\alpha}\right]^2 \left[\frac{10^{16}\ {\rm GeV}}{E_{\rm inf}}\right]^4 \mathcal{F}_{\log}(\eta_{15}), \end{aligned} \tag{4.78}$$

where

$$\mathcal{F}_{\log}(\eta) \equiv \log^3\left[(2.2 \times 10^{18}) \left(\frac{\eta}{10^{15}\ {\rm GeV}}\right) \left(\frac{\alpha}{0.1}\right)^2 \left(\frac{10^9\ {\rm GeV}}{E_{\rm KD}}\right)^2\right]$$

Conversely, the matter-kination peak signature in the primordial inflationary GW is visible if its amplitude exceeds the global-string blue-tilted part,

$$\begin{aligned} 1 > \left.\frac{\Omega_{\rm GW}^{\rm glob}}{\Omega_{\rm GW}^{\rm inf}}\right|_{f_{\rm KD}^{\rm inf}} &= \frac{\Omega_{\rm GW,KD}^{\rm glob}\left(\frac{f_{\rm KD}^{\rm inf}}{f_{\rm KD}^{\rm glob}}\right)}{\Omega_{\rm GW,KD}^{\rm inf}} \\ &= 1.1 \cdot 10^{-3} \left[\frac{\eta}{10^{15}\ {\rm GeV}}\right]^4 G^{-\frac{3}{4}}(T_\Delta) \left[\frac{\alpha}{0.1}\right] \left[\frac{10^{16}\ {\rm GeV}}{E_{\rm inf}}\right]^4 \mathcal{F}_{\log}(\eta_{15}) \end{aligned} \tag{4.79}$$

Both conditions in Eq. (4.78) and (4.79) must be satisfied for a visible two-peak signature, as illustrated in the white region of Fig. 4.29. Otherwise, only one peak is visible, either from global strings (red region) or from inflation (blue region). Fig. 4.29 only depends logarithmically on $E_{\rm KD}$, the white region moving to lower $E_{\rm inf}$ by only 10% when $E_{\rm KD}$ increases by three orders-of-magnitude.

4.8 Effect on SGWB from First-Order Phase Transitions

In the previous sections, we have shown that the presence of a non-standard cosmological history leads to many signatures in SGWB from the two main long-lasting sources: primordial inflation or cosmic strings. Any GW signal whose production period lasts longer than the duration of the non-standard era will receive a spectral distortion. This section will first show that this is also the case for super-horizon Fourier modes of GW from short-lasting sources such as a cosmological first-order phase transition (FOPT). Moreover, we later show that the amplitude of the GW peak is reduced whenever the FOPT is produced during the non-standard era, focussing on the matter-kination scenario (scheme E). One can generalize the analysis provided here to other short-lasting SGWB sources, e.g., the preheating and the leading contribution to thermal GW.

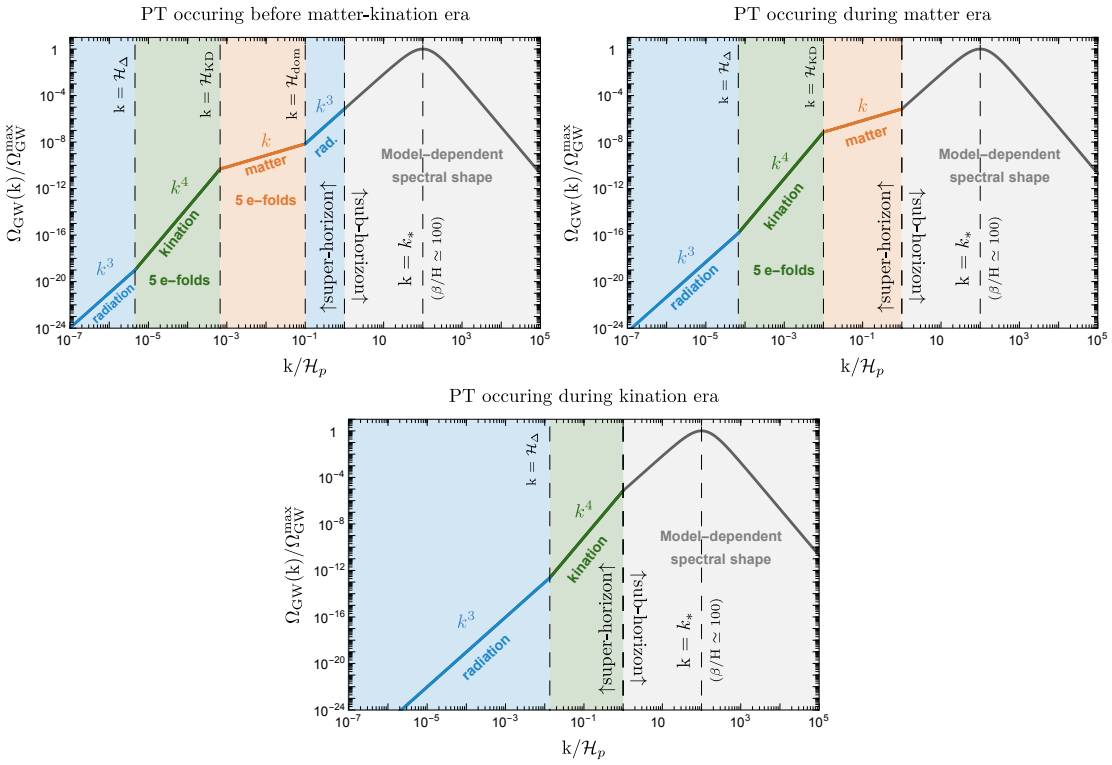

Figure 4.30: Spectral distortion of GW produced from a FOPT occurring before the matter-kination era (**Top left**), during a matter era which is followed by a kination era (**Top right**), and during a kination era (**Bottom**). To observe a triangular shape would be a smoking-gun of the scenarios studied in this work. The present figure does not show the peak suppression and the overall frequency blue-shift when the PT takes place during the non-standard era (e.g., middle and bottom panel here), and which we reserve for Fig. 4.31 and Fig. 4.32. $\mathcal{H}_{\rm dom}$, $\mathcal{H}_{\rm KD}$, and $\mathcal{H}_\Delta$ are the comoving Hubble scales ($\mathcal{H} \equiv aH$) at the beginning of the matter era, at the transition to the kination era, and at the end of the kination era, respectively. The angular wavenumber k is related to the linear frequency f by $k = 2\pi f$.

Spectral distortion

We consider a FOPT driven by a scalar field initially at thermal equilibrium with the radiation component. Depending on the amount of supercooling, GW is either sourced by the collision of bubble walls or by fluids motions, e.g., [152–154]. The peak amplitude of the GW can be formulated as

$$h^2\Omega_{\rm GW}(k)\big|_{t_0} \simeq h^2 \left(\frac{a_p}{a_0}\right)^4 \left(\frac{\rho_{{\rm tot},p}}{\rho_{{\rm tot},0}}\right) \left(\frac{H_p}{\beta}\right)^m \left(\frac{\kappa\alpha}{1+\alpha+\gamma}\right)^2 \mathcal{F}(k,\beta), \tag{4.80}$$

where $\rho_{{\rm tot},i}$ is the total energy density of the Universe at time i, T_p and H_p are the temperature and Hubble scale at the time of GW production, β^{-1} is the duration of the transition, α is the ratio of the vacuum energy difference over the radiation energy density, κ is the conversion coefficient and $\mathcal{F}(k,\beta)$ is the spectral shape. We expect $m = 1$ for GW from long-lived fluid motion and $m = 2$ for GW from short-lived fluid motion or bubble wall collisions. Since our focus is on the effects from the matter-kination era, we have neglected factors involving the wall velocity $v_{\rm w}$. The factor γ is the ratio of the energy density of the new sector, the spinning axion in our case, to that of radiation

$$\gamma \equiv \rho_{\rm NS}/\rho_{\rm rad}. \tag{4.81}$$

The case $\gamma = 0$ corresponds to the FOPT occurring during the standard radiation era. Additionally, the peak frequency is shifted with respect to the standard scenario by

$$f_{\rm NS} = f_{\rm ST} \left(\frac{a_0}{a_p H_p}\right)_{\rm ST} \left(\frac{a_p H_p}{a_0}\right)_{\rm NS} . \tag{4.82}$$

Super-horizon modes are sensitive to the EOS. Due to causality, the IR slope of GW spectrum from FOPT is expected to scale as $\Omega_{\rm GW} \propto k^3$ during radiation domination [556–558]. However, in generic background with EOS ω, we expect the spectral index of super-Hubble Fourier modes to be [462] (see also [559–561])

$$\Omega_{\rm GW}(k) \propto \begin{cases} k^3, & \text{for} \quad k \gtrsim \mathcal{H}_p, \\ k^{\frac{1+15\omega}{1+3\omega}}, & \text{for} \quad k \lesssim \mathcal{H}_p, \end{cases} \tag{4.83}$$

where $\mathcal{H}_p = \frac{a_p}{a_0} H_p$ is the comoving Hubble radius at the time of the PT. Therefore, during the matter and kination era, the slopes become k^1 and k^4 for superhorizon modes. To understand the scaling, it is possible to apply the argument in Sec. 4.2. The contribution from the superhorizon modes of GW continuously re-enters the horizon after the production process ceases. However, the slope from the mode – re-entering during the radiation era – has a k^3 slope. Therefore, the correction due to the non-standard era is added to this scaling, i.e., the red and blue tilts from the matter and kination era. The resulting spectral shape is shown in Fig. 4.30. Assuming on the intermediate matter-kination case (scheme E), we recognize the same triangular shape as the imprint in GW from primordial inflation and cosmic strings, cf. Sec. 4.7.1.

Uniform shift of the spectrum

Usually, a matter era is followed by a heated radiation era which implies a violation of entropy conservation, see, e.g., [532]. Instead, if the matter era is followed by a kination era, as considered in this paper, cf. Fig. 4.31, there is no entropy injection, which implies

$$\left(\frac{a_p}{a_0}\right)_{\rm NS} = \left(\frac{a_p}{a_0}\right)_{\rm ST} . \tag{4.84}$$

As we will see later in Eq. (4.90), (4.91) and (4.84), we deduce the displacement of the GW peak amplitude and frequency if emission occurs during the matter-kination era

$$\frac{\Omega^{\rm NS}_{\rm GW}}{\Omega^{\rm ST}_{\rm GW}} = \left(\frac{\rho^{\rm NS}_{\rm p,tot}}{\rho^{\rm ST}_{\rm p,tot}}\right) \left[\frac{(1+\alpha)_{\rm ST}}{(1+\alpha+\gamma)_{\rm NS}}\right]^2 = \left(\frac{\rho^{\rm ST}_{\rm p,tot}}{\rho^{\rm NS}_{\rm p,tot}}\right), \tag{4.85}$$

$$\frac{f_{\rm NS}}{f_{\rm ST}} = \left(\frac{H^{\rm NS}_{\rm p}}{H^{\rm ST}_{\rm p}}\right) = \left(\frac{\rho^{\rm NS}_{\rm p,tot}}{\rho^{\rm ST}_{\rm p,tot}}\right)^{1/2}, \tag{4.86}$$

where we have assumed unchanged α, κ, and β/H_p.[11] We see that if the PT occurs during the non-standard era, $\rho^{\rm NS}_{\rm p,tot} > \rho^{\rm ST}_{\rm p,tot}$, the amplitude of the GW peak is suppressed. Its frequency is blue-shifted, concerning the one assuming a standard cosmological history, which is in agreement with previous literature [458, 465, 512, 559]. In contrast, if the spinning axion energy density is sub-dominant at the time of GW production, $\gamma \to 0$ in Eq. (4.81), then there is no modification of the GW peak position concerning the standard scenario.

Due to the absence of entropy injection, cf. Eq. (4.84), the amplitude $\Omega^{\rm peak}_{\rm GW}$ and frequency f_p of the peak are dispensed from the additional suppression factor $1/D^{4/3}$ and redshift factor $1/D$, respectively, where $D \equiv \frac{S_{\rm after}}{S_{\rm before}} \geq 1$ is the usual dilution factor, e.g. [562].

[11] $\alpha \equiv \frac{\Delta V}{\rho_{\rm rad}(T_p)}$, where ΔV is the vacuum energy difference, is left unchanged if T_p is unchanged. $\kappa \equiv \frac{\rho_{\rm source}}{\rho_{\rm rad}}$ where $\rho_{\rm source}$ is the energy density of the GW source, is intrinsically independent of the background. $\beta/H_p \equiv \frac{T}{\Gamma}\frac{\partial \Gamma}{\partial T}\Big|_{T_p}$ where Γ is the tunneling rate, is left unchanged if $\Gamma(T)$ is unchanged.

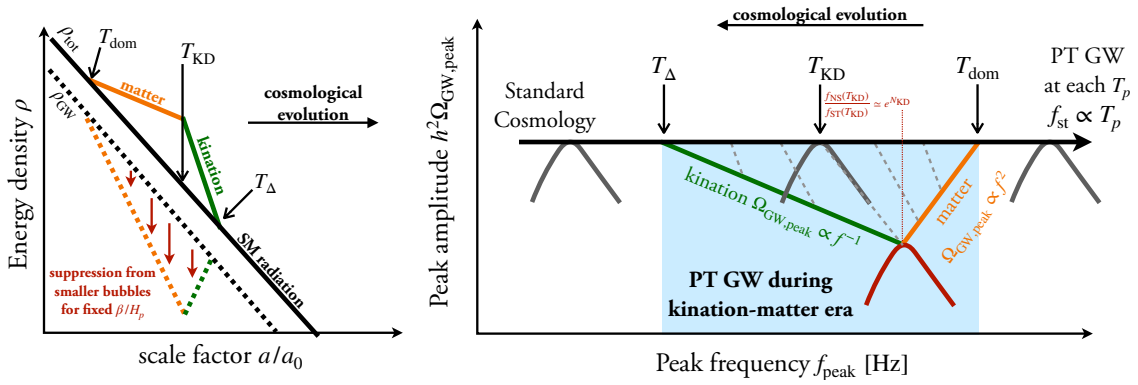

Figure 4.31: The **left** panel compares the evolution of the total energy density of the Universe in the kination-matter scenario (colored) and the one in the standard cosmological history (black). The black dashed line is the expected energy density in GW produced during a thermal FOPT at some temperature T_p. Since β/H_p is independent of the EOS of the Universe, the colliding bubbles during the new-sector domination are smaller in size, and the GW production is suppressed. The **right** panel shows the amplitude suppression (green and orange lines) and blue-shift (gray dashed lines) of the GW peak when the FOPT takes place during the matter-kination era, cf. Eq. (4.90) and (4.91), with respect to the standard radiation-dominated history (black line). The maximum suppression, shown in red, occurs when the PT occurs at the onset of the kination era.

A shift of the GW peak position, more precisely. — We consider a kination-matter era with energy scale at the onset of kination $E_{\rm KD} \equiv \rho_{\rm KD}^{1/4}$ and with $N_{\rm KD}$ efolds of kinations, as in Fig. 4.31. Using Eq. (4.47) and (4.49), we obtain the corresponding temperatures of the radiation bath at the onset of matter, at the onset of kination, and at the end of kination, respectively

$$T_{\rm dom} = \left(\frac{30}{\pi^2 g_*(T_{\rm dom})}\right)^{1/4} E_{\rm KD} \exp\left(\frac{3}{2}N_{\rm KD}\right), \tag{4.87}$$

$$T_{\rm KD} = \left(\frac{30}{\pi^2 g_*(T_{\rm KD})}\right)^{1/4} E_{\rm KD} \exp\left(-\frac{1}{2}N_{\rm KD}\right), \tag{4.88}$$

$$T_\Delta = \left(\frac{30}{\pi^2 g_*(T_\Delta)}\right)^{1/4} E_{\rm KD} \exp\left(-\frac{3}{2}N_{\rm KD}\right). \tag{4.89}$$

The amplitude of the GW peak in the presence of a kination-matter era reads

$$\frac{\Omega_{\rm GW}^{\rm NS}}{\Omega_{\rm GW}^{\rm ST}} = \begin{cases} 1 & \text{for } T_p < T_\Delta, \\ \left(\frac{g_*(T_{\rm KD})g_*(T_\Delta)}{g_*^2(T_p)}\right)\left(\frac{T_\Delta}{T_p}\right)^2 & \text{for } T_{\rm KD} > T_p \geq T_\Delta, \\ \left(\frac{T_p}{T_{\rm KD}}\right)\exp(-2N_{\rm KD}) & \text{for } T_{\rm dom} > T_p \geq T_{\rm KD}, \\ 1 & \text{for } T_p \geq T_{\rm dom}, \end{cases} \tag{4.90}$$

while its frequency is

$$\frac{f_{\rm NS}}{f_{\rm ST}} = \begin{cases} 1 & \text{for } T_p < T_\Delta, \\ \left(\frac{g_*^2(T_p)}{g_*(T_{\rm KD})g_*(T_\Delta)}\right)^{1/2}\left(\frac{T_p}{T_\Delta}\right) & \text{for } T_{\rm KD} > T_p \geq T_\Delta, \\ \left(\frac{T_{\rm KD}}{T_p}\right)^{1/2}\exp(N_{\rm KD}) & \text{for } T_{\rm dom} > T_p \geq T_{\rm KD}, \\ 1 & \text{for } T_p \geq T_{\rm dom}. \end{cases} \tag{4.91}$$

The largest modification occurs when the PT takes place at the start of the kination era, $T_p = T_{\rm KD}$,

for which the peak amplitude and frequency are given by

$$\left.\frac{\Omega_{\rm GW}^{\rm NS}}{\Omega_{\rm GW}^{\rm ST}}\right|_{\rm KD} = \exp(-2N_{\rm KD}), \text{ and } \left.\frac{f_{\rm NS}}{f_{\rm ST}}\right|_{\rm KD} = \exp(N_{\rm KD}), \tag{4.92}$$

The right panel of Fig. 4.31 shows the peak position of the modified GW spectrum in the presence of the kination-matter era, compared to the one assuming a standard cosmological history. The GW amplitude in the standard cosmological history (black line) is approximately constant with varying T_p, i.e. $\Omega_{\rm GW,ST} \propto (a_p/a_0)^4 \rho_{\rm p,tot} \propto$ constant, while the peak frequency grows linearly with the temperature $f_{\rm ST} \propto a_p H_p \propto T_p$. In contrast, during the kination and matter eras, the peak amplitude $\Omega_{\rm GW}^{\rm NS}$ scales with the peak frequency as $f_{\rm NS}^{-1}$ and $f_{\rm NS}^2$, respectively.

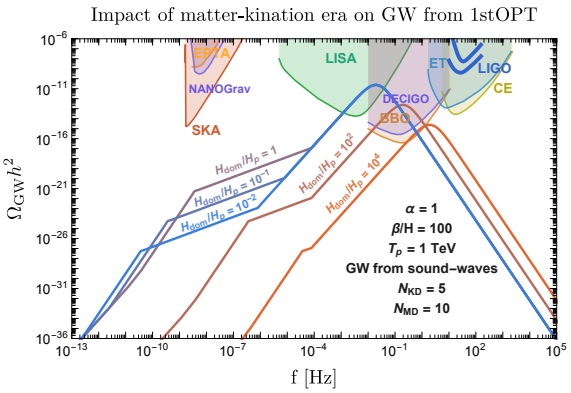

Figure 4.32: H_p and $H_{\rm dom}$ are the Hubble scales at the time of GW production and at the onset of the matter-kination era, respectively. Super-horizon modes (i.e. emitted with a frequency $f_* < H/2\pi$), are sensitive to the EOS of the Universe as stated in Eq. (4.83) (blue-ish lines). Here for $H_p < H_{\rm dom}$, the PT takes place during the non-standard era (either matter or kination) so its peak amplitude is suppressed and blue-shifted as stated by Eq. (4.85) and Eq. (4.86) (red-ish lines). The GW spectrum in standard radiation cosmology is computed according to [154].

Origin of the peak suppression. — The NS-to-standard GW density ratio in Eq. (4.85) can be rewritten as the ratio of Hubble horizon

$$\frac{\Omega_{\rm GW}^{\rm NS}}{\Omega_{\rm GW}^{\rm ST}} = \left(\frac{\rho_{\rm p,tot}^{\rm ST}}{\rho_{\rm p,tot}^{\rm NS}}\right) = \left(\frac{H_{\rm p}^{\rm ST}}{H_{\rm p}^{\rm NS}}\right)^2 . \tag{4.93}$$

At fixed β/H_p, the bubble size at collision is smaller during kination or matter era, implying a smaller GW amplitude. Finally, the overall impact of the matter-kination era on the short-lasting sources such as FOPT is shown in Fig. 4.32.

4.9 Chapter Summary

This chapter investigates primordial SGWB's ability to chart cosmological histories. As the Universe above the BBN scale is unconstrained, we consider two classes of non-standard scenarios – beyond the usually-assumed radiation-dominated Universe: the non-standard eras right after inflation and inside the radiation era, which are divided further into five schemes depending on their EOS. The corresponding effects on the SGWB of long-lasting sources are smoking-gun signatures derived from a simple argument. The matter and inflationary eras suppress the spectrum, while the kination boosts the SGWB energy density.

Assuming the standard radiation cosmology, the SGWB from the primordial inflation – at the highest inflationary scale allowed by observations – is barely observable by the future-planned observatories. Therefore, discovering any spectral suppression from the matter or the secondary inflation will remain uncharted. The kination era right after inflation enhances the relic GW too much and is strongly constrained by the $\Delta N_{\rm eff}$ bound. No enhancement feature can be probed; only the ultra-high frequency experiments beyond the ET band could do so. On the other hand, SGWB from cosmic strings has a far greater opportunity.

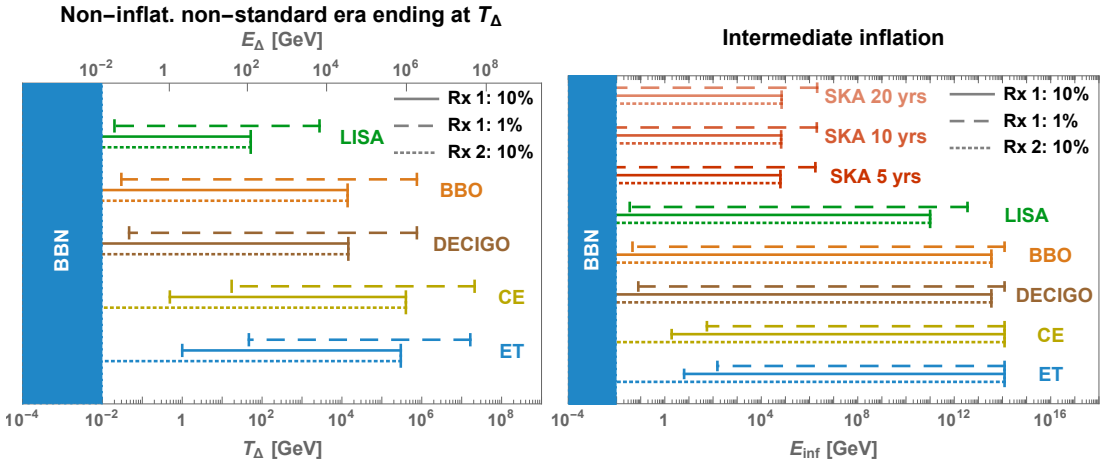

Figure 4.33: left: Sensitivity to the energy scale E_Δ of the Universe at the end of any non-inflationary non-standard era for each future GW interferometer. The connection to E_Δ is given by the observation of the turning-point frequency defined in Eq. (B.51). The width of the bands includes varying the string tension for $G\mu < 10^{-10}$. The dotted, dashed and solid lines correspond to different observational prescriptions defined in Sec. 4.2.3. *right:* Sensitivity to the energy scale $E_{\rm inf}$ of an intermediate inflationary era for each future GW interferometer as well as for future radio telescope SKA. The connection to $E_{\rm inf}$ is given by the observation of the turning-point frequency defined in Eq. (B.52). The width of the band also includes varying the number of efolds of inflation N_e up to 20.

Reach of different observatories at a glance (local cosmic strings). — Our analysis shows it is impossible to associate a given new physics energy scale with a given frequency band of observation. By probing the turning point in the spectrum, a given frequency band is associated with different energy scales, depending on the nature and duration of the non-standard era and the value of the string tension. Still, Fig. 4.33 compares the reach of each experiment on the energy scale of the non-standard era. The precise numbers depend on the definition of the observable used to probe the non-standard physics. For any non-inflationary non-standard era (left plot), we use the turning-point frequency in Eq. (B.51). It depends sensitively on the precision of the measurement. A realistic value is $\sim 10\%$; we also show results for the idealistic case of 1% for comparison. These plots include a variation of $G\mu$. In Fig. 4.33-right, we show the case of an intermediate inflationary era, which depends very sensitively on the number of efolds. In contrast to other non-standard cosmologies, the turning point frequency does not depend on the duration. The left plot applies to any non-standard era with the equation of state $\rho \sim a^{-n}$ with any n between 3 and 6, regardless of the duration of this non-standard era. Interestingly, radio telescope SKA can be sensitive to a low-scale inflationary era. Note that the bands in Fig. 4.33 are calculated by neglecting particle production, which will affect mostly ET and CE, cf. Figs. 4.6 and 4.19. The lower bound on T_Δ and $E_{\rm inf}$ should be weaker by one order of magnitude for ET and CE if there is a cutoff from particle production. For global cosmic strings, the turning point in Fig. 4.8 directly relates to the temperature at the end of the non-standard phase, regardless of its tension, thanks to the fast-decaying loops.

Another important question will be how to distinguish between a stage of matter era, inflationary expansion, and the effect of particle productions. All lead to a suppression of the SGWB and lead to similar spectra. Interestingly, particle production by cosmic string networks can be probed through cosmic rays and bring complementary non-gravitational information to the SGWB [563, 564]. Besides, the complementarity between different GW instruments will be crucial as the detection of the low-frequency peak of the spectrum (due to the transition from the standard radiation to the standard matter era) can enable to probe of the string tension and break the degeneracy between different spectral predictions. The possibility of reconstructing the spectral shape of an

SGWB was analyzed in [479] using LISA data only. In the case of a SGWB generated by CS, which can span more than twenty decades in frequency, it will be crucial to use data from different interferometers (and even from radio telescopes) to probe the full spectrum.

Interestingly, we investigate the intermediate kination era inside the standard radiation era – unrelated to the dynamics of inflaton – which has not been studied so far in the literature, except in the papers of the thesis' author and another coincident work [3, 4, 274]. In this scheme, the kination happens after the matter era and for a short period, allowing the observable enhanced spectra of SGWB from primordial inflation, and local and global cosmic strings without violating $\Delta N_{\rm eff}$ bound. A striking feature – a peaked spectrum – carries the information of the energy scale and duration of the kination era. Consider the inflationary GW from the highest inflation scale as an example. ET and CE can chart the intermediate kination era at energy scale $10^{6\div9}$ GeV, while LISA probes $10^{1\div5}$ GeV. In the presence of many long-lasting sources, there is a possibility to observe multiple-peak signatures within a range of one experiment.

Lastly, we also discuss the effects of non-standard eras on the SGWB from short-lasting sources such as the FOPT. The expansion rate beyond that of the radiation era shifts the spectrum as a whole since the GW has been produced all at once. The exception is only for the super-horizon contribution, seen in the causality tail of the spectrum, which acts as a long-lasting source and can be imprinted with a similar feature discussed above.

So far, we discuss the intermediate non-standard cosmological histories without much motivation for their origins. The second part of this thesis studies the intermediate matter era from the unstable particles and the intermediate kination era from the spinning axion. In both cases, GW observatories greatly extend the discovery/constraint bands on particle-physics parameter spaces.

PART II

Particle Physics Realizations of Non-Standard Cosmological Histories

Chapter 5

Intermediate Matter-Domination Era: Heavy-Unstable Particles

Based on
[2] Y. Gouttenoire, G. Servant and P. Simakachorn, ***BSM with Cosmic Strings: Heavy, up to EeV mass, Unstable Particles****,* JCAP **07** *(2020) 016, [*1912.03245*].*

The existence of massive particles X, with mass $m_X \gg$ TeV, is a generic prediction of many well-motivated extensions of the Standard Model (SM) of particle physics, such as Grand Unified Theories, extra-dimensional models inspired by String Theory or supersymmetric constructions. Suppose such particles are stable and still present in our Universe today. In that case, they can contribute to the dark matter, in which case a variety of detection strategies has been explored depending on their mass range and the nature of their interactions. On the other hand, *unstable* particles beyond the Standard Model (BSM) are very difficult to probe experimentally. The best chances are through their effects on cosmological observables. The strongest limits come from Big-Bang Nucleosynthesis (BBN) since any heavy relic which decays after BBN would ruin the predicted abundances of light elements. From BBN, one obtains general model-independent bounds in the plane $(\tau_X,\, m_X Y_X)$ where τ_X is their lifetime, m_X their mass and $m_X Y_X$ is their *would-be* contribution to the total energy density of the Universe today if they had not decayed [565–568]. We can therefore infer indirect information on their couplings through the constraints on their lifetime and the efficiency of their production mechanism in the early Universe. In the present chapter, we show how a sizeable new region unexplored so far in the $(\tau_X, m_X Y_X)$ plane can be probed using future GW observatories.

Our starting assumption is that these particles can temporarily dominate the energy density of the Universe and therefore induce a period of matter domination within the radiation era after post-inflationary reheating, so-called the *intermediate matter* era. This leads to a modified cosmic expansion compared to the vanilla single radiation era. Interestingly, such modified cosmological history can be probed if, during this period, there is an active GW source, in which case the resulting GW spectrum would imprint any modification of the equation of state of the Universe. Particularly well-motivated are the long-lasting GW production from cosmic-string (CS) networks, discussed in Chap. 3, whose scale-invariant GW spectrum would signal any deviation[1]. Moreover, we account for the extra time needed by the long-string network to respond to the change of cosmology, inducing a shift by one or two orders of magnitude of the turning-point frequency characterizing the non-standard matter era.

In this chapter, we assume the presence of a *heavy, unstable, and cold* particle X dominating the energy density of the Universe at the temperature $T_{\rm dom}$ and decaying at the temperature $T_{\rm dec}$. The success of BBN in a standard radiation-dominated Universe currently provides the most robust constraint on such a scenario, $T_{\rm dec} \gtrsim 1$ MeV. Our key point is that observing a flat GW spectrum from local CS would extend the BBN constraints on heavy relics by far. All assumptions relevant

[1]The inflationary SGWB also exhibits similar signature, but its amplitude is too weak to be probed by most of the observatories.

to our conclusions are discussed in Chap. 3 (based on Ref. [1]), where we refine and extend the work of [294, 295] beyond the scaling regime during the change of cosmology. We also consider the recent discussion on the effect of particle production on the SGWB [391].

In Sec. 5.1, we compute the GW spectrum in the presence of an *intermediate matter* era. We then derive the improvement by many orders of magnitude of the current model-independent BBN constraints on the abundance and lifetime of a particle, cf. Fig. 5.3, that can be inferred from the detection of GW produced by CS. In Sec. 5.3, we provide unprecedented exclusion bounds on four particle-physics models leading to an early matter domination era: oscillating scalar moduli in supersymmetric theories, secluded scalar sectors which are only gravitationally produced, scalars produced through the Higgs portal, and massive dark photons. At the very end, we also study the scenario where the dark photon mass and the cosmic string network are generated by the spontaneous breaking of the same $U(1)$ symmetry.

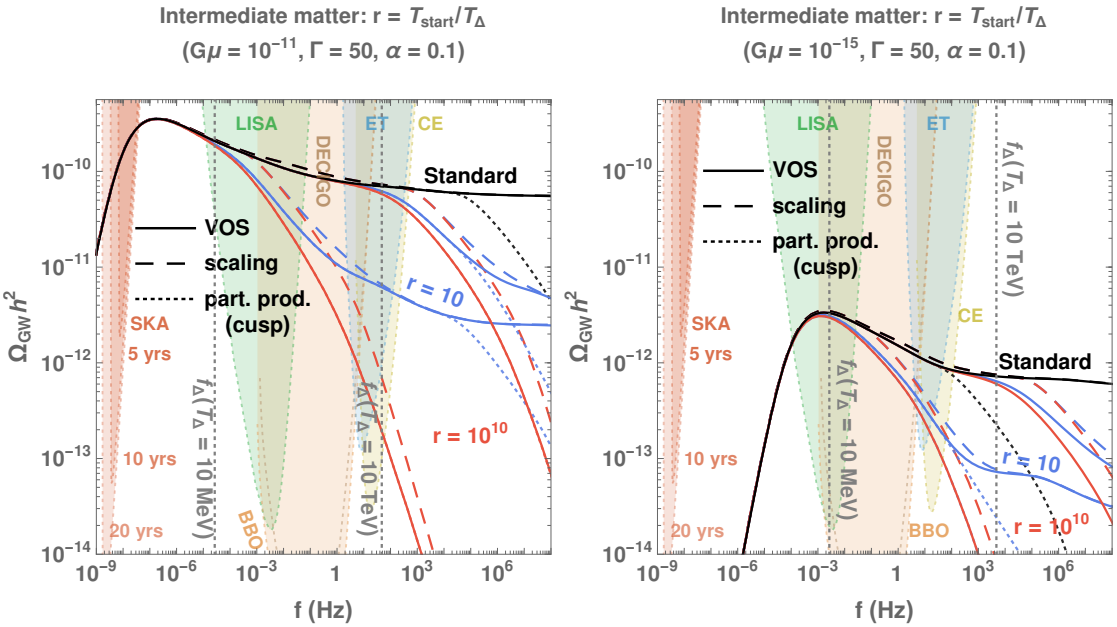

Figure 5.1: SGWB generated by the gravitational decay of cosmic strings compared to the reach of different GW interferometers. We show the impact of a long (red) or a short (blue) intermediate matter era, starting at the temperature rT_Δ and ending at $T_\Delta = 10$ MeV or $T_\Delta = 10$ TeV. Black lines show the results obtained assuming standard cosmological evolution. The dashed-lines assume that the scaling regime switches on instantaneously during the change of cosmology whereas the solid lines incorporate the transient behavior, solution of the VOS equations, as discussed in Chap. 3. Limitations due to particle production assuming that cusps dominate the small-scale structures are shown with dotted lines [1]. The dotted vertical lines indicate the relation in Eq. (5.1) between the temperature T_Δ and the frequency f_Δ of the turning point, where the matter-era-tilted spectrum meets the radiation-era-flat spectrum.

5.1 The imprints of an early era of matter domination

5.1.1 Modified spectral index

The part of the spectrum coming from loops produced and emitting during radiation is flat since there is an exact cancellation between the red-tilted redshift factor and the blue-tilted loop number density. However, in the case of a matter era, a mismatch induces a slope f^{-1} for the fundamental mode and $f^{-1/3}$ when higher modes are included, cf. Eq. (3.31) and App. B.3.7. The impact of a non-standard matter era is shown in Fig. 5.1.

The GW frequency detected today f_Δ of the turning point between the end of the matter domination and the beginning of the radiation domination can be related to the temperature of the Uni-

verse T_Δ when the change of cosmology occurs via the analytic relation Eq. (3.33) in Sec. 3.2.5. However, the turning point that would be seen in experiments shifts from Eq. (3.33) due to the transient regime of the network adapting to a change of cosmology. As an illustration, Fig. 5.1 compares the spectrum computed by assuming that the scaling regime is reached instantaneously during the change of cosmology with the full solution of the VOS equations. It shows that the turning point frequency, which is a signature of the evolution of cosmology from matter to radiation, is over-estimated by more than one order of magnitude in the scaling approximation. From Eq. (B.51) in appendix, we quote

$$f_\Delta = (2\times 10^{-3}\ \text{Hz})\left(\frac{T_\Delta}{\text{GeV}}\right)\left(\frac{0.1\times 50\times 10^{-11}}{\alpha\Gamma G\mu}\right)^{1/2}\left(\frac{g_*(T_\Delta)}{g_*(T_0)}\right)^{1/4}. \tag{5.1}$$

An extensive discussion of this frequency-temperature relation as provided in Sec. 3.2.5 and App. B.4. The above formula entirely relies on the assumptions that the back-reaction scale is $\Gamma G\mu$ as claimed by Blanco-Pillado et al. [345, 376, 399] and not much lower as claimed by Ringeval et al. [194, 398].

5.1.2 The reach of GW interferometers

GW spectra from CS for two values of $G\mu = 10^{-15}$, 10^{-11} are plotted in Fig. 5.1, together with the power-law sensitivity curves of NANOGrav [370], EPTA [569], SKA [207], LIGO [226], DECIGO, BBO [68], LISA [65], Einstein Telescope [66, 67] and Cosmic Explorer [228]. Only EPTA, NANOGrav, and LIGO O1/O2 (not visible on the plots) are current constraints, the other being projected sensitivities of future projects. The power-law integrated sensitivity curves are computed in [1] with a signal-to-noise ratio SNR=10 and an observation time of 10 years. At lower string tension $G\mu$, the GW power emission per loop is smaller; hence the amplitude is suppressed. Also, for lower values of $G\mu$, loops decay more slowly, and GW is emitted later, implying a lower red-shift factor and a global shift of the spectrum towards higher frequency.

The strongest constraints come from pulsar timing array EPTA, $G\mu \lesssim 8\times 10^{-10}$ [369], and NANOGrav, $G\mu \lesssim 5.3\times 10^{-11}$ [370], therefore we limit ourselves to $G\mu < 10^{-11}$. Our analysis is based on the assumption that the astrophysical foreground can be subtracted. The GW spectrum generated by the astrophysical foreground increases with frequency as $f^{2/3}$ [253], differently from the GW spectrum generated by CS during radiation (flat) or during matter (f^{-1}).

5.1.3 How to detect a matter era with a GW interferometer

For a first qualitative analysis, we start with two simple prescriptions for detecting a matter era from the measurement of a SGWB from CS by a GW interferometer:

- **Rx 1** *(turning-point prescription)*: The turning point, namely the frequency at which the spectral index of the GW spectrum changes, corresponding to the transition from the matter to the radiation era, defined in Eq. (5.1), must be inside the interferometer window, as shown for instance in Fig. 5.1.

- **Rx 2** *(spectra-index prescription)*: The measured spectral index must be smaller than -0.2, namely $\beta < -0.2$ where $\Omega_{\rm GW}h^2 \propto f^\beta$.

We compare the two prescriptions in Fig. 5.2. The prescription Rx 1 is more conservative but enough to measure the particle's lifetime. In our study, we use the prescription Rx 1 and, in Fig. 5.4, we show how to extend the constraints with Rx 2.

We note here that the presence of the turning point and the changed spectral index at high frequencies would be similar in the case of a long intermediate inflationary era instead of an intermediate matter era. Disentangling the two effects deserves further studies. Interestingly, high-frequency burst signals due to cusp formation could be a way-out [1]. In the analysis of this paper, we interpret the suppression of the GW spectrum as due to an intermediate matter era.

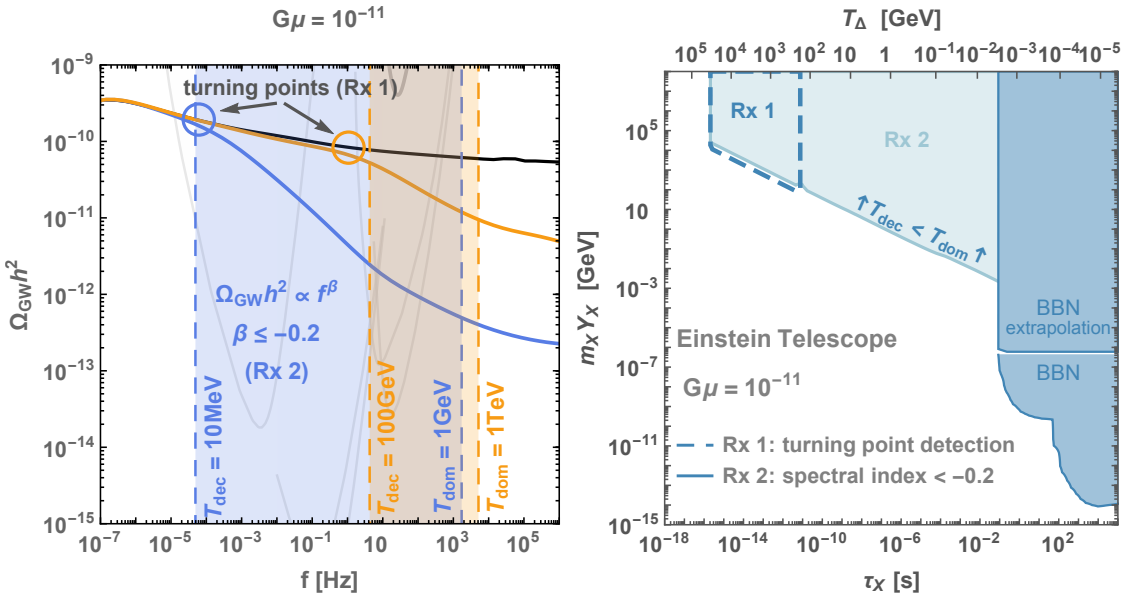

Figure 5.2: left: SGWB for $G\mu = 10^{-11}$ assuming that a heavy cold particle dominates the energy density of the Universe at the temperature $T_{\rm dom}$ and decays at the temperature $T_\Delta = T_{\rm dec}$. *right*: Considering the particular case of the Einstein Telescope, we illustrate how the constraints on the abundance and lifetime of a heavy relic depend on the choice of the prescription, Rx 1 or Rx 2 defined in Sec. 5.1.3.

5.2 Model-independent constraints on particle physics parameters

A matter-dominated era may result from an oscillating scalar field [517], such as a *moduli* field, or a relativistic plasma with a non-vanishing tensor bulk viscosity [459], or simply a massive particle dominating the energy density of the Universe. A matter-dominated era may be motivated by the possibility of enhancing structure growth at small scales since density perturbations start to grow linearly earlier [528, 570], hence boosting the dark matter indirect detection signals [571, 572], or the possibility to enhance the primordial black holes production [573–575].

We suppose an early-matter era is caused by the energy density of a cold particle X, i.e. X is non-relativistic and is decoupled chemically and kinetically from the visible sector. The energy density $m_X n_X$ of X dominates over the energy density of the SM radiation, with entropy $s_{\rm SM}$, at the temperature $T_{\rm dom}$

$$T_{\rm dom} = \frac{4}{3} m_X Y_X, \qquad Y_X \equiv n_X / s_{\rm SM}. \tag{5.2}$$

Then, the cold relic decays when its lifetime τ_X is equal to the age of the Universe, corresponding to the temperature

$$T_{\rm dec} = 1\ {\rm GeV} \left(\frac{80}{g_{\rm SM}}\right)^{1/4} \left(\frac{2.7\times 10^{-7}\ {\rm s}}{\tau_X}\right)^{1/2}. \tag{5.3}$$

Note that the above relation between $T_{\rm dec}$ and τ_X only assumes that the decay is followed by a radiation-dominated era and is independent of the previous thermal history of the Universe. $T_{\rm dec}$ is sometimes referred, mistakenly though [576], as the reheating temperature following the decay. We propose to use the third generation of GW interferometers to constrain cold relics responsible for early-matter domination. The constraints we will derive rely on the following assumptions:

1) A SGWB from CS with tension $G\mu$ is measured by a GW interferometer i.

2) The cold particle is abundant enough to lead to a matter-dominated era before it decays

$$T_{\rm dom} > T_{\rm dec}\ , \tag{5.4}$$

where $T_{\rm dom}$ and $T_{\rm dec}$ satisfy Eqs. (5.2) and (5.3).

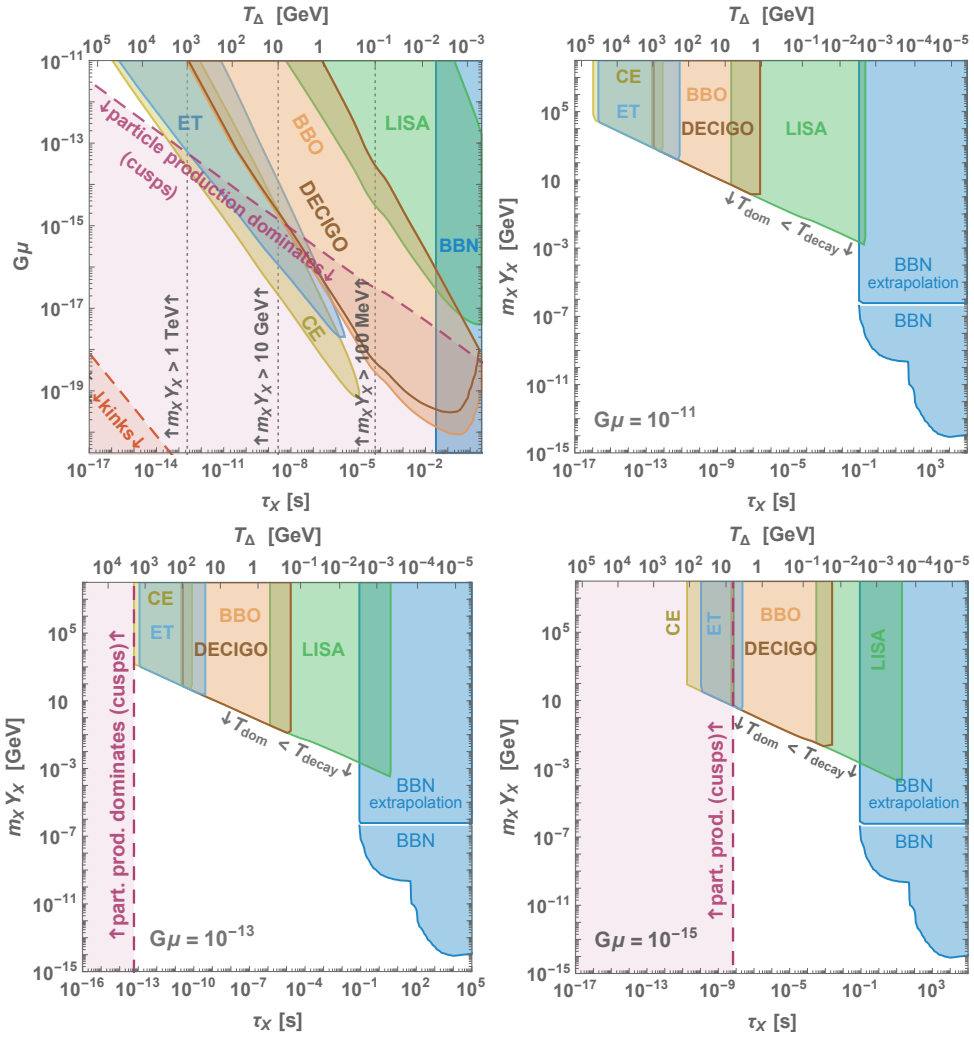

Figure 5.3: Constraints on the lifetime τ_X and would-be abundance $m_X Y_X$ of a heavy unstable particle inducing an early-matter era, assuming the observation of a SGWB from CS by a GW interferometer, cf. Sec. 5.2. We compare the new prospects with the current limits inferred from BBN [566–568]. We assume the detectability of the turning point in the GW spectrum at the frequency f_Δ, induced by the decay of the particle at $T_{\rm dec} = T_\Delta$, cf. *turning-point description Rx 1* in Sec. 5.1.3. Limitation due to particle production in the cusp-domination case – discussed in Sec. 3.2.1 – are shown in purple.

3) The prescription Rx 1 of Sec. 5.1.3 is used, i.e. the turning point in the GW spectrum is in the observation window of the detector and

$$\Omega_{GW}(f_\Delta(T_{\rm dec}, G\mu), G\mu)h^2 > \Omega^{(i)}_{\rm sens}h^2, \tag{5.5}$$

where $\Omega_{GW}(f, G\mu)h^2$ is the predicted scale-invariant GW spectrum from Eq. (3.47), and $\Omega^{(i)}_{\rm sens}h^2$ is the power-law sensitivity curve of the detector i.

Fig. 5.3 shows these new constraints in comparison with the current complementary constraints from BBN, usually represented in the plane $(\tau_X,\, m_X Y_X)$ [566–568]. We can translate the sensitivity of each interferometer to probe the particle lifetime into typical mass windows, assuming some decay width. This is illustrated in Fig. 5.4 with a Planck-suppressed decay width $\Gamma_X \propto m_X^3/M_{\rm pl}^2$.

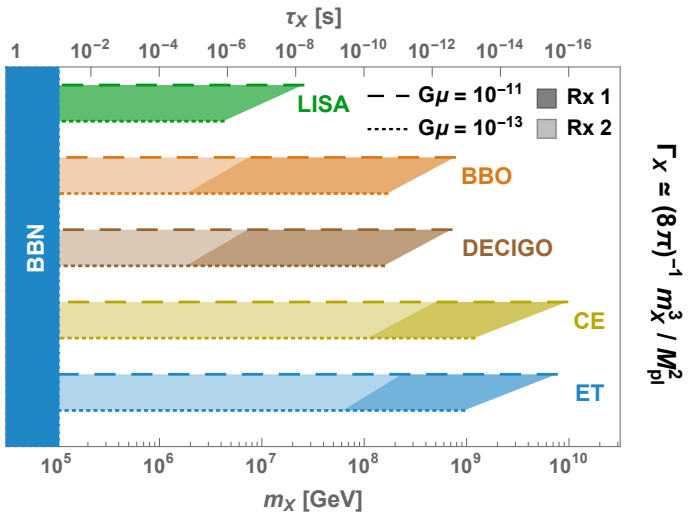

Figure 5.4: Reach of future GW interferometers on the mass of a heavy particle decaying through a Planck suppressed operator, $\Gamma_X \propto m_X^3/M_{\rm pl}^2$, supposing that it is sufficiently produced to induce a matter era before the decay. We compare the *turning-point prescription (Rx 1)* and the *spectral-index prescription (Rx 2)* discussed in Sec. 5.1.3. In Sec. 5.3, we study three different production mechanisms of such particle with Planck suppressed decay width: scalar oscillating moduli produced after supersymmetry breaking in Sec. 5.3.1, scalar particle gravitationally produced at the end of inflation in Sec. 5.3.2, or scalar particle produced via thermal freeze-in assuming a Higgs-mixing in Sec. 5.3.3.

5.3 Benchmark models

5.3.1 Oscillating scalar moduli

String theory vacua feature moduli fields that characterize the size and shape of the compactification manifold. From a 4D effective field theory perspective, they are fields with flat potential, e.g., axions or dilatons. After supersymmetry (SUSY) breaking, one expects moduli fields to acquire a mass of the order of the gravitino mass scale for the lightest [577], e.g., $m_{3/2} \sim$ TeV for low-scale SUSY. As soon as the Hubble rate satisfies $H \lesssim m_\phi$, the scalar field starts coherent oscillations, and its energy density redshifts as matter. We assume that the onset of oscillations occurs during radiation domination, at the temperature $T_{\rm osc}$

$$\frac{\pi^2 g_* T_{\rm osc}^4}{90\, M_{\rm pl}^2} \equiv m_\phi^2 \tag{5.6}$$

where we fix the number of relativistic degrees of freedom to the fiducial value $g_* = 106.75$. Then, the moduli start dominating the energy density of the Universe at the temperature, cf. Eq. (5.2)

$$T_{\rm dom} = \frac{4}{3}\frac{\rho_\phi^{\rm osc}}{s_{\rm osc}} \equiv \frac{\frac{1}{2}m_\phi^2\phi_0^2}{\frac{2\pi^2}{45}g_* T_{\rm osc}^3}, \tag{5.7}$$

where ϕ_0 is the vacuum expectation value of the moduli field when it starts to oscillate. For concreteness, we consider moduli fields which interact with the visible sector via Planck-suppressed operators and hence have decay widths of order

$$\Gamma_\phi \simeq \frac{c}{8\pi}\cdot\frac{m_\phi^3}{M_{\rm pl}^2}, \tag{5.8}$$

where $M_{\rm pl} \simeq 2.4 \times 10^{-18}$ GeV and c is a model-dependent factor which we suppose to be in the range $10^{-2} \lesssim c \lesssim 10^2$. For TeV-scale moduli mass, the moduli lifetime is long, $\tau_\phi \simeq \Gamma_\phi^{-1} \sim$

10^5 s, and the decay occurs much after BBN. Imposing that the energy density of the moduli decay products, ρ_ϕ, is smaller than a fraction 10^{-14} of the total entropy density of the Universe in order to preserve the predictions of BBN, cf. Fig. 5.3 and [566–568], one constrains the vacuum expectation value of the moduli field, just after it starts oscillating, to be, cf. Fig. 5.5

$$\text{BBN is preserved for TeV-scale moduli:} \qquad \phi_0 \lesssim 10^{-12}\, M_{\rm pl}. \tag{5.9}$$

A large moduli VEV is expected from the dependence of the moduli potential on the inflaton VEV [578–581], except if the scalar moduli field lies at a point of enhanced symmetry where the induced minimum at late times coincides with the minimum at earlier times [582]. However, even in the case where the moduli VEV after SUSY breaking remains small, one expects moduli to be copiously produced both through thermal [583–585] and gravitational production, cf. Sec. 5.3.2 and [586, 587], hence violating the bound in Eq. (5.9).

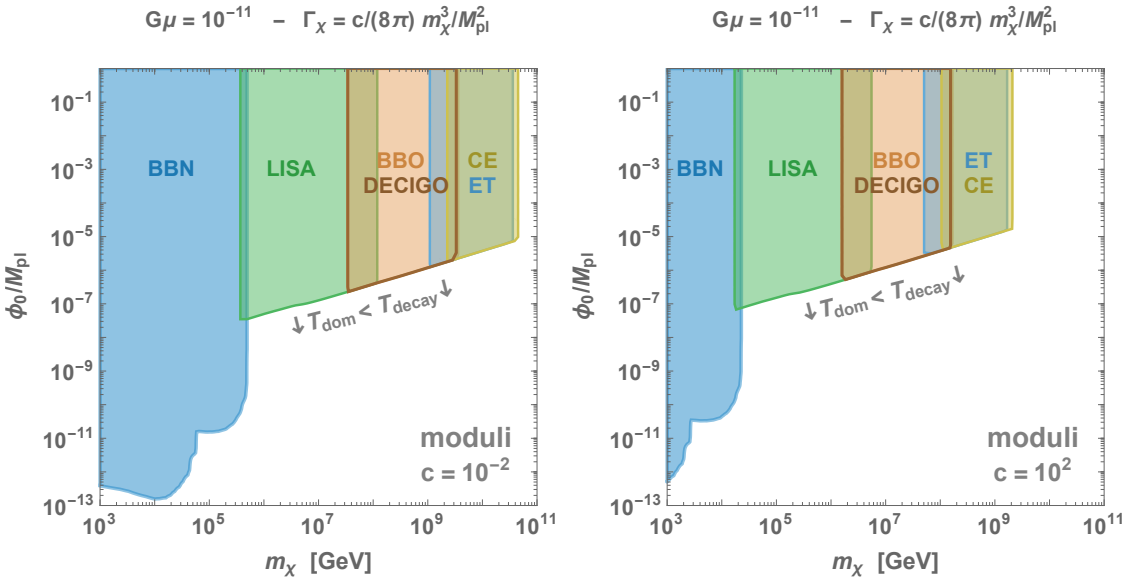

Figure 5.5: Constraints on a moduli field oscillating in the early Universe around its minima with initial amplitude ϕ_0 and mass m_ϕ, from the non-observation of its signature in the GW spectrum from CS with tension $G\mu = 10^{-11}$. In stringy UV completions, the lightest moduli field is related to the gravitino scale $m_\chi \sim m_{3/2}$ [577]. The BBN constraints are taken from [566–568]. We use the *turning-point prescription (Rx 1)* discussed in Sec. 5.1.3. Constraints are tightened when considering the *spectral-index prescription (Rx 2)*, as illustrated in Fig. 5.4.

The scalar moduli problem is similar to the gravitino problem [588], both are copiously produced relics, with weak-scale mass and Planck-suppressed decay rate, spoiling the BBN predictions. An important difference is that during inflation, the energy density is diluted in the fermionic case but is frozen in the scalar case as long as $H \gg m_\phi$. Hence, as opposed to the gravitino case, only a low-scale (weak-scale) inflation can exponentially dilute the scalar field and solve the moduli problem [589]. Other proposed solutions are to increase the moduli mass up to $m_\phi \sim O(10^3)\, m_{3/2}$, cf. Fig. 5.5 and [590], or to form substructures (modular stars) which enhances the decay [591, 592], or to produce gauge fields from the tachyonic instability [593].

A pragmatic approach to solve the moduli problem is to break SUSY at a much larger scale, at the expense of large fine-tuning, like in so-called High-scale SUSY [594] or Split SUSY [595]. A larger SUSY breaking scale improves gauge coupling unification [596], is compatible with the Higgs at 125 GeV [597] and is free from the main difficulties encountered by low-scale SUSY such as large flavor and CP violation [598]. In Split and High-scale SUSY, a 125 GeV Higgs is compatible with a SUSY breaking scale as large as 10^8 GeV and 10^{12} GeV respectively [597]. Moduli fields with masses of the same order would then induce an early matter era, leading to detectable features in the GW background.

As shown in Fig. 5.5, the observation of a SGWB from CS with one of the next generation GW interferometers would provide constraints on moduli masses up to $\lesssim 10^{10}$ GeV, well above the current $\lesssim 100$ TeV currently probed by BBN. Hence, GW from CS would be a promising tool to investigate superstring theories if detected.

In addition to being naturally motivated in SUSY constructions, moduli fields have interesting cosmological consequences: Affleck-Dine baryogenesis [580, 599], non-thermal production of Wino-DM [581, 600, 601], formation of oscillons or Q-balls [592], the required entropy injection to allow thermal DM much heavier than the standard unitarity bound ~ 100 TeV [532] or to revive Grand-Unified-Theory-scale QCD axion DM [602], see Ref. [603] for a review on the moduli problem and its cosmological implications.

5.3.2 Scalar particles produced gravitationally

In the previous subsection, Sec. 5.3.1, we considered a model of gravitationally-only interacting particle whose abundance is given by the misalignment mechanism after SUSY breaking. Instead, we now consider the possibility of producing such a particle, gravitationally only, at the end of inflation. In the following subsection, Sec. 5.3.3, we also consider the possibility of a thermal production via freeze-in through a Higgs mixing in the case of the conformal scalar $\xi = 1/6$ where the gravitational production is too small to lead to early matter domination.

A massive particle can be gravitationally produced at the end of the inflation due to the non-adiabatic change of its curvature-induced mass from deep de Sitter to deep radiation-domination [83, 485, 604–606], hence possibly leading to heavy dark matter WIMPzillas [607–611]. Our interest here is not to explain DM but to predict a non-standard matter era in the early Universe. If coupled non-conformally to gravity and if the condition of non-adiabaticity, $m_X \lesssim H_{\rm inf}$, is satisfied, then the particle χ will be produced abundantly, potentially leading to an early matter domination. The lagrangian is

$$\mathcal{S} = \int d^4x\sqrt{-g}\left[\frac{1}{2}\left(M_{\rm P}^2 - \xi\chi^2\right)R - \frac{1}{2}g^{\mu\nu}\partial_\mu\chi\partial_\nu\chi - \frac{1}{2}m_\chi^2\chi^2\right], \tag{5.10}$$

with ξ the non-minimal coupling to gravity. We consider the cases $\xi = 0$ (minimal coupling) and $\xi = 1/6$ (conformal coupling). We suppose that the scalar χ decays gravitationally through Planck suppressed operators

$$\Gamma_\chi \simeq \frac{1}{8\pi}\frac{m_\chi^3}{M_{\rm P}^2}. \tag{5.11}$$

A too light scalar would spoil the BBN prediction. The comoving number density, $Y_\chi \equiv n_\chi/s$, of a minimal scalar, $\xi = 0$, after gravitational production is [610]

$$Y_\chi^{\xi=0} \simeq \frac{H_{\rm reh}^2 H_{\rm inf}}{s}\begin{cases} 96\,\dfrac{H_{\rm inf}}{m_\chi} & \dfrac{m_\chi}{H_{\rm inf}} < 1, \\ 0.76\,\dfrac{H_{\rm inf}}{m_\chi}e^{-2m_\chi/H_{\rm inf}} & \dfrac{m_\chi}{H_{\rm inf}} > 1, \end{cases} \tag{5.12}$$

where $H_{\rm inf}$ and $H_{\rm reh}$ are the Hubble factors at the end of inflation and reheating. We have checked that particle production caused by the oscillations of the inflaton during preheating, potentially relevant when $H_{\rm inf} \lesssim m_\chi \lesssim m_\phi$ where m_ϕ is the inflaton mass [611–615], is not strong enough to ignite early matter domination before BBN.

For our study, we fix the inflation scale $H_{\rm inf} = 10^{13}$ GeV close to its upper bound value 6×10^{13} GeV from the non-detection of the fundamental B-mode polarization patterns in the CMB [20, 55]. If produced sufficiently, the scalar field can lead to an early-matter domination era. In Fig. 5.6, we show the GW constraints on the χ scalar particle, which is non-conformally coupled to gravity. We see that for reheating temperature larger than 10^7 GeV, the scalar field is

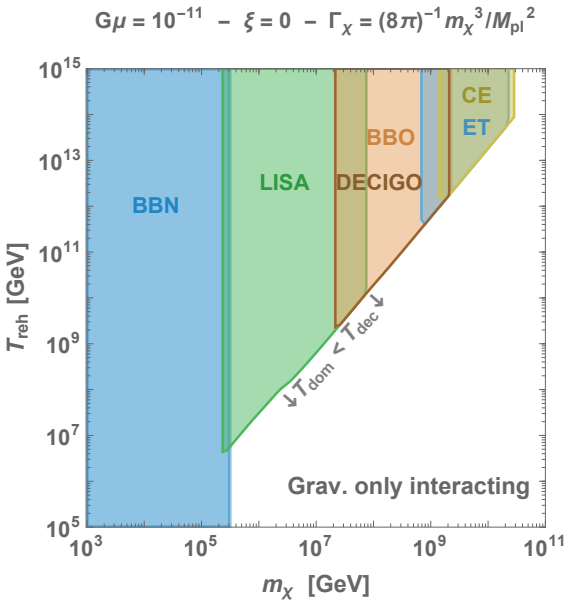

Figure 5.6: Constraints on a purely gravitationally produced ($\kappa = 0$) non-conformal scalar ($\xi = 0$) decaying via a Planck suppressed operator, cf. Sec. 5.3.2, assuming the observation of a SGWB from CS with tension $G\mu = 10^{-11}$ by third-generation GW detectors. We have fixed the inflation scale $H_{\rm inf} = 10^{13}$ GeV. We use the *turning-point prescription (Rx 1)* discussed in Sec. 5.1.3. Constraints are tightened when considering the *spectral-index prescription (Rx 2)*, as shown in Fig. 5.4.

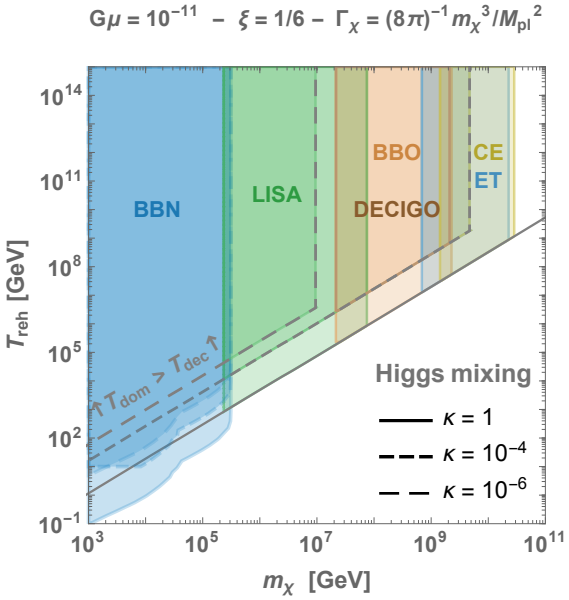

Figure 5.7: *Constraints on a scalar conformally coupled to gravity, $\xi = 1/6$, thermally produced via a mixing with the Higgs $\kappa = 10^{-6}, 10^{-4}, 1$, cf. Sec. 5.3.3, from the measurement of a SGWB from CS. We have also included the gravitational production, cf. Sec. 5.3.2, even though it is negligible. We have fixed the inflation scale $H_{\rm inf} = 10^{13}$ GeV. We use the turning-point prescription (Rx 1) discussed in Sec. 5.1.3. Constraints are tightened when considering the spectral-index prescription (Rx 2), as shown in Fig. 5.4.*

sufficiently produced by gravitational effects at the end of inflation to dominate the energy density of the Universe before BBN starts and be detected in GW experiments. Masses as large as 10^{10} GeV can be probed.

The gravitational production of particles conformally coupled to gravity, i.e. scalars with $\xi = 1/6$, transverse vectors or fermions, is less efficient than for a minimal scalar, $\xi = 0$ [610, 614, 616–618]. Here we give the abundance computed in [610] for a conformal scalar[2]

$$Y_\chi^{\xi=1/6} \simeq \frac{H_{\rm reh}^2 H_{\rm inf}}{s} \begin{cases} 0.0010 \, \dfrac{m_\chi}{H_{\rm inf}} & \text{for } \dfrac{m_\chi}{H_{\rm inf}} < 1, \\ 0.0040 \, \dfrac{H_{\rm inf}}{m_\chi} e^{-2m_\chi/H_{\rm inf}} & \text{for } \dfrac{m_\chi}{H_{\rm inf}} > 1, \end{cases} \tag{5.13}$$

We check that the gravitational production of such particles, conformally-coupled to gravity, is not strong enough to lead to a matter-domination era before BBN starts if the reheating temperature

[2]Here 'conformal scalar' means 'conformally coupled to gravity' with $\xi = 1/6$. In any case, the conformal symmetry is broken via the scalar mass term.

following inflation is below 10^{13} GeV. Hence, in the next section, we consider another production mechanism by introducing a mixing with the standard model Higgs.

5.3.3 Scalar particles produced through the Higgs portal

The gravitational production of a scalar conformally-coupled to gravity ($\xi = 1/6$) is too small to lead to early-matter domination. On the other hand, a mixing with the Higgs H

$$\mathcal{L} \supset \frac{\kappa}{2}\chi^2|H|^2, \tag{5.14}$$

can lead to a large abundance via thermal freeze-in [610]

$$Y_\chi \simeq \frac{H_{\rm reh}^2 H_{\rm inf}}{s} \begin{cases} \dfrac{105|\kappa|^2}{64\pi^4}\dfrac{T_{\rm max}^{12}}{H_{\rm inf}^4\, m_\chi^8} e^{-2m_\chi/T_{\rm max}} f_0\left(\frac{m_\chi}{T_{\rm max}}\right) & \text{for } T_{\rm reh} \ll m_\chi, \\ \dfrac{3|\kappa|^2}{2048\pi^3}\dfrac{T_{\rm max}^{12}}{T_{\rm reh}^7\, H_{\rm inf}^4\, m_\chi} & \text{for } m_\chi \ll T_{\rm reh}, \end{cases} \tag{5.15}$$

where $T_{\rm max} = T_{\rm reh}\,(H_{\rm inf}/H_{\rm reh})^{1/4}$ and $T_{\rm reh}$ are respectively the maximal temperature after inflation and the reheating temperature, and $f_0(x) \equiv 1 + 2x + 2x^2 + 4x^3/3 + 2x^4/3 + 4x^5/15 + 4x^6/45 + 8x^7/315 + 2x^8/315$. In Fig. 5.7, we show that a reheating temperature as low as 10^3 GeV (for $\kappa = 1$) can induce a matter-domination era before BBN and leave an imprint in the would-be SGWB from CS detectable by GW interferometers. For $\kappa = 1$, masses as large as 10^{10} GeV can be probed.

5.3.4 Heavy dark photons

The $U(1)_D$ dark photon: We consider a $U(1)_{\rm D}$ gauge boson V_μ – the dark photon of mass m_V – kinematically coupled to the $U(1)_{\rm Y}$ gauge boson of the SM [619, 620]

$$\mathcal{L} \supset -\frac{\epsilon}{2c_w} F_{{\rm Y}\mu\nu} F_{\rm D}^{\mu\nu}, \tag{5.16}$$

where c_w is the cosine of the weak angle and ϵ is the dark-SM coupling constant. The decay width into SM, Γ_V, is computed in [532]. We here report the expression for $m_V \gtrsim 2m_Z$

$$\Gamma_V \simeq \left(3 \times 10^{-8}\ {\rm s}\right)^{-1} \left(\frac{\epsilon}{10^{-9}}\right)^2 \left(\frac{m_V}{1\ {\rm TeV}}\right). \tag{5.17}$$

The dark photon leads to an early-matter-dominated era if it has a large energy density $m_V Y_V \gtrsim 10$ GeV and a long lifetime $\tau_V \sim 10^{-8}$ s, cf. Fig. 5.3 at $G\mu = 10^{-11}$. Supposing that the dark photon abundance is close to thermal, $Y_{\rm V} \sim 0.02$, cf. Eq. (5.19), this implies $\epsilon \lesssim 10^{-9}$. At such a low ϵ, the dark sector and the SM sector may have never been at thermal equilibrium (cf. [621] or footnote 8 in [622]) and may have their own distinct temperature. We assume that the dark sector and the SM have a different temperature by introducing the dark-to-SM temperature ratio [622]

$$\tilde{r} \equiv \frac{\tilde{T}_D}{\tilde{T}_{SM}}, \tag{5.18}$$

where quantities with a $\sim$ on top are evaluated at some high temperature $\tilde{T}$. Thus, the dark photon abundance before its decay is given by

$$Y_{\rm V} = \frac{n_{\rm V}}{s_{\rm SM}} = \frac{45\zeta(3)}{2\pi^4}\frac{\tilde{g}_D}{\tilde{g}_{\rm SM}}\tilde{r}^3 \simeq 0.0169\left(\frac{\tilde{g}_D}{6.5}\right)\tilde{r}^3, \tag{5.19}$$

where $\tilde{g}_D$ and $\tilde{g}_{\rm SM}$ are the relativistic number of degrees of freedom in the dark sector and the SM at temperature $\tilde{T}$. Plugging Eq. (5.19) into Eq. (5.2) implies a simple relation between the

temperature at which the dark photon dominates the Universe $T_{\rm dom}$ and its mass m_V. We choose to be agnostic about the mechanism setting the abundances in the dark sector, and we enclose all possibilities by introducing a dark-to-SM temperature ratio $\tilde{r}$[3]

As shown in the left panel of Fig. 5.8, low kinetic mixing ϵ, large mass m_V or large dark-to-SM temperature ratio $\tilde{r}$ lead to an early-matter-dominated era, triggered when $T_{\rm dom} \gtrsim T_{\rm dec}$. The non-detection with a future GW interferometer of the imprint left by such a matter era in the GW spectrum from CS would exclude the existence of the dark photon for given values of the kinetic mixing, the dark photon mass, and the dark-to-SM temperature ratio $(\epsilon,\, m_V,\, \tilde{r})$. We show the GW-from-CS constraints on the dark photon in the right panel of Fig. 5.8, together with existing constraints coming from supernova SN1987 [630, 631] and beam-dump experiments [622]. Other constraints on lighter dark photons do not appear on the plot and are summarized in the reviews [632–634]. We also include the BBN constraint, which imposes the dark photon to decay before $\tau_V \lesssim 0.1$ s [566–568] or later if the energy density fraction carried by the dark photon is smaller than $\sim 10\%$ [622]. Only the BBN and the GW-from-CS constraints depend on the dark-to-SM temperature ratio $\tilde{r}$ which fixes the abundance of the dark photon in the early Universe.

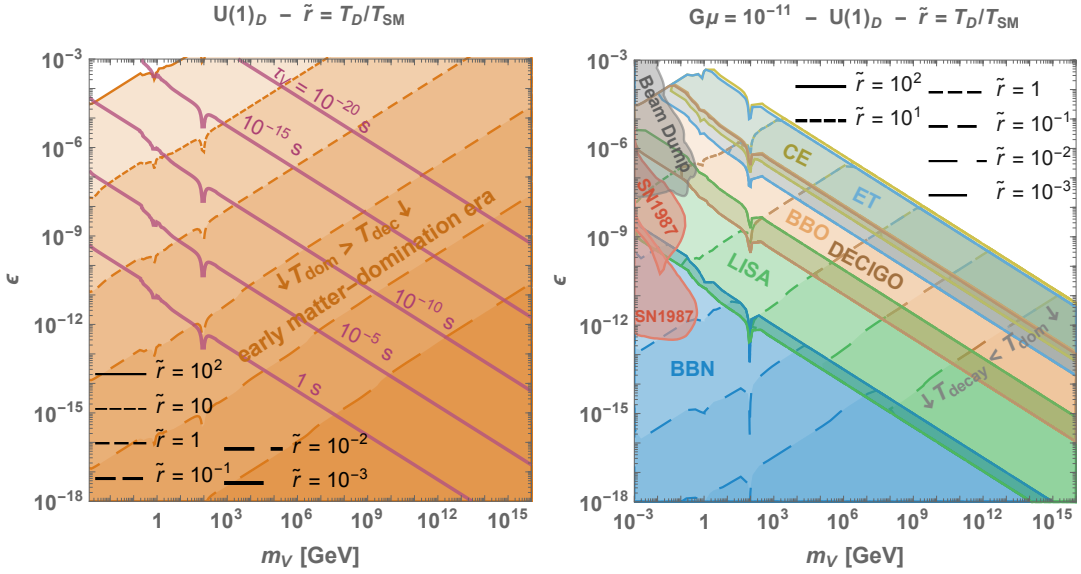

Figure 5.8: *left*: Constant dark photon lifetime τ_V contours. For a given dark-to-SM temperature ratio $\tilde{r} \equiv T_D/T_{\rm SM}$, a non-standard early matter domination is induced below the corresponding orange line where the dark photon dominates the Universe before it decays. *right*: Expected constraints on the dark photon mass m_V and kinetic mixing ϵ, assuming the measurement of a GW spectrum from CS with tension $G\mu = 10^{-11}$ by future GW interferometers. We use the *turning-point prescription (Rx 1)* discussed in Sec. 5.1.3.

We can appreciate the complementarity between the well-established supernova, beam dump, BBN constraints, and the expected constraints assuming the detection of a SGWB from CS by the GW interferometers. Indeed, whereas supernova and beam dump do not really constrain above $m_V \gtrsim 0.1$ GeV, the detection of a SGWB from CS with a string tension $G\mu \simeq 10^{-11}$ would exclude dark photon masses up to the maximal reheating temperature $m_V \sim 10^{16}$ GeV allowed by the maximal inflation scale $H_{\rm inf} \lesssim 6 \times 10^{13}$ GeV [20, 55], and kinetic mixing as low as $\epsilon \sim 10^{-18}$.

[3]The early Universe's production of the dark photon has been studied in the literature. For a small kinetic mixing ϵ, the abundance of the dark sector can be set non-thermally either by freeze-in [621, 623–625], or by a separate reheating mechanism. In the latter case, the temperature asymmetry in Eq. (5.18) results from an asymmetric reheating [626–629]. For moderate kinetic mixing $\epsilon \gtrsim 10^{-6}\sqrt{M_{\rm DM}/\text{TeV}}$ [621], the dark sector may have been at thermal equilibrium with the SM, but asymmetric temperatures can result from asymmetric changes in relativistic degrees of freedom [622]. On the other hand, a possibility for thermally equilibrating the $U(1)_D$ sector and the SM in the case of a small kinetic mixing ϵ would be to introduce a dark Higgs ϕ, mixing with the SM Higgs, which once at thermal equilibrium with SM, decays into dark photons.

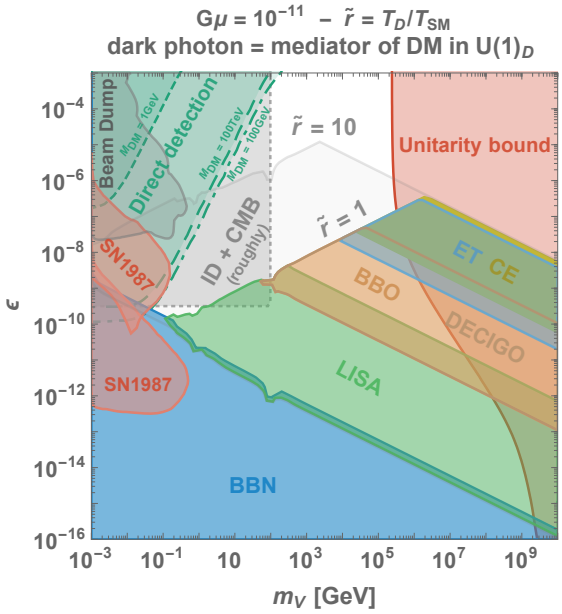

Figure 5.9: Additional constraints when the dark photon is embedded in a DM model as the mediator of $U(1)_D$-charged DM (see text). We compare the expected GW constraints from cosmic strings with the existing constraints on the $U(1)_{\rm D}$ DM model: Supernovae bounds from [630] and [631], direct detection bounds from [622] and the indirect detection + CMB constraints are a rough estimate from [532]. Beam dump constraints are also taken from [622]. The unitarity bound on the DM mass $M_{\rm DM}$ [635] can also be applied on the mediator mass because of the kinematic condition $m_V < M_{\rm DM}$. The unitarity bound gets relaxed at small ϵ because of the larger entropy injection following the dark photon decay [532].

The dark photon as a dark matter mediator: An interesting motivation for the dark photon is that it can play the role of a dark matter mediator. We can suppose that the dark sector also contains a Dirac fermion $\chi_{\rm D}$ charged under $U(1)_{\rm D}$, playing the role of DM [532, 622, 636–644]

$$L \supset \quad \bar{\chi}_{\rm D} i \not{D} \chi_{\rm D} - M_{\rm DM} \bar{\chi}_{\rm D} \chi_{\rm D}, \tag{5.20}$$

where $D_\mu = \partial_\mu + i g_{\rm D} V_{{\rm D}\mu}$ is the covariant derivative with $g_{\rm D}$ the $U(1)_{\rm D}$ gauge coupling constant. We suppose that the DM freezes-out by annihilating into pairs of dark photons, we impose $m_V < M_{\rm DM}$. We assume the dark photon to be non-relativistic when it decays but relativistic when it is produced, therefore, we set $\tilde{g}_D = 3 + \frac{7}{8} \cdot 4 = 6.5$ in Eq. (5.19).

The unitarity bound on the DM mass $M_{\rm DM}$ can be applied to the dark photon mass m_V upon assuming $m_V < M_{\rm DM}$. In the standard paradigm, the unitarity bound on s-wave annihilating dirac fermion DM is $M_{\rm DM} \lesssim 140$ TeV [635, 645]. However, if long-lived and heavy, the decay of the mediator can, by injecting entropy, dilute the DM abundance and relax the unitarity bound to [532]

$$M_{\rm DM} \lesssim 140 \text{ TeV } \sqrt{D}, \tag{5.21}$$

where D is the dilution factor: $D \simeq T_{\rm dom}/T_{\rm dec}$ with $T_{\rm dom}$ and $T_{\rm dec}$ are as defined in Eq. (5.2) and Eq. (5.3).

In Fig. 5.9, we add the contraints on the dark photon when the later plays the role of the mediator of DM. They come from direct detection [622], CMB [532], indirect detection, using neutrino, gamma-rays, positrons-electrons and anti-protons [532], as well as from unitarity [532]. They are complemented by the GW-from-CS constraints. For $\epsilon \lesssim 10^{-10}$, all the traditional indirect detection constraints evaporate and the unitarity bound is pushed to larger masses due to the entropy dilution following the dark photon decay such that the model is then currently only constrained by BBN. It is remarkable that GW interferometers could probe this unconstrained region where $\epsilon < 10^{-10}$ and $m_V > 1$ GeV. In Figs. 5.8 and 5.9, we use the *turning-point prescription (Rx 1)* discussed in Sec. 5.1.3. Constraints are stronger when considering the *spectral-index prescription (Rx 2)*, as shown in Fig. 5.4 or in Fig. 5.2.

Scenario where the cosmic string network and the dark photon mass have the same origin: As a last remark, we comment on the case where the spontaneous breaking of the $U(1)_D$ symmetry would be responsible for the formation of the cosmic string network. Therefore the dark photon

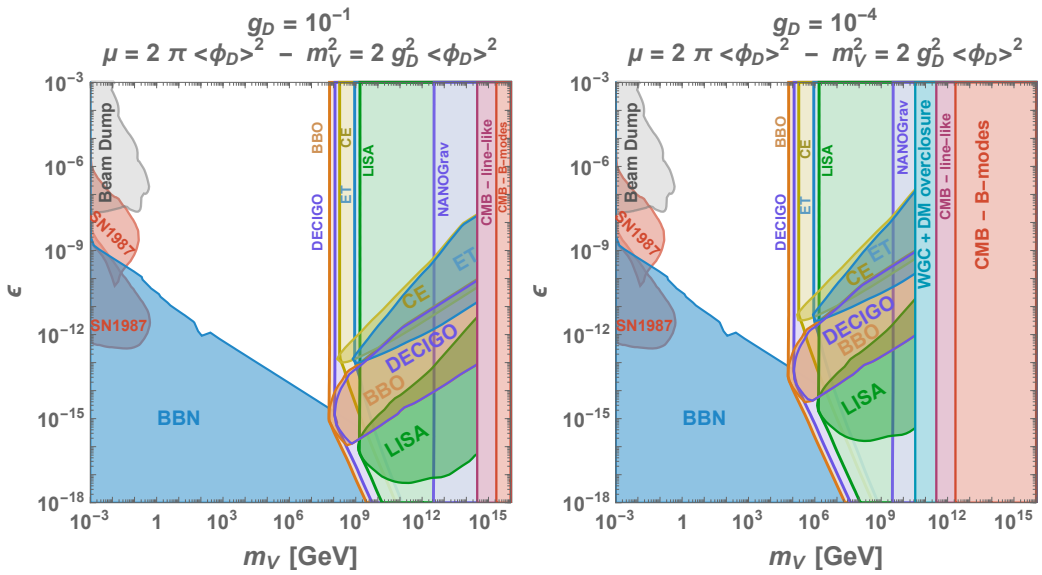

Figure 5.10: Scenario where the dark photon mass m_V and the cosmic string network are generated by the spontaneous breaking of the same $U(1)$ symmetry, such that m_V is related to the string tension μ. **Pale colors**: Constraints on the dark photon parameter space assuming the mere detection of the GW spectrum from CS by NANOGrav, LISA, ET, CE, DECIGO and BBO. **Opaque colors**: Constraints assuming the detection of the turning point in the GW spectrum induced by the transition from matter to radiation when the heavy dark photon decays. When combining Eq. (5.1) and Eq. (5.3), this last detection allows to measure the dark photon lifetime. The constraints described in the following part of this caption are independent of the GW emission. **Pale red**: The non-observation of the fundamental tensor B-modes in the CMB imposes the stringest upper bound on the energy density scale of inflation [20], $V_{\rm inf} \lesssim 1.6 \times 10^{16}$ GeV. This provides an upper-bound on the reheating temperature, which also must satisfy $\langle\phi_{\rm D}\rangle \lesssim T_{\rm reh}$ in order for the string network to be formed. Thus, we impose the CS formation to occur after the end of inflation with the following criteria: $\langle\phi_{\rm D}\rangle \lesssim V_{\rm inf}$. **Pale purple**: Constraints from the non-observation of line-like temperature anisotropies in the CMB, e.g. [646], $G\mu \lesssim 2 \times 10^{-7}$. **Pale sky blue**: In order to prevent DM overclosure, we must assume the $U(1)_D$ charged states to be heavier than the reheating temperature such that they are never produced. A possibility which is constrained by the Weak Gravity Conjecture, cf. main text, thus we impose $\langle\phi_{\rm D}\rangle \lesssim g_{\rm D} M_{\rm pl}$. The last inequality implicitly assumes $\langle\phi_{\rm D}\rangle \lesssim T_{\rm reh}$. Note however that such a charged state could be unstable, e.g. if it is a dark Higgs, in which case the WGC constraint is relaxed.

mass is no longer a free parameter but is related to the string tension μ, through the Abelian-Higgs relations [301]

$$\mu = 2\pi \langle\phi_{\rm D}\rangle \,, \tag{5.22}$$

$$m_V^2 = 2 g_{\rm D}^2 \langle\phi_{\rm D}\rangle^2 \,, \tag{5.23}$$

where $\phi_{\rm D}$ is the scalar field whose vacuum expectation value $\langle\phi_{\rm D}\rangle$ breaks the $U(1)_D$ symmetry spontaneously.

In this case, we find that most of the relevant parameter space is ruled out due to overabundance of dark matter.[4] The only viable solution would be to assume that the states charged under $U(1)_D$ and stable under decay are heavier than the reheating temperature such that they are never produced. The Weak Gravity Conjecture (WGC) requires the existence of a charged state with mass smaller than [647]

$$m_{\rm X} \lesssim g_{\rm D} M_{\rm pl}. \tag{5.24}$$

Hence, $g_{\rm D} M_{\rm pl}$ sets the maximal reheating temperature, above which charged states responsible for Universe overclosure might be produced. Therefore, we should exclude the parameter space where

[4] The cross-section of a pair of $U(1)_D$ fermions annihilating into dark photons is given by $\sigma v \simeq \pi \alpha_{\rm D}^2 / m_\psi^2$ with $\alpha_{\rm D} = g_{\rm D}^2/4\pi$. It is way too weak to prevent Universe overclosure, except if we tune the Yukawa coupling of the fermion, λ, defined by $m_\psi = \lambda \langle\phi\rangle / \sqrt{2}$, to minimal values.

the temperature of the $U(1)_D$ spontaneous breaking, taken as $\sim \langle\phi_{\rm D}\rangle$, is heavier than $g_{\rm D} M_{\rm pl}$, cf. pale sky blue region in right plot of Fig. 5.10. Note that the WGC does not specify if the suggested charged state is stable under decay or not. For instance, it would be stable and overclose the Universe if it is a $U(1)_D$ fermion but not if it is a $U(1)_D$ Higgs, which can still decay into a dark photon pair when $m_{\phi_{\rm D}} \gtrsim 2m_V$. Hence, the WGC constraint in our parameter space must be taken with a grain of salt.

Assuming a natural gauge coupling value, $g_{\rm D} = 10^{-1}$, we find that dark photons heavier than $\gtrsim 100$ PeV would be accompanied by a $U(1)_D$ cosmic string network producing a visible GW spectrum, see the left plot of Fig. 5.10. In the case where $g_{\rm D} = 10^{-4}$, we could probe dark photon masses down to $\gtrsim 100$ TeV, see right plot of Fig. 5.10.

On the same plot, we superpose the constraints, shown with pale colors, coming from the simple observation of the GW spectrum with future experiments (except NANOGrav, which is already operating), and the constraints, shown with opaque colors, coming from the detection of the turning point where the spectral index of the GW spectrum changes due to the decay of the dark photon which was dominating the energy density of the Universe. The former detection would allow measuring the dark photon mass, whereas the latter would enable accessing its lifetime.

5.4 Chapter Summary

Suppose future GW observatories have the sensitivity to detect stochastic GW backgrounds of primordial origin and measure distinct features in this spectrum. In that case, they can reveal unique information about high-scale physics. Particularly relevant sources of GW are cosmic strings. Cosmic strings are almost ubiquitous in many Grand-Unified Theories. As they keep emitting GW throughout the whole cosmological history of the Universe, the resulting spectrum covers a wide range of frequencies. It can be detected either by space-based or ground-based observatories. An early era of matter domination due to new heavy particles generates a clear signature in the GW spectrum of cosmic strings.

In this study, we assume the existence of an early matter era due to the presence of a cold particle X temporarily dominating the energy density of the Universe and decaying before the onset of BBN. We compute its impact on the GW spectrum of CS beyond the scaling regime. We show that detecting and interpreting such a feature in terms of a new heavy relic can lead to unparalleled constraints in the $(\tau_X,\, m_X Y_X)$ (lifetime, yield) plane. In Fig. 5.3, we provide model-independent constraints which extend the usual BBN constraints on the lifetime τ_X by 15 orders of magnitude for $G\mu = 10^{-11}$, as we can constrain the early matter-dominated era ending when the temperature of the Universe is between 50 TeV and 1 MeV.

Next, we show that this new search strategy will likely provide unprecedented constraints on particle physics models. We illustrate this on minimal models of massive particles. In the first class, the heavy particle has only gravitational interactions and decays through a Planck-suppressed coupling, cf. Fig. 5.4. In the second class, the heavy relic is a new $U(1)$ gauge boson that decays to the Standard Model via kinetic mixing to $U(1)_Y$ hypercharge. We point out that supersymmetric theories could be probed, well above the reach of present and future colliders, up to a gravitino mass scale of 10^{10} GeV, due to the presence of oscillating scalar moduli fields produced after dynamical supersymmetry breaking, cf. Fig. 5.5. Secondly, we study a simple model of a massive scalar particle interacting only gravitationally with the Standard Model and which therefore has no chance of being observed in collider or direct/indirect detection experiments. If non-conformally coupled to gravity, it can be abundantly produced by gravitational effects at the end of inflation, leading to a matter era in which stochastic gravitational-wave backgrounds from cosmic strings can uniquely probe, cf. Fig. 5.6. Finally, we study a dark photon model kinematically coupled to the Standard Model hypercharge, possibly embedded in the $U(1)_D$ dark-photon-mediated dark matter model. The constraints we obtain from GW on $U(1)_D$ dark matter fall in the large mass/small kinetic mixing ballpark, which is otherwise unreachable by any current and probably future direct/indirect

detection and CMB constraints, cf. Fig. 5.9. At last, we consider the possibility that the dark photon mass and the cosmic string network are generated by the spontaneous breaking of the same $U(1)$ symmetry and show that we can use future GW interferometers to probe dark photon masses above $100\ \mathrm{PeV}$, or even down to the TeV scale if we tune the gauge coupling to small values, see Fig. 5.10.

These are a few minimal examples of particle physics models generating early matter eras. There are many other well-motivated models which would deserve consideration in this respect. We will present the corresponding constraints on axion-like particles and primordial black holes in a separate study. Moreover, in the following two chapters, we will see that a period of the kination era inside the radiation era follows a matter-domination era. However, the effect of kination enhances the GW spectrum, as opposed to the suppression due to the matter era.

Chapter 6

Intermediate Kination-Domination Era: Rotating Axion I (model independent)

Based on
[3] Y. Gouttenoire, G. Servant and P. Simakachorn, ***Revealing the Primordial Irreducible Inflationary Gravitational-Wave Background with a Spinning Peccei-Quinn Axion****, [2108.10328] &*
[4] Y. Gouttenoire, G. Servant and P. Simakachorn, ***Kination cosmology from scalar fields and gravitational-wave signatures****, [2111.01150].*

One of the possible scenarios for the intermediate kination inside the radiation era is the matter-kination scenario, presented in Sec. 4.7 with its smoking-gun GW signature. This section and the next scrutinize how such a scenario can be realized in particle physics theory. As discussed in Chap. 4, the kination era right after inflation comes from the fast-moving scalar field whose energy density dominates that of the Universe. The intermediate kination inside the radiation era could also invoke similar physics, i.e., some fast-moving scalar field that is subdominant and only becomes more energetic at later times. Though it seems any scalar field might work, the key point is that this scalar is needed to dominate over the energy density of *per se* radiation bath and later behaves as kination. In other words, its equation of state must non-trivially change during its domination.

This chapter identifies the main classes of models where this happens naturally. They are linked to *axion* models where the axion acquires large kinetic energy before its low-energy potential – responsible for its mass – develops. As we shall see below, the trivial implementation involving axion dynamics only cannot lead to the intermediate kination. However, the interplayed dynamics between the axion – the angular mode of a complex scalar or Peccei-Quinn (PQ) field – and its unavoidable partner – the radial mode – generate the desired sequence of events that leads to a rotating stage along the circular orbit of the complex scalar-field potential and induce the matter-kination era, cf. Fig. 6.1.

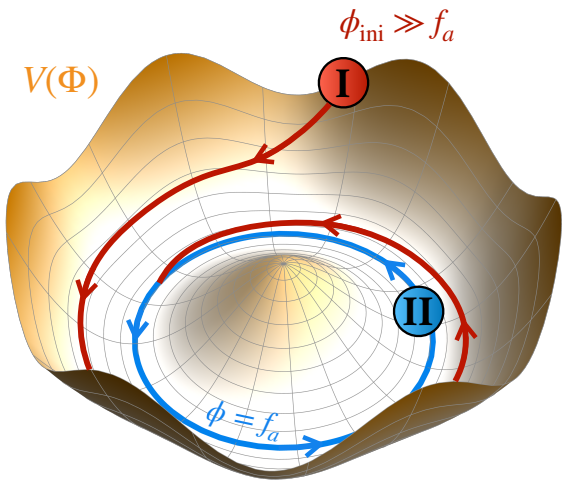

Figure 6.1: Axion models naturally provide a kination era preceded by a matter era. The complex scalar field, whose angular component is identified with the axion, starts at large radius, rotates down the potential, and behaves as pressure-less matter (red trajectory "I"). It reaches stage "II" and has the kination equation of state when its spinning settles down to the potential minimum.

The kination era from a rotating complex-scalar field was studied in a series of papers [507–510], in the context of self-interacting DM, where its very large rotational speed - whose origin remains unexplained by the authors – leads to the kination right after inflation. Later, it was suggested in Ref. [648] and studied thoroughly in [3, 4, 274] that the intermediate kination – following the matter era – can be UV-completed in the spinning-axion model and allows the GW kination signature to be a unique probe of axion physics.

We first make a short recap on axions in Sec. 6.1. Sec. 6.2 then outlines why the dynamics carried out by the axion only cannot lead to the intermediate kination era. We convey a simple concept of why the spinning-axion model realizes the matter-kination era in Sec. 6.3. The detailed and dedicated discussion on the UV completion of this model is postponed to Chap. 7. In the rest of this chapter, we focus on the phenomenology of the rotating axion: the axion DM and Baryogenesis, and its connection to the observable GW signal from the intermediate kination.

6.1 Axion: a short recap

Axion particles are ubiquitous in extensions of the Standard Model of particle physics. They arise as pseudo-Nambu-Goldstone bosons of a spontaneously broken global $U(1)$ symmetry and are typically very light compared to the symmetry-breaking energy scale f_a. A particularly well-motivated candidate is the QCD axion predicted by the Peccei-Quinn (PQ) mechanism introduced to solve the strong CP problem in the Standard Model [439–441, 649], which is the intriguing absence of CP-violation in the sector of strong interactions. The PQ mechanism relies on the existence of a new complex scalar field whose vacuum expectation value f_a breaks spontaneously a new broken global $U(1)_{\rm PQ}$ symmetry. Its main prediction is a new light particle, *the axion*, which is the angular mode of the new PQ scalar field. There has been growing interest in the axion over the years, as it can also explain the Dark Matter of the Universe [446–448]. The axion is at the origin of an extensive experimental program and has become the most hunted particle after the Higgs discovery, cf. [650, 651] for reviews and references therein[1]. For example, it is being searched by exploiting its coupling to the photon which scales as $1/f_a$. Given the astrophysical constraints on $f_a \gtrsim 10^8$ GeV, the small axion coupling makes its detection challenging [652–655].

Around the QCD epoch, the QCD axion acquires a temperature-depedent mass due to the QCD anomaly, which is model-dependent. For the canonical QCD axion [442–445, 656, 657], the mass is supposed to depend on temperature, e.g. from the dilute instanton gas approximation [658]

$$m_a^2(T) = m_{a,0}^2 \min\left[1, \frac{\chi(\text{GeV})}{\chi(0)}\left(\frac{1\ \text{GeV}}{T}\right)^{\alpha}\right] \equiv m_{a,0}^2 \Upsilon(T), \tag{6.1}$$

where[2] $\chi(0) \simeq (75.6\ \text{MeV})^4$, $\chi(\text{GeV}) \simeq (2\ \text{MeV})^4$, $\alpha = 8.16$ [658], $\Lambda_{\rm QCD} \simeq 211$ MeV is the QCD scale [659], and the zero-temperature mass is $m_{a,0}^2 = \chi(0)/f_a^2$. The QCD axion mass increases with time and becomes constant around $T \simeq 160$ MeV. QCD axion – heavier or lighter than this relation – requires an extension to the canonical scenario, e.g., [660]. Due to the observable ranges of the future and current axion experiments, a recent and interesting model is the lighter QCD axion where the QCD axion transforms non-linearly under a $\mathbb{Z}_{\mathcal{N}}$ symmetry [661–664] and modifies its mass to be [663]

$$\left(\frac{m_a}{m_a^{\rm QCD}}\right)^2 \simeq \frac{1}{\sqrt{\pi}}\sqrt{1-z^2}(1+z)\mathcal{N}^{3/2} z^{\mathcal{N}-1}, \tag{6.2}$$

where $m_a^{\rm QCD}$ is the canonical QCD axion mass, and $z \equiv m_u/m_d \simeq 0.47$ [39]. Stringent bounds on this non-canonical light QCD axion come from finite density effects, modifying the axion potential

[1] For the current updates on constraints and projections from axion experiments presented in an illustrative manner, cf. repository by O'Hare.

[2] χ is the susceptibility of the topological charge, defined by $\chi(T) \equiv m_a^2(T) f_a^2$ and $\Lambda_{\rm QCD}$ is the scale at which the perturbative QCD coupling constant diverges.

in dense astrophysical objects and, therefore, the neutron-star inspirals as well as nuclear matter properties, altering the stellar processes [661]. Recently, strong bounds have been derived from observations of white dwarfs [665], i.e., $\mathcal{N} \lesssim 31$ for $f_a \lesssim 10^{16}\,\text{GeV}$.

Later, we shall also see that DM production from the rotating axion can populate the lighter mass region. We report the final forms of canonical axion and $\mathbb{Z}_\mathcal{N}$ axion, which will be used extensively in this chapter and the next:

$$m_a \simeq \mu\text{eV}\left[\frac{10^{12}\,\text{GeV}}{f_a}\right] \times \begin{cases} 5.7\,\Upsilon^{1/2}(T) & \text{for conventional QCD axion,} \\ 4.9\cdot\mathcal{N}^{3/4}(0.47)^{(\mathcal{N}-1)/2} & \text{for } \mathbb{Z}_\mathcal{N} \text{ QCD axion,} \end{cases} \tag{6.3}$$

where $\Upsilon(T)$ is the temperature-depedent function, defined in Eq. (6.1). Indeed, the axion that does not solve the strong-CP problem can deviate from these mass relations, i.e., m_a and f_a are free parameters where m_a is the zero-temperature mass that could be present up to high scales.

Standard misalignment mechanism. — Due to the fast expansion rate of the Universe, the axion would sit frozen on the potential with its initial value; a single or randomly distributed value depends on whether the SSB of PQ symmetry happens before or after the end of inflation, respectively. The expansion rate later drops below the axion's mass, which determines the potential gradient. It allows the axion to oscillate in the underdamped motion at temperature T_mis when $3H(T_\text{mis}) = m_a(T_\text{mis})$. A homogeneous scalar field oscillating near the bottom minimum, where the potential is approximately quadratic, behaves as pressureless matter and serves as a good candidate for DM, i.e., the energy density goes like a^{-3}. The axion abundance is parametrized by the comoving axion number density $Y_\theta = n_a/s$ where s is the entropy density [446–448],

$$Y_\text{a}^\text{mis} = \frac{2m_a(T_\text{mis})f_a^2\theta_\text{mis}^2}{\frac{2\pi^2}{45}g_{*s}(T_\text{mis})T_\text{mis}^3} = \left(\frac{45}{30^{3/4}\pi^{1/2}}\right)\left(\frac{g_*^{3/4}(T_\text{mis})}{g_{*s}(T_\text{mis})}\right)\left(\frac{f_a^2}{m_a^{1/2}M_\text{Pl}^{3/2}}\right)\theta_\text{mis}^2, \tag{6.4}$$

where $n_a = \rho_a/m_a$ with ρ_a is the axion potential energy, and the second step uses the temperature-dependent mass relation $m_a(T)$. The misalignment angle θ_mis of the axion from its minimum is expected to be $\mathcal{O}(1)$ unless it is fine-tuned. The relic density of the axion can be computed from the general formula

$$\frac{\rho_{a,0}}{\rho_\text{DM,0}} = \frac{\Omega_{a,0}h^2}{\Omega_\text{DM,0}h^2} \simeq \frac{s_0 m_a Y_a h^2}{0.5745\,\text{keV/cm}^3} \simeq 205\,h^2\left(\frac{m_a}{1\,\text{eV}}\right)\left(\frac{Y_\theta}{40}\right), \tag{6.5}$$

where $2s_0 m_a Y_\theta$ is the axion energy density today, and $s_0 = 2\pi^2 g_{*s}(T_0)T_0^3/45$ is the entropy density today. This formula can also be applied to other production mechanisms of the axion. The correct DM abundance is satisfied on two dashed lines of Fig. 6.5 for the temperature-dependent and independnt masses. The conventional QCD axion explains DM for $f_a \simeq 10^{11}\,\text{GeV}$. The above DM production is the so-called *standard misalignment* mechanism, where the term *standard* is for distinguishing it from other misalignments. For example, the large-angle misalignment [666], the trapped misalignment [664], the frictional misalignment [667, 668], and, interestingly, the kinetic misalignment [132, 449, 450] that could lead to the kination era [3, 4, 274, 648, 669].

Next, we shall see the problem of the only-axion oscillation scenario in Sec. 6.2. Though its equation of state can be matter-kination, it cannot dominate the thermal bath and subsequently generate the intermediate kination. This motivates us to look at its natural extension in Sec. 6.3 where the axion spins fast, leads to the intermediate kination, and is compatible with the so-called *kinetic* misalignment.

6.2 No-go for intermediate kination from a real scalar field

Let us first consider the simplest realization – a real scalar field – that can lead to matter-kination equation-of-state. However, we shall see that this set-up cannot lead to any matter-kination domination era. The successful setup will be discussed in Sec. 6.3, using a complex scalar field instead

of the real one. Still, we suggest the interested reader go through this section and see why the real scalar fails.

A real scalar field – oscillating in the quadratic potential – generates the matter equation-of-state and obtains a considerable speed on average that could lead to the kination stage when the vanishing potential vanishes at later times. Interestingly, there is a class of models in which such dynamics are realized and interestingly related to axion physics. For example, the QCD axion mass (the real scalar field) is well-known to be generated by non-perturbative effects around the QCD scale. [663, 664]. At high temperature, the axion potential is unconstrained and can arise from a variety of PQ breaking effects [663, 664, 670–673]. Based on the idea of [661, 662], Refs. [663, 664] assume the existence of a discrete $\mathbb{Z}_{\mathcal{N}}$ shift symmetry for the axion field, where $\mathcal{N}$ is the number of mirror worlds to which the axion interacts with. As soon as the non-perturbative QCD effects from all worlds are effective at some critical temperature T_c, the axion mass receives an exponential suppression with respect to the usual prediction [442–445, 656, 657]. The sudden suppression of axion mass means a drop in the axion potential at T_c.

If the axion mass when $T > T_c$ is larger than $H(T_c)$, the axion oscillates around the potential minimum (approximately quadratic) and obtains some speed. The axion behaves as pressure-less matter and eventually rolls freely over the barrier of the axion potential that shrinks substantially for $T \lesssim T_c$. From this moment, the axion has the kination equation of state. Since a freely moving scalar has the EOM $\ddot{\phi}+3H\dot{\phi} = 0 \Leftrightarrow \dot{\phi} \propto a^{-3}$, the axion eventually gets trapped in low-T potential corresponding to axion mass today, which would allow it to be a natural DM candidate [132, 664].

No-Go argument. — The above scenario has a primary issue for realizing the intermediate kination; the energy density of the sector – responsible for the varying axion mass – cannot be sub-dominant compared to that of axion after the first axion potential is turned off, leading to the impossibility of a kination era[3]. Concretely, the averaged axion's energy density splits equally into kinetic and potential energy during the first oscillation. When the axion's potential vanishes at T_c, the axion rolls with half of its initial energy, and the other half goes to the sector responsible for the varying axion mass. E.g., the thermal bath of the confining sector always has more energy than the axion oscillations. To circumvent this problem, one has to involve a second scalar field. The simplest and most natural realization is to consider the radial mode (the partner of the axion) of the complex scalar field, as will be discussed in the remaining sections and chapters. Alternative UV-completions will be presented elsewhere [551].

6.3 Complex Scalar Field Dynamics: the rotating axion

The most straightforward extension of the axion dynamics is to consider its natural partner – the radial mode ϕ of the PQ complex-scalar field $\Phi \sim \phi \exp(i\theta)$, where θ is the angular degree-of-freedom or the axion. The interplay between them becomes non-trivial due to another mass scale, namely the mass of the radial mode $m_r \simeq \sqrt{V'(\Phi)/\Phi}$ with V is the complex-field potential, which can be much larger than the axion's mass. Elaborating more in Chap. 7, the motion of the complex-scalar field initiates by a large m_r and, at the same time, induces the axion rotation with help of an explicit breaking of $U(1)_{\rm PQ}$ symmetry, generating gradient along axion direction[4]. This high-temperature axion potential – expected due to the *no global symmetry* conjecture of the quantum gravity theories [675–679] – would later become ineffective; otherwise, it would contribute to the axion potential from QCD effect and invalidate the solution to the strong-CP problem [680, 681]. For instance, it can be the higher-dimensional operator which decouples from the dynamics when

[3] We thank Pablo Quilez, Raymond Co, Nicolas Fernandez, Akshay Ghalsasi, and Keisuke Harigaya for a discussion.

[4] Recently, Domcke et al. propose another exciting way: the axion is kicked by another complex scalar which interacts via the anomalous mixing [674]. This extra scalar must spin at priori with some significant global charges. Later its interaction with the axion becomes efficient in the thermal bath, so it equilibrates its charge with the rotating axion. The immense axion speed could induce a kination era. However, the enhanced axion speed affects the radial-mode dynamics and would lead to a non-trivial cosmological history, beyond the scope of this thesis.

the VEV of the complex scalar field gets smaller due to Hubble expansion. The axion motion gets excited and later rolls freely with a large speed $\phi\dot{\theta}$,

After this very first moment, the excitations of both radial and axion motions lead to an elliptic orbit with a smaller radius due to the Hubble friction, as shown in stage I of Fig. 6.1. The complex scalar field behaves as a pressureless matter if the potential is quadratic, cf. App. G.4.2. Later, the radial oscillation would be damped by dissipating its kinetic energy to thermal bath or fluctuations and prevented from over-closing the Universe. The remaining energy densities: the potential energy of the complex field and the kinetic energy in the axion field, balance with each other – making the orbit circular – and hinder the complex scalar from settling directly to its VEV after damping. The equation of state during this time is still matter-like, i.e., $\omega \propto p \propto KE - PE = 0$, and can lead to the matter-domination era if it does not earlier do so. Note the difference from the usual matter-like stage of the axion; the rotating axion moves in one direction and does not oscillates. Only after the circular orbit red-shifts to the potential minimum at $|\Phi| \simeq f_a$, the axion's kinetic energy dominates the dynamics and induces the kination-domination era

$$\rho_{\rm KD} = E_{\rm KD}^4 \simeq f_a^2 \dot{\theta}^2, \tag{6.6}$$

that lasts for some e-foldings $N_{\rm KD}$ before becoming sub-dominant to the radiation bath. The scalar-field energy density evolves along the sequence of events as shown in Fig. 6.2 (stepwise discussions in Chap. 7) and leads to the matter-kination era[5].

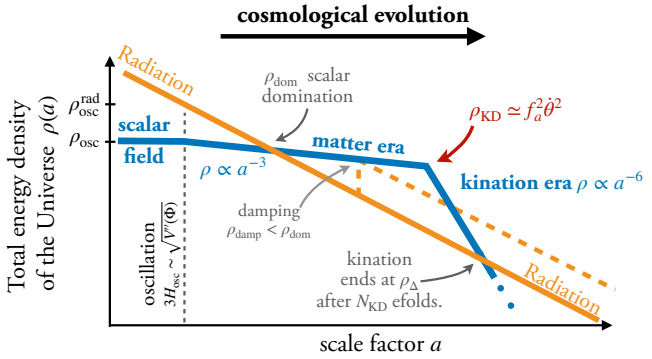

Figure 6.2: Complex-scalar field dynamics that generates a matter-kination era inside the radiation epoch. The solid orange line shows when the entropy injection is absent or happens before the scalar domination, while the entropy injection occurs after scalar domination and suppresses the kination duration for the dashed orange line. f_a denotes the radius of the circular orbit of the field spinning with velocity $\dot{\theta}$.

Other than the kination, the rotating axion scenario also possesses very interesting implications for the DM production via the so-called *kinetic misalignment* mechanism [449, 450] or kinetic fragmentation [129, 130, 132] and the Baryogenesis via the *axiogenesis* scenario [648, 669]. In the next section, we shall discuss these in turn and connect them to the observability of the kination GW peak. Before moving on, let us briefly comment on other similar set-ups where the spinning complex scalar field plays an important role. The effect of the axion fluctuations is enhanced by the motion of the axion field, which could amplify the axion relic density; this is the main idea of the work in progress [527]. The rotating axion could lead to many effects if its couplings to other fields are enhanced beyond what is considered in this paper, e.g., spontaneous baryogenesis [682], axion-assisted-Schwinger effect [683], and magnetogenesis [684]. Also, the spinning complex-scalar field is one of the key ingredients of the so-called Affleck-Dine Baryogenesis [589, 599] (cf. [685] for a review).

Why axion but not the Affleck-Dine scalar field? — The critical difference between the two frameworks is the position of the scalar-potential minimum. In the Affleck-Dine scenario, the nearly-flat (or angular) direction is a flat direction in the Minimal Supersymmetric Standard Model that is charged under baryon/lepton number – some combination of squarks and sleptons

[5] We comment on the impossibility in our opinion of the radiation-kination-radiation scenario (adopted in [352]). Indeed, a spinning field inside a quartic potential leads to radiation behavior. If the trajectory is circular, the EOS becomes kination-like once the scalar field reaches the bottom of the potential. Nevertheless, this scenario appears unfeasible because the damping of the radial motion responsible for the circular trajectory is expected to produce particles redshifting as radiation (or worse as matter) and to prevent the Universe from entering a kination stage.

– and lifted due to the supersymmetry breaking effect. The potential minimum is at the origin, conserving color and charge and leading to pressureless matter EOS until late. In the end, all the energy of the condensate goes into the plasma. This is not the case in axion models; the potential has a minimum at a large field value f_a that defines the axion decay constant and supports the circular orbit of axion along the flat direction. Crucially, a significant fraction of the U(1) charge in axion models is preserved in the rotating field at the potential minimum and enables a temporary kination equation of state. However, it is coupled to the thermal bath. The thermalization of the scalar field only depletes the kinetic energy of radial mode cf. Chap. 7.

6.4 Rotating axion DM

As we will discuss extensively in Chap. 7, the axion could receive a kick parametrized by the number density of Noether $U(1)_{\rm PQ}$ charge: $n_\theta = \phi^2\dot\theta$, due to some $U(1)_{\rm PQ}$-breaking effect at early times $\partial(a^3 n_\theta)/\partial t = -\partial V/\phi\partial\theta$. Assuming the explicit-breaking term is only active until some time t_r, we obtain the resulting comoving number density of $U(1)$ charge

$$Y_\theta(t) \equiv \frac{n_\theta}{s} \simeq \frac{a^3(t_r)}{a^3(t)}\cdot\frac{\partial V}{\partial\theta}(t_r)\cdot\frac{1}{H(t_r)}, \tag{6.7}$$

where s is the entropy density of the Universe and which is conserved through Hubble evolution, cf. Eq. (7.19) and Sec. 7.1.3 for more details. This conserved charge later converts into axion number density via the axion kinetic misalignment [449, 450] or fragmentation process [129, 130, 132].

Kinetic misalignment mechanism. – After the kination starts, the energy density in the rotating axion $\rho_\theta = f_a^2\dot\theta^2/2$ decreases as a^{-6}. Its large speed allows its skipping over the potential and delays the axions oscillation later than the usual $3H \sim m_a$ condition. Eventually, it drops below the axion potential at the top of the barrier $\rho_{\rm barrier} \simeq 2m_a^2 f_a^2$ where m_a is the axion mass, and the axion gets trapped and oscillates in one of the minima. This occurs when the axion spinning speed drops to $\dot\theta(T_{\rm trap}) = 2m_a(T_{\rm trap})$. Conservation of energy $\rho_\theta = \rho_a$ implies that the yield of $U(1)$ charge,

$$Y_\theta = 2\rho_\theta/(\dot\theta s) \simeq \phi^2\dot\theta/s, \tag{6.8}$$

is transferred to the yield of the axion oscillation $Y_a = \rho_a/(m_a s)$. The equality $Y_a = Y_\theta$ however neglects correction due to non-linear effects which can enhance the axion abundance into [449]

$$Y_a = 2Y_\theta. \tag{6.9}$$

The axion relic abundance can be obtained from Eq. (6.5). Moreover, the fast-moving axion skipping the potential barrier is known to fragment into higher-momentum modes [129]. It is found that the axion energy density in higher modes generated by the fragmentation is of the same order as the zero-mode component generated from the kinetic misalignment [132].

Effectiveness of kinetic misalignment. — Whenever $Y_{\rm a}^{\rm mis} > 2Y_\theta$, the axion relic abundance is dominated by the standard misalignment. By comparing Eq. (6.4) with Eq. (6.5) and (6.9), we deduce that the kinetic misalignment is the main DM production for

$$\sqrt{m_a f_a} \lesssim 1.1\times10^{-9}\left(\frac{g_{*s}(T_{\rm mis})}{g_*^{3/4}(T_{\rm mis})}\right)\left(\frac{M_{\rm Pl}}{f_a}\right)^{3/2}, \tag{6.10}$$

where we have taken $m_a(T_{\rm mis}) = m_a$. Outside this region, the axion relic abundance cannot relate to the rotating axion parameters using Eq. (6.8). As we shall see now, the rotating axion parameters are traded with those of kination. This means we cannot infer any axion parameter from the observed peak GW when $Y_{\rm a}^{\rm mis} > 2Y_\theta$.

6.4.1 Rotating axion DM and kination

Since the $U(1)_{\rm PQ}$ charge of the rotating axion is conserved throughout the field evolution until very late times, we can evaluate the comoving axion number density Y_θ at the beginning of the kination era

$$Y_\theta \;=\; \frac{n_\theta}{s} \;=\; \frac{\phi^2\dot\theta}{\frac{2\pi^2}{45}g_{*s}(T)T^3} \;=\; \left(\frac{2}{\dot\theta_{\rm KD}}\right)\left[\frac{E_{\rm KD}^4}{\frac{2\pi^2}{45}g_{*s}(T_{\rm KD})T_{\rm KD}^3}\right]. \tag{6.11}$$

when the complex scalar field sits in the circular minimum $\phi = f_a$ and the axion kinetic energy is given by $\rho_{\rm KD} = E_{\rm KD}^4 = f_a^2\dot\theta_{\rm KD}^2/2$. The thermal-bath temperature $T_{\rm KD}$ when kination starts follows from $\rho_{\rm KD}^{\rm rad} = E_{\rm KD}^4\exp(-2N_{\rm KD})$ and reads $T_{\rm KD} = \left(30/\pi^2 g_*(T_{\rm KD})\right)^{1/4} E_{\rm KD}\exp(-N_{\rm KD}/2)$. Solving for $E_{\rm KD}$, we obtain the relation between the $U(1)_{\rm PQ}$ charge and the kination era,

$$E_{\rm KD} \;=\; 0.436\, G^{3/4}(T_{\rm KD})\left(\frac{f_a}{Y_\theta}\right)\exp(3N_{\rm KD}/2), \tag{6.12}$$

where $G(T) \equiv (g_*(T)/106.75)(g_{*,s}(T)/106.75)^{-4/3}$. As we will see below, this relation allows for a one-to-one relation between the GW peak position induced by the kination era, and the $U(1)$ charge Y_θ. Interestingly, this result does not only apply for $U(1)_{\rm PQ}$, but also any $U(1)$ in general. It would be interesting to see if other particle-realization with the $U(1)$ extension can lead to the kination era and the exciting GW signature.

After the axion potential turns on at later times, the $U(1)_{\rm PQ}$ is converted into the axion abundance by the kinetic misalignment in Eq. (6.5). Therefore, the kination of energy scale in Eq. (6.13) becomes a function of the parameters axion and its abundance

$$E_{\rm KD} \simeq 2\cdot 10^9\ {\rm GeV}\ G^{3/4}(T_{\rm KD})\left(\frac{m_a f_a}{{\rm GeV}^2}\right)\left(\frac{\Omega_{\rm DM,0}h^2}{\Omega_{\rm a,0}h^2}\right)\exp(3N_{\rm KD}/2). \tag{6.13}$$

The kination energy scales for both conventional QCD axion and the $\mathbb{Z}_{\mathcal{N}}$ are

$$E_{\rm KD}^{\rm QCD} \simeq 10^7\ {\rm GeV} G^{3/4}(T_{\rm KD})\frac{\Omega_{\rm DM,0}h^2}{\Omega_{a,0}h^2}\exp(3N_{\rm KD}/2). \tag{6.14}$$

$$E_{\rm KD}^{\mathbb{Z}_{\mathcal{N}}} \simeq 10^7\ {\rm GeV}\ \mathcal{N}^{\frac{3}{4}} z^{\frac{\mathcal{N}-1}{2}} G^{\frac{3}{4}}(T_{\rm KD})\frac{\Omega_{\rm DM,0}h^2}{\Omega_{a,0}h^2}\exp(3N_{\rm KD}/2), \tag{6.15}$$

where $z \equiv m_u/m_d \simeq 0.47$ [39]

The $U(1)$ charge Y_θ can be partially transferred into baryon number and lead to successful baryogenesis as in the Affleck-Dine mechanism [599], or so-called axiogenesis mechanism [669]. We postpone the discussion of the baryon asymmetry to the next Sec. 6.5. Instead, in the present section, we discuss the transfer of Y_θ into axion coherent oscillations via the so-called kinetic misalignment mechanism, which can explain dark matter for smaller f_a than in the standard misalignment mechanism [449, 450].

6.4.2 Signature of the rotating axion DM in inflationary SGWB

The abundance-kination relation (6.13) allows us to recast the GW peak signature from primordial inflation in terms of axion parameters (f_a, m_a) for a given abundance – previously as $(E_{\rm KD}, N_{\rm KD})$ in Eqs. (4.55), (4.56),

$$f_{\rm KD} \simeq 9.7\ {\rm Hz}\ \left[\frac{G(T_\Delta)}{G(T_{\rm KD})}\right]^{\frac{1}{4}}\left[\frac{{\rm GeV}^2}{m_a f_a}\right]^{\frac{1}{3}}\left[\frac{\Omega_{a,0}}{\Omega_{DM,0}}\right]^{\frac{1}{3}}\left[\frac{E_{\rm KD}}{10^9\ {\rm GeV}}\right]^{\frac{4}{3}}, \tag{6.16}$$

$$\Omega_{\rm GW,KD}h^2 \simeq 5.9\cdot 10^{-19}\ \left[\frac{G(T_\Delta)}{G(T_{\rm KD})}\right]^{\frac{3}{4}}\left[\frac{E_{\rm inf}}{10^{16}\ {\rm GeV}}\right]^4\left[\frac{f_{\rm KD}}{1\ {\rm Hz}}\right]\left[\frac{{\rm GeV}^2}{m_a f_a}\right]\left[\frac{\Omega_{a,0}}{\Omega_{DM,0}}\right], \tag{6.17}$$

which applies for generic ALP with arbitrary mass relation. **For the QCD axion,** the fixed axion-mass relation, Eq. (6.3), leads to

$$f_{\rm KD}^{\rm QCD} \simeq 53\ {\rm Hz}\ \left[\frac{G(T_\Delta)}{G(T_{\rm KD})}\right]^{\frac{1}{4}} \left[\frac{\Omega_{a,0}}{\Omega_{DM,0}}\right]^{\frac{1}{3}} \left[\frac{E_{\rm KD}}{10^9\ {\rm GeV}}\right]^{\frac{4}{3}}, \tag{6.18}$$

$$\Omega_{\rm GW,KD}^{\rm QCD} h^2 \simeq 10^{-16} \left[\frac{G(T_\Delta)}{G(T_{\rm KD})}\right]^{\frac{3}{4}} \left[\frac{E_{\rm inf}}{10^{16}\ {\rm GeV}}\right]^4 \left[\frac{f_{\rm KD}}{1\ {\rm Hz}}\right] \left[\frac{\Omega_{a,0}}{\Omega_{DM,0}}\right]. \tag{6.19}$$

The relation between observability of GW from primordial inflation and axion DM abundance is shown in Fig 6.3. The matter-kination era generated by ALP DM with a mass $m_a \lesssim 10^{-6}$ eV can move the GW signal into observable windows of the future interferometers. In the specific case of the QCD axion DM, the GW signal is enhanced only at frequencies larger than ET/CE, which motivates high-frequency GW searches [40]. In the regions of observable GW signals, the conventional QCD axion is overabundant, as shown in Figs. 4.22 and 6.3. In the next paragraph, only lighter (non-conventional) QCD axion can satisfy the correct DM abundance while leading to an observable GW peak signature.

For the non-canonical lighter QCD axion, its mass – e.g. $\mathbb{Z}_\mathcal{N}$ axion [661–664] – is lighter than that of the conventional QCD axion in Eq. (6.3).

$$f_{\rm KD}^{\mathbb{Z}_\mathcal{N}} \simeq \frac{57\ {\rm Hz}}{\mathcal{N}^{\frac{1}{4}} z^{\frac{\mathcal{N}-1}{6}}} \left[\frac{G(T_\Delta)}{G(T_{\rm KD})}\right]^{\frac{1}{4}} \left[\frac{\Omega_{a,0}}{\Omega_{DM,0}}\right]^{\frac{1}{3}} \left[\frac{E_{\rm KD}}{10^9\ {\rm GeV}}\right]^{\frac{4}{3}}, \tag{6.20}$$

$$\Omega_{\rm GW,KD}^{\mathbb{Z}_\mathcal{N}} h^2 \simeq \frac{10^{-16}}{\mathcal{N}^{\frac{3}{4}} z^{\frac{\mathcal{N}-1}{2}}} \left[\frac{G(T_\Delta)}{G(T_{\rm KD})}\right]^{\frac{3}{4}} \left[\frac{E_{\rm inf}}{10^{16}\ {\rm GeV}}\right]^4 \left[\frac{f_{\rm KD}}{1\ {\rm Hz}}\right] \left[\frac{\Omega_{a,0}}{\Omega_{DM,0}}\right], \tag{6.21}$$

where $z \equiv m_u/m_d \simeq 0.47$ [39]. The lighter the axion mass (larger $\mathcal{N}$), the larger the GW peak amplitude for fixed $f_{\rm KD}$ that resides in the observable ranges. Note that a fixed $f_{\rm KD}$ means that the same frequency corresponds to a smaller $E_{\rm KD}$ for a larger $\mathcal{N}$. As examples, Tab. 6.1 provides the value of $\mathcal{N}$ of the spinning $\mathbb{Z}_\mathcal{N}$-axion DM that each GW experiment can infer if a GW peak signature, corresponded to benchmark spectra in Fig. 6.3.

We stressed that the QCD axion DM cannot induce an observable matter-kination GW peak, except maybe at BBO. Because the GW enhancement from the spinning-axion kination only takes place (i.e. $\Omega_{\rm st} < \Omega_{\rm KD}$) for

$$f_{\rm KD} \gtrsim 22\ {\rm Hz}(m_a f_a/{\rm GeV}^2). \tag{6.22}$$

Instead, for a given f_a, most of the interesting regions lie at a smaller m_a region, e.g. $f_{\rm KD} \gtrsim 0.1$ Hz for the conventional QCD axion and $f_{\rm KD} \gtrsim 10\,\mu$Hz for the $\mathbb{Z}_{31}$ QCD axion.

Observatories	$E_{\rm KD}$ (GeV)	$N_{\rm KD}$	$\mathcal{N}$
LISA	3×10^4	4	39[†]
BBO	3×10^6	5	31
ET	10^8	6	25

Table 6.1: Benchmark points in Fig. 4.22 and the corresponding $\mathcal{N}$-values of the non-canonical QCD axion DM models.[†]The $\mathbb{Z}_\mathcal{N}$ QCD axion with $\mathcal{N} \gtrsim 31$ appears to be ruled-out by finite-density effects [661, 665].

Reach of GW interferometers. From Eq. (6.17) and Fig. 6.3, we see that the GW peak amplitude scales as $\Omega_{\rm GW,KD} \propto f_{\rm KD}/m_a f_a$. For a given observatory with the best sensitivity $\Omega_{\rm sens,min}$,

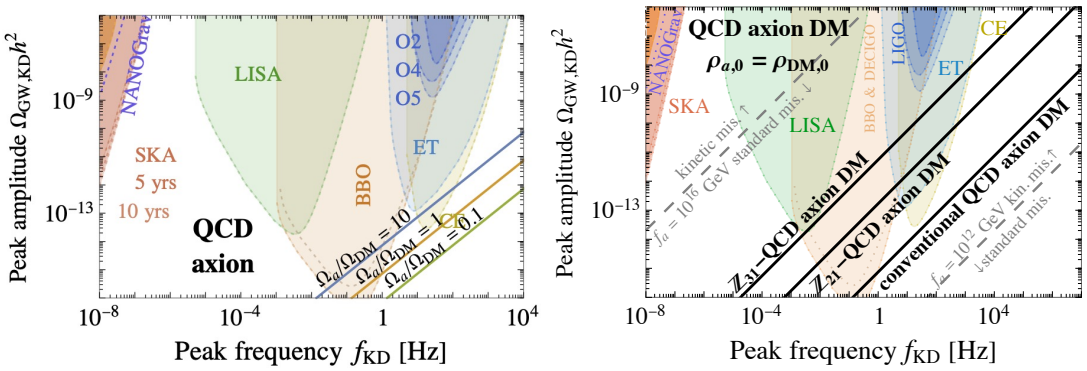

Figure 6.3: The solid lines indicate the position of the GW peak signature in the presence of a matter-kination generated by the rotating axion, for a fixed axion relic abundance, which is produced via kinetic misalignment for either the QCD axion, cf. Eq. (6.19). On the *right* plot, the axion is overabundant above the black solid lines. Below the dashed gray lines, the axion abundance is set by the standard misalignment mechanism for a given f_a, such that the relation between the GW-abundance relation in Eq. (6.19) and (6.18) is not applicable. The dependence on m_a and f_a is shown in Fig. 6.4.

there exists a maximal value of $m_a f_a$ below which the peak is observable. It depends on the frequency $f_{\rm sens,min}$ at which the signal-to-noise ratio is the largest[6]. Requiring $\Omega_{\rm GW,KD} > \Omega_{\rm sens,min}$ with $f_{\rm KD} = f_{\rm sens,min}$ in Eq. (6.17), we deduce the maximal axion mass which leads to a detectable peak signature in the SGWB from primordial inflation

$$m_a \lesssim (0.65\ \mu{\rm eV}) \left(\frac{E_{\rm inf}}{10^{16}\ {\rm GeV}}\right)^4 \left(\frac{10^{-12}}{\Omega_{\rm sens,min}}\right) \left(\frac{f_{\rm sens,min}}{1\ {\rm Hz}}\right) \left(\frac{10^9\ {\rm GeV}}{f_a}\right) \left(\frac{\Omega_{a,0}}{\Omega_{\rm DM,0}}\right). \quad (6.23)$$

The reach of future observatories in the $(m_a,\ f_a)$ plane is shown in Fig. 6.4. For example, ET ($f_{\rm sens,min} \simeq 1$ Hz and $\Omega_{\rm sens,min} \simeq 10^{-13}$) can probe $m_a^{\rm ET} \lesssim 6.5\ \mu{\rm eV}(10^9\ {\rm GeV}/f_a)$ for the maximum inflationary scale. Note that Eq. (6.23) is parallel to the $m_a(f_a)$ QCD axion mass relation.

Fig. 6.4 assumes that the frequency and amplitude of the GW peak are independent, which reflects the fact that we treat $(E_{\rm KD}, N_{\rm KD})$ as free parameters. As we shall see in Chap. 7, the UV completion fixes their relation. For example, Fig. 6.5 shows that a particular set of model parameters restricts the observability down to a subset of what is shown in Fig. 6.4.

BBN bound. The successful BBN requires that the kination era should ends above the BBN temperature $E_\Delta = E_{\rm KD} e^{-3N_{\rm KD}/2} \lesssim T_{\rm BBN} \sim 1$ MeV. Using Eq. (6.13), we deduce the BBN bound on the rotating axion that leads to the kination era

$$m_a \lesssim (0.5 \times 10^{-12}\ {\rm eV}) G^{-3/4}(T_{\rm KD}) \left(\frac{10^9\ {\rm GeV}}{f_a}\right) \left(\frac{\Omega_{a,0}}{\Omega_{\rm DM,0}}\right), \quad (6.24)$$

which is shown as the red-hatched region in Fig. 6.4.

Minimum inflationary scale. The amplitude of the GW spectrum from primordial inflation scales as $E_{\rm inf}^4$, see Eq. (6.17). The discovery band of a particular detector, Eq. (6.23), becomes weaker than the BBN bound, Eq. (6.24), when the inflationary scale becomes lower than

$$E_{\rm inf} \lesssim (3 \times 10^{14}\ {\rm GeV}) \left(\frac{\Omega_{\rm sens,min}}{10^{-12}}\right) \left(\frac{1\ {\rm Hz}}{f_{\rm sens,min}}\right). \quad (6.25)$$

For instance, ET can no longer probe the SGWB from primordial inflation enhanced by a period of kination induced by ALP DM if $E_{\rm inf} \lesssim 10^{13}$ GeV.

[6]This estimation is valid only when the slope of the sensitivity curve is steeper than the scaling of $\Omega_{\rm GW}$. If not, the tip of the sensitivity curve does not correspond to the largest $m_a f_a$.

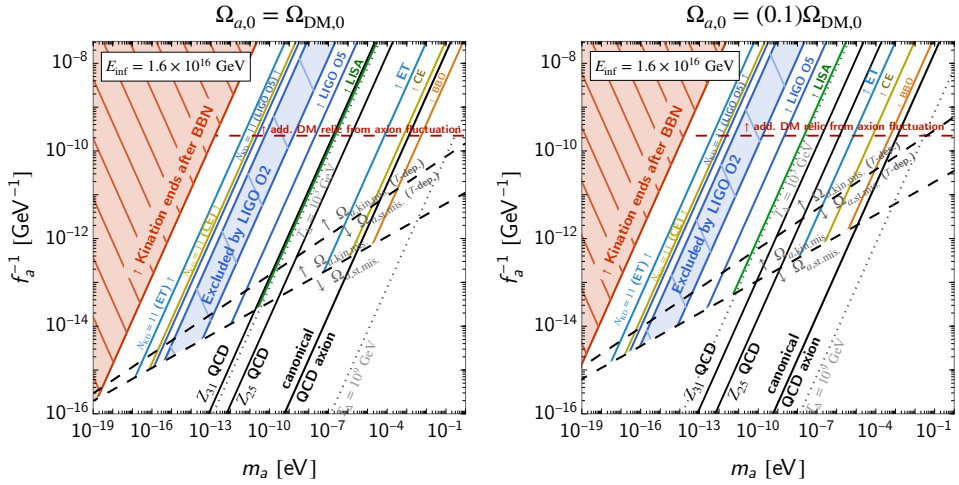

Figure 6.4: Ability of future planned GW experiments to probe axion DM through its matter-kination peak signature in inflationary SGWB, cf. Eq. (6.23). The BBN constraints, Eq. (6.24), are shown in red-hashed. The black solid lines are different $m_a - f_a$ relations corresponding to either canonical or non-canonical, see Eq. (6.3), QCD axion. Below the black dashed lines, the axion abundance is set by standard misalignment such that the 1-to-1 connection between the matter-kination parameters $(E_{\rm KD},\, f_{\rm KD})$ and the axion abundance $\Omega_{a,0}$ is lost, and the prediction of the GW peak signature via the kinetic misalignment, Eqs. (6.19) and (6.18), is not applicable. We consider either a QCD axion mass dependence $m_a(T)$ or a constant mass m_a. The axion fluctuation mentioned in Sec. 4.4.4 allows the longest kination era to be $N_{\rm KD} \simeq 11$ and prevents the detectability bands to continue to smaller m_a. Moreover, the axion fluctuation can dominate the relic density from the zero-mode when $f_a \lesssim 10^{9\div10}$ GeV [132]. We only show f_a values larger than $\sim 10^8$ GeV due to astrophysical constraints [652–655].

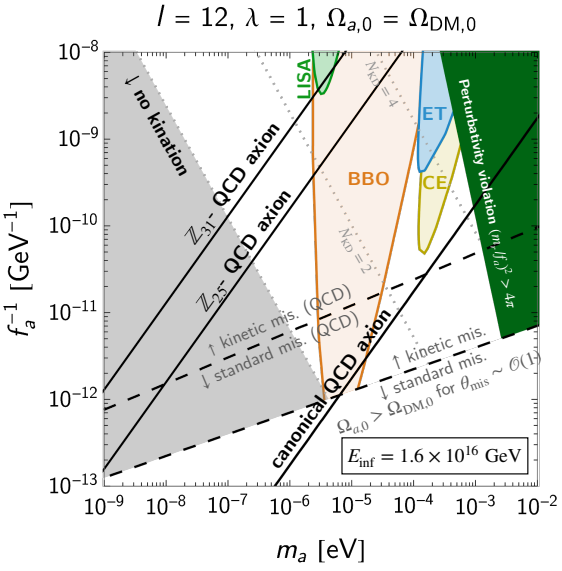

Figure 6.5: Sensitivity of the future-planned GW observatories for probing the GW kination peak – in inflationary SGWB – induced by the rotating axion DM whose UV completion is discussed in Chap. 7 with scenario I. The region is the subset of the model-independent plot in Fig. 6.4 because now $(E_{\rm KD}, N_{\rm KD})$ are not free parameters but are determined by model parameters. The region above the dashed lines explains DM via the kinetic misalignment. Two dashed line correspond to the axion DM from the standard misalignment, assuming the tempereature dependent (denoted QCD) and independent mass, cf. Eq. (6.3). See other colored regions in the next chapter, e.g. Fig. 7.10.

Scalar fluctuation bound. The presence of scalar fluctuation of the order $\rho/\delta\rho \sim 10^{9\div10}$, cf. Sec. 4.4.4, puts an upper limit on the duration of kination $N_{\rm KD} \lesssim 11$. Therefore, the predicted observable region should not include the signal that needs large $N_{\rm KD}$. Equivalently, the scalar fluctuation bound excludes the observable region for

$$m_a \lesssim \frac{1.3 \cdot 10^{-11}\ \text{eV}}{G^{3/4}(T_{\rm KD}) G^{1/4}(T_\Delta)} \left(\frac{f_{\rm sens,min}}{\text{Hz}}\right) \left(\frac{10^9\ \text{GeV}}{f_a}\right) \left(\frac{e^{11}}{e^{N_{\rm KD}^{\rm max}}}\right)^2 \left(\frac{\Omega_{a,0}}{\Omega_{\rm DM,0}}\right), \tag{6.26}$$

corresponding to the region on the left of each ($N_{\rm KD} = 11$) line in Fig. 6.4.

Trapping before kination ends. After the start of kination, the axion speed $\dot{\theta} \propto a^{-3}$ should not drop below m_a and gets trapped before the kination ends. Otherwise, the kination era stops earlier than expected, and the Universe is over closed by the axion oscillation energy density. The energy scale at the end of kination must be larger than the scale of the potential barrier; see also App. F: $\rho_\Delta = \rho_{\rm KD} \exp(-6N_{\rm KD}) \gtrsim m_a^2 f_a^2$, which leads to a lower bound on the axion mass

$$m_a \lesssim (2.9 \times 10^{-19}\ {\rm eV}) G^{-3/2}(T_{\rm KD}) \left(\frac{10^9\ {\rm GeV}}{f_a}\right) \left(\frac{\Omega_{\rm a,0}}{\Omega_{\rm DM,0}}\right)^2 . \tag{6.27}$$

For ALP DM, this bound is weaker than the BBN bound in Eq. (6.24).

Fragmentation before kination ends. Ref. [129] – recently confirmed by lattice simulations [130] – shows that the zero-mode axion, that rolls fast past the oscillatory potential barrier, can lead to its fragmentation into the axion fluctuation if it satisfies the condition $4H f_a^4 \dot{\theta}^3 < \pi \Lambda_b^8 W_0^{-1}$, where W_0 is the 0th branch of the product log-function. We impose that kination does not end because of fragmentation but because of SM radiation. It is straightforward to find the spinning speed $\dot{\theta}_\Delta$ and the Hubble parameter H_Δ at the end of kination. Therefore, the kination ends by fragmentation if

$$E_\Delta < \Lambda_b \left(\frac{\sqrt{3}\pi}{4}\right)^{1/8} \left(\frac{M_{\rm Pl}}{f_a}\right)^{1/8} W_0^{-1/8} \simeq \Lambda_b . \tag{6.28}$$

This leads to a similar bound as the trapping condition before kination ends in Eq. (6.27).

6.4.3 What if Axion DM generates both kination and GW?

An intriguing possibility would be if the $U(1)$-breaking leads to both: the cosmic-string network and the rotating axion generating the matter-kination era and DM. I.e., The global (axion) strings with scale $\eta = f_a$, though it is not clear if this is a viable possibility[7]. SGWB produced by CS and their enhancement by a pre-BBN kination era are studied in Sec. 4.7.1. Similar to the GW peak from primordial inflation in Eq. (6.17), the peak position in the SGWB from CS can be related to the axion abundance, using Eqs. (4.71) and (4.69),

$$f_{\rm KD} \simeq (1.83\ {\rm kHz}) G^{\frac{3}{4}}(T_{\rm KD}) \left[\frac{0.1}{\alpha}\right] \left[\frac{f_a}{10^{15}\ {\rm GeV}}\right] \left[\frac{m_a}{\mu{\rm eV}}\right] \left[\frac{\Omega_{\rm DM,0}}{\Omega_{a,0}}\right] e^{2N_{\rm KD}} , \tag{6.29}$$

$$\Omega_{\rm GW}^{\rm KD} \simeq 6.57 \cdot 10^{-22} G^{\frac{-3}{4}}(T_{\rm KD}) \left[\frac{\alpha}{0.1}\right] \left[\frac{f_{\rm KD}}{\rm Hz}\right] \left[\frac{f_a}{10^{15}\ {\rm GeV}}\right]^3 \left[\frac{\mu{\rm eV}}{m_a}\right] \left[\frac{\Omega_{a,0}}{\Omega_{\rm DM,0}}\right] \times \log^3 \left[(4.17 \cdot 10^{22}) \left[\frac{\alpha}{0.1}\right]^{\frac{1}{2}} G^3(T_{\rm KD}) \left[\frac{\rm Hz}{f_{\rm KD}}\right]^{\frac{3}{2}} \left[\frac{f_a}{10^{15}\ {\rm GeV}}\right]^{\frac{1}{2}} \left[\frac{\mu{\rm eV}}{m_a}\right]^{\frac{1}{2}} \left[\frac{\Omega_{a,0}}{\Omega_{\rm DM,0}}\right]^{\frac{1}{2}}\right] . \tag{6.30}$$

Fig. 6.6 shows the axion parameter space where the peak signal from axionic strings is observable by future detectors. As expected, the higher the f_a value, the larger the peak amplitude.

Two-peak signature. — In some regions of the parameter space, future experiments could observe two GW peaks: from the primordial inflation, cf. Fig. 6.4 and the axionic strings, cf. Fig. 6.6, resulting from the imprint of the matter-kination era. In particular, a gray band shows where the two peaks are distinguishable, i.e., the inter-peak distance is more than two orders of magnitude in frequencies, cf. Eq. (4.77). This occurs when the two conditions (4.78) and (4.79) are satisfied.

[7] The GW emission requires the existence of topological defects which imply the inhomogeneities. In contrast, the matter-kination era assumes a homogeneous condensate. We leave to future work a thorough investigation of how the presence of gradient terms in the energy density modifies the EOS of the complex scalar field. However, the rotation scalar field supports the cosmic-string (vortex) solution, regardless of its formation mechanism [686].

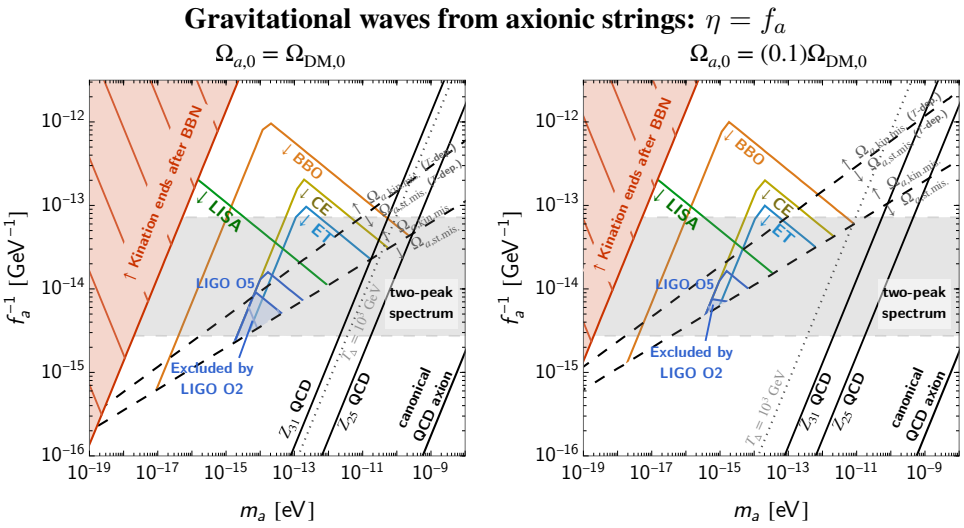

Figure 6.6: The rotating axion-DM field generating both the matter-kination era and the cosmic strings sourcing SGWB. Colored solid lines show the observability of the resulting matter-kination enhanced GW peak. The upper bounds on the duration of the kination era $N_{\rm KD} \lesssim 11$, discussed in Sec. 4.4.4, prevents the detectability windows going to smaller m_a. Additionally, the gray band shows the region where GW peaks from the axionic strings and inflation coexist, assuming $E_{\rm inf} = 1.6 \times 10^{16}$ GeV, cf. Eqs. (4.78) and (4.79). The descriptions of each line, see Fig. 6.4.

6.5 Kination GW Signature & Rotating axion Baryogenesis

Another phenomenology of the rotating axion is that it provides an alternative Baryogenesis mechanism, so-called *axiogenesis* [669, 687][8]. The fast-rotating axion carries a large $U(1)$-charge, which can be transferred to the chiral asymmetry of SM quarks through $SU(3)_{\rm c}$ sphaleron transitions. Later the $SU(2)_L$ sphalerons convert this asymmetry into the baryon asymmetry. As shown in the supplementary material of [669], when the scalar field thermalizes with the plasma, most of the $U(1)$ charge remains in the condensates if the scalar field VEV is much larger than the temperature $\phi \gg T$. Only a fraction $T_{\rm ws}^2/f_a^2$ of the $U(1)$ charge (initially $Y_\theta \equiv n_\theta/s$) is converted into the baryon number, $Y_B \equiv n_B/s$,

$$Y_B \;=\; \frac{n_\theta}{s}\left(c_B \frac{T_{\rm ws}^2}{f_a^2}\right) \;=\; 8\times 10^{-11}\left(\frac{c_B}{0.1}\right)\left(\frac{T_{\rm ws}}{130\ {\rm GeV}}\right)^2\left(\frac{10^8\ {\rm GeV}}{f_a}\right)^2\left(\frac{Y_\theta}{500}\right), \qquad (6.31)$$

where $c_B \sim \mathcal{O}(0.1)$ charaterizes the interactions between baryons and the axion, $T_{\rm ws}$ is the temperature when electroweak sphaleron freezes-out, which is around $T_{\rm ws} \sim 130$ GeV for SM [689]. The current value for the yield of baryon asymmetry is given by $Y_B = n_{B,0}/s_0 \simeq 10^{-10}$, where the number density of baryon today is $n_B \simeq 2.515 \times 10^{-7}{\rm cm}^{-3}$ [39].

Eqs. (6.12) and (6.31) relates the baryon asymmetry to the energy scale and duration of kination,

$$E_{\rm KD} \simeq 74\ {\rm TeV}\, G^{3/4}(T_{\rm KD})\left[\frac{c_B}{0.1}\right]\left[\frac{T_{\rm ws}}{130\ {\rm GeV}}\right]^2\left[\frac{10^8\ {\rm GeV}}{f_a}\right]\left[\frac{10^{-10}}{Y_B}\right]\exp\left[\frac{3N_{\rm KD}}{2}\right], \qquad (6.32)$$

[8]The three Sakharov conditions for Baryogenesis [688] are satisfied: B number is violated by SM sphaleron; CP is violated spontaneously by the rotation of the complex scalar field in one specific direction; the dynamic is far from equilibrium due to the presence of the condensate.

which leads to the peak signature in the inflationary SGWB, via Eqs. (4.55) and (4.56),

$$f_{\rm KD} \simeq 0.79\ {\rm mHz}\, G^{\frac{1}{4}}(T_\Delta) G^{\frac{3}{4}}(T_{\rm KD}) \left[\frac{c_B}{0.1}\right] \left[\frac{T_{\rm ws}}{130\ {\rm GeV}}\right]^2 \left[\frac{10^8\ {\rm GeV}}{f_a}\right] \left[\frac{10^{-10}}{Y_B}\right] e^{2N_{\rm KD}}, \tag{6.33}$$

$$\Omega_{\rm GW}^{\rm KD} h^2 \simeq 1.6 \cdot 10^{-14} \left[\frac{G(T_\Delta)}{G(T_{\rm KD})}\right]^{\frac{3}{4}} \left[\frac{E_{\rm inf}}{10^{16}\ {\rm GeV}}\right]^4 \left[\frac{f_{\rm KD}}{\rm Hz}\right] \left[\frac{f_a}{10^8\ {\rm GeV}}\right] \left[\frac{0.1}{c_B}\right] \left[\frac{130\ {\rm GeV}}{T_{\rm ws}}\right]^2 \left[\frac{Y_B}{10^{-10}}\right]. \tag{6.34}$$

Fig. 6.7 shows the kination-matter peak positions associated to the correct baryon asymmetry from the rotating axion of a given f_a.

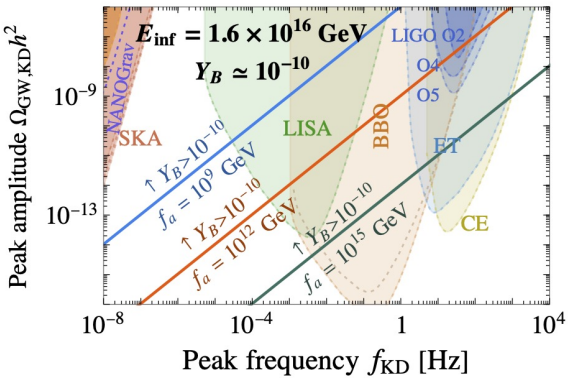

Figure 6.7: Reach of future interferometers to probe the GW peak signature in inflationary GW due to the presence of a matter-kination era induced by a rotating axion which also generates the correct baryon asymmetry. We fixed $c_B = 0.1$ and $T_{\rm ws} = 130$ GeV in Eq. (6.31).

Too much DM for Baryogenesis. — Using Eqs. (6.5) and (6.31), the axion abundance relates to the baryon asymmetry by

$$\frac{\Omega_a}{\Omega_{\rm DM}} \simeq 7006 \left(\frac{0.1}{c_B}\right) \left(\frac{130\ {\rm GeV}}{T_{\rm ws}}\right)^2 \left(\frac{m_a}{1\ {\rm eV}}\right) \left(\frac{f_a}{10^8\ {\rm GeV}}\right)^2 \left(\frac{Y_B}{10^{-10}}\right). \tag{6.35}$$

The QCD axion clearly overcloses the Universe for a correct baryon asymmetry, as argued in [669]:

$$\frac{\Omega_a}{\Omega_{\rm DM}} \simeq 399 \left(\frac{0.1}{c_B}\right) \left(\frac{130\ {\rm GeV}}{T_{\rm ws}}\right)^2 \left(\frac{f_a}{10^8\ {\rm GeV}}\right) \left(\frac{Y_B}{10^{-10}}\right). \tag{6.36}$$

Indeed, the QCD axion can solve DM and Baryogenesis altogether if the PQ-charge transfer to the baryon asymmetry becomes more efficient. Examples are: when the electroweak sphalerons freeze-out at a larger temperature $T_{\rm ws}$ [690–693], if the weak anomaly of $U(1)_{\rm PQ}$ is larger (larger c_B) [669], in the presence of the dimension-5 Weinberg operator giving a Majorana mass to the SM neutrinos [648, 694, 695], or in the presence of supersymmetric R-parity violating couplings [696].

6.6 Chapter Summary

This chapter presents a possible and (we believe) unique framework of the intermediate kination era – inside the standard radiation era – in cosmological history. So far, literature treats the kination mainly as a phenomenon coming from the dynamics after the end of inflation and before reheating to the SM thermal bath. Our main point is that a kination era can occur completely independently of the inflationary sector, inside the standard radiation era, and instead from the early dynamics of an axion field. Though the axion naturally has EOS of matter-kination-matter if it undergoes two-stage oscillation due to the varying axion mass, it cannot lead alone to an intermediate kination era because the sector – responsible for the disappearance of the axion's high-scale mass – necessarily

dominates over the axion's energy density. The most straightforward extension is to include the axion partner, the radial mode of the PQ field. Their interplay can naturally induce a stage of rotating axion, and the intermediate matter-kination era naturally follows, as justified in detail in Chap. 7.

We showed in Chap.4 that the intermediate matter-kination era leads to the distinctive *peaked* signature in the primordial SGWB, which would serve as a unique probe of axion physics. As the axion is one of the prime DM candidates, from the GW signature (peak frequency and amplitude) of the rotating axion kination we can directly infer the energy scale $\sqrt{m_a f_a}$ of the axion potential, cf. Eq. (6.17). The main DM production mechanism differs from the usual misalignment mechanism due to the dominant kinetic energy of the axion. It falls into the regime of the *kinetic misalignment* [449, 450] and *kinetic fragmentation* [129, 130, 132]. These mechanisms open up the parameter space of the axion with a lighter mass – than the standard scenario – for being an interesting DM candidate. Nonetheless, the rotating axion whose mass comes from the conventional QCD effect cannot lead to any observable signature in the conservative inflationary SGWB, except at BBO. The detectable regions are yet widely opened for the QCD axion with lighter mass, as motivated by the axion non-linearly realized $\mathbb{Z}_{\mathcal{N}}$ symmetry [661–664].

Furthermore, the rotating axion serves as a successful baryogenesis mechanism in the context of the *axiogenesis* model, where the $U(1)$ charge of the rotating axion transfers to the baryon asymmetry via the strong and weak sphalerons. One possible way to probe such a scenario is the GW signature of the spinning-axion kination, which is observable for a broad range of axion decay constant. Finally, a particularly intriguing scenario is when the $U(1)$-breaking – generating the rotating axion – also leads to the global string network whose GW emission is enhanced by the matter-kination era induced by the rotating axion itself. The axion strings with a non-vanishing axion speed – recently been shown to exist [686] – would entirely change the vanilla cosmic-string paradigm, e.g., the *scaling* regime, the particle production, and GW emission. It will be worth investigating such a *rotating axionic string scenario* in more detail.

After the general and model-independent rotating-axion discussions, the next chapter concerns model-building and connects the energy scale $E_{\rm KD}$ and duration $N_{\rm KD}$ of the kination era to the model parameters. We analyze in detail the conditions in particle-physics parameter space and chart observable regions at GW observatories.

Chapter 7

Intermediate Kination-Domination Era: Rotating Axion II (model-dependent)

Based on
[4] Y. Gouttenoire, G. Servant and P. Simakachorn, ***Kination cosmology from scalar fields and gravitational-wave signatures****, [2111.01150].*

The intermediate kination cannot arise from the only axion degree of freedom (angular direction of some complex scalar field), as discussed in Sec. 6.2. We emphasize that its interplay with the radial component is the crucial ingredient that induces a matter era – allowing its domination over the SM radiation. Eventually, the field reaches the bottom of the potential, and the kination era starts due to the axion speed. In addition to the kination era, the rotating axion persists to later times and allows interesting phenomenology: e.g., DM and Baryogenesis, discussed in Secs. 6.4 and 6.5.

In this chapter, we consider a UV-completion of the rotating axion that can lead to the kination-domination era, first suggested in appendixes of [648] and studied in detail in [3, 4, 274]. Our focus is on a class of models studied in detail by Co and Harigaya et al. [449, 648, 669, 697], where their main aims are for DM production and Baryogenesis[1]. We first review the model set-up and then the evolution of a rotating complex scalar field in an expanding Universe (cf. Fig. 6.1): from the early times during inflation when it has a large radial value $\phi \gg f_a$ until when it reaches the zero-temperature minimum in $\phi = f_a$. Sec. 7.1 discusses the necessary conditions for generating a kination era.

As we shall see, the vital obstacle for generating a kination EOS is that the energy density in the radial mode must be damped. The optimal case happens when this damping occurs before the scalar field energy density dominates. A kination era may still happen otherwise but the entropy injection will shorten its duration. In this work, two damping mechanisms can be invoked: through non-thermal process at early times (cf. Sec. 7.2) or through thermal effects (cf. 7.3 & 7.4). The latter case relies on the interaction of the radial mode with particles in the thermal bath. The predictions of the duration of the kination era and the observability of GW peak signature – from primordial inflation, local or global cosmic strings – have been provided exhaustively. All the supportive details that enter the discussion are collected in App. G.

7.1 Complex Scalar Field Dynamics

We consider a complex scalar field Φ with a Lagrangian

$$\mathcal{L} = (\partial_\mu \Phi)^\dagger \partial^\mu \Phi - V(|\Phi|) - V_{\rm th}(|\Phi|, T) - \cancel{V_{U(1)}}(\Phi) - V_H(\Phi), \tag{7.1}$$

where $V(|\Phi|)$ is a global $U(1)$-symmetric potential with spontaneous symmetry breaking (SSB) vacuum, $V_{\rm th}(|\Phi|, T)$ are the finite-temperature corrections, $\cancel{V_{U(1)}}$ is an explicit $U(1)$-breaking

[1] We also note that earlier works study the dynamics of a complex scalar field leading to a kination era following inflation, by assuming the initial rotational velocity in the context of self-interacting dark matter [507–510].

term, and V_H is a Hubble-dependent term driving the field VEV to large values at early time. The complex scalar field can be parameterized by two real fields describing radial ϕ and angular θ directions

$$\Phi \;=\; \phi e^{i\theta}, \tag{7.2}$$

where the $U(1)$ symmetry acts as a shift symmetry for θ. We consider only the homogeneous part of the field, such that the Lagrangian in the angular representation is

$$\mathcal{L} \;=\; \frac{1}{2}\dot{\phi}^2 + \frac{1}{2}\phi^2\dot{\theta}^2 - V(|\Phi|) - V_{\rm th}(|\Phi|\,,T) - \cancel{V_{U(1)}}(\Phi) - V_H(\Phi), \tag{7.3}$$

where the first two terms denote the kinetic energy in the radial and angular modes, respectively.

7.1.1 Requirements for a kination era.

First, let us chart the big picture and list the special features of the model required for generating a matter-kination era:

- ***A $U(1)$-conserving potential $V(|\Phi|)$ with spontaneous symmetry breaking (SSB):*** In our scenario, the kination era occurs when a rotating scalar field – which dominates the energy density of the Universe – rotates along the flat direction of its SSB minimum.
- ***An explicit $U(1)$-breaking potential $\cancel{V_{U(1)}}(\Phi)$:*** The rotation of the field condensate is induced by an early kick in the angular direction due to the presence of an explicit breaking potential, similarly to the *Affleck-Dine* mechanism [599].
- ***A large initial radial field-value $\phi_{\rm ini}$:*** For the explicit breaking of higher-order terms in the potential to kick the scalar field, we need a mechanism (encoded in $V_H(\Phi)$) to drive the scalar field to a considerable value in the early Universe.
- ***A mechanism for damping the radial mode:*** After the kick, the field condensate undergoes an elliptic motion. A damping mechanism of radial mode is necessary, so a circular trajectory is reached. Therefore, the energy density is dominated by the kinetic energy of the angular mode when the field settles down to the SSB vacuum, resulting in a kination era. The radial damping requires the (approximately) $U(1)$-conserved interaction that could arise from the non-thermal or thermal origins.

7.1.2 $U(1)$-conserving potential with spontaneous symmetry breaking

Zero-temperature potential

In App. G.4.2 and G.4.4, we show that a potential shallower than quartic is needed for the scalar-field energy density to redshift slower than radiation and to dominate the energy density of the Universe. Therefore, we consider a nearly-quadratic potential with a flat direction at the minimum,

$$V(|\Phi|) \;=\; m_r^2|\Phi|^2\left(\ln\frac{|\Phi|^2}{f_a^2} - 1\right) + m_r^2 f_a^2 \;+\; \frac{\lambda^2}{M_{\rm pl}^{2l-6}}|\Phi|^{2l-2}, \tag{7.4}$$

where f_a is the radial-field value at the minimum. For $\phi \gg f_a$, the scalar field has an equation-of-state of matter, with the corresponding effective mass defined as

$$m_{r,\rm eff}^2 \equiv \frac{d^2V}{d|\Phi|^2} = 4m_r^2\left(1 + \ln\frac{|\Phi|}{f_a}\right). \tag{7.5}$$

which is field dependent. The quadratic potential in Eq. (7.4) can be generated in gravity-mediated SUSY-broken theories, cf. App. G.1.1, with m_r being equal to the gravitino mass, $m_r \simeq m_{3/2}$.

Moreover, the U(1)-symmetric quartic term can also arise, but it is negligible in the limit $\phi \lesssim M_{\rm pl}$ which is considered in this paper, as shown in App. G.1.1. The logarithmic function is generated by the running of the soft mass [698], cf. App. G.1.4 for a review. The origin of the last term in Eq. (7.4) is discussed in App. G.1.2 and provides the third ingredient for kination, discussed in Sec. 7.1.3.

Finite-temperature corrections

The interactions between the complex scalar and other fields at equilibrium with the thermal plasma generate thermal corrections to the potential. For definiteness, we assume that the complex scalar field ϕ is coupled to fermions ψ charged under some (hidden or SM) gauge sector A_μ

$$\mathcal{L} \supset y_\psi \phi \psi_L^\dagger \psi_R + h.c. + g\, \bar{\psi} \gamma^\mu \psi\, A_\mu. \tag{7.6}$$

Depending on the fermion mass $y_\psi \phi$, the thermal corrections read [699, 700]

$$V_{\rm th}(\phi,\, T) \;=\; \begin{cases} \frac{1}{2} y_\psi^2 T^2 \phi^2, & \text{for } y_\psi \phi \lesssim T, \\ \alpha^2 T^4 \ln(\frac{y_\psi^2 \phi^2}{T^2}), & \text{for } y_\psi \phi \gtrsim T, \end{cases} \tag{7.7}$$

with $\alpha \equiv g^2/4\pi$ the gauge coupling constant. Two regimes are:

- **Thermal mass** $y_\psi \phi \lesssim T$: fermions are relativistic and abundant in the thermal plasma.
- **Thermal-log** $y_\psi \phi \gtrsim T$: the fermions abundance is Boltzmann suppressed. The thermal corrections are obtained from the running of the gauge coupling constant g, after integrating out the heavy fermions [701–705].

A sketch of the thermal corrections to the zero-temperature potential is shown in Fig. 7.1.

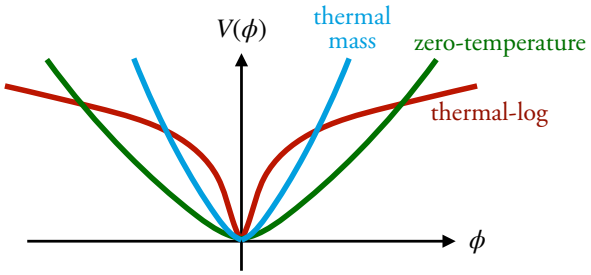

Figure 7.1: Sketch of the zero- and finite-temperature potentials.

Q-ball formation. Scalar fields – moving in a potential $V(\phi)$ where $V(\phi)/\phi^2$ has a non-trivial minimum – have stable non-topological localized field configurations, known as *Q-balls* [706]. This is the case of theories with negative radiative corrections to the mass term [707]: $m^2 = m_0^2(1 + \beta \ln(\phi))$, with $\beta < 0$. With a potential being flatter than quadratic, a condensate with a sizeable rotational charge has a centrifugal force larger than the potential gradient and fragments into higher modes [706]. Thermal-log potentials are flatter than quadratic are thus are expected to form Q-balls [699, 708, 709]. In order to preserve the condensate, the thermal-potential in the second line of Eq. (7.7) must be sub-dominant meaning that one of the two following conditions must be satisfied:

$$\begin{cases} y_\psi\, \phi \;\lesssim\; T, \\ 2\alpha T^2 \ln^{\frac{1}{2}}\left(\frac{y_\psi \phi}{T}\right) \;\lesssim\; m_{r,\rm eff}\, \phi, \end{cases} \quad \Rightarrow \quad \begin{cases} y_\psi \;\lesssim\; 3.4 \cdot 10^{-6} \left[\frac{T}{8.3\times 10^{12}}\right] \left[\frac{M_{\rm pl}}{\phi}\right], \\ T \;\lesssim\; 8.3 \cdot 10^{12} \left[\frac{m_{r,\rm eff}}{10^8\ \rm GeV}\right]^{\frac{1}{2}} \left[\frac{\phi}{M_{\rm pl}}\right]^{\frac{1}{2}} \left[\frac{0.1}{\alpha}\right]^{\frac{1}{2}} \left[\frac{25}{\ln\left(\frac{y_\psi \phi}{T}\right)}\right]^{\frac{1}{4}}. \end{cases} \tag{7.8}$$

Q-ball formation is avoided either by a small Yukawa coupling y_ψ, cf. scenario I in Sec. 7.2, or a small maximal plasma temperature $T_{\rm max}$, cf. scenario III in Sec. 7.4, and in particular outside the red region in Fig. 7.19-top-left. In contrast, scenario II presented in Sec. 7.3 controls neither Yukawa coupling nor the maximal plasma temperature. Both conditions in Eq. (7.8) could be violated and Q-balls could possibly form [699, 708, 709]. We do not investigate scenario II further, for it can not lead to any kination era.

7.1.3 Explicit $U(1)$-breaking potential

The general form of the explicit breaking term can be written as

$$V_{\cancel{U(1)}}(\Phi) \;=\; \Lambda_b^4 \sum_l \sum_{k\neq l} \left[\left(\frac{\Phi^\dagger}{M_{\rm pl}} \right)^l \left(\frac{\Phi}{M_{\rm pl}} \right)^k \;+\; \text{h.c.} \right], \tag{7.9}$$

where Λ_b is a mass scale, $M_{\rm pl}$ is the cut-off of the theory which we set equal to the Planck mass, and $l \neq k$ ensures the explicit breaking of the $U(1)$ symmetry. In this work, we will assume a simpler form where $k = 0$ and consider only one value of l. As discussed in App. G.1, the origin of Eq. (7.9) can be attributed to the interaction, in a SUSY theory, between soft-breaking terms and the higher-dimensional superpotential

$$\mathcal{L} \supset \int d^2\theta\, W(S_\Phi) \;+\; h.c., \;\; \text{with} \;\; W(S_\Phi) = \frac{\lambda}{l\, M_{\rm pl}^{l-3}} S_\Phi^l, \tag{7.10}$$

where S_Φ is the chiral superfield containing Φ and $\lambda = \mathcal{O}(1)$. The superpotential $W(S_\Phi)$ in Eq. (7.10) also generates a positive $\lambda^2\phi^{2l-2}$ term which insures stability at large field value and have already included in Eq. (7.4). In App. G.1.1, we obtain

$$V_{\cancel{U(1)}}(\phi,\theta) \;=\; \Lambda_b^4 \left[\left(\frac{\Phi^\dagger}{M_{\rm pl}} \right)^l + \left(\frac{\Phi}{M_{\rm pl}} \right)^l \right], \tag{7.11}$$

$$\text{with} \qquad \Lambda_b^4 = \lambda\, m_{3/2} M_{\rm pl}^3, \tag{7.12}$$

where the integer l corresponds both to the field order and the number of wiggles along the angular direction, cf. Fig 7.4.

7.1.4 Equations of motion

The evolution of the homogeneous field configuration is controlled by the Klein-Gordon equation in an expanding Universe,

$$\ddot{\Phi} + 3H\dot{\Phi} + \frac{\partial}{\partial\Phi^\dagger}\left(V + V_{\cancel{U(1)}} \right) \;=\; 0, \tag{7.13}$$

where H is the Hubble rate, and V is the total potential energy density that conserves $U(1)$ symmetry[2]. Plugging Eq. (7.11) in Eq. (7.13) and decomposing into radial and angular parts, the system of coupled equations of motion (EOM) becomes

$$\ddot{\phi} + 3H\dot{\phi} + \frac{\partial V}{\partial\phi} + 2l\cos\left[l\theta\right]\Lambda_b^3 \left(\frac{\Lambda_b}{M_{\rm pl}} \right) \left(\frac{\phi}{M_{\rm pl}} \right)^{l-1} \;=\; \phi\dot{\theta}^2, \tag{7.14}$$

$$\phi\ddot{\theta} + 3H\phi\dot{\theta} - 2l\sin\left[l\theta\right]\Lambda_b^3 \left(\frac{\Lambda_b}{M_{\rm pl}} \right) \left(\frac{\phi}{M_{\rm pl}} \right)^{l-1} \;=\; -\,2\dot{\phi}\dot{\theta}, \tag{7.15}$$

[2] An abuse of notation: $V = \sum_i V_i$ includes the zero-temperature V, the finite-temperature $V_{\rm th}$, and the higher-order V_H potentials in Eq. (7.3).

which is simply a Keplerian motion in a rotationally-invariant potential V, in the presence of small wiggles $V_{\cancel{U(1)}}$ and Hubble friction. The Friedmann equation controls the evolution of the Universe

$$H^2 \;=\; \frac{1}{3M_{\rm Pl}^2}\left(\rho_{\rm rad} + \dot{\phi}^2 + \phi^2\dot{\theta}^2 + V + V_{\rm th} + V_{\cancel{U(1)}} + V_H\right), \tag{7.16}$$

where $\rho_{\rm rad}$ is the radiation background energy density, and the scalar field has three components in its energy density: radial and angular kinetic energies and potential energy.

Generation of the $U(1)$ charge. The angular EOM in Eq. (7.15) can be recasted as Boltzmann equation of the $U(1)$ charge n_θ

$$\dot{n_\theta} + 3Hn_\theta \;=\; -\frac{\partial V_{\cancel{U(1)}}}{\partial\theta}, \qquad \text{with} \quad n_\theta \equiv \phi^2\dot{\theta}. \tag{7.17}$$

In App. G.4.1, we show that the field receives an angular kick at the onset of oscillation, $t_{\rm osc} \sim m_{r,\rm eff}^{-1}(\phi_{\rm ini})$ cf. Eq. (7.27), which for $V_{\cancel{U(1)}}(\theta)$ in Eq. (7.11) and $l \geq 4$, is given by

$$n_\theta \;=\; \phi_{\rm ini}^2\dot{\theta}_{\rm ini}\left(\frac{a_{\rm ini}}{a}\right)^3 \;=\; \left(\frac{12l}{6+q}\right)\Lambda_b^4\left(\frac{\phi_{\rm ini}}{M_{\rm pl}}\right)^l \frac{\sin(l\theta_{\rm ini})}{m_{r,\rm eff}(\phi_{\rm ini})}\left(\frac{a_{\rm ini}}{a}\right)^3, \tag{7.18}$$

where q is related to the equation of state of the Universe $H^2 \propto a^{-q}$ and where $m_{r,\rm eff}$ is defined in Eq. (7.5). After few Hubble times pass from the kick, ϕ has redshifted below $\phi \ll M_{\rm pl}$, and the angular EOM in Eq. (7.15) becomes a charge conservation equation

$$\frac{d}{dt}\left(a^3 n_\theta\right) \;=\; 0, \tag{7.19}$$

where n_θ is the comoving Noether charge of the restored $U(1)$ symmetry. As shown in Chap. 6, the U(1)-charge corresponds to the rotating axion and is the crucial quantity for characterizing kination era, DM, and Baryogenesis.

Quality problem of the Peccei-Quinn solution. If the global $U(1)$ symmetry is anomalous in a background of $SU(3)_c$ gluons, then a second $U(1)$-breaking potential is generated by QCD instantons around $T \simeq 100$ MeV [710–712]. In that case, the angular mode θ offers a solution to the strong CP problem known as the Peccei-Quinn QCD axion [439–441, 649]. The non-detection of the electric dipole moment of the neutron (nEDM) implies the upper bound [713–715]

$$\bar{\theta}_0 \;\lesssim\; 10^{-10}, \tag{7.20}$$

where $\bar{\theta}_0$ is the angle value today with respect to one of the CP-preserving [716] minimum of the QCD instanton potential. The presence of the higher dimentional $U(1)$-breaking potential in Eq. (7.11) is expected to shift the CP-preserving minimum by[3]

$$\Delta\theta \;\simeq\; l\frac{\Lambda_b^4}{\chi_0}\left(\frac{f_a}{M_{\rm pl}}\right)^l, \tag{7.21}$$

where $\chi_0 \equiv m_a^2 f_a^2 \simeq (75.6\ \text{MeV})^4$ is the susceptibility of the topological charge at zero temperature for the canonical QCD axion [658]. Using Eq. (7.12) with $m_{3/2} \simeq m_r$, the nEDM bound in Eq. (7.20) translates to

$$l\,\lambda\frac{m_r M_{\rm pl}^3}{\chi_0}\left(\frac{f_a}{M_{\rm pl}}\right)^l \;\lesssim\; 10^{-10}. \tag{7.22}$$

For $m_r/f_a \simeq 10^{-2}$, $\lambda = 10^{-4}$ and $f_a \simeq (10^8\ \text{GeV}, 10^{12}\ \text{GeV}, 10^{16}\ \text{GeV})$, the neutron EDM bound implies the following lower bounds $l \geq (7,\ 12,\ 34)$.

[3] We calculate the shift in the axion's potential minimum and obtain a similar condition as provided in Ref. [648] where the authors consider a different calculation, i.e. the mass contribution from the explicit breaking term.

7.1.5 Large initial vacuum expectation field-value

Supersymmetric theory

During the early Universe, the complex scalar field Φ can obtain a Hubble-induced negative mass and Hubble-induced higher dimensional terms [580, 582]

$$V_H(\Phi) \simeq -c\,H^2|\Phi|^2 + a\frac{H}{m_{3/2}}\Lambda_b^4\left[\left(\frac{\Phi}{M_{\rm pl}}\right)^l + h.c.\right], \qquad a,\, c = \mathcal{O}(1). \tag{7.23}$$

As shown in App. G.1.2, these naturally arise in SUSY theories in the presence of a gravity-mediated interaction in the Kähler potential

$$\mathcal{L} = \int d\theta^2 d\bar{\theta}^2 \left(a\frac{S_I + S_I^*}{M_{\rm pl}}|S_\phi|^2 + c\frac{|S_I|^2}{M_{\rm pl}^2}|S_\Phi|^2\right), \tag{7.24}$$

where S_Φ is the chiral superfield containing Φ and S_I is the chiral superfield whose F- or kinetic-term dominates the energy density of the Universe. At early time, the radial VEV of the scalar field is governed by the $U(1)$-conserving, $U(1)$-breaking and Hubble-induced terms in Eqs. (7.4), (7.11) and (7.23)

$$V(\Phi) = (m_{r,\rm eff}^2 - cH^2)|\Phi|^2 + \Lambda_b^4\left(1 + a\frac{H}{m_r}\right)\left[\left(\frac{\Phi}{M_{\rm pl}}\right)^l + h.c.\right] + \frac{\lambda^2}{M_{\rm pl}^{2n-6}}|\Phi|^{2l-2}. \tag{7.25}$$

With $c \sim \mathcal{O}(1)$ and $H \gtrsim m_{r,\rm eff}$, the Hubble friction $3H$ and the Hubble-induced mass term cH in the EOM are comparable, such that the scalar field is nearly critically-damped [589] and rolls exponentially fast (actually in $3/c$ e-folds of inflation) towards a non-trivial minimum at large field value

$$\phi_{\rm ini} = M_{\rm pl}\left(\sqrt{c}\frac{m_{r,\rm eff}(\phi_{\rm ini})}{\lambda\sqrt{2l-2}M_{\rm pl}}\right)^{\frac{1}{l-2}}, \tag{7.26}$$

for $a \lesssim c$, cf. App. G.1.3. When the Hubble scale crosses its mass

$$H_{\rm osc} \simeq m_{r,\rm eff}/3, \tag{7.27}$$

the field starts oscillating (under-damped motion) with an initial amplitude $\phi_{\rm ini}$. An oscillation in the angular direction with initial amplitude $\theta_{\rm ini} \sim \mathcal{O}(1)$ is generated by the same dynamics thanks to the Hubble-dependent $U(1)$-breaking terms in Eq. (7.23). We refer to App. G.1.3 for more details on the evolution of Φ at early stages.

Long kination requires large l. Even though it is not restricted to the Peccei-Quinn QCD axion, our study also motivates large values of l in order to maximize the amount of rotation ϵ, defined in Eq. (7.37), resulting from the angular kick, see Eq. (7.41), and to have initial radial value $\phi_{\rm ini}$ as large as possible, see Eq. (7.26). As we show in Eq. (7.34) and Eq. (7.35), the duration of the kination era depends crucially on those quantities. The impact of the value of l on the detectability of the GW peak signature can be seen from Fig. 7.10 to Fig. 7.12 of Sec. 7.2 or in Fig. 7.20 of Sec. 7.4.

Random fluctuations during inflation and some issues

Without any Hubble-induced mass term from the supersymmetry, the field can be driven at a large field value by the de Sitter (dS) fluctuations during inflation, namely the sub-horizon quantum modes in the dS background. During each Hubble time $H_{\rm inf}^{-1}$, the dynamics of a real scalar field

during inflation can be described as a superposition of quantum fluctuations $\delta\phi \simeq H_{\rm inf}/2\pi$ and classical motion $\Delta\phi \simeq V'/3H_{\rm inf}^2$, where $H_{\rm inf}$ is the Hubble scale during inflation. This interplay between random walk and restoring force determines the scalar field probability distribution as a solution to the associated Fokker-Planck equation. For a $U(1)$-preserving potential, the distribution spreads as [717, 718]

$$\left\langle \phi^2 \right\rangle = \frac{3H_{\rm inf}^4}{8\pi^2 m_\phi^2}\left[1-\exp\left[-\frac{2m_\phi^2}{3H_{\rm inf}}(t-t_0)\right]\right] \xrightarrow{N\gtrsim (H_{\rm inf}/m_\phi)^2} \frac{3H_{\rm inf}^4}{8\pi^2 m_\phi^2}, \tag{7.28}$$

where m_ϕ is the mass of the real scalar field. The arrow shows when the so-called Bunch-Davies equilibrium distribution is reached.[4] The correlation length l of dS fluctuations [717], $lH \sim \exp(\frac{3H_{\rm inf}^2}{2m_\phi^2})$, can be much larger than the Hubble horizon for relatively flat potential $m_\phi \ll H_{\rm inf}$, and therefore can give rise to a homogeneous condensate at a later time. The case of a complex scalar field is treated in [719] where it is shown that the averaged radial value is equal to Eq. (7.28), up to a factor 2

$$\left\langle \phi_{\rm ini}^2 \right\rangle \simeq \frac{3H_{\rm inf}^4}{4\pi^2 m_{r,\rm eff}^2}, \tag{7.29}$$

where $m_{r,\rm eff}$ is defined in Eq. (7.5). In the presence of an explicit $U(1)$-breaking, the averaged angle acquires a shift of order $\mathcal{O}(\epsilon)$, defined in Eq. (7.37), with respect to the values of θ along the valleys [719].[5] The scalar field remains frozen at $\left(\left\langle \phi_{\rm ini}^2 \right\rangle, \left\langle \theta_{\rm ini} \right\rangle\right)$ until the time of oscillation given by Eq. (7.27). Then, the $\mathcal{O}(\epsilon)$ shift of $\left\langle \theta_{\rm ini} \right\rangle$ acts as a kick in the angular direction.

In App. G.2, we show that in the absence of Hubble-size mass terms for the radial and angular modes in Eq. (7.23), quantum fluctuation during inflation leads to problematic adiabatic and isocurvature perturbations as well as to the formation of domain walls which are not bounded by cosmic strings. For those reasons, in this work we assume the presence of the Hubble-induced potential in Eq. (7.23) such that the radial VEV $\left\langle \phi_{\rm ini}^2 \right\rangle$ is set by Eq. (7.26) and not by Eq. (7.29).

7.1.6 Damping of the radial mode

After the complex field starts oscillating, it attains an elliptic orbit. Fig. 7.2 shows that the damping of radial kinetic energy $K_\phi = \dot\phi^2/2$ (green lines in left & right panels) is necessary for the complex scalar field to accomplish a circular orbit and to acquire a kination equation of state when it reaches the bottom of its potential $\phi \to f_a$. As motivated in the following, we consider the damping with the rate Γ via the (approximately[6]) $U(1)$-conserved interaction which enters in the radial-mode EOM as an additional friction term[7]:

$$\ddot\phi + (3H+\Gamma)\dot\phi + V'(\phi) = \dot\theta^2\phi, \quad \text{and} \quad \frac{d(a^3 n_\theta)}{dt} = 0, \tag{7.30}$$

[4] Basically, we can interpret the quantum fluctuations as due to the temperature of the dS space-time $H_{\rm inf}/2\pi$ such that the scalar field gets a thermal distribution satisfying $V(\phi) \simeq H_{\rm inf}^4$.

[5] The authors of [719] assume an explicit breaking of $U(1)$ of the form $V_{\not{U}(1)}(\Phi) = \lambda\left(\Phi^3\Phi^\dagger + \text{h.c.}\right)$, where λ can be either positive or negative. As a result, they find that the averaged angular amplitude is

$$\left\langle \tan\theta_{\rm ini} \right\rangle = \frac{\pm\sqrt{1-\frac{9\lambda H^4}{8\pi^2 m_{r,\rm eff}^4}}}{\pm\sqrt{1+\frac{9\lambda H^4}{8\pi^2 m_{r,\rm eff}^4}}} \Rightarrow \left\langle \theta_{\rm ini} \right\rangle \simeq (2n+1)\frac{\pi}{4} \pm \frac{9H^4}{8\pi^2 m_{r,\rm eff}^4}\lambda,$$

where $\lambda \ll m_{r,\rm eff}^4/H^4$ by assumption, and n is an integer.

[6] If the wash-out of $U(1)$ charge is suppressed, the rotation is left intact after the damping.

[7] Here, the friction invokes for the damping of radial mode – a partner of the axion. Recently, it has been shown that the presence of friction can substantially modify the usual prediction and opens-up parameter spaces for axion DM [667, 668].

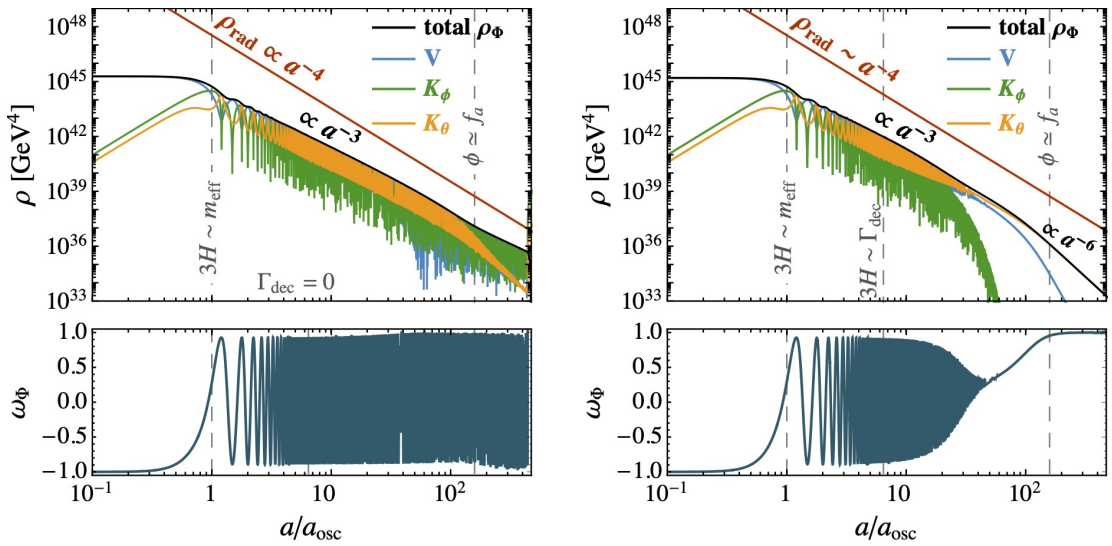

Figure 7.2: Evolution of complex field energy density without (**left**) and with (**right**) radial damping. Only the latter case gives rise to a kination equation of state when the complex scalar field reaches the degenerate minimum of its potential $\phi \to f_a$ (**bottom**). Obtained after numerically integrating the equations of motion in Eqs. (7.14), (7.15) and (7.16).

where we omit the explicit breaking-terms because they are only effective around the time of oscillation. The rate Γ can be identified as the decay or thermalization rate of a particle ϕ [81, 700]. Because the oscillation of a homogeneous scalar field is a coherent state of a scalar particle. When the damping rate becomes the dominant friction (i.e. $3H \sim \Gamma$ or the total energy density of the Universe is $\rho_{\rm damp} = 3M_{\rm Pl}^2\Gamma^2$), the radial motion is suppressed ($\dot\phi \to 0$), up to the cosmic expansion, cf. the right panel of Fig. 7.2. The field reaches the circular orbit because of the balance between the centrifugal force and the potential gradient, cf. App. G.4.4. Furthermore, the field's energy density could be reduced substantially if the orbit before damping is highly elliptic, cf. App. G.4.3.

In this work, we consider two mechanisms for damping the radial mode:

1) Parametric resonance: In App. G.3.2, we discuss qualitatively the possibility that parametric resonance could dampen the radial mode while preserving the $U(1)$ charge n_θ. However, we leave the quantitative study of the realistic efficiency of this damping mechanism for further studies.

2) Thermalization: We assume that the complex scalar field ϕ is coupled to fermions ψ charged under some (hidden or SM) gauge sector A_μ (KSVZ-type interactions)

$$\mathcal{L} \supset y_\psi \phi \psi_L^\dagger \psi_R + h.c. + g\,\bar\psi\gamma^\mu\psi\,A_\mu. \tag{7.31}$$

As a consequence, the scalar condensate thermalizes with the thermal plasma when the decay rate Γ into fermions[8], given in Eq. (G.69) of App. G.3.1, is larger than H. Higgs interactions are not sufficient enough, as discussed in App. G.3.1. Therefore, we focus on thermal effects from the fermionic portal. As shown in the supplementary material of [669], as long as $\phi \gg T$, it is energetically more favorable to keep the $U(1)$ charge in the condensate after thermalization. The condensate has an energy density $\rho_\phi = \phi^2\dot\theta^2$ larger than in the one converted to plasma, $\rho_{\rm rad} \supset \phi^4\dot\theta^2/T^2$. In the presence of this interaction, the scalar field dynamics can be dominated by its thermal mass

$$m_{r,{\rm eff},T}^2 = m_{r,{\rm eff}}^2 + y_\psi^2 T^2, \tag{7.32}$$

[8]The damping of condensate can be viewed in another direction. The slowly moving homogeneous scalar field changes the masses and parameters of the thermal plasma. It drives them slightly out of equilibrium, inducing the fluid viscosity, and the damping coefficient for scalar motion [703, 720].

after the onset of radial mode oscillation, if the Yukawa coupling y_ψ is larger than

$$y_\psi T_{\rm osc} \;>\; m_{r,\rm eff} \quad \Rightarrow \quad y_\psi \;\gtrsim\; g_*^{1/4}\sqrt{\frac{m_{r,\rm eff}}{M_{\rm pl}}}, \tag{7.33}$$

where $3H_{\rm osc} \simeq \left(\frac{\pi^2 g_*}{10}\right)^{1/2} T_{\rm osc}^2/M_{\rm pl} \simeq m_{r,\rm eff}$. We consider *three possible scenarios* for the damping of the radial mode:

1. **Scenario I.** The complex scalar field is assumed to evolve in the **zero-temperature** potential $V(\phi) = m_{r,\rm eff}^2(\phi)\phi^2/2$, which implies a small Yukawa coupling $y_\psi \lesssim \sqrt{m_{r,\rm eff}/M_{\rm pl}}$, cf. Eq. (7.33). As shown in gray region the lower panel of Fig. 7.18, thermalization with such small Yukawa coupling is not efficient to damp early enough the radial mode and cannot lead to kination. Instead, we assume that radial damping occurs **non-thermally** via some unknown mechanism, for which **parametric resonance** appears as a possible candidate, cf. App. G.3.2. This leads to the largest prediction for the number of kination e-folds $N_{\rm KD}$. This is the scenario considered in the next Sec. 7.2. The longest duration of kination is obtained in Eq. (7.57)

$$e^{N_{\rm KD}} \;=\; e^{8.2}\,\epsilon^{2/3}\left(\frac{10^9\ {\rm GeV}}{f_a}\right)^{1/3}\left(\frac{m_{r,\rm eff}(\phi_{\rm ini})}{5m_{r,\rm eff}(f_a)}\right)^{1/3}\left(\frac{\phi_{\rm ini}}{M_{\rm pl}}\right)^{4/3}. \tag{7.34}$$

2. Radial damping occurs via **thermalization**. Large $N_{\rm KD}$ requires that thermalization occurs before scalar field domination to prevent entropy injection. This implies a large Yukawa coupling y_ψ and potentially large thermal effects. We consider two possibilities:

   - **Scenario II.** The dynamics of the complex scalar field is controlled by its **thermal mass** $V(\phi) = \frac{1}{2}y_\psi^2 T^2\phi^2$. In Sec. 7.3 we show that the thermal mass prevents a kinaton-dominated era due to the initial angular kick ϵ being suppressed and also to the scalar field starting oscillating earlier.
   - **Scenario III.** The fermions responsible for the thermal corrections of the potential are Boltzmann-suppressed when the scalar field starts oscillating. Therefore, the scalar field evolves in its zero-temperature potential, and thermal effects do not spoil the efficiency of the angular kick. This scenario is presented in Sec. 7.4. The longest period of kination is cf. Eq. (7.112)

$$e^{N_{\rm KD}}\big|_{y_\psi = y_{\psi,*}} = e^{5.1}\frac{\epsilon^{\frac{2}{3}}}{\alpha^{\frac{1}{3}} g_*^{\frac{1}{4}}}\left(\frac{10^8}{f_a}\right)^{\frac{1}{6}}\left(\frac{m_{r,\rm eff}(f_a)}{f_a}\right)^{\frac{1}{6}}\left(\frac{m_{r,\rm eff}(\phi_{\rm ini})}{m_{r,\rm eff}(f_a)}\right)^{\frac{1}{2}}\left(\frac{0.1M_{\rm pl}}{\phi_{\rm ini}}\right)^{\frac{2}{3}}. \tag{7.35}$$

7.2 Scenario I: Non-Thermal Damping

When the couplings between the complex scalar condensate Φ and the thermal plasma are suppressed, we can ignore the thermal corrections to the potential in Eq. (7.7). We impose the thermal mass to be negligible at the onset of the radial mode oscillation. Focusing on the case where Φ couples to thermal fermions through a Yukawa coupling y_ψ as defined in Eq. (7.6), this implies

$$y_\psi T_{\rm osc} \;\lesssim\; m_{r,\rm eff}(\phi_{\rm ini}) \quad \Rightarrow \quad y_\psi \lesssim g_*^{1/4}\frac{m_{r,\rm eff}(\phi_{\rm ini})}{M_{\rm pl}}, \tag{7.36}$$

where we have used $y_\psi T_{\rm osc} \simeq 3H(T)$.

In App. G.3.1, we show that it is impossible to efficiently damp the radial mode via thermalization while neglecting thermal corrections at the onset of the scalar field oscillation. Instead, in the present section, we assume that radial damping takes place via a non-thermal mechanism (possibly parametric resonance cf. App. G.3.2), and we consider the radial damping rate Γ to be a free parameter.

7.2.1 Field trajectory

In Fig. 7.3, we outline the main stages of evolution of the rotating complex scalar field:

- First, the Hubble-induced and the higher-order potentials in Eq. (7.4) initially freeze the scalar field at a large field value $\phi_{\rm ini}$ and at a displaced angle $\theta_{\rm ini}$ with respect to the valleys of the potential, see Sec. 7.1.5.
- Second, the field starts oscillating when its dynamics become under-damped $3H_{\rm osc} \simeq m_{r,\rm eff}$. Thanks to the initial kick induced by the $U(1)$ breaking potential, see Sec. 7.1.3, the complex scalar field obtains an elliptic motion, whose size reduces with the cosmic expansion. For a nearly-quadratic potential, see Sec. 7.1.2, the scalar field energy density redshifts as matter $\rho_\phi \propto a^{-3}$ and starts dominating the energy density of the Universe.
- Third, the oscillation along the radial direction is damped due to either parametric resonance or thermalization in Secs. 7.3 and 7.4, while the angular motion remains, see Sec. 7.1.6. This happens when the damping mechanism becomes more efficient than the Hubble rate, $3H_{\rm damp} \sim \Gamma$.
- After this stage, the field rotates coherently in a circle with a continuously reducing size. When the orbiting field reaches the bottom of the potential, its kinetic energy dominates its potential energy and gives rise to a kination equation of state.

The numerical computation of the whole trajectory of the scalar field from the onset of the oscillation until the end of the kination era is shown in Figs. 7.5 and 7.7, cf. also our animation. For further details on the field evolution, we refer the interested readers to App. G.4.

Amount of rotation. We introduce the ratio between number densities in the angular mode and in the radial mode[9]

$$\epsilon \equiv \frac{\phi^2\dot\theta/2}{V(\phi)/m_{r,\rm eff}(\phi)} = \frac{\phi_{\rm ini}^2\dot\theta_{\rm ini}/2}{V(\phi)/m_{r,\rm eff}(\phi)}\left(\frac{a_{\rm ini}}{a}\right)^3 . \tag{7.37}$$

From using $(\phi_{\rm ini}/M_{\rm pl})^{l-2} = \sqrt{c}m_{r,\rm eff}(\phi_{\rm ini})/\lambda\sqrt{2l-2}M_{\rm pl}$, cf. Eq. (7.26), we find that the term in the potential – dominating the scalar dynamics at the onset of the radial-mode oscillation – depends on the value of c,

$$V(\phi_{\rm ini}) = \begin{cases} \lambda^2\frac{\phi_{\rm ini}^{2l-2}}{M_{\rm pl}^{2l-6}}, & \text{if } c > l-1, \\ \frac{1}{2}m_{r,\rm eff}^2(\phi_{\rm ini})\phi_{\rm ini}^2, & \text{otherwise.} \end{cases} \tag{7.38}$$

In the first case, the scalar field redshift as, cf. App. G.4.2

$$\phi \propto a^{-\frac{6}{2+n}}, \quad \text{with } n = 2l-2. \tag{7.39}$$

[9] ϵ is related to Y_θ defined in Eq. (6.11) through $\epsilon = sY_\theta m_{r,\rm eff}(\phi)/(2V(\phi))$, where $s = \frac{2\pi^2}{45}g_*T^3$. In successful setup, the quantity ϵ is bounded by above $\epsilon \lesssim 1$, where $\epsilon = 1$ corresponds to a field trajectory which would be already circular at the onset of the radial mode oscillation. In that sense, ϵ can be called the $U(1)$ charge fraction contained in the condensate, 1 being the maximal value.

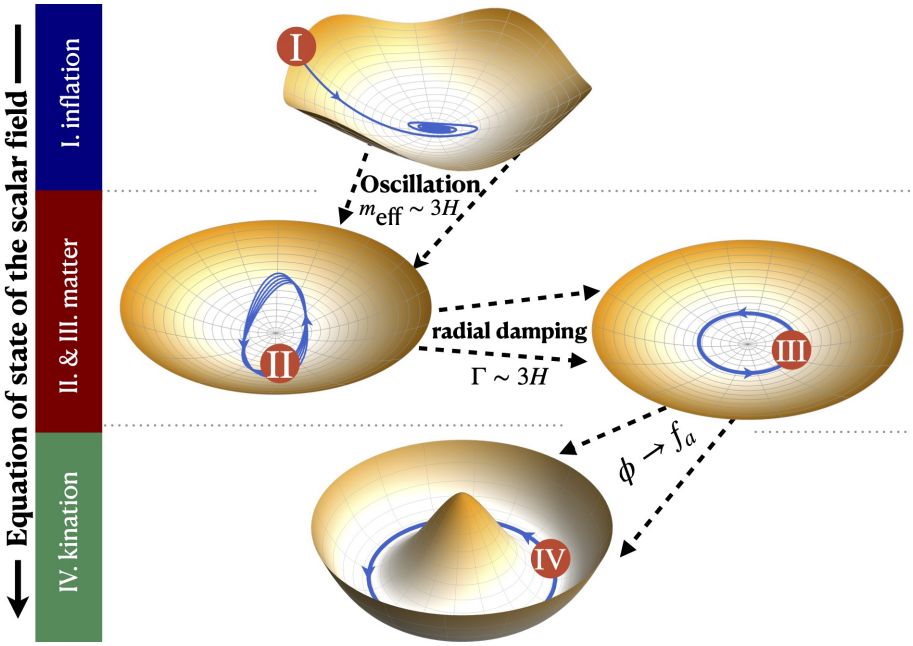

Stages		Hubble factor	Field value	Energy density
I.	Field frozen or track large-field minimum	$3H > m_{r,\rm eff},\ \Gamma$	$\phi = \phi_{\rm ini}$	$\rho_\Phi \propto a^0$
II.	Elliptic orbit: oscillation and rotation	$m_{r,\rm eff} \geq 3H > \Gamma$	$\phi_{\rm ini} > \phi > f_a$	$\rho_\Phi \propto a^{-3}$
III.	Circular orbit after radial damping	$m_{r,\rm eff},\ \Gamma > 3H$		
IV.	Rotation at potential minimum		$\phi = f_a$	$\rho \propto a^{-6}$

Figure 7.3: Different stages of evolution of the scalar field, leading to the matter-kination EOS. The side bar on the left shows the EOS of the scalar field. We invite the interested reader to visualize our animation.

until the nearly-quadratic term ϕ^2 dominates around the field value $\phi_{\rm quad}$

$$\frac{1}{2} m_{r,\rm eff}^2(\phi_{\rm quad}) \phi_{\rm quad}^2 \;=\; \lambda^2 \frac{\phi_{\rm quad}^{2l-2}}{M_{\rm pl}^{2l-6}}. \tag{7.40}$$

For $\phi < \phi_{\rm quad}$, the quantity ϵ defined in Eq. (7.37) becomes a conserved quantity since both numerator and denominator scale as a^{-3}. Plugging Eq. (7.39) into Eq. (7.40), we obtain the scale factor $a_{\rm quad}$ below which ϵ becomes constant. From injecting $a_{\rm quad}$ into the generated $U(1)$ charge in Eq. (7.18) and then back into the definition of ϵ in Eq. (7.37), we obtain

$$\epsilon \;=\; \begin{cases} \frac{1}{\sqrt{2}} \frac{m_{r,\rm eff}(f_a)}{m_{r,\rm eff}(\phi_{\rm ini})}\, l\, \sin l\theta_{\rm ini}, & \text{if} \quad c > l-1, \\ \frac{1}{\sqrt{2}} \sqrt{\frac{c}{l-1}} \frac{m_{r,\rm eff}(f_a)}{m_{r,\rm eff}(\phi_{\rm ini})}\, l\, \sin l\theta_{\rm ini}, & \text{otherwise.} \end{cases} \tag{7.41}$$

For $c \sim \mathcal{O}(1)$ and $\sin l\theta_{\rm ini} \sim \mathcal{O}(1)$, a large value of l, (for instance $l \simeq 10$), can easily compensate for the ratio of $m_{r,\rm eff}$, which is only $\log^{1/2}$ suppressed, cf. Eq. (7.5), such that $\epsilon = \mathcal{O}(1)$ is realistic.[10] Fig. 7.4 shows the size of the wiggles increasing with ϵ. The larger the wiggles, the larger the potential gradient along the angular direction and the larger the initial kick.

Motion after the kick. In App. G.4.2, we show that after a few oscillations in a nearly-quadratic potential, the angular velocity averaged over many oscillation periods $\left\langle \dot{\theta} \right\rangle$ becomes independent

[10] Values of ϵ larger than 1 corresponds to the field climbing up the field potential due to the centrifugal force being larger than the mass and we expect them to be unphysical, therefore we should replace Eq. (7.41) by Min $[\epsilon,\ 1]$.

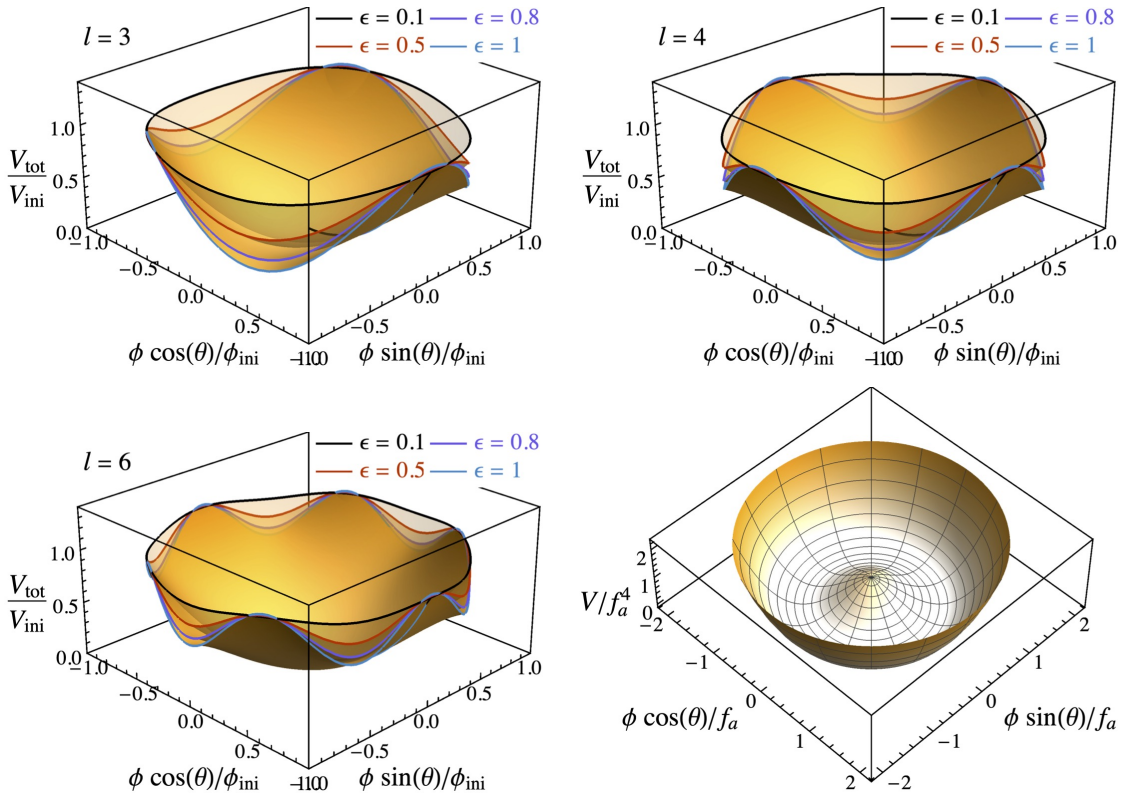

Figure 7.4: Nearly-quadratic potentials with the explicit-breaking term in Eq. (7.11). The integer l corresponds to both the number of wiggles and the order of ϕ^l. The amplitude of the angular velocity kick $\dot{\theta}_{\rm ini}$ is set by the explicit-breaking strength ϵ, defined in Eq. (7.37). The bottom-right figure shows a zoom of the circular vacuum at $\phi = f_a$.

of the initial kick $\dot{\theta}_{\rm ini}$ in Eq. (7.18). Instead, it converges to the attractor solution

$$\left\langle \dot{\theta} \right\rangle \equiv \frac{1}{T}\int_{m_{\rm eff}^{-1}}^{T} \dot{\theta}(t')dt' = m_{r,\rm eff}, \tag{7.42}$$

for which the quadratic potential $m_{r,\rm eff}^2\phi^2$ is exactly compensated by the centrifugal potential $\phi^2\dot{\theta}^2$. This is confirmed by the numerical integration of the equations of motion shown in Fig. 7.5. Even if the stationary value of $\left\langle \dot{\theta} \right\rangle$ is independent of $\dot{\theta}_{\rm ini}$, it is not the case of the fraction ϵ of $U(1)$ charge in the condensate, see Eq. (7.41).

In App. G.4.2, Virial theorem shows that the energy density ρ_Φ and the radial field value ϕ, assuming a nearly quadratic potential and averaged over oscillations, scale like

$$\langle \rho_\Phi \rangle \propto a^{-3}, \qquad \langle \phi \rangle \propto a^{-3/2}. \tag{7.43}$$

Motion due to radial damping. The damping of the radial mode $\dot{\phi} \to 0$, see Sec. 7.1.6, converts the elliptic trajectory into a circular one. In App. G.4.3, we show that radial damping leads to a drop in total energy of the complex scalar field Φ equal to the $U(1)$ charge fraction ϵ defined in Eq. (7.37)

$$\rho_\Phi^{\rm after} = \epsilon\rho_\Phi^{\rm before} \quad \Rightarrow \quad \phi_{\rm after}^2 = \epsilon\phi_{\rm before}^2, \tag{7.44}$$

where the label 'before' and 'after' denote the moments just before and after the time of damping. The suppression factor in Eq. (7.44) comes from the conservation of the rotational energy $\rho_\theta \equiv$

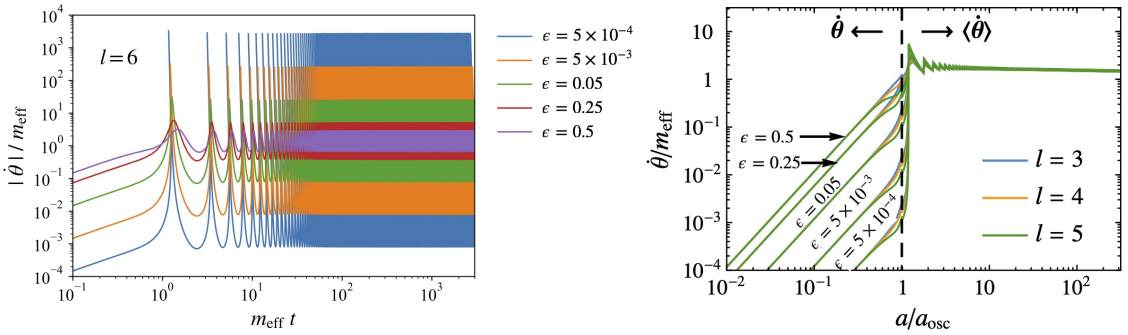

Figure 7.5: left: Non-averaged angular velocity $\dot{\theta}(t)$, obtained after numerically integrating the equations of motion in Eqs. (7.14), (7.15) and (7.16). ($m_r = 10^5$ GeV, $M = M_{\rm P1}$, $\phi_{\rm ini} = 10^{17}$ GeV, $\theta_{\rm ini} = \pi/2l$, $\dot{\phi}_{\rm ini} = \dot{\theta}_{\rm ini} = 0$). The trajectory becomes more circular as the $U(1)$ charge fraction $\epsilon \to 1$. *right:* Averaged angular velocity $\left\langle \dot{\theta} \right\rangle$, cf. Eq. (7.42). After the scalar oscillation $a > a_{\rm osc}$, the trajectory becomes independent of the values of ϵ and l and quickly converges to the attractor solution $\left\langle \dot{\theta} \right\rangle = m_{r,\rm eff}$.

$\dot{\theta}^2\phi^2/2$ during radial damping

$$\rho_\theta \;=\; \epsilon V(\phi). \tag{7.45}$$

In App. G.4.3, we show that due to Eq. (7.44), the number of e-folds of kination domination receives the suppression factor $-\frac{2}{3}\log\epsilon$. The impact of ϵ on the energy density and the duration of kination are depicted in Fig. 7.6.

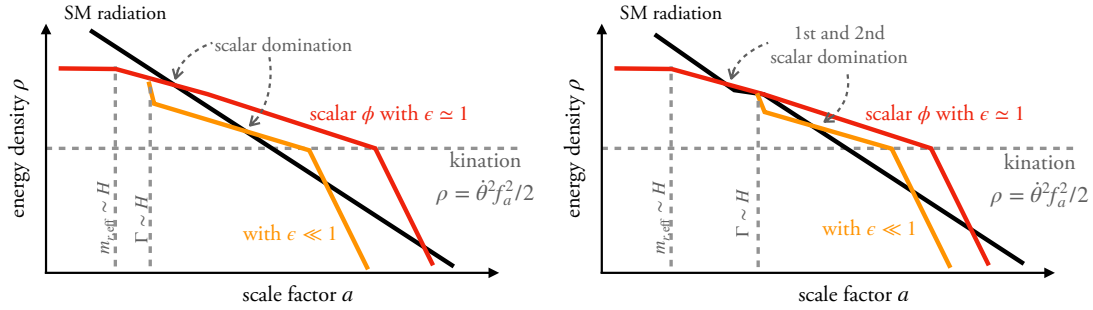

Figure 7.6: Impact of $\epsilon \ll 1$ on the evolution of the energy density of the complex scalar fields. We consider two cases according to whether the radial damping occurs before (*left*) or after (*right*) the complex scalar dominates the energy density of the Universe. In both cases, the number of e-folds of kination is reduced by $-\frac{2}{3}\log\epsilon$. The best case scenario $\epsilon = 1$ corresponds to a trajectory which is already circular even before radial damping.

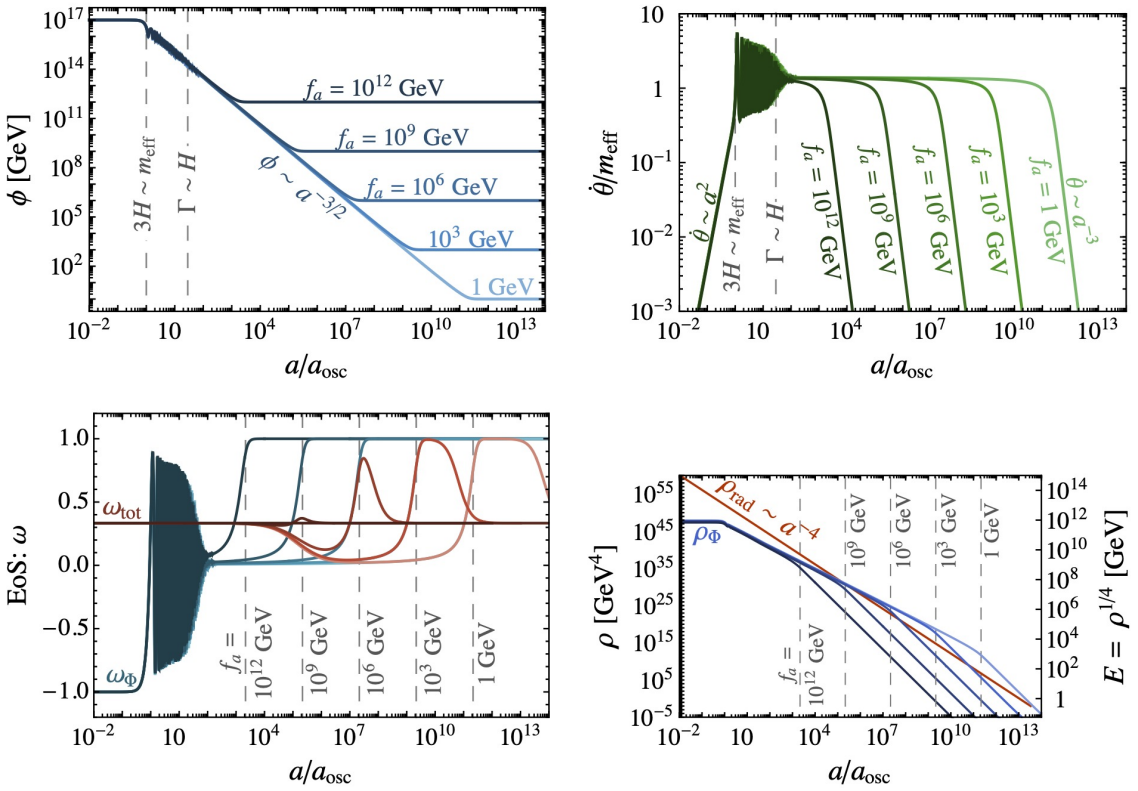

Figure 7.7: Numerical results of the radial field evolutions ϕ, the angular velocity $\dot\theta$, the equation-of-state ω_Φ, and the energy density ρ_Φ. The complex scalar field has a matter EOS $\omega_\Phi = 0$, when $\phi \gg f_a$ and reaches a kination EOS $\omega_\Phi = 1$, when $\phi \simeq f_a$. Kination ends when the radiation energy density shown in red starts dominating the energy budget of the Universe once again. For a fixed m_r, the smaller f_a, the longer the matter era, the larger the domination of the energy density of the Universe, and the longer the kination era. Obtained after numerically integrating the equations of motion in Eqs. (7.14), (7.15) and (7.16). (assuming $m_r = 10^6$ GeV, $M = M_{\rm P1}$, $\phi_{\rm ini} = 10^{17}$ GeV, $\theta_{\rm ini} = \pi/2l$, $\dot\phi_{\rm ini} = \dot\theta_{\rm ini} = 0$, $\epsilon = 0.4$, and $\Gamma = 10^4$ GeV.)

Motion towards kination. After radial damping, $\dot\phi \to 0$, the trajectory of the complex scalar field is reduced to a circular orbit whose radius decreases due to the Hubble friction. From the conservation of the $U(1)$ charge in Eq. (7.19), $a^3\phi^2\dot\theta$ = constant, we see that once $\phi \to f_a$, the complex scalar field reaches a kination equation of state, $\dot\theta \propto a^{-3}$ and $\rho_\Phi = \frac{\phi^2\dot\theta^2}{2} \propto a^{-6}$. More precisely, in App. G.4.4 and [669], the evolution of the complex scalar field $\Phi = \phi e^{i\theta}$ after radial damping $\dot\phi \to 0$ can be traced analytically

$$\frac{d\ln\phi}{d\ln a} = \frac{-3\log\left(\frac{\phi^2}{f^2}\right)}{2\log\left(\frac{\phi^2}{f^2}\right)+1} \quad \text{and} \quad \frac{d\ln\dot\theta^2}{d\ln a} = \frac{-6}{2\log\left(\frac{\phi^2}{f^2}\right)+1}, \tag{7.46}$$

as well as its energy density ρ_Φ and equation of state ω_Φ

$$\frac{d\ln\rho_\Phi}{d\ln a} = \frac{-6\log\left(\frac{\phi^2}{f^2}\right)}{2\log\left(\frac{\phi^2}{f^2}\right)-1+\frac{f^2}{\phi^2}} \quad \text{and} \quad \omega_\Phi = \frac{\phi^2-f_a^2}{2\phi^2\log\frac{\phi^2}{f_a^2}-f_a^2+\phi^2}. \tag{7.47}$$

For $\phi \gg f_a$ we have $\phi \propto a^{-3/2}$, $\dot\theta \propto a^0$, $\rho_\Phi \propto a^{-3}$, $\omega_\Phi \simeq 0$,, and for $\phi \to f_a$ we have $\phi \propto a^0$, $\dot\theta \propto a^{-3}$, $\rho_\Phi \propto a^{-6}$, $\omega_\Phi \simeq 1$. These analytical results agree with the numerical computations of the complex scalar evolution in an expanding Universe, from the oscillation onset until the end of the kination era, shown in Fig. 7.7.

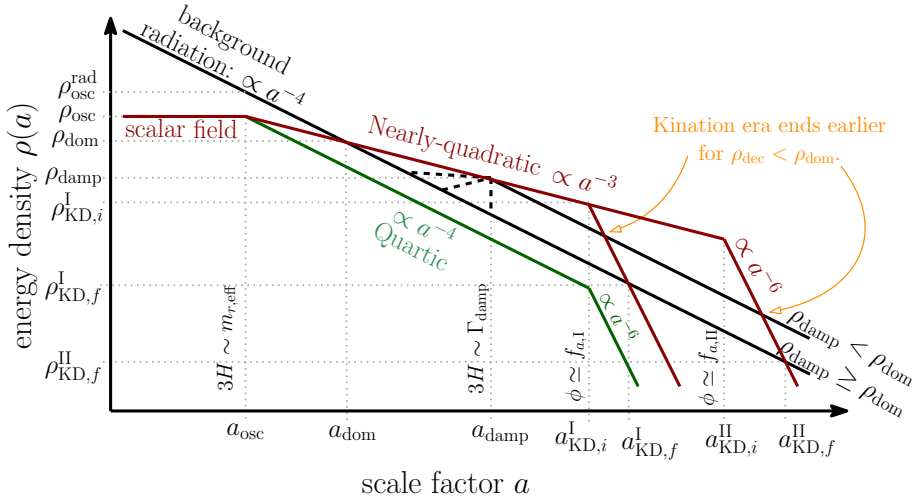

Figure 7.8: Evolution of energy densities of SM radiation (black) and the complex scalar field in nearly-quadratic potential (red) and quartic potential (green). A complex scalar field evolving in quartic potential redshifts like radiation and can never generate a kination-dominated era; see App. G.4.2 and G.4.4 for the analytical justification. Whenever it occurs after domination, $\rho_{\rm damp} < \rho_{\rm dom}$, the radial damping heats the thermal bath (black dashed lines), which reduces the duration of the kination era. In contrast, the kination duration is optimized for $\rho_{\rm damp} > \rho_{\rm dom}$. We show two f_a-values, $f_{a,\rm I} > f_{a,\rm II}$, corresponding to two durations of kination, $N_{\rm KD,I} < N_{\rm KD,II}$.

7.2.2 Cosmological history

In this section, we discuss the cosmological history of the Universe in terms of the energy density of the scalar field ρ_Φ. We defer the derivations of the expressions below to App. G.4.5 (and App. G.4.3 for the factor $\epsilon/2$). We show a sketch of the evolution of ρ_Φ in Fig. 7.8.

Onset of field oscillation. We assume that the Universe is initially radiation-dominated. The complex scalar field starts to roll when

$$3H = m_{r,\rm eff} \quad \Rightarrow \quad T_{\rm osc} = g_*^{-1/4}\sqrt{m_{r,\rm eff} M_{\rm pl}} \leq T_{\rm reh}, \tag{7.48}$$

and $\rho_{\rm osc} = V(\phi_{\rm ini})$, with $m_{r,\rm eff}$ and $\phi_{\rm ini}$ given in Eq. (7.5) and (7.26), respectively. Our framework assumes that the scalar field starts oscillating during a radiation-dominated era after reheating. The maximum reheating temperature is of the order of the inflationary scale $E_{\rm inf}$. Hence in our plots, we have the constraint, $T_{\rm osc} \leq E_{\rm inf}$, which can be seen as the purple upper-right region from Fig. 7.10, to 7.12.

No second inflation. In order for the scalar field to not induce a second period of slow-roll inflation, we must impose Φ to be sub-dominant at the onset of the oscillation

$$V(\phi_{\rm ini}) \; < \; \frac{m^2_{r,\rm eff} M^2_{\rm pl}}{3}. \tag{7.49}$$

Note that this condition guarantees that the initial radial field excursion is never superplanckian.

Matter domination. The scalar field redshifts like matter and dominates the energy density of the Universe at

$$\rho_{\rm dom} \; = \; \frac{27 m_{r,\rm eff} (\phi_{\rm ini})^2 \phi^8_{\rm ini}}{16 M^6_{\rm Pl}} A^4_\epsilon \qquad \text{and} \qquad \frac{a_{\rm dom}}{a_{\rm osc}} \; = \; \frac{2M^2_{\rm Pl}}{3\phi^2_{\rm ini}} A^{-1}_\epsilon \tag{7.50}$$

with

$$A_\epsilon = \begin{cases} \epsilon, & \text{if } \rho_{\rm damp} > \rho_{\rm dom}, \\ 1, & \text{if } \rho_{\rm damp} < \rho_{\rm dom}, \end{cases} \tag{7.51}$$

where ϵ is the amount of Noether charge, defined by Eq. (7.37) and whose value is dynamically generated at the onset of oscillation, see Eq. (7.41). The impact of ϵ on the evolution of the scalar field energy density is discussed in App. G.4.3.

Radial damping. Denoting by Γ the rate at which the radial motion is damped by some unspecified mechanism, cf. Sec. 7.1.6, we obtain that the trajectory becomes circular when

$$\rho_{\rm damp} \;=\; 3 M_{\rm Pl}^2 \Gamma^2 \, B_\epsilon^4, \;\; \text{and} \;\; \frac{a_{\rm damp}}{a_{\rm dom}} \;=\; \left(\frac{\rho_{\rm dom}}{\rho_{\rm damp}} \right)^{1/3}, \tag{7.52}$$

with

$$B_\epsilon = \begin{cases} 1, & \text{if } \rho_{\rm damp} > \rho_{\rm dom}, \\ \epsilon, & \text{if } \rho_{\rm damp} < \rho_{\rm dom}. \end{cases} \tag{7.53}$$

In this section, Γ is considered as a free parameter, and we assume that damping can occur before the onset of the matter domination, $\rho_{\rm damp} > \rho_{\rm dom}$.

Duration of the kination era. The Universe acquires a kination equation-of-state when the field reaches $\phi \to f_a$, corresponding to the energy density $\rho_{{\rm KD},i} = f_a^2 m_{r,\rm eff}^2(f_a)/2$. Depending on whether radial damping occurs before or after the onset of matter domination, we obtain

$$\frac{a_{{\rm KD},i}}{\max(a_{\rm dom}, a_{\rm damp})} = \left(\frac{\min(\rho_{\rm dom},\, \rho_{\rm damp})}{\rho_{\rm KD,i}} \right)^{1/3}. \tag{7.54}$$

The kination era stops when the Universe becomes radiation-dominated again. The energy scale at which it occurs depends on whether radial damping occurs before and after the onset of matter domination

$$\rho_{{\rm KD},f} = \frac{\rho_{{\rm KD},i}^2}{\min(\rho_{\rm dom},\, \rho_{\rm damp})} = \begin{cases} \frac{4 f_a^4 m_{r,\rm eff}^4(f_a) M_{\rm Pl}^6}{27 m_{r,\rm eff}^2(\phi_{\rm ini}) \phi_{\rm ini}^8} \left(\frac{1}{\epsilon}\right)^4, & \text{if } \rho_{\rm damp} > \rho_{\rm dom}, \\ \frac{f_a^4 m_{\rm eff}^4(f_a)}{12 M_{\rm Pl}^2 \Gamma_{\rm damp}^2} \left(\frac{1}{\epsilon}\right)^4, & \text{if } \rho_{\rm damp} < \rho_{\rm dom}. \end{cases} \tag{7.55}$$

The duration of the kination era $N_{\rm KD} \equiv \log a_{{\rm KD},f}/a_{{\rm KD},i}$ reads

$$e^{N_{\rm KD}} = \left(\frac{\min(\rho_{\rm dom},\, \rho_{\rm damp})}{\rho_{{\rm KD},i}} \right)^{\frac{1}{6}} = \begin{cases} \sqrt{\frac{3}{2}} \left(\frac{m_{r,\rm eff}(\phi_{\rm ini})}{m_{r,\rm eff}(f_a)} \frac{M_{\rm pl}}{f_a} \right)^{1/3} \left(\frac{\phi_{\rm ini}}{M_{\rm pl}} \right)^{4/3} \epsilon^{2/3}, & \text{if } \rho_{\rm damp} > \rho_{\rm dom}, \\ \left(\frac{6 M_{\rm Pl}^2 \Gamma_{\rm damp}^2}{f_a^2 m_{r,\rm eff}^2(f_a)} \right)^{1/6} \epsilon^{2/3}, & \text{if } \rho_{\rm damp} < \rho_{\rm dom}. \end{cases} \tag{7.56}$$

The first line of Eq. (7.56), corresponding to efficient radial damping before scalar field domination, gives the longest duration of kination for the complex scalar field model studied in this work

$$\rho_{\rm damp} > \rho_{\rm dom} \quad \Rightarrow \quad e^{N_{\rm KD}} \simeq e^{8.2} \, \epsilon^{2/3} \left(\frac{10^9 \text{ GeV}}{f_a} \right)^{1/3} \left(\frac{m_{r,\rm eff}(\phi_{\rm ini})}{5 m_{r,\rm eff}(f_a)} \right)^{1/3} \left(\frac{\phi_{\rm ini}}{M_{\rm pl}} \right)^{4/3}, \tag{7.57}$$

where ϵ can be $\mathcal{O}(1)$, see Eq. (7.41). Note that for efficient thermalization, the number of matter e-folds $N_{\rm MD} \equiv \log a_{{\rm KD},i}/a_{\rm dom}$, cf. first line of Eq. (7.54), verifies the property

$$\rho_{\rm damp} > \rho_{\rm dom} \quad \Rightarrow \quad N_{\rm MD} = 2 N_{\rm KD}. \tag{7.58}$$

The duration of the matter and kination eras are shown in Fig. 7.9.

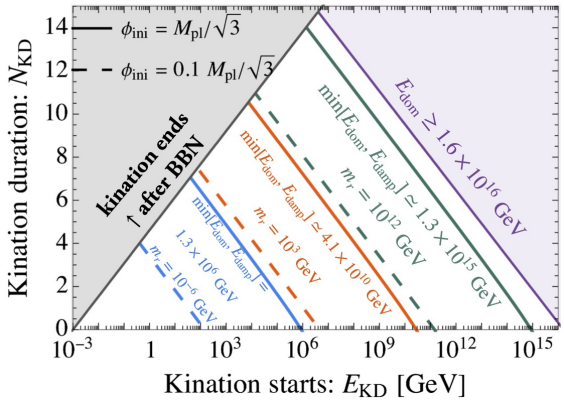

Figure 7.9: The duration of kination $N_{\rm KD}$, cf. Eq. (7.56), depends on the energy scale at the 'effective' start of the matter era Min $[E_{\rm dom},\ E_{\rm damp}]$ and at the onset of the kination era $E_{\rm KD} = (2m_r^2 f_a^2)^{1/4}$. If $E_{\rm damp} < E_{\rm dom}$, entropy injection at the time of damping re-equilibrates the amount of matter vs radiation in the Universe, hence the 'Min' function. The larger m_r, the larger $E_{\rm dom}$ and the longer the duration of the matter-kination era. In the present Sec. 7.2, we consider $E_{\rm damp}$ as a free parameter. The maximum duration of kination compatible with both BBN and the maximal inflationary scale allowed by CMB data, $N_{\rm KD} \lesssim 14.6$, is computed precisely in App. F.1.

7.2.3 Gravitational-wave signature and detectability

As discussed in Sec. 4.7.1, the primary motivation for generating a kination era is enhancing the amplitude of SGWB produced beforehand. The subsequent figures show the detectability of SGWB produced by primordial inflation (Fig. 7.10), local strings (Fig. 7.11), and globals strings (Fig. 7.12) in the presence of a kination era generated by scenario I: a spinning complex scalar field assuming the existence of an efficient non-thermal damping mechanism that enables to neglect thermal corrections to the potential.

Axion dark matter. One interesting point in this paper is that the axion generating the matter-kination era and the peak GW signature could also explain DM. In Sec. 6.4, the nature of kination – parametrized by its energy scale $E_{\rm KD}$ and duration $N_{\rm KD}$ – is related model-independently to the axion parameters, namely axion mass m_a and its decay constant f_a. This means that the axion parameter space could be probed easily by reading the peak position of the GW background that gets boosted by this kination era.

This section provides the kination nature $(E_{\rm KD}, N_{\rm KD})$ in terms of UV-completion parameters, i.e. the radial-mode mass m_r and f_a. Therefore we translate the detectability plots in the UV-completion parameters into the usual axion parameter space. Let us compare the model-independent expression of the energy scale at the end of kination, Eq. (6.13), and the model-dependent expression, Eq. (7.55), and we also use the initial VEV in Eq. (7.26). Equating these two expressions, the mass of radial mode is fixed when axion of mass m_a contributes to the total DM density,

$$m_r \simeq M_{\rm Pl}\left[\frac{7.1\times10^9 h^2}{[\lambda^2(2l-2)]^{\frac{1}{l-2}}}\left(\frac{m_a}{\rm GeV}\right)\left(\frac{\Omega_{\rm DM}}{\Omega_a}\right)\right]^{\frac{2(l-2)}{l-6}}. \tag{7.59}$$

Here we see a non-trivial result, namely m_r grows with m_a. One might naively expect a larger m_r for smaller m_a because the larger PQ-charge yield is required for the correct $\Omega_{\rm a} = m_a Y_\theta s_0$. However, a larger charge does not mean larger m_r. A yield is proportional to $m_r/T_{\rm KD}^3$. For larger m_r, the kination energy scale also increases and hence enhances $T_{\rm KD}$ in the process. Applying the new m_r expression, the duration of kination in Eq. (7.56) transforms into the axion DM parameters,

$$e^{N_{\rm KD}} \simeq \sqrt{\frac{3}{2}}\left(\frac{M_{\rm Pl}}{f_a}\right)^{\frac{1}{3}}\left(\frac{\phi_{\rm ini}}{M_{\rm Pl}}\right)^{\frac{4}{3}} \simeq \sqrt{\frac{3}{2}}\left(\frac{M_{\rm Pl}}{f_a}\right)^{\frac{1}{3}}\left[\frac{7.1\times10^9 h^2}{(\lambda\sqrt{2l-2})^{1/2}}\left(\frac{m_a}{\rm GeV}\right)\left(\frac{\Omega_{\rm DM}}{\Omega_a}\right)\right]^{\frac{8}{3(l-6)}}. \tag{7.60}$$

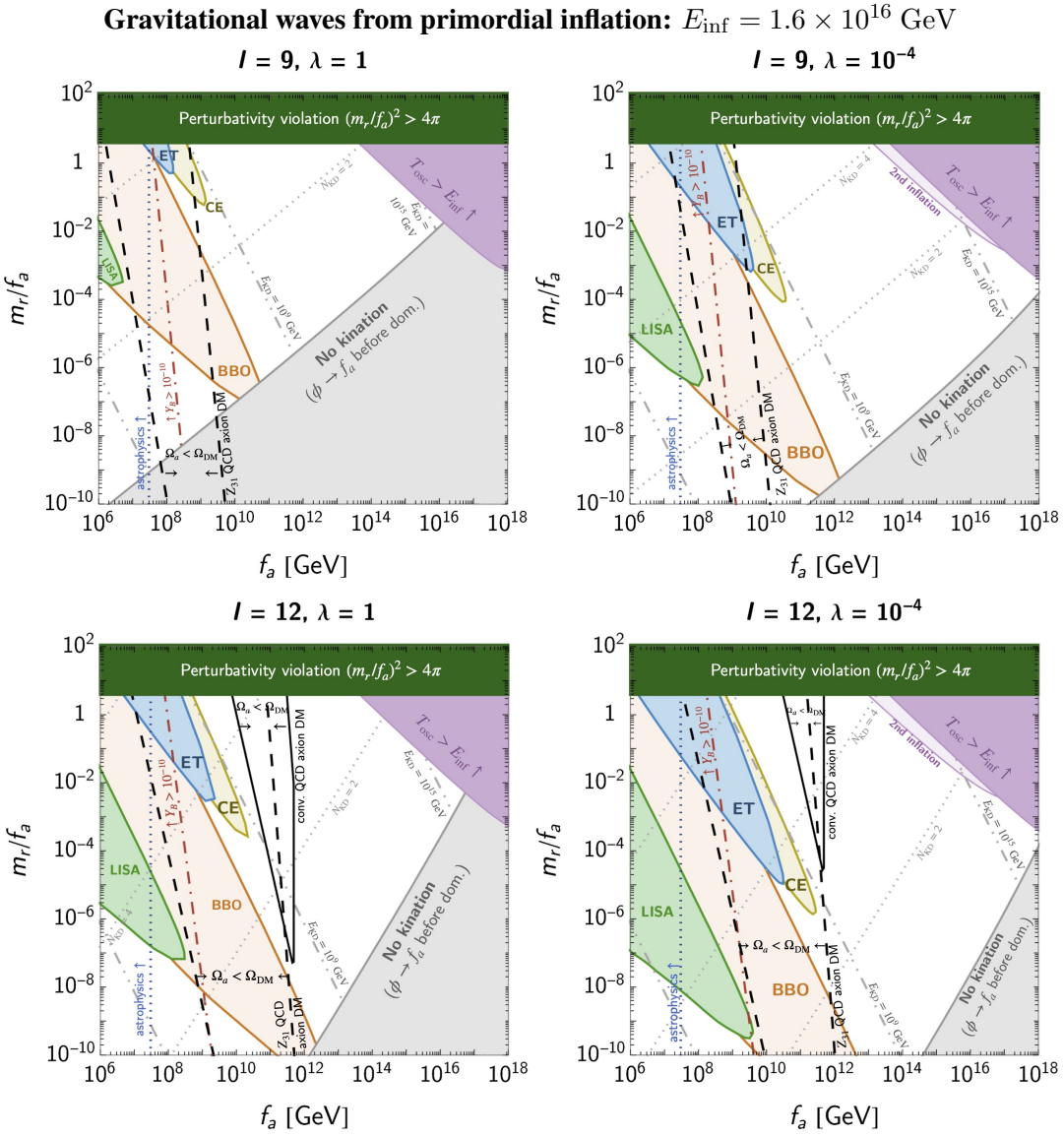

Figure 7.10: Ability of future-planned GW observatories to detect the peak signature in the SGWB from primordial inflation with energy scale $E_{\rm inf}$ of a matter-kination era induced by **scenario I**. In this scenario, a kick in the angular direction of a complex scalar field is induced with a large radial value by operators of order l and self-coupling λ, and the radial motion is assumed to be damped non-thermally. Black dashed lines indicate where the lighter non-canonical QCD axion abundance in Eq. (6.3) is satisfied, cf. Eq. (6.5). The left boundary is set by the kinetic misalignment mechanism, while the right one is set by the axion quality problem (for larger m_r depending on f_a), cf. Eq. (7.22). Only the region between these two lines does not over-produce DM.

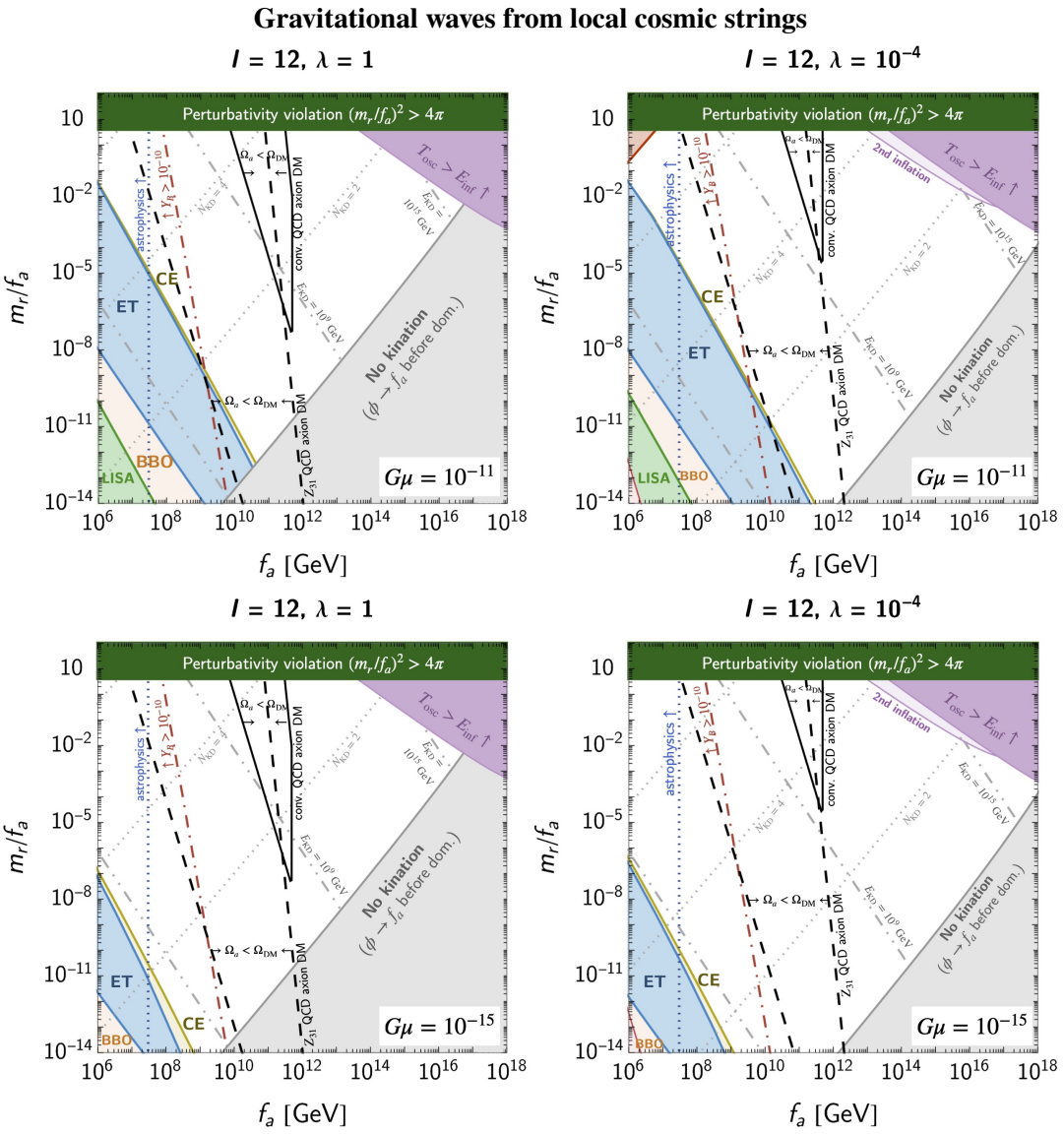

Figure 7.11: Ability of future-planned GW observatories to detect the peak signature in the SGWB from local cosmic strings with tension $G\mu$ of a matter-kination era induced by **scenario I**. In this scenario, a kick in the angular direction of a complex scalar field is induced with a large radial value by operators of order $l = 12$ and self-coupling λ, and the radial motion is assumed to be damped non-thermally. Black solid lines indicate where the canonical QCD axion abundance is satisfied, cf. Eq. (6.5). The left boundary is set by the kinetic misalignment mechanism, while the right one is by the standard misalignment (for small m_r with a specific f_a) and by the axion quality problem (for larger m_r depending on f_a), cf. Eq. (7.22). Only the region between the two lines does not over-produce DM. Dashed lines are the equivalent for lighter non-canonical QCD axion, cf. Eq. (6.3).

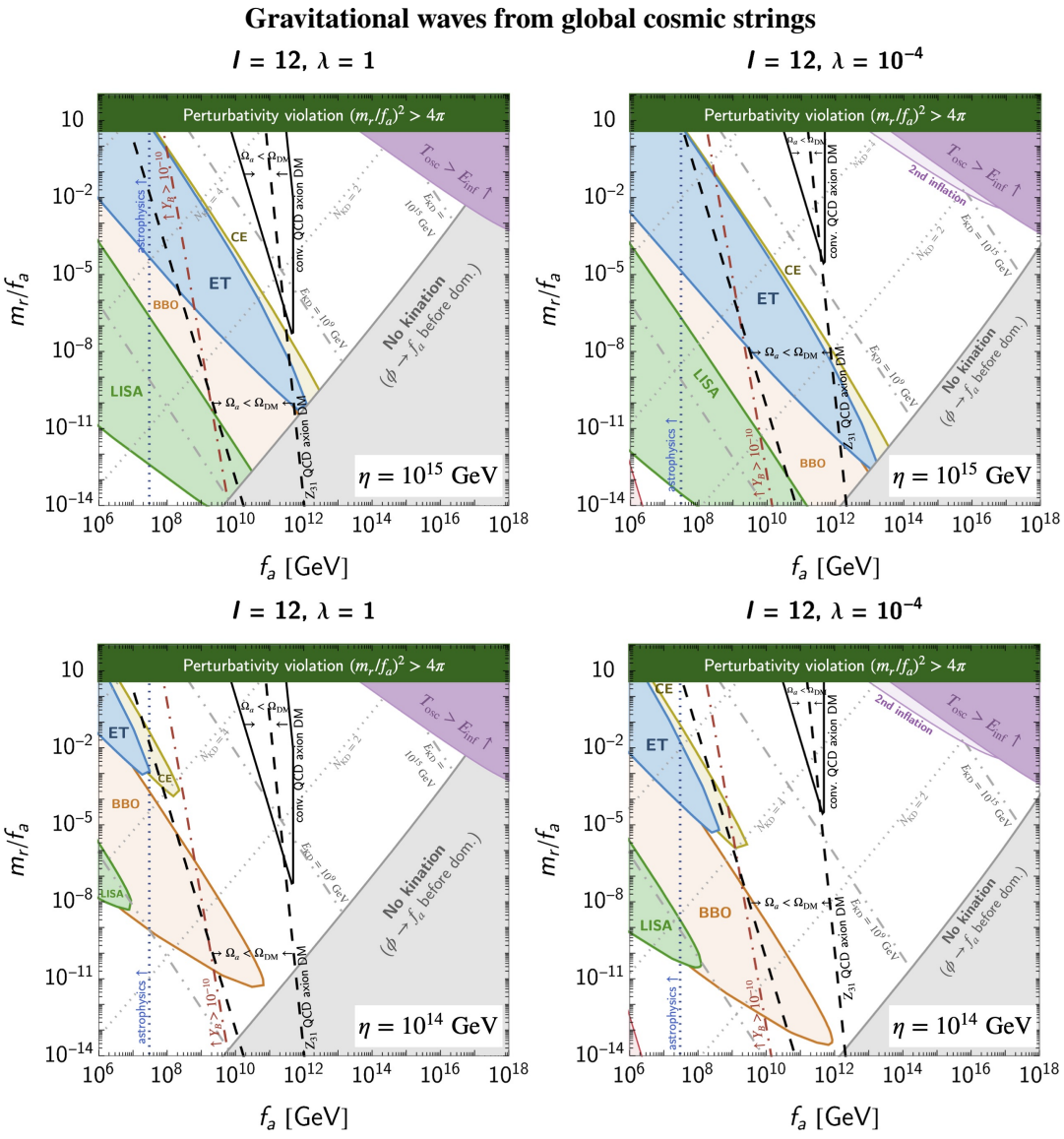

Figure 7.12: Ability of future-planned GW observatories to detect the peak signature in the SGWB from global cosmic strings with string scale η of a matter-kination era induced by **scenario I**. In this scenario, a kick in the angular direction of a complex scalar field is induced with a large radial value by operators of order $l = 12$ and self-coupling λ, and the radial motion is assumed to be damped non-thermally. Black solid lines indicate where the canonical QCD axion abundance is satisfied, cf. Eq. (6.5). The left boundary is set by the kinetic misalignment mechanism, while the right one is by the standard misalignment (for small m_r with a specific f_a) and by the axion quality problem (for larger m_r depending on f_a), cf. Eq. (7.22). Only the region between the two lines does not over-produce DM. Dashed lines are the equivalent for lighter non-canonical QCD axion, cf. Eq. (6.3).

7.3 Scenario II: thermal damping and relativistic fermions

7.3.1 Effects of the thermal corrections

In scenario I in the previous Sec. 7.2, we have assumed the existence of an unspecified non-thermal mechanism (maybe parametric resonance) responsible for efficiently damping the radial mode of the scalar condensate. The advantage was that we could neglect the effect of the thermal corrections to the potential, presented in Sec. 7.1.2, on the dynamics of the scalar field. In the current section, we switch on the interaction with the thermal plasma by relaxing the condition of small Yukawa coupling y_ψ in Eq. (7.36). The advantage is that it leads to an early thermalization of the condensate with the plasma, which is a well-understood and efficient mechanism [669] for damping the radial mode. The difficulty relies upon the presence of the thermal mass, which leads to a modification of the cosmological history of the scalar field:[11]

- the scalar field starts oscillating earlier,
- the initial angular kick ϵ is substantially reduced,
- the scalar field redshifts like radiation until the thermal mass becomes negligible below $T_{\rm zero} = m_{r,\rm eff}/y_\psi$. This leads to a delay in the onset of the matter era.

We discuss those effects below, showing that they prevent the onset of the matter-kination era. A sketch of the cosmological history in the presence of thermal effects is demonstrated in Fig. 7.13.

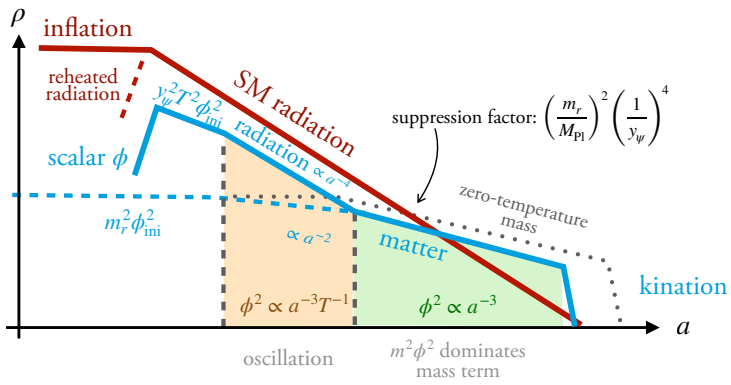

Figure 7.13: Evolution of the energy density of the complex scalar field with (blue) and without (gray) thermal mass. Due to the earlier oscillation, the thermal mass suppresses the energy density at the time of scalar domination by a factor proportional to $(m_r/M_{\rm Pl})^2(1/y_\psi)^4$, and so is the duration of the kination era, see text for more details. The corresponding numerical trajectory is shown in Fig. 7.14. Not shown on this figure is the suppression of the angular kick by the thermal mass, see Eq. (7.72).

An earlier oscillation The earlier oscillation of the condensate due to the thermal effect has been pointed-out in [702, 721]. The field starts rolling when $3H \sim m_{\rm eff,T}$ where the effective mass, in a radiation era is

$$m_{{\rm eff},T}^2 \;=\; m_{\rm eff}^2 + y_\psi^2 T^2. \tag{7.61}$$

Assuming that the thermal mass dominates, we obtain that the field starts oscillating at the temperature

$$3H_{\rm osc} \;=\; y_\psi T_{\rm osc}, \quad \Rightarrow \quad T_{\rm osc} \;=\; g_*^{-1/2} M_{\rm Pl} y_\psi, \tag{7.62}$$

[11] The difficulty inherent to scenario II studied in the present section is the fragmentation of the scalar condensate into Q-balls whenever the thermal-log dominate, see Sec. 7.1.2. We do not investigate this possibility further as the present scenario II does not lead to any matter-kination era.

which is larger than the oscillation temperature in the zero-temperature potential, see Eq. (7.48), for

$$y_\psi \gtrsim y_{\psi,T=0} \equiv g_*^{1/4} \sqrt{\frac{m_{r,\text{eff}}(\phi_\text{ini})}{M_\text{pl}}}. \tag{7.63}$$

An earlier oscillation due to thermal effects can be visualized in Fig. 7.14.

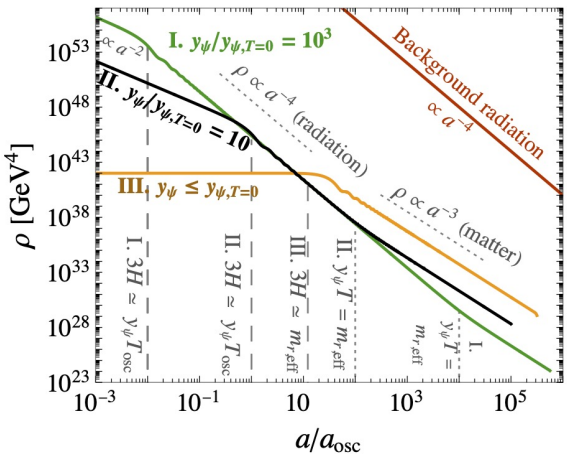

Figure 7.14: Evolution of scalar field energy density with thermal mass $y_\psi T$ (case I in green and II in black) and without thermal mass (case III in yellow). After the onset of oscillation (vertical dashed), the field redshifts as radiation until the zero-temperature mass dominates (vertical dotted), where it starts redshifting as matter. The smaller y_ψ, the later the start of oscillation and the earlier the start of the matter behavior. Below the value $y_\psi < y_{\psi,T=0}$, where $y_{\psi,T=0}$ is defined in Eq. (7.63), the thermal mass never plays any role in the evolution, and the field redshifts as a matter already at the onset of oscillation. We normalize the scale factor a with a_osc of case II. Figure obtained after numerically integrating the EOM of the scalar field in quadratic potential in the presence of the thermal mass in Eq. (7.61).

A different redshift law. When dominated by its thermal mass, the complex scalar field redshifts like radiation, see App. G.4.2

$$\phi^2 \propto a^{-3} T^{-1} \propto a^{-2}, \quad \Rightarrow \quad \rho_\Phi \simeq \frac{1}{2} y_\psi^2 T^2 \phi^2 \propto a^{-4}. \tag{7.64}$$

On the other hand, the zero-temperature contribution redshifts slower than radiation

$$V(\phi, T=0) = \frac{1}{2} m_{r,\text{eff}}^2 \phi^2 \propto a^{-2}. \tag{7.65}$$

The thermal potential becomes sub-dominant at the temperature, scale factor, and field value

$$T_\text{zero} = \frac{m_{r,\text{eff}}(\phi_\text{zero})}{y_\psi}, \quad \frac{a_\text{zero}}{a_\text{osc}} = g_*^{-1/2} \frac{y_\psi^2 M_\text{Pl}}{m_{r,\text{eff}}(\phi_\text{zero})} \text{ and } \phi_\text{zero} = \phi_\text{ini} \frac{T_\text{zero}}{T_\text{osc}}. \tag{7.66}$$

Changes in the redshift law are also seen in our numerical simulations, cf. Fig. 7.15.

No symmetry restoration when $\phi \to f_a$. To generate a kination equation of state, we must check that the complex scalar field reaches the minimum of the potential $\phi \to f_a$ after the thermal mass becomes sub-dominant, i.e. $\phi(T_\text{zero}) \gtrsim f_a$. We checked that in the parameter space of interest, this never occurs.

A smaller angular kick. We calculate the $U(1)$ charge fraction in Eq. (7.37)

$$\epsilon \equiv \frac{\phi^2 \dot\theta/2}{V(\phi)/m_{r,\text{eff}}(\phi)} = \frac{\phi_\text{ini}^2 \dot\theta_\text{ini}/2}{V(\phi)/m_{r,\text{eff}}(\phi)} \left(\frac{a_\text{ini}}{a}\right)^3. \tag{7.67}$$

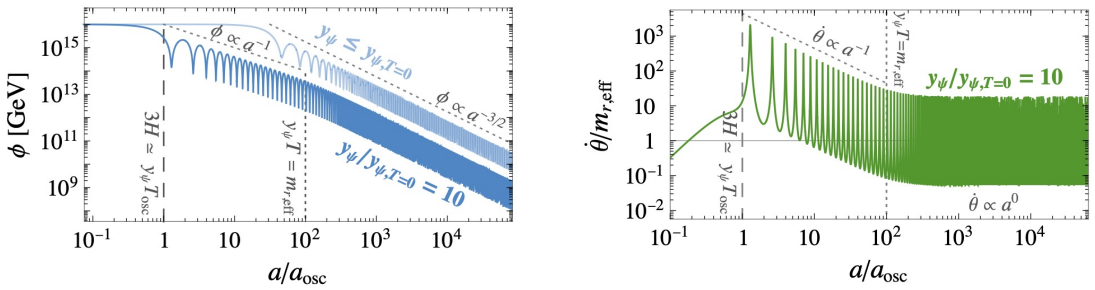

Figure 7.15: *left:* In the presence of the thermal mass (dark blue), at the onset of oscillation (vertical dashed line), the radial mode ϕ starts evolving as $\langle\phi\rangle \propto a^{-3/2}T^{-1/2} \propto a^{-1}$ in radiation era, until the zero-temperature mass dominates (vertical dotted line), after which the field starts redshifting as $\langle\phi\rangle \propto a^{-3/2}$. Instead, when the potential is always dominated by its zero-temperature contribution (light blue), i.e. $y_\psi < y_{\psi,T=0}$ where $y_{\psi,T=0}$ is defined in Eq. (7.63), the field starts redshifting as $\langle\phi\rangle \propto a^{-3/2}$ immediately after the start of oscillation. *right:* During the period of thermal mass domination, the angular velocity $\dot\theta$ redshifts as $\left\langle\dot\theta\right\rangle \propto T \propto a^{-1}$ during radiation, and then oscillates around $m_{r,\rm eff}$ when the zero-temperature mass dominates.

From using $(\phi_{\rm ini}/M_{\rm pl})^{l-2} = \sqrt{c}m_{r,\rm eff}(\phi_{\rm ini})/\lambda\sqrt{2l-2}M_{\rm pl}$, see Eq. (7.26), we find that the term in the potential which dominates the dynamics of the scalar field at the onset of the radial mode oscillation depends on the value of c

$$V(\phi_{\rm ini}) = \begin{cases} \lambda^2 \frac{\phi_{\rm ini}^{2l-2}}{M_{\rm pl}^{2l-6}}, & \text{if } c > l-1, \\ \frac{1}{2}y_\psi^2 T_{\rm osc}^2 \phi_{\rm ini}^2, & \text{otherwise.} \end{cases} \tag{7.68}$$

In the first case of the previous equation, the scalar field redshifts as, cf. App. G.4.2

$$\phi \propto a^{-\frac{6}{2+n}}, \quad \text{with} \quad n = 2l-2. \tag{7.69}$$

until the nearly-quadratic term ϕ^2 dominates around the field value $\phi_{\rm quad}$

$$\frac{1}{2}y_\psi^2 T_{\rm quad}^2 \phi_{\rm quad}^2 \;=\; \lambda^2 \frac{\phi_{\rm quad}^{2l-2}}{M_{\rm pl}^{2l-6}}. \tag{7.70}$$

For $\phi < \phi_{\rm quad}$, the $U(1)$ charge fraction ϵ becomes constant since both numerator and denominator in Eq. (7.67) scale like a^{-3}. Plugging Eq. (7.69) into Eq. (7.70), we obtain the scale factor $a_{\rm quad}$ below which the potential is dominated by the quadratic term. From injecting $a_{\rm quad}$ into the generated $U(1)$ charge in Eq. (7.18) and the definition of ϵ in Eq. (7.67), we obtain

$$\epsilon \;=\; \begin{cases} \sqrt{\frac{g_*}{2}} \frac{m_{r,\rm eff}(f_a)}{y_\psi^2 M_{\rm pl}}\, l\, \sin l\theta_{\rm ini}, & \text{if} \quad c > l-1, \\ \sqrt{\frac{g_* c}{2(l-1)}} \frac{m_{r,\rm eff}(f_a)}{y_\psi^2 M_{\rm pl}}\, l\, \sin l\theta_{\rm ini}, & \text{otherwise.} \end{cases} \tag{7.71}$$

We conclude that for a fix value of c, l and $\theta_{\rm ini}$, the value of ϵ in the presence of a thermal mass is suppressed by a factor $\frac{g_*^{1/2} m_{r,\rm eff}(\phi_{\rm ini})}{y_\psi^2 M_{\rm pl}}$ with respect to the value of ϵ without thermal mass, cf. Eq. (7.41), which we denote ϵ_0

$$\epsilon \;=\; \left(\frac{g_*^{1/2} m_{r,\rm eff}(\phi_{\rm ini})}{y_\psi^2 M_{\rm pl}}\right) \epsilon_0. \tag{7.72}$$

The reason of the suppression of ϵ in Eq. (7.72) can be understood from Eq. (7.67) where the denominator $V(\phi)$ is enlarged by the presence of the thermal mass while the explicit $U(1)$ breaking potential generating the numerator $\dot\theta$ is not.

7.3.2 Evolution of the field and its energy density

Delay of matter domination The scalar field dominates the energy density of the Universe at the scale factor $a_{\rm dom}$ defined by

$$V(\phi_{\rm zero},\, T=0)\left(\frac{a_{\rm zero}}{a_{\rm dom}}\right)^3 = \rho_{\rm rad}(T_{\rm zero})\left(\frac{a_{\rm zero}}{a_{\rm dom}}\right)^4 \quad \text{with} \quad \rho_{\rm rad} = \frac{\pi^2}{30} g_* T^4, \tag{7.73}$$

where $T_{\rm zero}$ denotes the temperature, defined in Eq. (7.66), below which the zero-temperature mass dominates over the thermal mass. We obtain

$$\frac{a_{\rm dom}}{a_{\rm zero}} = \frac{2}{3}\left(\frac{M_{\rm pl}}{\phi_{\rm ini}}\right)^2 A_\epsilon^{-1}, \quad T_{\rm dom} = \frac{m_{r,\rm eff}(\phi_{\rm zero})}{y_\psi}\frac{3}{2}\left(\frac{\phi_{\rm ini}}{M_{\rm pl}}\right)^2 A_\epsilon, \tag{7.74}$$

and

$$\rho_{\rm dom} = \frac{27 g_*}{16}\left(\frac{m_{r,\rm eff}(\phi_{\rm zero})}{y_\psi}\right)^4 \left(\frac{\phi_{\rm ini}}{M_{\rm pl}}\right)^8 A_\epsilon^4, \tag{7.75}$$

with A_ϵ defined by

$$A_\epsilon = \begin{cases} \epsilon, & \text{if } \rho_{\rm damp} > \rho_{\rm dom}, \\ 1, & \text{if } \rho_{\rm damp} < \rho_{\rm dom}, \end{cases} \tag{7.76}$$

stands for the ϵ-suppression discussed in App. G.4.3. The value of ϵ is given by Eq. (7.71). Note that we can rewrite Eq. (7.75) as

$$\rho_{\rm dom} = \left(g_*^{1/2}\frac{m_{r,\rm eff}^2(\phi_{\rm zero})}{y_\psi^2 m_{r,\rm eff}(\phi_{\rm ini}) M_{\rm pl}}\right)^2 \rho_{\rm dom,1} \tag{7.77}$$

with $\rho_{\rm dom,\,1}$ being the energy density at domination, defined in Eq. (7.50), in the case of the first scenario where the thermal mass can be neglected due to a small Yukawa coupling. From Eq. (7.77), we can see that the effect of the thermal mass is to delay the onset of the matter domination by a factor $\propto y_\psi^{-4}$ in the energy density. As we will see in Eq. (7.86), the delay of the matter domination in Eq. (7.77) together with the suppression of ϵ in Eq. (7.72) are responsible for preventing the kination era to take place in the presence of thermal effects.

Radial damping In the presence of the Yukawa interactions with fermions ψ, cf. Eq. (7.6), the scalar condensate thermalizes with the thermal plasma with the rate, see App. G.3.1

$$\Gamma_\phi \simeq \begin{cases} \text{for } y_\psi\phi < T: \begin{cases} \text{for } \alpha T > y_\psi\phi, & \frac{y_\psi^2 \alpha T}{2\pi^2}, \\ \text{for } \alpha T < y_\psi\phi, & \frac{y_\psi^4\phi^2}{\pi^2\alpha T}, \end{cases} & + \ \frac{y_\psi^2 m_\phi}{8\pi}\Theta\left(m_\phi/2 - \text{Max}\left[y_\psi\phi,\, gT\right]\right). \\ \text{for } y_\psi\phi > T: \quad b\alpha^2\frac{\text{Max}\left[T,\, m_\phi\right]^3}{\phi^2}, \end{cases} \tag{7.78}$$

with $b \simeq 0.01$. As shown in the supplementary material of [669], thermalization conserves the $U(1)$ charge $\phi^2\dot\theta$. Radial damping takes place at the energy scale and scale factor

$$\rho_{\rm damp} = 3M_{\rm pl}^2\Gamma^2 B_\epsilon^4 \ \text{ and } \ \frac{a_{\rm damp}}{a_{\rm dom}} = \left(\frac{\rho_{\rm dom}}{\rho_{\rm damp}}\right)^{1/3} B_\epsilon^{-1}, \tag{7.79}$$

$$\text{with} \qquad B_\epsilon = \begin{cases} 1, & \text{if } \rho_{\rm damp} > \rho_{\rm dom}, \\ \epsilon, & \text{if } \rho_{\rm damp} < \rho_{\rm dom}. \end{cases} \tag{7.80}$$

For the sake of simplicity, in the present Sec. 7.3, we suppose that the thermal width is larger than the fermion mass $\alpha T > y_\psi \phi$. The decay rate is given by the first line in Eq. (7.78) and we compute

$$\Gamma_{\rm damp} = \begin{cases} \frac{3\alpha^2}{4\pi^4} g_*^{-1/2} y_\psi^4 M_{\rm pl}, & \text{for } y_\psi > y_{\psi,1}, \\ \frac{y_\psi^2 m_{r,\rm eff}(f_a)}{8\pi}, & \text{otherwise}, \end{cases} \tag{7.81}$$

and

$$T_{\rm damp} = \begin{cases} \frac{\alpha}{2\pi} \frac{y_\psi^2 M_{\rm pl}}{g_*^{1/2}}, & \text{for } y_\psi > y_{\psi,1}, \\ \frac{y_\psi}{\pi g_*^{1/4}} \sqrt{m_{r,\rm eff}(f_a) M_{\rm pl}}, & \text{otherwise}, \end{cases} \tag{7.82}$$

where

$$y_{\psi,1} \equiv 2 \frac{g_s^{1/4}}{\alpha} \left(\frac{m_{r,\rm eff}(f_a)}{M_{\rm pl}} \right)^{1/2}. \tag{7.83}$$

Duration of the kination era. The Universe acquires a kination equation-of-state when the field reaches $\phi \to f_a$, corresponding to the energy density and scale factor

$$\rho_{{\rm KD},i} = \frac{1}{2} f_a^2 m_{r,\rm eff}^2(f_a) \text{ and } \frac{a_{{\rm KD},i}}{\max(a_{\rm dom}, a_{\rm damp})} = \left(\frac{\min(\rho_{\rm dom}, \rho_{\rm damp})}{\rho_{\rm KD,i}} \right)^{1/3}. \tag{7.84}$$

The kination era stops when the Universe becomes radiation-dominated again. The energy scale at which it occurs depends on whether radial damping occurs before and after the onset of matter domination: $\rho_{{\rm KD},f} = \rho_{{\rm KD},i}^2 / \min(\rho_{\rm dom}, \rho_{\rm damp})$. The duration of the kination era $N_{\rm KD} \equiv \log \frac{a_{{\rm KD},f}}{a_{{\rm KD},i}}$ reads

$$e^{N_{\rm KD}} = \begin{cases} \sqrt{\frac{3}{2}} \left(\frac{g_*^{1/2}}{y_\psi^2} \frac{m_{r,\rm eff}(\phi_{\rm zero})}{m_{r,\rm eff}(f_a)} \frac{m_{r,\rm eff}(\phi_{\rm zero})}{f_a} \right)^{1/3} \left(\frac{\phi_{\rm ini}}{M_{\rm pl}} \right)^{4/3} \epsilon^{2/3}, & \text{if } \rho_{\rm damp} > \rho_{\rm dom}, \\ \left(\frac{6 M_{\rm Pl}^2 \Gamma_{\rm damp}^2}{f_a^2 m_{r,\rm eff}^2(f_a)} \right)^{1/6} \epsilon^{2/3}, & \text{if } \rho_{\rm damp} < \rho_{\rm dom}. \end{cases} \tag{7.85}$$

Using the first lines of Eq. (7.78) and (7.82) and plugging the most optimistic value of ϵ, cf. first line of Eq. (7.71), we obtain

$$\begin{aligned} e^{N_{\rm KD}} = 0.74 g_*^{1/18} \alpha^{2/9} \epsilon^{2/3} \left(\frac{M_{\rm pl}}{f_a} \right)^{1/3} \left(\frac{m_{r,\rm eff}(f_a)}{M_{\rm pl}} \right)^{1/9} \left(\frac{m_{r,\rm eff}(\phi_{\rm zero})}{m_{r,\rm eff}(f_a)} \right)^{4/9} \left(\frac{\phi_{\rm ini}}{M_{\rm pl}} \right)^{8/9} \times \\ \times \begin{cases} \left(\frac{y_{\psi,\rm th}}{y_\psi} \right)^{2/3}, & \text{if } y_\psi \gtrsim y_{\psi,\rm th}, \\ \left(\frac{y_\psi}{y_{\psi,\rm th}} \right)^{4/3}, & \text{if } y_{\psi,\rm th} \gtrsim y_\psi \gtrsim y_{\psi,1}, \\ \left(\frac{y_{\psi,1}}{y_{\psi,\rm th}} \right)^{4/3} \left(\frac{y_\psi}{y_{\psi,1}} \right)^{2/3}, & \text{if } y_\psi \lesssim y_{\psi,1}, \end{cases} \end{aligned} \tag{7.86}$$

where $y_{\psi,1}$ is defined in Eq. (7.83) and where $y_{\psi,\rm th}$ is the Yukawa coupling above which thermalization starts to occur before scalar field domination

$$\rho_{\rm damp} > \rho_{\rm dom} \;\Rightarrow\; y_\psi > y_{\psi,\rm th} = \pi^{2/3} \frac{g_*^{1/6}}{\alpha^{1/3}} \left(\frac{m_{r,\rm eff}(\phi_{\rm zero})}{M_{\rm pl}} \right)^{1/3} \left(\frac{\phi_{\rm ini}}{M_{\rm pl}} \right)^{2/3}. \tag{7.87}$$

From plugging in Eq. (7.86) the most optimistic value of ϵ, cf. first line of Eq. (7.71), we obtain

$$e^{N_{\rm KD}} = 0.2 g_*^{1/6} \alpha^{2/3} \left(\frac{m_{r,\rm eff}(f_a)}{f_a}\right)^{1/3} \left(\frac{m_{r,\rm eff}(\phi_{\rm ini})}{m_{r,\rm eff}(f_a)}\right)^{2/3} (l \, \sin l\theta_{\rm ini})^{2/3} \times \\ \times \begin{cases} \left(\frac{y_{\psi,\rm th}}{y_\psi}\right)^2, & \text{if } y_\psi \gtrsim y_{\psi,\rm th}, \\ 1, & \text{if } y_{\psi,\rm th} \gtrsim y_\psi \gtrsim y_{\psi,1}, \\ \left(\frac{y_{\psi,1}}{y_\psi}\right)^{2/3}, & \text{if } y_{\psi,1} \gtrsim y_\psi \gtrsim y_{\psi,0}, \\ \left(\frac{y_{\psi,1}}{y_{\psi,0}}\right)^{2/3} \left(\frac{y_\psi}{y_{\psi,0}}\right)^{2/3} & \text{if } y_{\psi,0} \gtrsim y_\psi, \end{cases} \tag{7.88}$$

where $y_{\psi,0}$, defined in Eq. (7.63), is the Yukawa coupling below which oscillation is induced by the zero-temperature potential. The longest duration of kination occurs for

$$y_\psi \simeq y_{\psi,0} \quad \Rightarrow \quad e^{N_{\rm KD}} = 0.4 g_*^{1/6} \left(\frac{m_{r,\rm eff}(\phi_{\rm ini})}{f_a}\right)^{1/3} (l \, \sin l\theta_{\rm ini})^{2/3} \lesssim 1. \tag{7.89}$$

To conclude, a period of kination-domination can not be induced by the spinning complex scalar field, starting oscillating in a radiation-dominated Universe when the damping of the radial mode relies on thermalization. To reduce the Yukawa coupling y_ψ would reduce the thermal mass but delay thermalization too much. To increase y_ψ would make thermalization more efficient but would increase the thermal mass too much. In the next section, we show how the inhibition of the initial rotation due to the thermal mass can be avoided when the fermion abundance is Boltzmann-suppressed at the onset of the oscillation due to either a large Yukawa coupling $y_\psi \phi_{\rm osc} \gtrsim T_{\rm osc}$ or a small reheating temperature $T_{\rm reh} \lesssim y_\psi \phi_{\rm reh}$.

7.4 Scenario III: Thermal Damping & Non-Relativistic Fermions

In Sec. 7.2, the first scenario considers a small Yukawa coupling such that thermal corrections could be neglected. However, as discussed in App. G.3.1, the difficulty is that thermalization takes place too late, and we must rely on a different mechanism for damping the radial mode.

In the second scenario in Sec. 7.3, we have enforced radial damping through thermalization. However, the suppression of the initial angular kick ϵ, cf. Sec. 7.3.1, and the delay of the onset of the matter era, cf. Eq. (7.77), due to the large thermal mass at an early time, prevent the scalar field from inducing a kination era, cf. Eq. (7.89).

In the present section, we consider a third scenario, depicted in Fig. 7.16, which turns out to be the promising one and where radial damping occurs through thermalization. Still, the thermal mass is absent at the onset of the radial mode oscillation due to the Boltzmann suppression of the fermion abundance.

7.4.1 Boltzmann-suppression of the fermion abundance

The presence of the thermal mass $y_\psi T$ supposes the fermions ψ to be abundant in the plasma. Instead, if their abundance is Boltzmann-suppressed, the thermal mass is set by the thermal log potential, cf. Eq. (7.7)

$$m_{r,\rm eff}(\phi, \, T) \; = \; \begin{cases} y_\psi T, & \text{for } y_\psi \phi \lesssim T, \\ \sqrt{2}\alpha \frac{T^2}{\phi}, & \text{for } y_\psi \phi \gtrsim T, \end{cases} \tag{7.90}$$

The Boltzmann-suppression of the fermion abundance can arise in two situations:

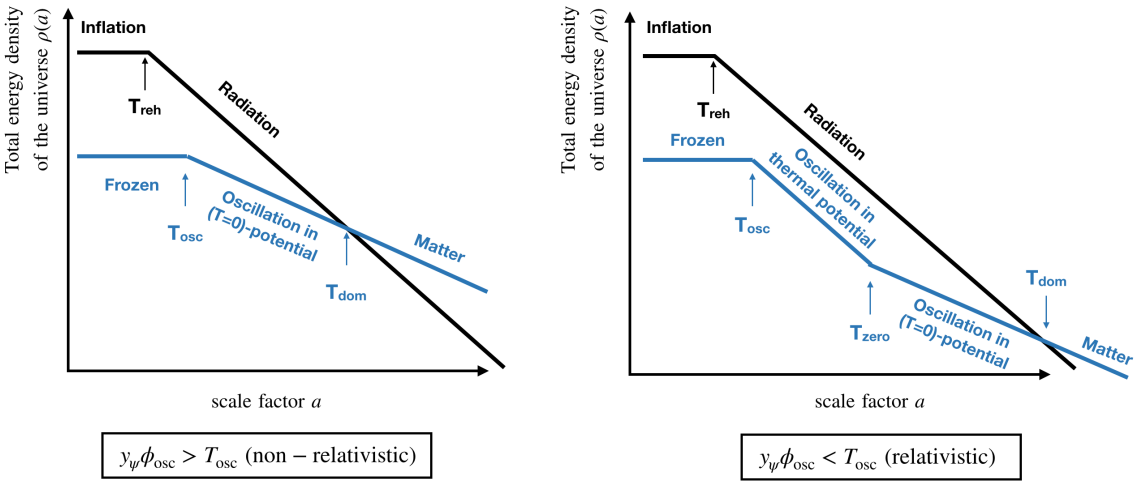

Figure 7.16: In scenario III of the present Sec. 7.4, we consider the fermions responsible for the thermal mass to be Boltzmann-suppressed at the onset of the oscillation (**left** panel). Therefore, the thermal mass is turned off at the time of the angular kick and the $U(1)$ charge fraction ϵ in Eq. (7.97) can be $\mathcal{O}(1)$ without any tuning of the Yukawa coupling to small values, in contrast to scenario II, cf. Sec 7.3 (**right** panel). Later, when the fermions become relativistic, Yukawa interactions are efficient enough to dampen the radial motion before the onset of the matter era.

1. **At large Yukawa coupling** y_ψ

$$\begin{cases} y_\psi \phi_{\rm osc} > T_{\rm osc}, \\ \phi_{\rm osc} = M_{\rm pl} \left(\sqrt{c} \frac{y_\psi T_{\rm osc}}{\lambda \sqrt{2l-2} M_{\rm pl}} \right)^{\frac{1}{l-2}}, \\ T_{\rm osc} = g_*^{-1/2} y_\psi M_{\rm pl}, \end{cases} \quad \Rightarrow \quad y_\psi > 2^{1/4} \sqrt{\lambda} g_*^{\frac{(3-l)}{4}} \left(\frac{l-1}{c} \right)^{1/4}. \tag{7.91}$$

   For $(\lambda,\, c,\, l,\, g_*) = (1,\, 1,\, 10,\, 100)$, we obtain $y_\psi \simeq 6.5 \times 10^{-4}$.

2. **At small reheating temperature** $T_{\rm reh}$

$$\begin{cases} y_\psi \phi_{\rm reh} > T_{\rm reh}, \\ \phi_{\rm reh} = M_{\rm pl} \left(\sqrt{c} \frac{3 H_{\rm reh}}{\lambda \sqrt{2l-2} M_{\rm pl}} \right)^{\frac{1}{l-2}}, \\ T_{\rm reh} = g_*^{-1/4} \sqrt{3 H_{\rm reh} M_{\rm pl}}. \end{cases} \quad \Rightarrow \quad \frac{T_{\rm reh}}{M_{\rm pl}} < y_\psi^{\frac{l-2}{l-4}} \left(\frac{g_*^{1/4}}{\sqrt{3}} \right)^{\frac{2}{l-4}} \left(\frac{\lambda \sqrt{2l-2}}{3\sqrt{c}} \right)^{\frac{1}{l-4}}. \tag{7.92}$$

   For $(\lambda,\, c,\, l,\, g_*,\, y_\psi) = (1,\, 1,\, 10,\, 100,\, 10^{-4})$, we obtain $T_{\rm reh} < 1.5 \times 10^{13}$ GeV. The upper bound (7.92) on the reheating temperature prevents the thermal mass $y_\psi T$ to be active at the time of the kick. In our work we assume the Universe to be radiation-dominated at the time of the kick. Therefore, for consistency we must also insure that the reheating temperature is larger than the temperature at the time of the kick

$$T_{\rm reh} > T_{\rm osc} = g_*^{-1/4} \sqrt{m_{r,\rm eff}(\phi_{\rm ini}) M_{\rm pl}} = 4.9 \times 10^{12}\ {\rm GeV} \left(\frac{100}{g_*} \right)^{1/4} \left(\frac{m_{r,\rm eff}(\phi_{\rm ini})}{10^8\ {\rm GeV}} \right)^{1/2}. \tag{7.93}$$

   Compatibility between Eq. (7.92) and Eq. (7.93) implies that the conditions for successful kination are lost as soon as

$$g_*^{-1/4} \sqrt{m_{r,\rm eff}(\phi_{\rm ini})/M_{\rm pl}} > y_\psi^{\frac{l-2}{l-4}} \left(\frac{g_*^{1/4}}{\sqrt{3}} \right)^{\frac{2}{l-4}} \left(\frac{\lambda \sqrt{2l-2}}{3\sqrt{c}} \right)^{\frac{1}{l-4}}. \tag{7.94}$$

The latter condition does not add any constraint to our plots.

No thermal-log domination. When fermions are Boltzmann-suppressed, the thermal potential is given by the thermal log potential, which is suppressed with respect to the quadratic thermal correction by $(\alpha T/y_\psi \phi)^2$. Suppose the thermal log dominates the potential at the onset of oscillation. In that case, we expect suppression of the kick ϵ and a delay of the onset of the matter era as in scenario II, cf. Sec. 7.3.1, but also the formation of Q-balls, see Sec. 7.1.2. The thermal-log potential can be neglected whenever its associated thermal mass is smaller than the zero-temperature mass

$$\sqrt{2}\alpha \frac{T_{\rm osc}^2}{\phi_{\rm ini}} \lesssim m_{r,\rm eff}(\phi_{\rm ini}) \quad \Rightarrow \quad \alpha \lesssim \frac{g_*^{1/2}}{\sqrt{2}} \left(\frac{\phi_{\rm ini}}{M_{\rm pl}}\right). \tag{7.95}$$

where we have used $m_{r,\rm eff}(\phi_{\rm ini}) \simeq 3H_{\rm osc} \simeq g_*^{1/2} T_{\rm osc}^2/M_{\rm pl}$.

Consequence I: Non-suppressed angular kick. Since the thermal mass is absent at the onset of the radial mode oscillation, the onset of oscillation occurs when the Hubble scale crosses the zero-temperature mass

$$H_{\rm osc} \simeq m_{r,\rm eff}(\phi_{\rm ini})/3. \tag{7.96}$$

where $\phi_{\rm ini}$ is given by Eq. (7.26) and the fraction of $U(1)$ charge is the same as in the scenario I, cf. Eq. (7.41)

$$\epsilon \;=\; \begin{cases} \frac{1}{\sqrt{2}} \frac{m_{r,\rm eff}(f_a)}{m_{r,\rm eff}(\phi_{\rm ini})}\, l\, \sin l\theta_{\rm ini}, & \text{if} \quad c > l-1, \\ \frac{1}{\sqrt{2}} \sqrt{\frac{c}{l-1}} \frac{m_{r,\rm eff}(f_a)}{m_{r,\rm eff}(\phi_{\rm ini})}\, l\, \sin l\theta_{\rm ini}, & \text{otherwise.} \end{cases} \tag{7.97}$$

so that values $\epsilon \sim \mathcal{O}(1)$ are allowed.

Consequence II: No thermal mass domination at all. After the onset of oscillation, the scalar field $\phi \propto a^{-3/2}$ redshifts faster than the temperature $T \propto a^{-1}$. This implies the existence of a temperature $T_{\rm rel}$

$$T_{\rm rel} \;\equiv\; y_\psi \phi_{\rm rel}, \tag{7.98}$$

below which the fermion are relativistic and abundant in the plasma. Using that the scalar field ϕ reshifts as matter in a radiation-dominated Universe, we get

$$\phi_{\rm rel} = \phi_{\rm ini} \left(\frac{H_{\rm rel}}{H_{\rm osc}}\right)^{3/4}, \tag{7.99}$$

where $H_{\rm osc} \simeq m_{r,\rm eff}(\phi_{\rm ini})/3$, $H_{\rm rel} \simeq g_*^{1/2} T_{\rm damp}^2/3M_{\rm pl}$. From Eq. (7.98) and Eq. (7.99), we obtain

$$T_{\rm rel} \simeq \frac{1}{g_*^{3/4}} \frac{m_{r,\rm eff}^{3/2}(\phi_{\rm ini})}{y_\psi^2 M_{\rm pl}^{1/2}} \left(\frac{M_{\rm pl}}{\phi_{\rm ini}}\right)^2. \tag{7.100}$$

When the fermions become relativistic, the thermal mass jumps, cf. Eq. (7.90), and will have no impact if the thermal mass remains smaller than the zero-temperature mass $y_\psi T_{\rm rel} \lesssim m_{r,\rm eff}(\phi_{\rm rel})$. From plugging Eq. (7.100) in the previous equation, we obtain that the scalar field evolves in its zero-temperature potential during the whole time if

$$y_\psi \gtrsim \frac{1}{g_*^{3/4}} \left(\frac{m_{r,\rm eff}(\phi_{\rm ini})}{m_{r,\rm eff}(\phi_{\rm rel})}\right) \left(\frac{m_{r,\rm eff}(\phi_{\rm ini})}{M_{\rm pl}}\right)^{1/2} \left(\frac{M_{\rm pl}}{\phi_{\rm ini}}\right)^2. \tag{7.101}$$

7.4.2 Evolution of the field and its energy density

Delay of matter domination. If the conditions in Eq. (7.91), (7.92) and (7.101) are satisfied, then the scalar field redshifts like matter during its whole evolution. Therefore, the situation is similar to scenario I in Eq. (7.50) and the scalar dominates the energy density of the Universe at

$$\rho_{\rm dom} = \frac{27 m_{r,\rm eff}(\phi_{\rm ini})^2 \phi_{\rm ini}^8}{16 M_{\rm Pl}^6} A_\epsilon^4 \qquad \text{and} \qquad \frac{a_{\rm dom}}{a_{\rm osc}} = \frac{2M_{\rm Pl}^2}{3\phi_{\rm ini}^2} A_\epsilon^{-1} \tag{7.102}$$

with

$$A_\epsilon = \begin{cases} \epsilon, & \text{if } \rho_{\rm damp} > \rho_{\rm dom}, \\ 1, & \text{if } \rho_{\rm damp} < \rho_{\rm dom}. \end{cases} \tag{7.103}$$

We recall that the impact of ϵ on the evolution of the scalar field energy density is discussed in App. G.4.3.

Radial damping. The scalar field decay rate is given by Eq. (7.78) (see App. G.3.1 for more details) which we rewrite here

$$\Gamma_\phi \simeq \begin{cases} \text{for } y_\psi \phi < T : \begin{cases} \text{for } \alpha T > y_\psi \phi, & \frac{y_\psi^2 \alpha T}{2\pi^2}, \\ \text{for } \alpha T < y_\psi \phi, & \frac{y_\psi^4 \phi^2}{\pi^2 \alpha T}, \end{cases} & + \frac{y_\psi^2 m_\phi}{8\pi} \Theta\left(m_\phi/2 - \text{Max}\left[y_\psi \phi,\, gT\right]\right). \\ \text{for } y_\psi \phi > T : \quad b\alpha^2 \frac{\text{Max}\left[T,\, m_\phi\right]^3}{\phi^2}, \end{cases} \tag{7.104}$$

The different decay channels in Eq. (7.78) are the ones induced by scattering with virtual fermions of the plasma $\phi\psi_{\rm th} \to \psi_{\rm th}$ $\left(\Gamma = \frac{y_\psi^2 \alpha T}{2\pi^2} \text{ or } \frac{y_\psi^4 \phi^2}{\pi^2 \alpha T}\right)$, tree-level decay $\phi \to \psi\psi$ $\left(\Gamma = \frac{y_\psi^2 m_\phi}{8\pi}\right)$ or loop-induced decay into gauge boson pair $\phi \to AA$ $\left(\Gamma = b\alpha^2 \frac{\text{Max}\left[T,\, m_\phi\right]^3}{\phi^2}\right)$. In Fig. 7.17, we show the different decay rates and compute the decay temperature for three different values of the Yukawa coupling y_ψ.

For a better understanding, we now derive the expression for the maximum damping temperature analytically. We suppose that the conditions introduced in Sec. 7.4.1 are satisfied such that the fermion abundance is initially Boltzmann-suppressed at the onset of scalar field oscillation. When the fermions become relativistic at the temperature $T_{\rm rel} \equiv y_\psi \phi_{\rm rel}$ given in Eq. (7.98), the damping rate suddenly increases due the scattering with virtual fermions of the plasma, see Fig. 7.17. We suppose $\alpha \lesssim 1$ in Eq. (7.104), such that the decay rate at $T_{\rm rel}$ is controlled by $\Gamma_{\phi\psi_{\rm th}\to\psi_{\rm th}} = y_\psi^4 \phi^2/(\pi^2 \alpha T) \propto T^2$. Since $\Gamma/H =$ constant, the decay through that channel only depends on whether $\Gamma/H > 1$ at the relativistic threshold $T_{\rm rel}$. This defines the quantity $y_{\psi,*}$

$$\Gamma/H\Big|_{T=T_{\rm rel}} > 1 \quad \Rightarrow \quad y_\psi > y_{\psi,*} = \frac{1.35\alpha^{1/4}}{g_*^{1/16}} \left(\frac{m_{\rm eff,ini}}{M_{\rm Pl}}\right)^{3/8} \left(\frac{M_{\rm pl}}{\phi_{\rm ini}}\right)^{1/2}. \tag{7.105}$$

We deduce the maximum damping temperature

$$\begin{cases} \alpha \lesssim 1, \\ y_\psi > y_{\psi,*}, \end{cases} \quad \Rightarrow \quad T_{\rm damp} = T_{\rm rel}, \tag{7.106}$$

with $T_{\rm rel}$ given in Eq. (7.98). The damping temperature peaks for $y_\psi = y_{\psi,*}$, see maximum of the dashed yellow line in Fig. 7.18-top. The energy density just after damping is given by, see Eq. (G.151), $\rho_{\rm damp} = \frac{\pi^2}{30} g_* T_{\rm damp}^4 B_\epsilon^4$, with $B_\epsilon = 1, \epsilon$ if $\rho_{\rm damp} > \rho_{\rm dom}$ and $\rho_{\rm damp} \leq \rho_{\rm dom}$, respectively

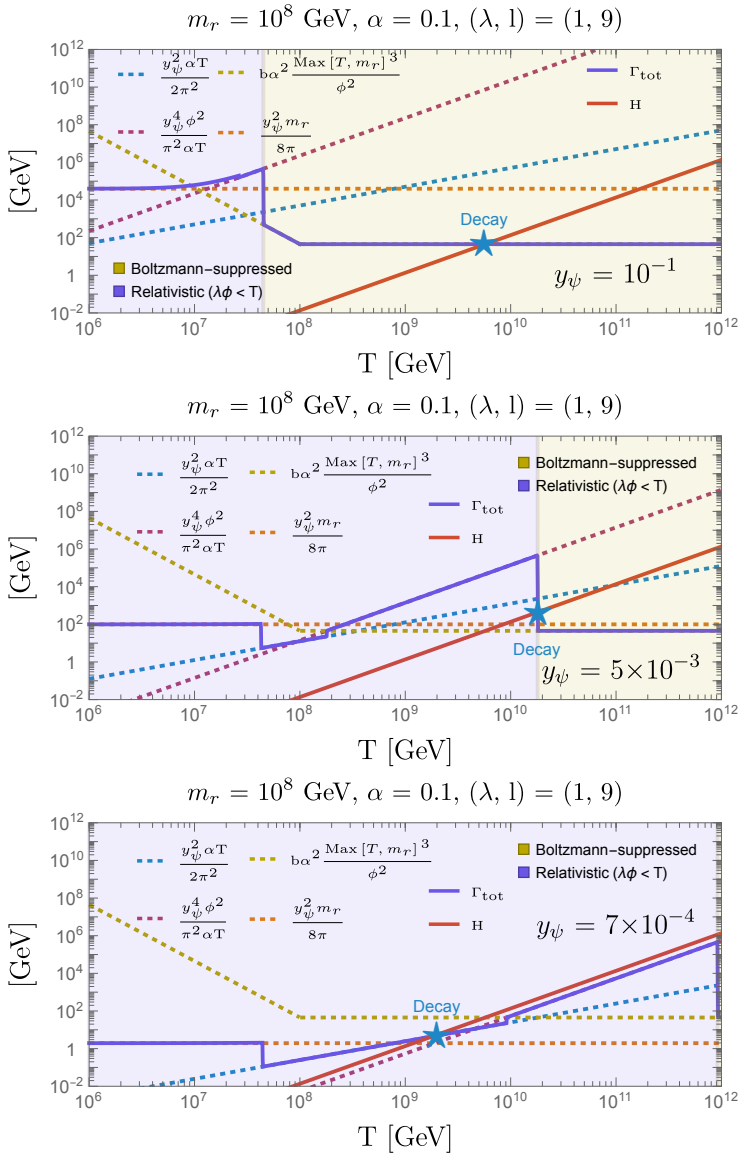

Figure 7.17: The total decay rate (solid purple) of the scalar condensate in the fermion portal compared to the Hubble scale (solid red). The decay temperature is depicted by a blue star. We show three values of y_ψ, corresponding to the three decay channels given in Eq. (7.104) and depicted in Fig. G.3 (see App. G.3.1 for more details). From **top** to **bottom**, the dominant channel is the decay into gauge boson pairs at one loop $\phi \to AA$ (dotted gold), scattering with virtual fermions of the plasma $\phi\psi_{\mathrm{th}} \to \psi_{\mathrm{th}}$ in the small thermal width $\alpha T \lesssim y_\psi \phi$ (dotted purple) and large thermal width limit $\alpha T \gtrsim y_\psi \phi$ (dotted blue). Visible on these plots is the suppression of the decay into fermions when the later are non-relativistic (yellow region).

Preservation of the $U(1)$ charge in the condensate. The $U(1)$ charge carried by the condensate is preserved during thermalization if [669] (see also App. G.3.1)

$$f_a \gg T_{\phi \to f_a}, \tag{7.107}$$

where $T_{\phi \to f_a}$ is the temperature when ϕ reaches f_a. Using that ϕ redshifts like matter, $\phi = \phi_{\mathrm{ini}} \left(\frac{T}{T_{\mathrm{osc}}}\right)^{3/2}$, we obtain

$$\frac{f_a}{T_{\phi \to f_a}} = 0.8 \times 10^5 \left(\frac{f_a}{10^8 \text{ GeV}}\right)^{1/3} \left(\frac{10^{10} \text{ GeV}}{T_{\mathrm{osc}}}\right) \left(\frac{\phi_{\mathrm{ini}}}{M_{\mathrm{pl}}}\right)^{2/3} \gg 1. \tag{7.108}$$

We checked that all the parameter spaces shown from Figs. 7.18 to Fig. 7.22 satisfy that condition.

Duration of the kination era. The Universe acquires a kination equation-of-state when the field reaches $\phi \to f_a$, corresponding to the energy density and scale factor

$$\rho_{\mathrm{KD},i} \;=\; \frac{1}{2} f_a^2 m_{r,\mathrm{eff}}^2(f_a), \quad \text{and} \quad \frac{a_{\mathrm{KD},i}}{\max(a_{\mathrm{dom}}, a_{\mathrm{damp}})} = \left(\frac{\min(\rho_{\mathrm{dom}},\, \rho_{\mathrm{damp}})}{\rho_{\mathrm{KD,i}}} \right)^{1/3}. \tag{7.109}$$

The kination era stops when the Universe becomes radiation dominated. The energy scale at which it occurs depends on whether radial damping occurs before and after the onset of matter domination $\rho_{\mathrm{KD},f} = \rho_{\mathrm{KD},i}^2 / \min(\rho_{\mathrm{dom}},\, \rho_{\mathrm{damp}})$.

The duration of the kination era $\exp(N_{\mathrm{KD}}) \equiv a_{\mathrm{KD},f}/a_{\mathrm{KD},i}$ reads

$$e^{N_{\mathrm{KD}}} = \begin{cases} \sqrt{\frac{3}{2}} \left(\frac{m_{r,\mathrm{eff}}(\phi_{\mathrm{ini}})}{m_{r,\mathrm{eff}}(f_a)} \frac{M_{\mathrm{pl}}}{f_a} \right)^{1/3} \left(\frac{\phi_{\mathrm{ini}}}{M_{\mathrm{pl}}} \right)^{4/3} \epsilon^{2/3}, & \text{if } \rho_{\mathrm{damp}} > \rho_{\mathrm{dom}}, \\ \left(\frac{\frac{\pi^2}{30} g_* T_{\mathrm{damp}}^4}{f_a^2 m_{r,\mathrm{eff}}^2(f_a)/2} \right)^{1/6} \epsilon^{2/3}, & \text{if } \rho_{\mathrm{damp}} < \rho_{\mathrm{dom}}. \end{cases} \tag{7.110}$$

where ϵ can be $\mathcal{O}(1)$ and where T_{damp} is given by Eq. (7.106). In the case where $y_\psi > y_{\psi,*}$ with $y_{\psi,*}$ given by Eq. (7.105), we obtain

$$e^{N_{\mathrm{KD}}} = \begin{cases} e^{8.1} \epsilon^{\frac{2}{3}} \left[\frac{10^8 \mathrm{GeV}}{f_a} \right]^{\frac{1}{3}} \left[\frac{m_{r,\mathrm{eff}}(\phi_{\mathrm{ini}})}{m_{r,\mathrm{eff}}(f_a)} \right] \left[\frac{\phi_{\mathrm{ini}}}{M_{\mathrm{pl}}} \right]^{\frac{4}{3}}, & \text{if } \rho_{\mathrm{damp}} > \rho_{\mathrm{dom}}, \\ e^{4.2} \frac{\epsilon^{2/3}}{g_*^{1/3}} \left[\frac{f_a}{10^8\ \mathrm{GeV}} \right]^{\frac{1}{3}} \left[\frac{m_{r,\mathrm{eff}}(f_a)}{f_a} \right]^{\frac{2}{3}} \left[\frac{m_{r,\mathrm{eff}}(\phi_{\mathrm{ini}})}{m_{r,\mathrm{eff}}(f_a)} \right] \left[\frac{10^{-4}}{y_\psi} \right]^{\frac{4}{3}} \left[\frac{M_{\mathrm{pl}}}{\phi_{\mathrm{ini}}} \right]^{\frac{4}{3}} & \text{if } \rho_{\mathrm{damp}} < \rho_{\mathrm{dom}}. \end{cases} \tag{7.111}$$

The maximal duration of kination is reached for $y_\psi = y_{\psi,*}$

$$e^{N_{\mathrm{KD}}}\big|_{y_\psi = y_{\psi,*}} = e^{5.1} \frac{\epsilon^{2/3}}{\alpha^{1/3} g_*^{1/4}} \left[\frac{10^8}{f_a} \right]^{\frac{1}{6}} \left[\frac{m_{r,\mathrm{eff}}(f_a)}{f_a} \right]^{\frac{1}{6}} \left[\frac{m_{r,\mathrm{eff}}(\phi_{\mathrm{ini}})}{m_{r,\mathrm{eff}}(f_a)} \right]^{\frac{1}{2}} \left[\frac{0.1}{\phi_{\mathrm{ini}}/M_{\mathrm{pl}}} \right]^{\frac{2}{3}}. \tag{7.112}$$

7.4.3 Gravitational-wave signature and detectability

We show the detectability of the SGWB produced by primordial inflation (Fig. 7.20), local strings (Fig. 7.21), and globals strings (Figs.7.22) in the presence of a kination era generated by scenario III: a spinning complex scalar field with thermal damping and Boltzmann-suppression of the thermal corrections to the potential.

The parameter space splits into two parts separated by the blue dashed line: the Boltzmann suppression by a considerable y_ψ in Eq. (7.91) and by a small reheating temperature in Eq. (7.92). The kination duration in the former region is independent of T_{reh}, and the inflationary or the string scales are not bounded. On the contrary, the maximum energy scale is constrained if the Universe reheats instantaneously in a region with a small reheating temperature. In the figures below, some parts of the parameter space have the inflation scale and the string scale fixed at high-energy above the $T_{\mathrm{reh,max}}$. This is allowed when a period between the end of inflation and the completion of reheating exists. Its existence would induce the SGWB distortion at high frequencies above the kination peak and might allow us to distinguish the large y_ψ from the small T_{reh} cases.

Finally, we also show the constraints that apply for very low m_r, in which the radial mode has a large thermal abundance and long lifetime, which is excluded either by overabundance if cosmologically stable or by late decay into photons after BBN [722]. The corresponding constraint $m_r > 10\ \mathrm{GeV}(f_a/10^9\ \mathrm{GeV})^{2/3}$ is reported in the green hashed region in the plots.

These plots demonstrate that concrete scenario III, where radial damping is not assumed but explicitly calculated via thermal effects, leads to observable signatures of an intermediate matter-kination era.

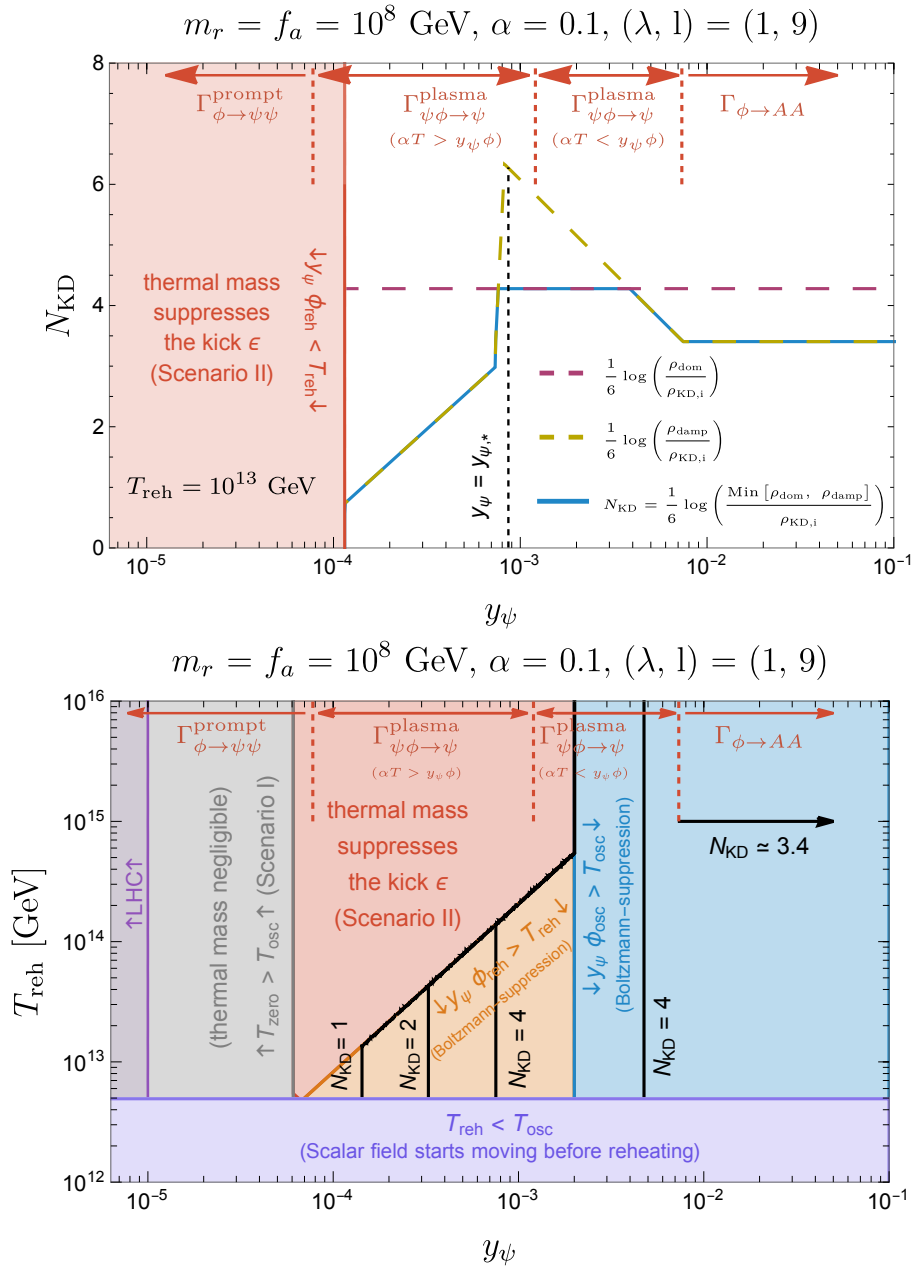

Figure 7.18: Number of kination e-folds when radial damping occurs via thermalization through fermion portal. The presence of the thermal mass at the onset of the oscillation (scenario II in Sec. 7.1) suppresses the angular kick and prevents kination (red region). Instead, at large Yukawa coupling (blue region and condition (7.91)) or at low reheating temperature (orange region and condition (7.92)), the fermion abundance is Boltzmann-suppressed and the thermal mass is absent. The $N_{\rm KD}$ black contour lines follow from Eq. (7.110), with the decay temperature $T_{\rm damp}$ being determined numerically as shown in Fig. 7.17. We write in red the dominant decay channel, based on Eq. (7.104). The maximal duration of kination is reached at $y_\psi = y_{\psi,*}$, cf. Eq. (7.105), and is given by Eq. (7.112). The thermal mass is also negligible at small Yukawa (gray region and scenario I in Sec. 7.2), but there, the thermalization rate is too small and a circular trajectory is not obtained before $\phi \to f_a$. In the pale purple region, the kick at $T_{\rm osc}$ occurs before the Universe is reheated which goes beyond the scope of our study, see Eq. (7.93). We show the LHC constraints on heavy colored fermions, $m_\psi = y_\psi f_a \gtrsim$ TeV.

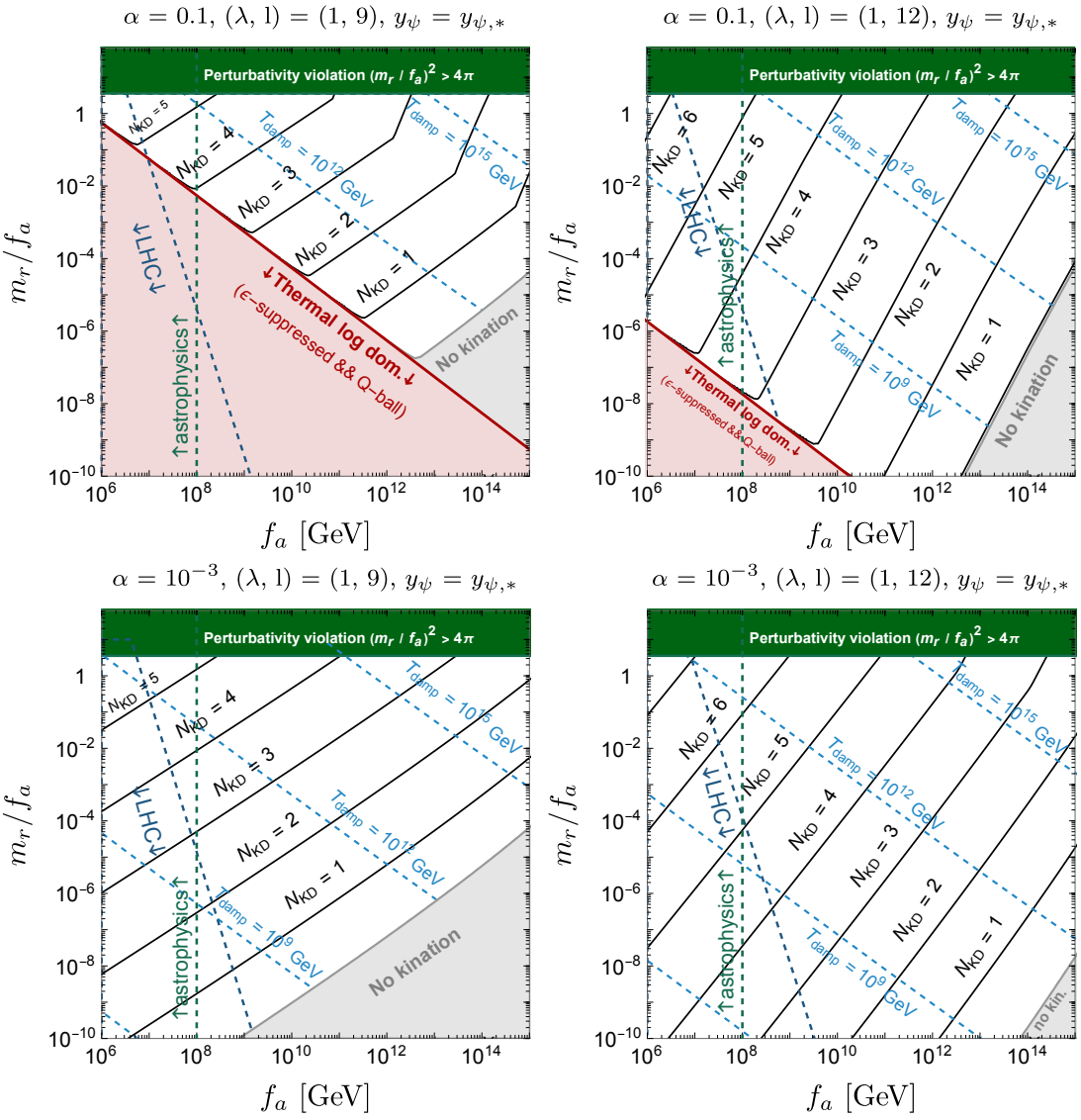

Figure 7.19: Maximum number of kination e-folds in **scenario III**. In order to have matter-kination as long as possible, we chose values of the Yukawa coupling $y_\psi = y_{\psi,*}$ in Eq. (7.105) to maximize the duration of kination, see Eq. (7.112). The dashed blue lines show the temperature at which the radial mode is dampened by thermal effects. The dark blue region shows the LHC constraints $m_\psi \gtrsim$ TeV. The vertical green dashed line shows expected astrophysical constraints $f_a \gtrsim 10^8$ GeV. The dark green region shows the limit of validity of the EFT. In the purple region, the thermal-log potential dominates the onset of oscillation, which suppresses the angular kick ϵ, delays the onset of matter era, cf. Sec. 7.3.1, and generates Q-balls, see Sec. 7.1.2.

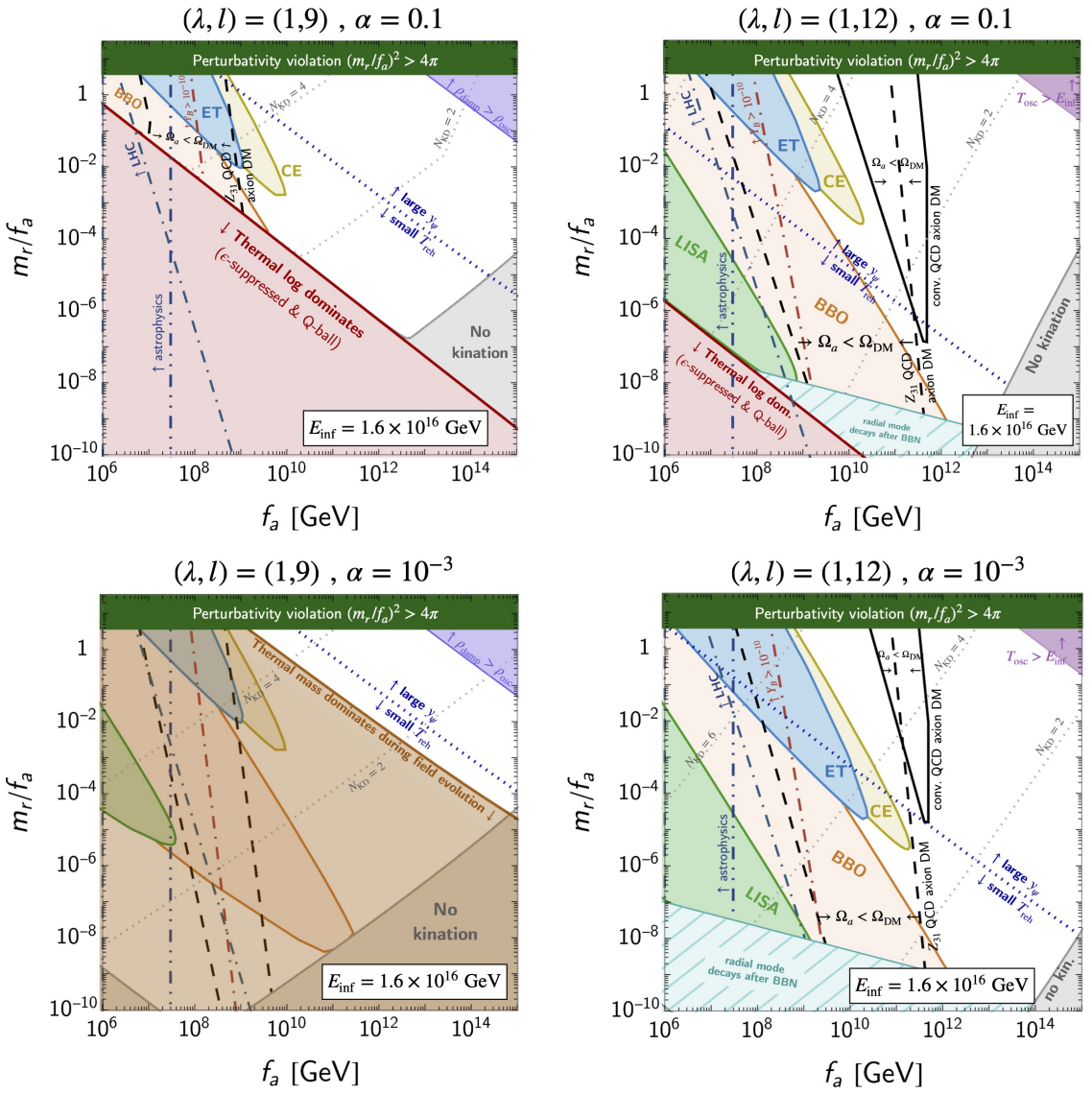

Figure 7.20: Ability of future-planned GW observatories to detect the peak signature of a matter-kination era induced by **scenario III** in the SGWB from inflation with energy scale $E_{\rm inf}$. Black solid lines indicate where the canonical QCD axion DM abundance is satisfied, cf. Eq. (6.5). The left boundary is set by the kinetic misalignment mechanism, while the right one is by the standard misalignment (for small m_r with a specific f_a) and by the axion quality problem (for larger m_r depending on f_a), cf. Eq. (7.22). Only the region between the two lines does not over-produce DM. Dashed lines are the equivalent for lighter non-canonical QCD axion, cf. Eq. (6.3). A dotted-dashed red line denotes the parameter space where the rotating axion allows the correct baryon asymmetry, cf. Eq. (6.32). Gray dotted lines show the kination duration contours. Smaller m_r and λ implies larger initial scalar vev $\phi_{\rm ini}$, cf. Eq. (7.26), and longer matter-kination duration. For smaller α, the coupling $y_{\psi,*}$ decreases and cannot prevent the thermal mass to dominate during the field evolution as shown in bottom-left panel, cf. Eq. (7.101). The blue dashed line separates the large y_ψ region where the kination duration is $T_{\rm reh}$-independent, from the small $T_{\rm reh}$ region.

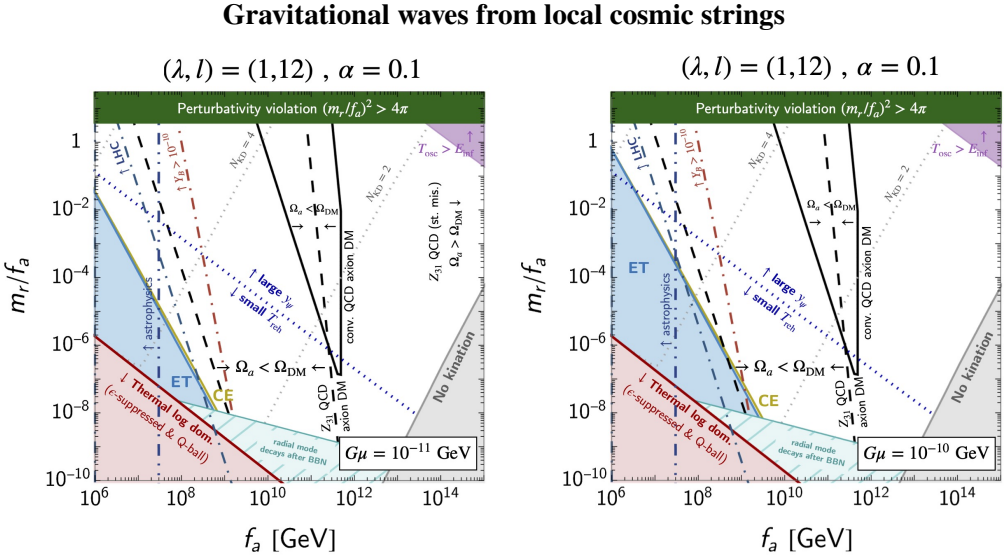

Figure 7.21: Same as Fig. 7.20 using the SGWB from local cosmic strings with tension $G\mu$.

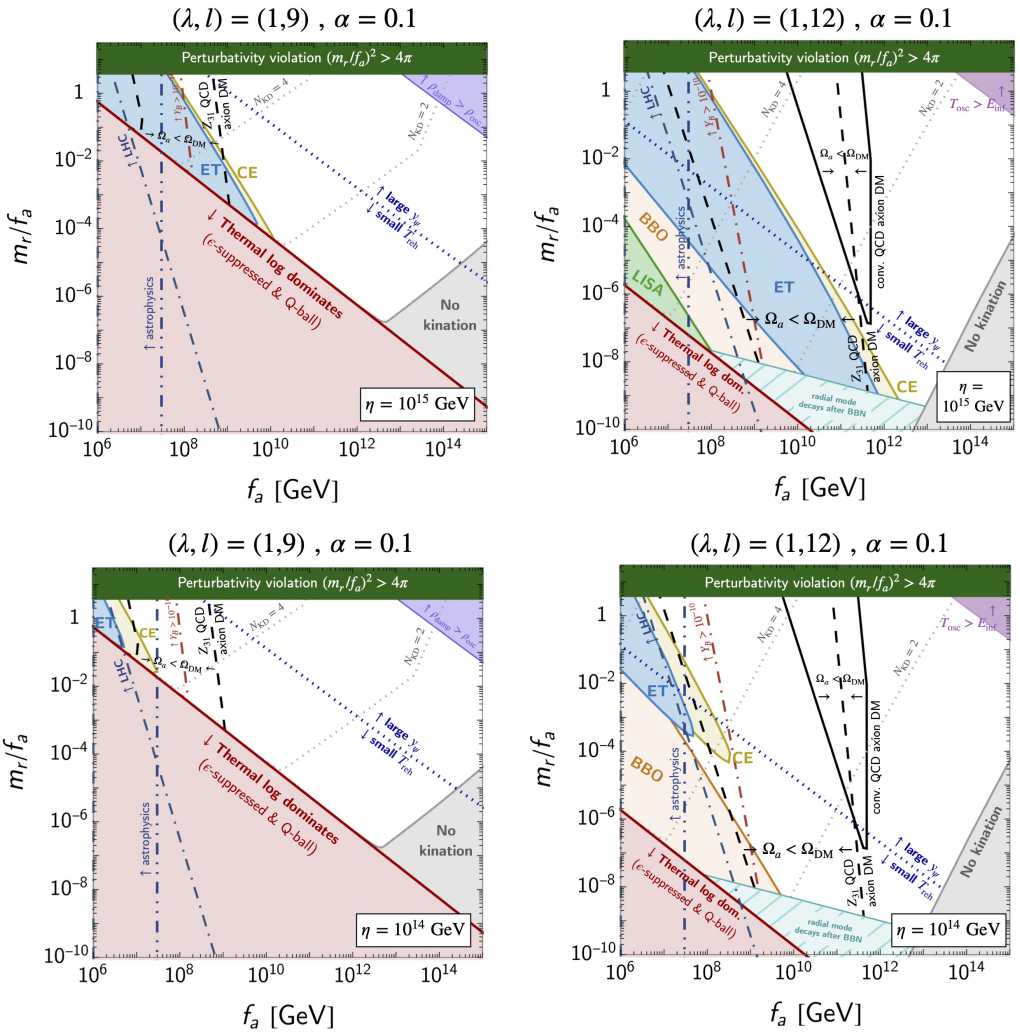

Figure 7.22: Same as Fig. 7.20 using the SGWB from global cosmic strings with string scale η.

7.5 Chapter Summary

The potential candidate for the intermediate kination era that leads to a striking signature in SGWB from all prime sources (Sec. 4.4) is the rotating axion, which provides exciting phenomenology such as DM production and Baryogenesis, as discussed in Chap. 6, This chapter discusses the particle physics implementations of such intermediate kination era in one main class of axion models, where the unavoidable partner of the axion, the radial mode of the complex scalar field, plays a crucial role in providing a kick to the axion. While the corresponding setup where the radial mode dynamics start at large VEV $\gg f_a$ can be well-motivated in SUSY frameworks, for instance, one non-trivial aspect is that the radial motion needs to be damped for successful kination.

As Ref. [4] was being completed, Refs. [3, 274] appeared, which also discusses GW from a kination era triggered in axion models and partially overlaps with the present chapter. As we have discussed extensively, the radial-mode damping is crucial for kination to be realized. While most of the literature on axion cosmology typically ignores the dynamics of its radial partner and focuses on the angular mode, the analysis in this chapter, as well as references [128, 274, 449, 450, 648, 669, 693, 697] show that the radial mode may be a key to understand the early cosmological history in axion models, with significant consequences for the experimental program. Thermal damping of the radial mode requires introducing new interactions of the Peccei-Quinn field. We have shown that these interactions induce a thermal mass for the Peccei-Quinn field, thus delaying the time of the axion kick. Together with a modified thermalization temperature, this prevents a kination era unless the reheating temperature is sufficiently low or the Yukawa coupling y_ψ is large, cf. Sec. 7.4.

We have derived in detail the model's parameter space that leads to a kination era and resulting observable gravitational waves. Moreover, the connection between GW signature, DM production, and Baryogenesis from the rotating axion is also established. We showed that $N_{\rm KD} < 6$ for most of the model's parameter space. In Sec. 4.4 we considered the energy scale and duration of kination as free parameters, with $N_{\rm KD}$ as high as $N_{\rm KD} < 11$. It would be interesting to investigate whether there are alternative models which can give longer kination eras.

Regarding the thermal damping mechanism of radial mode, we have used the thermalization rate that follows from a Yukawa interaction between the scalar field and new fermions, cf. Refs. [699, 700]. While the literature on axion cosmology is large, there is no study of the radial mode thermalization beyond references [128, 274, 449, 450, 648, 669, 693, 697], on which we have extended by including the thermal mass effect in the radial-mode EOM. We hope our work will motivate further investigations on these thermalization effects as they are crucial for the early Universe physics of axion, with far-reaching observable consequences. Another option is to assume non-thermal damping through parametric resonance. We have derived predictions in this case, treating the damping temperature as a free parameter. It remains to be checked whether this is indeed realizable. We have exposed the problem in App. G.3.2. This will require a careful investigation of the coupled dynamics and back-reaction effects.

We note that if the complex scalar field belongs to a completely secluded sector, we expect the LHC and astrophysical bounds on f_a in Fig. 7.19, 7.20, 7.21, and 7.22 to be relaxed. Additionally, the $N_{\rm eff}$ bounds can be evaded if the matter domination occurs after thermalization. Low f_a regions are interesting from the point of view of GW detection, see Fig. 4.22. When the matter-kination era occurs after the end of BBN, below 6 keV, the peak signature appears in the very low-frequency region and could be probed by pulsar timing array experiments like SKA and NANOGrav [274]. We leave the dedicated study of the viability of this possibility for further works.

Fig. 7.23 summarizes the values of f_a and of the kination energy scales that can be probed by GW experiments in the main class of axion model considered. The key expressions and figures of this chapter are shown in Tables 8.1. Concerning the particle physics implementations, Secs. 7.1, 7.2, 7.3 and 7.4 improve the recent study [274] in different aspects, summarized as follows:

- We compute the Noether $U(1)$ charge ϵ (or Y_θ) explicitly from a particle physics model, and we show that it is suppressed when the thermal mass is present, see Sec. 7.3.1. The impact

of ϵ on the kination duration is presented in Sec. 7.2.1.

- We show that the thermal mass is necessarily present at the time of the angular kick if we require efficient thermalization. As a consequence, a period of matter-kination domination cannot be generated, see Sec. 7.3.
- A first solution is to consider radial damping through non-thermal processes as parametric resonance, see scenario I in Sec. 7.2, even though a more quantitative analysis would be needed to assess this possibility.
- A second solution is to consider the possibility that the fermions inducing the thermal mass are Boltzmann-suppressed at the angular kick when the value of ϵ is generated. See scenario III in Sec. 7.4.
- We study the possibility of generating a matter-kination era from a spinning complex scalar field in all the possible values of the Yukawa coupling y_ψ and reheating temperature $T_{\rm reh}$. We found four different regimes, pictured by colored regions in Fig. 7.18.

As shown in Fig. 7.19, the parameter space associated with the longest matter-kination era lies in the region $f_a \lesssim 10^8$ GeV and $y_\psi f_a \lesssim$ TeV, potentially already excluded by astrophysics and LHC constraints. This motivates the study of an axion sector secluded from the SM. Also, the UV completion requires several assumptions (on the shape of the radial mode potential, the absence of higher-dimensional operators with $l < 6$, and the need for an appropriate damping mechanism of the radial motion). It will be interesting to motivate further constructions leading to high axion masses at early times compatible with a matter-kination era. We leave this for future work.

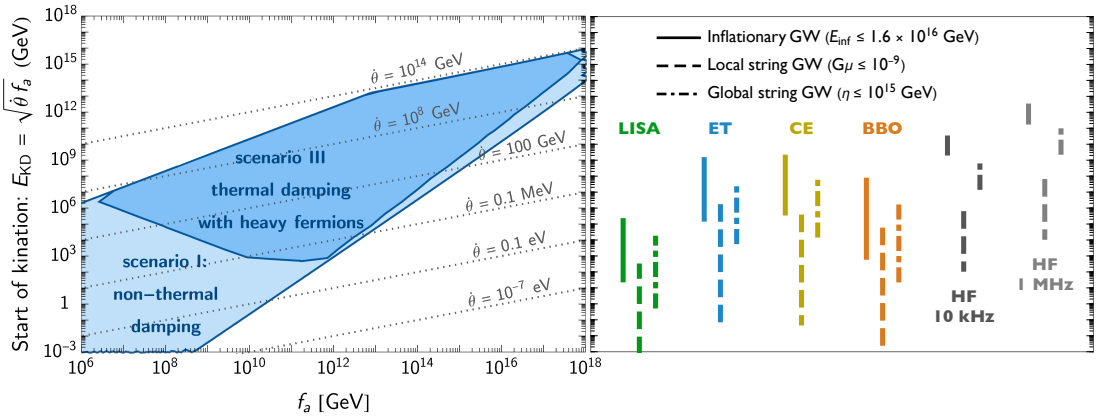

Figure 7.23: *left*: Parameter space leading to observable GW peak signature in the rotating axion model, scanning over m_r and l values and the corresponding values of the axion velocity at the start of kination. *right*: Detectable ranges of $E_{\rm KD}$ by the future planned GW experiments, for the three GW sources: primordial inflation, local and global cosmic strings. For the fictional high-frequency experiments, we assume detectors operating at 10 kHz and 1 MHz with $\Omega_{\rm sens}h^2 \simeq 10^{-10}$.

Field evolution Fig. 7.3	$E_{\rm KD} = 2^{1/4}(f_a m_r)^{1/2}$	
Scenario I (non-thermal damping) Fig. 7.9, 7.20, 7.11, 7.12	$N_{\rm KD}$	Eq. (7.34)
Scenario II (thermal damping) Fig. 7.13	$N_{\rm KD}$	Eq. (7.89)
Scenario III (thermal damping with non-relativistic fermions) Fig. 7.16, 7.18, 7.19, 7.20, 7.21, 7.22	$N_{\rm KD}$	Eq. (7.35)

Table 7.1: List of key relations and figures in the model-dependent analysis.

Chapter 8

Final Remarks and Outlooks

Primordial SGWBs are tools for charting the early-Universe cosmology and the high-energy particle physics. With the landscape in Fig. 2.1 spanning almost 31 decades in frequency from 10^{13} Hz to 10^{-18} Hz, SGWBs encapsulate information around their production times from the Planck scale until today. The earlier the production, the smaller the horizon size, leading to the higher GW frequency due to causality. We can trace the cosmological history using almost all SGWBs from and beyond the SM of particle physics, except the thermal-plasma GW; see Fig. 2.2. Assuming the standard radiation-dominated Universe, SGWBs from the SM have either too-weak amplitude (for inflation) or too-high frequency (for thermal plasma) to be observed in future experiments. Nonetheless, these GW observatories have excellent reach to the SGWB from BSM sources and the effects of the non-standard cosmological histories.

The landscape's amplitude – representing the relic density of GW today – is strongly bounded ($\Omega_{\rm GW} \lesssim 10^{-7}$) by the extra relativistic degrees-of-freedom $\Delta N_{\rm eff}$. The GW experiments that can overcome this bound populate the frequency region of $f_{\rm GW} \simeq 10^{(-18,3)}$ Hz. Recently, there are active efforts in the ultra-high-frequency (UHF) regime $f_{\rm GW} > {\rm kHz}$ to improve the sensitivities beyond $\Delta N_{\rm eff}$ bound [40]. The idea of probing ${\rm MHz} - {\rm GHz}$ SGWB with the existing axion experiments is extremely appealing.

Cosmic strings and SGWB.

Cosmic strings are ubiquitous in BSM physics and have prominent SGWB signals due to the broadband spectrum and amplitude that grows with the symmetry-breaking scale. We adopt the semi-analytic VOS model for tracing the string-network evolution and accurately calculating the loop numbers and GW. Moreover, the SGWB calculation via this method applies to strings in non-trivial scenarios, e.g., strings under thermal friction, metastable strings, and global strings. The particle-production effect also generates interesting GW signatures despite its unobservability for the conservative cosmic strings. The additional couplings between strings and other particles enhance particle production, render the GW signature detectable, and provide an exciting way of dark matter production and baryogenesis. Nonetheless, there might be an issue with cosmic-ray observation [457, 723]. We leave this for future work.

Cosmic archeology with primordial GW

For long-lasting sources (primordial inflation, cosmic strings, and the super-horizon contribution), the shape of SGWB traces the evolution of the total energy density of the Universe, cf. Figs. 4.2 and 4.3. The suppression feature is due to matter and inflationary eras, while the kination enhances the signal. We classify five schemes depending on sequences of the equation-of-state parameter. The non-standard eras right after inflation usually relate to the inflaton dynamics, while the intermediate eras arise from other late-time BSM physics.

We first focus on the cosmic-string SGWB because the suppression signature is observable, unlike inflationary SGWB. The turning-point frequencies of suppression and enhancement correspond to the end of the non-standard era. For local cosmic strings, the turning point receives a multiplicative factor of $(G\mu)^{-1/2}$ – compared to the primordial inflation and global strings (Fig. 4.8) – due to the delayed decay of loops. For example, ET is sensitive to loops formed at the 1-100 TeV scale, unlike the usual TeV window of LISA. The overall reach of all planned GW observatories is shown in Fig. 4.33-left. For intermediate inflation, ET and CE are sensitive up to 10^{14} GeV, cf. Fig. 4.33-right, due to the stretching regime of cosmic strings. Nonetheless, the SGWB has a suppression signature, similar to the matter era. It will be interesting to disentangle their degeneracies, e.g., using other observables generated during this secondary inflation.

The kination era after inflation enhances the SGWB from primordial inflation; however, the $\Delta N_{\rm eff}$ bound excludes any observable signature within the future-planned experiments, cf. Fig. 4.10, except those in the challenging UHF regime. Furthermore, the kination is obstructed by the induced scalar fluctuation, which could be interestingly responsible for a new dark matter production mechanism. We leave this issue for future study.

For the intermediate kination era, we show that it must follow a matter era, which leads to a GW-peaked signature from both long-lasting and short-lasting sources. We express the peak position as a function of the energy scale and duration of kination. ET and CE are windows to $10^{(5,9)}$ GeV kination for inflationary and global-string SGWB and $10^{(-1,6)}$ GeV for local strings, cf. Fig. 7.23. Moreover, multiple peak signatures could be observed when two or more GW sources are present.

Intermediate matter era from heavy and unstable particles

The intermediate matter era – ending well above the BBN scale – can be naturally induced by particles of large energy density (or yield) and short lifetime. By observing the step-like suppression in cosmic-string SGWB, we can infer the (yield, lifetime) of the heavy and unstable particles, which relate to the (energy scale, duration) of the matter era. For example, ET can probe the intermediate matter up to 100 TeV scale for $G\mu = 10^{-11}$, meaning that the GW probe extends the usual BBN bound on the particle's lifetime by 15 orders of magnitude, cf. Fig. 5.3. We consider several UV completions and find that cosmic-string GW is either a unique or complementary probe of the direct/indirect detection experiments. E.g., oscillating scalar moduli fields in Fig. 5.5, a massive scalar particle interacting only gravitationally in Fig. 5.6, a dark photon model kinematically coupled to the Standard Model in Fig. 5.9, and a dark photon with a dark $U(1)$ strings in Fig. 5.10. The analyses for the axion-like particles and primordial black holes can be done similarly.

Intermediate kination era from the rotating axion

Unlike the kination treated so far in the literature, this kination scenario can occur independently of the inflationary sector, inside the standard radiation era, and instead from the early dynamics of an axion field. We emphasize that its interplay with the natural partner – the radial component of the PQ field – is the crucial ingredient that induces a matter-kination era; the sole axion degree of freedom cannot. The extended scenario of the kination following some other era will be considered elsewhere.

The intermediate kination era leads to a unique GW-peak signature in SGWB from all prime sources, serving as a unique axion physics probe. See Tab. 8.1 for the summary. Connecting to axion DM from the kinetic misalignment and fragmentation, the peak position can directly infer the scale $\sqrt{m_a f_a}$. Nonetheless, the rotating axion signature in the inflationary SGWB from the *standard* QCD axion is not observable, except at BBO. The promising observable regions are, however, widely open for the QCD axion with lighter mass or for generic axion-like particles. The rotating axion also serves as a baryogenesis mechanism in the axiogenesis model, which can be tested via the GW signature of the spinning-axion kination. We find a broad range of axion decay constant compatible with observable windows by future observatories.

Four ingredients are required for the UV completion of the rotating axion, cf. Sec. 7.1.1. The most significant obstacle for a kination era is that the radial motion needs to be damped. The optimal case happens when this damping occurs before the scalar field energy density dominates; otherwise, a kination era may still happen, but the entropy injection will shorten its duration. We consider three possible ways of damping. The first option is to assume non-thermal damping through parametric resonance. We have derived predictions in this case, treating the damping temperature as a free parameter. It remains to be checked whether this is indeed realizable. The second option relies on the thermalization rate from a Yukawa interaction between the scalar field and new fermions. Nonetheless, these interactions induce a thermal mass for the Peccei-Quinn field, thus delaying the time of the axion kick. Together with a modified thermalization temperature, this prevents a kination era.

The axion kination's last and most realistic option is the thermal damping with the sufficiently low reheating temperature or large Yukawa coupling, cf. Fig. 7.18. These conditions allow considerable interaction and sufficient damping, while the thermal potential is suppressed due to the Boltzmann-suppressed fermions. We showed that $N_{\rm KD} < 6$ for most of the model's parameter space, and the summary of detectability is shown in Fig. 7.23. It would be interesting to investigate whether there are alternative models which can give more extended kination eras.

Finally, a particularly intriguing scenario is where the U(1)-breaking – generating the rotating axion – also leads to the global string network whose GW emission is enhanced by the matter-kination era induced by the rotating axion itself. The axion strings with a non-vanishing axion speed – recently been shown to exist [686] – would entirely change the vanilla cosmic-string paradigm, e.g., the scaling regime, the particle production, and GW emission. It will be worth investigating such a so-called rotating axionic string scenario in more detail.

GW from primordial inflation Fig. 4.22, 4.23	$f_{\rm peak}$	Eq. (4.55)
	$\Omega_{\rm peak}$	Eq. (4.56)
GW from local cosmic strings Fig. 4.24, 4.25	$f_{\rm peak}$	Eq. (4.62)
	$\Omega_{\rm peak}$	Eq. (4.63)
GW from global cosmic strings Fig. 4.26, 4.27	$f_{\rm peak}$	Eq. (4.69)
	$\Omega_{\rm peak}$	Eq. (4.71)
GW peak and axion relic abundance Fig. 6.3, 6.4, 6.6	$E_{\rm KD} - \Omega_{a,0}$	Eq. (6.13)
	$\Omega_{\rm peak} - \Omega_{a,0}$	Eq. (6.17)
GW peak and baryon asymmetry Fig. 6.7	$E_{\rm KD} - Y_B$	Eq. (6.32)
	$\Omega_{\rm peak} - Y_B$	Eq. (6.34)

Table 8.1: List of key relations and figures for the intermediate kination from the rotating axion (model-independent).

Appendix A

Sensitivity curves of GW Detectors

We first review the notion of signal-to-noise ratio (SNR), which determines the detectability of the GW signal at a given GW detector. We consider a graphical representation of the detector's sensitivity, the integrated sensitivity curve.

A.1 The signal-to-noise ratio

The total output of a detector is given by the GW signal plus the noise, $h(t)+n(t)$ where the level of noise $n(t)$ is measured by its noise spectral density $S_n(f)$ [29, 31, 552].

$$\left\langle \tilde{n}^*(f)\tilde{n}(f')\right\rangle \equiv \delta(f-f')\,S_n(f). \tag{A.1}$$

The detector sensitivity $\Omega_{\rm sens}(f)$ is defined as the magnitude of the SGWB energy density which would mimic the noise spectral density $S_n(f)$

$$\Omega_{\rm sens}(f) = \frac{2\pi^2}{3H_0^2}\,f^3\,S_n(f). \tag{A.2}$$

The capability of an interferometer to detect a SGWB of energy density $\Omega_{\rm GW}(f)$ after an observation time T is measured by the signal-to-noise ratio (SNR)

$$\mathrm{SNR} \equiv \sqrt{T\int_{f_{\rm min}}^{f_{\rm max}} df\,\left[\frac{\Omega_{\rm GW}(f)}{\Omega_{\rm sens}(f)}\right]^2}. \tag{A.3}$$

We now comment on different definitions of SNR in the literature and shall see that our definition is more pragmatic.

Issue of the different formalisms. — Here we review the generic and systematic way to define SNR and discuss its short-coming. We consider two formulae of SNR – adopted in the GW community. Generically, the SNR is written as the mean value to the variance of the noise output – including both the detector noise and the stochastic noise of the signal [552]. Two formulae of SNR below can be used:

- **general formula**: For any size of $\Omega_{\rm GW}$ [466, 552, 553]. A very large SGWB signal dominates the intrinsic noise of the detector.

$$\mathrm{SNR}^2 = T\int df \frac{\Omega_{\rm GW}(f)^2}{2\Omega_{\rm GW}(f)^2+2\Omega_{\rm GW}(f)\Omega_{\rm sens}(f)+\Omega_{\rm sens}(f)^2} \tag{A.4}$$

- **common formula**: Assuming the limit $\Omega_{\rm GW}\ll\Omega_{\rm sens}$.

$$\mathrm{SNR}^2 = T\int df \frac{\Omega_{\rm GW}(f)^2}{\Omega_{\rm sens}(f)^2} \tag{A.5}$$

In Fig. A.1, we compare the results from these two formulae assuming a scale-invariant sensitivity:

$$\Omega_{\rm sens}(f) = \Omega_{\rm sens} = \text{constant}, \tag{A.6}$$

while the signal is assumed to be the power-law shape

$$\Omega_{\rm GW}(f) = \Omega_{\rm GW,\star} \left(\frac{f}{f_{\rm peak}} \right)^p , \tag{A.7}$$

which is cut-off at $f_{\rm peak}$ with the peak amplitude $\Omega_{\rm GW,\star}$. The main difference is when $\Omega_{\rm GW} \gtrsim \mathcal{O}(\Omega_{\rm sens})$. The generic formula (A.4) saturates at $\mathrm{SNR} = T f_{\rm peak}$, while Eq. (A.5) grows with the ratio $\Omega_{\rm GW}/\Omega_{\rm sens}$. Indeed, the common definition of SNR in Eq. (A.5) can capture the signal's size compared to the sensitivity and is a more pragmatic choice, in the sense that one can quantitatively differentiate between the detector noise and the stochastic noise from the signal.

Which SNR means discovery? — Although the common criterion relies on the approximated SNR formula in the large detector noise limit, it has been compared with and gives the same results as the full likelihood analysis, which yields the threshold of $\mathrm{SNR} \simeq 10$. It means that the signal can be reconstructed for the power-law SGWB spectrum with the detection probability of 97% C.L. [479].

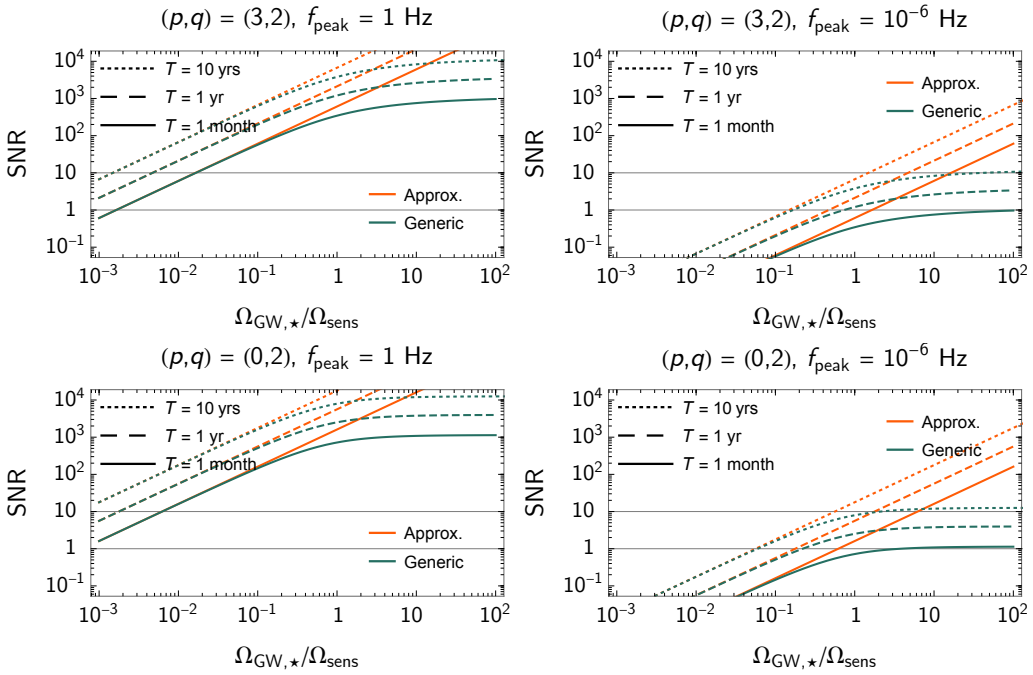

Figure A.1: SNR from the generic formula (A.4) and the approximated one (A.5). The two formulae deviate for $\Omega_{\rm GW} \gtrsim \mathcal{O}(\Omega_{\rm sens})$. Also, the size of the SNR from the generic formula saturates at $\mathrm{SNR} = T f_{\rm peak}/2$.

A.2 Power-Law Integrated Sensitivity Curves

Due to its non-trivial integral over the signal's spectrum in Eq. (A.3), the SNR calculation increases the difficulty and computation time for predicting the detectability of some GW models, i.e., the integral must be evaluated for every set of parameters. On the other hand, the more convenient path – the integrated sensitivity curve – has been laid out in Ref. [478] and relies on graphical representations. We first assume the generic shape of the spectrum and, then, calculate a function

of GW amplitude $\Omega_{\rm GW}$ – the integrated sensitivity curve – corresponding to some observation time T and to some SNR at a given detector. Any signal above this curve has SNR larger than the benchmark value after an observation time T. There are several types of integrated sensitivity curves in literature, depending on the initially assumed shape. E.g., the peak-integrated sensitivity curve assumes the signal with a broken power-law shape [724]. In this section, we consider the generic shape of a power law and derive the power-law integrated sensitivity (PLS) curves. All results and analyses in this thesis are drawn from the PLS curves.

Assuming SGWB with a power law spectrum

$$\Omega_{\rm GW}(f) = \Omega_\beta \left(\frac{f}{f_{\rm ref}}\right)^\beta , \tag{A.8}$$

with spectral index β, amplitude Ω_β and reference frequency $f_{\rm ref}$, we deduce from Eq. (A.3) the amplitude Ω_β needed to reach a given SNR after a given observation time T

$$\Omega_\beta = \frac{\rm SNR}{\sqrt{T}} \left(\int_{f_{\rm min}}^{f_{\rm max}} df \left[\frac{h^2}{h^2 \Omega_{\rm sens}(f)} \left(\frac{f}{f_{\rm ref}}\right)^\beta \right]^2 \right)^{-1/2} , \tag{A.9}$$

which upon re-injecting into Eq. (A.8) gives

$$h^2\Omega_{\rm GW}(f) = f^\beta \frac{\rm SNR}{\sqrt{T}} \left(\int_{f_{\rm min}}^{f_{\rm max}} df \left[\frac{f^\beta}{h^2 \Omega_{\rm sens}(f)} \right]^2 \right)^{-1/2} . \tag{A.10}$$

For a given pair (SNR, T), one obtains a series in β of power-law integrated curves. One defines the power-law integrated sensitivity curve $\Omega_{PI}(f)$ as the envelope of those functions [478]

$$\Omega_{PI}(f) \equiv \max_\beta \left[f^\beta \frac{\rm SNR}{\sqrt{T}} \left(\int_{f_{\rm min}}^{f_{\rm max}} df \left[\frac{f^\beta}{h^2 \Omega_{\rm sens}(f)} \right]^2 \right)^{-1/2} \right] . \tag{A.11}$$

Any SGWB signal $\Omega_{\rm GW}(f)$ which lies above $\Omega_{PI}(f)$ would give a signal to noise ratio $>$ SNR after an observation time T.

For the purpose of our study, we computed the power-law integrated sensitivity curve $\Omega_{PI}(f)$, starting from the noise spectral density in [66] for ET, [228] for CE and [68] for BBO/DECIGO, [221] for AEDGE, and [210] for GAIA/THEIA. The required SNR $= 10$ and the observation time is 10 years; though the sensitivity is only lost by a small factor when the observation time is reduced by 10%. For pulsar timing arrays EPTA, NANOGrav and SKA, we directly took the sensitivity curves from [201]. The signal-to-noise ratio can be improved by using cross-correlation between multiple detectors, e.g. LIGO-Hanford, LIGO-Livingston, VIRGO and KAGRA in run O3, or LIGO-India which may be operational for run O5 [725]. We computed the SNR for LIGO from the expression [478]

$$\text{SNR} = \left[2T \int_{f_{\rm min}}^{f_{\rm max}} df \frac{\Gamma^2(f) S_{\rm h}^2(f)}{S_n^1(f) S_n^2(f)} \right]^{1/2} , \tag{A.12}$$

where S_n^1 and S_n^2 are the noise spectral densities of the detectors in Hanford and in Livingston for the runs O2, O4 or O5 and $\Gamma(f)$ is the overlap function between the two LIGO detectors which we took from [726]. The GW power spectral density $S_h(f)$ is related to the GW energy density through

$$S_h(f) = \frac{3H_0^2}{2\pi^2} \cdot \frac{\Omega_{\rm GW}(f)}{f^3} . \tag{A.13}$$

We fixed the signal-to-noise ratio SNR $= 10$ and the observational time $T = 268$ days for LIGO O2, 1 year for LIGO O4 and O5, and 10 years for other sensitivity curves.

A.2.1 Landscape of primordial GW backgrounds in the characteristic strain h_c unit

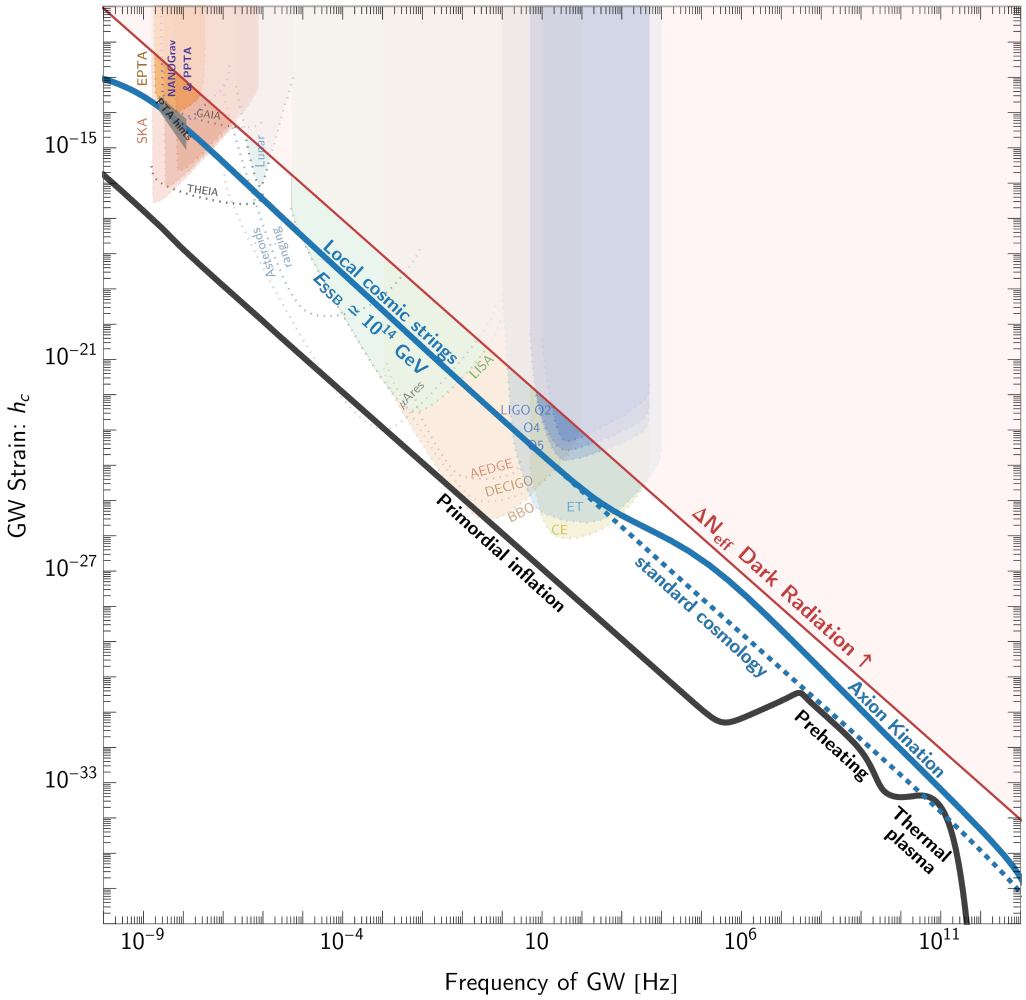

Figure A.2: This figure displays how the GW frequency spectra discussed in this thesis and shown in $\Omega_{\rm GW}h^2$ unit would look like when presented in terms of the characteristic strain h_c defined in Eq. (2.11).

Appendix B

Further Details on Cosmic Strings

B.1 Field-theoretic strings

For the completeness of the thesis, this section discusses the simple field-theoretic model of cosmic strings, which can be either local (or gauged) or global strings. Let us start with the local string and then put some limit on it to obtain the global-string case.

B.1.1 Abelian Higgs model

Consider a complex scalar field φ charged under gauge fields A_μ,

$$\mathcal{L} = |D_\mu \varphi|^2 - \frac{1}{4} F_{\mu\nu} F^{\mu\nu} - \frac{1}{4}\lambda(|\varphi|^2 - \eta^2)^2, \tag{B.1}$$

where $D_\mu = \partial_\mu + ieA_\mu$, $F_{\mu\nu} = \partial_\mu A_\mu - \partial_\nu A_\mu$, and the Mexican-hat potential is assumed. The scalar field could receive the radiative correction that restores its symmetry at high temperatures. At later times, the correction is suppressed and leads to the phase transition and cosmic strings formation. Moreover, the scalar φ and the vector boson A_μ obtain masses $m_\varphi = \lambda^{1/2}\eta,\ m_A = e\eta$.

The EOMs for φ and A_μ read

$$(\partial_\mu - ieA_\mu)(\partial^\mu - ieA^\mu)\varphi + \frac{\lambda}{2}\varphi(\varphi^\dagger\varphi - \eta^2) = 0, \tag{B.2}$$

$$\partial_\mu F^{\mu\nu} - 2e\Im(\varphi^\dagger D^\nu \varphi) = 0, \tag{B.3}$$

We see that the system of equations is controlled by the mass scale η and the ratio $\beta \equiv \lambda^2/2e^2$. On top of the vacuum solution $\langle\phi\rangle = \eta$, a static cylindrical-symmetric field configuration exists, namely *Nielsen-Olesen* vortex [319, 320]

$$\varphi = \eta f(\eta r)\exp(in\theta),\ \ A_i = -n\hat{\theta}_i \alpha(\eta r)/(er), \tag{B.4}$$

where n is the winding number, and the gauge field circulates around the string core with a gauge $A_r = 0$. The boundary conditions for these solutions are

$$f(\eta r),\ \alpha(\eta r) \to \begin{cases} 0, & r \to 0, \\ 1, & r \to \infty, \end{cases} \tag{B.5}$$

where the symmetric and broken phases are recovered at the string's core and at infinity, respectively. For pedagogical reason, let us write the EOM in terms of f and α:

$$f'' + \frac{f'}{r} - \frac{n^2 f}{r^2}(\alpha - 1)^2 - \frac{\lambda}{2} f(f^2 - 1) = 0, \tag{B.6}$$

$$\alpha'' - \frac{\alpha'}{r} - 2e^2 f^2(\alpha - 1) = 0. \tag{B.7}$$

The solutions are obtained numerically[1] and are shown in Fig. B.1. The gauge boson profile is solely controlled by its mass m_A – the last term of its EOM, while the scalar field profile $f(\eta r)$ depends on two scales: its mass m_φ (last term) and the gauge boson mass m_A (as α in the third term). Fig. B.1 shows that the gauge-boson profile exponentially reaches its asymptotic value beyond $r > m_A^{-1}$, while the scalar profile does so when $r > \max(m_\varphi^{-1}, m_A^{-1})$. In case of $m_A^{-1} > m_\varphi^{-1}$, the φ-profile behaves as $1 - f(\eta r) \sim r^{-2}$, instead of exponentially decay. Because the angular gradient (the third term) is effective in the small-α regime – despite $r > m_\varphi^{-1}$ – and gets screened only when $r > m_A^{-1}$. On the other hand, for $m_A^{-1} < m_\varphi^{-1}$, the φ-profile reaches its limit exponentially once $r > m_\varphi^{-1}$.

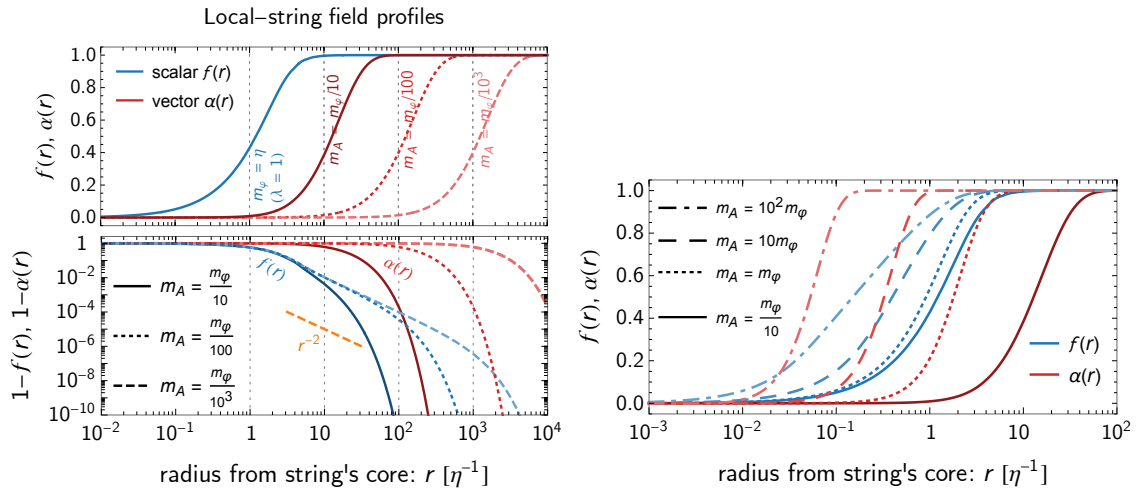

Figure B.1: Local-string profile in the Abelian-Higgs Model. *left:* In regime $m_A^{-1} > m_\varphi^{-1}$, the φ-profile goes exponentially to its asymptotic value when $r > m_A^{-1}$ due to the gauge field screening. *right:* In regime $m_A^{-1} < m_\varphi^{-1}$, the φ-profile reaches its its asymptotic value quickly for $r > m_\varphi^{-1}$.

The energy stored in the string's core per unit length or the string tension[2] is

$$\mu = \int d^2r \left[|(\nabla - ie\vec{A})\varphi|^2 + \frac{1}{2}(|\vec{E}|^2 + |\vec{B}|^2) + V(\varphi) \right]. \tag{B.8}$$

whose leading contribution is found to be

$$\mu \approx 2\pi n^2 \eta^2 g(e,\lambda) \;\; \text{where } g(e,\lambda) = \begin{cases} 1 & \text{for } m_A^{-1} < m_\varphi^{-1}, \\ \log(m_\varphi/m_A) & \text{for } m_A^{-1} > m_\varphi^{-1}. \end{cases} \tag{B.9}$$

The log-correction comes from the $(1 - r^{-2})$ profile for $r < m_A^{-1}$ which leads to the slightly diverging energy density. Contrary to the global strings, there is no screening from the gauge field, and their energy density diverges up to the largest IR scale of the system, instead of m_A^{-1}.

B.1.2 Global strings

The global string solution can be obtained easily by decoupling the gauge field from the Abelian-Higgs model, i.e., setting $e \to 0$ and $m_A^{-1} \to \infty$. Now there is no gauge field to cancel the angular-gradient contribution. The field profile never goes exponentially to its asymptotic value,

[1] The numerical algorithm using the *shooting* method might find difficulties due to singularity at $r \to 0$, but other methods work well, e.g. the *finite difference* method in this link.

[2] The energy per unit length and the tension are not necessary the same. For wiggly strings, one finds $\mu > T$ on average over large string's length scale [301].

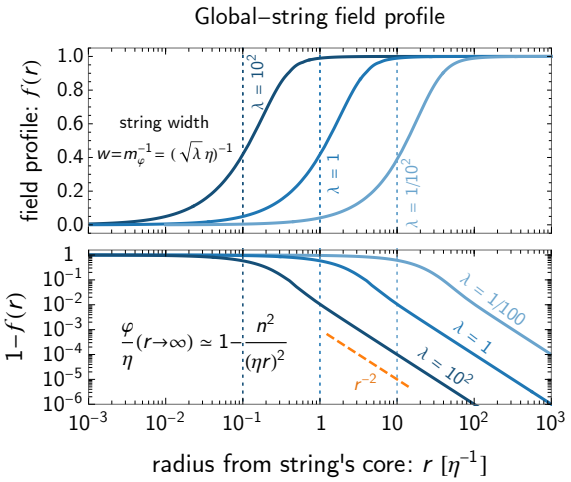

Figure B.2: Global-string profile. The string core sits near the origin, and the field continuously reaches its VEV for $r \to \infty$. The width of the profile is controlled by the scalar mass: $m_\varphi = \sqrt{\lambda}\eta$. Outside the core region, the profile decreases as $1 - f \sim r^{-2}$, unlike the exponential suppression for the local string, cf. Fig. B.1.

as shown in Fig. B.2. The energy density per length diverges as the distance grows away from the core. Within the Hubble horizon, the global-string tension is

$$\mu = 2\pi n^2 \eta^2 \log(H^{-1}/m_\varphi^{-1}). \tag{B.10}$$

The string tension grows with time, and so does the SGWB from global strings, as shown in Fig. 3.12.

Thin-string effective action

Masses of the underlying fields determine the size of the core width. However, strings can be rather small compared to the cosmological scale. An observer is unable to resolve any physics within the core. Hence, we can consider the effective description in the zero-width limit. For local strings, the appropriate effective action is the Nambu-Goto (NG) action [727–729], i.e. a featureless one-dimensional object,

$$\mathcal{S}_{\rm NG} = -\mu \int \sqrt{-g^{(2)}} d^2\chi, \tag{B.11}$$

where coordinates on a 2-dimensional world sheet of propagating strings are $x^\mu(\chi^0, \chi^1)$, $g^{(2)}$ is the 2-dimensional metric induced background metric, and μ is the string tension.

For global strings, the extended core due to the Goldstone boson satisfies the so-called Kalb-Ramond action [303, 348], i.e. NG string plus contribution from the Goldstone field.

$$\mathcal{S}_{\rm KR} = -\mu \int \sqrt{-g^{(2)}} d^2\chi + \frac{1}{6}\int H^2 d^4x + 2\pi\eta \int B_{\mu\nu} d\sigma^{\mu\nu}, \tag{B.12}$$

where $B_{\mu\nu}$ is the antisymmetric field representing the topological interaction between the string and the Goldstone boson, $H^{\mu\nu\lambda} = \partial^\mu B^{\nu\lambda} + \partial^\lambda B^{\mu\nu} + \partial^\nu B^{\lambda\mu}$ is the field strength tensor of $B_{\mu\nu}$, and $d\sigma^{\mu\nu} = \epsilon^{ab} x^\mu_{,a} x^\nu_{,b} d^2\chi$ is the worldsheet area element. Here is another application of *Goldstone equivalence theorem* [348].

B.2 Constraints from BBN, CMB, gravitational lensing & cosmic rays

By confronting our theoretical predictions for the GW spectrum from CS with the sensitivity curves of EPTA [369] and NANOGrav [370] (which we take from [201]), we derived the respective bounds $G\mu \lesssim 2 \times 10^{-10}$ (EPTA) and $G\mu \lesssim 5 \times 10^{-11}$ (NANOGrav), as discussed in Sec. 3.1.4. For this reason, we only considered in our analysis $G\mu$ values smaller than 5×10^{-11}. In Sec. B.2.1, we give the constraints on the string tension from a too large SGWB at CMB/BBN. They are much

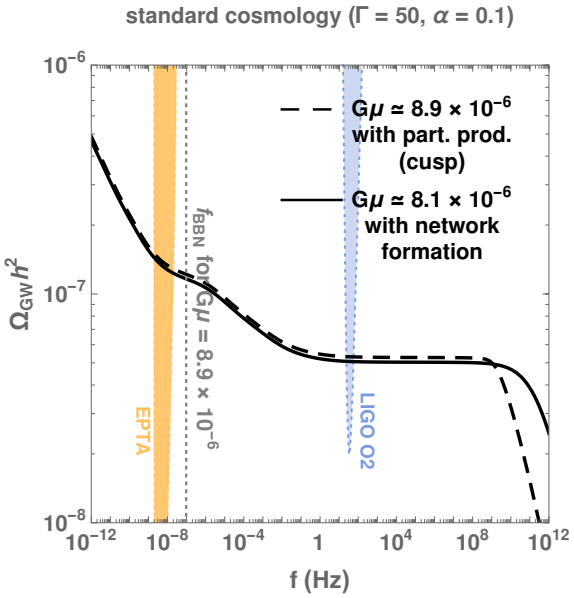

Figure B.3: Two GW spectra which saturate the BBN bounds, assuming a VOS string network, cf. Sec. 3.3.3, evolving in standard cosmology. The solid line assumes a cut-off due to network formation whereas the dashed line assumes a cut-off due to particle production from cusps. The dotted vertical line is the frequency emitted when BBN starts. We compare the BBN bounds to the bounds from EPTA and LIGO O2.

weaker than the ones from Pulsar Timing Arrays (PTAs) but can become relevant in the presence of kination.

In Sec. B.2.2 and Sec. B.2.3, bounds from gravitational lensing and direct CMB observables are much weaker than the ones from PTAs. Still, they have the decisive advantage of being independent of our assumptions for the theoretical prediction of the GW background. Finally, in Sec. B.2.4, we discuss the possibility of probing CS from the particle productions in the presence of kinks and cusps.

B.2.1 GW constraints from BBN

SGWB from cosmic strings spans a broad frequency range due to its long-lasting source. Its total energy density present before BBN/CMB is bounded from above by the $\Delta N_{\rm eff}$-constraint discussed in Sec. 2.2.2. As shown in Eq. (2.22), the integral starts from the lowest frequency, corresponding to the emission at BBN, to the high frequency when the GW production has started. For CS, the temperature at BBN, $T_{\rm BBN} \simeq 1$ MeV, translates via Eq. (3.33) to the frequency

$$f_{\rm BBN} \simeq 8.9 \times 10^{-5}\ {\rm Hz} \left(\frac{0.1 \times 50 \times 10^{-11}}{\alpha \Gamma G\mu}\right)^{1/2}. \tag{B.13}$$

Fig. B.3 shows the GW spectra, which saturate the BBN bound for two different high-frequency cut-offs. The lower the cut-off, the higher the upper bound on $G\mu$ due to less GW present at BBN time. Assuming the presence of the cut-off due to particle production from cusps, we obtain

$$\text{BBN:} \qquad h^2 \Omega_{\rm GW}(f) \lesssim 8.9 \times 10^{-6}. \tag{B.14}$$

We expect the BBN bounds to become weaker in non-standard matter or inflationary era but tighter in the presence of an early kination era. For instance, scenarios of inflation followed by a stiff equation of state (e.g. quintessential inflation [522]) are dramatically jeopardized by the BBN bounds [4, 71]. Similarly, in the case of CS, we find that the maximally allowed string tension is $G\mu \simeq 3.9 \times 10^{-15}$, 3.8×10^{-17}, and 2.9×10^{-20} for long-lasting kination era ending at temperature $T_\Delta = 100$ TeV, 1 TeV, and 1 GeV, respectively.

B.2.2 Gravitational lensing

The presence of energy confined within the core of CS affects the spacetime around them. The metric near a straight CS is locally flat but globally conical [730]. Photons from a distant celestial

object traveling in the vicinity of a CS are subject to gravitational lensing effects. The corresponding constraint $G\mu \lesssim 3 \times 10^{-7}$ has been derived from the search of gravitational lensing signatures of CS in the high-resolution wide-field astronomical surveys GOODS [731] and COSMOS [732]. It has been claimed that constraints from gravitational lensing surveys at radio frequencies like LOFAR and SKA could reach $G\mu \lesssim 10^{-9}$ [733].

B.2.3 Temperature anisotropies in the CMB

There are two possible effects of CS on temperature fluctuations in the CMB:

- CS moving through the line-of-sight can induce Doppler shifts on the photons coming from the last scattering surface, known as the *Kaiser-Stebbins-Gott* effect [734–736], potentially leaving line-like discontinuities in the CMB.
- A CS moving in the primordial plasma leaves surdensity perturbations, the so-called *wakes* [737], possibly imprinted in the CMB temperature anisotropy. Due to the stochastic behavior of the Kibble mechanism, these perturbations are decoherent and give rise to a CMB spectrum without acoustic peaks [738].

Lattice numerical computation of the temperature anisotropy in Abelian-Higgs [646, 739], Nambu-Goto [738, 740, 741] or global strings [742] have constrained the string tension to $G\mu \lesssim$ few$\times 10^{-7}$ [743]. Constraints of the same magnitude can be found from non-gaussianity [743–745]. Also, the same signatures as in the CMB can be imprinted in the 21-cm power spectrum, and an experiment with a collecting area of $10^4 - 10^6$ km^2 might constrain $G\mu \lesssim 10^{-10} - 10^{-12}$ [746].

B.2.4 Non-gravitational radiation

As discussed in Sec. 3.2.1, the presence of small-scale structures on local strings, cusps, and kinks, invalidates the Nambu-Goto approximation and implies the radiation of massive particles. Therefore, CS have been proposed as a possible mechanism for generating non-thermal DM and Baryon Asymmetry of the Universe [180, 195–197, 358–365, 747].

At a cusp, the string can reach ultrarelativistic velocities. Therefore, CS have been pointed [564, 723, 748–750] as a possible candidate for the detection of ultra-high energy cosmic rays [751] above the Greisen-Zatsepin-Kuzmin (GZK) cut-off, around 10^{20} eV [752–754], even though the expected flux at earth is generally too small to be detected [359, 755, 756].

More precisely, a coupling between the SM and the dark $U(1)'$ from which the CS result – e.g., a Higgs portal or a kinetic mixing – leads to effective interaction between SM particles and the CS [757]. In that case, the formation of cusps and kinks on the string radiate SM particles [360]. The expected gamma-ray flux at the earth is too low to be observed by Fermi-LAT [758], also if we assume that all the massive particles radiated by the CS subsequently decay into gamma-ray [391]. However, for cusp domination and large coupling between the SM and $U(1)'$, the flux of high-energy neutrino might be measured by the future experiments SKA and LOFAR for $G\mu \sim 10^{-16 \div -14}$ [758]. Also, the distortions in the CMB may be detected by the future telescope PIXIE for $G\mu \sim 10^{-14 \div -12}$ [758]. Finally, depending on the magnitude of the SM-$U(1)'$ coupling, the BBN constraints can already exclude values of string tensions: $10^{-14} \lesssim G\mu \lesssim 10^{-8}$ [758].

Constraints from particle emission apply on an interval of values for $G\mu$, and not as upper bound like for gravitational emission [755]. There are more loops for longer lifetimes $\propto (\Gamma G\mu)^{-1}$, and we expect a larger flux of emitted particles while gravitational emission grows with $G\mu$. Loops with small $G\mu$ decay preferentially into particles, cf. sec. 3.2.1. In that case, the expected flux of emitted particles increases with the string tension, which controls the power of the particle emission. Therefore, a value of $G\mu$ exists for which the expected flux of emitted particles is maximal. This is the value of $G\mu$ when particle production is as efficient as gravitational production. For example, for loops created at the recombination time, the value of $G\mu$ maximizing the cosmic ray production is 10^{-18} [759].

Superconducting Cosmic Strings: Another possibility for large particle production is to couple the CS with electromagnetic charge carriers and to spontaneously break electromagnetic gauge invariance inside the vortex [760]. Upon moving through cosmic magnetic fields, Superconducting Cosmic Strings (SCS) are able to develop a large electric current $\mathcal{I}$. The cusp formation on SCS is expected to emit electromagnetic bursts [761–764], up to very high energies, set by the string tension $\sqrt{\mu} \sim 10^{13}$ GeV $\sqrt{G\mu/10^{-15}}$, hence leading to high-energy gamma-rays [765–767]. Hence, SCS could be an explanation for the observed gamma-ray bursts at high redshifts, which depart from the predictions from star-formation-history [767]. However, the expected photon flux at earth is larger in the radio band than in the gamma-ray band [768–770] (but also mostly generated by kinks instead of cusps [771]). Thus, it has been proposed that SCS could be an explanation for the Fast-Radio-Burst events [772–774] for string tensions in the range $G\mu \sim 10^{-14\div-12}$ and string currents $\mathcal{I} \sim 10^{-1\div2}$ GeV [773]. Electromagnetic emission from SCS lead to CMB distortions [775–777]. A next-generation telescope like PIXIE [778] would exclude string tensions $G\mu \sim 10^{-18}$, for string currents as low as $\mathcal{I} \sim 10^{-8}$ GeV [777]. Also, electromagnetic radiation, by increasing the ionization fraction of neutral hydrogen, can affect the CMB temperature and polarization correlation functions at large angular scales, leading to the contraint $\mathcal{I} \lesssim 10^{7}$ GeV [779]. Note that ionization of neutral hydrogen has been studied in [759] in the case of non-superconducting strings. Additionally, the radio emission from SCS can increase the depth of the 21 cm absorption signal, and EDGES data excludes the SCS tension $G\mu \sim 10^{-13}$ for string currents as low at $\mathcal{I} \sim 10$ GeV. Finally, emission of boosted charge carriers from SCS cusps moving in a cosmic magnetic field B, has been studied in [780], and provide a possible explanation for high-energy neutrino above 10^{20} eV, for $G\mu \sim 10^{-20\div-14}$.

B.3 Derivation of SGWB from CS (precisely)

This section provides a pedagogical derivation for GW from the local cosmic-string network. Since the main GW contribution comes from string loops, let us now go from the loop production until their GW reaches the GW observatories today. Then we will see that the estimation for the SGWB can be obtained using the quadrupole formula. Lastly, we consider the effect of higher modes and the possibility of distinguishing small-scale structures on strings.

B.3.1 The loop production

In Sec. 3.2.2, the string network produces number density of loops of size αt_i at time t_i with rate

$$\frac{dn_{\rm loop}}{dt_i} = (0.1)\frac{C_{\rm eff}(t_i)}{\alpha\, t_i^4}, \tag{B.15}$$

where $C_{\rm eff}(t_i)$ is the loop-formation efficiency. The loop number density per unit frequency reads

$$\frac{dn_{\rm loop}(\tilde{f},\,\tilde{t})}{d\tilde{f}} = \left[\frac{a(t_i)}{a(\tilde{t})}\right]^3 \sum_k (0.1)\frac{C_{\rm eff}(t_i)}{t_i^4}\cdot\frac{1}{\alpha\,(\alpha+\Gamma G\mu)}\cdot\frac{2k}{f^2}\left[\frac{a(\tilde{t})}{a(t_o)}\right]^2, \tag{B.16}$$

where the number density of loops red-shifts as a^{-3} before they maximally decay. Moreover, we consider that the GW spectrum is dominated by the largest loops formed with size equal to 10% of the horizon [194], i.e. the monochromatic loop size distribution

$$P_\alpha(\alpha) = \delta(\alpha - 0.1). \tag{B.17}$$

B.3.2 From loop production to GW emission

After its formation at t_i, a loop shrinks through GW emission with a rate $\Gamma G\mu$ so that its length evolves as, cf. Sec. 3.1.3

$$l(t) = \alpha t_i - \Gamma G\mu(t - t_i), \tag{B.18}$$

where α is the length at formation in units of the horizon size. The resulting GW are emitted at a frequency $\tilde{f}$ corresponding to one of the proper modes of the loop, i.e.

$$\tilde{f} = \frac{2k}{l}, \qquad k \in \mathbb{Z}^+. \tag{B.19}$$

The GW energy rate emitted by one loop through the mode k is

$$\frac{dE_{\rm GW}^{(k)}}{dt} = \Gamma^{(k)}\, G\mu^2, \quad \text{with} \quad \sum_k \Gamma^{(k)} = \Gamma, \tag{B.20}$$

$$\text{where} \quad \Gamma^{(k)} = \frac{\Gamma\, k^{-4/3}}{\sum_{p=1}^{\infty} p^{-4/3}} \simeq \frac{\Gamma\, k^{-4/3}}{3.60}, \tag{B.21}$$

which assumes that the GW emission is dominated by cusps [277]. The GW energy density spectrum resulting from the emission of all the decaying loops until today is

$$\frac{d\rho_{\rm GW}(\tilde{f},\, \tilde{t})}{d\tilde{f}} = \int_{t_F}^{t_0} d\tilde{t}\, \frac{dE_{\rm GW}}{d\tilde{t}} \cdot \frac{dn(\tilde{f},\, \tilde{t})}{d\tilde{f}}, \tag{B.22}$$

where $dn(\tilde{f},\, \tilde{t})/d\tilde{f}$ is the number density of loops emitting GW at frequency $\tilde{f}$ at time $\tilde{t}$ and t_0 is the age of the Universe today. Loops start being created at time of CS network formation t_F or after the damped evolution has stopped, cf. Sec. B.5.

B.3.3 From GW emission to detection

The GW energy density spectrum today is defined as $\Omega_{\rm GW}(f) = (f/\rho_c)\, |d\rho_{\rm GW}(f,\, t_0)/df|$. After emission, the GW energy density redshifts as radiation, $\rho_{\rm GW} \propto a^{-4}$, so the GW energy density per unit of frequency redshifts as

$$\frac{d\rho_{\rm GW}(f,\, t_0)}{df} = \frac{d\rho_{\rm GW}(\tilde{f},\, \tilde{t})}{d\tilde{f}} \left(\frac{a(\tilde{t})}{a(t_0)}\right)^3 \tag{B.23}$$

where the frequency at emission $\tilde{f}$ red-shifts to the frequency today: $f = \tilde{f}[a(\tilde{t})/a(t_0)]$.

B.3.4 The master equation

Following all steps from loop production until the GW reaches the detector, GW energy density spectrum from CS can be written pedagogically as $\Omega_{\rm GW}(f) = \sum_k \Omega_{\rm GW}^k(f)$ where

$$\Omega_{\rm GW}^k(f) = \frac{1}{\rho_c} \int_{t_{\rm osc}}^{t_0} d\tilde{t} \int_0^1 d\alpha\, \Theta\left[t_i - \frac{l_*}{\alpha}\right] \Theta(t_i - t_{\rm osc}) \left[\frac{a(\tilde{t})}{a(t_0)}\right]^4 P_{\rm GW}^{(m)} \left[\frac{a(t_i)}{a(\tilde{t})}\right]^3 P_\alpha(\alpha) \frac{dt_i}{df} \frac{dn_{\rm loop}}{dt_i}, \tag{B.24}$$

such that the chronology of the involved processes can be understood from right to left. Loops are formed at rate $dn_{\rm loop}/dt_i$ at t_i with a size distribution $P_\alpha(\alpha)$. They dilute like a^{-3} due to Hubble expansion, before emitting GW with power spectrum $P_{\rm GW}^{(m)}$ which subsequently redshifts like a^{-4}. The two Heaviside functions represent high-frequency cut-offs. The right-handed Heaviside function stands for the time $t_{\rm osc}$ at which long-strings start oscillating, either just after the formation of the long-string network or after that friction becomes negligible, cf. Sec. B.5.4. The left-handed Heaviside function stands for the energy loss into particle production, which is more efficient than GW emission for loops of length smaller than a characteristic length l_*, which depends on the small-scale string structure, cf. sec 3.2.1.

Integrating over all loop sizes α, all emission times $\tilde{t}$ and we sum over all loop modes m, we deduce a ready-to-use form of the GW energy density spectrum from CS:

$$\begin{aligned}\Omega_{\rm GW}(f) &= \sum_k \Omega_{\rm GW}^{(k)}(f) \\ &= \sum_k \frac{1}{\rho_c}\frac{2k}{f}\frac{\mathcal{F}_\alpha\,\Gamma^{(k)}\,G\mu^2}{\alpha(\alpha+\Gamma\,G\mu)}\int_{t_{\rm osc}}^{t_0} d\tilde{t}\,\frac{C_{\rm eff}(t_i)}{t_i^4}\left[\frac{a(\tilde{t})}{a(t_0)}\right]^5\left[\frac{a(t_i)}{a(\tilde{t})}\right]^3\Theta(t_i-t_{\rm osc})\Theta(t_i-\frac{l_*}{\alpha}).\end{aligned} \tag{B.25}$$

The time t_i of formation of the loops, which emit at time $\tilde{t}$ and which give the detected frequency f, can be determined from Eq. (B.18) and Eq. (B.19)

$$t_i(f,\,\tilde{t}) = \frac{1}{\alpha+\Gamma G\mu}\left[\frac{2k}{f}\frac{a(\tilde{t})}{a(t_0)}+\Gamma G\mu\,\tilde{t}\right]. \tag{B.26}$$

Note that the contribution coming from the higher modes are related to the contribution of the first mode by

$$\Omega_{\rm GW}^{(k)}(f) = k^{-4/3}\,\Omega_{\rm GW}^{(1)}(f/k). \tag{B.27}$$

B.3.5 The GW spectrum from the quadrupole formula

In standard radiation-dominated Universe, the scaling behavior $\Omega_{\rm GW}\propto\sqrt{G\mu}\times f^0$, e.g. Eq. (3.47), can be understood qualitatively from the *quadrupole formula* for the power emission of GW [277, 342]

$$P_{\rm GW}\sim N_{\rm loop}\,\frac{G}{5}\left(Q'''_{\rm loop}\right)^2, \tag{B.28}$$

where the triple derivative of the quadrupole of a loop is simply the string tension

$$Q'''_{\rm loop}\sim \text{mass}\times\text{length}^2/\text{time}^3\sim\mu. \tag{B.29}$$

During the scaling regime, the number of loops formed at time t_i scales as t_i^{-3} and red-shifts as a^{-3} until time $\tilde{t}$ to be

$$N_{\rm loop}\sim\left(\frac{\tilde{t}}{t_i}\right)^3\left(\frac{t_i}{\tilde{t}}\right)^{3/2}. \tag{B.30}$$

Since GW redshift as radiation, their energy density today is

$$\Omega_{\rm GW}\sim\Omega_{\rm rad}\,\frac{\rho_{\rm GW}(\tilde{t})}{\rho_{\rm rad}(\tilde{t})}\sim\Omega_{\rm rad}\,(G\mu)^2\left(\frac{\tilde{t}}{t_i}\right)^{3/2}, \tag{B.31}$$

where we assumed radiation-domination at $\tilde{t}$

$$\rho_{\rm rad}(\tilde{t})\sim G^{-1}\,\tilde{H}^2\,\frac{\rho_{\rm rad}(\tilde{t})}{\rho_{\rm tot}(\tilde{t})}\sim G^{-1}\,\tilde{t}^{-2}, \tag{B.32}$$

and where we used that the energy density of GW at $\tilde{t}$ is

$$\rho_{\rm GW}(\tilde{t})\sim\left(P_{\rm GW}\,\tilde{t}\right)/\,\tilde{t}^3. \tag{B.33}$$

with the GW power $P_{\rm GW}$ defined in Eq. (B.28). From Eq. (B.30), one can see that, at a fixed formation time t_i, the later the GW emission, the more numerous the loops. Hence, the dominant

contribution to the SGWB from a given population of loops formed at t_i occurs after one loop-lifetime, cf. Eq. (3.15), at

$$\tilde{t}_{\rm M} \sim \frac{\alpha\, t_i}{\Gamma G\mu}. \tag{B.34}$$

Upon plugging Eq. (B.34) into Eq. (B.31), one gets

$$\Omega_{\rm GW} \propto \sqrt{G\mu} \times f^0. \tag{B.35}$$

From Eq. (B.31), the GW spectrum during radiation is set by a combination of the strength of the GW emission from loops, $(G\mu)^2$, and the loop-lifetime $\tilde{t}_{\rm M}/t_i$, cf. Eq. (B.34). Both are set by the triple derivative of the loop-quadrupole $Q'''_{\rm loop} \sim \mu$. Hence we understand that the flatness in frequency during radiation is closely linked to the independence of the triple derivative of the loop-quadrupole[3], cf. Eq. (B.29), on the loop length, and therefore on the frequency.

B.3.6 Contributions from each loop population.

Each loop population – produced at time t_i and decayed at time $\tilde{t}$ – contributes to the SGWB from a cosmic-string network at different frequencies and amplitudes today (for the latter, this is true for the non-radiation-dominated Universe). As discussed in Secs. 3.2.4 and 4.2.2, the spectrum from each population peaks when $\tilde{t} = \tilde{t}_M$, and the sum of these peaks concludes in the power-law spectrum that can infer the cosmological history, Eq. (3.31). Nonetheless, we must be cautious because, in some cases, the observed spectral slope does not come from the sum of peaks. Each loop population also produces the peaked GW spectrum with its UV (high-frequency) and IR (low-frequency) tails. In this subsection, let us compute the slopes of these tails and see how they affect the ability to track cosmological history.

UV tail. The frequency higher than the spectral peak corresponds to the GW emission at time $\tilde{t} < \tilde{t}_M$. Choosing the values for t_i and $\tilde{t}$ which makes them f-independent, the master equation in Eq. (B.25) has the f-dependence as $\Omega_{\rm GW} \propto f^{-1}$, that is the UV tail from each loop population. If the peak contributions in Eq. (3.31) lead to the power-law spectrum with a slope smaller than -1, the final spectrum from each mode k is dominated by the UV tail of the contribution produced at the latest time and has the slope of -1.

In Fig. B.4, we see that the slope of each mode is exactly -1; however, the peak contribution in this case also leads to a slope of -1 as the loops produced in matter era and decaying in radiation era. Another case is when the spectrum has the high-frequency cut-offs. A more illuminating example is shown in the case of global strings. We obtain from Eq. (3.76) that the peak contribution leads to a spectrum with slope -2, while the resulting ($k = 1$) spectrum in Fig. 3.12 shows a slope of -1 due to this UV tail. Nevertheless, this UV tail gets enhanced into $-1/3$ due to the higher harmonics; see App. B.3.7.

IR tail. The low-frequency behavior is also derived from Eq. (B.25), but in the regime, $\tilde{t} > \tilde{t}_M$. Unlike a freedom of $\tilde{t}$-value, t_i is now related to $\tilde{t}_M$, Eq. (B.34), and is f-dependent, i.e. $t_i \propto f^{-1}$. Eq. (B.25) reads

$$\Omega_{\rm GW} \propto f^{3(n-2)/n},$$

where loop population is produced during $\rho \propto a^{-n}$. This result is obvious for all plots of the cosmic-string SGWB in the standard cosmology; the IR tail has a slope of $3/2$ corresponding to $\tilde{t} > t_0$ and the loop population from the radiation-domination era. For the case of loops produced in the matter era, the IR tail has a slope of 1, as shown in Fig. 3.9.

[3] In contrast, the GW spectrum generated by domain walls during radiation is not flat since in that case the triple derivative of the wall-quadrupole depends on the emission time: $Q'''_{\rm DW} \sim \sigma\,\tilde{t}$, where σ is the wall energy per unit of area. Hence, the energy density fraction in GW before wall annihilation [781] increases with time $\Omega_{\rm GW}^{\rm DW} \sim \left(G\sigma\tilde{t}\right)^2$.

B.3.7 Impact of the high-frequency proper modes of the loop

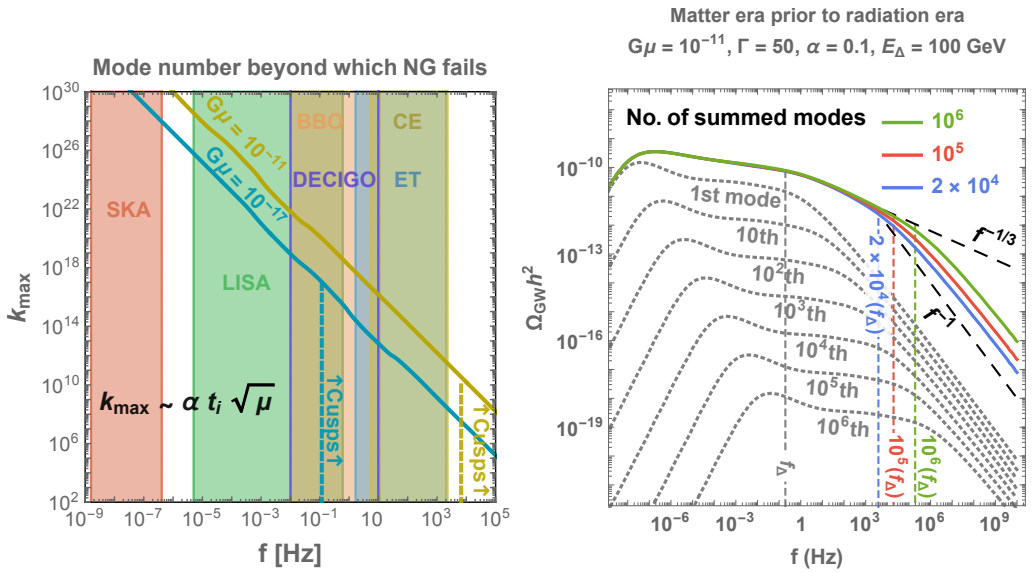

Figure B.4: left: Maximal mode number $k_{\rm max}$ in Eq. (B.36) beyond which the Nambu-Goto approximation cannot be trusted. We see that in the different interferometer windows, $k_{\rm max}$ is extremely large, often much larger than the maximal mode number tractable numerically $\sim 10^6$. *right:* Decomposition of a GW spectrum under the contributions coming from the different proper modes of the loop. We can see that high-k modes are responsible for the change of slope $f^{-1/3} \to f^{-1}$ between the physical turning point frequency f_Δ and a second, artificial, turning-point $f_{\rm max}$, given by $f_{\rm max} = k_{\rm max}\, f_\Delta$, cf. Eq. (B.45), where $k_{\rm max}$ is the total number of modes chosen for doing the computation, here 2×10^4, 10^5 and 10^6. Except when explicitly specified, for technical reasons we fix $k_{\rm max} = 2 \times 10^4$ modes in all the plots of our study.

When computing the GW spectrum from CS, Eq. (3.29), we are confronted with an infinite sum over the proper modes k of the loop. Indeed, a mode with infinitely large k becomes unphysical because it corresponds to the oscillation of infinitely large energy: $E_k \sim k/L$. The highest oscillation mode should not have energy more considerable than the energy scale of string, $E_k < \eta$, otherwise, the infinitely thin-string approximation is violated [359]. Therefore, we obtain the highest-mode number:

$$k_{\rm max} = \eta L \simeq \eta(\alpha H^{-1}), \tag{B.36}$$

which grows as a^2 in radiation-dominated Universe. At the formation time $H_{\rm form} \simeq \eta^2/M_{\rm Pl}$, the summation must be performed up to $(\alpha M_{\rm Pl}/\eta)$ modes. The number of modes before the violation of the Nambu-Goto approximation can be huge, as shown in the left panel of Fig. B.4. Nonetheless, we leave the possibility to probe the time-dependent $n_{\rm max}$ for future studies.

In what follows, we study the impact of the high-frequency modes on the GW spectrum. From Eqs. (B.19), (B.21), and (B.25), the $k^{\rm th}$-mode spectrum is related to the fundamental spectrum $k = 1$ through Eq. (B.27), which we rewrite here

$$\Omega^{(k)}_{\rm GW}(f) = k^{-\delta}\, \Omega^{(1)}_{\rm GW}(f/k), \tag{B.37}$$

In this study, we fix $\delta = 4/3$ since we assume that cusps dominate the small-scale structure. However, the results of the present section apply to any small-scale structure described by δ.

Case of a flat fundamental spectrum: If the one-mode spectrum is flat, $\Omega^{(1)}_{\rm GW}(f) \propto f^0$, the total spectrum is a simple rescaling of the fundamental spectrum by the Riemann zeta function

$$\Omega_{\rm GW}(f) = \zeta\,(\delta)\; \Omega^{(1)}_{\rm GW}(f), \tag{B.38}$$

where in particular, $\zeta(4/3) = \sum_k k^{-4/3} \simeq 3.60$.

Case of a fundamental spectrum with a slope f^{-1}: The study [334] was the first to point out the impact of the high-frequency modes on the value of a decreasing slope. We now consider the case where the fundamental spectrum has a slope f^{-1}, as expected in the presence of an early matter era, cf. Eq. (3.31) and in UV tail due to high-frequency cut-offs, cf. App. B.3.6.

The high-frequency cut-offs are described by Heaviside functions in the master formula in Eq. (B.25), of the type $\Theta\left(t_i - t_\Delta\right)$, where t_i is the cosmic time when loop formation starts. The time t_Δ can correspond to either the time of formation of the network, cf. Eq. (3.4), the time when friction-dominated dynamics become irrelevant, cf. App. B.5.4, the time when gravitational emission dominates over massive particle production, cf. Sec. 3.2.1, or the time when the string correlation length re-enters the Hubble horizon after a short period of second inflation, cf. Sec. 4.6. The slope of the $k = 1$ spectrum beyond the cut-off frequency follows from Eq. (B.25) after injecting Eq. (B.26) and $t_i = t_\Delta$, where we find

$$\Omega_{\rm GW}^{(1)}(f) = \Omega_\Delta \Theta\left(-f + f_\Delta\right) + \Omega_\Delta \frac{f_\Delta}{f} \Theta\left(f - f_\Delta\right). \tag{B.39}$$

The fundamental spectrum is flat until f_Δ and then shows a slope f^{-1} beyond. The total spectrum, summed over all the proper modes, can be obtained from Eq. (B.37) and Eq. (B.39)

$$\Omega_{\rm GW}(f) = \sum_{k=1}^{\rm k_\Delta} \frac{\Omega_\Delta}{k^\delta} k \frac{f_\Delta}{f} + \sum_{k=k_\Delta}^{\rm k_{max}} \frac{\Omega_\Delta}{k^\delta}, \tag{B.40}$$

where $k_{\rm max}$ is the maximal mode, chosen arbitrarily, and k_Δ is the critical mode defined such that modes with $k < k_\Delta$ have a slope f^{-1} whereas modes with $k > k_\Delta$ have a flat slope. For a given frequency f, the critical mode number k_Δ obeys

$$k_\Delta \simeq \frac{f}{f_\Delta}. \tag{B.41}$$

We now evaluate Eq. (B.40) in the large k_Δ limit, while still keeping $k_\Delta < k_{\rm max}$

$$\Omega_{\rm GW}^{1 \ll k_\Delta < k_{\rm max}}(f) \simeq \Omega_\Delta \frac{f_\Delta}{f} k_\Delta^{2-\delta} + \frac{1}{\delta - 1} \frac{\Omega_\Delta}{k_\Delta^{\delta-1}}, \tag{B.42}$$

where we have used the asymptotic expansion of the Euler-Maclaurin formula for the first term and the asymptotic expansion of the Hurwitz zeta function for the second term. Finally, after injecting Eq. (B.41), we get

$$\Omega_{\rm GW}^{1 \ll k_\Delta < k_{\rm max}}(f) \simeq \frac{\delta}{\delta - 1} \Omega_\Delta \left(\frac{f_\Delta}{f}\right)^{\delta-1} \propto \begin{cases} f^{-1/3} & \text{cusps } (\delta = 4/3) \\ f^{-2/3} & \text{kinks } (\delta = 5/3) \\ f^{-1} & \text{kink-kink collisions } (\delta = 2) \end{cases} \tag{B.43}$$

We conclude that the spectral index beyond a high-frequency turning point f_Δ – due to an early matter era, a second inflation era, particle production, thermal friction domination, or the formation of the network – is modified by the presence of the high-k modes in a way that depends on the small-scale structure. If cusps dominate the small-scale structure, we find a slope $-1/3$. Therefore, we can get information about the nature of the small structure by detecting a GW spectrum from CS with a decreasing slope.

Impact of fixing the total number of proper modes: For technical reasons we are unavoidably forced to choose a maximal number of modes $k_{\rm max}$. We now study the dependence of the GW spectrum on the choice of $k_{\rm max}$. The evaluation of Eq. (B.40) for $k_\Delta > k_{\rm max}$ leads to

$$\Omega_{\rm GW}^{1 \ll k_{\rm max} < k_\Delta}(f) = \zeta\left(\delta - 1\right) \Omega_\Delta \frac{f_\Delta}{f}. \tag{B.44}$$

Hence, in addition to the initial physical turning point f_Δ, where the slope changes from flat to $f^{-1/3}$, there is a second artificial turning point $f_{\rm max}$ given by

$$f_{\rm max} = k_{\rm max}\, f_\Delta, \tag{B.45}$$

where the slope changes from $f^{-1/3}$ to f^{-1}. We show the different behaviors in the right panel of Fig. B.4.

Case of a fundamental spectrum with a slope f^{+1}: As last, we comment on the case where the fundamental spectrum has a slope f^1, as in the case of an early kination era. Repeating the same steps as in Eq. (B.40), we obtain

$$\Omega_{\rm GW}(f) = \zeta\,(\delta+1)\;\Omega_\Delta\,\frac{f}{f_\Delta}, \tag{B.46}$$

hence the slope of the full spectrum is the same as the slope of the fundamental spectrum.

B.4 Derivation of the frequency–temperature relation

In this appendix, we compute the correspondence between an observed GW frequency f and the temperature T of the Universe when the loops responsible for that frequency have been formed.

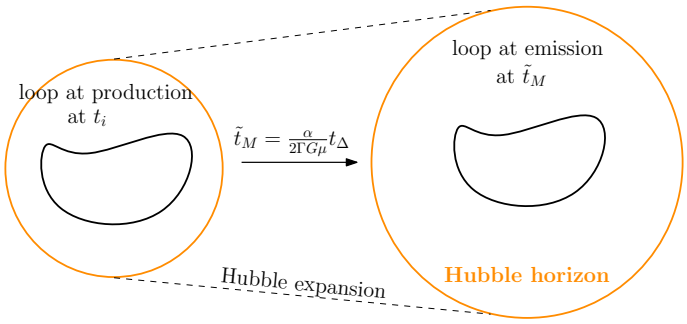

Figure B.5: Loops produced at time t_i contribute to the GW spectrum much later, when they have accomplished half of their lifetime, at $\tilde{t}_{\rm M} \simeq \alpha\, t_i/(2\Gamma G\mu)$. Hence GW emitted from cosmic-string loops are exempt from a redshift factor $a(\tilde{t}_{\rm M})/a(t_i)$ so have much higher frequency than GW produced from other sources at the same energy scale.

B.4.1 In standard cosmology

According to the scaling of the loop-formation rate $dn/dt_i \propto t_i^{-4}$, the main contribution to the GW emission at time $\tilde{t}$ comes from the loops created at the earliest epoch. Correspondingly, loops created at t_i contribute to the spectrum as late as possible, at the *main emission time* $\tilde{t}_{\rm M}$. The latest emission time is set by the loop lifetime $\alpha\, t_i/\Gamma G\mu$, where α is the loop-length at formation in horizon unit, cf. Eq. (3.15). Hence, a loop produced at time t_i mainly contributes to the spectrum, much later cf. Fig. B.5, at a time

$$\tilde{t}_{\rm M} \simeq \frac{\alpha\, t_i}{2\Gamma G\mu}, \tag{B.47}$$

where the factor $1/2$ is found upon maximizing the loop-formation rate $dn/dt_i \propto t_i^{-4}$ and upon assuming $\alpha \gg \Gamma G\mu$. The loop length after half the loop lifetime, in Eq. (B.47), is equal to half the length at formation $\alpha\, t_i/2$, cf. Eq. (B.18). Hence the emitted frequency is set by

$$\alpha\, t_i \simeq \frac{4}{f}\frac{a(\tilde{t}_M)}{a(t_0)} \simeq \frac{4}{f}\frac{a(\tilde{t}_M)}{a(t_{\rm eq})}\frac{a(t_{\rm eq})}{a(t_0)} \simeq \frac{4}{f}\left(\frac{\tilde{t}_M}{t_{\rm eq}}\right)^{1/2}\left(\frac{t_{\rm eq}}{t_0}\right)^{2/3} \tag{B.48}$$

where $f\, a(t_0)/a(\tilde{t}) = 2k/l$ and we considered the first mode $k = 1$, cf. Eqs. (3.11). By merging Eq. (B.47) and (B.48), the relation between an observed frequency f and the time t_i of loop formation reads

$$f \simeq \sqrt{\frac{8 z_{\rm eq}}{\alpha \Gamma G \mu}} \left(\frac{t_{\rm eq}}{t_i}\right)^{1/2} t_0^{-1}, \tag{B.49}$$

where the redshift at matter-radiation equality is $z_{\rm eq} = \Omega_{\rm C}/\Omega_\gamma \simeq 3360$, and $t_{\rm eq} \simeq 51.8$ kyrs and $t_0 \simeq 13.8$ Gyrs [39]. Finally, using entropy conservation, we obtain the frequency–temperature correspondence for local cosmic strings:

$$\begin{aligned} f &\simeq \sqrt{\frac{8}{z_{\rm eq}\alpha \Gamma G \mu}} \left(\frac{g_*(T)}{g_*(T_0)}\right)^{1/4} \left(\frac{T}{T_0}\right) t_0^{-1} \\ &\simeq (6.7 \times 10^{-2}\ \text{Hz}) \left(\frac{T}{\text{GeV}}\right) \left(\frac{0.1 \times 50 \times 10^{-11}}{\alpha \Gamma G \mu}\right)^{1/2} \left(\frac{g_*(T)}{g_*(T_0)}\right)^{1/4}. \end{aligned} \tag{B.50}$$

In the case of global cosmic strings, discussed in Sec. 3.6, the frequency-temperature relation is more trivial. Since loops decay quickly after their formation, its GW contribution from those loops depends directly on their size at production, that is, the horizon size. Therefore, the frequency-temperature relation is numerically similar to that of inflationary GW.

B.4.2 During a change of cosmology

The derivation of Eq. (B.50) does not take into account the time-variation of loop formation $C_{\rm eff}$. It assumes that loops are produced and decayed during the scaling regime in the radiation era. An observable to test the non-standard cosmology is the frequency f_Δ of the *turning-point* defined as the frequency at which the GW spectrum deviates from the standard-cosmology behavior and the spectral index changes. We obtain different fitted values for this turning-point frequency depending on the prescription. We quote below different expressions, depending on whether the GW spectrum can be measured with a 10% precision and 1% respectively[4]. We compare the predictions obtained using a scaling and VOS network:

$$f_\Delta \simeq \text{Hz} \left[\frac{T_\Delta}{\text{GeV}}\right] \left[\frac{0.1 \cdot 50 \cdot 10^{-11}}{\alpha \Gamma G \mu}\right]^{1/2} \left[\frac{g_*(T_\Delta)}{g_*(T_0)}\right]^{1/4} \cdot \begin{cases} 2 \times 10^{-3} & (\text{VOS}, 10\%) \\ 45 \times 10^{-3} & (\text{scaling}, 10\%) \\ 0.04 \times 10^{-3} & (\text{VOS}, 1\%) \\ 15 \times 10^{-3} & (\text{scaling}, 1\%) \end{cases} \tag{B.51}$$

Therefore, the turning-point frequency is lower in VOS than in scaling by a factor ~ 22.5 if we define the turning-point frequency by an amplitude deviation of 10% with respect to standard cosmology and by a factor ~ 375 for a deviation of 1%. The loops contributing to this part of the spectrum have been formed at the time of cosmology change. When the cosmology changes, the network achieves a transient evolution to reach the new scaling regime. The long-string network needs extra time to transit from one scaling regime to the other, hence the shift in the frequency-temperature relation of the turning point.

B.4.3 In the presence of an intermediate inflation period

The derivation of Eq. (B.50) assumes that cosmic-string loops are constantly being produced throughout the cosmic history. It does not apply if the network experiences an intermediate era of inflation.

[4] This criterion compares the GW spectrum to the standard prediction and has nothing to do with the sensitivity of GW observatories. Indeed, the required precision for detecting this deviation will depend on the signal-to-noise ratio.

This case is discussed in Sec. 4.6.2 and the turning-point formulae are, for a given precision

$$f_\Delta \simeq \text{Hz}\left[\frac{T_\Delta}{\text{GeV}}\right]\left[\frac{0.1\cdot 50\cdot 10^{-11}}{\alpha\Gamma G\mu}\right]^{1/2}\left[\frac{g_*(T_\Delta)}{g_*(T_0)}\right]^{1/4}\cdot\begin{cases}1.5\times 10^{-4} & (10\%)\\ 5\times 10^{-6} & (1\%)\end{cases} \tag{B.52}$$

B.4.4 Cut-off from particle production

The cutoff frequency due to particle production is given in Sec. 3.2.5.

B.5 Derivation of the VOS equations

B.5.1 The Nambu-Goto string in an expanding Universe

The Velocity-dependent One-Scale equations (VOS) in Eq. (3.40), describe the evolution of a network of long strings in term of two parameters[5]: the mean velocity $\bar{v}$ and the correlation length $\xi = L/t$, see the original papers [405–407] and [408] for a review. The set of points visited by the Nambu-Goto string during its time evolution form a 2D manifold, called the *world-sheet*, described by time-like $\mathtt{t}$ and space-like σ coordinates. The embedding of the 2D world-sheet in the 4D space-time is described by $x^\mu(\mathtt{t},\,\sigma)$ where $\mu = 1,\,2,\,3,\,4$. The choice of the word-sheet coordinates being arbitrary, and we can gauge-fix by imposing $\dot{\mathbf{x}}\cdot\mathbf{x}' = 0$ and $\mathtt{t} = \tau$ where τ is the conformal time of the expanding Universe, $\dot{\mathbf{x}} \equiv d\mathbf{x}/d\mathtt{t}$ and $\mathbf{x}' \equiv d\mathbf{x}/d\sigma$. Then, the equations of motion of the Nambu-Goto string in a FRW Universe are [784]

$$\ddot{\mathbf{x}} + 2\mathcal{H}(1-\dot{\mathbf{x}}^2)\dot{\mathbf{x}} = \frac{1}{\epsilon}\left(\frac{\mathbf{x}'}{\epsilon}\right)', \tag{B.53}$$

$$\dot{\epsilon} + 2\mathcal{H}\,\dot{\mathbf{x}}^2\,\epsilon = 0, \tag{B.54}$$

where $\mathcal{H} \equiv \dot{a}/a = Ha$ and $\epsilon \equiv \sqrt{\mathbf{x}'^2/(1-\dot{\mathbf{x}}^2)}$ is the coordinate energy per unit of length.

B.5.2 The long-string network

The macroscopic evolution of the long string network can be described by the energy density

$$\rho_\infty = \frac{E}{a^3} = \frac{\mu}{a^2(\tau)}\int \epsilon\, d\sigma \equiv \frac{\mu}{L^2}, \tag{B.55}$$

and the root-mean-square averaged velocity

$$\bar{v}^2 \equiv \langle\dot{\mathbf{x}}^2\rangle = \frac{\int \dot{\mathbf{x}}^2\epsilon\, d\sigma}{\int \epsilon\, d\sigma}, \tag{B.56}$$

where we recall that μ is the CS linear mass density.

[5] For the superconducting strings, the VOS model can be extended with two more charge-current parameters into Charge-VOS model [782]. Very recently, it has been shown that the current inside strings affects the scaling solution and loop production [783], resulting in the peak-like enhancement simialr to the intermediate kination scenario.

B.5.3 VOS 1: the correlation length

Differentiating Eq. (B.55) gives the evolution of the energy density in an expanding Universe

$$\frac{d\rho_\infty}{dt} = \frac{d\rho_\infty}{d\tau}\cdot\frac{d\tau}{dt} = \frac{1}{a}\cdot\frac{d\rho_\infty}{d\tau}, \tag{B.57}$$

$$= \frac{\mu}{a}\left[\frac{d}{d\tau}\left(\frac{1}{a^2}\right)\int \epsilon\, d\sigma + \frac{1}{a^2}\int \frac{d\epsilon}{d\tau}\, d\sigma\right], \tag{B.58}$$

$$= -2\frac{\mu}{a^3}\mathcal{H}\left[\int \epsilon\, d\sigma + \int \dot{\mathbf{x}}^2\epsilon\, d\sigma\right], \tag{B.59}$$

$$= -2H\rho_\infty\,(1+\bar{v}^2). \tag{B.60}$$

Moreover, after each string crossing, the network transfers energy into loops with a rate given by Eq. (3.38) and we get

$$\frac{d\rho_\infty}{dt} = -2H\rho_\infty\,(1+\bar{v}^2) - \tilde{c}\,\bar{v}\frac{\rho_\infty}{L}, \tag{B.61}$$

which after using Eq. (B.55), leads to the first VOS equation

$$\text{VOS 1:}\qquad \frac{dL}{dt} = HL\,(1+\bar{v}^2) + \frac{1}{2}\tilde{c}\,\bar{v}. \tag{B.62}$$

The back-reaction on long strings from gravitational emission is suppressed with respect to the loop-chopping loss term by $O(G\mu)$. The case of global strings, for which the back-reaction due to particle production may play a role, is considered in Sec. 3.6.2.

B.5.4 Thermal friction

In addition to the Hubble friction, strings can experience friction due to their interactions with particles of the plasma, leading to the retarding force [411]

$$F = \rho\sigma\bar{v} = \beta T^3\bar{v}, \tag{B.63}$$

where $\rho \sim T^4$ is the plasma energy density, and $\sigma \sim T^{-1}$ is the cross-section per unit of length. The friction damps the string motion and suppresses the GW spectrum [785]. For gauge strings, a well-known realisation of friction is the interaction of charged particles with the pure gauge fields existing outside the string, the so-called *Aharonov-Bohm* effect [786]. In such a case, the friction coefficient β is given by [411]

$$\beta = 2\pi^{-2}\zeta(3)\sum_i g_i \sin^2(\pi\nu_i), \tag{B.64}$$

with $i \equiv$ relativistic particle species ($m_i \ll T$),

$g_i \equiv$ number of relativistic degrees of freedom of $i \times \begin{cases} 3/4 \text{ (fermion)}, \\ 1 \text{ (boson)}, \end{cases}$

$2\pi\,\nu_i \equiv e_i\,\Phi \equiv$ phase-shift of the wave-function of particle i when transported on a close path around the string. e_i being its charge under the associated gauge group and Φ the magnetic field flux along the string.

The friction term in the first VOS equation, Eq. (B.62), becomes

$$2H\bar{v}^2 \longrightarrow \frac{\bar{v}^2}{l_d} \equiv 2H\bar{v}^2 + \frac{\bar{v}^2}{l_f}, \tag{B.65}$$

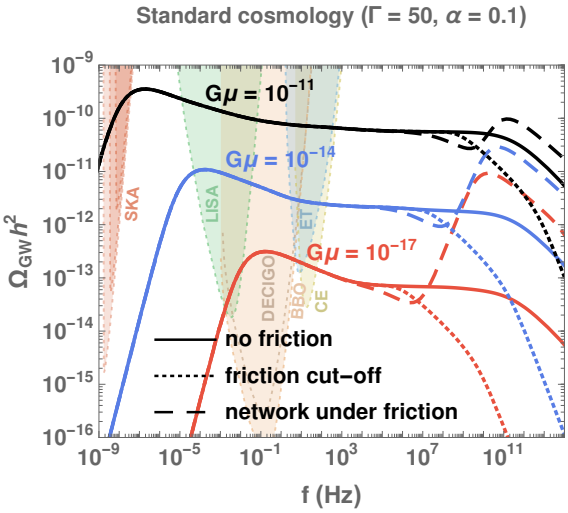

Figure B.6: GW spectrum from CS assuming no thermal friction (solid lines), thermal friction only at the level of the long-string network, i.e. upon including Eq. (B.65) in the VOS equations (dashed lines) or thermal friction taken at the loop-motion level, i.e. by removing GW emissions anterior to $t_{\rm fric}$ defined in Eq. (B.66) (dotted lines). See text for more details. A standard cosmology is assumed.

where a friction length due to particle scattering is defined by $l_f \equiv \mu/(\sigma\,\rho) = \mu/(\beta T^3)$ [405, 406], and the associated effective friction length l_d. At high temperature, the large friction prevents the CS network to reach the scaling regime until $2H \lesssim 1/l_f$, so after the time

$$t_{\rm fric} \simeq (2.5\times10^{-5}) \left(\frac{106.75}{g_*(t_{\rm fric})}\right)^{3/2} \beta^2\,(G\mu)^{-2}\,t_{\rm pl}, \tag{B.66}$$

$$\simeq (1.4\times10^{-4}) \left(\frac{g_*(t_{\rm F})}{106.65}\right)^{1/2} \left(\frac{106.75}{g_*(t_{\rm fric})}\right)^{3/2} \beta^2\,(G\mu)^{-1}\,t_F, \tag{B.67}$$

where $t_{\rm pl} \equiv \sqrt{G}$, and the network formation time t_F is when the energy scale of the Universe is equal to the string tension $\rho_{\rm tot}^{1/2}(t_F) \equiv \mu$. For friction coefficient $\beta = 1$, the friction becomes negligible at the temperatures $T_* \simeq 4$ TeV for $G\mu = 10^{-17}$, $T_* \simeq 400$ TeV for $G\mu = 10^{-15}$, $T_* \simeq 40$ PeV for $G\mu = 10^{-13}$. Hence, it respectively impacts SGWB above the frequencies 20, 200, 2000 kHz, cf. Eq. (4.21), which are outside the GW interferometer windows, cf. Fig. 3.4.

In Fig. B.6, we show the impact of thermal friction on the GW spectrum from CS in two different ways:

- **Network under friction** *(dashed lines in Fig. B.6):* the thermal friction is only taken into account at the level of the long-string network, i.e., by including the friction term in Eq. (B.65) in the VOS equations. The GW peak at high frequency is due to the loop over-production by the frozen network, followed by a fast relaxation (with a little oscillatory behavior) to the scaling regime once friction becomes negligible with respect to Hubble expansion. This approach is insufficient since it assumes that $\Gamma G\mu^2$ still gives the GW power emitted by loops with $\Gamma \simeq 50$. Therefore, it does not consider the damping of the oscillations of the loops under which we expect $\Gamma \to 0$.

- **GW emission cut-off** *(dotted lines in Fig. B.6):* The damping of the loop oscillations discards all GW emissions happening prior to $t_{\rm fric}$ in Eq. (B.66), when thermal friction is larger than Hubble friction. Technically, the time $t_{\rm osc}$ of first loop oscillations in Eq. (3.30) is set equal to $t_{\rm fric}$ in Eq. (B.66).

In many of our plots, e.g., Fig. 3.2 and Fig. 3.4, we show the GW spectrum in the presence of thermal friction with a gray line, computed according to the second prescription above, entitled *GW emission cut-off*. Note that in most cases, the effect of friction manifests itself at very high frequencies, outside the observability band of planned interferometers. It could, however, become relevant if those high frequencies could be probed in future experiments.

B.5.5 VOS 2: the mean velocity

Differentiating Eq. (B.56) gives the evolution of the averaged velocity, which constitutes the second VOS equation

$$\text{VOS 2:} \qquad \frac{d\bar{v}}{dt} = (1-\bar{v}^2)\left[\frac{k(\bar{v})}{L} - \frac{\bar{v}}{l_d}\right], \tag{B.68}$$

$$\text{with} \quad k(\bar{v}) \equiv \frac{\left\langle (1-\dot{\mathbf{x}}^2)\,(\dot{\mathbf{x}}\cdot\mathbf{u})\right\rangle}{\bar{v}\,(1-\bar{v}^2)},$$

where $\mathbf{u}$ is the unit vector aligned with the radius of curvature $\propto d^2\mathbf{x}/d\sigma^2$, and $k(\bar{v})$ indicates the degree of wiggliness of the string. More precisely, $k(\bar{v}) = 1$ for a straight string and $k(\bar{v}) \lesssim 1$ once we add small-scale structures. We use the results from numerical simulations [407]

$$k(\bar{v}) = \frac{2\sqrt{2}}{\pi}(1-\bar{v}^2)(1+2\sqrt{2}\bar{v}^3)\frac{1-8\bar{v}^6}{1+8\bar{v}^6}. \tag{B.69}$$

Eq. (B.68) is a relativistic generalization of Newton's law where the string is accelerated by its curvature $1/L$ but is damped by the Hubble expansion and plasma friction after a typical length $1/l_d$[6].

B.6 Extension of the original VOS model

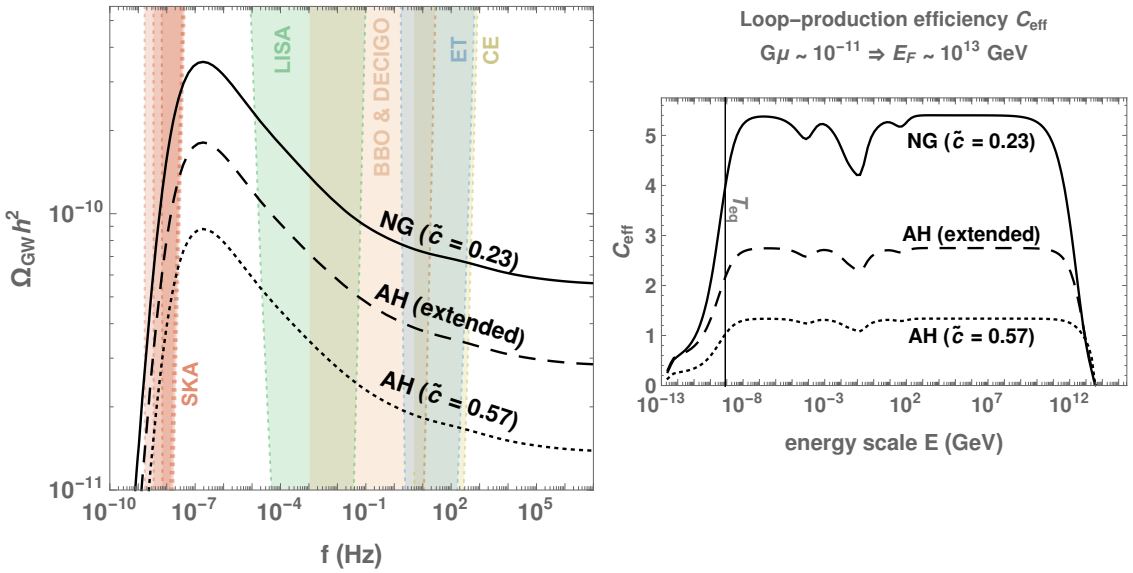

Figure B.7: left: GW spectra with different VOS modellings of the long-string network evolution. The VOS models are either based on Nambu-Goto simulations (solid line - $\tilde{c} = 0.23$) [407] or abelian-Higgs (AH) field theory simulations (dashed line - $\tilde{c} = 0.57$) [382, 788], possibly extended to include particle production [409] (dotted line). *right:* The corresponding loop-production efficiency for each VOS model.

B.6.1 VOS model from Nambu-Goto simulations

In our study, the evolution of the long-string network through the VOS model is described by Eq. (3.40). The only free parameter is the loop-chopping efficiency $\tilde{c}$, which is computed from Nambu-Goto network simulations in an expanding Universe [407], to be

$$\textbf{NG:} \qquad \tilde{c} = 0.23 \pm 0.04. \tag{B.70}$$

[6] Eq. (B.68) neglects the change in long string velocity $\bar{v}$ due to loop formation as proposed in [787].

scaling in radiation dominated Universe	NG $\tilde{c} = 0.23$	AH $\tilde{c} = 0.57$	AH extended $\tilde{c} = 0.31$ $(d,\ k_0,\ r,\ q,\ \beta)$
$\bar{v}$	0.66	0.62	0.59
ξ	0.27	0.57	0.36
$C_{\rm eff}$	5.4	1.3	2.8

Table B.1: Values of mean velocity $\bar{v}$, correlation length ξ, and loop-production efficiency $C_{\rm eff}$ in radiation scaling regime with different VOS calibrations.

B.6.2 VOS model from Abelian-Higgs simulations

Abelian-Higgs (AH) field theory simulations in both expanding and flat spacetime suggest a larger value [382, 788]

$$\textbf{AH:} \qquad \tilde{c} = 0.57 \pm 0.04. \tag{B.71}$$

Indeed, in Abelian-Higgs simulations, no loops are produced below the string core size, so the energy loss into loop formation is lower. Consequently, the loop-chopping efficiency must be increased to maintain scaling.

B.6.3 VOS model from Abelian-Higgs simulations with particle production

In Abelian-Higgs simulations, the loops produced at the string core scale are non-linear lumps of field, called *proto-loops*, which decay fast into massive radiation. Therefore, a recent work [409] extends the VOS model by including a term in Eq. (B.62) to account for the emission of massive radiation at the string core scale. The energy-loss function $F(v)$ is modified as

$$F(\bar{v})|_{\rm original} = \frac{\tilde{c}\bar{v}}{2} \quad \Rightarrow \quad F(\bar{v})|_{\rm extended} = \frac{\tilde{c}\bar{v} + d[k_0 - k(\bar{v})]^r}{2}, \tag{B.72}$$

and the momentum operator $k(v)$, cf. Eq. (B.69), accounting for the amount of small-scale structures in the string, is modified to

$$k(\bar{v})|_{\rm original} = \frac{2\sqrt{2}}{\pi}\frac{1 - 8\bar{v}^6}{1 + 8\bar{v}^6} \quad \Rightarrow \quad k(\bar{v})|_{\rm extended} = k_0\frac{1 - (q\bar{v}^2)^\beta}{1 + (q\bar{v}^2)^\beta}. \tag{B.73}$$

With Abelian-Higgs simulations, one finds [409]

$$\textbf{AH extended:} \qquad \tilde{c} = 0.31, \tag{B.74}$$

as well as $d = 0.26$, $k_0 = 1.27$, $r = 1.66$, $q = 2.27$, and $\beta = 1.54$. In Abelian-Higgs extended, the loop-chopping efficiency, cf. Eq. (B.74), is smaller than the one in the original Abelian-Higgs model, cf. Eq. (B.71). Indeed, because of the additional energy loss through massive-radiation, less energy loss via loop-chopping is needed to maintain scaling.

In Fig. B.7, we compare the GW spectra in the different VOS models. The difference in amplitude comes from the difference in the number of loops, set by $C_{\rm eff}$. The larger the loop-chopping efficiency $\tilde{c}$, the smaller the loop-formation efficiency $C_{\rm eff}$. This counter-intuitive result can be better understood by looking at Tab. B.1. A larger loop-chopping efficiency $\tilde{c}$ implies a larger loop formation rate only during the transient regime. In the scaling regime, a larger loop-chopping efficiency $\tilde{c}$ implies a more depleted long-string network and a larger correlation length ξ. Hence, the long-string network is more sparse, so the rate of loop formation via string crossing is lower.

B.7 Impact of the cosmology on the loop size at formation

B.7.1 Loop size as a fraction of the Hubble horizon

In this section, we discuss the validity of defining the loop-size at formation, l_i, as a constant fraction α of the Hubble horizon size t_i

$$\text{Terminology I}: \quad l_i = \alpha\, t_i. \tag{B.75}$$

Nambu-Goto simulations [194] suggest $\alpha \simeq 0.1$. In this first prescription, we neglect the effects of cosmology change on α. The advantage of the second prescription presented in Sec. B.7.2 is to account analytically for these effects.

The time derivative of the length of the loop at its formation is simply

$$\frac{dl}{dt} = \alpha + \Gamma G\mu, \tag{B.76}$$

which leads to the GW spectrum in Eq. (3.29). Outside the redshift factors, in this first prescription the loop-production efficiency $C_{\rm eff}$ is the only parameter depending on the cosmology in the GW spectrum formula.

B.7.2 Loop size as a fraction of long-string correlation length

Loops being formed by inter-commutation of long strings, the appropriate length scale setting their size at formation should be the correlation length L of the long-string network, and not the Hubble horizon size t_i. Therefore, the loop-size at formation l_i in Eq. (B.75) should be replaced by the more natural definition, pointed out first in [410]

$$\text{Terminology II}: \quad l_i \equiv \alpha_L\, L_i = \alpha_L\, \xi\, t_i, \tag{B.77}$$

where α_L is the new constant loop-size parameter. The two definitions of the loop-size parameter in Eqs. (B.75) and (B.77) are related through

$$\alpha = \alpha_L\, \xi. \tag{B.78}$$

We assume that α_L is a constant independent of the equation of state of the Universe [296]. We set its value to $\alpha_{\rm L} = 0.37$ in order to match $\alpha = 0.1$ during radiation-domination. Therefore, the dependence of l_i on the change of cosmology is directly tied to ξ.

The GW spectrum formula, cf. Eq. (B.25), which depends on the time derivative of the loop length at the production, cf. Eq. (B.16)

$$\frac{dl}{dt} = \alpha_L \frac{d}{dt}(\xi t) + \Gamma G\mu, \tag{B.79}$$

becomes

$$\begin{aligned}\Omega_{\rm GW}^{(k)}(f) =& \frac{1}{\rho_c}\frac{2k}{f}(0.1)\,\Gamma^{(k)} G\mu^2 \int_{t_{\rm osc}}^{t_0} d\tilde{t}\, \frac{\tilde{c}\bar{v}(t_i)}{\gamma\alpha_L}\left[\frac{1}{\xi(t_i)t_i}\right]^4 \left[\frac{1}{\alpha_L \frac{d}{dt}(\xi t) + \Gamma G\mu}\right] \\ &\times \left[\frac{a(\tilde{t})}{a(t_0)}\right]^5 \left[\frac{a(t_i)}{a(\tilde{t})}\right]^3 \Theta(t_i - t_{\rm osc})\Theta(t_i - \frac{l_*}{\alpha}),\end{aligned} \tag{B.80}$$

where t_i is the solution to

$$l(t) = \alpha_L \xi(t_i) t_i - \Gamma G\mu(t - t_i). \tag{B.81}$$

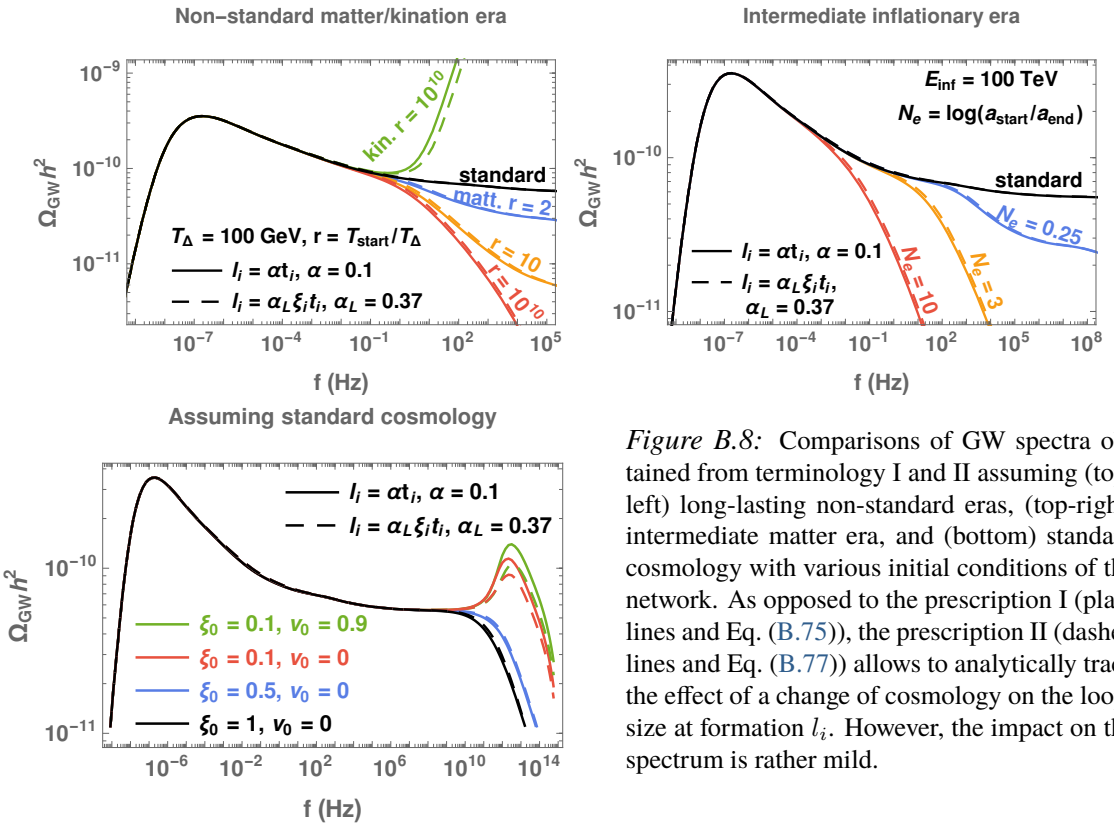

Figure B.8: Comparisons of GW spectra obtained from terminology I and II assuming (top-left) long-lasting non-standard eras, (top-right) intermediate matter era, and (bottom) standard cosmology with various initial conditions of the network. As opposed to the prescription I (plain lines and Eq. (B.75)), the prescription II (dashed lines and Eq. (B.77)) allows to analytically track the effect of a change of cosmology on the loop-size at formation l_i. However, the impact on the spectrum is rather mild.

	terminology I $\alpha_{\rm I}$	terminology II $\alpha_{\rm II} = \alpha_L \xi$	$\frac{\Omega_{\rm GW,II}}{\Omega_{\rm GW,I}} = \sqrt{\frac{\alpha_{\rm II}}{\alpha_{\rm I}}}$
radiation	0.1	(0.37)(0.27)	1
matter	0.1	(0.37)(0.63)	1.53
kination	0.1	(0.37)(0.15)	0.75

Table B.2: Values of loop-size parameter $\alpha_{\rm I}$, $\alpha_{\rm II} \equiv \xi t$ assuming radiation-, matter-, and kination-scaling and ratios between their corresponding GW spectra. Note that the intermediate inflationary scenario provides similar results to that of the matter era. The characteristic length scale ξ is constant during the scaling regime, which makes the comparison between the two terminologies possible.

B.7.3 Impact on the GW spectrum

In Fig. B.8, we compare the impact of the two prescriptions for the loop-size at formation, defined in Eqs. (B.75) and (B.77), on the GW spectrum. We show GW spectra assuming intermediate or long-lasting non-standard era, or standard cosmology with various initial conditions of the cosmic-string network. The impact of the loop-size at formation on the spectrum mainly comes from the behavior $\Omega_{\rm GW} \propto \sqrt{\alpha}$, cf. Eq. (3.47). Since the actual long-string correlation scale ξ is longer/shorter in matter-/kination-dominated Universe respectively, terminology II leads to an enhancement/suppression of the spectrum. Table B.2 displays values of α and expected ratios of amplitudes from two terminologies, for different equations of state. Because of the technical difficulties in applying terminology II and the relatively small spectral impact, we restrict to the terminology I throughout this work, as used in Sec. 3.2.2.

Appendix C

Constraint on Intermediate Inflation

In Sec. 4.6, we discuss the effect on SGWB of an intermediate inflationary period – occurring much after the primordial inflation and unrelated to CMB and large-scale structure (LSS) observations. This appendix quantifies the bound on such a scenario. The idea is that any perturbation leaving the horizon during the secondary inflation is not observable in the CMB and in the LSS if the second inflation lasts no longer than ~ 30 efolds. Fig. C.1 shows the comoving Hubble horizon in the two-stage inflation cosmology where the interim period is the radiation domination era; the derivation of the bound can be understood graphically. We will follow the similar derivations for bounds on the single-inflationary era followed by standard hot-Big-Bang cosmology and the non-standard cosmology [789, 790].

We define the critical mode as the smallest-scale mode in the CMB power spectrum – the largest harmonic moment l – that does not reenter the horizon during the reheating and leave the horizon again due to the second inflation,

$$k_{\rm crit} \;=\; a_{\rm reh} H_{\rm reh}. \tag{C.1}$$

We obtain the maximum e-folding $N_{\rm II}$ of the secondary inflation,

$$a_{\rm CMB} H_{\rm CMB} = a_{\rm reh} H_{\rm reh} \;\;\Rightarrow\;\; N_{\rm II,max} = -\frac{1}{12}\ln\left(\frac{\rho_{\rm eq}\rho_{\rm CMB}^2}{M_{\rm Pl}^{12}}\right) + \frac{1}{4}\ln\left(\frac{\rho_{\rm II}}{M_{\rm Pl}^4}\right), \tag{C.2}$$

where we assume the instantaneous reheating at the end of second inflation, and we use the total energy density of the Universe at matter-radiation equality $\rho_{\rm eq} = \Omega_{m,0}\rho_c z_{\rm eq}^3$. The total energy density of the Universe corresponding to the smallest scale in CMB power spectra is found by comparing the multipole moments of the smallest scale, $l_{\rm smallest} \simeq 2500$, to the scale at recombination – the highest peak of the CMB power spectrum $l_* \simeq 200$ [791],

$$\frac{l_*}{l_{\rm smallest}} \;=\; \frac{k_*}{k_{\rm CMB}} \;=\; \frac{a_* H_*}{a_{\rm CMB} H_{\rm CMB}} \;=\; \left(\frac{\rho_*}{\rho_{\rm CMB}}\right)^{2/3}, \tag{C.3}$$

$$\rho_{\rm CMB} \;=\; \left(\frac{l_{\rm smallest}}{l_*}\right)^{3/2}\rho_* \;=\; \left(\frac{l_{\rm smallest}}{l_*}\right)^{3/2}\Omega_{m,0}\rho_c z_*^3 \tag{C.4}$$

where we have used that the Universe is matter-dominated. Therefore, the maximum bound allowed by the successful observation of the CMB power spectrum is

$$N_{\rm II}^{\rm CMB} \;=\; 63.08 + \frac{1}{4}\ln\left(\frac{\rho_{\rm II}}{M_{\rm Pl}^4}\right) \;=\; 27.65 + \frac{1}{4}\ln\left(\frac{\rho_{\rm II}}{\rm TeV^4}\right). \tag{C.5}$$

A similar but weaker bound from the smallest scale from LSS observation, i.e., the Lyman-α forest probes down to $k \simeq 1.4$ Mpc^{-1}, see Ref. [25] for a review and references therein. The maximum e-foldings of the second inflation allowed by Lyman-α is

$$N_{\rm II}^{\text{Ly-}\alpha} \;=\; 65.47 + \frac{1}{4}\ln\left(\frac{\rho_{\rm II}}{M_{\rm Pl}^4}\right) \;=\; 30.04 + \frac{1}{4}\ln\left(\frac{\rho_{\rm II}}{\rm TeV^4}\right). \tag{C.6}$$

Lastly, we comment on the two-stage inflation with a specific case of cosmic-string domination [543]. The Hubble horizon during string domination, $(aH)^{-1}$, is constant, and the super-horizon mode that hovers just above the horizon can reprocess the perturbations if the cosmic-string domination is long enough and impacts the density power spectrum.

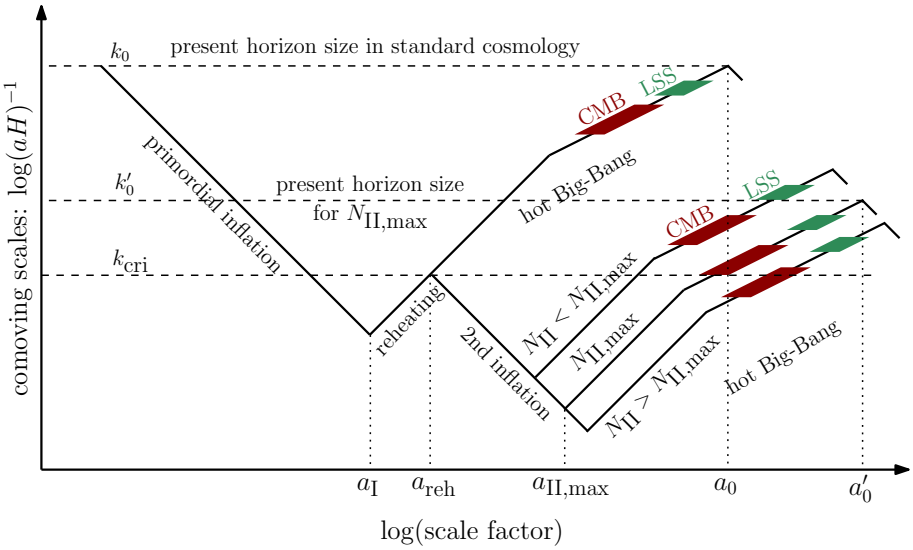

Figure C.1: Comoving horizons in the standard hot-Big-Bang cosmology and the cosmological history with second-stage inflation. The CMB and LSS can bound the maximum e-fold number of the second inflation by requiring that there is no observable signal corresponding to modes reprocessed by the non-standard cosmological history, i.e., mode with $k > k_{\rm crit}$. For simplicity, we assume the reheating to be a radiation-dominated era, and the Universe is instantaneously reheated after the second inflation.

Appendix D

Kination after inflation: quintessential inflation with α-attractor

Kination has been discussed in the literature as a follow-up of inflation before reheating. Except for the new constraint derived in Sec. 4.4.4, this appendix reviews the motivation for models of kination following inflation for completeness. As stated in Sec. 4.4.2, it is impossible to have a kination era from a canonical scalar field rolling down its potential without superplanckian field excursions. On the other hand, kination arises in a popular class of inflation models called α-attractor models which not only fit CMB data well but also link to quintessence at a late time. Besides, they can be motivated by supergravity models. We summarise them in the following.

D.1 A sharp transition between two plateaus

α-attractor is a class of supergravity theory where kinetic terms have poles

$$\mathcal{L} = \frac{\frac{1}{2}(\partial\phi)^2}{(1-\frac{\phi^2}{6\alpha M_{\rm pl}^2})^2} - V(\phi) + \Lambda, \qquad \alpha > 0. \tag{D.1}$$

The use of α-attractor for quintessential inflation has been studied in [792–797]. Since the scalar field cannot cross the poles, the field range is limited to $-\sqrt{6\alpha}M_{\rm pl} \lesssim \phi \lesssim +\sqrt{6\alpha}M_{\rm pl}$. For $\alpha \lesssim 1/6$, it has the great advantage to prevent super-Planckian field excursion which plagues usual quintessential inflation scenarios.

Scalar potential. — Following [794, 795, 797], we choose the following scalar potential

$$V(\phi) = V_0\, e^{-\kappa\phi/M_{\rm pl}}, \tag{D.2}$$

where $\kappa > 0$, which can be motivated by supergravity [798, 799], brane inflation [800], string theory [315, 801, 802] or gaugino condensation [803–805]. At late time, the scalar field slows downs when reaching an infinite kinetic term at $\phi \to +\sqrt{6\alpha}M_{\rm pl}$. We suppose the existence of an unknown mechanism which set the cosmological constant (CC) to zero at $\phi \to +\sqrt{6\alpha}M_{\rm pl}$

$$\Lambda = V(\sqrt{6\alpha}M_{\rm pl}) = V_0\, e^{-\kappa\sqrt{6\alpha}}, \tag{D.3}$$

such that the scalar field potential energy + CC reads

$$V(\phi) = V_0\, e^{-n}\left[e^{n\left(1-\frac{\phi}{\sqrt{6\alpha}M_{\rm pl}}\right)} - 1\right], \qquad \text{with} \quad n \equiv \kappa\sqrt{6\alpha}. \tag{D.4}$$

Upon introducing the field transformation

$$\frac{\partial\phi}{\partial\varphi} = 1 - \frac{\phi^2}{6\alpha M_{\rm pl}^2}, \quad \leftrightarrow \quad \phi = \sqrt{6\alpha} M_{\rm pl} \tanh\left(\frac{\varphi}{\sqrt{6\alpha} M_{\rm pl}}\right), \tag{D.5}$$

we obtain a canonically normalized scalar field with potential energy

$$V(\varphi) = e^{-2n} M^4 \left[e^{n\left(1-\tanh\frac{\varphi}{\sqrt{6\alpha}M_{\rm pl}}\right)} - 1 \right], \quad M^4 \equiv e^n V_0. \tag{D.6}$$

The poles at $\phi \to \pm\sqrt{6\alpha} M_{\rm pl}$ have been sent to $\varphi \to \pm\infty$ and the potential $V(\varphi)$ features two plateaus

$$V(\varphi) \simeq \begin{cases} M^4 \exp\left(-2n e^{\frac{2\varphi}{\sqrt{6\alpha}M_{\rm pl}}}\right), & \text{when } \varphi \to -\infty, \\ 2n e^{-2n} M^4 \exp\left(-\frac{2\varphi}{\sqrt{6\alpha}M_{\rm pl}}\right), & \text{when } \varphi \to +\infty. \end{cases} \tag{D.7}$$

This potential and the history of the Universe in the quintessential inflation scenario are shown in Fig. D.1 and Fig. D.2 respectively.

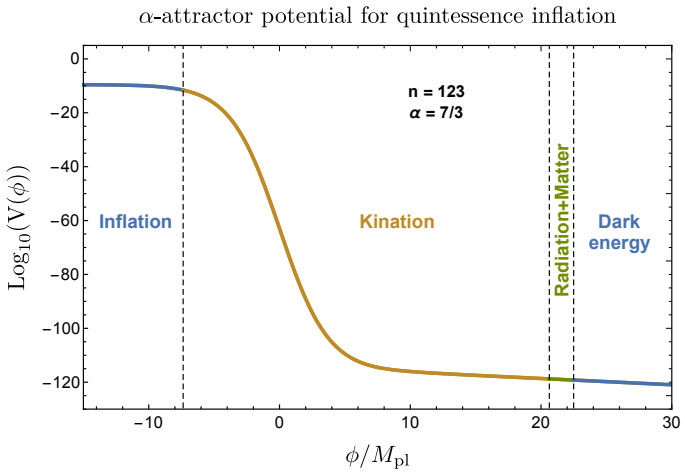

Figure D.1: α-attractor potential for quintessential inflation. We took the same parameters as in Fig. (D.2).

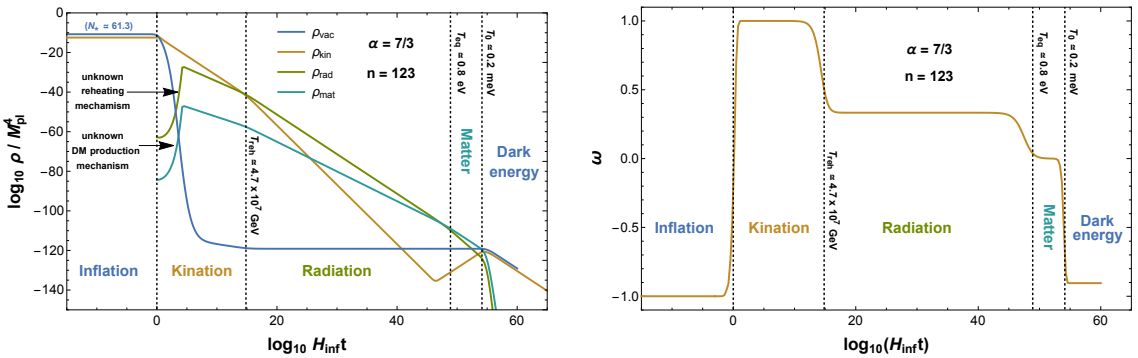

Figure D.2: **left**: evolution of the different energy densities composing the Universe in the quintessential inflation scenario based on the potential in Eq. (D.6) for $\alpha = 7/3$ (motivated by string theory [796]) and $n = 123$. We solved numerically the equation of motion of the scalar field evolving in the potential in Eq. (D.6) in the expanding Universe. **right**: evolution of the equation of state $\omega = p/\rho$ of the Universe.

D.2 Kination followed by reheating

After inflation, the Universe is dominated by the kinetic energy of the scalar field which evolves according to Eq. (4.24)

$$\varphi = \varphi_{\rm end} + \sqrt{\frac{2}{3}} M_{\rm pl} \ln\left(\frac{t}{t_{\rm end}}\right) \tag{D.8}$$

with the field position at the end of inflation estimated as

$$\varphi_{\rm end} = \sqrt{\frac{3\alpha}{2}} M_{\rm pl} \ln\left(\frac{\sqrt{3\alpha}}{2n}\right). \tag{D.9}$$

Since the inflation potential is non-oscillatory, the standard reheating can not occur through the decay of the inflaton.

The kination era ends when the Universe becomes dominated by the energy density of the reheated plasma. An immediate possibility for producing radiation is *gravitational reheating* [485, 486] in which the reheated density reads

$$\rho_{\rm grav} \simeq \delta \times 10^{-2}\, H_{\rm end}^4, \tag{D.10}$$

where δ is an efficiency factor that depends on the number of fields, their coupling with gravity, their mass, and their self-coupling; see [511] for a review. However, unless we introduce a large number $\delta \gtrsim 50$ of self-interacting and non-minimally-coupled light fields, reheating through gravitational coupling only is inconsistent with the BBN bound on GW from inflation [506, 511, 806–809].

Other reheating mechanism, which may be the one realized in the SM [810], is to introduce a large non-minimal coupling to gravity to exploit the tachyonic instability generated by the change of sign of the Ricci scalar during kination [487–491]. The tachyonic instability can also be generated by a thermal phase transition [797] or more generally when the inflaton crosses an enhanced symmetry point, see instant reheating [795, 811–813] or trapping reheating [814, 815]. Another well-known efficient reheating is curvaton reheating where a spectator field decay into SM [816–818].

Appendix E

GW probe of stiff era

The scalar Virial theorem in Eq. (G.141) states that the averaged energy density of the scalar field – in the power-law potential and in the expanding Universe – redshifts as $\langle \rho_\Phi \rangle \propto a^{-6n/(2+n)}$ for $V(\Phi) \propto \Phi^n$, which is equivalent to the EOS: $\omega = (n-2)/(n+2)$. For $n > 4$, the EOS is larger than that of radiation: $\omega > 1/3$ and is called the stiff era.

In Chap. 4, we have studied the spectrum of inflationary GW in presence of an arbitrary EOS and found the spectral indices to be, see Eq. (4.12)

$$\Omega_{\rm GW} \propto f^{-2(1-3\omega)/1+3\omega} \propto f^\beta, \text{ with } \beta \equiv -2\left(\frac{1-3\omega}{1+3\omega}\right). \tag{E.1}$$

The energy-frequency relation is

$$f(\rho) = f_\Delta \left(\frac{\rho}{\rho_\Delta}\right)^{\frac{1+3\omega}{6(1+\omega)}}, \tag{E.2}$$

where f_Δ and ρ_Δ are the GW frequency and the total energy density at the end of the stiff era. Examples of inflationary GW spectra in the presence of a stiff era are shown in Fig. E.1-top. In Fig. E.1-bottom, we show the reach of future-planned GW observatories. In contrast to the case $\omega = 1$ shown in Fig. 4.10, the ability of GW interferometers to probe $\omega = 2/3$ and $\omega = 1/2$ a stiff era can be better than $\Delta N_{\rm eff}$.

E.1 Growth of scalar fluctuation

The fluctuations of the massless field red-shifts as radiation grow during stiff era, eventually dominates, ends the stage of stiff domination era. Similar to the kination case in Sec. 4.4.4 (see Ref. [132] for a precise derivation), the stiff era ends by fluctuation after some $N_{\rm stiff}$ efolds,

$$\left(\frac{\rho_{\rm inf}}{\rho_{\rm reh}}\right)^{\frac{1}{3(1+\omega)}} = \left(\frac{3M_{\rm Pl}H_{\rm inf}^2}{\pi^2 g_*(T_{\rm reh})T_{\rm reh}^4/30}\right)^{\frac{1}{3(1+\omega)}} = \frac{a_{\rm reh}}{a_{\rm inf}} = \exp\left(N_{\rm stiff}\right) < \xi^{-\frac{1}{3\omega-1}}, \tag{E.3}$$

where $\xi \equiv \delta\rho/\rho$ is the initial fluctuation's energy density at the end of inflation. With the curvature perturbations observed in CMB $\sim 10^{-9\div-10}$ [20], we obtain the bound on duration of stiff era, $N_{\rm stiff}^{\rm max} \sim 11, 23, 46$ for $\omega = 1, 2/3, 1/2$, respectively. The constraint is also illustrated in Fig. E.1. We leave a more careful study of fluctuations during the matter-kination era for future work [527].

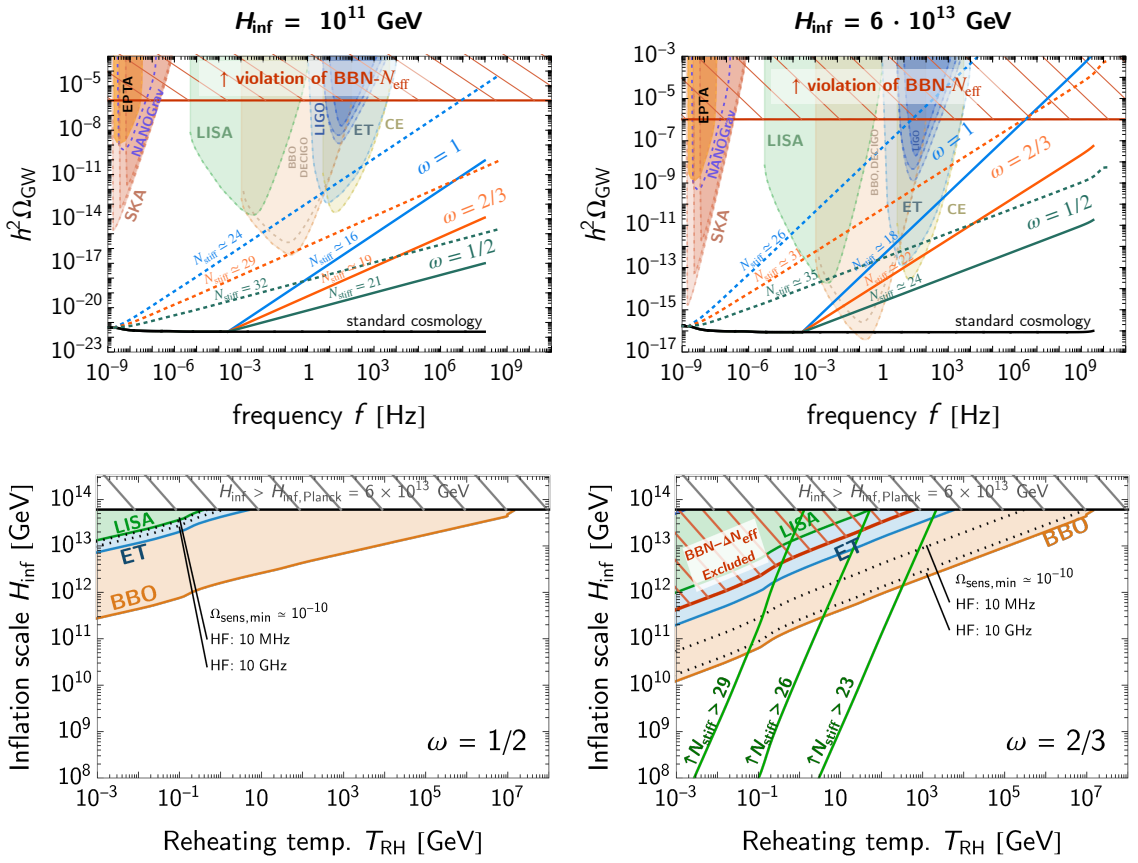

Figure E.1: **Top:** In the presence of a stiff era with EOS ω occurring right after inflation, the GW spectrum from primordial inflation receives a blue-tilt, cf. Eq. (4.12). The dashed and solid lines correspond to the reheating temperatures $T_{\rm RH} = 10^{-1}$ GeV and 10^4 GeV, respectively. Some spectra associated with too long kination are subject to the fluctuation constraint Eq. (E.3), which depends on the initial scalar fluctuation [132, 527]. **Bottom:** Ability of the future-planned experiments to compete with the BBN bound, for probing SGWB enhanced by post-inflation stiff era with EOS ω ending at the reheating temperature $T_{\rm RH}$. The lower ω, the more competitive the GW interferometers concerning BBN. The stiff era on the left of the solid green line cannot be realized due to the radiation-like fluctuation, cf. Eq. (E.3). An experiment operating at higher frequencies loses sensitivity for smaller ω because of the smaller enhancement.

Appendix F

Further constraints on kination

In this appendix, we derive the following upper bounds on the number of e-folds of kination:

1. The limited duration between the end of inflation/reheating and BBN, cf. App. F.1

$$\text{Kination after inflation (scheme B):} \quad N_{\rm KD} \lesssim 29 + \frac{2}{3}\log\frac{E_{\rm inf}}{1.4\times10^{16}\ {\rm GeV}} \tag{F.1}$$

$$\text{Intermediate kination (scheme E):} \quad N_{\rm KD} \lesssim 14.6 + \frac{1}{3}\log\frac{E_{\rm reh}}{1.4\times10^{16}\ {\rm GeV}}. \tag{F.2}$$

2. The $N_{\rm eff}$ constraint of kination-enhanced inflationary GW, cf. App. (F.2)

$$\text{For scheme B and E:} \quad N_{\rm KD} \lesssim 11.9 + \log\frac{5\times10^{13}\ {\rm GeV}}{H_{\rm inf}}. \tag{F.3}$$

3. The angular mode energy density drops below the wiggle step size of the axion potential, cf. App. F.3

$$\text{For scheme E (model-dependent):} \quad N_{\rm KD} \lesssim \frac{1}{3}\ln\frac{\dot\theta_0}{2m_a}, \tag{F.4}$$

   for the rotating axion models leading to the intremediate kination, see Chaps. 6 and 7.

4. The Universe contains a non-vanishing vacuum energy V_0, cf. Sec. F.4,

$$N_{\rm KD} \lesssim \frac{1}{6}\log\left(\frac{\rho_{\rm KD}}{V_0}\right). \tag{F.5}$$

5. The growth of scalar fluctuation during kination, cf. Sec. 4.4.4

$$\text{For scheme B and E:} \quad N_{\rm KD} \lesssim 10 \text{ or } 11. \tag{F.6}$$

F.1 Duration between inflation/reheating and BBN

The non-detection of primordial B modes by 2021 BICEP/Keck Collaboration [21] constrains the tensor-to-scalar ratio to be smaller than

$$r \equiv \frac{A_s}{A_t} \lesssim 0.036, \tag{F.7}$$

where $A_s \simeq 2.196\times10^{-9}$ [819] and $A_t = \frac{2H_{\rm inf}^2}{\pi M_{\rm pl}^2}$ [820]. This implies the maximal Hubble and energy scale at the end of inflation to be

$$H_{\rm inf} \lesssim 5\times10^{-13}\ {\rm GeV}, \ \text{ and } \ E_{\rm inf} \equiv \left(3M_{\rm pl}^2H_{\rm inf}^2\right)^{1/4} \lesssim 1.4\times10^{16}\ {\rm GeV}. \tag{F.8}$$

The maximum reheating scale, corresponding to the extreme scenario where reheating takes place instantaneously at the very end of inflation, is given by

$$E_{\rm reh} \lesssim 1.4 \times 10^{16}\ {\rm GeV}. \tag{F.9}$$

By using the code AlterBBN [821], it can be shown that successful BBN requires the amount of kination energy density to be less than 92% of the radiation energy density at the temperature $T = 1$ MeV [132]

$$\rho_{\rm kin} \lesssim 92\%\ \rho_{\rm rad}, \qquad \text{at} \quad T = 1\ {\rm MeV}. \tag{F.10}$$

We conclude that kination must end before

$$E_\Delta \gtrsim E_{\rm BBN} \equiv 1.4\ {\rm MeV}, \tag{F.11}$$

where E_Δ is the energy scale at the end of kination when $\rho_{\rm kin} = \rho_{\rm rad}$, and where we remind the reader of our notation $E_i \equiv \rho_i^{1/4}$.

Kination right after inflation (scheme B). — A simple constraint on $N_{\rm KD}$ comes from kination not lasting more than the time between the end of inflation in Eq. (F.8), and the end of BBN in Eq. (F.11). We obtain the bound

$$\text{Scheme B:} \quad N_{\rm KD} \lesssim \frac{1}{6}\log\frac{E_{\rm inf}^4}{\rho_{\rm BBN}} = 29 + \frac{2}{3}\log\frac{E_{\rm inf}}{1.4\times 10^{16}\ {\rm GeV}}. \tag{F.12}$$

Intermediate matter-kination (scheme E). — As we already discussed along Eq. (4.51), the duration of the matter-kination is maximized when there is no entropy injection which would produce an additional radiation component. For such an adiabatic evolution, the number of e-folds of matter and kination is related through

$$N_{\rm MD} = 2N_{\rm KD}, \quad \text{with} \quad N_{\rm MD} \equiv \frac{1}{3}\log\frac{\rho_{\rm dom}}{\rho_{\rm KD}}, \quad \text{and} \quad N_{\rm KD} \equiv \frac{1}{6}\log\frac{\rho_{\rm KD}}{\rho_\Delta}. \tag{F.13}$$

In this scenario, the energy scale $E_{\rm KD}$ at the onset of the kination era is given by

$$E_{\rm KD} = \sqrt{E_{\rm dom}E_\Delta}, \tag{F.14}$$

where $E_{\rm dom}$ and E_Δ are energy scales at the onset of the matter era and at the end of the kination era The duration of the kination era can be written as

$$N_{\rm KD} = \frac{1}{3}\log\frac{E_{\rm dom}}{E_\Delta}. \tag{F.15}$$

The longest matter-kination era allowed by CMB and BBN is when the matter era starts right after the end of inflation $E_{\rm dom} = E_{\rm reh}$ and the kination ends just before the onset of BBN $E_\Delta = E_{\rm BBN}$. We obtain the upper bound

$$\text{Scheme E:} \quad N_{\rm KD} \lesssim 14.6 + \frac{1}{3}\log\frac{E_{\rm reh}}{1.4\times 10^{16}\ {\rm GeV}}. \tag{F.16}$$

F.2 $N_{\rm eff}$ bound on inflationary GW

As we discuss in Chap. 2, the GW energy density produced prior to the onset of BBN can contribute to the effective number of neutrino species, which leads to the bound, cf. Eq. (2.22)

$$\int_{f_{\rm BBN}}^{f_{\rm max}} \frac{df}{f} h^2\Omega_{\rm GW}(f) \leq 5.6\times 10^{-6}\ \Delta N_\nu, \tag{F.17}$$

where $\Delta N_\nu \leq 0.2$ [39]. In Sec. 4.7, we have studied the impact of a kination EOS on the spectrum of primordial GW and we have found that a period of $N_{\rm KD}$ e-folds of kination leads to a blue-tilt $\Omega_{\rm GW} \propto f$ whose peak value is, cf. Eq. (4.56)

$$\Omega_{\rm GW,KD} \simeq 2.8 \times 10^{-13} \left(\frac{g_*(T_\Delta)}{106.75}\right) \left(\frac{g_{*,s}(T_\Delta)}{106.75}\right)^{-\frac{4}{3}} \left(\frac{E_{\rm inf}}{10^{16}\ \text{GeV}}\right)^4 \left(\frac{\exp(2N_{\rm KD})}{e^{10}}\right). \quad \text{(F.18)}$$

The $\Delta N_{\rm eff}$ bound yields the maximal duration of kination, which can be seen in Fig. 4.10,

$$\text{Scheme B and E:} \quad N_{\rm KD} \lesssim 11.9 + \log \frac{5 \times 10^{13}\ \text{GeV}}{H_{\rm inf}}. \quad \text{(F.19)}$$

F.3 Presence of axion wiggles

In Chaps. 6 and 7, the intermediate kination era is well-motivated by the model of rotating axion. This is a pseudo-Nambu-Goldstone boson whose mass becomes relevant to the dynamics at later times. Assuming the presence of an axion potential $V(\theta) = f_a^2 m_a^2 (1 + \cos\theta)$, where m_a is the mass of the axion $a \equiv \theta f_a$. The circular motion is only possible if its kinetic energy density is larger than the top of the potential barrier

$$\frac{f_a^2 \dot\theta^2}{2} > 2 f_a^2 m_a^2 \qquad \Rightarrow \qquad \dot\theta > 2 m_a. \quad \text{(F.20)}$$

Since the axion velocity redshift as $\theta \propto a^{-3}$, the kination ends by trapping in the axion wiggles unless its duration is smaller than

$$N_{\rm KD}^{\rm max} = \frac{1}{3} \ln \frac{\dot\theta_0}{2 m_a}, \quad \text{(F.21)}$$

which is also shown in Fig. F.1. We obtained a similar bound from fragmentation in Eq. (6.28). We also checked that the early wiggles from higher-dimensional $U(1)$-explicit breaking terms do not lead to fragmentation.

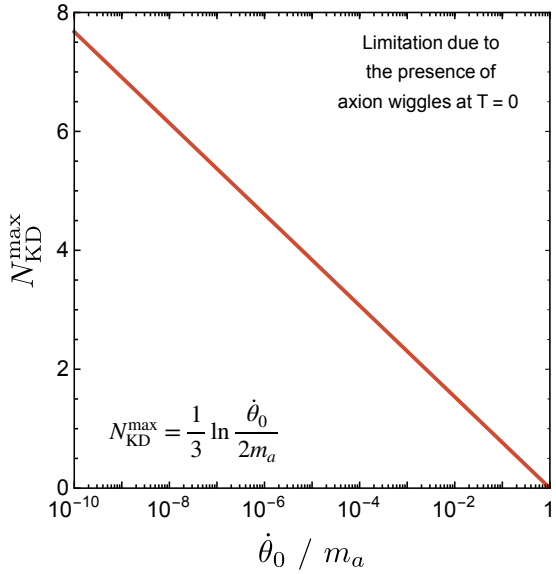

Figure F.1: Maximal number of kination e-folds due to the presence of axion wiggles cf. Eq. (F.21). In the parameter space of interest, the number of e-folds $N_{\rm KD}$ is always smaller than $N_{\rm KD}^{\rm max}$ shown here, such that the bound (F.21) is always satisfied. Instead, we expect the duration of kination to be dominantly constrained by the other bounds given in Eqs. (F.1), (F.3) and (F.6)

F.4 Inflationary behavior after kination phase

So far, we have neglected the vacuum energy at the potential minimum, so the kinetic energy of a scalar field always dominates. The non-zero potential energy can, however, lead to an inflationary

period at later times. The kinetic energy density redshifts as a^{-6} and eventually becomes as small as the vacuum energy

$$\omega(a) \;=\; \frac{K(a)-V_0}{K(a)+V_0} \;=\; \frac{\rho_{\rm KD}(\frac{a_{\rm KD}}{a})^6-V_0}{\rho_{\rm KD}(\frac{a_{\rm KD}}{a})^6+V_0} \;=\; \frac{\exp(-6N_{\rm KD})-V_0/\rho_{\rm KD}}{\exp(-6N_{\rm KD})+V_0/\rho_{\rm KD}}, \tag{F.22}$$

where $N_{\rm KD}$ is the e-foldings of the cosmic expansion after the kination era started. For a non-zero V_0, Fig. F.2 shows that after a number of kination e-folds given by

$$N_{\rm KD}^{\rm max} = \frac{1}{6}\log\left(\frac{\rho_{\rm KD}}{V_0}\right), \tag{F.23}$$

the EOS decreases abruptly to $\omega = -1$.

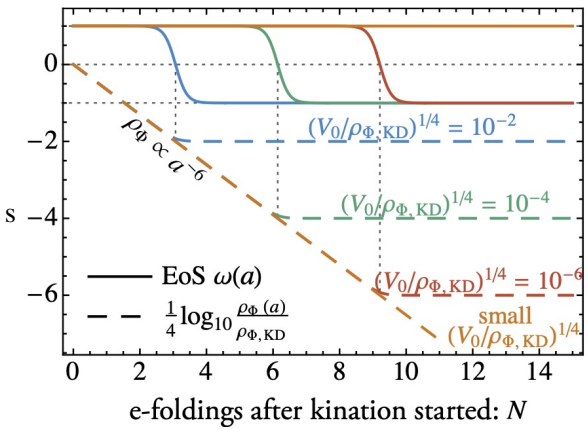

Figure F.2: The kination EOS ends when the kinetic energy density $\rho_{\phi,\rm KD}$ drops below the non-zero vacuum energy V_0.

Appendix G

More Details on Intermediate Kination from the Rotating Axion

This appendix provides exhaustive details on the spinning-axion model buildings that led to the intermediate kination era, discussed in Chap. 7. The origin of the potential for the complex scalar field – motivated by Supersymmetry and providing three of the four requirements for kination – is discussed in App. G.1. We discuss issues of the fluctuations that might constraint the model parameters if the Hubble-induced terms of potential are absent, cf. App. G.2. Two mechanisms for damping the radial mode are discussed in App. G.3. The last part G.4 considers the detailed complex-scalar field evolution in the expanding Universe: both numerically and analytically.

G.1 Origin of the scalar potential

We consider a complex scalar field Φ with the Lagrangian introduced in Eq. (7.1)

$$\mathcal{L} \;=\; (\partial_\mu \Phi)^\dagger \partial^\mu \Phi - V(|\Phi|) - V_{\rm th}(|\Phi|) - \cancel{V_{U(1)}}(\Phi) - V_H(\Phi), \tag{G.1}$$

with V the global $U(1)$-symmetric potential with spontaneous symmetry breaking (SSB) vacuum, $V_{\rm th}$ the thermal corrections, $\cancel{V_{U(1)}}$ the explicit $U(1)$-breaking term, and V_H the Hubble-dependent potential:

$$V(|\Phi|) = m_r^2 |\Phi|^2 \left(\ln \frac{|\Phi|^2}{f_a^2} - 1 \right) + m_r^2 f_a^2 + \frac{\lambda^2}{M^{2l-6}} |\Phi|^{2l-2}, \tag{G.2}$$

$$\cancel{V_{U(1)}}(\Phi) = \Lambda_b^4 \left[\left(\frac{\Phi^\dagger}{M} \right)^l + \left(\frac{\Phi}{M} \right)^l \right], \tag{G.3}$$

$$V_H(\Phi) = -cH^2 |\Phi|^2 - a \frac{M}{M_{\rm pl}} \frac{H}{m_{3/2}} \Lambda_b^4 \left[\left(\frac{\Phi^\dagger}{M} \right)^l + \left(\frac{\Phi}{M} \right)^l \right], \tag{G.4}$$

and

$$V_{\rm th}(\phi,\, T) \;=\; \begin{cases} \frac{1}{2} y_\psi^2 T^2 \phi^2, & \text{for } y_\psi \phi \lesssim T, \\ \alpha^2 T^4 \ln(\frac{y_\psi^2 \phi^2}{T^2}), & \text{for } y_\psi \phi \gtrsim T \end{cases}, \tag{G.5}$$

which can be derived in SUSY framework. In the main text, we take $M = M_{\rm pl}$.

G.1.1 Neglecting Hubble curvature

The first two terms, in Eq. (G.2) and Eq. (G.3), can be derived from the SUSY Lagrangian

$$\mathcal{L} \supset \int d^2\theta d^2\bar{\theta}\, K(S_\Phi,\, S_\Phi^*) + \int d^2\theta\, W(S_\Phi) + h.c. \tag{G.6}$$

with the Kahler potential K and the superpotential W being given by

$$K(S_\Phi, S_\Phi^*) = |S_\Phi|^2 - \frac{1}{M}|S_\Phi|^2\left(S_\chi + S_\chi^*\right) - \frac{1}{M^2}|S_\Phi|^2|S_\chi|^2 - \frac{1}{M^4}|S_\Phi|^4|S_\chi|^2, \tag{G.7}$$

$$W(S_\Phi) = \lambda\frac{S_\Phi^l}{l\,M^{l-3}}, \qquad l \in \mathbb{N}. \tag{G.8}$$

where $(\theta,\,\bar{\theta})$ are the Graßmannian coordinates in the superspace. S_Φ is the chiral superfield containing the complex scalar Φ

$$S_\Phi = \Phi + \sqrt{2}\theta\psi + \theta^2 F. \tag{G.9}$$

M is the messenger scale (e.g. the Planck scale for gravity mediation) and S_χ is a SUSY-breaking chiral superfield

$$S_\chi = \chi + \sqrt{2}\theta\psi_\chi + \theta^2 F_\chi, \tag{G.10}$$

which we assume to get a non-vanishing F-term VEV

$$\langle S_\chi\rangle = \theta^2\langle F_\chi\rangle \quad \text{with} \quad \langle F_\chi\rangle = m_{32}M_{\rm pl}, \tag{G.11}$$

where m_{32} is the gravitino mass. From using Eq. (G.10), together with $\int d\theta^2\theta^2 = 1$, the last two terms of the Kahler potential in Eq. (G.7) contribute to the scalar potential

$$V(\Phi) \supset \frac{\langle F_\chi\rangle^2}{M^2}|\Phi|^2 + \frac{\langle F_\chi\rangle^2}{M^4}|\Phi|^4, \tag{G.12}$$

while the second term of the Kahler potential in Eq. (G.7) acts as a non-holomorphic effective superpotential

$$\int d^2\theta d^2\bar{\theta}\frac{1}{M}|S_\Phi|^2\left(S_\chi + S_\chi^*\right) \simeq \int d^2\theta\frac{1}{M}|S_\Phi|^2\langle F_\chi\rangle + h.c., \tag{G.13}$$

and Eq. (G.8) can be replaced by

$$W(S_\Phi) = \frac{\langle F_\chi\rangle}{M}|S_\Phi|^2 + \lambda\frac{S_\Phi^l}{l\,M^{l-3}}. \tag{G.14}$$

In turn, from the equations of motion for the F-terms of S_Φ and S_Φ^*

$$F = \left(\frac{\partial K}{\partial\Phi^\dagger\partial\Phi^\dagger}\right)^{-1}\frac{\partial W}{\partial\Phi^\dagger}, \qquad F^* = \left(\frac{\partial K}{\partial\Phi\partial\Phi}\right)^{-1}\frac{\partial W}{\partial\Phi}, \tag{G.15}$$

we obtain the scalar potential

$$V(\Phi) \supset \left(\frac{\partial K}{\partial\Phi\partial\Phi^\dagger}\right)^{-1}\left|\frac{\partial W}{\partial\Phi}\right|^2 = \frac{\langle F_\chi\rangle^2}{M^2}|\Phi|^2 + \lambda\langle F_\chi\rangle\frac{\Phi^l + h.c.}{M^{l-2}} + |\lambda|^2\frac{|\Phi|^{2l-2}}{M^{2l-6}}. \tag{G.16}$$

From Eq. (G.12) and Eq. (G.16), we deduce $V_{U(1)}(\Phi)$ and $V_{\cancel{U(1)}}(\Phi)$ in Eq. (G.2) and Eq. (G.3)

$$V(|\Phi|) = m_r^2|\Phi|^2\left(\ln\frac{|\Phi|^2}{f_a^2} - 1\right) + m_r^2 f_a^2 + \frac{|\lambda|^2}{M^{2l-6}}|\Phi|^{2l-2}, \tag{G.17}$$

$$V_{\cancel{U(1)}}(\Phi) = \Lambda_b^4\left[\left(\frac{\Phi^\dagger}{M}\right)^l + \left(\frac{\Phi}{M}\right)^l\right], \tag{G.18}$$

with

$$m_r^2 = \frac{\langle F_\chi\rangle^2}{M^2} = m_{32}^2\frac{M_{\rm pl}^2}{M^2}, \tag{G.19}$$

$$\Lambda_b^4 = \lambda\langle F_\chi\rangle M^2 = \lambda\, m_{32}M_{\rm pl}M^2. \tag{G.20}$$

The quartic term in Eq. (G.12) is negligible as long as $|\Phi| \ll M$. The presence of the logarithmic function in Eq. (G.17), which is responsible for the spontaneous breaking of the $U(1)$ symmetry $\Phi \to e^{i\alpha}\Phi$, is generated radiatively [698], see App. G.1.4 for a review. The constant term in the same equation is needed in order to tune the cosmological constant to zero.

G.1.2 Including Hubble expansion

Let's assume that the energy density is dominated by a complex scalar I, which can be the inflaton during inflation or matter-dominated preheating [580, 582] or a field in equilibrium with the thermal plasma during radiation domination [822]

$$H^2 M_{\rm pl}^2 = \rho_I = \begin{cases} \langle F_I^* F_I \rangle \,, & \text{during inflation or matter-domination,} \\ \\ \langle \partial I^* \partial I \rangle \,, & \text{during radiation-domination,} \end{cases} \tag{G.21}$$

where F_I is the F-term of the chiral superpotential S_I containing I. Our complex scalar of interest Φ, which is a sub-dominant fraction of the energy density of the Universe $\rho_\Phi \ll H^2 M_{\rm pl}^2$, interacts with I through gravity, which leads to the non-renormalizable Kahler potential

$$\mathcal{L} \supset \int d\theta^2 d\bar{\theta}^2 \left(a \frac{S_I + S_I^*}{M_{\rm pl}} |S_\phi|^2 + c \frac{|S_I|^2}{M_{\rm pl}^2} |S_\Phi|^2 \right), \qquad a,\, c = \mathcal{O}(1). \tag{G.22}$$

Upon solving for the S_Φ-F-term equations of motion from the total Lagrangian Eq. (G.7), (G.8) and Eq. (G.22), in which we replace[1]

$$S_I = i\theta\sigma^\mu\bar{\theta}\partial_\mu I + \theta^2 F_I, \tag{G.23}$$

we find that the scalar potential receives the additional terms

$$V(\phi) \supset \frac{-c\partial I^\dagger \partial I + (a^2 - c) F_I^* F_I + a \frac{M_{\rm pl}}{M} (F_I\, F_\chi^* + F_I^*\, F_\chi)}{M_{\rm pl}^2} |\Phi|^2 - a\lambda \frac{F_I\, \Phi^l + h.c.}{M_{\rm pl} M^{l-3}}. \tag{G.24}$$

If the dynamics occurs during radiation-domination, then $\langle \partial I^* \partial I \rangle$ dominates and the scalar potential receives a negative curvature-induced mass whenever $c > 0$

$$V(\phi) \supset -c H^2 \Phi^2, \tag{G.25}$$

If the dynamics occurs during inflation or matter-domination, then $\langle F_I^* F_I \rangle$ dominates[2]

$$V(\phi) \supset \left((a^2 - c) H^2 + a m_{32} H \right) \Phi^2 - a \frac{M}{M_{\rm pl}} \frac{H}{m_{3/2}} \Lambda_b^4 \left(\frac{\Phi}{M} \right)^l, \tag{G.26}$$

with Λ_b defined in Eq. (G.20). The Hubble-induced mass is negative whenever $c > a^2$ and $H \gtrsim m_{32}$. For $M = M_{\rm pl}$, the latter condition is verified whenever the SUSY-breaking field χ does not dominate the energy density of the Universe $F_\chi \lesssim F_I$. We refer to [580, 582] for a discussion of supergravity corrections, which should become important during inflation whenever $I \gtrsim M_{\rm pl}$.

In summary, we see that a large and negative Hubble-induced mass term is naturally generated in models where the complex scalar field Φ couples to a field that dominates the energy density of the Universe. This is very important for justifying the initial conditions.

G.1.3 Evolution of the scalar field in the negative Hubble-induced potential.

We recall the damped harmonic oscillator

$$\ddot{\phi} + \Gamma \dot{\phi} + m^2 \phi \;=\; 0, \tag{G.27}$$

[1] We remind the reader that chiral superfields in superspace read $S_I(y,\theta) = I(y) + \sqrt{2}\theta\psi(y) + \theta^2 F(y)$ with $y^\mu = x^\mu + i\theta\sigma^\mu\bar{\theta}$, which implies $S_I(y,\theta,\bar{\theta}) = I(x) + i\bar{\theta}\bar{\sigma}^\mu\theta\partial_\mu I(x) + \frac{1}{4}\theta^2\bar{\theta}^2\Box I(x) + \sqrt{2}\theta\psi(x) = \frac{i}{\sqrt{2}}\theta^2\bar{\theta}\bar{\sigma}^\mu\partial_\mu\psi(x) + \theta^2 F(x)$. In Eq. (G.23), we have neglected the fermionic component ψ, the inflaton VEV ϕ and the mass term $\Box I$.

[2] The term $aHm_{32}\Phi^2$ in Eq. (G.26) is generated by the interaction between the three non trivial terms $|S_\Phi|^2 S_\chi$, $|S_\Phi|^2 |S_\chi|^2$ and $|S_\Phi|^2 S_I$ in the Kahler potential.

has three regimes according to the value of Γ

$$\phi(t) \;=\; \begin{cases} \phi_1 \exp\left(\sigma_+ t\right) + \phi_2 \exp\left(\sigma_- t\right), & \text{for } \Gamma^2 > 4m^2 \text{ (over-damped)}, \\ \left(\phi_1 + \phi_2 \Gamma t\right) \exp\left(\frac{-\Gamma t}{2}\right), & \text{for } \Gamma^2 = 4m^2 \text{ (critically-damped)}, \\ \phi_1 \cos(\sqrt{m^2 - \frac{\Gamma^2}{4}} t - \alpha) \exp\left(\frac{-\Gamma t}{2}\right), & \text{for } \Gamma^2 < 4m^2 \text{ (under-damped)}, \end{cases} \tag{G.28}$$

where ϕ_1, ϕ_2, α are constants set by the initial conditions, and $\sigma_\pm \equiv -\Gamma/2 \pm \sqrt{(\Gamma/2)^2 - m^2}$. Taking $\Gamma = 3H$ and introducing $N_e \equiv Ht$, we obtain, e.g. [589]

$$\phi(N_e) \;\simeq\; \begin{cases} \phi_1 e^{-\frac{m^2}{3H^2} N_e} & \text{for } H \gg m \text{ (over-damped)}, \\ \left(\phi_1 + 3\phi_2 N_e\right) e^{-\frac{3}{2} N_e} & \text{for } H = \frac{2}{3} m \text{ (critically-damped)}, \\ \phi_1 \cos(mt - \alpha) e^{-\frac{3}{2} N_e} & \text{for } H \ll m \text{ (under-damped)}. \end{cases} \tag{G.29}$$

Initial radial VEV. Neglecting the $U(1)$-breaking term and assuming $a \ll \sqrt{c}$ in Eq. (G.26), the potential at early time reads, cf. Eq. (G.17), Eq. (G.18) and Eq. (G.26)

$$V(\phi) \;=\; (\frac{1}{2} m_{\rm eff}^2(T) - cH^2)\phi^2 + \lambda^2 \frac{\phi^{2l-2}}{M_{\rm Pl}^{2l-6}}, \qquad m_{\rm eff}^2(T) \equiv m^2 + y^2 T^2, \tag{G.30}$$

where we included a thermal mass y^2T^2 coming from a possible interaction with the thermal bath. We study the dynamics of the scalar field at early time by numerically integrating the field equation of motion in the presence of the potential in Eq. (G.30). To simplify the numerical study, we assume that the Universe is radiation-dominated, so that the temperature T is related to the Hubble parameter H through

$$T^2 \simeq H M_{\rm Pl}. \tag{G.31}$$

From Eq. (G.29), we deduce that there are three stages of field evolution after which the field starts oscillating with an amplitude $\phi_{\rm ini}$ in a potential with minimum $\phi_{\rm min} = 0$.[3] The resulting field trajectory is plotted in Fig. G.1.

1. $\sqrt{c}H \gg m_{\rm eff}$: the negative Hubble-mass dominates the mass term so the fields rolls within $N_e \simeq 3/c$ e-folds towards the non-trivial minimum at

$$\phi_{\rm ini}(H) \;\simeq\; \left(\frac{M_{\rm Pl}^{l-3} \sqrt{cH^2 - m^2/2 - H M_{\rm Pl} y^2/2}}{\lambda \sqrt{2l-2}} \right)^{1/(l-2)}. \tag{G.32}$$

2. $m_{\rm eff} \gtrsim \sqrt{c}H$: the Hubble-mass becomes sub-dominant and the time-dependent minimum vanishes $\phi_{\rm min} = 0$.

3. $m_{\rm eff} > 3H$: the Hubble friction drops, the field becomes under-damped, $V''(\langle\phi\rangle) > 9H^2$, and starts to roll away from

$$\phi_{\rm ini}(H \simeq m_{\rm eff}) \;\simeq\; M_{\rm pl} \left(\sqrt{c} \frac{m_{\rm eff}}{\lambda \sqrt{2l-2} M_{\rm pl}} \right)^{1/(l-2)}. \tag{G.33}$$

The trajectories shown in Fig. (G.1) assume that the dynamics occur during a radiation-dominated era. If the Hubble-induced mass is generated from the inflaton sector, the Hubble-induced mass decreases instead during preheating and the field starts rolling away from the non trivial value in Eq. (G.33) as soon as Max $[\sqrt{c}, 3]\, H$ drops below $m_{\rm eff}$.

[3] At early stage, we can forget about the existence of the SSB minimum at $\phi = f_a \ll \phi_{\rm ini}$.

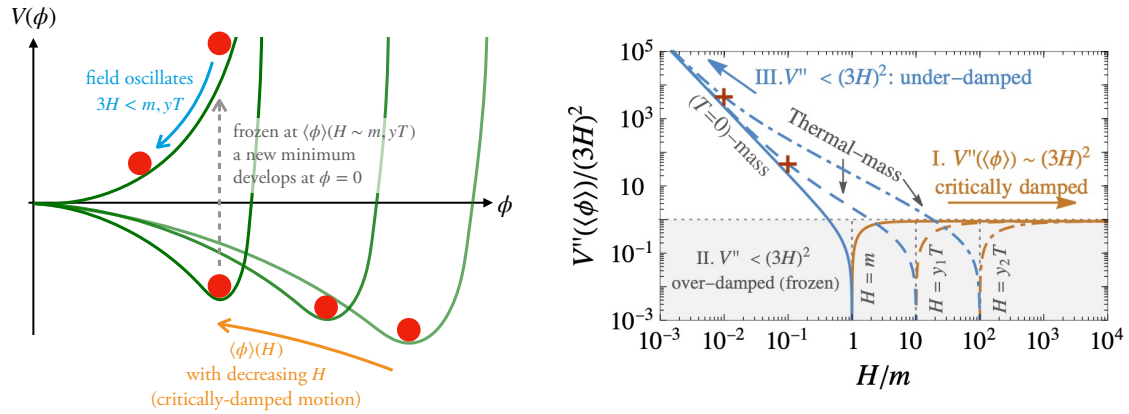

Figure G.1: We numerically integrate the Klein-Gordon equation of motion in the presence of the negative Hubble-induced potential in Eq. (G.30), in radiation-dominated Universe. There are three stages of field evolution, which depend on the value of V''/H: 1) critically-damped 2) over-damped 3) under-damped. Effects from the thermal mass become important for $y > \sqrt{m/M_{\rm Pl}}$. They lead to an earlier oscillation and a larger $\phi_{\rm ini}$, compared to the zero-temperature mass alone. The field later evolves in a zero-temperature potential at the points marked by the red crosses. We chose the values $y_1 = \sqrt{10m/M_{\rm Pl}}$, and $y_2 = 10\sqrt{m/M_{\rm Pl}}$.

Initial angular VEV. For F-term dominated Universe, cf. Eq. (G.26), the $U(1)$ breaking term receives Hubble-dependent corrections

$$V_{\cancel{U(1)}}(\Phi) \simeq \left(1 + a\frac{H}{m_{32}}\right)\Lambda_b^4\left[\left(\frac{\Phi}{M_{\rm pl}}\right)^l + h.c.\right], \qquad a,\, c = \mathcal{O}(1). \tag{G.34}$$

Therefore, the valleys of minimum potential $\theta_{\rm min}$ are time-dependent. The same dynamics described above for the radial mode also apply to the angular mode. The angular field rolls towards a temporary valley $\theta_0 + \theta_H$ during inflation when $H_{\rm inf} \gtrsim m_{32}$, and starts rolling towards the Hubble-independent valley θ_0 when H drops below m_{32}. In this work, we assume the initial angular amplitude[4]

$$\theta_{\rm ini} \sim \mathcal{O}(1). \tag{G.35}$$

G.1.4 Nearly-quadratic potentials

In this appendix, we review the results presented in [698] which show how spontaneous symmetry breaking can arise due to the running of the soft masses. The authors consider supersymmetric theories coupled to $\mathcal{N} = 1$ supergravity where $U(1)_{\rm PQ}$ is a global symmetry of the superpotential. They show that $U(1)_{\rm PQ}$ can be broken by the logarithmic running of renormalization group equations. Their results are not specific to the Peccei-Quinn symmetry and can be generalized to other global $U(1)$.

The superpotential is given by $W = \lambda\bar{Q}Q\phi$, where the $SU(3)_c$ quantum numbers of the chiral superfields are $Q(\mathbf{3}), \bar{Q}(\bar{\mathbf{3}}), \phi(\mathbf{1})$ and are singlets under $SU(2)_L$. The fields transform under the $U(1)_{\rm PQ}$ as

$$(Q,\, \bar{Q}) \to e^{i\alpha}(Q,\, \bar{Q}), \qquad \phi \to e^{-2i\alpha}\phi. \tag{G.36}$$

[4]Note that for radiation-dominated Universe, the A-term in Eq. (G.24), at least in our analysis and in the ones of [702, 721], seems to be Hubble-independent. We leave for further study the question of whether such Hubble-dependent A-term is induced during radiation domination. In any case, the angular kick could be generated by random fluctuations during inflation, see Sec. 7.1.5.

There is a continuum of supersymmetric minima $\phi =$ undetermined, $Q = \bar{Q} = 0$. Supergravity couplings lift this flat direction by inducing soft supersymmetric breaking terms characterized by the gravitino mass $m_{3/2}$

$$V_{\text{soft}} \;=\; m_{3/2} A\lambda \bar{Q} Q \phi + \text{h.c.} + m_{3/2}^2 (g_Q |Q|^2 + g_{\bar{Q}} |\bar{Q}|^2 + g_\phi |\phi|^2). \tag{G.37}$$

The initial conditions for the RGE are set at the Planck scale M_{pl} and $g_Q = g_{\bar{Q}} = g_\phi \;= 1$. The effective scalar potential is

$$V \;=\; \sum_i \left| \frac{\partial W}{\partial \phi_i} \right|^2 + \frac{1}{2} \Sigma_a D_a^2 + V_{\text{soft}}, \tag{G.38}$$

and along the supersymmetric minimum $(Q,\ \bar{Q}) = (0,\ 0)$, it is reduced to $V(\phi) \;=\; m_{3/2}^2 g_\phi |\phi|^2$.

Renormalization group equations. Loop corrections to the couplings lead to the running [698]

$$\frac{de}{dt} \;=\; \frac{-2}{16\pi^2} e^3, \tag{G.39}$$

$$\frac{d\lambda}{dt} \;=\; \frac{\lambda}{16\pi^2} \left(5\lambda^2 - \frac{16}{3} e^2 \right), \tag{G.40}$$

$$\frac{dA}{dt} \;=\; \frac{5A\lambda^2}{8\pi^2} e^3, \tag{G.41}$$

$$\frac{dg_Q}{dt} \;=\; \frac{dg_{\bar{Q}}}{dt} \;=\; \frac{1}{3} \cdot \frac{dg_\phi}{dt} \;=\; \frac{\lambda^2}{8\pi^2} \left(g_Q + g_{\bar{Q}} + g_\phi + A^2 \right), \tag{G.42}$$

where $t \equiv \ln(|\phi|/M_{\text{pl}})$ and e is the gauge-coupling of the $SU(3)_c$. The equation for e can be solved analytically with $e^2(t) \;=\; e_0^2/(1 + \frac{e_0^2}{4\pi^2} t)$. All the couplings g are related $g_Q = g_{\bar{Q}} = \frac{1}{3} g_\phi$, hence we have $dg_\phi/dt \;=\; \lambda^2 \left(5g_\phi + 3A^2 \right) / 8\pi^2$. The system of first-order differential equations above has a fixed point at $3\lambda^2 = 2e^2$, where g_ϕ is running as

$$\frac{dg_\phi}{dt} \;=\; \frac{e_0^2}{12\pi^2} \left(\frac{5g_\phi + 3A^2}{1 + \frac{e_0^2}{4\pi^2} t} \right), \tag{G.43}$$

and A is approximately constant. In the limit $\frac{e_0^2}{4\pi^2} \ll 1$, the above equation is solved analytically by

$$g_\phi(\phi) \;\simeq\; (3A + 5) \left(\frac{e_0^2}{24\pi^2} \right) \ln \left(\frac{\phi^2}{M_{\text{pl}}^2} \right) + 1, \tag{G.44}$$

where the approximation $\frac{e_0^2}{4\pi^2} \ll 1$ is used. Then we define scale M_{PQ} by when the radiative correction changes the sign of effective potential, i.e. at

$$g_\phi(\phi \to M_{\text{PQ}}) \;=\; 0 \;\simeq\; (3A + 5) \left(\frac{e_0^2}{24\pi^2} \right) \ln \left(\frac{M_{\text{PQ}}^2}{M_{\text{pl}}^2} \right) + 1, \tag{G.45}$$

where M_{PQ} is related to M_{pl} by

$$M_{\text{PQ}}^2 \;=\; M_{\text{pl}}^2 \exp \left[\left(\frac{-1}{3A + 5} \right) \frac{24\pi^2}{e_0^2} \right]. \tag{G.46}$$

With the definition of M_{PQ}, the coupling g_ϕ is simplified to

$$g_\phi(\phi) \;=\; (3A + 5) \left(\frac{e_0^2}{24\pi^2} \right) \ln \left(\frac{\phi^2}{M_{\text{PQ}}^2} \right). \tag{G.47}$$

The effective potential. We obtain the effective potential that is quadratic at a large field and has a circular SSB minimum at $\phi = f_a$, allowing axion to spin at late times and induce kination domination era.

$$V_{\rm eff} \;=\; m_{3/2}^2 g_\phi \phi^2 \;\simeq\; m_{3/2}^2 \phi^2 \left[\ln\left(\frac{\phi^2}{f_a^2}\right) - 1\right], \;\; \text{and} \;\; f_a \;\equiv\; M_{\rm PQ} e^{-1/2}. \tag{G.48}$$

For $A = 2$ and $e_0 = 0.8$, we have $f_a \simeq 7 \times 10^{10}$ GeV.

G.2 Fluctuations in Absence of Hubble-Induced Terms

G.2.1 Adiabatic curvature perturbations

Any light scalar present during inflation receives quantum fluctuations which classicalize upon horizon exit, e.g., [823]. When such perturbations re-enter the horizon, they source either the adiabatic or the isocurvature power spectrum according to whether the extra specie thermalizes with the SM. In our model, cf. Sec. 7.1, the radial mode of the complex scalar field decays into thermal radiation and therefore contributes to the adiabatic part of the curvature perturbations. Assuming a quadratic scalar potential with $m_r \ll H_{\rm inf}$, the perturbation from the decaying scalar field reads [824]

$$\mathcal{P}_\zeta^\phi \;=\; r_{\rm dec}^2 \left(\frac{H_{\rm inf}}{3\pi\phi_{\rm ini}}\right)^2, \;\text{with}\; r_{\rm dec} \;\simeq\; \left(\frac{3\rho_\phi}{3\rho_\phi + 4\rho_{\rm rad}}\right)_{\rm dec}, \tag{G.49}$$

where $r_{\rm dec}$ is the energy density fraction carried by the scalar, evaluated at the time of radial damping. The upper bound on $\mathcal{P}_\zeta^\phi$ corresponds to the value measured by CMB [20]

$$\mathcal{P}_\zeta^\phi \;<\; \mathcal{P}_\zeta^{\rm tot} \;\simeq\; 2.2 \times 10^{-9}. \tag{G.50}$$

To constrain the model, we consider two limits.

1) Damping before domination. Assuming the extreme case in which radial damping occurs right after the onset of radial mode oscillation, cf. Eq. (7.27), in order to minimize $r_{\rm dec}$, the adiabatic curvature power spectrum reads

$$\mathcal{P}_\zeta^\phi \;=\; \left(\frac{\phi_{\rm osc}^2}{\phi_{\rm osc}^2 + \frac{4}{9}M_{\rm Pl}^2}\right)^2 \left(\frac{H_{\rm inf}}{3\pi\phi_{\rm ini}}\right)^2, \tag{G.51}$$

where $\phi_{\rm osc}$ is the value at oscillation.

- If the initial field value is set by the stochastic-inflation process, i.e. $\phi_{\rm ini}^2 = 3H_{\rm ini}^4/(4\pi^2 m^2)$ in Eq. (7.29), the above equation becomes

$$\mathcal{P}_\zeta^\phi \;=\; \left(\frac{27}{64\pi^4}\right)\left(\frac{H_{\rm inf}^6}{m^2 M_{\rm Pl}^4}\right)\left(1 + \frac{27 H_{\rm inf}^4}{16\pi^2 m_r^2 M_{\rm Pl}^2}\right)^{-2}. \tag{G.52}$$

  In Fig. G.2, we show that the constraints on $H_{\rm inf}$ from Eq. (G.50) and Eq. (G.52) are weaker than the Planck constraints coming from the B-mode non-observation.

- Suppose the initial field value is driven by the negative-Hubble mass and is stabilized by higher-order terms. In that case, the quantum fluctuation of the radial and angular fluctuation is suppressed, see Sec. G.2.4. This is the scenario that we assume in this paper.

2) Damping when dominating. Assuming $\rho_\phi \gg \rho_{\rm rad}$ in Eq. (G.49) leads to $r_{\rm dec} \simeq 1$ and to the adiabatic curvature perturbations $\mathcal{P}_\zeta^\phi = \left(H_{\rm inf}/3\pi\phi_{\rm ini}\right)^2$.

- If the initial field value is set by the stochastic-inflation process, i.e. $\phi_{\rm ini}^2 = 3H_{\rm ini}^4/(4\pi^2 m_r^2)$, the above equation becomes

$$\mathcal{P}_\zeta^\phi \;=\; \left(\frac{4}{27}\right)\left(\frac{m_r}{H_{\rm inf}}\right)^2 . \tag{G.53}$$

  As shown in light blue in Fig. G.2, the constraint from Eq. (G.50) and Eq. (G.53) can be quite limiting.

- As mentioned in the previous paragraph and as we will discuss more precisely in Sec. G.2.4, for scenarios with Hubble-size masses, quantum fluctuations are suppressed, and the Planck constraints are avoided.

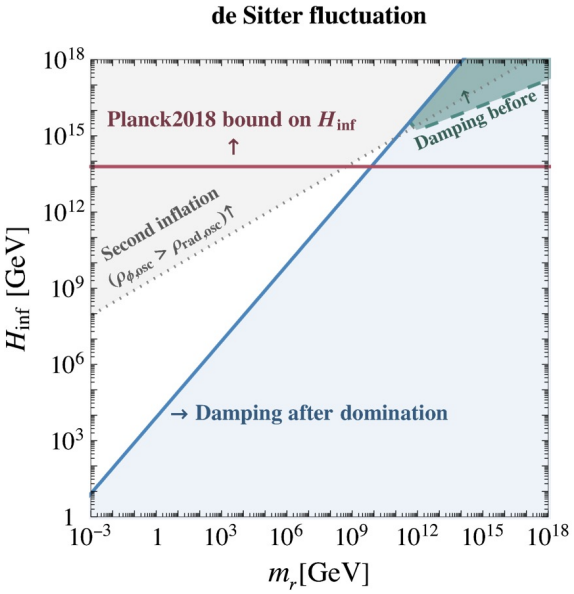

Figure G.2: Parameter space of a thermalized complex scalar which generates too much adiabatic curvature perturbations. The weakest constraint (**green**) arises when damping occurs at the onset of oscillation. As damping takes place later, the constraint grows and reach **light blue** region when damping takes place at the onset of scalar domination. For the Hubble-induced mass scenario, the green and light blue constraints are avoided due to a large Hubble-sized mass during inflation, see Sec. 7.1.5. The red line corresponds to Planck constraints from B modes non-observation [20]. The gray region corresponds to the requirement of not generating a second inflation era, see Eq. (7.49).

G.2.2 Domain wall problem

Quantum fluctuations of the initial angular phase $\delta\theta_i$ and of the initial radial value $\delta\phi_i$ lead to a fluctuation of the final angular phase $\delta\theta$ at the time when the axion potential develops. This can lead to the formation of domain walls (DW). In the absence of CS, e.g., in the pre-inflationary PQ-breaking scenario, the DW is infinite and can not decay, so we must impose $\delta\theta \lesssim \mathcal{O}(1)$.

Assuming $V(\Phi) \propto \Phi^p$, from $U(1)$ charge conservation in Eq. (7.19) and from the scaling $\langle\phi\rangle \propto a^{-\frac{6}{2+p}}$ in Eq.(G.141), we deduce the scaling of the angular velocity

$$Y_\theta \;=\; \phi^2\dot\theta \;\propto a^{-3} \quad\Rightarrow\; \dot\theta \;\propto\; a^{-3(p-2)/(p+2)} \;\propto\; t^{-3(p-2)/2(p+2)}, \tag{G.54}$$

where we assume a radiation-dominated Universe. The angular phase elapsed after the onset of radial mode oscillation which we denote by $t_i \simeq m_{\rm eff}^{-1}(\phi_i)$ reads

$$\theta \;=\; \int_{t_i}^{t} \dot\theta dt' \;\simeq\; \dot\theta_i t_i \left(\frac{\phi_i}{\phi}\right)^{(10-p)/6} , \tag{G.55}$$

The fluctuation in the angular phase can be written as

$$\frac{\delta\theta}{\theta} \;=\; \frac{\delta\dot\theta_i}{\dot\theta_i} + \frac{\delta t_i}{t_i} + \left(\frac{10-p}{6}\right)\left(\frac{\phi_i}{\phi}\right)^{\frac{10-p}{6}}\left(\frac{\delta\phi_i}{\phi_i}\right). \tag{G.56}$$

From Eq. (G.109), $t_i \simeq m_{\rm eff}^{-1}(\phi_i)$ and Eq. (7.5), we can write

$$\frac{\delta\dot{\theta}_i}{\dot{\theta}_i} = (l-p)\frac{\delta\phi_i}{\phi_i} + l\cot(l\theta_i)\delta\theta_i + \frac{\delta t_i}{t_i}, \quad \text{and} \quad \frac{\delta t_i}{t_i} = -\frac{\delta\phi_i/\phi_i}{2\left(1+\log(\phi_i/f_a)\right)}. \tag{G.57}$$

The late time phase fluctuation in Eq. (G.56) becomes

$$\frac{\delta\theta}{\theta} \simeq \left[(l-p) - \frac{1}{1+\log(\phi_i/f_a)} + \left(\frac{10-p}{6}\right)\left(\frac{\phi_i}{f_a}\right)^{\frac{10-p}{6}}\right]\left(\frac{\delta\phi_i}{\phi_i}\right) + l\cot l\theta_i\delta\theta_i, \tag{G.58}$$

where the last term in the squared bracket dominates for $p < 10$ and $\phi_i \gg f_a$. Plugging the typical standard deviation for a massless field during inflation, e.g. [823]

$$\delta\phi_i = H_{\rm inf}/2\pi = \phi_i\delta\theta_i, \tag{G.59}$$

we obtain the necessary condition for preventing DW formation once the axion potential switches on

$$\delta\theta \simeq \left[\left(\frac{10-p}{6}\right)\left(\frac{\phi_i}{f_a}\right)^{(10-p)/6} + l\cot(l\theta_i)\right]\left(\frac{H_{\rm inf}}{2\pi\phi_i}\right) < 1, \tag{G.60}$$

where we replaced $\theta \sim \mathcal{O}(1)$. The flatter the potential, the slower the redshift of the angular velocity, and the larger the final time fluctuation $\delta\theta$.

G.2.3 Isocurvature perturbations

If the axion contributes to the DM abundance then the quantum fluctuation during inflation in Eq. (G.59) generate isocurvature perturbations [825–828][5] whose amplitude is bounded by Planck data [20]

$$\mathcal{P}_{\rm iso} = \left\langle\left(\frac{\Omega_a}{\Omega_{\rm DM}}\cdot\frac{\delta\Omega_a}{\Omega_a}\right)^2\right\rangle < 8.69\times10^{-11}. \tag{G.61}$$

For a rotating axion, the axion abundance is set by the kinetic misalignment mechanism $\Omega_a \propto \dot{\theta}_c$, cf. Eq. (6.8). From Eq. (G.57) and Eq. (G.59), we deduce

$$\mathcal{P}_{\rm iso} = \left(\frac{\Omega_a}{\Omega_{\rm DM}}\right)^2\left\langle\left(\frac{\delta\dot{\theta}_i}{\dot{\theta}_i}\right)^2\right\rangle = A\left(\frac{\Omega_a}{\Omega_{\rm DM}}\right)^2\left(\frac{H_{\rm inf}}{2\pi\phi_i}\right)^2 < 8.69\times10^{-11}, \tag{G.62}$$

where $A \equiv l - p - [1+\log(\phi_i/f_a)]^{-1} + l\cot(l\theta_i) = \mathcal{O}(1)$.

G.2.4 Solution

A way to cure the three problems listed above - too large adiabatic and isocurvature perturbations and DW overclosure - is to suppress the initial quantum fluctuations by introducing a large mass for both the radial mode ϕ and the angular mode θ during inflation [671, 833–838].

As discussed along Eq. (7.23), Hubble size masses for ϕ and θ arise naturally in SUSY scenario

$$m_\phi^2 = \partial^2 V_H/\partial\phi^2 \simeq 4(l-2)H_{\rm inf}^2, \tag{G.63}$$

$$m_\theta^2 = |\phi|^{-2}\partial^2 V_H/\partial\theta^2 \simeq H_{\rm inf}^2\sqrt{l^2/(l-1)}. \tag{G.64}$$

So, the solution to these problems is built-in in into these models. Quantum fluctuations of massive states are blue-tilted, e.g., [823], such that the amplitude of the associated curvature perturbations entering the Hubble horizon long after the end of inflation is expected to be negligible. This is the scenario that we consider in this paper. Therefore we assume that the initial field value $\phi_{\rm i}$ is set by the classical minimum of the Hubble-induced SUSY potential in Sec. 7.1.5 and not by the Bunch-Davies quantum distribution in Sec. 7.1.5.

[5] This problem also arises in the context of the Affleck-Dine Baryogenesis, where the inflationary perturbation leads to the baryonic isocurvature perturbations [829–833].

G.3 Damping of the radial motion

G.3.1 Thermalization

Fermion portal. We assume that the complex scalar field ϕ is coupled to heavy fermions ψ charged under some (hidden or SM) gauge sector A_μ (KSVZ-type interactions)

$$\mathcal{L} \supset y_\psi \phi \psi_L^\dagger \psi_R + h.c. + g\, \bar{\psi} \gamma^\mu \psi\, A_\mu. \tag{G.65}$$

At zero temperature, the scalar condensate decays into fermions pairs with a rate, cf. diagram a in Fig. G.3

$$\Gamma_{\phi \to \psi\psi} \simeq \frac{y_\psi^2}{8\pi} m_\psi, \quad \text{for} \quad m_\phi/2 \; > \; \text{Max}[y_\psi \phi,\, gT]. \tag{G.66}$$

If the fermion mass, either from vacuum $y_\psi \phi$ or thermal origin gT, is larger than the scalar field mass, then the scalar field cannot excite thermal ψ and it is dominantly depleted through scattering with thermally-dressed fermions of the plasma, cf. diagram b in Fig. G.3, with a rate [699, 700]

$$\Gamma_{\phi \psi_{\rm th} \to \psi_{\rm th}} \simeq \begin{cases} \frac{y_\psi^2 \alpha T}{2\pi^2}, & \text{for } \alpha T > y_\psi \phi, \\ \frac{y_\psi^4 \phi^2}{\pi^2 \alpha T}, & \text{for } \alpha T < y_\psi \phi < T, \end{cases} \qquad \text{where} \;\; \alpha \equiv \frac{g^2}{4\pi}. \tag{G.67}$$

The two regimes in Eq. (G.67) depend on whether the thermal width αT - the typical relaxation rate of the fermion density towards thermal equilibrium - is larger or smaller than the fermion zero-temperature mass $y_\psi \phi$. If the temperature is smaller than the fermion mass, $T < y_\psi \phi$, the heavy fermions are absent of the thermal plasma. In that case, the scalar field can decay into gauge bosons through a loop of fermions [701, 703, 704], cf. diagram c in Fig. G.3

$$\Gamma_{\phi \to AA} \simeq \frac{b \alpha^2 T^3}{\phi^2}, \quad b \simeq 0.01, \quad \text{for} \;\; y_\psi \phi > T. \tag{G.68}$$

For $T < m_\phi$, we replace T in Eq. (G.68) by m_ϕ. The dependence on y_ψ in Eq. (G.68) appears in the logarithmic running of α. So we conclude

$$\Gamma_\phi \simeq \begin{cases} \text{for } y_\psi \phi < T : \begin{cases} \text{for } \alpha T > y_\psi \phi, & \frac{y_\psi^2 \alpha T}{2\pi^2}, \\ \text{for } \alpha T < y_\psi \phi, & \frac{y_\psi^4 \phi^2}{\pi^2 \alpha T}, \end{cases} \\ \text{for } y_\psi \phi > T : \;\; b\alpha^2 \frac{\text{Max}[T,\, m_\phi]^3}{\phi^2}, \end{cases} \quad + \frac{y_\psi^2 m_\phi}{8\pi} \Theta\left(m_\phi/2 - \text{Max}\left[y_\psi \phi,\, gT\right]\right). \tag{G.69}$$

The scalar field keeps spinning after thermalization. The coherent oscillation is a very ordered state. Once the oscillation energy begins to be transferred into the thermal bath, the inverse process which creates coherent oscillation is unlikely to occur. Therefore, the thermalization of the scalar field, when the Universe reaches the energy density

$$\rho_{\rm damp} = 3\Gamma^2 M_{\rm pl}^2, \tag{G.70}$$

transfers all the kinetic energy of the radial mode to the plasma $\dot{\phi} \to 0$. The kinetic energy of the angular mode, aka the $U(1)$ charge, can also be transferred to the thermal bath, e.g. in the form of chiral charges of SM fermions. However, as shown by the supplementary material of [669], the creation of an asymmetric fermion abundance costs chemical potential which leads to an energy

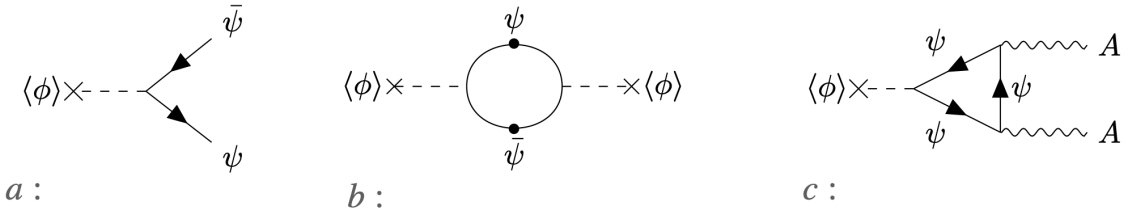

Figure G.3: Quantum processes responsible for the thermalization of the coherent scalar field in KSVZ type models. The scattering rates of a, b and c are respectively given by $\frac{y_\psi^2 m_\phi}{8\pi}$, $\frac{y_\psi^2 \alpha T}{2\pi^2}$ and $\frac{b\alpha^2 T^3}{\phi^2}$, cf. Eq. (G.69). The black blobs in the middle diagram stand for the thermal field corrections to the fermion propagator accounting for plasma effects. The decay width is obtained from the finite-temperature analogue of Cutkosky's rule [839].

density $\phi^4\dot{\theta}^2/T^2$ and it turns out that it is thermodynamically favorable to keep the $U(1)$ charge in the condensate with energy density $\phi^2\dot{\theta}^2$ as long as

$$f_a \gg T_{\phi\to f_a}, \tag{G.71}$$

where $T_{\phi\to f_a}$ is the temperature when ϕ reaches f_a. We check that this condition is satisfied in Eq. (7.108). The washout of $U(1)$ charge due to chirality flip mediated by Yukawa interactions is shown to be negligible if the temperature of thermalization is smaller than [669]

$$T_{\rm damp} \lesssim 10^{12}\ {\rm GeV}\left(\frac{\langle\phi\rangle}{10^9\ {\rm GeV}}\right)^2. \tag{G.72}$$

Using that the scalar field evolves in its quadratic potential as

$$\phi = \phi_{\rm ini}(T/T_{\rm osc})^{3/2},\ \ T_{\rm osc} = g_*^{-1/4}\sqrt{m_r(\phi_{\rm ini})M_{\rm pl}}, \tag{G.73}$$

we obtain that the axion rotation is preserved from wash-out from the onset of oscillation until the final stage $\phi \to f_a$ as long as

$$f_a > 10^4\ {\rm GeV}\left(\frac{m_r}{f_a}\right)^{3/5}\left(\frac{M_{\rm pl}}{\phi_{\rm ini}}\right)^{4/5}. \tag{G.74}$$

The latter condition is primarily satisfied in the parameter space of our interest, and wash-out never occurs.

Thermal corrections to the potential. The presence of the interactions in Eq. (G.65) generates thermal corrections to the scalar potential [699, 700]

$$V(\phi) = m_r^2\phi^2\left(\ln\frac{\phi^2}{f_a^2} - 1\right) + m_r^2 f_a^2 + V_{\rm th}(\phi, T), \tag{G.75}$$

$$V_{\rm th}(\phi, T) = \frac{1}{2}y_\psi^2 T^2\phi^2\Theta(T - y_\psi\phi) + a\alpha^2 T^4\ln\lambda_\phi^2\phi^2/T^2\Theta(y_\psi\phi - T), \tag{G.76}$$

where $a = \mathcal{O}(1)$ and $\alpha \equiv \frac{g^2}{4\pi}$. The first Heaviside function stands for the Boltzmann suppression of the fermion ψ abundance in the thermal plasma in the large vev limit $y_\psi\phi \gg T$. In that case the thermal corrections are given by the thermal-log potential, obtained after integrating out the heavy fermions [701, 703–705]. At small vev value $\lambda\phi < T$, the running of the gauge coupling constant g becomes independent of ϕ, which explains the second Heaviside function.

Impossibility to generate efficient thermalization when neglecting thermal corrections. Let's first assume that thermal corrections to the potential in Eq. (G.76) do not impact the scalar field dynamics. This happens whenever the thermal mass of the scalar fields can be neglected at the time of oscillation $T_{\rm osc} \sim \sqrt{m_{\rm r,\,eff} M_{\rm pl}}$, see Eq. (7.36), [6]

$$y_\psi T_{\rm osc} \lesssim m_{\rm r,eff}, \quad \Rightarrow \quad y_\psi \lesssim \left(\frac{\pi^2 g_*}{10}\right)^{1/4} \sqrt{\frac{m_{\rm r,eff}}{M_{,\rm pl}}}. \tag{G.77}$$

The duration of the kination era reads, cf. Sec. 7.2.2

$$e^{N_{\rm KD}} \equiv \frac{a_{\rm Kf}}{a_{\rm Ki}} = \left(\frac{\text{Min}\left[\rho_{\rm dom},\, \rho_{\rm damp}\right]}{\rho_{\rm K,i}}\right)^{1/6} \left(\frac{\epsilon}{2}\right)^{2/3}, \tag{G.78}$$

with

$$\rho_{\rm dom} = \frac{27 V(\phi_{\rm ini})^4}{m_{r,\rm eff}^6 M_{\rm pl}^6}, \quad \rho_{\rm damp} = 3\Gamma^2 M_{\rm pl}^2 \;\text{ and }\; \rho_{\rm K,i} = \frac{1}{2} f_a^2 m_{r,\rm eff}^2. \tag{G.79}$$

From plugging[7] $\Gamma \simeq \frac{y_\psi^2 m_\phi}{8\pi}$, cf. Eq. (G.69), $\phi_{\rm ini} \simeq M_{\rm pl}$, which corresponds to the $l \to \infty$ limit of Eq. (7.26) and $y_\psi \lesssim \sqrt{\frac{m_{\rm r,eff}}{M_{,\rm pl}}}$, cf. Eq. (G.77) we obtain

$$e^{N_{\rm KD}} \;\lesssim\; 0.3\, g_*^{1/6} \left(\frac{m_{r,\rm eff}(f_a)}{f_a}\right)^{1/3} \epsilon^{2/3} \;<\; 1. \tag{G.80}$$

So we conclude that whenever the conditions of neglecting the thermal mass in Eq. (G.77) are satisfied, thermalization via the fermion portal is not efficient enough to generate a kination era.

For this reason, in scenario I of Sec. 7.2, we must postulate the existence of an unknown mechanism other than thermalization via fermion or Higgs portal to damp the radial mode.

The thermal mass effects are considered in scenario II of Sec. 7.3. Unfortunately, the suppression of the angular kick and the delay of the matter domination prevent the onset of kination.

In scenario III in Sec. 7.4, instead of choosing a low Yukawa coupling y_ψ, we get rid of the thermal effects at the onset of the radial mode oscillation by Boltzmann-suppressing the fermion abundance.

Higgs portal. In the previous paragraph, we have considered the fermion portal. If instead the scalar condensate thermalizes through a Higgs mixing (DFSZ-type interactions)

$$\mathcal{L} \;\supset\; \lambda_{\rm H} |\phi|^2 H^\dagger H. \tag{G.81}$$

The thermal mass correction to the condensate is

$$V_{\rm th}(\phi,\, T) = \lambda_{\rm H} T^2 \phi^2. \tag{G.82}$$

The quantum processes responsible for the thermalization of the condensate are described in [840]. In contrast to the fermion portal (denoted by ψ), in the case of the Higgs portal (denoted by H) the thermalization rates scale as the the forth power of the thermal mass. Indeed

$$\Gamma_\psi \propto m_{\rm th,\psi}^2, \;\text{ and }\; \Gamma_{\rm H} \propto m_{\rm th,H}^4, \tag{G.83}$$

[6] We backward check that this coincides with $y_\psi \phi_{\rm ini} \lesssim T_{\rm osc}$ (the first Heaviside function in Eq. (G.76)) whenever the initial field value $\phi_{\rm ini}$ is sub-planckian $T_{\rm osc}/y_\psi \gtrsim T_{\rm osc}^2/m_{\rm r,eff} \simeq M_{\rm pl}\left(10/\pi^2 g_*\right)^{1/4} \gtrsim \phi_{\rm ini}$.

[7] We checked that $y_\psi \lesssim \sqrt{m_{\rm r,eff}/M_{\rm pl}}$ implies $y_\psi \phi_{\rm damp}/T_{\rm damp} \lesssim (b\alpha^2)^{1/3} \left(m_{r,\rm eff}/M_{\rm pl}\right)^{1/6}$ and $T_{\rm damp}/m_{r,\rm eff} \lesssim 1$, leading to $\Gamma \simeq y_\psi^2 m_\phi/8\pi$ in Eq. (G.69).

with

$$m^2_{\mathrm{th},\psi} = y^2_\psi T^2, \;\; \text{and} \;\; m^2_{\mathrm{th,H}} = \lambda^2_H T^2. \tag{G.84}$$

We conclude that the situation of the previous paragraph - imposing a small thermal mass prevents thermalization from occurring before the start of the would-be kination era - is even worse in the case of the Higgs portal.

The larger dependence of the damping rate on the thermal mass in the Higgs portal, in Eq. (G.83), is the reason why we focus on the fermion portal in the main text, cf. Sec. 7.3 and Sec. 7.4.

G.3.2 Parametric resonance

In this paper, we focus on the zero-mode dynamics. However, there may be circumstances where higher modes get produced. We now introduce the framework to study early parametric resonance, which may occur in the UV completion and have significant consequences on the whole dynamics. The equation of motion of a complex scalar reads

$$\ddot{\Phi} - a^{-2}\nabla^2\Phi + 3H\dot{\Phi} + \frac{\partial V}{\partial \Phi^\dagger} \tag{G.85}$$

which after decomposing in polar coordinates $\Phi = \phi e^{i\theta}$, becomes

$$\ddot{\phi} - a^{-2}\nabla^2\phi + 3H\dot{\phi} + V'(\phi) = \phi\dot{\theta}^2 - a^{-2}\phi(\nabla\theta)^2, \tag{G.86}$$

$$\phi\ddot{\theta} - a^{-2}\phi\nabla^2\theta + 3H\phi\dot{\theta} = -2\dot{\phi}\dot{\theta} + 2a^{-2}\nabla\phi\nabla\theta. \tag{G.87}$$

We can decompose $(\phi(x,\,t),\,\theta(x,\,t))$ into the superposition of a classical homogeneous mode $(\phi(t),\,\theta(t))$ and small fluctuations $(\delta\phi(x,\,t),\,\delta\theta(x,\,t))$ around it

$$\phi(x,\,t) = \phi(t) + \delta\phi(x,\,t) = \phi(t) + \left(\int \frac{d^3k}{(2\pi)^3} a^\phi_k\, u^\phi_k(t)\, e^{ikx} + \text{h.c.}\right), \tag{G.88}$$

$$\theta(x,\,t) = \theta(t) + \delta\theta(x,\,t) = \theta(t) + \left(\int \frac{d^3k}{(2\pi)^3} a^\theta_k\, u^\theta_k(t)\, e^{ikx} + \text{h.c.}\right), \tag{G.89}$$

with a^i_k, $a^{i\dagger}_k$ being the annihilation and creation operators of field i

$$\left[a^i_k,\, a^{j\dagger}_{k'}\right] = (2\pi)^3\delta_{ij}\delta^{(3)}(k-k'), \tag{G.90}$$

and the initial condition for the mode function u^i_k at $t \to -\infty$ is given by

$$u^i_k(t) = \frac{e^{i(k/a)t}}{a\sqrt{2k}}. \tag{G.91}$$

We now treat $(\delta\phi(x,\,t),\,\delta\theta(x,\,t))$ as perturbations. We expand the potential around the background solution

$$V'(\phi(x,\,t)) = V'(\phi) + V''(\phi)\partial\phi + \frac{1}{2}V'''(\phi)\partial\phi\partial\phi, \tag{G.92}$$

such that after spatial and quantum averaging $\langle\cdots\rangle$ we get, e.g. [129, 648, 685].

$$\ddot{\phi} + 3H\dot{\phi} + V'(\phi) + \frac{1}{2}V'''(\phi)\left\langle\delta\phi^2\right\rangle = \phi\dot{\theta}^2 + \phi\left\langle\delta\dot{\theta}^2\right\rangle + 2\dot{\theta}\left\langle\delta\phi\delta\dot{\theta}\right\rangle - \frac{2}{a^2}\phi\left\langle\nabla\delta\theta\nabla\delta\theta\right\rangle, \tag{G.93}$$

$$\phi\ddot{\theta} + 3H\phi\dot{\theta} + 3H\left\langle\delta\phi\delta\dot{\theta}\right\rangle = -2\dot{\phi}\dot{\theta} - 2\left\langle\delta\dot{\phi}\delta\dot{\theta}\right\rangle - \left\langle\delta\phi\delta\ddot{\theta}\right\rangle + \frac{2}{a^2}\left\langle\nabla\delta\phi\nabla\delta\theta\right\rangle, \tag{G.94}$$

for the zero mode, and

$$\delta\ddot{\phi} + 3H\delta\dot{\phi} + V''(\phi)\delta\phi + \frac{k^2}{a^2}\delta\phi = \delta\phi\dot{\theta}^2 + 2\phi\dot{\theta}\delta\dot{\theta}, \tag{G.95}$$

$$\delta\phi\ddot{\theta} + \phi\delta\ddot{\theta} + 3H\delta\phi\dot{\theta} + 3H\phi\delta\dot{\theta} + \frac{k^2}{a^2}\delta\theta = -2\delta\dot{\phi}\dot{\theta} - 2\dot{\phi}\delta\dot{\theta}, \tag{G.96}$$

for the higher modes, where

$$\langle\delta\phi^2\rangle = \int \frac{d^3k}{(2\pi)^3}\left|u_k^{\phi}\right|^2, \quad \langle\delta\theta^2\rangle = \int \frac{d^3k}{(2\pi)^3}\left|u_k^{\theta}\right|^2, \quad \langle\delta\theta\delta\phi\rangle = 0. \tag{G.97}$$

Since $[\phi,\, \theta] = 0$, all the quantum average of cross terms in Eq. (G.93) and (G.94) vanish and we get

$$\ddot{\phi} + 3H\dot{\phi} + V'(\phi) + \frac{1}{2}V'''(\phi)\langle\delta\phi^2\rangle = \phi\dot{\theta}^2 + \phi\left\langle\delta\dot{\theta}^2\right\rangle - 2\phi\left\langle\frac{k^2}{a^2}\delta\theta^2\right\rangle, \tag{G.98}$$

$$\phi\ddot{\theta} + 3H\phi\dot{\theta} = -2\dot{\phi}\dot{\theta}, \tag{G.99}$$

We conclude that the Noether charge $n_\theta = \phi^2\dot{\theta}$ is conserved during parametric resonance. Note that from using Eq. (G.99), Eq. (G.96) simplifies to [685]

$$\delta\ddot{\theta} + 3H\delta\dot{\theta} + \frac{k^2}{a^2}\delta\theta = -\frac{2\delta\dot{\phi}\dot{\theta}}{\phi} - \frac{2\dot{\phi}\delta\dot{\theta}}{\phi} + \frac{2\dot{\phi}\dot{\theta}}{\phi^2}\delta\phi \tag{G.100}$$

In order to address whether parametric resonance is a successful mechanism for damping the radial mode $\dot{\phi} \to 0$, an important question for scenario I in Sec. 7.2 is to solve the system of Eqs. (G.95), (G.96), (G.98) and (G.99). We leave this question for further study.

G.4 Detailed Field Evolution

G.4.1 The angular kick

The angular EOM, Eq. (7.15), can be rewritten as a Boltzmann equation for the $U(1)$ charge n_θ

$$\dot{n_\theta} + 3Hn_\theta \;=\; -\frac{\partial V_{\cancel{U(1)}}}{\partial\theta}, \quad \text{with} \quad n_\theta \equiv \phi^2\dot{\theta}. \tag{G.101}$$

which is equivalent to

$$\frac{d}{dt}\left(a^3 n_\theta\right) = -a^3\frac{\partial V_{\cancel{U(1)}}}{\partial\theta} \;\Rightarrow\; \frac{d}{da}\left(a^3 n_\theta\right) = -\frac{a^2}{H^2}\frac{\partial V_{\cancel{U(1)}}}{\partial\theta}. \tag{G.102}$$

This equation suggests that the $U(1)$ charge production rate is proportional to the potential gradient in the angular direction. Numerical simulations plotted in Fig. 7.5 show that the charge generation can possibly start even before that the field starts to roll in the radial direction at $3H \simeq m_{r,\text{eff}}$. Once the field value ϕ drops substantially, the explicit breaking term becomes negligible, see Fig. G.4, and the $U(1)$ charge $n_\theta a^3$ becomes conserved.

We can determine the angular kick by integrating Eq. (G.102)

$$a^3 n_\theta(a) - a_i^3 n_\theta(a_i) \;=\; -\int_{a_i}^{a} d\tilde{a}\,\frac{\tilde{a}^2}{H}\frac{\partial V_{\cancel{U(1)}}}{\partial\theta} \;=\; \int_{a_i}^{a} d\tilde{a}\,\frac{\tilde{a}^2}{H}2l\Lambda_b^4\left(\frac{\phi}{M}\right)^l\sin(l\theta), \tag{G.103}$$

where a_i is the scale factor of the Universe in the far past, where we plugged the explicit breaking potential in Eq. (G.3). The production rate of the $U(1)$ charge n_θ behaves differently accordingly to whether the radial mode ϕ has started rolling $3H < m_{r,\text{eff}}$ or not.

- **Before oscillation:** the field initially stands at $\phi_{\rm ini}$, see Sec. 7.1.5. Assuming the Universe is dominated by the background energy density $\rho \propto a^{-q}$, the corresponding charge generation is

$$a^3 n_\theta(a) - a_i^3 n_\theta(a_i) \;=\; 2l\Lambda_b^4 \left(\frac{\phi_{\rm ini}}{M}\right)^l \int_{a_i}^{a} d\tilde{a}\, \frac{\tilde{a}^2}{H} \sin(l\theta), \tag{G.104}$$

$$\simeq\; 2l\Lambda_b^4 \left(\frac{\phi_{\rm ini}}{M}\right)^l \frac{\sin(l\theta_{\rm ini})}{H_{\rm ini} a_{\rm ini}^{p/2}} \int_{a_i}^{a} d\tilde{a}\, \tilde{a}^{2+q/2}, \tag{G.105}$$

$$\simeq\; 2l\Lambda_b^4 \left(\frac{\phi_{\rm ini}}{M}\right)^l \frac{\sin(l\theta_{\rm ini})}{H_{\rm ini} a_{\rm ini}^{q/2}} \left(\frac{2}{6+q}\right) \left(a^{6+q} - a_i^{6+q}\right)^{1/2}, \tag{G.106}$$

where we approximate $\sin(l\theta) \sim \mathcal{O}(1) \sim \sin(l\theta_{\rm ini})$ and take it out of the integration. The late-time contribution dominates the charge generation such that we have the $U(1)$ charge evolution

$$n(a) \;\simeq\; \left(\frac{4l}{6+q}\right) \Lambda_b^4 \left(\frac{\phi_{\rm ini}}{M}\right)^l \frac{\sin(l\theta_{\rm ini})}{H}, \tag{G.107}$$

and we see that the field receives a kick even before the time of oscillation with $\dot{\theta} \propto a^{q/2}$. The $U(1)$ charge is maximally generated at the onset of oscillation

$$n_\theta(a_{\rm osc}) \;\simeq\; \left[\frac{4l}{6+q}\right] \Lambda_b^4 \left[\frac{\phi_{\rm ini}}{M}\right]^l \frac{\sin(l\theta_{\rm ini})}{H_{\rm osc}} \;\simeq\; \left[\frac{12l}{6+q}\right] \Lambda_b^4 \left[\frac{\phi_{\rm ini}}{M}\right]^l \frac{\sin(l\theta_{\rm ini})}{m_{r,\rm eff}}, \tag{G.108}$$

and the corresponding angular velocity reads

$$\dot{\theta}_{\rm osc} \;\simeq\; \left(\frac{12l}{6+q}\right) \Lambda_b^4 \left(\frac{\phi_{\rm ini}}{M}\right)^l \frac{\sin(l\theta_{\rm ini})}{m_{r,\rm eff}\phi_{\rm ini}^2}, \tag{G.109}$$

- **After the oscillation:** gradients of the potential in angular and radial directions kick the field into an elliptic orbit whose size redshifts over time. In App. G.4.2, we determine the dynamics of the radial mode as a function of the shape of the $U(1)$-symmetric potential

$$V(\phi) \;\propto\; \phi^p \;\;\Rightarrow\;\; \langle\phi\rangle \;\propto\; a^{-6/(2+p)}. \tag{G.110}$$

Assuming that the Hubble factor evolves as $H \propto a^{-q/2}$, then the $U(1)$ charge generated after oscillation $3H < m_{r,\rm eff}$, in Eq. (G.103), reads

$$a^3 n_\theta(a) - a_{\rm osc}^3 n_\theta(a_{\rm osc}) \;\sim\; \int_{a_{\rm osc}}^{a} d\tilde{a}\, \tilde{a}^{\frac{(6+q)(2+p)-12l}{2(2+p)}-1}. \tag{G.111}$$

Depending on the values of q, p, and l, we obtain three regimes

$$a^3 n_\theta(a) - a_{\rm osc}^3 n_\theta(a_{\rm osc}) \;\sim\; \begin{cases} a^{\frac{(6+q)(2+p)-12l}{2(2+p)}} & \text{for } l < \frac{(6+q)(2+p)}{12}, \\ \log a & \text{for } l = \frac{(6+q)(2+p)}{12}, \\ a^{-\frac{12l-(6+q)(2+p)}{2(2+p)}} & \text{for } l > \frac{(6+q)(2+p)}{12}. \end{cases} \tag{G.112}$$

In the first and second cases, the $U(1)$ charge continues to increase after the oscillation, while in the third case, at large l, the $U(1)$ charge stops being efficiently produced after a few Hubble times and the $U(1)$-symmetry is restored. Assuming a radiation-dominated Universe ($q = 4$), the estimated $U(1)$-symmetry after the oscillation demands that l is greater than $10/3$ and 5 for quadratic ($p = 2$) and quartic ($p = 4$) potentials, respectively. Hence, in this work, we consider cases $l \geq 4$ to neglect explicit breaking terms at later times.

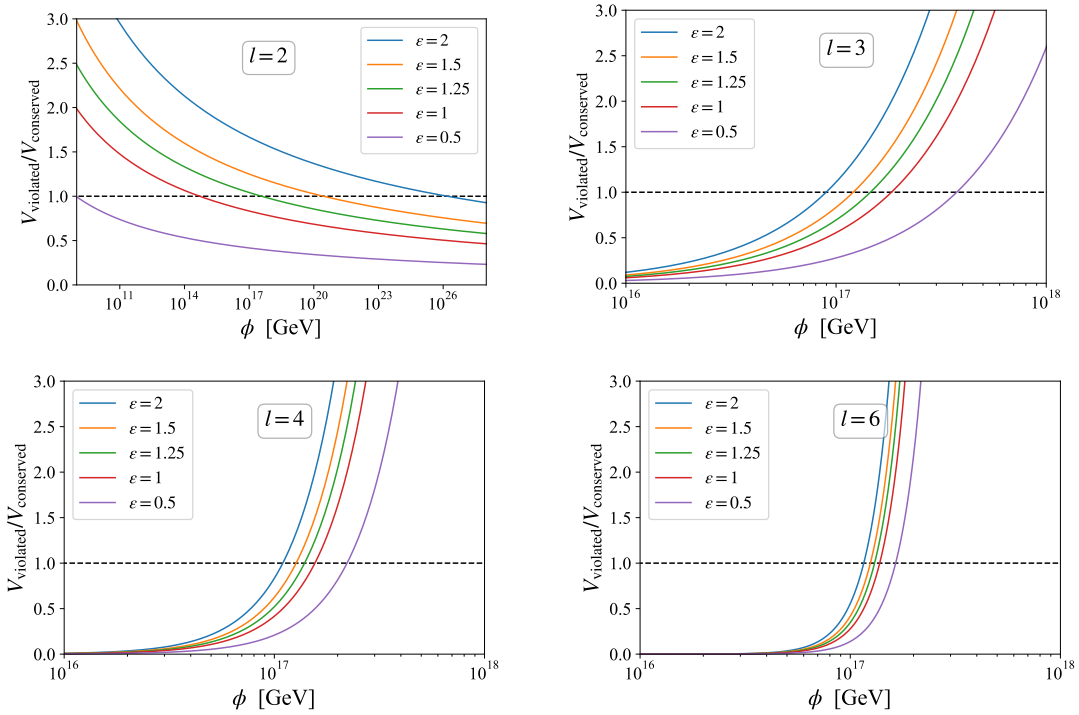

Figure G.4: For each l, we show the ratio of the $U(1)$-violating potential to the $U(1)$-conserving one, assuming nearly-quadratic potential, along the $\theta = 0$ direction, which has the maximum $V_{U(1)}$. For $l > 2$, the conserving potential always dominates at small field values $\phi \ll M$, and the $U(1)$ charge, defined in Eq. (7.19), is conserved in the subsequent evolution.

G.4.2 After the kick

The $U(1)$-conserving and the $U(1)$-breaking potentials excite the field in the radial and angular directions, respectively. As argued in App. G.4.1, after a few Hubble times of field evolution, for $l \geq 4$, we can neglect effects coming from the $U(1)$-breaking terms.

Exact solution. We now derive an exact analytical solution of the complex scalar equation of motion in a quadratic potential without Hubble friction, e.g., [841, 842]. For $\phi \gg f_a$, the nearly-quadratic potential in Eq. (7.4) is approximated to $V = m^2\Phi^\dagger\Phi/2 = m^2\phi^2/2$, where m is a constant or a slowly-changing variable. The $U(1)$-charge conservation in Eq. (7.19), and the radial EOM in Eq. (7.14), give

$$\ddot{\phi} + 3H\dot{\phi} + \frac{\partial V}{\partial \phi} - \frac{Y^2}{\phi^3 a^6} = 0, \tag{G.113}$$

where $Y \equiv a^3\phi^2\dot{\theta} =$ is the conserved comoving $U(1)$ charge. We use a set of dimensionless parameters

$$\tau \equiv mt, \quad h \equiv \frac{H}{m}, \quad u \equiv \sqrt{\frac{m}{Y}}a^{3/2}\phi, \tag{G.114}$$

which simplifies the charge conservation equation to $\dot{\theta}u^2 = m$ and the EOM to

$$0 = u'' + \left[1 - u^{-4} - \frac{3}{2}\left(h' + \frac{3}{2}h^2\right)\right]u \simeq u'' + u - \frac{1}{u^3}, \tag{G.115}$$

where $\cdots'$ denotes the derivative w.r.t. τ, and where we considered the oscillation time scale to be much faster than a Hubble time $h \to 0$, which becomes true after oscillation has started

$3H \simeq m_{r,\text{eff}}$. The differential equation in Eq. (G.115) can be understood as the equation of motion of a scalar u evolving in a potential

$$\mathcal{V}(u) = \frac{u^2 + u^{-2}}{2}, \tag{G.116}$$

whose minimum is at $u = 1$, or equivalently $\dot{\theta} = m$. Its corresponding constant-of-motion E_u satisfies

$$\frac{dE_u}{d\tau} \equiv \frac{d}{d\tau}\left(\frac{u'^2}{2} + \frac{u^2 + u^{-2}}{2}\right) = 0, \tag{G.117}$$

with $E_u \geq 1$. The parameter E_u can be related to the energy density of the scalar field

$$\rho_\Phi = \frac{\dot{\phi}^2}{2} + \frac{\phi^2\dot{\theta}^2}{2} + V = mYE_u a^{-3}. \tag{G.118}$$

We just found that the energy density of a complex scalar field evolving in quadratic potential redshifts as matter $\rho_\Phi \propto a^{-3}$.

To find the exact solution to the EOM, we rewrite Eq. (G.117) as

$$u'^2 = 2E_u - u^2 - u^{-2} \quad \Rightarrow \quad U'^2 = -4U^2 + 8E_u U - 4, \tag{G.119}$$

where $U \equiv u^2$. Integrating this equation, we deduce

$$\int dt = \int \frac{dU}{\sqrt{-4U^2 + 8E_u U - 4}} \quad \Rightarrow \quad u(\tau) = \sqrt{(E_u^2 - 1)^{1/2}\sin(2\tau + \psi) + E_u}. \tag{G.120}$$

where ψ is a phase which depends on the initial conditions. In u-space, the orbit is a fixed-sized ellipse, so the orbit in field space ϕ is an ellipse whose size scale as $a^{-3/2}$, i.e. an ellipse that spirals towards the origin as illustrated in Fig. 7.3 or by our animation.. The parameter E_u is related to the orbit eccentricity and to the previously defined parameter $0 < \epsilon \leq 2$ in Eq. (7.37)

$$m^2\phi^2 = \rho_\Phi = mn_\theta E_u \quad \Rightarrow \quad \frac{1}{E_u} = \frac{n_\theta}{m\phi^2} = \frac{\epsilon}{2} \quad \Rightarrow \quad \epsilon = 2/E_u. \tag{G.121}$$

For $E_u = 1$ or $\epsilon = 2$, the orbit is essentially circular, while for large E_u or $\epsilon \to 0$ the orbit has a large eccentricity and starts to resemble the trajectory of a real scalar field.

We can calculate the average angular speed

$$\dot{\theta} \;=\; \frac{m}{u^2} \;=\; \frac{m}{(E_u^2 - 1)^{1/2}\sin(2\tau + \psi) + E_u}, \tag{G.122}$$

by averaging over a time $T = n\pi$, $n \in \mathbb{N}^+$, which is larger than the oscillation period but less than the Hubble time scale

$$\left\langle \dot{\theta} \right\rangle \;=\; \frac{1}{n\pi}\int_0^{n\pi} d\tau \frac{m}{(E_u^2 - 1)^{1/2}\sin(2\tau + \psi) + E_u} \;=\; m, \tag{G.123}$$

where we have integrated an elliptic integral[8]. We find that the averaged angular velocities become independent of the initial value θ_{ini} in Eq. (G.109) and converge towards an attractor solution. This is confirmed by the numerical integration of the equations of motion in Fig. 7.5.

[8] We can freely choose the phase ψ such that the sine becomes a cosine and the elliptic integral reads

$$\int_0^{2\pi} \frac{dx}{a + b\cos x} \;=\; \frac{2\pi}{\sqrt{a^2 - b^2}}.$$

Exact solution (bis) : quartic potential. Even if we do not use it in our work, it may be helpful in further studies (of axion dark matter, for example, [843]) to give the analog of Eq. (G.120) for a quartic potential. When adding a quartic term to the potential $V = \frac{1}{2}m^2\phi^2 + \frac{1}{4}\lambda\phi^4$, the Eq. (G.115) becomes

$$u'' + u + \frac{4\alpha}{a^3}u^3 - \frac{1}{u^3} = 0, \quad \text{with } \alpha \equiv \lambda Y/(4m^3). \tag{G.124}$$

We now consider $\phi \gg m/\sqrt{\lambda}$, such that the linear term u corresponding to $\frac{1}{2}m^2\phi^2$ can be dropped and Eq. (G.124) becomes

$$\nu'' + 4\alpha\nu^3 - \frac{1}{\nu^3} = 0 \;\Rightarrow\; \frac{1}{2}\nu'^2 = E_\nu - V_\nu = 2E_\nu - 2\alpha\nu^4 - \frac{1}{\nu^2}, \tag{G.125}$$

with $\nu \equiv a^{-1/2}u$ and with $'$ denoting the derivative with respect to the conformal time η ($mdt = d\tau = ad\eta$) and where we have dropped Hubble depending terms. The motion can be interpreted as a scalar ν oscillating in a potential $V_\nu = \alpha\nu^4 + 1/(2\nu^2)$, with the constant of motion $E_\nu = \nu'^2/2 + V_\nu$. Introducing the new variables $V \equiv -\nu^2/\sqrt{2}$ and $s \equiv \eta\sqrt{\alpha}$, we deduce

$$\left(\frac{dV}{ds}\right)^2 = 4V^3 - \frac{4E_\nu}{\alpha}V - \frac{2}{\alpha}. \tag{G.126}$$

It is known that the *Weierstrass elliptic function* $\wp(s;\, g_2,\, g_3)$ solves the differential equation of the form [844]

$$\left(\frac{d\wp(s)}{ds}\right)^2 = 4\wp^3(s) - g_2\wp(s) - g_3. \tag{G.127}$$

Therefore, Eq. (G.126) has a solution as an elliptic orbit described by $\wp(s;\, 4E_\nu/\alpha,\, 2/\alpha)$. Applying one of the properties of $\wp$, namely $\wp(u; g_2, g_3) = k^2\,\wp(ku;\, g_2/k^4,\, g_3/k^6)$, the exact solution to Eq. (G.125) reads

$$\nu^2 = -\sqrt{2}V = -\frac{\sqrt{2}}{\alpha}\wp(\eta;\, 4\alpha E_\nu,\, 2\alpha^2). \tag{G.128}$$

Virial theorem. The Virial theorem in classical mechanics is a well-known tool, e.g., [845] for studying the averaged behavior of a stable system. We now use it to analyze the dynamics of a complex scalar field in a central potential during the early Universe. The EOM in Eq. (7.14) and (7.15) can be written in terms of kinetic K and potential V energy densities as

$$\frac{d}{dt}(K+V) = \dot\phi\left(\ddot\phi + \frac{\partial V}{\partial\phi} + \phi\dot\theta^2 + \frac{\phi^2}{\dot\phi}\dot\theta\ddot\theta\right) + \dot T\frac{\partial V}{\partial T}, \tag{G.129}$$

$$= -(3H+\Gamma)\dot\phi^2 - 3H\phi^2\dot\theta^2 + \dot T\frac{\partial V}{\partial T}, \tag{G.130}$$

$$= -(6H+2\Gamma)K_\phi - 6HK_\theta + \dot T\frac{\partial V}{\partial T}, \tag{G.131}$$

where $K_\phi \equiv \dot\phi^2/2$ and $K_\theta \equiv \phi^2\dot\theta^2/2$ are the kinetic energy in radial and angular modes, respectively. After $3H \simeq m_{r,\text{eff}}$, the field oscillates fast compared to the expansion and damping rate. The average over many field cycles but over a time shorter than the H^{-1} reads

$$\frac{d}{dt}\langle K+V\rangle = -(6H+2\Gamma)\langle K_\phi\rangle - 6H\langle K_\theta\rangle + \dot T\frac{\partial V}{\partial T}. \tag{G.132}$$

We introduce the *Virial* parameter G, e.g. [845]

$$G \equiv \sum_{i=\phi,\theta} p_i\cdot r_i = \dot\phi\phi + \phi^2\dot\theta\theta, \tag{G.133}$$

where $r_\phi = \phi$ and $r_\theta = \theta$, and $p_i \equiv \partial\mathcal{L}/\partial r_i$. By taking its time derivative, we deduce

$$\frac{dG}{dt} = \dot{\phi}^2 + \phi^2\dot{\theta}^2 + \phi\ddot{\phi} + \phi^2\theta\left(\ddot{\theta} + 2\frac{\dot{\phi}}{\phi}\dot{\theta}\right), \tag{G.134}$$

$$= \dot{\phi}^2 + \phi^2\dot{\theta}^2 - \phi\frac{\partial V}{\partial\phi} - (3H+\Gamma)\phi\dot{\phi} - 3H\phi^2\dot{\theta}\theta, \tag{G.135}$$

$$\simeq 2K - \phi\frac{\partial V}{\partial\phi}, \tag{G.136}$$

where we used Eq. (7.14) and (7.15) in the second step, and where we neglected the damping terms in the last step. The Virial theorem states that whenever the system is stable, the averaged kinetic and potential energies are related

$$\left\langle\frac{dG}{dt}\right\rangle = \lim_{\Delta T\to\infty}\frac{G(T+\Delta T)-G(T)}{\Delta T} = 0, \quad \Rightarrow \quad \langle 2K\rangle = \left\langle\phi\frac{\partial V}{\partial\phi}\right\rangle. \tag{G.137}$$

which resembles the Virial theorem for a real scalar [699, 700]. For convenience, we consider the field behavior before the damping term becomes effective and deduces the average EOM from Eq. (G.132) and (G.137)

$$\frac{d}{dt}\langle K+V\rangle = -6H\langle K\rangle + \dot{T}\frac{\partial V}{\partial T} \quad \Rightarrow \quad \frac{d}{dt}\left\langle\phi\frac{\partial V}{\partial\phi} + 2V\right\rangle = -6H\left\langle\phi\frac{\partial V}{\partial\phi}\right\rangle + \dot{T}\frac{\partial V}{\partial T}. \tag{G.138}$$

Monomial potential. From plugging the potential $V \propto \phi^n$ into Eq. (G.138), we obtain

$$(n+2)\frac{d}{dt}\langle V\rangle = -6Hn\langle V\rangle \quad \Rightarrow \quad \frac{d}{dt}\langle\rho_\Phi\rangle = -\frac{6n}{2+n}H\langle\rho\rangle \quad \Rightarrow \quad \frac{d\ln\langle\rho_\Phi\rangle}{d\ln a} = -\frac{6n}{2+n}, \tag{G.139}$$

with $\langle\rho_\Phi\rangle$ is the average total energy density of the field

$$\langle\rho_\Phi\rangle = \langle K+V\rangle = (2+n)\langle V\rangle/2. \tag{G.140}$$

We deduce the redshift laws of $\langle\rho_\Phi\rangle$ and $\langle\phi\rangle$

$$\langle\rho_\Phi\rangle \propto a^{-\frac{6n}{2+n}}, \text{ and } \langle\phi\rangle \propto a^{-\frac{6}{2+n}}. \tag{G.141}$$

For the quadratic and quartic potentials, the complex scalar field behaves like matter ($\rho_\Phi \propto a^{-3}$, $\phi \propto a^{-3/2}$) and radiation ($\rho_\Phi \propto a^{-4}$, $\phi \propto a^{-1}$), respectively. The scaling $\rho_\Phi \propto a^{-3}$ is confirmed by the exact solution in Eq. (G.118). We show that, cf. Eq. (G.154), that Eq. (G.139) holds without any average after radial damping $\dot{\phi} \to 0$.

Thermal mass. From plugging the potential $V = \lambda T^2\phi^2/2$ into Eq. (G.138), we obtain

$$\frac{d}{dt}\langle\phi^2\rangle = -3H\langle\phi^2\rangle - \frac{\dot{T}}{T}\langle\phi^2\rangle \quad \Rightarrow \quad \phi^2 \propto a^{-3}T^{-1} \text{ and } V \propto a^{-3}T. \tag{G.142}$$

We conclude that a scalar field dominated by its thermal mass redshifts like radiation in a radiation-dominated Universe.

G.4.3 The radial damping

Amount of rotation. The parameter ϵ expresses the amount of rotation generated by the explicit breaking at the time of oscillation $t_{\rm osc}$, cf. Eq. (7.37)

$$\epsilon \;=\; \frac{\phi^2\dot\theta/2}{V(\phi)/m_{r,\rm eff}}, \tag{G.143}$$

From Eq. (7.43), we deduce that ϵ becomes a conserved quantity through Hubble expansion $d\epsilon/da = 0$, as soon as $V(\phi)$ become dominated by its quadratic term. It can be rewritten in terms of the ratio between energy densities as

$$\epsilon \;=\; \left(\frac{\rho_\theta}{V}\right)\left(\frac{m_{r,\rm eff}}{\dot\theta}\right), \quad \text{with} \;\; \rho_\theta \equiv \dot\theta^2\phi^2/2. \tag{G.144}$$

Since $\left\langle\dot\theta\right\rangle = m_{r,\rm eff}$, see Fig. 7.5, we deduce the rotational energy density to be an ϵ fraction of the potential energy density

$$\rho_\theta \;=\; \epsilon V(\phi). \tag{G.145}$$

Note that $\epsilon \leq 1$ prevents the field from spinning upward.

$$\begin{cases} \epsilon = \phi^2\dot\theta/(2\rho_r(\phi)/m_{r,\rm eff}), \\ \phi^2\dot\theta = \text{constant}, \\ \dot\theta_{\rm after} = m_{r,\rm eff}, \end{cases} \qquad \Rightarrow \;\; \rho_\theta\Big|_{\rm after} = \epsilon\rho_r(\phi) \tag{G.146}$$

Drop of energy density during radial damping. During the radial damping $\dot\phi \to 0$, see Sec. 7.1.6, the elliptic orbits becomes a circular one. During this process, the scalar field kinetic energy is damped but the rotational kinetic energy is preserved. Therefore, after the radial damping the total energy density of the complex scalar field drops by

$$\rho_\Phi^{\rm after} = \epsilon\,\rho_\Phi^{\rm before} \;\; \Rightarrow \;\; \phi^2_{\rm after} = \epsilon\,\phi^2_{\rm before}, \tag{G.147}$$

where the second equation assumes the quadratic potential. $\phi_{\rm before}$ is the field value just before thermalization, and it can be computed from Eq. (G.141)

$$\frac{\rho_\Phi^{\rm osc}}{\rho_\Phi^{\rm before}} \;=\; \left(\frac{a_{\rm damp}}{a_{\rm osc}}\right)^3 \;=\; \left(\frac{\phi_{\rm osc}}{\phi_{\rm before}}\right)^2 \qquad \Rightarrow \qquad \phi_{\rm before} \;=\; \frac{(\rho_\Phi^{\rm before})^{1/2}}{m_{r,\rm eff}(\phi_{\rm osc})}, \tag{G.148}$$

where we used that the energy density just after oscillation can be written as $\rho_\Phi^{\rm osc} = \phi^2_{\rm osc} m_{\rm eff}(\phi_{\rm osc})^2$. In Fig. G.5, we show that the result in Eq.(G.147) is confirmed by numerical integration of the equations of motion.

Impact on kination duration. We now study the impact of the energy drop in Eq. (G.147) on the duration of the kination era. As shown in Fig. 7.6, we must consider two possible scenarios, depending on whether the radial damping occurs before or after the scalar domination. For the sake of simplicity we assume an instantaneous drop in energy density at the time of radial damping.

- **Damping before domination.** The energy transferred to the thermal bath is negligible. However, the ϵ factor in the energy density in Eq. (G.147) delays the time when the scalar field dominates the energy density of the Universe

$$\rho'_{\rm dom} \;=\; \epsilon^4\,\frac{\rho_\Phi^4}{\rho_{\rm rad}^3}\bigg|_{\text{at oscillation}} \;=\; \epsilon^4\rho_{\rm dom}, \tag{G.149}$$

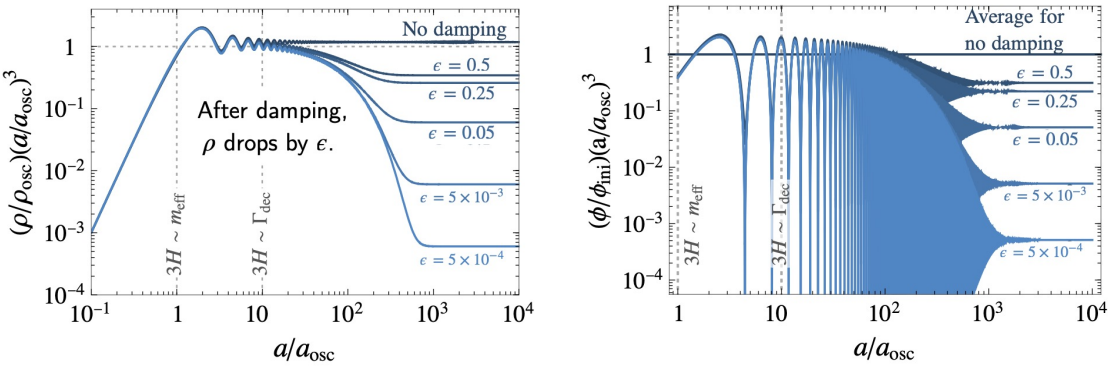

Figure G.5: Numerical integration of the equations of motion in Eqs. (7.14), (7.15) and (7.16). The energy density (**left**) and the radial value (**right**) of the complex scalar field drops by a factor ϵ after the radial damping. The larger ϵ, the larger the rotational energy density produced during the initial kick and the smaller the energy drop during the radial damping. The extreme case $\epsilon = 1$ corresponds to a trajectory which is already circular right after the initial angular kick.

where $\rho_{\rm dom}$ is the domination energy scale without energy drop during damping (case $\epsilon = 1$) and where we have used Eq. (G.177).

As a consequence of the energy drop, the kination era ends earlier and is then shorter

$$\rho_{{\rm KD},f} = \frac{\rho_{{\rm KD},i}^2}{\rho'_{\rm dom}} = \frac{\rho_{{\rm KD},i}^2}{\rho_{\rm dom}}\left(\frac{1}{\epsilon}\right)^4 \quad \text{and} \quad \frac{a_{{\rm KD},f}}{a_{{\rm KD},i}} = \left(\frac{\rho'_{\rm dom}}{\rho_{{\rm KD},i}}\right)^{1/6} = \left(\frac{\rho_{\rm dom}}{\rho_{{\rm KD},i}}\right)^{1/6}\epsilon^{2/3}. \tag{G.150}$$

- **Damping after domination.** A substantial amount of energy is injected into the thermal bath. For $\epsilon = \mathcal{O}(0.1)$, the radial damping reduces the scalar energy by a factor $\mathcal{O}(10)$ so that the produced SM radiation dominates the energy density. Later, the domination of the energy density by the rotating scalar generates a second matter era at

$$\rho'_{\rm dom} = \epsilon^4 \rho_{\rm damp}, \tag{G.151}$$

The scale of kination ending and its duration are given by Eq. (G.150) after replacing $\rho_{\rm dom}$ by $\rho_{\rm damp}$

$$\rho_{{\rm KD},f} = \frac{\rho_{{\rm KD},i}^2}{\rho_{\rm damp}}\left(\frac{1}{\epsilon}\right)^4 \quad \text{and} \quad \frac{a_{{\rm KD},f}}{a_{{\rm KD},i}} = \left(\frac{\rho_{\rm damp}}{\rho_{{\rm KD},i}}\right)^{1/6}\epsilon^{2/3}. \tag{G.152}$$

Note that the presence of the radiation era in between the two matter eras could leave a distinctive imprint on the SGWB.

Too small ϵ kills the kination era. In Eqs. (G.150) and (G.152), we have seen that the kination duration receives a suppression factor $\epsilon^{2/3}$. This implies the existence of a lower bound on ϵ below which no kination era is generated

$$\text{Requiring} \quad \frac{a_{{\rm KD},f}}{a_{{\rm KD},i}} \geq 1 \quad \Rightarrow \quad \epsilon \geq \left[\frac{\rho_{{\rm KD},i}}{\max(\rho_{\rm dom}, \rho_{\rm damp})}\right], \tag{G.153}$$

for both damping before and after the scalar domination. In Sec. 7.3, we show that the scenario II, in which thermal corrections to the potential are present at the onset of the radial mode oscillation, necessarily predicts a value of ϵ smaller than Eq. (G.153).

G.4.4 After the radial damping

In this section, we reproduce the results from [669] and derive the evolution of the radial ϕ and angular $\dot{\theta}$ field values, their energy density ρ_Φ and equation of state ω_Φ, in an arbitrary $U(1)$-symmetric potential $V(\phi)$, after that the radial mode has been damped $\dot{\phi}/\phi \ll \sqrt{V''}$.

Radial evolution. In the limit $\dot{\phi} \to 0$, the radial EOM in Eq. (7.14) takes a simple form

$$\dot{\theta}^2\phi = \frac{\partial V}{\partial \phi} \qquad \Rightarrow \qquad \dot{\theta}^2 = 2\frac{\partial V}{\partial \phi^2}, \tag{G.154}$$

We inject it in the equation of conservation of $n_\theta = \phi^2\dot{\theta}$

$$\frac{d(a^3 n_\theta)}{da} = 3a^2\phi^2\dot{\theta} + 2a^3\phi\dot{\theta}\frac{d\phi}{da} + a^3\phi^2\frac{d\dot{\theta}}{da}, \tag{G.155}$$

$$\Rightarrow \quad 0 = 3a^2\phi^2\dot{\theta} + 2a^3\phi\dot{\theta}\frac{d\phi}{da} + a^3\phi^2\frac{4\phi}{2\dot{\theta}}\cdot\frac{d\phi}{da}\cdot\frac{\partial^2 V}{(\partial\phi^2)^2}, \tag{G.156}$$

$$\Rightarrow \quad a\frac{d\phi}{da} = \frac{-3\phi\dot{\theta}^2}{2\dot{\theta}^2 + 2\phi^2\frac{\partial^2 V}{(\partial\phi^2)^2}} = \frac{-3\phi\frac{\partial V}{\partial\phi^2}}{2\frac{\partial V}{\partial\phi^2} + \phi^2\frac{\partial^2 V}{(\partial\phi^2)^2}}, \tag{G.157}$$

From which we obtain

$$\frac{d\ln\phi}{d\ln a} = \frac{-3\frac{\partial V}{\partial\phi^2}}{2\frac{\partial V}{\partial\phi^2} + \phi^2\frac{\partial^2 V}{(\partial\phi^2)^2}}. \tag{G.158}$$

Angular evolution. Starting from Eq.(G.154), we can write

$$\frac{d\ln\dot{\theta}^2}{d\ln a} = 2\frac{a}{\dot{\theta}^2}\frac{d\phi^2}{da}\cdot\frac{\partial^2 V}{(\partial\phi^2)^2} = 4\frac{\phi^2}{\dot{\theta}^2}\frac{d\ln\phi}{d\ln a}\cdot\frac{\partial^2 V}{(\partial\phi^2)^2} = 2\frac{\phi^2}{\frac{\partial V}{\partial\phi^2}}\frac{d\ln\phi}{d\ln a}\cdot\frac{\partial^2 V}{(\partial\phi^2)^2}, \tag{G.159}$$

where $\frac{d\ln\phi}{d\ln a}$ is given by Eq. (G.158).

Energy density evolution. After radial damping, the kinetic energy of the radial mode vanishes such that the energy density of the complex field reads

$$\rho_\Phi = \frac{1}{2}\phi^2\dot{\theta}^2 + V(\phi) = \phi^2\frac{\partial V}{\partial\phi^2} + V(\phi). \tag{G.160}$$

Taking the derivative with respect to ϕ, we get

$$\frac{d\rho_\Phi}{d\phi} = 2\phi\frac{\partial V}{\partial\phi^2} + 2\phi^3\frac{\partial^2 V}{(\partial\phi^2)^2} + \frac{\partial V}{\partial\phi} = 2\phi\left(2\frac{\partial V}{\partial\phi^2} + \phi^2\frac{\partial^2 V}{(\partial\phi^2)^2}\right). \tag{G.161}$$

Now taking the derivative with respect to a

$$a\frac{d\rho_\Phi}{da} = \frac{d\rho_\Phi}{d\phi}\cdot a\frac{d\phi}{da} = \left[2\phi\left(2\frac{\partial V}{\partial\phi^2} + \phi^2\frac{\partial^2 V}{(\partial\phi^2)^2}\right)\right]\left[\frac{-3\phi\frac{\partial V}{\partial\phi^2}}{2\frac{\partial V}{\partial\phi^2} + \phi^2\frac{\partial^2 V}{(\partial\phi^2)^2}}\right] = -6\phi^2\frac{\partial V}{\partial\phi^2} \equiv -6\rho_\theta, \tag{G.162}$$

where ρ_θ is the kinetic energy density of the angular field

$$\rho_\theta \equiv \frac{1}{2}\phi^2\dot{\theta}^2 = \phi^2\frac{\partial V}{\partial\phi^2}, \tag{G.163}$$

we deduce

$$\frac{d\ln\rho_\Phi}{d\ln a} = \frac{-6\phi^2\frac{\partial V}{\partial\phi^2}}{\phi^2\frac{\partial V}{\partial\phi^2} + V}. \tag{G.164}$$

Equation of state. Using $\dot{\phi} \to 0$ and Eq. (G.154), the equation of state of the complex scalar field becomes[9]

$$\omega_\Phi \;=\; \frac{\frac{1}{2}\phi^2\dot{\theta}^2 - V}{\frac{1}{2}\phi^2\dot{\theta}^2 + V} \;=\; \frac{\phi^2\frac{\partial V}{\partial\phi^2} - V}{\phi^2\frac{\partial V}{\partial\phi^2} + V}. \tag{G.165}$$

Example: Nearly-quadratic potential. This is the scenario considered in this work. The potential and its derivatives read[10]

$$V \;=\; m^2\phi^2\left[\log\left(\frac{\phi^2}{f^2}\right) - 1\right] + m^2 f^2, \;\; \frac{\partial V}{\partial\phi^2} = m^2\log\left(\frac{\phi^2}{f^2}\right), \;\; \frac{\partial^2 V}{(\partial\phi^2)^2} = \frac{m^2}{\phi^2}. \tag{G.166}$$

From using Eq. (G.158) and (G.159), we deduce the evolution of the radial and angular component of the scalar field after radial damping

$$\frac{d\ln\phi}{d\ln a} \;=\; \frac{-3\log\left(\frac{\phi^2}{f^2}\right)}{2\log\left(\frac{\phi^2}{f^2}\right)+1} \;\text{ and }\; \frac{d\ln\dot{\theta}^2}{d\ln a} \;=\; \frac{-6}{2\log\left(\frac{\phi^2}{f^2}\right)+1}. \tag{G.167}$$

Using Eq. (G.164) and (G.165), we deduce the evolution of the complex scalar field energy density ρ_Φ and its equation of state ω_Φ

$$\frac{d\ln\rho_\Phi}{d\ln a} \;=\; \frac{-6\log\left(\frac{\phi^2}{f^2}\right)}{2\log\left(\frac{\phi^2}{f^2}\right) - 1 + \frac{f^2}{\phi^2}} \;\text{ and }\; \omega_\Phi = \frac{\phi^2 - f_a^2}{2\phi^2\log\frac{\phi^2}{f_a^2} - f_a^2 + \phi^2}. \tag{G.168}$$

For $\phi \gg f_a$ we have

$$\phi \;\propto\; a^{-3/2}, \;\; \dot{\theta} \;\propto\; a^0, \;\; \rho_\Phi \;\propto\; a^{-3}, \;\; \omega_\Phi \;\simeq\; 0, \tag{G.169}$$

and for $\phi \simeq f_a$ we have

$$\phi \;\propto\; a^0, \;\; \dot{\theta} \;\propto\; a^{-3}, \;\; \rho_\Phi \;\propto\; a^{-6}, \;\; \omega_\Phi \;\simeq\; 1. \tag{G.170}$$

Example: quartic potential. For the sake of the comparison, we consider the potential

$$V = \lambda^2\left(\phi^2 - f^2\right)^2, \;\; \frac{\partial V}{\partial\phi^2} = 2\lambda^2\left(\phi^2 - f^2\right), \;\; \frac{\partial^2 V}{(\partial\phi^2)^2} = 2\lambda^2. \tag{G.171}$$

Eq. (G.158) and (G.159) From using Eq. (G.158) and (G.159), we deduce the evolution of the radial and angular component of the scalar field after radial damping

$$\frac{d\ln\phi}{d\ln a} \;=\; \frac{-3\left[\frac{\phi^2}{f_a^2} - 1\right]}{3\frac{\phi^2}{f_a^2} - 2} \;\text{ and }\; \frac{d\ln\dot{\theta}^2}{d\ln a} \;=\; \frac{-6\frac{\phi^2}{f_a^2}}{3\frac{\phi^2}{f_a^2} - 1}. \tag{G.172}$$

[9] As a sanity check, we can use

$$\dot{\rho} + 3H(\rho + P) = 0 \;\;\Rightarrow\;\; \frac{d\ln\rho}{d\ln a} = -3(1+\omega),$$

to show that Eq. (G.164) and Eq. (G.165) are consistent with each others.

[10] Note that is the minimum of potential is not vanishing $V_{\rm min} \neq 0$, then the evolution of the energy density and EOS becomes

$$\frac{d\ln\rho}{d\ln a} = \frac{-6\log\left(\frac{\phi^2}{f^2}\right)}{2\log\left(\frac{\phi^2}{f^2}\right) - 1 + \frac{f^2}{\phi^2} + \frac{V_{\rm min}}{m^2 f^2}} \;\text{ and }\; \omega_\Phi = \frac{\phi^2 - f_a^2}{2\phi^2\log\frac{\phi^2}{f_a^2} - f_a^2 + \phi^2 - V_{\rm min}/f_a^2}.$$

To generate a kination EOS, in this work, we assume $V_{\rm min} \ll m^2 f^2$.

Using Eq. (G.164) and (G.165), we deduce the evolution of the complex scalar field energy density ρ_Φ and equation of state ω_Φ

$$\frac{d\ln\rho_\Phi}{d\ln a} = \frac{-12\frac{\phi^2}{f_a^2}}{3\frac{\phi^2}{f_a^2}-1} \text{ and } \omega_\Phi = \frac{\phi^2+f_a^2}{3\phi^2-f_a^2}. \tag{G.173}$$

For $\phi \gg f_a$ we have

$$\phi \propto a^{-1},\ \dot\theta \propto a^{-1},\ \rho_\Phi \propto a^{-4},\ \omega_\Phi \simeq \frac{1}{3}, \tag{G.174}$$

and for $\phi \simeq f_a$ we have

$$\phi \propto a^{0},\ \dot\theta \propto a^{-3},\ \rho_\Phi \propto a^{-6},\ \omega_\Phi \simeq 1. \tag{G.175}$$

The evolution of ρ_Φ and ω_Φ in nearly-quadratic and quartic potentials are shown in Fig. G.6. Only the matter phase induced by the nearly-quadratic potential can allow the initially sub-dominant Φ to dominate the energy density of the Universe and, later, generate a kination-dominated era. For this reason, in this work, we focus on a nearly-quadratic potential. In Fig. 7.7, we show the evolution of ϕ, $\dot\theta$, ρ_Φ and ω_Φ in the nearly-quadratic potential, obtained after numerically integrating the equations of motion in Eqs. (7.14), (7.15) and (7.16).

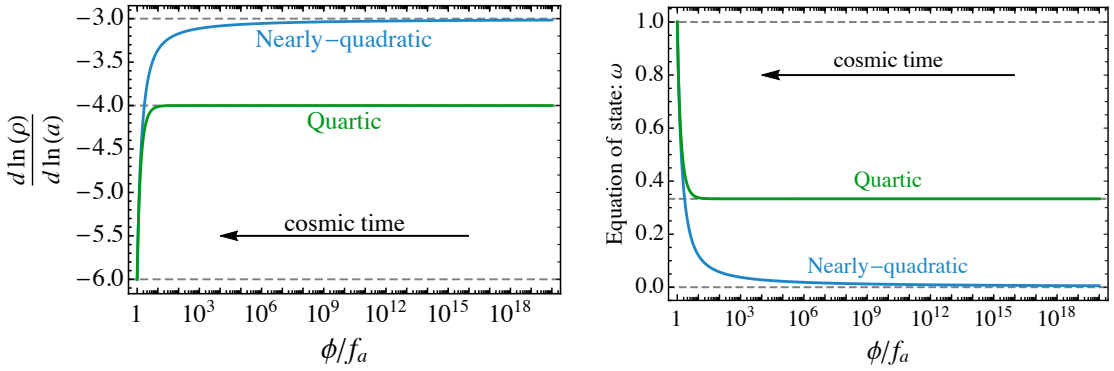

Figure G.6: Evolutions of the energy density (**left**) and the equation-of-state (**right**) of the complex scalar field, rotating in a nearly-quadratic or quartic potential after its radial motion has been damped. Both cases lead to a kination EOS ($\omega = 1$) when $\phi \to f_a$. While the quadratic potential gives a matter EOS for $\phi \gg f_a$, the quartic potential gives a radiation EOS and cannot lead to any kination-domination era when $\phi \to f_a$, cf. Fig. 7.8.

G.4.5 Derivation of the cosmological-history relations

In this appendix, we derive the expression used in Sec. 7.2.2, neglecting the factor $(\epsilon/2)$, and for which we refer to App. G.4.3.

Matter domination. After the field starts oscillating at $3H_{\rm osc} = m_{r,\rm eff}$, it redshifts like matter and induces a matter-domination era as soon as it dominates the energy density of the Universe when

$$\rho_{\rm dom} \equiv V(\phi_{\rm ini})\left(\frac{a_{\rm osc}}{a_{\rm dom}}\right)^3 \simeq 3H_{\rm osc}^2 M_{\rm pl}^2\left(\frac{a_{\rm osc}}{a_{\rm dom}}\right)^4, \tag{G.176}$$

where we have neglected the change of relativistic degrees of freedom in the thermal bath. We obtain

$$\frac{a_{\rm dom}}{a_{\rm osc}} \simeq \frac{M_{\rm Pl}^2 m_{\rm eff}^2(\phi_{\rm ini})}{3V(\phi_{\rm ini})} \text{ and } \rho_{\rm dom} = \frac{27V^4(\phi_{\rm ini})}{M_{\rm Pl}^6 m_{\rm eff}^6(\phi_{\rm ini})}. \tag{G.177}$$

Radial damping. The decay of the radial mode, occuring at the rate Γ, dissipates the radial kinetic energy when

$$\Gamma \simeq H \qquad \Rightarrow \qquad \rho_{\rm damp} = 3M_{\rm Pl}^2\Gamma^2, \tag{G.178}$$

after that the Universe has expanded by

$$\frac{a_{\rm damp}}{a_{\rm dom}} = \left(\frac{\rho_{\rm dom}}{\rho_{\rm damp}}\right)^{1/3} = \left[\frac{9V^4(\phi_{\rm ini})}{M_{\rm Pl}^8\Gamma^2 m_{\rm eff}^6(\phi_{\rm ini})}\right]^{1/3}. \tag{G.179}$$

Start of kination (starting). The scalar field reaches the kination-liked equation of state when the radial field-value settles down to its final VEV $\phi \to f_a$, when the energy density is

$$\rho_{{\rm KD},i} = \frac{1}{2}\cancel{\dot\phi^2} + \frac{1}{2}\phi^2\dot\theta^2 + V(\phi \to f_a) \simeq \frac{1}{2}\phi^2\dot\theta^2 \;\Rightarrow\; \rho_{{\rm KD},i} \simeq \frac{1}{2}f^2 m_{\rm eff}^2(f), \tag{G.180}$$

where the radial kinetic energy vanishes after $H < \Gamma$ and where we assume the vacuum energy to vanish at the minimum. The duration of the matter era reads

$$\frac{a_{{\rm KD},i}}{\min(a_{\rm dom},\, a_{\rm damp})} = \left(\frac{\rho_{\rm damp}}{\rho_{\rm KD}}\right)^{1/3}. \tag{G.181}$$

End of kination. The period of kination lasts until the energy density of the scalar field drops below that of thermal bath. The value of the radiation energy density depends on whether entropy has been injected during the damping of the radial mode. This depends on whether radial damping has occured after domination $\rho_{\rm damp} < \rho_{\rm dom}$, or not. Its energy density at the end of kination era follows the scaling law

$$\rho_{\rm rad} = \rho_{{\rm KD},f} = \begin{cases} \rho_{\rm dom}\left(\frac{a_{\rm dom}}{a_{{\rm KD},f}}\right)^4, & \text{if } \rho_{\rm damp} > \rho_{\rm dom}, \\ \rho_{\rm damp}\left(\frac{a_{\rm damp}}{a_{{\rm KD},f}}\right)^4, & \text{if } \rho_{\rm damp} < \rho_{\rm dom}. \end{cases} \tag{G.182}$$

Similarly, the scalar field which has undergone a period of matter folowed by a period of kination has the energy density

$$\rho_\Phi = \rho_{{\rm KD},f} = \begin{cases} \rho_{\rm dom}\left(\frac{a_{\rm dom}}{a_{{\rm KD},i}}\right)^3\left(\frac{a_{{\rm KD},i}}{a_{{\rm KD},f}}\right)^6, & \text{if } \rho_{\rm damp} > \rho_{\rm dom}, \\ \rho_{\rm damp}\left(\frac{a_{\rm damp}}{a_{{\rm KD},i}}\right)^3\left(\frac{a_{{\rm KD},i}}{a_{{\rm KD},f}}\right)^6, & \text{if } \rho_{\rm damp} < \rho_{\rm dom}. \end{cases} \tag{G.183}$$

From the above two equations, we deduce the energy density at the end of kination $\rho_{{\rm KD},f}$

$$\rho_{{\rm KD},f} = \begin{cases} \frac{\rho_{\rm KD,i}^2}{\rho_{\rm dom}}, & \text{if } \rho_{\rm damp} > \rho_{\rm dom}, \\ \frac{\rho_{\rm KD,i}^2}{\rho_{\rm damp}}, & \text{if } \rho_{\rm damp} < \rho_{\rm dom}, \end{cases} \tag{G.184}$$

and the duration of the kination era

$$\frac{a_{{\rm KD},f}}{a_{{\rm KD},i}} = \begin{cases} \left(\frac{\rho_{\rm dom}}{\rho_{{\rm KD},i}}\right)^{1/6}, & \text{if } \rho_{\rm damp} > \rho_{\rm dom}, \\ \left(\frac{\rho_{\rm damp}}{\rho_{{\rm KD},i}}\right)^{1/6}, & \text{if } \rho_{\rm damp} < \rho_{\rm dom}. \end{cases} \tag{G.185}$$

Bibliography

[1] Y. Gouttenoire, G. Servant and P. Simakachorn, *Beyond the Standard Models with Cosmic Strings*, *JCAP* **07** (2020) 032, [1912.02569].

[2] Y. Gouttenoire, G. Servant and P. Simakachorn, *BSM with Cosmic Strings: Heavy, up to EeV mass, Unstable Particles*, *JCAP* **07** (2020) 016, [1912.03245].

[3] Y. Gouttenoire, G. Servant and P. Simakachorn, *Revealing the Primordial Irreducible Inflationary Gravitational-Wave Background with a Spinning Peccei-Quinn Axion*, 2108.10328.

[4] Y. Gouttenoire, G. Servant and P. Simakachorn, *Kination Cosmology from Scalar Fields and Gravitational-Wave Signatures*, 2111.01150.

[5] LISA Cosmology Working Group collaboration, P. Auclair et al., *Cosmology with the Laser Interferometer Space Antenna*, 2204.05434.

[6] ATLAS collaboration, G. Aad et al., *Observation of a new particle in the search for the Standard Model Higgs boson with the ATLAS detector at the LHC*, *Phys. Lett. B* **716** (2012) 1–29, [1207.7214].

[7] CMS collaboration, S. Chatrchyan et al., *Observation of a New Boson at a Mass of 125 GeV with the CMS Experiment at the LHC*, *Phys. Lett. B* **716** (2012) 30–61, [1207.7235].

[8] LIGO Scientific, Virgo collaboration, B. P. Abbott et al., *Observation of Gravitational Waves from a Binary Black Hole Merger*, *Phys. Rev. Lett.* **116** (2016) 061102, [1602.03837].

[9] LIGO Scientific, Virgo collaboration, B. P. Abbott et al., *GW150914: First results from the search for binary black hole coalescence with Advanced LIGO*, *Phys. Rev. D* **93** (2016) 122003, [1602.03839].

[10] D. W. Hogg, D. J. Eisenstein, M. R. Blanton, N. A. Bahcall, J. Brinkmann, J. E. Gunn et al., *Cosmic homogeneity demonstrated with luminous red galaxies*, *Astrophys. J.* **624** (2005) 54–58, [astro-ph/0411197].

[11] P. Ntelis et al., *Exploring cosmic homogeneity with the BOSS DR12 galaxy sample*, *JCAP* **06** (2017) 019, [1702.02159].

[12] Planck collaboration, Y. Akrami et al., *Planck 2018 results. I. Overview and the cosmological legacy of Planck*, 1807.06205.

[13] A. Friedmann, *On the Possibility of a world with constant negative curvature of space*, *Z. Phys.* **21** (1924) 326–332.

[14] G. Lemaitre, *A Homogeneous Universe of Constant Mass and Growing Radius Accounting for the Radial Velocity of Extragalactic Nebulae*, *Annales Soc. Sci. Bruxelles A* **47** (1927) 49–59.

[15] H. P. Robertson, *Relativistic Cosmology*, *Rev. Mod. Phys.* **5** (1933) 62–90.

[16] A. G. Walker, *On milne's theory of world-structure*, *Proceedings of the London Mathematical Society* **2** (1937) 90–127.

[17] Planck collaboration, N. Aghanim et al., *Planck 2018 results. VI. Cosmological parameters*, *Astron. Astrophys.* **641** (2020) A6, [1807.06209].

[18] A. Einstein, *The Field Equations of Gravitation*, *Sitzungsber. Preuss. Akad. Wiss. Berlin (Math. Phys.)* **1915** (1915) 844–847.

[19] A. H. Guth, *The Inflationary Universe: A Possible Solution to the Horizon and Flatness Problems*, *Phys. Rev. D* **23** (1981) 347–356.

[20] Planck collaboration, Y. Akrami et al., *Planck 2018 results. X. Constraints on inflation*, 1807.06211.

[21] BICEP, Keck collaboration, P. A. R. Ade et al., *Improved Constraints on Primordial Gravitational Waves using Planck, WMAP, and BICEP/Keck Observations through the 2018 Observing Season*, *Phys. Rev. Lett.* **127** (2021) 151301, [2110.00483].

[22] K. Saikawa and S. Shirai, *Primordial gravitational waves, precisely: The role of thermodynamics in the Standard Model*, *JCAP* **1805** (2018) 035, [1803.01038].

[23] Particle Data Group collaboration, P. A. Zyla et al., *Review of Particle Physics*, *PTEP* **2020** (2020) 083C01.

[24] R. H. Cyburt, B. D. Fields, K. A. Olive and T.-H. Yeh, *Big Bang Nucleosynthesis: 2015*, *Rev. Mod. Phys.* **88** (2016) 015004, [1505.01076].

[25] M. Ouchi, Y. Ono and T. Shibuya, *Observations of the Lyman-α Universe*, *Ann. Rev. Astron. Astrophys.* **58** (2020) 617–659, [2012.07960].

[26] A. Einstein, *Approximative Integration of the Field Equations of Gravitation*, *Sitzungsber. Preuss. Akad. Wiss. Berlin (Math. Phys.)* **1916** (1916) 688–696.

[27] A. Einstein, *Über Gravitationswellen*, *Sitzungsber. Preuss. Akad. Wiss. Berlin (Math. Phys.)* **1918** (1918) 154–167.

[28] KAGRA, LIGO Scientific, Virgo, VIRGO collaboration, B. P. Abbott et al., *Prospects for observing and localizing gravitational-wave transients with Advanced LIGO, Advanced Virgo and KAGRA*, *Living Rev. Rel.* **21** (2018) 3, [1304.0670].

[29] M. Maggiore, *Gravitational wave experiments and early universe cosmology*, *Phys. Rept.* **331** (2000) 283–367, [gr-qc/9909001].

[30] P. D. Lasky et al., *Gravitational-wave cosmology across 29 decades in frequency*, *Phys. Rev.* **X6** (2016) 011035, [1511.05994].

[31] C. Caprini and D. G. Figueroa, *Cosmological Backgrounds of Gravitational Waves*, *Class. Quant. Grav.* **35** (2018) 163001, [1801.04268].

[32] A. I. Renzini, B. Goncharov, A. C. Jenkins and P. M. Meyers, *Stochastic Gravitational-Wave Backgrounds: Current Detection Efforts and Future Prospects*, *Galaxies* **10** (2022) 34, [2202.00178].

[33] Particle Data Group collaboration, M. Tanabashi et al., *Review of Particle Physics*, *Phys. Rev.* **D98** (2018) 030001.

[34] E. W. Kolb and M. S. Turner, *The Early Universe*, vol. 69. 1990, 10.1201/9780429492860.

[35] N. Bartolo, V. Domcke, D. G. Figueroa, J. García-Bellido, M. Peloso, M. Pieroni et al., *Probing non-Gaussian Stochastic Gravitational Wave Backgrounds with LISA*, *JCAP* **11** (2018) 034, [1806.02819].

[36] C. S. Machado, W. Ratzinger, P. Schwaller and B. A. Stefanek, *Audible Axions*, *JHEP* **01** (2019) 053, [1811.01950].

[37] LISA Cosmology Working Group collaboration, N. Bartolo et al., *Probing Anisotropies of the Stochastic Gravitational Wave Background with Lisa*, *JCAP* **11** (2022) 009, [2201.08782].

[38] Z.-Y. Wu, R. Saito and N. Sakai, *Antipodal Angular Correlations of Inflationary Stochastic Gravitational Wave Background*, 2207.04669.

[39] Particle Data Group collaboration, M. Tanabashi et al., *Review of Particle Physics*, *Phys. Rev.* **D98** (2018) 030001.

[40] N. Aggarwal et al., *Challenges and Opportunities of Gravitational-Wave Searches at Mhz to Ghz Frequencies*, *Living Rev. Rel.* **24** (2021) 4, [2011.12414].

[41] G. Franciolini, A. Maharana and F. Muia, *Hunt for Light Primordial Black Hole Dark Matter with Ultrahigh-Frequency Gravitational Waves*, *Phys. Rev. D* **106** (2022) 103520, [2205.02153].

[42] G. Mangano and P. D. Serpico, *A robust upper limit on $N_{\rm eff}$ from BBN, circa 2011*, *Phys. Lett.* **B701** (2011) 296–299, [1103.1261].

[43] A. Peimbert, M. Peimbert and V. Luridiana, *The Primordial Helium Abundance and the Number of Neutrino Families*, *Rev. Mex. Astron. Astrofis.* **52** (2016) 419–424, [1608.02062].

[44] G. Mangano, G. Miele, S. Pastor, T. Pinto, O. Pisanti and P. D. Serpico, *Relic neutrino decoupling including flavor oscillations*, *Nucl. Phys.* **B729** (2005) 221–234, [hep-ph/0506164].

[45] P. F. de Salas and S. Pastor, *Relic neutrino decoupling with flavour oscillations revisited*, *JCAP* **07** (2016) 051, [1606.06986].

[46] M. Escudero Abenza, *Precision Early Universe Thermodynamics made simple: $N_{\rm eff}$ and Neutrino Decoupling in the Standard Model and beyond*, 2001.04466.

[47] CMB-S4 collaboration, K. N. Abazajian et al., *Cmb-S4 Science Book, First Edition*, 1610.02743.

[48] G. Domènech, *Scalar Induced Gravitational Waves Review*, *Universe* **7** (2021) 398, [2109.01398].

[49] J. T. Giblin and E. Thrane, *Estimates of maximum energy density of cosmological gravitational-wave backgrounds*, *Phys. Rev. D* **90** (2014) 107502, [1410.4779].

[50] Y. Gouttenoire, *Beyond the Standard Model Cocktail*, 2207.01633.

[51] L. P. Grishchuk, *Amplification of Gravitational Waves in an Istropic Universe*, *Zh. Eksp. Teor. Fiz.* **67** (1974) 825–838.

[52] A. A. Starobinsky, *Spectrum of Relict Gravitational Radiation and the Early State of the Universe*, *JETP Lett.* **30** (1979) 682–685.

[53] V. A. Rubakov, M. V. Sazhin and A. V. Veryaskin, *Graviton Creation in the Inflationary Universe and the Grand Unification Scale*, *Phys. Lett. B* **115** (1982) 189–192.

[54] R. Fabbri and M. d. Pollock, *The Effect of Primordially Produced Gravitons upon the Anisotropy of the Cosmological Microwave Background Radiation*, *Phys. Lett. B* **125** (1983) 445–448.

[55] BICEP2, Keck Array collaboration, P. A. R. Ade et al., *BICEP2 / Keck Array x: Constraints on Primordial Gravitational Waves using Planck, WMAP, and New BICEP2/Keck Observations through the 2015 Season*, *Phys. Rev. Lett.* **121** (2018) 221301, [1810.05216].

[56] S. Matarrese, O. Pantano and D. Saez, *A General relativistic approach to the nonlinear evolution of collisionless matter*, *Phys. Rev. D* **47** (1993) 1311–1323.

[57] S. Matarrese, O. Pantano and D. Saez, *General relativistic dynamics of irrotational dust: Cosmological implications*, *Phys. Rev. Lett.* **72** (1994) 320–323, [astro-ph/9310036].

[58] S. Matarrese, S. Mollerach and M. Bruni, *Second order perturbations of the Einstein-de Sitter universe*, *Phys. Rev. D* **58** (1998) 043504, [astro-ph/9707278].

[59] H. Noh and J.-c. Hwang, *Second-order perturbations of the Friedmann world model*, *Phys. Rev. D* **69** (2004) 104011.

[60] C. Carbone and S. Matarrese, *A Unified treatment of cosmological perturbations from super-horizon to small scales*, *Phys. Rev. D* **71** (2005) 043508, [astro-ph/0407611].

[61] S. Mollerach, D. Harari and S. Matarrese, *CMB polarization from secondary vector and tensor modes*, *Phys. Rev. D* **69** (2004) 063002, [astro-ph/0310711].

[62] K. N. Ananda, C. Clarkson and D. Wands, *The Cosmological gravitational wave background from primordial density perturbations*, *Phys. Rev. D* **75** (2007) 123518, [gr-qc/0612013].

[63] D. Baumann, P. J. Steinhardt, K. Takahashi and K. Ichiki, *Gravitational Wave Spectrum Induced by Primordial Scalar Perturbations*, *Phys. Rev. D* **76** (2007) 084019, [hep-th/0703290].

[64] S. Weinberg, *Damping of tensor modes in cosmology*, *Phys. Rev. D* **69** (2004) 023503, [astro-ph/0306304].

[65] LISA collaboration, H. Audley et al., *Laser Interferometer Space Antenna*, 1702.00786.

[66] S. Hild et al., *Sensitivity Studies for Third-Generation Gravitational Wave Observatories*, *Class. Quant. Grav.* **28** (2011) 094013, [1012.0908].

[67] M. Punturo et al., *The Einstein Telescope: A third-generation gravitational wave observatory*, *Class. Quant. Grav.* **27** (2010) 194002.

[68] K. Yagi and N. Seto, *Detector configuration of DECIGO/BBO and identification of cosmological neutron-star binaries*, *Phys. Rev.* **D83** (2011) 044011, [1101.3940].

[69] K. Nakayama, S. Saito, Y. Suwa and J. Yokoyama, *Probing reheating temperature of the universe with gravitational wave background*, *JCAP* **0806** (2008) 020, [0804.1827].

[70] L. A. Boyle and P. J. Steinhardt, *Probing the early universe with inflationary gravitational waves*, *Phys. Rev.* **D77** (2008) 063504, [astro-ph/0512014].

[71] D. G. Figueroa and E. H. Tanin, *Ability of Ligo and Lisa to Probe the Equation of State of the Early Universe*, *JCAP* **08** (2019) 011, [1905.11960].

[72] S. Weinberg, *Gravitation and Cosmology*. John Wiley and Sons, New York, 1972.

[73] J. Ghiglieri and M. Laine, *Gravitational wave background from Standard Model physics: Qualitative features*, *JCAP* **07** (2015) 022, [1504.02569].

[74] J. Ghiglieri, G. Jackson, M. Laine and Y. Zhu, *Gravitational wave background from Standard Model physics: Complete leading order*, *JHEP* **07** (2020) 092, [2004.11392].

[75] A. Ringwald, J. Schütte-Engel and C. Tamarit, *Gravitational Waves as a Big Bang Thermometer*, *JCAP* **03** (2021) 054, [2011.04731].

[76] A. Ringwald and C. Tamarit, *Revealing the Cosmic History with Gravitational Waves*, *Phys. Rev. D* **106** (2022) 063027, [2203.00621].

[77] L. D. Landau and E. M. Lifshitz, *Statistical Physics: Volume 5*, vol. 5. Elsevier, 2013.

[78] P. B. Arnold, G. D. Moore and L. G. Yaffe, *Transport coefficients in high temperature gauge theories. 1. Leading log results*, *JHEP* **11** (2000) 001, [hep-ph/0010177].

[79] P. B. Arnold, G. D. Moore and L. G. Yaffe, *Transport coefficients in high temperature gauge theories. 2. Beyond leading log*, *JHEP* **05** (2003) 051, [hep-ph/0302165].

[80] A. D. Dolgov and A. D. Linde, *Baryon Asymmetry in Inflationary Universe*, *Phys. Lett. B* **116** (1982) 329.

[81] L. Abbott, E. Farhi and M. B. Wise, *Particle Production in the New Inflationary Cosmology*, *Phys. Lett. B* **117** (1982) 29.

[82] L. Kofman, A. D. Linde and A. A. Starobinsky, *Reheating after inflation*, *Phys. Rev. Lett.* **73** (1994) 3195–3198, [hep-th/9405187].

[83] L. Kofman, A. D. Linde and A. A. Starobinsky, *Towards the theory of reheating after inflation*, *Phys. Rev.* **D56** (1997) 3258–3295, [hep-ph/9704452].

[84] R. Allahverdi, R. Brandenberger, F.-Y. Cyr-Racine and A. Mazumdar, *Reheating in Inflationary Cosmology: Theory and Applications*, *Ann. Rev. Nucl. Part. Sci.* **60** (2010) 27–51, [1001.2600].

[85] M. A. Amin, M. P. Hertzberg, D. I. Kaiser and J. Karouby, *Nonperturbative Dynamics Of Reheating After Inflation: A Review*, *Int. J. Mod. Phys. D* **24** (2014) 1530003, [1410.3808].

[86] K. D. Lozanov, *Lectures on Reheating After Inflation*, 1907.04402.

[87] A. D. Linde, *Particle physics and inflationary cosmology*, vol. 5. 1990.

[88] Y. Ema, R. Jinno and K. Nakayama, *High-frequency Graviton from Inflaton Oscillation*, *JCAP* **09** (2020) 015, [2006.09972].

[89] P. B. Greene, L. Kofman, A. D. Linde and A. A. Starobinsky, *Structure of resonance in preheating after inflation*, *Phys. Rev. D* **56** (1997) 6175–6192, [hep-ph/9705347].

[90] J. H. Traschen and R. H. Brandenberger, *Particle Production During Out-of-equilibrium Phase Transitions*, *Phys. Rev.* **D42** (1990) 2491–2504.

[91] Y. Shtanov, J. H. Traschen and R. H. Brandenberger, *Universe reheating after inflation*, *Phys. Rev.* **D51** (1995) 5438–5455, [hep-ph/9407247].

[92] D. I. Kaiser, *Post inflation reheating in an expanding universe*, *Phys. Rev. D* **53** (1996) 1776–1783, [astro-ph/9507108].

[93] D. I. Kaiser, *Preheating in an expanding universe: Analytic results for the massless case*, *Phys. Rev. D* **56** (1997) 706–716, [hep-ph/9702244].

[94] D. I. Kaiser, *Resonance structure for preheating with massless fields*, *Phys. Rev. D* **57** (1998) 702–711, [hep-ph/9707516].

[95] G. N. Felder, J. Garcia-Bellido, P. B. Greene, L. Kofman, A. D. Linde and I. Tkachev, *Dynamics of symmetry breaking and tachyonic preheating*, *Phys. Rev. Lett.* **87** (2001) 011601, [hep-ph/0012142].

[96] G. N. Felder, L. Kofman and A. D. Linde, *Tachyonic instability and dynamics of spontaneous symmetry breaking*, *Phys. Rev. D* **64** (2001) 123517, [hep-th/0106179].

[97] E. J. Copeland, S. Pascoli and A. Rajantie, *Dynamics of tachyonic preheating after hybrid inflation*, *Phys. Rev. D* **65** (2002) 103517, [hep-ph/0202031].

[98] J. Garcia-Bellido, M. Garcia Perez and A. Gonzalez-Arroyo, *Symmetry breaking and false vacuum decay after hybrid inflation*, *Phys. Rev. D* **67** (2003) 103501, [hep-ph/0208228].

[99] R. Easther, J. T. Giblin and E. A. Lim, *Gravitational Waves From the End of Inflation: Computational Strategies*, *Phys. Rev. D* **77** (2008) 103519, [0712.2991].

[100] J. Garcia-Bellido and D. G. Figueroa, *A stochastic background of gravitational waves from hybrid preheating*, *Phys. Rev. Lett.* **98** (2007) 061302, [astro-ph/0701014].

[101] J.-F. Dufaux, D. G. Figueroa and J. Garcia-Bellido, *Gravitational Waves from Abelian Gauge Fields and Cosmic Strings at Preheating*, *Phys. Rev. D* **82** (2010) 083518, [1006.0217].

[102] S. Y. Khlebnikov and I. I. Tkachev, *Relic gravitational waves produced after preheating*, *Phys. Rev. D* **56** (1997) 653–660, [hep-ph/9701423].

[103] P. B. Greene and L. Kofman, *Preheating of fermions*, *Phys. Lett. B* **448** (1999) 6–12, [hep-ph/9807339].

[104] P. B. Greene and L. Kofman, *On the theory of fermionic preheating*, *Phys. Rev. D* **62** (2000) 123516, [hep-ph/0003018].

[105] M. Peloso and L. Sorbo, *Preheating of massive fermions after inflation: Analytical results*, *JHEP* **05** (2000) 016, [hep-ph/0003045].

[106] R. Easther and E. A. Lim, *Stochastic gravitational wave production after inflation*, *JCAP* **04** (2006) 010, [astro-ph/0601617].

[107] R. Easther, J. T. Giblin, Jr. and E. A. Lim, *Gravitational Wave Production At The End Of Inflation*, *Phys. Rev. Lett.* **99** (2007) 221301, [astro-ph/0612294].

[108] J. Garcia-Bellido, D. G. Figueroa and A. Sastre, *A Gravitational Wave Background from Reheating after Hybrid Inflation*, *Phys. Rev. D* **77** (2008) 043517, [0707.0839].

[109] J. F. Dufaux, A. Bergman, G. N. Felder, L. Kofman and J.-P. Uzan, *Theory and Numerics of Gravitational Waves from Preheating after Inflation*, *Phys. Rev. D* **76** (2007) 123517, [0707.0875].

[110] J.-F. Dufaux, G. Felder, L. Kofman and O. Navros, *Gravity Waves from Tachyonic Preheating after Hybrid Inflation*, *JCAP* **03** (2009) 001, [0812.2917].

[111] J. Berges, D. Gelfand and J. Pruschke, *Quantum theory of fermion production after inflation*, *Phys. Rev. Lett.* **107** (2011) 061301, [1012.4632].

[112] D. G. Figueroa, J. Garcia-Bellido and A. Rajantie, *On the Transverse-Traceless Projection in Lattice Simulations of Gravitational Wave Production*, *JCAP* **11** (2011) 015, [1110.0337].

[113] K. Enqvist, D. G. Figueroa and T. Meriniemi, *Stochastic Background of Gravitational Waves from Fermions*, *Phys. Rev. D* **86** (2012) 061301, [1203.4943].

[114] L. Bethke, D. G. Figueroa and A. Rajantie, *Anisotropies in the Gravitational Wave Background from Preheating*, *Phys. Rev. Lett.* **111** (2013) 011301, [1304.2657].

[115] L. Bethke, D. G. Figueroa and A. Rajantie, *On the Anisotropy of the Gravitational Wave Background from Massless Preheating*, *JCAP* **06** (2014) 047, [1309.1148].

[116] D. G. Figueroa and T. Meriniemi, *Stochastic Background of Gravitational Waves from Fermions – Theory and Applications*, *JHEP* **10** (2013) 101, [1306.6911].

[117] D. G. Figueroa, *A gravitational wave background from the decay of the standard model Higgs after inflation*, *JHEP* **11** (2014) 145, [1402.1345].

[118] D. G. Figueroa and F. Torrenti, *Gravitational wave production from preheating: parameter dependence*, *JCAP* **10** (2017) 057, [1707.04533].

[119] D. G. Figueroa, A. Florio, N. Loayza and M. Pieroni, *Spectroscopy of Particle Couplings with Gravitational Waves*, *Phys. Rev. D* **106** (2022) 063522, [2202.05805].

[120] S. Antusch, K. Marschall and F. Torrenti, *Characterizing the Post-Inflationary Reheating History, Part Ii: Multiple Interacting Daughter Fields*, 2206.06319.

[121] C. Cosme, D. G. Figueroa and N. Loayza, *Gravitational Wave Production from Preheating with Trilinear Interactions*, 2206.14721.

[122] D. G. Figueroa, A. Florio, F. Torrenti and W. Valkenburg, *The art of simulating the early Universe – Part I*, *JCAP* **04** (2021) 035, [2006.15122].

[123] D. G. Figueroa, A. Florio, F. Torrenti and W. Valkenburg, *Cosmolattice*, *Comput. Phys. Commun.* **283** (2023) 108586, [2102.01031].

[124] J. L. Cook and L. Sorbo, *Particle production during inflation and gravitational waves detectable by ground-based interferometers*, *Phys. Rev. D* **85** (2012) 023534, [1109.0022].

[125] N. Barnaby and M. Peloso, *Large Nongaussianity in Axion Inflation*, *Phys. Rev. Lett.* **106** (2011) 181301, [1011.1500].

[126] N. Barnaby, E. Pajer and M. Peloso, *Gauge Field Production in Axion Inflation: Consequences for Monodromy, non-Gaussianity in the CMB, and Gravitational Waves at Interferometers*, *Phys. Rev. D* **85** (2012) 023525, [1110.3327].

[127] C. S. Machado, W. Ratzinger, P. Schwaller and B. A. Stefanek, *Gravitational wave probes of axionlike particles*, *Phys. Rev. D* **102** (2020) 075033, [1912.01007].

[128] R. T. Co, K. Harigaya and A. Pierce, *Gravitational Waves and Dark Photon Dark Matter from Axion Rotations*, *JHEP* **12** (2021) 099, [2104.02077].

[129] N. Fonseca, E. Morgante, R. Sato and G. Servant, *Axion fragmentation*, *JHEP* **04** (2020) 010, [1911.08472].

[130] E. Morgante, W. Ratzinger, R. Sato and B. A. Stefanek, *Axion Fragmentation on the Lattice*, *JHEP* **12** (2021) 037, [2109.13823].

[131] E. Madge, W. Ratzinger, D. Schmitt and P. Schwaller, *Audible axions with a booster: Stochastic gravitational waves from rotating ALPs*, *SciPost Phys.* **12** (2022) 171, [2111.12730].

[132] C. Eröncel, R. Sato, G. Servant and P. Sørensen, *ALP dark matter from kinetic fragmentation: opening up the parameter window*, *JCAP* **10** (2022) 053, [2206.14259].

[133] K. Kajantie, M. Laine, K. Rummukainen and M. E. Shaposhnikov, *The Electroweak phase transition: A Nonperturbative analysis*, *Nucl. Phys. B* **466** (1996) 189–258, [hep-lat/9510020].

[134] F. Csikor, Z. Fodor and J. Heitger, *Endpoint of the hot electroweak phase transition*, *Phys. Rev. Lett.* **82** (1999) 21–24, [hep-ph/9809291].

[135] M. A. Stephanov, *QCD phase diagram: An Overview*, *PoS* **LAT2006** (2006) 024, [hep-lat/0701002].

[136] A. H. Guth and E. J. Weinberg, *Could the Universe Have Recovered from a Slow First Order Phase Transition?*, *Nucl. Phys. B* **212** (1983) 321–364.

[137] V. A. Kuzmin, V. A. Rubakov and M. E. Shaposhnikov, *On the Anomalous Electroweak Baryon Number Nonconservation in the Early Universe*, *Phys. Lett. B* **155** (1985) 36.

[138] V. A. Rubakov and M. E. Shaposhnikov, *Electroweak baryon number nonconservation in the early universe and in high-energy collisions*, *Usp. Fiz. Nauk* **166** (1996) 493–537, [hep-ph/9603208].

[139] J. M. Cline, C. Grojean and G. Servant, *Cosmological expansion in the presence of extra dimensions*, *Phys. Rev. Lett.* **83** (1999) 4245, [hep-ph/9906523].

[140] C. Grojean and G. Servant, *Gravitational Waves from Phase Transitions at the Electroweak Scale and Beyond*, *Phys. Rev.* **D75** (2007) 043507, [hep-ph/0607107].

[141] L. Randall and G. Servant, *Gravitational waves from warped spacetime*, *JHEP* **05** (2007) 054, [hep-ph/0607158].

[142] K. Petraki, M. Trodden and R. R. Volkas, *Visible and dark matter from a first-order phase transition in a baryon-symmetric universe*, *JCAP* **02** (2012) 044, [1111.4786].

[143] M. J. Baker, J. Kopp and A. J. Long, *Filtered Dark Matter at a First Order Phase Transition*, *Phys. Rev. Lett.* **125** (2020) 151102, [1912.02830].

[144] B. Von Harling, A. Pomarol, O. Pujolàs and F. Rompineve, *Peccei-Quinn Phase Transition at LIGO*, *JHEP* **04** (2020) 195, [1912.07587].

[145] L. Delle Rose, G. Panico, M. Redi and A. Tesi, *Gravitational Waves from Supercool Axions*, *JHEP* **04** (2020) 025, [1912.06139].

[146] I. Baldes, Y. Gouttenoire and F. Sala, *String Fragmentation in Supercooled Confinement and Implications for Dark Matter*, *JHEP* **04** (2021) 278, [2007.08440].

[147] I. Baldes, Y. Gouttenoire, F. Sala and G. Servant, *Supercool composite Dark Matter beyond 100 TeV*, *JHEP* **07** (2022) 084, [2110.13926].

[148] E. Witten, *Cosmic Separation of Phases*, *Phys. Rev. D* **30** (1984) 272–285.

[149] C. J. Hogan, *Gravitational Radiation from Cosmological Phase Transitions*, *Mon. Not. Roy. Astron. Soc.* **218** (1986) 629–636.

[150] J. R. Espinosa, T. Konstandin, J. M. No and G. Servant, *Energy Budget of Cosmological First-order Phase Transitions*, *JCAP* **06** (2010) 028, [1004.4187].

[151] F. Giese, T. Konstandin, K. Schmitz and J. Van De Vis, *Model-independent energy budget for LISA*, *JCAP* **01** (2021) 072, [2010.09744].

[152] C. Caprini et al., *Science with the space-based interferometer eLISA. II: Gravitational waves from cosmological phase transitions*, *JCAP* **1604** (2016) 001, [1512.06239].

[153] C. Caprini et al., *Detecting gravitational waves from cosmological phase transitions with LISA: an update*, *JCAP* **03** (2020) 024, [1910.13125].

[154] J. Ellis, M. Lewicki and J. M. No, *Gravitational waves from first-order cosmological phase transitions: lifetime of the sound wave source*, *JCAP* **07** (2020) 050, [2003.07360].

[155] C. Caprini, R. Durrer and G. Servant, *Gravitational wave generation from bubble collisions in first-order phase transitions: An analytic approach*, *Phys. Rev.* **D77** (2008) 124015, [0711.2593].

[156] S. J. Huber and T. Konstandin, *Gravitational Wave Production by Collisions: More Bubbles*, *JCAP* **09** (2008) 022, [0806.1828].

[157] R. Jinno and M. Takimoto, *Gravitational waves from bubble collisions: An analytic derivation*, *Phys. Rev.* **D95** (2017) 024009, [1605.01403].

[158] D. J. Weir, *Revisiting the envelope approximation: gravitational waves from bubble collisions*, *Phys. Rev. D* **93** (2016) 124037, [1604.08429].

[159] T. Konstandin, *Gravitational radiation from a bulk flow model*, *JCAP* **03** (2018) 047, [1712.06869].

[160] R. Jinno and M. Takimoto, *Gravitational waves from bubble dynamics: Beyond the Envelope*, *JCAP* **1901** (2019) 060, [1707.03111].

[161] M. Kamionkowski, A. Kosowsky and M. S. Turner, *Gravitational radiation from first order phase transitions*, *Phys. Rev. D* **49** (1994) 2837–2851, [astro-ph/9310044].

[162] M. Hindmarsh, S. J. Huber, K. Rummukainen and D. J. Weir, *Gravitational waves from the sound of a first order phase transition*, *Phys. Rev. Lett.* **112** (2014) 041301, [1304.2433].

[163] J. T. Giblin and J. B. Mertens, *Gravitional radiation from first-order phase transitions in the presence of a fluid*, *Phys. Rev. D* **90** (2014) 023532, [1405.4005].

[164] M. Hindmarsh, S. J. Huber, K. Rummukainen and D. J. Weir, *Numerical simulations of acoustically generated gravitational waves at a first order phase transition*, *Phys. Rev. D* **92** (2015) 123009, [1504.03291].

[165] M. Hindmarsh, *Sound shell model for acoustic gravitational wave production at a first-order phase transition in the early Universe*, *Phys. Rev. Lett.* **120** (2018) 071301, [1608.04735].

[166] M. Hindmarsh, S. J. Huber, K. Rummukainen and D. J. Weir, *Shape of the acoustic gravitational wave power spectrum from a first order phase transition*, *Phys. Rev. D* **96** (2017) 103520, [1704.05871].

[167] M. Hindmarsh and M. Hijazi, *Gravitational waves from first order cosmological phase transitions in the Sound Shell Model*, *JCAP* **12** (2019) 062, [1909.10040].

[168] D. Cutting, M. Hindmarsh and D. J. Weir, *Vorticity, kinetic energy, and suppressed gravitational wave production in strong first order phase transitions*, *Phys. Rev. Lett.* **125** (2020) 021302, [1906.00480].

[169] A. Kosowsky, A. Mack and T. Kahniashvili, *Gravitational radiation from cosmological turbulence*, *Phys. Rev.* **D66** (2002) 024030, [astro-ph/0111483].

[170] C. Caprini and R. Durrer, *Gravitational waves from stochastic relativistic sources: Primordial turbulence and magnetic fields*, *Phys. Rev. D* **74** (2006) 063521, [astro-ph/0603476].

[171] C. Caprini, R. Durrer and G. Servant, *The stochastic gravitational wave background from turbulence and magnetic fields generated by a first-order phase transition*, *JCAP* **12** (2009) 024, [0909.0622].

[172] G. Gogoberidze, T. Kahniashvili and A. Kosowsky, *The Spectrum of Gravitational Radiation from Primordial Turbulence*, *Phys. Rev. D* **76** (2007) 083002, [0705.1733].

[173] T. Kahniashvili, A. Kosowsky, G. Gogoberidze and Y. Maravin, *Detectability of Gravitational Waves from Phase Transitions*, *Phys. Rev. D* **78** (2008) 043003, [0806.0293].

[174] T. Kahniashvili, L. Campanelli, G. Gogoberidze, Y. Maravin and B. Ratra, *Gravitational Radiation from Primordial Helical Inverse Cascade MHD Turbulence*, *Phys. Rev. D* **78** (2008) 123006, [0809.1899].

[175] T. Kahniashvili, L. Kisslinger and T. Stevens, *Gravitational Radiation Generated by Magnetic Fields in Cosmological Phase Transitions*, *Phys. Rev. D* **81** (2010) 023004, [0905.0643].

[176] T. Kalaydzhyan and E. Shuryak, *Gravity waves generated by sounds from big bang phase transitions*, *Phys. Rev. D* **91** (2015) 083502, [1412.5147].

[177] U.-L. Pen and N. Turok, *Shocks in the Early Universe*, *Phys. Rev. Lett.* **117** (2016) 131301, [1510.02985].

[178] P. Niksa, M. Schlederer and G. Sigl, *Gravitational Waves produced by Compressible MHD Turbulence from Cosmological Phase Transitions*, *Class. Quant. Grav.* **35** (2018) 144001, [1803.02271].

[179] A. Roper Pol, S. Mandal, A. Brandenburg, T. Kahniashvili and A. Kosowsky, *Numerical simulations of gravitational waves from early-universe turbulence*, *Phys. Rev. D* **102** (2020) 083512, [1903.08585].

[180] A. J. Long and L.-T. Wang, *Dark Photon Dark Matter from a Network of Cosmic Strings*, *Phys. Rev.* **D99** (2019) 063529, [1901.03312].

[181] T. W. B. Kibble, *Topology of Cosmic Domains and Strings*, *J. Phys.* **A9** (1976) 1387–1398.

[182] T. W. B. Kibble, *Some Implications of a Cosmological Phase Transition*, *Phys. Rept.* **67** (1980) 183.

[183] M. B. Hindmarsh and T. W. B. Kibble, *Cosmic strings*, *Rept. Prog. Phys.* **58** (1995) 477–562, [hep-ph/9411342].

[184] T. W. B. Kibble, *Evolution of a system of cosmic strings*, *Nucl. Phys.* **B252** (1985) 227.

[185] D. P. Bennett and F. R. Bouchet, *Evidence for a Scaling Solution in Cosmic String Evolution*, *Phys. Rev. Lett.* **60** (1988) 257.

[186] D. P. Bennett and F. R. Bouchet, *Cosmic string evolution*, *Phys. Rev. Lett.* **63** (1989) 2776.

[187] A. Albrecht and N. Turok, *Evolution of Cosmic String Networks*, *Phys. Rev.* **D40** (1989) 973–1001.

[188] B. Allen and E. P. S. Shellard, *Cosmic string evolution: a numerical simulation*, *Phys. Rev. Lett.* **64** (1990) 119–122.

[189] C. Ringeval, M. Sakellariadou and F. Bouchet, *Cosmological evolution of cosmic string loops*, *JCAP* **0702** (2007) 023, [astro-ph/0511646].

[190] V. Vanchurin, K. D. Olum and A. Vilenkin, *Scaling of cosmic string loops*, *Phys. Rev.* **D74** (2006) 063527, [gr-qc/0511159].

[191] C. J. A. P. Martins and E. P. S. Shellard, *Fractal properties and small-scale structure of cosmic string networks*, *Phys. Rev.* **D73** (2006) 043515, [astro-ph/0511792].

[192] K. D. Olum and V. Vanchurin, *Cosmic string loops in the expanding Universe*, *Phys. Rev.* **D75** (2007) 063521, [astro-ph/0610419].

[193] J. J. Blanco-Pillado, K. D. Olum and B. Shlaer, *Large parallel cosmic string simulations: New results on loop production*, *Phys. Rev.* **D83** (2011) 083514, [1101.5173].

[194] J. J. Blanco-Pillado, K. D. Olum and B. Shlaer, *The number of cosmic string loops*, *Phys. Rev.* **D89** (2014) 023512, [1309.6637].

[195] M. Gorghetto, E. Hardy and G. Villadoro, *Axions from Strings: the Attractive Solution*, *JHEP* **07** (2018) 151, [1806.04677].

[196] M. Gorghetto, E. Hardy and G. Villadoro, *More axions from strings*, *SciPost Phys.* **10** (2021) 050, [2007.04990].

[197] M. Buschmann, J. W. Foster, A. Hook, A. Peterson, D. E. Willcox, W. Zhang et al., *Dark matter from axion strings with adaptive mesh refinement*, *Nature Commun.* **13** (2022) 1049, [2108.05368].

[198] M. Hindmarsh, J. Lizarraga, A. Lopez-Eiguren and J. Urrestilla, *Approach to scaling in axion string networks*, *Phys. Rev. D* **103** (2021) 103534, [2102.07723].

[199] C.-F. Chang and Y. Cui, *Stochastic Gravitational Wave Background from Global Cosmic Strings*, *Phys. Dark Univ.* **29** (2020) 100604, [1910.04781].

[200] J. A. Dror, H. Murayama and N. L. Rodd, *Cosmic axion background*, *Phys. Rev. D* **103** (2021) 115004, [2101.09287].

[201] M. Breitbach, J. Kopp, E. Madge, T. Opferkuch and P. Schwaller, *Dark, Cold, and Noisy: Constraining Secluded Hidden Sectors with Gravitational Waves*, *JCAP* **1907** (2019) 007, [1811.11175].

[202] P. Campeti, E. Komatsu, D. Poletti and C. Baccigalupi, *Measuring the spectrum of primordial gravitational waves with CMB, PTA and Laser Interferometers*, *JCAP* **01** (2021) 012, [2007.04241].

[203] T. Kite, A. Ravenni, S. P. Patil and J. Chluba, *Bridging the gap: spectral distortions meet gravitational waves*, *Mon. Not. Roy. Astron. Soc.* **505** (2021) 4396–4405, [2010.00040].

[204] S. Chen et al., *Common-red-signal analysis with 24-yr high-precision timing of the European Pulsar Timing Array: Inferences in the stochastic gravitational-wave background search*, *Mon. Not. Roy. Astron. Soc.* **508** (2021) 4970–4993, [2110.13184].

[205] NANOGrav collaboration, Z. Arzoumanian et al., *The NANOGrav 12.5 yr Data Set: Search for an Isotropic Stochastic Gravitational-wave Background*, *Astrophys. J. Lett.* **905** (2020) L34, [2009.04496].

[206] B. Goncharov et al., *On the Evidence for a Common-Spectrum Process in the Search for the Nanohertz Gravitational-Wave Background with the Parkes Pulsar Timing Array*, *Astrophys. J. Lett.* **917** (2021) L19, [2107.12112].

[207] G. Janssen et al., *Gravitational wave astronomy with the SKA*, *PoS* **AASKA14** (2015) 037, [1501.00127].

[208] M. Ajello et al., *A Gamma-ray Pulsar Timing Array Constrains the Nanohertz Gravitational Wave Background*, 2204.05226.

[209] C. J. Moore, D. P. Mihaylov, A. Lasenby and G. Gilmore, *Astrometric Search Method for Individually Resolvable Gravitational Wave Sources with Gaia*, *Phys. Rev. Lett.* **119** (2017) 261102, [1707.06239].

[210] J. García-Bellido, H. Murayama and G. White, *Exploring the Early Universe with Gaia and Theia*, *JCAP* **12** (2021) 023, [2104.04778].

[211] M. A. Fedderke, P. W. Graham and S. Rajendran, *Gravity Gradient Noise from Asteroids*, *Phys. Rev. D* **103** (2021) 103017, [2011.13833].

[212] D. Blas and A. C. Jenkins, *Detecting Stochastic Gravitational Waves with Binary Resonance*, *Phys. Rev. D* **105** (2022) 064021, [2107.04063].

[213] S. Rao, M. Brüggen and J. Liske, *Detection of gravitational waves in circular particle accelerators*, *Phys. Rev. D* **102** (2020) 122006, [2012.00529].

[214] A. Berlin et al., *Storage Rings and Gravitational Waves: Summary and Outlook*, in *ARIES WP6 Workshop: Storage Rings and Gravitational Waves*, 5, 2021. 2105.00992.

[215] W.-R. Hu and Y.-L. Wu, *The Taiji Program in Space for gravitational wave physics and the nature of gravity*, *Natl. Sci. Rev.* **4** (2017) 685–686.

[216] W.-H. Ruan, Z.-K. Guo, R.-G. Cai and Y.-Z. Zhang, *Taiji program: Gravitational-wave sources*, *Int. J. Mod. Phys. A* **35** (2020) 2050075, [1807.09495].

[217] TianQin collaboration, J. Luo et al., *TianQin: a space-borne gravitational wave detector*, *Class. Quant. Grav.* **33** (2016) 035010, [1512.02076].

[218] X.-C. Hu, X.-H. Li, Y. Wang, W.-F. Feng, M.-Y. Zhou, Y.-M. Hu et al., *Fundamentals of the orbit and response for TianQin*, *Class. Quant. Grav.* **35** (2018) 095008, [1803.03368].

[219] TianQin collaboration, J. Mei et al., *The TianQin project: current progress on science and technology*, *PTEP* **2021** (2021) 05A107, [2008.10332].

[220] A. Sesana et al., *Unveiling the gravitational universe at μ-Hz frequencies*, *Exper. Astron.* **51** (2021) 1333–1383, [1908.11391].

[221] AEDGE collaboration, Y. A. El-Neaj et al., *AEDGE: Atomic Experiment for Dark Matter and Gravity Exploration in Space*, *EPJ Quant. Technol.* **7** (2020) 6, [1908.00802].

[222] P. W. Graham, J. M. Hogan, M. A. Kasevich and S. Rajendran, *Resonant mode for gravitational wave detectors based on atom interferometry*, *Phys. Rev. D* **94** (2016) 104022, [1606.01860].

[223] MAGIS collaboration, P. W. Graham, J. M. Hogan, M. A. Kasevich, S. Rajendran and R. W. Romani, *Mid-Band Gravitational Wave Detection with Precision Atomic Sensors*, 1711.02225.

[224] L. Badurina et al., *AION: An Atom Interferometer Observatory and Network*, *JCAP* **05** (2020) 011, [1911.11755].

[225] MAGIS-100 collaboration, M. Abe et al., *Matter-wave Atomic Gradiometer Interferometric Sensor (MAGIS-100)*, *Quantum Sci. Technol.* **6** (2021) 044003, [2104.02835].

[226] LIGO Scientific, VIRGO collaboration, J. Aasi et al., *Characterization of the LIGO detectors during their sixth science run*, *Class. Quant. Grav.* **32** (2015) 115012, [1410.7764].

[227] LIGO Scientific, Virgo collaboration, B. P. Abbott et al., *Search for the isotropic stochastic background using data from Advanced LIGO's second observing run*, *Phys. Rev. D* **100** (2019) 061101, [1903.02886].

[228] LIGO Scientific collaboration, B. P. Abbott et al., *Exploring the Sensitivity of Next Generation Gravitational Wave Detectors*, *Class. Quant. Grav.* **34** (2017) 044001, [1607.08697].

[229] LIGO Scientific, Virgo collaboration, B. P. Abbott et al., *GW150914: First results from the search for binary black hole coalescence with Advanced LIGO*, *Phys. Rev.* **D93** (2016) 122003, [1602.03839].

[230] LIGO Scientific, Virgo collaboration, B. P. Abbott et al., *GW151226: Observation of Gravitational Waves from a 22-Solar-Mass Binary Black Hole Coalescence*, *Phys. Rev. Lett.* **116** (2016) 241103, [1606.04855].

[231] LIGO Scientific, Virgo collaboration, B. P. Abbott et al., *Binary Black Hole Mergers in the first Advanced LIGO Observing Run*, *Phys. Rev.* **X6** (2016) 041015, [1606.04856].

[232] LIGO Scientific, VIRGO collaboration, B. P. Abbott et al., *GW170104: Observation of a 50-Solar-Mass Binary Black Hole Coalescence at Redshift 0.2*, *Phys. Rev. Lett.* **118** (2017) 221101, [1706.01812].

[233] LIGO Scientific, Virgo collaboration, B. P. Abbott et al., *GW170608: Observation of a 19-solar-mass Binary Black Hole Coalescence*, *Astrophys. J.* **851** (2017) L35, [1711.05578].

[234] LIGO Scientific, Virgo collaboration, B. P. Abbott et al., *GW170814: A Three-Detector Observation of Gravitational Waves from a Binary Black Hole Coalescence*, *Phys. Rev. Lett.* **119** (2017) 141101, [1709.09660].

[235] LIGO Scientific, Virgo collaboration, B. P. Abbott et al., *Gwtc-1: a Gravitational-Wave Transient Catalog of Compact Binary Mergers Observed by Ligo and Virgo during the First and Second Observing Runs*, *Phys. Rev. X* **9** (2019) 031040, [1811.12907].

[236] LIGO Scientific, Virgo collaboration, B. P. Abbott et al., *GW170817: Observation of Gravitational Waves from a Binary Neutron Star Inspiral*, *Phys. Rev. Lett.* **119** (2017) 161101, [1710.05832].

[237] LIGO Scientific, Virgo collaboration, R. Abbott et al., *GWTC-2: Compact Binary Coalescences Observed by LIGO and Virgo During the First Half of the Third Observing Run*, *Phys. Rev. X* **11** (2021) 021053, [2010.14527].

[238] LIGO Scientific, VIRGO collaboration, R. Abbott et al., *Gwtc-2.1: Deep Extended Catalog of Compact Binary Coalescences Observed by Ligo and Virgo during the First Half of the Third Observing Run*, 2108.01045.

[239] LIGO Scientific, VIRGO, KAGRA collaboration, R. Abbott et al., *Gwtc-3: Compact Binary Coalescences Observed by Ligo and Virgo during the Second Part of the Third Observing Run*, 2111.03606.

[240] C. Cutler and J. Harms, *BBO and the neutron-star-binary subtraction problem*, *Phys. Rev.* **D73** (2006) 042001, [gr-qc/0511092].

[241] T. Regimbau, M. Evans, N. Christensen, E. Katsavounidis, B. Sathyaprakash and S. Vitale, *Digging deeper: Observing primordial gravitational waves below the binary black hole produced stochastic background*, *Phys. Rev. Lett.* **118** (2017) 151105, [1611.08943].

[242] A. J. Farmer and E. S. Phinney, *The gravitational wave background from cosmological compact binaries*, *Mon. Not. Roy. Astron. Soc.* **346** (2003) 1197, [astro-ph/0304393].

[243] P. A. Rosado, *Gravitational wave background from binary systems*, *Phys. Rev.* **D84** (2011) 084004, [1106.5795].

[244] C. J. Moore, R. H. Cole and C. P. L. Berry, *Gravitational-wave sensitivity curves*, *Class. Quant. Grav.* **32** (2015) 015014, [1408.0740].

[245] D. I. Kosenko and K. A. Postnov, *On the Gravitational Wave Noise from Unresolved Extragalactic Binaries*, *Astron. Astrophys.* **336** (1998) 786, [astro-ph/9801032].

[246] M. R. Adams and N. J. Cornish, *Discriminating between a Stochastic Gravitational Wave Background and Instrument Noise*, *Phys. Rev.* **D82** (2010) 022002, [1002.1291].

[247] M. R. Adams and N. J. Cornish, *Detecting a Stochastic Gravitational Wave Background in the presence of a Galactic Foreground and Instrument Noise*, *Phys. Rev.* **D89** (2014) 022001, [1307.4116].

[248] Z. Pan and H. Yang, *Probing Primordial Stochastic Gravitational Wave Background with Multi-band Astrophysical Foreground Cleaning*, *Class. Quant. Grav.* **37** (2020) 195020, [1910.09637].

[249] A. Sharma and J. Harms, *Searching for cosmological gravitational-wave backgrounds with third-generation detectors in the presence of an astrophysical foreground*, *Phys. Rev. D* **102** (2020) 063009, [2006.16116].

[250] K. Martinovic, P. M. Meyers, M. Sakellariadou and N. Christensen, *Simultaneous estimation of astrophysical and cosmological stochastic gravitational-wave backgrounds with terrestrial detectors*, *Phys. Rev. D* **103** (2021) 043023, [2011.05697].

[251] S. Sachdev, T. Regimbau and B. S. Sathyaprakash, *Subtracting compact binary foreground sources to reveal primordial gravitational-wave backgrounds*, *Phys. Rev. D* **102** (2020) 024051, [2002.05365].

[252] M. Lewicki and V. Vaskonen, *Impact of Ligo-Virgo Binaries on Gravitational Wave Background Searches*, 2111.05847.

[253] X.-J. Zhu, E. J. Howell, D. G. Blair and Z.-H. Zhu, *On the gravitational wave background from compact binary coalescences in the band of ground-based interferometers*, *Mon. Not. Roy. Astron. Soc.* **431** (2013) 882–899, [1209.0595].

[254] C. Ungarelli and A. Vecchio, *A Family of filters to search for frequency dependent gravitational wave stochastic backgrounds*, *Class. Quant. Grav.* **21** (2004) S857–S860, [gr-qc/0312061].

[255] A. Parida, S. Mitra and S. Jhingan, *Component Separation of a Isotropic Gravitational Wave Background*, *JCAP* **04** (2016) 024, [1510.07994].

[256] M. Pieroni and E. Barausse, *Foreground cleaning and template-free stochastic background extraction for LISA*, *JCAP* **07** (2020) 021, [2004.01135].

[257] G. Boileau, N. Christensen, R. Meyer and N. J. Cornish, *Spectral separation of the stochastic gravitational-wave background for LISA: Observing both cosmological and astrophysical backgrounds*, *Phys. Rev. D* **103** (2021) 103529, [2011.05055].

[258] D. Poletti, *Measuring the primordial gravitational wave background in the presence of other stochastic signals*, *JCAP* **05** (2021) 052, [2101.02713].

[259] P. Adshead, N. Afshordi, E. Dimastrogiovanni, M. Fasiello, E. A. Lim and G. Tasinato, *Multimessenger cosmology: Correlating cosmic microwave background and stochastic gravitational wave background measurements*, *Phys. Rev. D* **103** (2021) 023532, [2004.06619].

[260] A. Malhotra, E. Dimastrogiovanni, M. Fasiello and M. Shiraishi, *Cross-correlations as a Diagnostic Tool for Primordial Gravitational Waves*, *JCAP* **03** (2021) 088, [2012.03498].

[261] J. Antoniadis et al., *The International Pulsar Timing Array second data release: Search for an isotropic gravitational wave background*, *Mon. Not. Roy. Astron. Soc.* **510** (2022) 4873–4887, [2201.03980].

[262] R. w. Hellings and G. s. Downs, *UPPER LIMITS ON THE ISOTROPIC GRAVITATIONAL RADIATION BACKGROUND FROM PULSAR TIMING ANALYSIS*, *Astrophys. J. Lett.* **265** (1983) L39–L42.

[263] E. S. Phinney, *A Practical Theorem on Gravitational Wave Backgrounds*, astro-ph/0108028.

[264] S. Blasi, V. Brdar and K. Schmitz, *Has NANOGrav found first evidence for cosmic strings?*, *Phys. Rev. Lett.* **126** (2021) 041305, [2009.06607].

[265] J. Ellis and M. Lewicki, *Cosmic String Interpretation of NANOGrav Pulsar Timing Data*, *Phys. Rev. Lett.* **126** (2021) 041304, [2009.06555].

[266] W. Buchmuller, V. Domcke and K. Schmitz, *From NANOGrav to LIGO with metastable cosmic strings*, *Phys. Lett. B* **811** (2020) 135914, [2009.10649].

[267] V. De Luca, G. Franciolini and A. Riotto, *NANOGrav Data Hints at Primordial Black Holes as Dark Matter*, *Phys. Rev. Lett.* **126** (2021) 041303, [2009.08268].

[268] S. Vagnozzi, *Implications of the NANOGrav results for inflation*, *Mon. Not. Roy. Astron. Soc.* **502** (2021) L11–L15, [2009.13432].

[269] G. Domènech and S. Pi, *NANOGrav hints on planet-mass primordial black holes*, *Sci. China Phys. Mech. Astron.* **65** (2022) 230411, [2010.03976].

[270] W. Ratzinger and P. Schwaller, *Whispers from the dark side: Confronting light new physics with NANOGrav data*, *SciPost Phys.* **10** (2021) 047, [2009.11875].

[271] A. Addazi, Y.-F. Cai, Q. Gan, A. Marciano and K. Zeng, *NANOGrav results and dark first order phase transitions*, *Sci. China Phys. Mech. Astron.* **64** (2021) 290411, [2009.10327].

[272] Y. Nakai, M. Suzuki, F. Takahashi and M. Yamada, *Gravitational Waves and Dark Radiation from Dark Phase Transition: Connecting NANOGrav Pulsar Timing Data and Hubble Tension*, *Phys. Lett. B* **816** (2021) 136238, [2009.09754].

[273] A. Neronov, A. Roper Pol, C. Caprini and D. Semikoz, *NANOGrav signal from magnetohydrodynamic turbulence at the QCD phase transition in the early Universe*, *Phys. Rev. D* **103** (2021) 041302, [2009.14174].

[274] R. T. Co, D. Dunsky, N. Fernandez, A. Ghalsasi, L. J. Hall, K. Harigaya et al., *Gravitational Wave and Cmb Probes of Axion Kination*, *JHEP* **09** (2022) 116, [2108.09299].

[275] A. Vilenkin, *Gravitational radiation from cosmic strings*, *Phys. Lett.* **107B** (1981) 47–50.

[276] C. J. Hogan and M. J. Rees, *Gravitational interactions of cosmic strings*, *Nature* **311** (1984) 109–113.

[277] T. Vachaspati and A. Vilenkin, *Gravitational Radiation from Cosmic Strings*, *Phys. Rev.* **D31** (1985) 3052.

[278] F. S. Accetta and L. M. Krauss, *The stochastic gravitational wave spectrum resulting from cosmic string evolution*, *Nucl. Phys.* **B319** (1989) 747–764.

[279] D. P. Bennett and F. R. Bouchet, *Constraints on the gravity wave background generated by cosmic strings*, *Phys. Rev.* **D43** (1991) 2733–2735.

[280] R. R. Caldwell and B. Allen, *Cosmological constraints on cosmic string gravitational radiation*, *Phys. Rev.* **D45** (1992) 3447–3468.

[281] B. Allen and E. P. S. Shellard, *Gravitational radiation from cosmic strings*, *Phys. Rev.* **D45** (1992) 1898–1912.

[282] R. A. Battye, R. R. Caldwell and E. P. S. Shellard, *Gravitational waves from cosmic strings*, in *Topological defects in cosmology*, pp. 11–31, 1997. astro-ph/9706013.

[283] M. R. DePies and C. J. Hogan, *Stochastic Gravitational Wave Background from Light Cosmic Strings*, *Phys. Rev.* **D75** (2007) 125006, [astro-ph/0702335].

[284] X. Siemens, V. Mandic and J. Creighton, *Gravitational wave stochastic background from cosmic (super)strings*, *Phys. Rev. Lett.* **98** (2007) 111101, [astro-ph/0610920].

[285] S. Olmez, V. Mandic and X. Siemens, *Gravitational-Wave Stochastic Background from Kinks and Cusps on Cosmic Strings*, *Phys. Rev. D* **81** (2010) 104028, [1004.0890].

[286] T. Regimbau, S. Giampanis, X. Siemens and V. Mandic, *The stochastic background from cosmic (super)strings: popcorn and (Gaussian) continuous regimes*, *Phys. Rev.* **D85** (2012) 066001, [1111.6638].

[287] S. A. Sanidas, R. A. Battye and B. W. Stappers, *Constraints on cosmic string tension imposed by the limit on the stochastic gravitational wave background from the European Pulsar Timing Array*, *Phys. Rev.* **D85** (2012) 122003, [1201.2419].

[288] S. A. Sanidas, R. A. Battye and B. W. Stappers, *Projected constraints on the cosmic (super)string tension with future gravitational wave detection experiments*, *Astrophys. J.* **764** (2013) 108, [1211.5042].

[289] P. Binetruy, A. Bohe, C. Caprini and J.-F. Dufaux, *Cosmological Backgrounds of Gravitational Waves and eLISA/NGO: Phase Transitions, Cosmic Strings and Other Sources*, *JCAP* **1206** (2012) 027, [1201.0983].

[290] S. Kuroyanagi, K. Miyamoto, T. Sekiguchi, K. Takahashi and J. Silk, *Forecast constraints on cosmic string parameters from gravitational wave direct detection experiments*, *Phys. Rev.* **D86** (2012) 023503, [1202.3032].

[291] S. Kuroyanagi, K. Miyamoto, T. Sekiguchi, K. Takahashi and J. Silk, *Forecast constraints on cosmic strings from future CMB, pulsar timing and gravitational wave direct detection experiments*, *Phys. Rev.* **D87** (2013) 023522, [1210.2829].

[292] L. Sousa and P. P. Avelino, *Probing Cosmic Superstrings with Gravitational Waves*, *Phys. Rev.* **D94** (2016) 063529, [1606.05585].

[293] L. Sousa, P. P. Avelino and G. S. Guedes, *Full analytical approximation to the stochastic gravitational wave background generated by cosmic string networks*, *Phys. Rev. D* **101** (2020) 103508, [2002.01079].

[294] Y. Cui, M. Lewicki, D. E. Morrissey and J. D. Wells, *Cosmic Archaeology with Gravitational Waves from Cosmic Strings*, *Phys. Rev.* **D97** (2018) 123505, [1711.03104].

[295] Y. Cui, M. Lewicki, D. E. Morrissey and J. D. Wells, *Probing the pre-BBN universe with gravitational waves from cosmic strings*, *JHEP* **01** (2019) 081, [1808.08968].

[296] P. Auclair et al., *Probing the gravitational wave background from cosmic strings with LISA*, *JCAP* **04** (2020) 034, [1909.00819].

[297] G. S. F. Guedes, P. P. Avelino and L. Sousa, *Signature of inflation in the stochastic gravitational wave background generated by cosmic string networks*, *Phys. Rev.* **D98** (2018) 123505, [1809.10802].

[298] R. E. Packard and T. Sanders Jr, *Observations on single vortex lines in rotating superfluid helium*, *Physical Review A* **6** (1972) 799.

[299] E. Yarmchuk, M. Gordon and R. Packard, *Observation of stationary vortex arrays in rotating superfluid helium*, *Physical Review Letters* **43** (1979) 214.

[300] D. Awschalom and K. Schwarz, *Observation of a remanent vortex-line density in superfluid helium*, *Physical review letters* **52** (1984) 49.

[301] A. Vilenkin and E. P. S. Shellard, *Cosmic Strings and Other Topological Defects*. Cambridge University Press, 7, 2000.

[302] T. Vachaspati, L. Pogosian and D. Steer, *Cosmic Strings*, *Scholarpedia* **10** (2015) 31682, [1506.04039].

[303] E. Witten, *Cosmic Superstrings*, *Phys. Lett.* **153B** (1985) 243–246.

[304] G. Dvali and A. Vilenkin, *Formation and evolution of cosmic D strings*, *JCAP* **0403** (2004) 010, [hep-th/0312007].

[305] E. J. Copeland, R. C. Myers and J. Polchinski, *Cosmic F and D strings*, *JHEP* **06** (2004) 013, [hep-th/0312067].

[306] J. Polchinski, *Introduction to cosmic F- and D-strings*, in *String theory: From gauge interactions to cosmology. Proceedings, NATO Advanced Study Institute, Cargese, France, June 7-19, 2004*, pp. 229–253, 2004. hep-th/0412244.

[307] M. Sakellariadou, *Cosmic Superstrings*, *Phil. Trans. Roy. Soc. Lond.* **A366** (2008) 2881–2894, [0802.3379].

[308] A.-C. Davis, P. Brax and C. van de Bruck, *Brane Inflation and Defect Formation*, *Phil. Trans. Roy. Soc. Lond.* **A366** (2008) 2833–2842, [0803.0424].

[309] M. Sakellariadou, *Cosmic Strings and Cosmic Superstrings*, *Nucl. Phys. Proc. Suppl.* **192-193** (2009) 68–90, [0902.0569].

[310] E. J. Copeland and T. W. B. Kibble, *Cosmic Strings and Superstrings*, *Proc. Roy. Soc. Lond.* **A466** (2010) 623–657, [0911.1345].

[311] J. Polchinski, *Cosmic superstrings revisited*, *Int. J. Mod. Phys.* **A20** (2005) 3413–3415, [hep-th/0410082].

[312] L. Pogosian, S. H. H. Tye, I. Wasserman and M. Wyman, *Cosmic Strings as the Source of Small-Scale Microwave Background Anisotropy*, *JCAP* **0902** (2009) 013, [0804.0810].

[313] J. Yokoyama, *INFLATION CAN SAVE COSMIC STRINGS*, *Phys. Rev. Lett.* **63** (1989) 712.

[314] W. Buchmüller, V. Domcke, K. Kamada and K. Schmitz, *The Gravitational Wave Spectrum from Cosmological $B - L$ Breaking*, *JCAP* **1310** (2013) 003, [1305.3392].

[315] D. Baumann and L. McAllister, *Inflation and String Theory*. Cambridge Monographs on Mathematical Physics. Cambridge University Press, 5, 2015, 10.1017/CBO9781316105733.

[316] T. Vachaspati, *Electroweak strings*, *Nucl. Phys. B* **397** (1993) 648–671.

[317] T. Vachaspati and A. Achucarro, *Semilocal cosmic strings*, *Phys. Rev. D* **44** (1991) 3067–3071.

[318] M. James, L. Perivolaropoulos and T. Vachaspati, *Detailed stability analysis of electroweak strings*, *Nucl. Phys. B* **395** (1993) 534–546, [hep-ph/9212301].

[319] A. A. Abrikosov, *On the Magnetic Properties of Superconductors of the Second Group*, *Sov. Phys. JETP* **5** (1957) 1174–1182.

[320] H. B. Nielsen and P. Olesen, *Vortex Line Models for Dual Strings*, *Nucl. Phys.* **B61** (1973) 45–61.

[321] R. J. Scherrer and J. A. Frieman, *COSMIC STRINGS AS RANDOM WALKS*, *Phys. Rev.* **D33** (1986) 3556.

[322] E. P. S. Shellard, *Cosmic String Interactions*, *Nucl. Phys.* **B283** (1987) 624–656.

[323] M. Eto, K. Hashimoto, G. Marmorini, M. Nitta, K. Ohashi and W. Vinci, *Universal Reconnection of Non-Abelian Cosmic Strings*, *Phys. Rev. Lett.* **98** (2007) 091602, [hep-th/0609214].

[324] M. G. Jackson, N. T. Jones and J. Polchinski, *Collisions of cosmic F and D-strings*, *JHEP* **10** (2005) 013, [hep-th/0405229].

[325] E. J. Copeland, T. W. B. Kibble and D. A. Steer, *Constraints on string networks with junctions*, *Phys. Rev.* **D75** (2007) 065024, [hep-th/0611243].

[326] P. Laguna and R. A. Matzner, *PEELING U(1) GAUGE COSMIC STRINGS*, *Phys. Rev. Lett.* **62** (1989) 1948–1951.

[327] A. Achucarro and R. de Putter, *Effective non-intercommutation of local cosmic strings at high collision speeds*, *Phys. Rev.* **D74** (2006) 121701, [hep-th/0605084].

[328] V. B. Klaer and G. D. Moore, *The dark-matter axion mass*, *JCAP* **1711** (2017) 049, [1708.07521].

[329] M. Kawasaki, T. Sekiguchi, M. Yamaguchi and J. Yokoyama, *Long-term dynamics of cosmological axion strings*, *PTEP* **2018** (2018) 091E01, [1806.05566].

[330] A. Vaquero, J. Redondo and J. Stadler, *Early Seeds of Axion Miniclusters*, *JCAP* **04** (2019) 012, [1809.09241].

[331] M. Buschmann, J. W. Foster and B. R. Safdi, *Early-Universe Simulations of the Cosmological Axion*, *Phys. Rev. Lett.* **124** (2020) 161103, [1906.00967].

[332] C. J. A. P. Martins, *Scaling properties of cosmological axion strings*, *Phys. Lett.* **B788** (2019) 147–151, [1811.12678].

[333] M. Hindmarsh, J. Lizarraga, A. Lopez-Eiguren and J. Urrestilla, *Scaling Density of Axion Strings*, *Phys. Rev. Lett.* **124** (2020) 021301, [1908.03522].

[334] S. Blasi, V. Brdar and K. Schmitz, *Fingerprint of low-scale leptogenesis in the primordial gravitational-wave spectrum*, *Phys. Rev. Res.* **2** (2020) 043321, [2004.02889].

[335] L. M. Krauss, *Gravitational waves from global phase transitions*, *Phys. Lett.* **B284** (1992) 229–233.

[336] K. Jones-Smith, L. M. Krauss and H. Mathur, *A Nearly Scale Invariant Spectrum of Gravitational Radiation from Global Phase Transitions*, *Phys. Rev. Lett.* **100** (2008) 131302, [0712.0778].

[337] E. Fenu, D. G. Figueroa, R. Durrer and J. Garcia-Bellido, *Gravitational waves from self-ordering scalar fields*, *JCAP* **0910** (2009) 005, [0908.0425].

[338] D. G. Figueroa, M. Hindmarsh and J. Urrestilla, *Exact Scale-Invariant Background of Gravitational Waves from Cosmic Defects*, *Phys. Rev. Lett.* **110** (2013) 101302, [1212.5458].

[339] D. C. N. da Cunha, C. Ringeval and F. R. Bouchet, *Stochastic gravitational waves from long cosmic strings*, 2205.04349.

[340] T. Vachaspati and A. Vilenkin, *Gravitational radiation from cosmic strings*, *Physical Review D* **31** (1985) 3052.

[341] J. J. Blanco-Pillado, K. D. Olum and X. Siemens, *New limits on cosmic strings from gravitational wave observation*, *Phys. Lett.* **B778** (2018) 392–396, [1709.02434].

[342] M. Maggiore, *Gravitational waves: Volume 1: Theory and experiments*, vol. 1. Oxford university press, 2008.

[343] T. W. B. Kibble and N. Turok, *Selfintersection of Cosmic Strings*, *Phys. Lett.* **116B** (1982) 141–143.

[344] T. Damour and A. Vilenkin, *Gravitational wave bursts from cusps and kinks on cosmic strings*, *Phys. Rev.* **D64** (2001) 064008, [gr-qc/0104026].

[345] C. Ringeval and T. Suyama, *Stochastic gravitational waves from cosmic string loops in scaling*, *JCAP* **1712** (2017) 027, [1709.03845].

[346] C. J. Burden, *Gravitational Radiation From a Particular Class of Cosmic Strings*, *Phys. Lett.* **164B** (1985) 277–281.

[347] T. Damour and A. Vilenkin, *Gravitational wave bursts from cosmic strings*, *Phys. Rev. Lett.* **85** (2000) 3761–3764, [gr-qc/0004075].

[348] A. Vilenkin and T. Vachaspati, *Radiation of Goldstone Bosons From Cosmic Strings*, *Phys. Rev.* **D35** (1987) 1138.

[349] A. Saurabh, T. Vachaspati and L. Pogosian, *Decay of Cosmic Global String Loops*, *Phys. Rev. D* **101** (2020) 083522, [2001.01030].

[350] D. Bettoni, G. Domènech and J. Rubio, *Gravitational waves from global cosmic strings in quintessential inflation*, *JCAP* **1902** (2019) 034, [1810.11117].

[351] N. Ramberg and L. Visinelli, *Probing the Early Universe with Axion Physics and Gravitational Waves*, *Phys. Rev.* **D99** (2019) 123513, [1904.05707].

[352] C.-F. Chang and Y. Cui, *Gravitational Waves from Global Cosmic Strings and Cosmic Archaeology*, *JHEP* **03** (2022) 114, [2106.09746].

[353] A. Vilenkin and A. E. Everett, *Cosmic Strings and Domain Walls in Models with Goldstone and PseudoGoldstone Bosons*, *Phys. Rev. Lett.* **48** (1982) 1867–1870.

[354] A. Vilenkin, *Cosmic Strings and Domain Walls*, *Phys. Rept.* **121** (1985) 263–315.

[355] P. Sikivie, *Of Axions, Domain Walls and the Early Universe*, *Phys. Rev. Lett.* **48** (1982) 1156–1159.

[356] A. Dabholkar and J. M. Quashnock, *Pinning Down the Axion*, *Nucl. Phys.* **B333** (1990) 815–832.

[357] M. Gorghetto, E. Hardy and H. Nicolaescu, *Observing invisible axions with gravitational waves*, *JCAP* **06** (2021) 034, [2101.11007].

[358] M. Peloso and L. Sorbo, *Moduli from cosmic strings*, *Nucl. Phys. B* **649** (2003) 88–100, [hep-ph/0205063].

[359] M. Srednicki and S. Theisen, *Nongravitational Decay of Cosmic Strings*, *Phys. Lett.* **B189** (1987) 397.

[360] A. J. Long, J. M. Hyde and T. Vachaspati, *Cosmic Strings in Hidden Sectors: 1. Radiation of Standard Model Particles*, *JCAP* **1409** (2014) 030, [1405.7679].

[361] R. H. Brandenberger and A. Riotto, *A New mechanism for baryogenesis in low-energy supersymmetry breaking models*, *Phys. Lett. B* **445** (1999) 323–330, [hep-ph/9801448].

[362] R. Jeannerot, X. Zhang and R. H. Brandenberger, *Non-thermal production of neutralino cold dark matter from cosmic string decays*, *JHEP* **12** (1999) 003, [hep-ph/9901357].

[363] Y. Cui, S. P. Martin, D. E. Morrissey and J. D. Wells, *Cosmic Strings from Supersymmetric Flat Directions*, *Phys. Rev. D* **77** (2008) 043528, [0709.0950].

[364] Y. Cui and D. E. Morrissey, *Non-Thermal Dark Matter from Cosmic Strings*, *Phys. Rev.* **D79** (2009) 083532, [0805.1060].

[365] X.-J. Bi, R. Brandenberger, P. Gondolo, T.-j. Li, Q. Yuan and X.-m. Zhang, *Non-Thermal Production of WIMPs, Cosmic e+- Excesses and gamma-rays from the Galactic Center*, *Phys. Rev. D* **80** (2009) 103502, [0905.1253].

[366] R. H. Brandenberger, *On the Decay of Cosmic String Loops*, *Nucl. Phys.* **B293** (1987) 812–828.

[367] J. J. Blanco-Pillado and K. D. Olum, *The Form of cosmic string cusps*, *Phys. Rev.* **D59** (1999) 063508, [gr-qc/9810005].

[368] D. Matsunami, L. Pogosian, A. Saurabh and T. Vachaspati, *Decay of Cosmic String Loops Due to Particle Radiation*, *Phys. Rev. Lett.* **122** (2019) 201301, [1903.05102].

[369] L. Lentati et al., *European Pulsar Timing Array Limits On An Isotropic Stochastic Gravitational-Wave Background*, *Mon. Not. Roy. Astron. Soc.* **453** (2015) 2576–2598, [1504.03692].

[370] NANOGRAV collaboration, Z. Arzoumanian et al., *The NANOGrav 11-year Data Set: Pulsar-timing Constraints On The Stochastic Gravitational-wave Background*, *Astrophys. J.* **859** (2018) 47, [1801.02617].

[371] M. Sakellariadou, *A Note on the evolution of cosmic string/superstring networks*, *JCAP* **0504** (2005) 003, [hep-th/0410234].

[372] T. Damour and A. Vilenkin, *Gravitational radiation from cosmic (super)strings: Bursts, stochastic background, and observational windows*, *Phys. Rev.* **D71** (2005) 063510, [hep-th/0410222].

[373] LIGO Scientific, Virgo collaboration, B. P. Abbott et al., *Constraints on cosmic strings using data from the first Advanced LIGO observing run*, *Phys. Rev.* **D97** (2018) 102002, [1712.01168].

[374] LIGO Scientific, Virgo collaboration, B. P. Abbott et al., *All-sky search for short gravitational-wave bursts in the second Advanced LIGO and Advanced Virgo run*, 1905.03457.

[375] LIGO Scientific, Virgo, KAGRA collaboration, R. Abbott et al., *Constraints on Cosmic Strings Using Data from the Third Advanced LIGO–Virgo Observing Run*, *Phys. Rev. Lett.* **126** (2021) 241102, [2101.12248].

[376] L. Lorenz, C. Ringeval and M. Sakellariadou, *Cosmic string loop distribution on all length scales and at any redshift*, *JCAP* **1010** (2010) 003, [1006.0931].

[377] G. Vincent, N. D. Antunes and M. Hindmarsh, *Numerical simulations of string networks in the Abelian Higgs model*, *Phys. Rev. Lett.* **80** (1998) 2277–2280, [hep-ph/9708427].

[378] M. Hindmarsh, S. Stuckey and N. Bevis, *Abelian Higgs Cosmic Strings: Small Scale Structure and Loops*, *Phys. Rev.* **D79** (2009) 123504, [0812.1929].

[379] M. Hindmarsh, J. Lizarraga, J. Urrestilla, D. Daverio and M. Kunz, *Scaling from gauge and scalar radiation in Abelian Higgs string networks*, *Phys. Rev.* **D96** (2017) 023525, [1703.06696].

[380] J. N. Moore and E. P. S. Shellard, *On the Evolution of Abelian Higgs String Networks*, hep-ph/9808336.

[381] K. D. Olum and J. J. Blanco-Pillado, *Radiation from cosmic string standing waves*, *Phys. Rev. Lett.* **84** (2000) 4288–4291, [astro-ph/9910354].

[382] J. N. Moore, E. P. S. Shellard and C. J. A. P. Martins, *On the evolution of Abelian-Higgs string networks*, *Phys. Rev.* **D65** (2002) 023503, [hep-ph/0107171].

[383] J. J. Blanco-Pillado, K. D. Olum and B. Shlaer, *Cosmic string loop shapes*, *Phys. Rev.* **D92** (2015) 063528, [1508.02693].

[384] D. Matsunami, L. Pogosian, A. Saurabh and T. Vachaspati, *Decay of Cosmic String Loops Due to Particle Radiation*, *https://ayushsaurabh.home.blog*.

[385] J. V. Rocha, *Analytic Approaches to the Study of Small Scale Structure on Cosmic String Networks*, 0812.4020.

[386] J. M. Quashnock and D. N. Spergel, *Gravitational Selfinteractions of Cosmic Strings*, *Phys. Rev.* **D42** (1990) 2505–2520.

[387] J. J. Blanco-Pillado, K. D. Olum and J. M. Wachter, *Gravitational backreaction near cosmic string kinks and cusps*, *Phys. Rev.* **D98** (2018) 123507, [1808.08254].

[388] J. J. Blanco-Pillado, K. D. Olum and J. M. Wachter, *Gravitational backreaction simulations of simple cosmic string loops*, *Phys. Rev.* **D100** (2019) 023535, [1903.06079].

[389] J. M. Wachter and K. D. Olum, *Gravitational backreaction on piecewise linear cosmic string loops*, *Phys. Rev.* **D95** (2017) 023519, [1609.01685].

[390] J. M. Wachter and K. D. Olum, *Gravitational smoothing of kinks on cosmic string loops*, *Phys. Rev. Lett.* **118** (2017) 051301, [1609.01153].

[391] P. Auclair, D. A. Steer and T. Vachaspati, *Particle emission and gravitational radiation from cosmic strings: observational constraints*, *Phys. Rev. D* **101** (2020) 083511, [1911.12066].

[392] K. D. Olum and J. J. Blanco-Pillado, *Field theory simulation of Abelian Higgs cosmic string cusps*, *Phys. Rev. D* **60** (1999) 023503, [gr-qc/9812040].

[393] T. Elghozi, W. Nelson and M. Sakellariadou, *Cusps and pseudocusps in strings with Y-junctions*, *Phys. Rev.* **D90** (2014) 123517, [1403.3225].

[394] M. J. Stott, T. Elghozi and M. Sakellariadou, *Gravitational Wave Bursts from Cosmic String Cusps and Pseudocusps*, *Phys. Rev.* **D96** (2017) 023533, [1612.07599].

[395] P. Binetruy, A. Bohe, T. Hertog and D. A. Steer, *Gravitational wave signatures from kink proliferation on cosmic (super-) strings*, *Phys. Rev.* **D82** (2010) 126007, [1009.2484].

[396] P. Binetruy, A. Bohe, T. Hertog and D. A. Steer, *Proliferation of sharp kinks on cosmic (super-)string loops with junctions*, *Phys. Rev.* **D82** (2010) 083524, [1005.2426].

[397] C. J. Hogan, *Gravitational Waves from Light Cosmic Strings: Backgrounds and Bursts with Large Loops*, *Phys. Rev.* **D74** (2006) 043526, [astro-ph/0605567].

[398] J. J. Blanco-Pillado and K. D. Olum, *Stochastic gravitational wave background from smoothed cosmic string loops*, *Phys. Rev.* **D96** (2017) 104046, [1709.02693].

[399] P. Auclair, C. Ringeval, M. Sakellariadou and D. Steer, *Cosmic string loop production functions*, *JCAP* **1906** (2019) 015, [1903.06685].

[400] J. Polchinski and J. V. Rocha, *Analytic study of small scale structure on cosmic strings*, *Phys. Rev.* **D74** (2006) 083504, [hep-ph/0606205].

[401] J. Polchinski and J. V. Rocha, *Cosmic string structure at the gravitational radiation scale*, *Phys. Rev.* **D75** (2007) 123503, [gr-qc/0702055].

[402] F. Dubath, J. Polchinski and J. V. Rocha, *Cosmic String Loops, Large and Small*, *Phys. Rev.* **D77** (2008) 123528, [0711.0994].

[403] J. V. Rocha, *Scaling solution for small cosmic string loops*, *Phys. Rev. Lett.* **100** (2008) 071601, [0709.3284].

[404] J. J. Blanco-Pillado, K. D. Olum and J. M. Wachter, *Energy-Conservation Constraints on Cosmic String Loop Production and Distribution Functions*, *Phys. Rev. D* **100** (2019) 123526, [1907.09373].

[405] C. J. A. P. Martins and E. P. S. Shellard, *String evolution with friction*, *Phys. Rev.* **D53** (1996) 575–579, [hep-ph/9507335].

[406] C. J. A. P. Martins and E. P. S. Shellard, *Quantitative string evolution*, *Phys. Rev.* **D54** (1996) 2535–2556, [hep-ph/9602271].

[407] C. J. A. P. Martins and E. P. S. Shellard, *Extending the velocity dependent one scale string evolution model*, *Phys. Rev.* **D65** (2002) 043514, [hep-ph/0003298].

[408] C. J. Martins, *Defect evolution in cosmology and condensed matter: quantitative analysis with the velocity-dependent one-scale model*. Springer, 2016.

[409] J. R. C. C. C. Correia and J. A. P. Martins, *Extending and Calibrating the Velocity dependent One-Scale model for Cosmic Strings with One Thousand Field Theory Simulations*, *Phys. Rev.* **D100** (2019) 103517, [1911.03163].

[410] L. Sousa and P. P. Avelino, *Stochastic Gravitational Wave Background generated by Cosmic String Networks: Velocity-Dependent One-Scale model versus Scale-Invariant Evolution*, *Phys. Rev.* **D88** (2013) 023516, [1304.2445].

[411] A. Vilenkin, *Cosmic string dynamics with friction*, *Phys. Rev.* **D43** (1991) 1060–1062.

[412] M. B. Hindmarsh and T. W. B. Kibble, *Cosmic strings*, *Rept. Prog. Phys.* **58** (1995) 477–562, [hep-ph/9411342].

[413] A. Vilenkin, *COSMOLOGICAL EVOLUTION OF MONOPOLES CONNECTED BY STRINGS*, *Nucl. Phys.* **B196** (1982) 240–258.

[414] X. Martin and A. Vilenkin, *Gravitational wave background from hybrid topological defects*, *Phys. Rev. Lett.* **77** (1996) 2879–2882, [astro-ph/9606022].

[415] X. Martin and A. Vilenkin, *Gravitational radiation from monopoles connected by strings*, *Phys. Rev.* **D55** (1997) 6054–6060, [gr-qc/9612008].

[416] L. Leblond, B. Shlaer and X. Siemens, *Gravitational Waves from Broken Cosmic Strings: The Bursts and the Beads*, *Phys. Rev.* **D79** (2009) 123519, [0903.4686].

[417] A. Kamada and M. Yamada, *Gravitational waves as a probe of the SUSY scale*, *Phys. Rev.* **D91** (2015) 063529, [1407.2882].

[418] A. Kamada and M. Yamada, *Gravitational wave signals from short-lived topological defects in the MSSM*, *JCAP* **1510** (2015) 021, [1505.01167].

[419] T. Hiramatsu, M. Kawasaki and K. Saikawa, *Evolution of String-Wall Networks and Axionic Domain Wall Problem*, *JCAP* **1108** (2011) 030, [1012.4558].

[420] T. Hiramatsu, M. Kawasaki, K. Saikawa and T. Sekiguchi, *Axion cosmology with long-lived domain walls*, *JCAP* **1301** (2013) 001, [1207.3166].

[421] T. Hiramatsu, M. Kawasaki, K. Saikawa and T. Sekiguchi, *Production of dark matter axions from collapse of string-wall systems*, *Phys. Rev.* **D85** (2012) 105020, [1202.5851].

[422] D. I. Dunsky, A. Ghoshal, H. Murayama, Y. Sakakihara and G. White, *Guts, Hybrid Topological Defects, and Gravitational Waves*, *Phys. Rev. D* **106** (2022) 075030, [2111.08750].

[423] J. Preskill and A. Vilenkin, *Decay of metastable topological defects*, *Phys. Rev.* **D47** (1993) 2324–2342, [hep-ph/9209210].

[424] T. Vachaspati and A. Vilenkin, *Evolution of cosmic networks*, *Phys. Rev.* **D35** (1987) 1131.

[425] T. W. B. Kibble and T. Vachaspati, *Monopoles on strings*, *J. Phys.* **G42** (2015) 094002, [1506.02022].

[426] X. Siemens, X. Martin and K. D. Olum, *Dynamics of cosmic necklaces*, *Nucl. Phys.* **B595** (2001) 402–414, [astro-ph/0005411].

[427] J. J. Blanco-Pillado and K. D. Olum, *Monopole annihilation in cosmic necklaces*, *JCAP* **1005** (2010) 014, [0707.3460].

[428] M. Hindmarsh, K. Rummukainen and D. J. Weir, *Numerical simulations of necklaces in SU(2) gauge-Higgs field theory*, *Phys. Rev.* **D95** (2017) 063520, [1611.08456].

[429] M. Hindmarsh, A. Kormu, A. Lopez-Eiguren and D. J. Weir, *Scaling in necklaces of monopoles and semipoles*, *Phys. Rev.* **D98** (2018) 103533, [1809.03384].

[430] C. J. A. P. Martins, *Evolution of Cosmic Necklaces and Lattices*, *Phys. Rev.* **D82** (2010) 067301, [1009.1707].

[431] V. Berezinsky and A. Vilenkin, *Cosmic necklaces and ultrahigh-energy cosmic rays*, *Phys. Rev. Lett.* **79** (1997) 5202–5205, [astro-ph/9704257].

[432] J. J. Blanco-Pillado and K. D. Olum, *Monopole - anti-monopole bound states as a source of ultrahigh-energy cosmic rays*, *Phys. Rev.* **D60** (1999) 083001, [astro-ph/9904315].

[433] C. Gomez Sanchez and B. Holdom, *Monopoles, strings and dark matter*, *Phys. Rev.* **D83** (2011) 123524, [1103.1632].

[434] J. Terning and C. B. Verhaaren, *Detecting Dark Matter with Aharonov-Bohm*, *JHEP* **12** (2019) 152, [1906.00014].

[435] W. Buchmuller, V. Domcke, H. Murayama and K. Schmitz, *Probing the scale of grand unification with gravitational waves*, *Phys. Lett. B* **809** (2020) 135764, [1912.03695].

[436] D. Cutting, M. Hindmarsh and D. J. Weir, *Gravitational waves from vacuum first-order phase transitions: from the envelope to the lattice*, *Phys. Rev.* **D97** (2018) 123513, [1802.05712].

[437] V. B. Klaer and G. D. Moore, *How to simulate global cosmic strings with large string tension*, *JCAP* **1710** (2017) 043, [1707.05566].

[438] V. B. Klaer and G. D. Moore, *Global cosmic string networks as a function of tension*, *JCAP* **06** (2020) 021, [1912.08058].

[439] F. Wilczek, *Problem of Strong P and T Invariance in the Presence of Instantons*, *Phys. Rev. Lett.* **40** (1978) 279–282.

[440] R. Peccei and H. R. Quinn, *CP Conservation in the Presence of Instantons*, *Phys. Rev. Lett.* **38** (1977) 1440–1443.

[441] S. Weinberg, *A New Light Boson?*, *Phys. Rev. Lett.* **40** (1978) 223–226.

[442] J. E. Kim, *Weak Interaction Singlet and Strong CP Invariance*, *Phys. Rev. Lett.* **43** (1979) 103.

[443] M. A. Shifman, A. Vainshtein and V. I. Zakharov, *Can Confinement Ensure Natural CP Invariance of Strong Interactions?*, *Nucl. Phys. B* **166** (1980) 493–506.

[444] M. Dine, W. Fischler and M. Srednicki, *A Simple Solution to the Strong CP Problem with a Harmless Axion*, *Phys. Lett. B* **104** (1981) 199–202.

[445] A. R. Zhitnitsky, *On Possible Suppression of the Axion Hadron Interactions. (In Russian)*, *Sov. J. Nucl. Phys.* **31** (1980) 260.

[446] J. Preskill, M. B. Wise and F. Wilczek, *Cosmology of the Invisible Axion*, *Phys. Lett. B* **120** (1983) 127–132.

[447] L. F. Abbott and P. Sikivie, *A Cosmological Bound on the Invisible Axion*, *Phys. Lett. B* **120** (1983) 133–136.

[448] M. Dine and W. Fischler, *The Not So Harmless Axion*, *Phys. Lett. B* **120** (1983) 137–141.

[449] R. T. Co, L. J. Hall and K. Harigaya, *Kinetic Misalignment Mechanism*, *Phys. Rev. Lett.* **124** (2020) 251802, [1910.14152].

[450] C.-F. Chang and Y. Cui, *New Perspectives on Axion Misalignment Mechanism*, *Phys. Rev. D* **102** (2020) 015003, [1911.11885].

[451] A. Vilenkin, *Cosmic Strings*, *Phys. Rev.* **D24** (1981) 2082–2089.

[452] R. L. Davis, *Goldstone Bosons in String Models of Galaxy Formation*, *Phys. Rev.* **D32** (1985) 3172.

[453] R. L. Davis, *Cosmic Axions from Cosmic Strings*, *Phys. Lett.* **B180** (1986) 225–230.

[454] D. Harari and P. Sikivie, *On the Evolution of Global Strings in the Early Universe*, *Phys. Lett.* **B195** (1987) 361–365.

[455] R. A. Battye and E. P. S. Shellard, *Axion string constraints*, *Phys. Rev. Lett.* **73** (1994) 2954–2957, [astro-ph/9403018].

[456] M. Kawasaki, K. Saikawa and T. Sekiguchi, *Axion dark matter from topological defects*, *Phys. Rev. D* **91** (2015) 065014, [1412.0789].

[457] P. Auclair, K. Leyde and D. A. Steer, *A window for cosmic strings*, 2112.11093.

[458] R. Allahverdi et al., *The First Three Seconds: a Review of Possible Expansion Histories of the Early Universe*, 2006.16182.

[459] L. A. Boyle and A. Buonanno, *Relating gravitational wave constraints from primordial nucleosynthesis, pulsar timing, laser interferometers, and the CMB: Implications for the early Universe*, *Phys. Rev.* **D78** (2008) 043531, [0708.2279].

[460] F. D'Eramo and K. Schmitz, *Imprint of a Scalar Era on the Primordial Spectrum of Gravitational Waves*, *Phys. Rev. Research.* **1** (2019) 013010, [1904.07870].

[461] N. Bernal and F. Hajkarim, *Primordial Gravitational Waves in Nonstandard Cosmologies*, *Phys. Rev. D* **100** (2019) 063502, [1905.10410].

[462] A. Hook, G. Marques-Tavares and D. Racco, *Causal gravitational waves as a probe of free streaming particles and the expansion of the Universe*, *JHEP* **02** (2021) 117, [2010.03568].

[463] A. Ringwald, K. Saikawa and C. Tamarit, *Primordial gravitational waves in a minimal model of particle physics and cosmology*, *JCAP* **02** (2021) 046, [2009.02050].

[464] G. Choi, R. Jinno and T. T. Yanagida, *Probing PeV scale SUSY breaking with satellite galaxies and primordial gravitational waves*, *Phys. Rev. D* **104** (2021) 095018, [2107.12804].

[465] P. Simakachorn, *Probing particle theory with primordial gravitational waves*, Master's thesis, Universität Hamburg, 2019.

[466] D. Brzeminski, A. Hook and G. Marques-Tavares, *Precision Early Universe Cosmology from Stochastic Gravitational Waves*, *JHEP* **11** (2022) 061, [2203.13842].

[467] M. Kawasaki, K. Kohri and N. Sugiyama, *Cosmological constraints on late time entropy production*, *Phys. Rev. Lett.* **82** (1999) 4168, [astro-ph/9811437].

[468] M. Kawasaki, K. Kohri and N. Sugiyama, *MeV scale reheating temperature and thermalization of neutrino background*, *Phys. Rev. D* **62** (2000) 023506, [astro-ph/0002127].

[469] S. Hannestad, *What is the lowest possible reheating temperature?*, *Phys. Rev. D* **70** (2004) 043506, [astro-ph/0403291].

[470] Planck collaboration, N. Aghanim et al., *Planck 2018 results. VI. Cosmological parameters*, *Astron. Astrophys.* **641** (2020) A6, [1807.06209].

[471] Q. Shafi and A. Vilenkin, *Spontaneously Broken Global Symmetries and Cosmology*, *Phys. Rev. D* **29** (1984) 1870.

[472] E. T. Vishniac, K. A. Olive and D. Seckel, *Cosmic Strings and Inflation*, *Nucl. Phys.* **B289** (1987) 717–734.

[473] L. A. Kofman and A. D. Linde, *Generation of Density Perturbations in the Inflationary Cosmology*, *Nucl. Phys. B* **282** (1987) 555.

[474] J. Yokoyama, *Natural Way Out of the Conflict Between Cosmic Strings and Inflation*, *Phys. Lett.* **B212** (1988) 273–276.

[475] M. Nagasawa and J. Yokoyama, *Phase transitions triggered by quantum fluctuations in the inflationary universe*, *Nucl. Phys. B* **370** (1992) 472–490.

[476] R. Basu and A. Vilenkin, *Evolution of topological defects during inflation*, *Phys. Rev. D* **50** (1994) 7150–7153, [gr-qc/9402040].

[477] K. Freese, T. Gherghetta and H. Umeda, *Moduli inflation with large scale structure produced by topological defects*, *Phys. Rev.* **D54** (1996) 6083–6087, [hep-ph/9512211].

[478] E. Thrane and J. D. Romano, *Sensitivity curves for searches for gravitational-wave backgrounds*, *Phys. Rev.* **D88** (2013) 124032, [1310.5300].

[479] C. Caprini, D. G. Figueroa, R. Flauger, G. Nardini, M. Peloso, M. Pieroni et al., *Reconstructing the spectral shape of a stochastic gravitational wave background with LISA*, *JCAP* **11** (2019) 017, [1906.09244].

[480] R. Flauger, N. Karnesis, G. Nardini, M. Pieroni, A. Ricciardone and J. Torrado, *Improved reconstruction of a stochastic gravitational wave background with LISA*, *JCAP* **01** (2021) 059, [2009.11845].

[481] Y. B. Zel'dovich, *The equation of state at ultrahigh densities and its relativistic limitations*, *Soviet physics JETP* **14** (1962) .

[482] M. Joyce, *Electroweak Baryogenesis and the Expansion Rate of the Universe*, *Phys. Rev.* **D55** (1997) 1875–1878, [hep-ph/9606223].

[483] B. Spokoiny, *Deflationary universe scenario*, *Phys. Lett.* **B315** (1993) 40–45, [gr-qc/9306008].

[484] L. Visinelli, *(Non-)thermal production of WIMPs during kination*, *Symmetry* **10** (2018) 546, [1710.11006].

[485] L. H. Ford, *Gravitational Particle Creation and Inflation*, *Phys. Rev.* **D35** (1987) 2955.

[486] E. Chun, S. Scopel and I. Zaballa, *Gravitational reheating in quintessential inflation*, *JCAP* **07** (2009) 022, [0904.0675].

[487] K. Dimopoulos and T. Markkanen, *Non-minimal gravitational reheating during kination*, *JCAP* **06** (2018) 021, [1803.07399].

[488] T. Nakama and J. Yokoyama, *Reheating through the Higgs amplified by spinodal instabilities and gravitational creation of gravitons*, *PTEP* **2019** (2019) 033E02, [1803.07111].

[489] T. Opferkuch, P. Schwaller and B. A. Stefanek, *Ricci Reheating*, *JCAP* **07** (2019) 016, [1905.06823].

[490] D. Bettoni and J. Rubio, *Hubble-induced phase transitions: Walls are not forever*, *JCAP* **01** (2020) 002, [1911.03484].

[491] D. Bettoni, A. Lopez-Eiguren and J. Rubio, *Hubble-induced phase transitions on the lattice with applications to Ricci reheating*, *JCAP* **01** (2022) 002, [2107.09671].

[492] M. Joyce and T. Prokopec, *Turning around the sphaleron bound: Electroweak baryogenesis in an alternative postinflationary cosmology*, *Phys. Rev. D* **57** (1998) 6022–6049, [hep-ph/9709320].

[493] P. Salati, *Quintessence and the relic density of neutralinos*, *Phys. Lett. B* **571** (2003) 121–131, [astro-ph/0207396].

[494] S. Profumo and P. Ullio, *SUSY dark matter and quintessence*, *JCAP* **11** (2003) 006, [hep-ph/0309220].

[495] C. Pallis, *Quintessential kination and cold dark matter abundance*, *JCAP* **10** (2005) 015, [hep-ph/0503080].

[496] D. J. H. Chung, L. L. Everett and K. T. Matchev, *Inflationary cosmology connecting dark energy and dark matter*, *Phys. Rev. D* **76** (2007) 103530, [0704.3285].

[497] D. J. H. Chung, L. L. Everett, K. Kong and K. T. Matchev, *Connecting LHC, ILC, and Quintessence*, *JHEP* **10** (2007) 016, [0706.2375].

[498] S. Lola, C. Pallis and E. Tzelati, *Tracking Quintessence and Cold Dark Matter Candidates*, *JCAP* **11** (2009) 017, [0907.2941].

[499] C. Pallis, *Cold Dark Matter in non-Standard Cosmologies, PAMELA, ATIC and Fermi LAT*, *Nucl. Phys. B* **831** (2010) 217–247, [0909.3026].

[500] L. Visinelli and P. Gondolo, *Axion cold dark matter in non-standard cosmologies*, *Phys. Rev. D* **81** (2010) 063508, [0912.0015].

[501] K. Redmond and A. L. Erickcek, *New Constraints on Dark Matter Production during Kination*, *Phys. Rev. D* **96** (2017) 043511, [1704.01056].

[502] F. D'Eramo, N. Fernandez and S. Profumo, *When the Universe Expands Too Fast: Relentless Dark Matter*, *JCAP* **05** (2017) 012, [1703.04793].

[503] F. D'Eramo, N. Fernandez and S. Profumo, *Dark Matter Freeze-in Production in Fast-Expanding Universes*, *JCAP* **02** (2018) 046, [1712.07453].

[504] K. Redmond, A. Trezza and A. L. Erickcek, *Growth of Dark Matter Perturbations during Kination*, *Phys. Rev. D* **98** (2018) 063504, [1807.01327].

[505] L. Visinelli and J. Redondo, *Axion Miniclusters in Modified Cosmological Histories*, *Phys. Rev. D* **101** (2020) 023008, [1808.01879].

[506] H. Tashiro, T. Chiba and M. Sasaki, *Reheating after quintessential inflation and gravitational waves*, *Class. Quant. Grav.* **21** (2004) 1761–1772, [gr-qc/0307068].

[507] B. Li, T. Rindler-Daller and P. R. Shapiro, *Cosmological Constraints on Bose-Einstein-Condensed Scalar Field Dark Matter*, *Phys. Rev. D* **89** (2014) 083536, [1310.6061].

[508] T. Rindler-Daller and P. R. Shapiro, *Complex scalar field dark matter on galactic scales*, *Mod. Phys. Lett. A* **29** (2014) 1430002, [1312.1734].

[509] B. Li, P. R. Shapiro and T. Rindler-Daller, *Bose-Einstein-condensed scalar field dark matter and the gravitational wave background from inflation: new cosmological constraints and its detectability by LIGO*, *Phys. Rev.* **D96** (2017) 063505, [1611.07961].

[510] B. Li and P. R. Shapiro, *Precision cosmology and the stiff-amplified gravitational-wave background from inflation: NANOGrav, Advanced LIGO-Virgo and the Hubble tension*, *JCAP* **10** (2021) 024, [2107.12229].

[511] D. G. Figueroa and E. H. Tanin, *Inconsistency of an inflationary sector coupled only to Einstein gravity*, *JCAP* **10** (2019) 050, [1811.04093].

[512] D. J. H. Chung and P. Zhou, *Gravity Waves as a Probe of Hubble Expansion Rate During An Electroweak Scale Phase Transition*, *Phys. Rev. D* **82** (2010) 024027, [1003.2462].

[513] J. D. Barrow and M. S. Turner, *Inflation in the Universe*, *Nature* **292** (1981) 35–38.

[514] M. S. Turner and L. M. Widrow, *Old Inflation Is Not Prevented by Large Amounts of Anisotropy*, *Nature* **326** (1987) 206.

[515] F. Niedermann and M. S. Sloth, *New Early Dark Energy*, *Phys. Rev. D* **103** (2021) L041303, [1910.10739].

[516] F. Niedermann and M. S. Sloth, *Resolving the Hubble tension with new early dark energy*, *Phys. Rev. D* **102** (2020) 063527, [2006.06686].

[517] M. S. Turner, *Coherent Scalar Field Oscillations in an Expanding Universe*, *Phys. Rev.* **D28** (1983) 1243.

[518] K. D. Lozanov and M. A. Amin, *Equation of State and Duration to Radiation Domination after Inflation*, *Phys. Rev. Lett.* **119** (2017) 061301, [1608.01213].

[519] J. van de Vis, R. Nguyen, E. I. Sfakianakis, J. T. Giblin and D. I. Kaiser, *Time scales for nonlinear processes in preheating after multifield inflation with nonminimal couplings*, *Phys. Rev. D* **102** (2020) 043528, [2005.00433].

[520] P. Saha, S. Anand and L. Sriramkumar, *Accounting for the time evolution of the equation of state parameter during reheating*, *Phys. Rev. D* **102** (2020) 103511, [2005.01874].

[521] S. Antusch, D. G. Figueroa, K. Marschall and F. Torrenti, *Energy distribution and equation of state of the early Universe: matching the end of inflation and the onset of radiation domination*, *Phys. Lett. B* **811** (2020) 135888, [2005.07563].

[522] P. J. E. Peebles and A. Vilenkin, *Quintessential inflation*, *Phys. Rev.* **D59** (1999) 063505, [astro-ph/9810509].

[523] K. Dimopoulos and J. W. F. Valle, *Modeling quintessential inflation*, *Astropart. Phys.* **18** (2002) 287–306, [astro-ph/0111417].

[524] H. Ooguri and C. Vafa, *On the Geometry of the String Landscape and the Swampland*, *Nucl. Phys. B* **766** (2007) 21–33, [hep-th/0605264].

[525] T. D. Brennan, F. Carta and C. Vafa, *The String Landscape, the Swampland, and the Missing Corner*, *PoS* **TASI2017** (2017) 015, [1711.00864].

[526] E. Palti, *The Swampland: Introduction and Review*, *Fortsch. Phys.* **67** (2019) 1900037, [1903.06239].

[527] C. Eröncel, R. Sato, G. Servant and P. Simakachorn `to appear`.

[528] A. L. Erickcek and K. Sigurdson, *Reheating Effects in the Matter Power Spectrum and Implications for Substructure*, *Phys. Rev.* **D84** (2011) 083503, [1106.0536].

[529] N. Musoke, S. Hotchkiss and R. Easther, *Lighting the Dark: Evolution of the Postinflationary Universe*, *Phys. Rev. Lett.* **124** (2020) 061301, [1909.11678].

[530] B. Eggemeier, B. Schwabe, J. C. Niemeyer and R. Easther, *Gravitational Collapse in the Postinflationary Universe*, *Phys. Rev. D* **105** (2022) 023516, [2110.15109].

[531] T. Harada, C.-M. Yoo, K. Kohri, K.-i. Nakao and S. Jhingan, *Primordial black hole formation in the matter-dominated phase of the Universe*, *Astrophys. J.* **833** (2016) 61, [1609.01588].

[532] M. Cirelli, Y. Gouttenoire, K. Petraki and F. Sala, *Homeopathic Dark Matter, Or How Diluted Heavy Substances Produce High Energy Cosmic Rays*, *JCAP* **02** (2019) 014, [1811.03608].

[533] L. A. Kofman, A. D. Linde and A. A. Starobinsky, *Inflationary Universe Generated by the Combined Action of a Scalar Field and Gravitational Vacuum Polarization*, *Phys. Lett. B* **157** (1985) 361–367.

[534] A. A. Starobinsky, *Multicomponent De Sitter (Inflationary) Stages and the Generation of Perturbations*, *JETP Lett.* **42** (1985) 152–155.

[535] J. Silk and M. S. Turner, *Double Inflation*, *Phys. Rev. D* **35** (1987) 419.

[536] D. S. Salopek, J. R. Bond and J. M. Bardeen, *Designing Density Fluctuation Spectra in Inflation*, *Phys. Rev. D* **40** (1989) 1753.

[537] V. F. Mukhanov and M. I. Zelnikov, *What kinds of perturbation spectra can be produced by inflation?*, *Phys. Lett. B* **263** (1991) 169–175.

[538] D. Polarski and A. A. Starobinsky, *Spectra of perturbations produced by double inflation with an intermediate matter dominated stage*, *Nucl. Phys. B* **385** (1992) 623–650.

[539] R. K. Jain, P. Chingangbam, J.-O. Gong, L. Sriramkumar and T. Souradeep, *Punctuated inflation and the low CMB multipoles*, *JCAP* **01** (2009) 009, [0809.3915].

[540] S. Pi, M. Sasaki and Y.-l. Zhang, *Primordial Tensor Perturbation in Double Inflationary Scenario with a Break*, *JCAP* **06** (2019) 049, [1904.06304].

[541] T. Damour and V. F. Mukhanov, *Inflation without slow roll*, *Phys. Rev. Lett.* **80** (1998) 3440–3443, [gr-qc/9712061].

[542] J. A. Adams, G. G. Ross and S. Sarkar, *Multiple inflation*, *Nucl. Phys. B* **503** (1997) 405–425, [hep-ph/9704286].

[543] C. P. Burgess, R. Easther, A. Mazumdar, D. F. Mota and T. Multamaki, *Multiple inflation, cosmic string networks and the string landscape*, *JHEP* **05** (2005) 067, [hep-th/0501125].

[544] M. Cicoli, S. Downes, B. Dutta, F. G. Pedro and A. Westphal, *Just enough inflation: power spectrum modifications at large scales*, *JCAP* **12** (2014) 030, [1407.1048].

[545] G. D'Amico and N. Kaloper, *Rollercoaster cosmology*, *JCAP* **08** (2021) 058, [2011.09489].

[546] T. Konstandin and G. Servant, *Cosmological Consequences of Nearly Conformal Dynamics at the TeV scale*, *JCAP* **1112** (2011) 009, [1104.4791].

[547] B. von Harling and G. Servant, *QCD-induced Electroweak Phase Transition*, *JHEP* **01** (2018) 159, [1711.11554].

[548] S. Bruggisser, B. Von Harling, O. Matsedonskyi and G. Servant, *Electroweak Phase Transition and Baryogenesis in Composite Higgs Models*, *JHEP* **12** (2018) 099, [1804.07314].

[549] P. Creminelli, A. Nicolis and R. Rattazzi, *Holography and the electroweak phase transition*, *JHEP* **03** (2002) 051, [hep-th/0107141].

[550] Y. Cui, M. Lewicki and D. E. Morrissey, *Gravitational Wave Bursts as Harbingers of Cosmic Strings Diluted by Inflation*, *Phys. Rev. Lett.* **125** (2020) 211302, [1912.08832].

[551] Y. Gouttenoire, O. Matsedonskyi, G. Servant and P. Simakachorn `to appear`.

[552] B. Allen and J. D. Romano, *Detecting a stochastic background of gravitational radiation: Signal processing strategies and sensitivities*, *Phys. Rev. D* **59** (1999) 102001, [gr-qc/9710117].

[553] H. Kudoh, A. Taruya, T. Hiramatsu and Y. Himemoto, *Detecting a gravitational-wave background with next-generation space interferometers*, *Phys. Rev. D* **73** (2006) 064006, [gr-qc/0511145].

[554] NANOGRAV collaboration, Z. Arzoumanian et al., *The NANOGrav 11-year Data Set: Pulsar-timing Constraints On The Stochastic Gravitational-wave Background*, *Astrophys. J.* **859** (2018) 47, [1801.02617].

[555] W. Buchmuller, V. Domcke and K. Schmitz, *Stochastic Gravitational-Wave Background from Metastable Cosmic Strings*, *JCAP* **12** (2021) 006, [2107.04578].

[556] R. Durrer and C. Caprini, *Primordial magnetic fields and causality*, *JCAP* **11** (2003) 010, [astro-ph/0305059].

[557] C. Caprini, R. Durrer, T. Konstandin and G. Servant, *General Properties of the Gravitational Wave Spectrum from Phase Transitions*, *Phys. Rev. D* **79** (2009) 083519, [0901.1661].

[558] R.-G. Cai, S. Pi and M. Sasaki, *Universal infrared scaling of gravitational wave background spectra*, *Phys. Rev. D* **102** (2020) 083528, [1909.13728].

[559] G. Barenboim and W.-I. Park, *Gravitational waves from first order phase transitions as a probe of an early matter domination era and its inverse problem*, *Phys. Lett. B* **759** (2016) 430–438, [1605.03781].

[560] G. Domènech, S. Pi and M. Sasaki, *Induced gravitational waves as a probe of thermal history of the universe*, *JCAP* **08** (2020) 017, [2005.12314].

[561] J. Ellis, M. Lewicki and V. Vaskonen, *Updated predictions for gravitational waves produced in a strongly supercooled phase transition*, *JCAP* **11** (2020) 020, [2007.15586].

[562] F. Ertas, F. Kahlhoefer and C. Tasillo, *Turn Up the Volume: Listening to Phase Transitions in Hot Dark Sectors*, *JCAP* **02** (2022) 014, [2109.06208].

[563] G. Sigl, D. N. Schramm and P. Bhattacharjee, *On the origin of highest energy cosmic rays*, *Astropart. Phys.* **2** (1994) 401–414, [astro-ph/9403039].

[564] P. Bhattacharjee and G. Sigl, *Origin and propagation of extremely high-energy cosmic rays*, *Phys. Rept.* **327** (2000) 109–247, [astro-ph/9811011].

[565] R. H. Cyburt, J. R. Ellis, B. D. Fields and K. A. Olive, *Updated nucleosynthesis constraints on unstable relic particles*, *Phys. Rev.* **D67** (2003) 103521, [astro-ph/0211258].

[566] K. Jedamzik, *Big bang nucleosynthesis constraints on hadronically and electromagnetically decaying relic neutral particles*, *Phys. Rev.* **D74** (2006) 103509, [hep-ph/0604251].

[567] K. Jedamzik and M. Pospelov, *Big Bang Nucleosynthesis and Particle Dark Matter*, *New J. Phys.* **11** (2009) 105028, [0906.2087].

[568] M. Kawasaki, K. Kohri, T. Moroi and Y. Takaesu, *Revisiting Big-Bang Nucleosynthesis Constraints on Long-Lived Decaying Particles*, *Phys. Rev.* **D97** (2018) 023502, [1709.01211].

[569] R. van Haasteren et al., *Placing limits on the stochastic gravitational-wave background using European Pulsar Timing Array data*, *Mon. Not. Roy. Astron. Soc.* **414** (2011) 3117–3128, [1103.0576].

[570] J. Fan, O. Özsoy and S. Watson, *Nonthermal histories and implications for structure formation*, *Phys. Rev.* **D90** (2014) 043536, [1405.7373].

[571] M. Sten Delos, T. Linden and A. L. Erickcek, *Breaking a dark degeneracy: The gamma-ray signature of early matter domination*, 1910.08553.

[572] C. Blanco, M. S. Delos, A. L. Erickcek and D. Hooper, *Annihilation Signatures of Hidden Sector Dark Matter Within Early-Forming Microhalos*, *Phys. Rev. D* **100** (2019) 103010, [1906.00010].

[573] A. G. Polnarev and M. Yu. Khlopov, *COSMOLOGY, PRIMORDIAL BLACK HOLES, AND SUPERMASSIVE PARTICLES*, *Sov. Phys. Usp.* **28** (1985) 213–232.

[574] A. M. Green, A. R. Liddle and A. Riotto, *Primordial black hole constraints in cosmologies with early matter domination*, *Phys. Rev.* **D56** (1997) 7559–7565, [astro-ph/9705166].

[575] J. Georg, G. Şengör and S. Watson, *Nonthermal WIMPs and primordial black holes*, *Phys. Rev.* **D93** (2016) 123523, [1603.00023].

[576] R. J. Scherrer and M. S. Turner, *Decaying Particles Do Not Heat Up the Universe*, *Phys. Rev.* **D31** (1985) 681.

[577] B. S. Acharya, G. Kane and E. Kuflik, *Bounds on scalar masses in theories of moduli stabilization*, *Int. J. Mod. Phys.* **A29** (2014) 1450073, [1006.3272].

[578] M. Dine, W. Fischler and D. Nemeschansky, *Solution of the Entropy Crisis of Supersymmetric Theories*, *Phys. Lett.* **136B** (1984) 169–174.

[579] G. D. Coughlan, R. Holman, P. Ramond and G. G. Ross, *Supersymmetry and the Entropy Crisis*, *Phys. Lett.* **140B** (1984) 44–48.

[580] M. Dine, L. Randall and S. D. Thomas, *Baryogenesis from flat directions of the supersymmetric standard model*, *Nucl. Phys. B* **458** (1996) 291–326, [hep-ph/9507453].

[581] B. S. Acharya, P. Kumar, K. Bobkov, G. Kane, J. Shao and S. Watson, *Non-thermal Dark Matter and the Moduli Problem in String Frameworks*, *JHEP* **06** (2008) 064, [0804.0863].

[582] M. Dine, L. Randall and S. D. Thomas, *Supersymmetry breaking in the early universe*, *Phys. Rev. Lett.* **75** (1995) 398–401, [hep-ph/9503303].

[583] J. R. Ellis, A. D. Linde and D. V. Nanopoulos, *Inflation Can Save the Gravitino*, *Phys. Lett.* **118B** (1982) 59–64.

[584] D. V. Nanopoulos, K. A. Olive and M. Srednicki, *After Primordial Inflation*, *Phys. Lett.* **127B** (1983) 30–34.

[585] J. R. Ellis, J. E. Kim and D. V. Nanopoulos, *Cosmological Gravitino Regeneration and Decay*, *Phys. Lett.* **145B** (1984) 181–186.

[586] G. F. Giudice, I. Tkachev and A. Riotto, *Nonthermal production of dangerous relics in the early universe*, *JHEP* **08** (1999) 009, [hep-ph/9907510].

[587] G. N. Felder, L. Kofman and A. D. Linde, *Gravitational particle production and the moduli problem*, *JHEP* **02** (2000) 027, [hep-ph/9909508].

[588] S. Weinberg, *Cosmological Constraints on the Scale of Supersymmetry Breaking*, *Phys. Rev. Lett.* **48** (1982) 1303.

[589] L. Randall and S. D. Thomas, *Solving the cosmological moduli problem with weak scale inflation*, *Nucl. Phys.* **B449** (1995) 229–247, [hep-ph/9407248].

[590] P. Binetruy, M. K. Gaillard and Y.-Y. Wu, *Supersymmetry breaking and weakly versus strongly coupled string theory*, *Phys. Lett.* **B412** (1997) 288–295, [hep-th/9702105].

[591] T. Banks, M. Berkooz and P. J. Steinhardt, *The Cosmological moduli problem, supersymmetry breaking, and stability in postinflationary cosmology*, *Phys. Rev.* **D52** (1995) 705–716, [hep-th/9501053].

[592] S. Krippendorf, F. Muia and F. Quevedo, *Moduli Stars*, *JHEP* **08** (2018) 070, [1806.04690].

[593] J. T. Giblin, G. Kane, E. Nesbit, S. Watson and Y. Zhao, *Was the Universe Actually Radiation Dominated Prior to Nucleosynthesis?*, *Phys. Rev.* **D96** (2017) 043525, [1706.08536].

[594] L. J. Hall and Y. Nomura, *A Finely-Predicted Higgs Boson Mass from A Finely-Tuned Weak Scale*, *JHEP* **03** (2010) 076, [0910.2235].

[595] J. D. Wells, *PeV-scale supersymmetry*, *Phys. Rev.* **D71** (2005) 015013, [hep-ph/0411041].

[596] N. Arkani-Hamed and S. Dimopoulos, *Supersymmetric unification without low energy supersymmetry and signatures for fine-tuning at the LHC*, *JHEP* **06** (2005) 073, [hep-th/0405159].

[597] E. Bagnaschi, G. F. Giudice, P. Slavich and A. Strumia, *Higgs Mass and Unnatural Supersymmetry*, *JHEP* **09** (2014) 092, [1407.4081].

[598] N. Arkani-Hamed, S. Dimopoulos, G. F. Giudice and A. Romanino, *Aspects of split supersymmetry*, *Nucl. Phys.* **B709** (2005) 3–46, [hep-ph/0409232].

[599] I. Affleck and M. Dine, *A New Mechanism for Baryogenesis*, *Nucl. Phys.* **B249** (1985) 361–380.

[600] T. Moroi and L. Randall, *Wino cold dark matter from anomaly mediated SUSY breaking*, *Nucl. Phys.* **B570** (2000) 455–472, [hep-ph/9906527].

[601] J. Fan and M. Reece, *In Wino Veritas? Indirect Searches Shed Light on Neutralino Dark Matter*, *JHEP* **10** (2013) 124, [1307.4400].

[602] B. S. Acharya, K. Bobkov and P. Kumar, *An M Theory Solution to the Strong CP Problem and Constraints on the Axiverse*, *JHEP* **11** (2010) 105, [1004.5138].

[603] G. Kane, K. Sinha and S. Watson, *Cosmological Moduli and the Post-Inflationary Universe: A Critical Review*, *Int. J. Mod. Phys.* **D24** (2015) 1530022, [1502.07746].

[604] L. Parker, *Quantized fields and particle creation in expanding universes. 1.*, *Phys. Rev.* **183** (1969) 1057–1068.

[605] Y. B. Zeldovich and A. A. Starobinsky, *Particle Production and Vacuum Polarization in an Anisotropic Gravitational Field*, *Zh. Eksp. Teor. Fiz.* **61** (1971) 2161–2175.

[606] N. D. Birrell and P. C. W. Davies, *Quantum Fields in Curved Space*. Cambridge Monographs on Mathematical Physics. Cambridge Univ. Press, Cambridge, UK, 2, 1984, 10.1017/CBO9780511622632.

[607] D. J. H. Chung, E. W. Kolb and A. Riotto, *Superheavy dark matter*, *Phys. Rev.* **D59** (1999) 023501, [hep-ph/9802238].

[608] E. W. Kolb, D. J. H. Chung and A. Riotto, *WIMPzillas!*, *AIP Conf. Proc.* **484** (1999) 91–105, [hep-ph/9810361].

[609] D. J. H. Chung, P. Crotty, E. W. Kolb and A. Riotto, *On the Gravitational Production of Superheavy Dark Matter*, *Phys. Rev.* **D64** (2001) 043503, [hep-ph/0104100].

[610] E. W. Kolb and A. J. Long, *Superheavy dark matter through Higgs portal operators*, *Phys. Rev.* **D96** (2017) 103540, [1708.04293].

[611] Y. Ema, K. Nakayama and Y. Tang, *Production of Purely Gravitational Dark Matter*, *JHEP* **09** (2018) 135, [1804.07471].

[612] Y. Ema, R. Jinno, K. Mukaida and K. Nakayama, *Gravitational Effects on Inflaton Decay*, *JCAP* **1505** (2015) 038, [1502.02475].

[613] Y. Ema, R. Jinno, K. Mukaida and K. Nakayama, *Gravitational particle production in oscillating backgrounds and its cosmological implications*, *Phys. Rev.* **D94** (2016) 063517, [1604.08898].

[614] Y. Ema, K. Nakayama and Y. Tang, *Production of Purely Gravitational Dark Matter: The Case of Fermion and Vector Boson*, *JHEP* **07** (2019) 060, [1903.10973].

[615] D. J. H. Chung, E. W. Kolb and A. J. Long, *Gravitational production of super-Hubble-mass particles: an analytic approach*, *JHEP* **01** (2019) 189, [1812.00211].

[616] K. Dimopoulos, *Can a vector field be responsible for the curvature perturbation in the Universe?*, *Phys. Rev.* **D74** (2006) 083502, [hep-ph/0607229].

[617] D. J. H. Chung, L. L. Everett, H. Yoo and P. Zhou, *Gravitational Fermion Production in Inflationary Cosmology*, *Phys. Lett.* **B712** (2012) 147–154, [1109.2524].

[618] P. W. Graham, J. Mardon and S. Rajendran, *Vector Dark Matter from Inflationary Fluctuations*, *Phys. Rev.* **D93** (2016) 103520, [1504.02102].

[619] B. Holdom, *Two U(1)'s and Epsilon Charge Shifts*, *Phys. Lett.* **166B** (1986) 196–198.

[620] R. Foot and X.-G. He, *Comment on Z Z-prime mixing in extended gauge theories*, *Phys. Lett.* **B267** (1991) 509–512.

[621] T. Hambye, M. H. G. Tytgat, J. Vandecasteele and L. Vanderheyden, *Dark matter from dark photons: a taxonomy of dark matter production*, *Phys. Rev. D* **100** (2019) 095018, [1908.09864].

[622] M. Cirelli, P. Panci, K. Petraki, F. Sala and M. Taoso, *Dark Matter's secret liaisons: phenomenology of a dark U(1) sector with bound states*, *JCAP* **1705** (2017) 036, [1612.07295].

[623] L. J. Hall, K. Jedamzik, J. March-Russell and S. M. West, *Freeze-In Production of FIMP Dark Matter*, *JHEP* **03** (2010) 080, [0911.1120].

[624] X. Chu, T. Hambye and M. H. G. Tytgat, *The Four Basic Ways of Creating Dark Matter Through a Portal*, *JCAP* **1205** (2012) 034, [1112.0493].

[625] J. Berger, K. Jedamzik and D. G. E. Walker, *Cosmological Constraints on Decoupled Dark Photons and Dark Higgs*, *JCAP* **1611** (2016) 032, [1605.07195].

[626] H. M. Hodges, *Mirror baryons as the dark matter*, *Phys. Rev.* **D47** (1993) 456–459.

[627] Z. G. Berezhiani, A. D. Dolgov and R. N. Mohapatra, *Asymmetric inflationary reheating and the nature of mirror universe*, *Phys. Lett.* **B375** (1996) 26–36, [hep-ph/9511221].

[628] J. L. Feng, H. Tu and H.-B. Yu, *Thermal Relics in Hidden Sectors*, *JCAP* **0810** (2008) 043, [0808.2318].

[629] P. Adshead, Y. Cui and J. Shelton, *Chilly Dark Sectors and Asymmetric Reheating*, *JHEP* **06** (2016) 016, [1604.02458].

[630] D. Kazanas, R. N. Mohapatra, S. Nussinov, V. L. Teplitz and Y. Zhang, *Supernova Bounds on the Dark Photon Using its Electromagnetic Decay*, *Nucl. Phys.* **B890** (2014) 17–29, [1410.0221].

[631] J. H. Chang, R. Essig and S. D. McDermott, *Revisiting Supernova 1987A Constraints on Dark Photons*, *JHEP* **01** (2017) 107, [1611.03864].

[632] J. Jaeckel and A. Ringwald, *The Low-Energy Frontier of Particle Physics*, *Ann. Rev. Nucl. Part. Sci.* **60** (2010) 405–437, [1002.0329].

[633] R. Essig et al., *Working Group Report: New Light Weakly Coupled Particles*, in *Proceedings, 2013 Community Summer Study on the Future of U.S. Particle Physics: Snowmass on the Mississippi (CSS2013): Minneapolis, MN, USA, July 29-August 6, 2013*, 2013. 1311.0029.

[634] J. Alexander et al., *Dark Sectors 2016 Workshop: Community Report*, 8, 2016. 1608.08632.

[635] K. Griest and M. Kamionkowski, *Unitarity Limits on the Mass and Radius of Dark Matter Particles*, *Phys. Rev. Lett.* **64** (1990) 615.

[636] B. Kors and P. Nath, *A Stueckelberg extension of the standard model*, *Phys. Lett.* **B586** (2004) 366–372, [hep-ph/0402047].

[637] D. Feldman, B. Kors and P. Nath, *Extra-weakly Interacting Dark Matter*, *Phys. Rev.* **D75** (2007) 023503, [hep-ph/0610133].

[638] P. Fayet, *U-boson production in e+ e- annihilations, psi and Upsilon decays, and Light Dark Matter*, *Phys. Rev.* **D75** (2007) 115017, [hep-ph/0702176].

[639] L. Ackerman, M. R. Buckley, S. M. Carroll and M. Kamionkowski, *Dark Matter and Dark Radiation*, *Phys. Rev.* **D79** (2009) 023519, [0810.5126].

[640] M. Goodsell, J. Jaeckel, J. Redondo and A. Ringwald, *Naturally Light Hidden Photons in LARGE Volume String Compactifications*, *JHEP* **11** (2009) 027, [0909.0515].

[641] D. E. Morrissey, D. Poland and K. M. Zurek, *Abelian Hidden Sectors at a GeV*, *JHEP* **07** (2009) 050, [0904.2567].

[642] S. Andreas, M. D. Goodsell and A. Ringwald, *Dark matter and dark forces from a supersymmetric hidden sector*, *Phys. Rev.* **D87** (2013) 025007, [1109.2869].

[643] M. Goodsell, S. Ramos-Sanchez and A. Ringwald, *Kinetic Mixing of U(1)s in Heterotic Orbifolds*, *JHEP* **01** (2012) 021, [1110.6901].

[644] P. Fayet, *The light U boson as the mediator of a new force, coupled to a combination of Q, B, L and dark matter*, *Eur. Phys. J.* **C77** (2017) 53, [1611.05357].

[645] B. von Harling and K. Petraki, *Bound-state formation for thermal relic dark matter and unitarity*, *JCAP* **1412** (2014) 033, [1407.7874].

[646] J. Lizarraga, J. Urrestilla, D. Daverio, M. Hindmarsh and M. Kunz, *New CMB constraints for Abelian Higgs cosmic strings*, *JCAP* **1610** (2016) 042, [1609.03386].

[647] N. Arkani-Hamed, L. Motl, A. Nicolis and C. Vafa, *The String landscape, black holes and gravity as the weakest force*, *JHEP* **06** (2007) 060, [hep-th/0601001].

[648] R. T. Co, N. Fernandez, A. Ghalsasi, L. J. Hall and K. Harigaya, *Lepto-Axiogenesis*, *JHEP* **03** (2021) 017, [2006.05687].

[649] R. D. Peccei and H. R. Quinn, *Constraints Imposed by CP Conservation in the Presence of Instantons*, *Phys. Rev. D* **16** (1977) 1791–1797.

[650] K. Choi, S. H. Im and C. Sub Shin, *Recent Progress in the Physics of Axions and Axion-Like Particles*, *Ann. Rev. Nucl. Part. Sci.* **71** (2021) 225–252, [2012.05029].

[651] L. Di Luzio, M. Giannotti, E. Nardi and L. Visinelli, *The landscape of QCD axion models*, *Phys. Rept.* **870** (2020) 1–117, [2003.01100].

[652] A. Ayala, I. Domínguez, M. Giannotti, A. Mirizzi and O. Straniero, *Revisiting the bound on axion-photon coupling from Globular Clusters*, *Phys. Rev. Lett.* **113** (2014) 191302, [1406.6053].

[653] H.-J. Li, J.-G. Guo, X.-J. Bi, S.-J. Lin and P.-F. Yin, *Limits on axion-like particles from Mrk 421 with 4.5-year period observations by ARGO-YBJ and Fermi-LAT*, *Phys. Rev. D* **103** (2021) 083003, [2008.09464].

[654] J. W. Foster, Y. Kahn, O. Macias, Z. Sun, R. P. Eatough, V. I. Kondratiev et al., *Green Bank and Effelsberg Radio Telescope Searches for Axion Dark Matter Conversion in Neutron Star Magnetospheres*, *Phys. Rev. Lett.* **125** (2020) 171301, [2004.00011].

[655] J. Darling, *New Limits on Axionic Dark Matter from the Magnetar PSR J1745-2900*, *Astrophys. J. Lett.* **900** (2020) L28, [2008.11188].

[656] J. E. Kim, *A COMPOSITE INVISIBLE AXION*, *Phys. Rev. D* **31** (1985) 1733.

[657] K. Choi and J. E. Kim, *DYNAMICAL AXION*, *Phys. Rev. D* **32** (1985) 1828.

[658] S. Borsanyi et al., *Calculation of the axion mass based on high-temperature lattice quantum chromodynamics*, *Nature* **539** (2016) 69–71, [1606.07494].

[659] Flavour Lattice Averaging Group collaboration, S. Aoki et al., *FLAG Review 2019: Flavour Lattice Averaging Group (FLAG)*, *Eur. Phys. J. C* **80** (2020) 113, [1902.08191].

[660] V. A. Rubakov, *Grand unification and heavy axion*, *JETP Lett.* **65** (1997) 621–624, [hep-ph/9703409].

[661] A. Hook and J. Huang, *Probing Axions with Neutron Star Inspirals and Other Stellar Processes*, *JHEP* **06** (2018) 036, [1708.08464].

[662] A. Hook, *Solving the Hierarchy Problem Discretely*, *Phys. Rev. Lett.* **120** (2018) 261802, [1802.10093].

[663] L. Di Luzio, B. Gavela, P. Quilez and A. Ringwald, *An even lighter QCD axion*, *JHEP* **05** (2021) 184, [2102.00012].

[664] L. Di Luzio, B. Gavela, P. Quilez and A. Ringwald, *Dark Matter from an Even Lighter QCD Axion: Trapped Misalignment*, *JCAP* **10** (2021) 001, [2102.01082].

[665] R. Balkin, J. Serra, K. Springmann, S. Stelzl and A. Weiler, *White Dwarfs as a Probe of Light QCD Axions*, 2211.02661.

[666] A. Arvanitaki, S. Dimopoulos, M. Galanis, L. Lehner, J. O. Thompson and K. Van Tilburg, *Large-misalignment mechanism for the formation of compact axion structures: Signatures from the QCD axion to fuzzy dark matter*, *Phys. Rev. D* **101** (2020) 083014, [1909.11665].

[667] A. Papageorgiou, P. Quílez and K. Schmitz, *Axion dark matter from frictional misalignment*, 2206.01129.

[668] K. Choi, S. H. Im, H. J. Kim and H. Seong, *Axion Dark Matter with Thermal Friction*, 2206.01462.

[669] R. T. Co and K. Harigaya, *Axiogenesis*, *Phys. Rev. Lett.* **124** (2020) 111602, [1910.02080].

[670] S. M. Barr and J. E. Kim, *New Confining Force Solution of the QCD Axion Domain-Wall Problem*, *Phys. Rev. Lett.* **113** (2014) 241301, [1407.4311].

[671] F. Takahashi and M. Yamada, *Strongly broken Peccei-Quinn symmetry in the early Universe*, *JCAP* **10** (2015) 010, [1507.06387].

[672] A. Caputo and M. Reig, *Cosmic implications of a low-scale solution to the axion domain wall problem*, *Phys. Rev. D* **100** (2019) 063530, [1905.13116].

[673] L. Heurtier, F. Huang and T. M. P. Tait, *Resurrecting Low-Mass Axion Dark Matter via a Dynamical QCD Scale*, *JHEP* **12** (2021) 216, [2104.13390].

[674] V. Domcke, K. Harigaya and K. Mukaida, *Charge Transfer Between Rotating Complex Scalar Fields*, *JHEP* **08** (2022) 234, [2205.00942].

[675] S. B. Giddings and A. Strominger, *Loss of Incoherence and Determination of Coupling Constants in Quantum Gravity*, *Nucl. Phys. B* **307** (1988) 854–866.

[676] S. R. Coleman, *Why There Is Nothing Rather Than Something: A Theory of the Cosmological Constant*, *Nucl. Phys. B* **310** (1988) 643–668.

[677] G. Gilbert, *WORMHOLE INDUCED PROTON DECAY*, *Nucl. Phys. B* **328** (1989) 159–170.

[678] D. Harlow and H. Ooguri, *Constraints on Symmetries from Holography*, *Phys. Rev. Lett.* **122** (2019) 191601, [1810.05337].

[679] D. Harlow and H. Ooguri, *Symmetries in quantum field theory and quantum gravity*, *Commun. Math. Phys.* **383** (2021) 1669–1804, [1810.05338].

[680] M. Kamionkowski and J. March-Russell, *Planck scale physics and the Peccei-Quinn mechanism*, *Phys. Lett. B* **282** (1992) 137–141, [hep-th/9202003].

[681] R. Kallosh, A. D. Linde, D. A. Linde and L. Susskind, *Gravity and global symmetries*, *Phys. Rev. D* **52** (1995) 912–935, [hep-th/9502069].

[682] A. G. Cohen and D. B. Kaplan, *SPONTANEOUS BARYOGENESIS*, *Nucl. Phys. B* **308** (1988) 913–928.

[683] V. Domcke, Y. Ema and K. Mukaida, *Axion assisted Schwinger effect*, *JHEP* **05** (2021) 001, [2101.05192].

[684] K. Kamada and C. S. Shin, *Magnetogenesis from a rotating scalar: à la scalar chiral magnetic effect*, *JHEP* **04** (2020) 185, [1905.06966].

[685] M. Dine and A. Kusenko, *The Origin of the matter - antimatter asymmetry*, *Rev. Mod. Phys.* **76** (2003) 1, [hep-ph/0303065].

[686] R. T. Co, K. Harigaya and A. Pierce, *Cosmic Perturbations from a Rotating Field*, *JCAP* **10** (2022) 037, [2202.01785].

[687] R. T. Co, L. J. Hall and K. Harigaya, *Predictions for Axion Couplings from ALP Cogenesis*, *JHEP* **01** (2021) 172, [2006.04809].

[688] A. D. Sakharov, *Violation of CP Invariance, C asymmetry, and baryon asymmetry of the universe*, *Pisma Zh. Eksp. Teor. Fiz.* **5** (1967) 32–35.

[689] M. D'Onofrio, K. Rummukainen and A. Tranberg, *Sphaleron Rate in the Minimal Standard Model*, *Phys. Rev. Lett.* **113** (2014) 141602, [1404.3565].

[690] I. Baldes and G. Servant, *High scale electroweak phase transition: baryogenesis \& symmetry non-restoration*, *JHEP* **10** (2018) 053, [1807.08770].

[691] A. Glioti, R. Rattazzi and L. Vecchi, *Electroweak Baryogenesis above the Electroweak Scale*, *JHEP* **04** (2019) 027, [1811.11740].

[692] O. Matsedonskyi and G. Servant, *High-Temperature Electroweak Symmetry Non-Restoration from New Fermions and Implications for Baryogenesis*, *JHEP* **09** (2020) 012, [2002.05174].

[693] K. Harigaya and I. R. Wang, *Axiogenesis from $SU(2)_R$ phase transition*, *JHEP* **10** (2021) 022, [2107.09679].

[694] S. Weinberg, *Baryon and Lepton Nonconserving Processes*, *Phys. Rev. Lett.* **43** (1979) 1566–1570.

[695] V. Domcke, Y. Ema, K. Mukaida and M. Yamada, *Spontaneous Baryogenesis from Axions with Generic Couplings*, *JHEP* **08** (2020) 096, [2006.03148].

[696] R. T. Co, K. Harigaya, Z. Johnson and A. Pierce, *R-Parity Violation Axiogenesis*, *JHEP* **11** (2021) 210, [2110.05487].

[697] R. T. Co, L. J. Hall, K. Harigaya, K. A. Olive and S. Verner, *Axion Kinetic Misalignment and Parametric Resonance from Inflation*, *JCAP* **08** (2020) 036, [2004.00629].

[698] P. Moxhay and K. Yamamoto, *Peccei-Quinn Symmetry Breaking by Radiative Corrections in Supergravity*, *Phys. Lett. B* **151** (1985) 363–366.

[699] K. Mukaida and K. Nakayama, *Dynamics of oscillating scalar field in thermal environment*, *JCAP* **01** (2013) 017, [1208.3399].

[700] K. Mukaida and K. Nakayama, *Dissipative Effects on Reheating after Inflation*, *JCAP* **03** (2013) 002, [1212.4985].

[701] M. A. Shifman, A. I. Vainshtein, M. B. Voloshin and V. I. Zakharov, *Low-Energy Theorems for Higgs Boson Couplings to Photons*, *Sov. J. Nucl. Phys.* **30** (1979) 711–716.

[702] A. Anisimov and M. Dine, *Some issues in flat direction baryogenesis*, *Nucl. Phys. B* **619** (2001) 729–740, [hep-ph/0008058].

[703] D. Bodeker, *Moduli decay in the hot early Universe*, *JCAP* **06** (2006) 027, [hep-ph/0605030].

[704] M. Laine, *On bulk viscosity and moduli decay*, *Prog. Theor. Phys. Suppl.* **186** (2010) 404–416, [1007.2590].

[705] M. Carena, I. Low and C. E. M. Wagner, *Implications of a Modified Higgs to Diphoton Decay Width*, *JHEP* **08** (2012) 060, [1206.1082].

[706] S. R. Coleman, *Q Balls*, *Nucl. Phys. B* **262** (1985) 263.

[707] S. Kasuya and M. Kawasaki, *Q Ball formation in the gravity mediated SUSY breaking scenario*, *Phys. Rev. D* **62** (2000) 023512, [hep-ph/0002285].

[708] S. Kasuya and M. Kawasaki, *Q ball formation: Obstacle to Affleck-Dine baryogenesis in the gauge mediated SUSY breaking?*, *Phys. Rev. D* **64** (2001) 123515, [hep-ph/0106119].

[709] S. Kasuya, *Formation of the Q ball in the thermal logarithmic potential and its properties*, *Phys. Rev. D* **81** (2010) 083507, [1002.4032].

[710] S. Coleman, *Aspects of Symmetry: Selected Erice Lectures*. Cambridge University Press, Cambridge, U.K., 1985, 10.1017/CBO9780511565045.

[711] P. Di Vecchia and G. Veneziano, *Chiral Dynamics in the Large n Limit*, *Nucl. Phys. B* **171** (1980) 253–272.

[712] G. Grilli di Cortona, E. Hardy, J. Pardo Vega and G. Villadoro, *The QCD axion, precisely*, *JHEP* **01** (2016) 034, [1511.02867].

[713] C. Baker et al., *An Improved experimental limit on the electric dipole moment of the neutron*, *Phys. Rev. Lett.* **97** (2006) 131801, [hep-ex/0602020].

[714] J. M. Pendlebury et al., *Revised experimental upper limit on the electric dipole moment of the neutron*, *Phys. Rev. D* **92** (2015) 092003, [1509.04411].

[715] nEDM collaboration, C. Abel et al., *Measurement of the permanent electric dipole moment of the neutron*, *Phys. Rev. Lett.* **124** (2020) 081803, [2001.11966].

[716] C. Vafa and E. Witten, *Restrictions on Symmetry Breaking in Vector-Like Gauge Theories*, *Nucl. Phys. B* **234** (1984) 173–188.

[717] A. D. Linde, *INFLATION CAN BREAK SYMMETRY IN SUSY*, *Phys. Lett. B* **131** (1983) 330–334.

[718] A. A. Starobinsky and J. Yokoyama, *Equilibrium state of a selfinteracting scalar field in the De Sitter background*, *Phys. Rev. D* **50** (1994) 6357–6368, [astro-ph/9407016].

[719] Y.-P. Wu and K. Petraki, *Stochastic Baryogenesis*, *JCAP* **01** (2021) 022, [2008.08549].

[720] D. Bödeker and J. Nienaber, *Scalar field damping at high temperatures*, *Phys. Rev. D* **106** (2022) 056016, [2205.14166].

[721] R. Allahverdi, B. A. Campbell and J. R. Ellis, *Reheating and supersymmetric flat direction baryogenesis*, *Nucl. Phys. B* **579** (2000) 355–375, [hep-ph/0001122].

[722] D. Cadamuro and J. Redondo, *Cosmological bounds on pseudo Nambu-Goldstone bosons*, *JCAP* **02** (2012) 032, [1110.2895].

[723] C. Creque-Sarbinowski, J. Hyde and M. Kamionkowski, *High-Energy Astrophysical Neutrinos from Cosmic Strings*, 2206.06377.

[724] K. Schmitz, *New Sensitivity Curves for Gravitational-Wave Signals from Cosmological Phase Transitions*, *JHEP* **01** (2021) 097, [2002.04615].

[725] KAGRA, LIGO Scientific, VIRGO collaboration, B. P. Abbott et al., *Prospects for Observing and Localizing Gravitational-Wave Transients with Advanced LIGO, Advanced Virgo and KAGRA*, *Living Rev. Rel.* **21** (2018) 3, [1304.0670].

[726] LIGO Scientific, VIRGO collaboration, J. Abadie et al., *Upper limits on a stochastic gravitational-wave background using LIGO and Virgo interferometers at 600-1000 Hz*, *Phys. Rev.* **D85** (2012) 122001, [1112.5004].

[727] A. Vilenkin and E. P. S. Shellard, *Cosmic strings and other topological defects*. Cambridge University Press, 2000.

[728] K.-i. Maeda and N. Turok, *Finite Width Corrections to the Nambu Action for the Nielsen-Olesen String*, *Phys. Lett.* **B202** (1988) 376–380.

[729] D. Forster, *Dynamics of Relativistic Vortex Lines and their Relation to Dual Theory*, *Nucl. Phys.* **B81** (1974) 84–92.

[730] A. Vilenkin, *Gravitational Field of Vacuum Domain Walls and Strings*, *Phys. Rev.* **D23** (1981) 852–857.

[731] J. L. Christiansen, E. Albin, K. A. James, J. Goldman, D. Maruyama and G. F. Smoot, *Search for Cosmic Strings in the GOODS Survey*, *Phys. Rev.* **D77** (2008) 123509, [0803.0027].

[732] J. L. Christiansen, E. Albin, T. Fletcher, J. Goldman, I. P. W. Teng, M. Foley et al., *Search for Cosmic Strings in the COSMOS Survey*, *Phys. Rev.* **D83** (2011) 122004, [1008.0426].

[733] K. J. Mack, D. H. Wesley and L. J. King, *Observing cosmic string loops with gravitational lensing surveys*, *Phys. Rev.* **D76** (2007) 123515, [astro-ph/0702648].

[734] J. R. Gott, III, *Gravitational lensing effects of vacuum strings: Exact solutions*, *Astrophys. J.* **288** (1985) 422–427.

[735] N. Kaiser and A. Stebbins, *Microwave Anisotropy Due to Cosmic Strings*, *Nature* **310** (1984) 391–393.

[736] F. R. Bouchet, D. P. Bennett and A. Stebbins, *Microwave Anisotropy Patterns from Evolving String Networks*, *Nature* **335** (1988) 410–414.

[737] J. Silk and A. Vilenkin, *COSMIC STRINGS AND GALAXY FORMATION*, *Phys. Rev. Lett.* **53** (1984) 1700–1703.

[738] L. Pogosian and T. Vachaspati, *Cosmic microwave background anisotropy from wiggly strings*, *Phys. Rev.* **D60** (1999) 083504, [astro-ph/9903361].

[739] J. Lizarraga, J. Urrestilla, D. Daverio, M. Hindmarsh, M. Kunz and A. R. Liddle, *Constraining topological defects with temperature and polarization anisotropies*, *Phys. Rev.* **D90** (2014) 103504, [1408.4126].

[740] R. Battye and A. Moss, *Updated constraints on the cosmic string tension*, *Phys. Rev.* **D82** (2010) 023521, [1005.0479].

[741] T. Charnock, A. Avgoustidis, E. J. Copeland and A. Moss, *CMB constraints on cosmic strings and superstrings*, *Phys. Rev.* **D93** (2016) 123503, [1603.01275].

[742] A. Lopez-Eiguren, J. Lizarraga, M. Hindmarsh and J. Urrestilla, *Cosmic Microwave Background constraints for global strings and global monopoles*, *JCAP* **1707** (2017) 026, [1705.04154].

[743] Planck collaboration, P. A. R. Ade et al., *Planck 2013 results. XXV. Searches for cosmic strings and other topological defects*, *Astron. Astrophys.* **571** (2014) A25, [1303.5085].

[744] C. Ringeval and F. R. Bouchet, *All Sky CMB Map from Cosmic Strings Integrated Sachs-Wolfe Effect*, *Phys. Rev.* **D86** (2012) 023513, [1204.5041].

[745] R. Ciuca and O. F. Hernández, *Information theoretic bounds on cosmic string detection in CMB maps with noise*, *Mon. Not. Roy. Astron. Soc.* **492** (2020) 1329–1334, [1911.06378].

[746] R. Khatri and B. D. Wandelt, *Cosmic (super)string constraints from 21 cm radiation*, *Phys. Rev. Lett.* **100** (2008) 091302, [0801.4406].

[747] T. Matsuda, *Dark matter production from cosmic necklaces*, *JCAP* **0604** (2006) 005, [hep-ph/0509064].

[748] J. H. MacGibbon and R. H. Brandenberger, *High-energy neutrino flux from ordinary cosmic strings*, *Nucl. Phys.* **B331** (1990) 153–172.

[749] V. Berezinsky, P. Blasi and A. Vilenkin, *Ultrahigh-energy gamma-rays as signature of topological defects*, *Phys. Rev.* **D58** (1998) 103515, [astro-ph/9803271].

[750] V. Berezinsky, E. Sabancilar and A. Vilenkin, *Extremely High Energy Neutrinos from Cosmic Strings*, *Phys. Rev.* **D84** (2011) 085006, [1108.2509].

[751] D. Bird, S. Corbato, H. Dai, B. Dawson, J. Elbert, B. Emerson et al., *The cosmic-ray energy spectrum observed by the fly's eye*, *The Astrophysical Journal* **424** (1994) 491–502.

[752] K. Greisen, *End to the cosmic-ray spectrum?*, *Phys. Rev. Lett.* **16** (Apr, 1966) 748–750.

[753] G. T. Zatsepin and V. A. Kuzmin, *Upper limit of the spectrum of cosmic rays*, *Journal of Experimental and Theoretical Physics Letters (JETP Letters)* **4** (1966) 78–80.

[754] HiRes collaboration, R. Abbasi et al., *First observation of the Greisen-Zatsepin-Kuzmin suppression*, *Phys. Rev. Lett.* **100** (2008) 101101, [astro-ph/0703099].

[755] P. Bhattacharjee, *Cosmic Strings and Ultrahigh-Energy Cosmic Rays*, *Phys. Rev.* **D40** (1989) 3968.

[756] A. J. Gill and T. W. B. Kibble, *Cosmic rays from cosmic strings*, *Phys. Rev.* **D50** (1994) 3660–3665, [hep-ph/9403395].

[757] J. M. Hyde, A. J. Long and T. Vachaspati, *Dark Strings and their Couplings to the Standard Model*, *Phys. Rev.* **D89** (2014) 065031, [1312.4573].

[758] A. J. Long and T. Vachaspati, *Cosmic Strings in Hidden Sectors: 2. Cosmological and Astrophysical Signatures*, *JCAP* **1412** (2014) 040, [1409.6979].

[759] S. Laliberte and R. Brandenberger, *Ionization from Cosmic Strings at Cosmic Dawn*, *Phys. Rev. D* **101** (2020) 023528, [1907.08022].

[760] E. Witten, *Superconducting Strings*, *Nucl. Phys.* **B249** (1985) 557–592.

[761] A. Vilenkin and T. Vachaspati, *Electromagnetic Radiation from Superconducting Cosmic Strings*, *Phys. Rev. Lett.* **58** (1987) 1041–1044.

[762] D. N. Spergel, T. Piran and J. Goodman, *Dynamics of Superconducting Cosmic Strings*, *Nucl. Phys.* **B291** (1987) 847–875.

[763] E. J. Copeland, D. Haws, M. Hindmarsh and N. Turok, *Dynamics of and Radiation From Superconducting Strings and Springs*, *Nucl. Phys.* **B306** (1988) 908–930.

[764] J. J. Blanco-Pillado and K. D. Olum, *Electromagnetic radiation from superconducting string cusps*, *Nucl. Phys.* **B599** (2001) 435–445, [astro-ph/0008297].

[765] A. Babul, B. Paczynski and D. Spergel, *Gamma-ray bursts from superconducting cosmic strings at large redshifts*, *Astrophys. J.* **316** (1987) L49–L54.

[766] V. Berezinsky, B. Hnatyk and A. Vilenkin, *Gamma-ray bursts from superconducting cosmic strings*, *Phys. Rev.* **D64** (2001) 043004, [astro-ph/0102366].

[767] K. S. Cheng, Y.-W. Yu and T. Harko, *High Redshift Gamma-Ray Bursts: Observational Signatures of Superconducting Cosmic Strings?*, *Phys. Rev. Lett.* **104** (2010) 241102, [1005.3427].

[768] T. Vachaspati, *Cosmic Sparks from Superconducting Strings*, *Phys. Rev. Lett.* **101** (2008) 141301, [0802.0711].

[769] L. V. Zadorozhna and B. I. Hnatyk, *Electromagnetic Emission Bursts from the Near-Cusp Regions of Superconducting Cosmic Strings*, *Ukr. J. Phys.* **54** (2009) 1149–1156.

[770] Y.-F. Cai, E. Sabancilar and T. Vachaspati, *Radio bursts from superconducting strings*, *Phys. Rev.* **D85** (2012) 023530, [1110.1631].

[771] Y.-F. Cai, E. Sabancilar, D. A. Steer and T. Vachaspati, *Radio Broadcasts from Superconducting Strings*, *Phys. Rev.* **D86** (2012) 043521, [1205.3170].

[772] Y.-W. Yu, K.-S. Cheng, G. Shiu and H. Tye, *Implications of fast radio bursts for superconducting cosmic strings*, *JCAP* **1411** (2014) 040, [1409.5516].

[773] J. Ye, K. Wang and Y.-F. Cai, *Superconducting cosmic strings as sources of cosmological fast radio bursts*, *Eur. Phys. J.* **C77** (2017) 720, [1705.10956].

[774] R. Brandenberger, B. Cyr and A. V. Iyer, *Fast Radio Bursts from the Decay of Cosmic String Cusps*, 1707.02397.

[775] N. G. Sanchez and M. Signore, *The Cosmological Microwave Background Radiation, Cosmic and Superconducting Strings*, *Phys. Lett.* **B219** (1989) 413–418.

[776] N. G. Sanchez and M. Signore, *The Absence of Distortion in the Cosmic Microwave Background Spectrum and Superconducting Cosmic Strings*, *Phys. Lett.* **B241** (1990) 332–335.

[777] H. Tashiro, E. Sabancilar and T. Vachaspati, *CMB Distortions from Superconducting Cosmic Strings*, *Phys. Rev.* **D85** (2012) 103522, [1202.2474].

[778] A. Kogut et al., *The Primordial Inflation Explorer (PIXIE): A Nulling Polarimeter for Cosmic Microwave Background Observations*, *JCAP* **1107** (2011) 025, [1105.2044].

[779] H. Tashiro, E. Sabancilar and T. Vachaspati, *Constraints on Superconducting Cosmic Strings from Early Reionization*, *Phys. Rev.* **D85** (2012) 123535, [1204.3643].

[780] V. Berezinsky, K. D. Olum, E. Sabancilar and A. Vilenkin, *UHE neutrinos from superconducting cosmic strings*, *Phys. Rev.* **D80** (2009) 023014, [0901.0527].

[781] K. Saikawa, *A review of gravitational waves from cosmic domain walls*, *Universe* **3** (2017) 40, [1703.02576].

[782] C. J. A. P. Martins, P. Peter, I. Y. Rybak and E. P. S. Shellard, *Charge-velocity-dependent one-scale linear model*, *Phys. Rev. D* **104** (2021) 103506, [2108.03147].

[783] P. Auclair, S. Blasi, V. Brdar and K. Schmitz, *Gravitational Waves from Current-Carrying Cosmic Strings*, 2207.03510.

[784] N. Turok and P. Bhattacharjee, *STRETCHING COSMIC STRINGS*, *Phys. Rev.* **D29** (1984) 1557.

[785] J. Garriga and M. Sakellariadou, *Effects of friction on cosmic strings*, *Phys. Rev.* **D48** (1993) 2502–2515, [hep-th/9303024].

[786] Y. Aharonov and D. Bohm, *Significance of electromagnetic potentials in the quantum theory*, *Phys. Rev.* **115** (1959) 485–491.

[787] P. Avelino, *Assessing and improving on current semi-analytical models for cosmic defect network evolution*, *JCAP* **04** (2020) 012, [2001.06318].

[788] C. J. A. P. Martins, J. N. Moore and E. P. S. Shellard, *A Unified model for vortex string network evolution*, *Phys. Rev. Lett.* **92** (2004) 251601, [hep-ph/0310255].

[789] S. Dodelson and L. Hui, *A Horizon ratio bound for inflationary fluctuations*, *Phys. Rev. Lett.* **91** (2003) 131301, [astro-ph/0305113].

[790] A. R. Liddle and S. M. Leach, *How long before the end of inflation were observable perturbations produced?*, *Phys. Rev. D* **68** (2003) 103503, [astro-ph/0305263].

[791] Planck collaboration, Y. Akrami et al., *Planck 2018 results. VII. Isotropy and Statistics of the CMB*, 1906.02552.

[792] E. V. Linder, *Dark Energy from α-Attractors*, *Phys. Rev. D* **91** (2015) 123012, [1505.00815].

[793] S. S. Mishra, V. Sahni and Y. Shtanov, *Sourcing Dark Matter and Dark Energy from α-attractors*, *JCAP* **06** (2017) 045, [1703.03295].

[794] K. Dimopoulos and C. Owen, *Quintessential Inflation with α-attractors*, *JCAP* **06** (2017) 027, [1703.00305].

[795] K. Dimopoulos, L. Donaldson Wood and C. Owen, *Instant preheating in quintessential inflation with α-attractors*, *Phys. Rev. D* **97** (2018) 063525, [1712.01760].

[796] Y. Akrami, R. Kallosh, A. Linde and V. Vardanyan, *Dark energy, α-attractors, and large-scale structure surveys*, *JCAP* **06** (2018) 041, [1712.09693].

[797] K. Dimopoulos, M. Karčiauskas and C. Owen, *Quintessential inflation with a trap and axionic dark matter*, *Phys. Rev. D* **100** (2019) 083530, [1907.04676].

[798] A. S. Goncharov, A. D. Linde and M. I. Vysotsky, *COSMOLOGICAL PROBLEMS FOR SPONTANEOUSLY BROKEN SUPERGRAVITY*, *Phys. Lett.* **147B** (1984) 279–283.

[799] J. R. Ellis, A. B. Lahanas, D. V. Nanopoulos and K. Tamvakis, *No-Scale Supersymmetric Standard Model*, *Phys. Lett. B* **134** (1984) 429.

[800] C. P. Burgess, P. Martineau, F. Quevedo, G. Rajesh and R. J. Zhang, *Brane - anti-brane inflation in orbifold and orientifold models*, *JHEP* **03** (2002) 052, [hep-th/0111025].

[801] M. Cicoli, C. P. Burgess and F. Quevedo, *Fibre Inflation: Observable Gravity Waves from IIB String Compactifications*, *JCAP* **03** (2009) 013, [0808.0691].

[802] C. P. Burgess, M. Cicoli, S. de Alwis and F. Quevedo, *Robust Inflation from Fibrous Strings*, *JCAP* **05** (2016) 032, [1603.06789].

[803] L. Gorlich, S. Kachru, P. K. Tripathy and S. P. Trivedi, *Gaugino condensation and nonperturbative superpotentials in flux compactifications*, *JHEP* **12** (2004) 074, [hep-th/0407130].

[804] Z. Lalak, G. G. Ross and S. Sarkar, *Racetrack inflation and assisted moduli stabilisation*, *Nucl. Phys. B* **766** (2007) 1–20, [hep-th/0503178].

[805] M. Haack, D. Krefl, D. Lust, A. Van Proeyen and M. Zagermann, *Gaugino Condensates and D-terms from D7-branes*, *JHEP* **01** (2007) 078, [hep-th/0609211].

[806] V. Sahni, M. Sami and T. Souradeep, *Relic gravity waves from brane world inflation*, *Phys. Rev.* **D65** (2002) 023518, [gr-qc/0105121].

[807] M. Sami and V. Sahni, *Quintessential inflation on the brane and the relic gravity wave background*, *Phys. Rev. D* **70** (2004) 083513, [hep-th/0402086].

[808] M. Artymowski, O. Czerwinska, Z. Lalak and M. Lewicki, *Gravitational wave signals and cosmological consequences of gravitational reheating*, *JCAP* **04** (2018) 046, [1711.08473].

[809] L. Aresté Saló and J. de Haro, *Quintessential inflation at low reheating temperatures*, *Eur. Phys. J. C* **77** (2017) 798, [1707.02810].

[810] D. G. Figueroa and C. T. Byrnes, *The Standard Model Higgs as the origin of the hot Big Bang*, *Phys. Lett. B* **767** (2017) 272–277, [1604.03905].

[811] G. N. Felder, L. Kofman and A. D. Linde, *Instant preheating*, *Phys. Rev. D* **59** (1999) 123523, [hep-ph/9812289].

[812] G. N. Felder, L. Kofman and A. D. Linde, *Inflation and preheating in NO models*, *Phys. Rev. D* **60** (1999) 103505, [hep-ph/9903350].

[813] J. Haro, *Different reheating mechanisms in quintessence inflation*, *Phys. Rev. D* **99** (2019) 043510, [1807.07367].

[814] J. Bueno Sanchez and K. Dimopoulos, *Trapped Quintessential Inflation*, *Phys. Lett. B* **642** (2006) 294–301, [hep-th/0605258].

[815] J. Bueno Sanchez and K. Dimopoulos, *Trapped quintessential inflation in the context of flux compactifications*, *JCAP* **10** (2007) 002, [hep-th/0606223].

[816] B. Feng and M.-z. Li, *Curvaton reheating in nonoscillatory inflationary models*, *Phys. Lett. B* **564** (2003) 169–174, [hep-ph/0212213].

[817] J. Bueno Sanchez and K. Dimopoulos, *Curvaton reheating allows TeV Hubble scale in NO inflation*, *JCAP* **11** (2007) 007, [0707.3967].

[818] T. Matsuda, *NO Curvatons or Hybrid Quintessential Inflation*, *JCAP* **08** (2007) 003, [0707.1948].

[819] Particle Data Group collaboration, M. Tanabashi et al., *Review of Particle Physics*, *Phys. Rev. D* **98** (2018) 030001.

[820] D. Baumann, *Primordial Cosmology*, *PoS* **TASI2017** (2018) 009, [1807.03098].

[821] A. Arbey, *AlterBBN: A program for calculating the BBN abundances of the elements in alternative cosmologies*, *Comput. Phys. Commun.* **183** (2012) 1822–1831, [1106.1363].

[822] M. Kawasaki and T. Takesako, *Hubble Induced Mass in Radiation Dominated Universe*, *Phys. Lett. B* **711** (2012) 173–177, [1112.5823].

[823] A. Riotto, *Inflation and the Theory of Cosmological Perturbations*, *ICTP Lect. Notes Ser.* **14** (2003) 317–413, [hep-ph/0210162].

[824] J. Torrado, C. T. Byrnes, R. J. Hardwick, V. Vennin and D. Wands, *Measuring the duration of inflation with the curvaton*, *Phys. Rev. D* **98** (2018) 063525, [1712.05364].

[825] A. D. Linde, *Generation of Isothermal Density Perturbations in the Inflationary Universe*, *Phys. Lett. B* **158** (1985) 375–380.

[826] D. H. Lyth, *A Limit on the Inflationary Energy Density From Axion Isocurvature Fluctuations*, *Phys. Lett. B* **236** (1990) 408–410.

[827] M. Kawasaki, N. Sugiyama and T. Yanagida, *Isocurvature and adiabatic fluctuations of axion in chaotic inflation models and large scale structure*, *Phys. Rev. D* **54** (1996) 2442–2446, [hep-ph/9512368].

[828] M. Beltran, J. Garcia-Bellido and J. Lesgourgues, *Isocurvature bounds on axions revisited*, *Phys. Rev. D* **75** (2007) 103507, [hep-ph/0606107].

[829] K. Enqvist and J. McDonald, *Observable isocurvature fluctuations from the Affleck-Dine condensate*, *Phys. Rev. Lett.* **83** (1999) 2510–2513, [hep-ph/9811412].

[830] S. Kasuya, M. Kawasaki and F. Takahashi, *Isocurvature fluctuations in Affleck-Dine mechanism and constraints on inflation models*, *JCAP* **10** (2008) 017, [0805.4245].

[831] K. Kamada, K. Kohri and S. Yokoyama, *Affleck-Dine baryogenesis with modulated reheating*, *JCAP* **01** (2011) 027, [1008.1450].

[832] J. McDonald, *Anthropically Selected Baryon Number and Isocurvature Constraints*, *JCAP* **10** (2012) 005, [1207.2135].

[833] K. Harigaya, A. Kamada, M. Kawasaki, K. Mukaida and M. Yamada, *Affleck-Dine Baryogenesis and Dark Matter Production after High-scale Inflation*, *Phys. Rev. D* **90** (2014) 043510, [1404.3138].

[834] M. Dine and A. Anisimov, *Is there a Peccei-Quinn phase transition?*, *JCAP* **07** (2005) 009, [hep-ph/0405256].

[835] K. S. Jeong and F. Takahashi, *Suppressing Isocurvature Perturbations of QCD Axion Dark Matter*, *Phys. Lett. B* **727** (2013) 448–451, [1304.8131].

[836] T. Higaki, K. S. Jeong and F. Takahashi, *Solving the Tension between High-Scale Inflation and Axion Isocurvature Perturbations*, *Phys. Lett. B* **734** (2014) 21–26, [1403.4186].

[837] M. Dine and L. Stephenson-Haskins, *Hybrid Inflation with Planck Scale Fields*, *JHEP* **09** (2015) 208, [1408.0046].

[838] K. Choi, E. J. Chun, S. H. Im and K. S. Jeong, *Diluting the inflationary axion fluctuation by a stronger QCD in the early Universe*, *Phys. Lett. B* **750** (2015) 26–30, [1505.00306].

[839] M. Laine and A. Vuorinen, *Basics of Thermal Field Theory*, vol. 925. Springer, 2016, 10.1007/978-3-319-31933-9.

[840] K. Mukaida, K. Nakayama and M. Takimoto, *Fate of Z_2 Symmetric Scalar Field*, *JHEP* **12** (2013) 053, [1308.4394].

[841] A. Arbey, J. Lesgourgues and P. Salati, *Cosmological constraints on quintessential halos*, *Phys. Rev. D* **65** (2002) 083514, [astro-ph/0112324].

[842] A. J. Brizard, *A primer on elliptic functions with applications in classical mechanics*, *European journal of physics* **30** (2009) 729.

[843] C. Eröncel, R. Sato, G. Servant and P. Sørensen to appear.

[844] I. S. Gradshteyn, I. M. Ryzhik, D. Zwillinger and V. Moll, *Table of integrals, series, and products; 8th ed.* Academic Press, Amsterdam, Sep, 2014, 0123849330.

[845] H. Goldstein, C. Poole and J. Safko, *Classical mechanics addison-wesley*, *Reading, MA* **426** (1980) .